frontiers | Research Topics

Differences in shale oil and gas reservoirs across various sedimentary environments: theories and applications, volume II

Edited by
Hu Li, Peng Tan and Ahmed E. Radwan

Published in
Frontiers in Earth Science

ISSN 1664-8714
ISBN 978-2-8325-6299-4
DOI 10.3389/978-2-8325-6299-4

About Frontiers

Frontiers is more than just an open access publisher of scholarly articles: it is a pioneering approach to the world of academia, radically improving the way scholarly research is managed. The grand vision of Frontiers is a world where all people have an equal opportunity to seek, share and generate knowledge. Frontiers provides immediate and permanent online open access to all its publications, but this alone is not enough to realize our grand goals.

Frontiers journal series

The Frontiers journal series is a multi-tier and interdisciplinary set of open-access, online journals, promising a paradigm shift from the current review, selection and dissemination processes in academic publishing. All Frontiers journals are driven by researchers for researchers; therefore, they constitute a service to the scholarly community. At the same time, the *Frontiers journal series* operates on a revolutionary invention, the tiered publishing system, initially addressing specific communities of scholars, and gradually climbing up to broader public understanding, thus serving the interests of the lay society, too.

Dedication to quality

Each Frontiers article is a landmark of the highest quality, thanks to genuinely collaborative interactions between authors and review editors, who include some of the world's best academicians. Research must be certified by peers before entering a stream of knowledge that may eventually reach the public - and shape society; therefore, Frontiers only applies the most rigorous and unbiased reviews. Frontiers revolutionizes research publishing by freely delivering the most outstanding research, evaluated with no bias from both the academic and social point of view. By applying the most advanced information technologies, Frontiers is catapulting scholarly publishing into a new generation.

What are Frontiers Research Topics?

Frontiers Research Topics are very popular trademarks of the *Frontiers journals series*: they are collections of at least ten articles, all centered on a particular subject. With their unique mix of varied contributions from Original Research to Review Articles, Frontiers Research Topics unify the most influential researchers, the latest key findings and historical advances in a hot research area.

Find out more on how to host your own Frontiers Research Topic or contribute to one as an author by contacting the Frontiers editorial office: frontiersin.org/about/contact

Differences in shale oil and gas reservoirs across various sedimentary environments: theories and applications, volume II

Topic editors

Hu Li — Sichuan University of Science and Engineering, China

Peng Tan — CNPC Engineering Technology R & D Company Limited, China

Ahmed E. Radwan — Jagiellonian University, Poland

Citation

Li, H., Tan, P., Radwan, A. E., eds. (2025). *Differences in shale oil and gas reservoirs across various sedimentary environments: theories and applications, volume II*. Lausanne: Frontiers Media SA. doi: 10.3389/978-2-8325-6299-4

Table of contents

frontiers | Frontiers in Earth Science

TYPE Editorial
PUBLISHED 22 April 2025
DOI 10.3389/feart.2025.1602806

OPEN ACCESS

EDITED AND REVIEWED BY:
David R. Lentz,
University of New Brunswick
Fredericton, Canada

*CORRESPONDENCE
Hu Li,
lihu860628@126.com,
lihu@suse.edu.cn

RECEIVED 30 March 2025
ACCEPTED 10 April 2025
PUBLISHED 22 April 2025

CITATION
Li H, Tan P, Radwan AE and Wang H (2025) Editorial: Differences in shale oil and gas reservoirs across various sedimentary environments: theories and applications, volume II.
Front. Earth Sci. 13:1602806.
doi: 10.3389/feart.2025.1602806

Editorial: Differences in shale oil and gas reservoirs across various sedimentary environments: theories and applications, volume II

Hu Li[1,2]*, Peng Tan[3], Ahmed E. Radwan[4] and Haijun Wang[1,2]

[1]School of Economics, Sichuan University of Science and Engineering, Yibin, China, [2]Sichuan Key Provincial Research Base of Intelligent Tourism, Sichuan University of Science and Engineering, Yibin, China, [3]CNPC Engineering Technology R & D Company Limited, Beijing, China, [4]Faculty of Geography and Geology, Institute of Geological Sciences, Jagiellonian University, Kraków, Poland

KEYWORDS

shale oil and gas, pore structure, multi-scale fracture, sedimentary environment, diagenesis

Editorial on the Research Topic
Editorial: Differences in shale oil and gas reservoirs across various sedimentary environments: theories and applications, volume II

1 Introduction

The success of the North American shale revolution has not only reshaped the global energy landscape but also driven a systematic paradigm shift in unconventional hydrocarbon exploration (Fan et al., 2020). As a major shale gas resource country, China has achieved commercial development in marine shale systems (such as the Ordovician Wufeng Formation and Silurian Longmaxi Formation), and in 2022, their shale gas production surpassed 24 billion cubic meters (Li, 2023; Li H. et al., 2024; Li et al., 2024b; Li et al., 2025a; He et al., 2025). Currently, exploration and development efforts are underway in new marine shale intervals (e.g., the Qiongzhusi and Wujiaping formations), continental shale intervals (e.g., the Qingshankou Formation in the Songliao Basin), and marine–continental transitional shales (e.g., the Shanxi Formation in the Ordos Basin) (Zhai et al., 2019; Chen et al., 2019; 2023; Feng et al., 2023; Yan et al., 2024). Breakthroughs in the exploration of continental shale in India's Cambay Basin and Jurassic marine–continental transitional shale in Saudi Arabia's Jafurah Basin further validate the resource potential of shale oil and gas in different depositional settings (Singh and Chakraborty, 2023; Madukwe et al., 2023). With the application of technologies such as pre-stack 3D seismic inversion, nano-CT pore characterization, and multi-stage fracturing in horizontal wells, research focus has shifted from macroscopic reservoir description to advanced topics including organic matter enrichment dynamics, evolution of nanometer-scale pore throats, and multiscale reservoir heterogeneity (Guo et al., 2019; Chen et al., 2022; Dang et al., 2022). Notably, shales deposited in different depositional facies exhibit systematic differences in organic matter type, diagenetic

processes, and preservation conditions, which directly affect the accuracy of sweet spot prediction models.

This research topic is organized precisely against this backdrop, aiming to compile the latest research findings and insights in this field, and comprises nine papers covering a wide range of themes and diverse depositional environments, with study areas including representative Chinese basins such as the Ordos, Bohai Bay, Sichuan, and Beibuwan basins. The following sections review each paper's research content, methodology, principal conclusions, and significance.

2 Paper reviews

2.1 Multiscale fracture patterns in tight sandstones and their impact on natural gas accumulation

In tight sandstones, the connectivity of multiscale natural fractures is critical for forming high-quality reservoirs and achieving sustained high hydrocarbon production. This study (Manuscript ID: 1,448,238), taking the Upper Paleozoic tight sandstones of the Ordos Basin as an example, quantitatively characterized fracture parameters across various scales and innovatively proposed a classification of four fracture network patterns: (i) high-density, multi-orientations (multi-scale fracture); (ii) moderate-high density and dual orientations (multi-scale fracture); (iii) moderate density and dual orientations (small-scale fracture); and (iv) low density and single orientation (small-scale fracture). The results show that fracture length, density, porosity, and connectivity exhibit clear regularities, and different network patterns have distinct effects on gas accumulation (Li et al., 2025a; Li et al., 2025b). In particular, high-density, multi-orientations fractures tend to compromise caprock integrity, while moderate-density, dual orientations small-scale fractures are more favorable for gas accumulation. This multiscale perspective deepens our understanding of the coupling between fracture systems and hydrocarbon enrichment, thereby providing a scientific basis for sweet spot selection and production enhancement in tight gas reservoirs (Liu et al., 2024a; Yin et al., 2024).

2.2 The influence of CO_2 on sandstone reservoirs under different fluid regimes

Mantle-derived CO_2, an important component of hydrothermal fluids, has traditionally been studied in open systems where its role in mineral dissolution is believed to improve reservoir properties. However, its adverse effects *via* carbonate cementation have often been overlooked. This study (Manuscript ID: 1,436,573), using a mantle-derived CO_2 gas reservoir in the Dongying Sag of the Bohai Bay Basin as a case, systematically investigates the mechanisms by which CO_2 affects sandstone reservoirs in both open and closed fluid environments. The results demonstrate that CO_2-enriched hydrothermal fluids actively participate in water-rock interactions, significantly influencing diagenetic evolution. In open environments, mantle-derived CO_2 promotes the dissolution of feldspar and carbonate minerals, facilitates the timely removal of dissolution products (e.g., clays), and inhibits new carbonate cementation, thereby enhancing porosity and permeability. In contrast, in closed systems, as depth increases and CO_2 concentration decreases, the dissolution effect weakens while carbonate cementation intensifies, resulting in reduced porosity and permeability. This study corrects the one-sided view derived solely from open-system experiments and emphasizes the dual (both positive and negative) impact of CO_2 on reservoir properties. The findings enrich our theoretical understanding of CO_2–rock diagenetic interactions in sedimentary basins and provide practical guidance for evaluating reservoirs in CO_2-active areas, facilitating the identification of sweet spots with favorable properties.

2.3 Enrichment characteristics and genesis of key elements in coals

The discovery of co-associated valuable metals in coal and their genetic mechanisms represents a cutting-edge topic in sedimentary environmental research. This study conducted mineralogical and geochemical tests on coal samples from seven typical mines in the Late Permian coalfields of northeastern Guizhou (Manuscript ID: 1,520,502). It reveals the anomalous enrichment and mineralization mechanisms of key elements such as niobium (Nb), tantalum (Ta), zirconium (Zr), hafnium (Hf), rare earth elements (REE), and yttrium (Y). The results show significant variations in elemental composition and abundance among different mines and coal seams, with key elements preferentially concentrated in the clay-rich layers interbedded with coal. The enrichment types and abundance differences are mainly controlled by terrigenous detrital input, depositional conditions, seawater influence, and hydrothermal fluid activity. This study not only elucidates the enrichment patterns and genesis of key rare metals in coal-bearing strata, but also provides valuable insights for the comprehensive recovery of strategic metals from coal and the expansion of unconventional mineral resources.

2.4 Machine learning-driven lithology identification in complex reservoirs

Accurate lithology identification is crucial for selecting exploration targets, evaluating reservoirs, and optimizing development strategies in complex reservoirs. However, the limited availability of core data introduces uncertainties when relying solely on conventional well logs. Recently, machine learning techniques have been introduced to enhance lithology prediction accuracy. This study (Manuscript ID: 1,491,334), using the Niuxintuo block in the Liaohe Oilfield as an example, evaluated the applicability of five algorithms, which are Bayesian discriminant analysis, Random Forest (RF), Support Vector Machine (SVM), Back-Propagation Neural Network (BPNN), and Convolutional Neural Network (CNN), for lithology identification in complex reservoirs. The results indicate that all models, except the Bayesian classifier, achieved prediction accuracies above 85%, with the SVM model performing exceptionally well, attaining an accuracy of 93%. Moreover, the optimized SVM model was successfully applied to predict lithology in blind wells, demonstrating its strong generalizability. These findings confirm that machine learning approaches based on

well log data can significantly enhance lithology identification accuracy, providing new tools for reservoir characterization and modeling, predicting residual oil distribution, and guiding further exploration (Liu Z. D. et al., 2024).

2.5 Characteristics and main controlling factors of mudstone reservoirs

This study examines the mudstone reservoir of the first Member of the Maokou Formation in the southeastern Sichuan Basin (Manuscript ID: 1,494,518). By integrating outcrop observations, core descriptions, thin-section analysis, scanning electron microscopy (SEM), X-ray diffraction (XRD) testing, total organic carbon (TOC) measurements, low-temperature nitrogen adsorption and well log data, the research comprehensively analyzes the reservoir characteristics and controlling factors of the mudstones. The results indicate that mudstones with high TOC content and superior porosity represent the best reservoir rock type, and their formation is jointly promoted by organic enrichment and clay diagenesis. This work not only deepens our geological understanding of tight mudstone reservoirs in southeastern Sichuan, but also enriches diagenetic models for marine carbonate unconventional reservoirs (Shan et al., 2022).

2.6 A fine interpretation method for tight reservoirs based on core analysis and imaging well logs

Addressing the limitations of conventional well log interpretation, which often fails to accurately delineate productive intervals in tight carbonate reservoirs (with porosities of only 2%–6% and permeabilities less than 2 mD) in Lower Paleozoic Ordovician marine carbonates at the eastern margin of the Ordos Basin. This study proposes an integrated method combining core experimental analysis with imaging well logs (Manuscript ID: 1,534,598). The methodology involves: (i) detailed lithofacies classification using XRD analysis of core samples; (ii) comprehensive evaluation of pore types and permeability using electrical imaging logs and multi-array sonic logs; and (iii) calculation of gas saturation using a modified Archie equation with a variable cementation exponent. This approach significantly overcomes the limitations of conventional well log interpretation in tight reservoirs, improves the accuracy of fluid identification, and offers a new pathway for the quantitative evaluation of complex unconventional reservoirs. Practically, it aids in identifying sweet spot intervals and increasing drilling success rates.

2.7 Controls of sedimentation, diagenesis, and geochemistry on lacustrine shale reservoir characteristics

Taking the Qianfoya Formation in the Langzhong–Yuanba area of the northeastern Sichuan Basin as a case study, this study employs comprehensive sedimentological, geochemical, and rock-physical analyses of core samples to identify three main depositional facies, and each corresponding to different depositional energy environments (Manuscript ID: 1,499,533). The findings reveal that the laminated, clay-rich shales in a semi-deep lacustrine setting exhibit the best reservoir properties, characterized by high TOC and a pore structure dominated by silt intergranular pores, clay interlayer pores, intra-pyrite pores, and microfractures; in contrast, the organic pores typical of marine shales are not the primary storage space in this lacustrine system. The primary controlling factors include the synergistic interaction between organic matter and clay minerals, the depositional environment, and diagenetic processes. This study systematically elucidates the formation mechanisms of lacustrine shale reservoirs, highlighting significant differences in reservoir quality between lacustrine and marine shales, and offers important insights for the exploration of similar continental shale gas plays worldwide.

2.8 Formation processes and controlling factors of tight buried-basement hill reservoirs

In stable cratonic basins, hydrocarbon reservoirs hosted in buried basement hills typically form after the basement structure is established and before overlying sediments are deposited. This study (Manuscript ID: 1,552,826), using a buried hill in the Weixinan Depression of the northern Beibu Gulf Basin as a case, employs balanced section restoration and paleo stress field analysis to reconstruct the tectonic evolution and burial history of the hill, and to analyze the main factors controlling reservoir development. In carbonate basement hills, the combined effect of multistage tectonic stresses and karstification forms a tight reservoir system dominated by dissolution pores and tectonic fractures, primarily distributed along lateral underflow zones on the hill flanks; in contrast, in granite or metamorphic basement hills, tectonic stresses and karstification remain the primary controls, with pore–fracture reservoirs mainly developing in weathered, leached zones at the hilltops. This study clarifies the entire process from tectonic evolution to reservoir formation in buried basement hills, deepening our understanding of unconventional hydrocarbon accumulation in cratonic basins, and provides strong guidance for seismic interpretation and sweet spot selection in similar deep target areas.

2.9 Characterization and exploration implications of marine shale reservoirs

Taking the Upper Permian Wujiaping Formation marine shales in the Longmen–Wushankan area of the eastern Sichuan Basin as an example, this study comprehensively characterizes the key reservoir properties by integrating well rock electrical properties, TOC, porosity, brittle mineral content, and sedimentary-structural analyses (Manuscript ID: 1,453,098). The results indicate that the high natural gas productivity in the Wujiaping shales is primarily attributed to favorable depositional environments, excellent pore conditions, an optimal combination of cap and floor rocks, and a robust fracturing response. However, compared with the Wufeng–Longmaxi shales, the Wujiaping shales exhibit

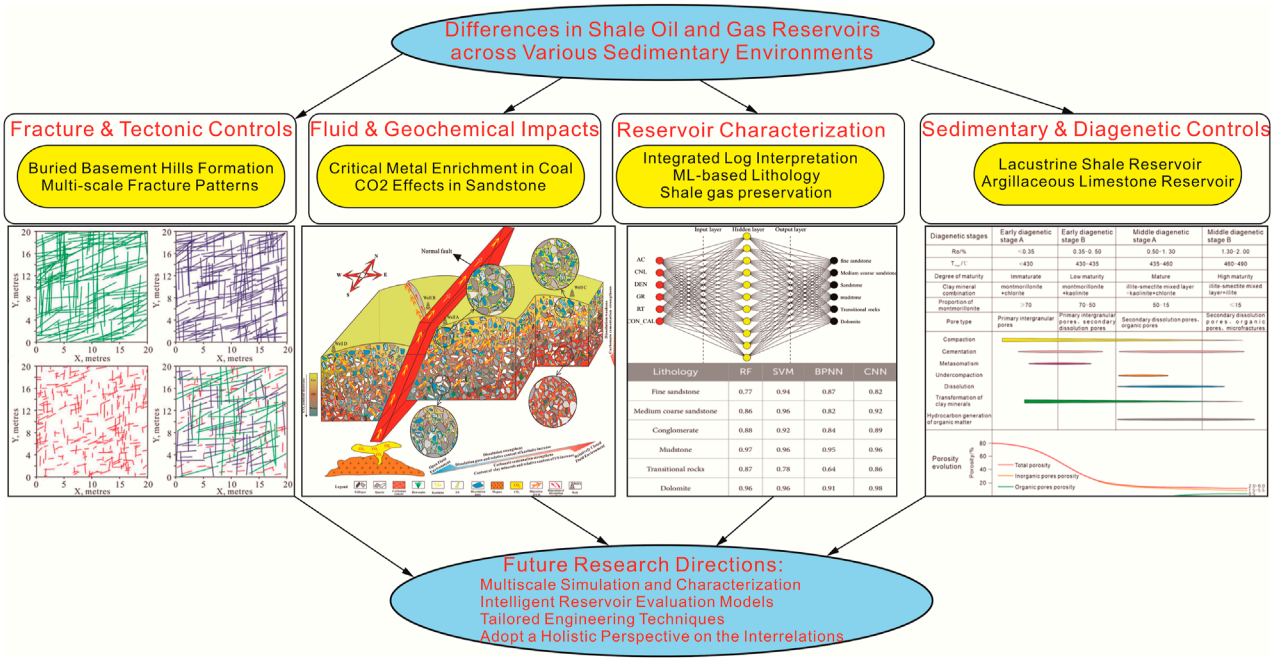

FIGURE 1
The main content of the papers published in this rsearch topic.

lower porosity, thinner single shale intervals, and greater burial depths, which pose additional challenges for development. Based on a multi-parameter evaluation, the study establishes a set of criteria for assessing Wujiaping shale gas potential and identifies four favorable exploration zones within the study area. These findings provide both theoretical and practical guidance for future marine shale gas development, contributing to more rational development strategies and optimized well placement.

3 Conclusions and outlook

The majority of the papers in this Research Topic have demonstrated the latest advances in understanding the geological characteristics and accumulation mechanisms of unconventional hydrocarbon reservoirs formed in diverse depositional environments. Overall, these studies reveal several common insights (Figure 1).

3.1 Multiscale geological controls on reservoir characteristics

Whether through pore–fracture structures, diagenetic environments, sedimentary sequences, or tectonic evolution, geological factors across different scales collectively influence hydrocarbon accumulation and preservation (Li et al., 2022a; Liu et al., 2025). Hence, research on unconventional reservoirs should adopt a multi-scale, integrated approach to fully reveal their accumulation mechanisms.

3.2 Depositional environment variability shapes reservoir diversity

Reservoirs formed in marine, continental, and transitional settings exhibit systematic differences in organic matter type, mineral composition, pore structure, and fluid occurrence. For example, lacustrine shales differ markedly from marine shales in their primary storage spaces, and the evolution pathways of reservoir porosity in open *versus* closed systems are distinct. Therefore, it is crucial to consider depositional environment characteristics when devising effective exploration and development strategies.

3.3 Advanced technologies support unconventional reservoir evaluation

Faced with the limitations of conventional methods for characterizing complex reservoirs, an increasing number of studies have introduced innovative techniques, such as machine learning for well log lithology identification, integrated analysis of geological and geophysical data, and geochemical tracers for microscale diagenetic process investigation, that significantly enhance our understanding and predictive accuracy, providing robust tools for quantitative reservoir evaluation.

3.4 Importance of reservoir identification and quantitative control factors

Several studies have quantitatively delineated the controlling factors of reservoirs, for example, the impact of fracture network

patterns on productivity, the enrichment conditions of key metals in coals, diagenetic influences on carbonate reservoir quality, and tectonic–karst controls on buried hill reservoirs. These efforts provide a scientific basis for predicting favorable reservoir zones and guiding engineering improvements, which are key to increasing exploration success rates.

Looking ahead, although significant progress has been made in unconventional oil and gas, particularly in shale gas, many scientific challenges remain. Firstly, it is essential to strengthen multiscale simulation and characterization studies from nanoscale pore throats to basin-scale structures, and to develop integrated modeling techniques to elucidate the coupling among pore evolution, fracture propagation, and hydrocarbon migration (Li et al., 2022b; Xu et al., 2025). Secondly, with the widespread application of machine learning and big data in geosciences, constructing robust and universally applicable intelligent reservoir evaluation models resilient to complex geological scenarios has become an inevitable trend; this requires the integration of various data types (e.g., 3D seismic, production dynamics) and the optimization of algorithm integration. Thirdly, in terms of unconventional reservoir stimulation and enhanced recovery, future efforts should focus on developing tailored engineering techniques and enhanced oil recovery (EOR) methods that address the microscale differences among various reservoir types (e.g., tight sandstones, mudstones, shales, coalbed methane, basement reservoirs). Finally, against the backdrop of the global energy transition, coordinated assessments of unconventional oil and gas alongside other resources, such as critical metals, geothermal energy, and carbon storage potential, may emerge as new research hotspots, requiring geoscientists to adopt a holistic perspective on the interrelations among various resources within sedimentary basins.

In summary, comparing the formation and differences of hydrocarbon reservoirs across various depositional environments not only deepens our overall understanding of unconventional hydrocarbon accumulation but also provides valuable lessons for global exploration. The research outcomes in this Research Topic demonstrate the latest progress and diversified exploration approaches in this field, and we look forward to more interdisciplinary, multiscale studies that continuously refine shale oil and gas geological theories and drive efficient development and sustained innovation of unconventional resources.

Author contributions

HL: Conceptualization, Formal Analysis, Funding acquisition, Project administration, Writing – original draft, Writing – review and editing. PT: Data curation, Formal Analysis, Investigation, Methodology, Writing – review and editing. AR: Conceptualization, Formal Analysis, Methodology, Writing – review and editing. HW: Formal Analysis, Funding acquisition, Methodology, Writing – review and editing.

Funding

The author(s) declare that financial support was received for the research and/or publication of this article. This study was financially supported by the Sichuan Key Provincial Research Base of Intelligent Tourism, Sichuan University of Science and Engineering (No. ZHYR24-05), the Open Fund of the National Key Laboratory of Oil and Gas Reservoir Geology and Exploitation (Southwest Petroleum University) (No. PLN 2023-31), the Open Funds of the Shale Gas Evaluation and Exploitation Key Laboratory of Sichuan Province (No. YSK2023001).

Conflict of interest

Author PT was employed by CNPC Engineering Technology R & D Company Limited.

The remaining authors declare that the research was conducted in the absence of any commercial or financial relationships that could be construed as a potential conflict of interest.

The author(s) declared that they were an editorial board member of Frontiers, at the time of submission. This had no impact on the peer review process and the final decision.

Generative AI statement

The author(s) declare that no Generative AI was used in the creation of this manuscript.

Publisher's note

References

Chen, Y., Yang, K., Wu, W., Yang, Y., Yang, X., and Ma, K. (2023). Favorable lithofacies and pore characteristics of the Permian Longtan formation shale in the southern Sichuan Basin. *Energy Geosci.* 4 (3), 100193. doi:10.1016/j.engeos.2023.100193

Chen, Y. H., Zhu, Z. W., and Zhang, L. (2019). Control actions of sedimentary environments and sedimentation rates on lacustrine oil shale distribution, an example of the oil shale in the Upper Triassic Yanchang Formation, southeastern Ordos Basin (NW China). *Mar. Petrol. Geol.* 102, 508–520. doi:10.1016/j.marpetgeo.2019.01.006

Chen, Z. P., Liao, Y., Li, L., Chen, L., Wang, P., Zuo, Y., et al. (2022). Implication of alkane carbon and hydrogen isotopes for genesis and accumulation of over-mature shale gas: a case study of Longmaxi Formation shale gas in Upper Yangtze area. *Front. Earth Sci.* 10, 901989. doi:10.3389/feart.2022.901989

Dang, W., Nie, H. K., Zhang, J. C., Tang, X., Jiang, S., Wei, X., et al. (2022). Pore-scale mechanisms and characterization of light oil storage in shale nanopores: new method and insights. *Geosci. Front.* 13 (5), 101424. doi:10.1016/j.gsf.2022.101424

Fan, C. H., Li, H., Qin, Q. R., He, S., and Zhong, C. (2020). Geological conditions and exploration potential of shale gas reservoir in Wufeng and Longmaxi Formation of southeastern Sichuan Basin, China. *J. Petrol. Sci. Eng.*, 191, 107138. doi:10.1016/j.petrol.2020.107138

Feng, W., Li, R., Zhao, Z., Yu, Q., Liu, W., and Cao, J. (2023). Geological characterization and exploration potential of shale gas in the Carboniferous Jiusi Formation, northern Guizhou and Yunnan provinces, SW China. *Energy Geosci.* 4 (3), 100177. doi:10.1016/j.engeos.2023.100177

Guo, X. B., Huang, Z. L., Zhao, L. B., Han, W., Ding, C., Sun, X., et al. (2019). Pore structure and multi-fractal analysis of tight sandstone using MIP, NMR and NMRC methods: a case study from the Kuqa depression, China. *J. Petrol. Sci. Eng.* 178, 544–558. doi:10.1016/j.petrol.2019.03.069

He, S., Tan, W. C., Li, H., Li, H., Wang, Y., Niu, P. F., et al. (2025). Mineralogical and lithofacies controls on gas storage mechanisms in organic-rich marine shales. *Energy Fuel* 39 (8), 3846–3858. doi:10.1021/acs.energyfuels.4c05685

Li, H. (2023). Advancing "Carbon Peak" and "Carbon Neutrality" in China: a comprehensive review of current global research on carbon capture, utilization, and storage technology and its implications. *ACS Omega* 8 (45), 42086–42101. doi:10.1021/acsomega.3c06422

Li, H., Duan, H. T., Qin, Q. R., Zhao, T. B., Fan, C. H., and Luo, J. (2025b). Characteristics and distribution of tectonic fracture networks in low permeability conglomerate reservoirs. *Sci. Rep.* 15, 5914. doi:10.1038/s41598-025-90458-6

Li, H., He, S., Radwand, A. E., Xie, J. T., and Qin, Q. R. (2024a). Quantitative analysis of pore complexity in lacustrine organic-rich shale and comparison to marine shale: insights from experimental tests and fractal theory. *Energy Fuel* 38 (17), 16171–16188. doi:10.1021/acs.energyfuels.4c03095

Li, J., Li, H., Jiang, W., Cai, M. L., He, J., Wang, Q., et al. (2024b). Shale pore characteristics and their impact on the gas-bearing properties of the Longmaxi Formation in the Luzhou area. *Sci. Rep.* 14, 16896. doi:10.1038/s41598-024-66759-7

Li, J., Li, H., Xu, J. L., Wu, Y. J., and Gao, Z. (2022a). Effects of fracture formation stage on shale gas preservation conditions and enrichment in complex structural areas in the southern Sichuan Basin, China. *Front. Earth Sci.* 10, 921988. doi:10.3389/feart.2022.921988

Li, J., Qin, Q. R., Li, H., and Wan, Y. F. (2022b). Numerical simulation of the stress field and faultsealing of complex fault combinations in Changningarea, Southern Sichuan Basin, China. *Energy Sci. Eng.* 10, 278–291. doi:10.1002/ese3.1044

Li, J., Zhang, Q., Jiang, W., Li, H., Li, L., Xue, T. F., et al. (2025a). Lithological controls on pore structure and their implications for deep shale gas reservoir quality in the Longmaxi Formation, Luzhou area, Southern Sichuan Basin, China. *Energy Fuel* 39 (3), 1541–1558. doi:10.1021/acs.energyfuels.4c05247

Liu, J. F., He, X., Xue, F. J., Dai, J. J., Yang, J. X., Huang, H. Y., et al. (2024a). The influence of natural fractures of multi-feature combination on seepage behavior in shale reservoirs. *J. Min. Strata Control Eng.* 6 (1), 131–140. doi:10.13532/j.jmsce.cn10-1638/td.20240018.001

Liu, J. F., Zhao, C. X., Dai, H. Y., Wei, J. B., and Yang, J. X. (2025). Experimental study on shale fault instability and reactivation induced by fluid injection. *J. Min. Strata Control Eng.* 7 (1), 53–66. doi:10.13532/j.jmsce.cn10-1638/td.2024-1387

Liu, Z. D., Yang, B. R., Tang, X. Y., Wang, W., Ji, L., and Jiang, Z. H. (2024b). Evaluating the fracture resistance and drainage difficulty of coal reservoirs using log data. *Appl. Geophys.* 21 (2), 265–278. doi:10.1007/s11770-021-0961-8

Madukwe, H. Y., Adegoke, A. K., Adeleye, M. A., and Aturamu, A. O. (2023). Paleo-productivity and petroleum source evaluation of the Nkporo and Awgu shales, lower Benue trough, Nigeria: insight from inorganic geochemistry. *Energy Geosci.* 4 (3), 100161. doi:10.1016/j.engeos.2023.100161

Shan, C., Ye, C., Zhang, Z., Zou, C., He, F., Zhang, H., et al. (2022). Reservoir characteristics and resource potential analysis of transitional shale gas in Southern Sichuan Basin. *Front. Earth Sci.* 10, 909469. doi:10.3389/feart.2022.909469

Singh, A. K., and Chakraborty, P. P. (2023). Geochemistry and hydrocarbon source rock potential of shales from the Palaeo-Mesoproterozoic Vindhyan Supergroup, central India. *Energy Geosci.* 4 (3), 100073. doi:10.1016/j.engeos.2021.10.007

Xu, X. Y., Hu, B., Dong, C. W., Zhang, H. J., and Li, H. Y. (2025). Fractional-order creep model of carbonaceous shale considering age damage. *J. Min. Strata Control Eng.* 7 (1), 145–156. doi:10.13532/j.jmsce.cn10-1638/td.2024-1233

Yan, W., Wang, C., Yin, S., Wen, Z., Zheng, J., Fu, X., et al. (2024). A log-based method for fine-scale evaluation of lithofacies and its applications to the Gulong shale in the Songliao Basin, Northeast China. *Energy Geosci.* 5 (3), 100291. doi:10.1016/j.engeos.2024.100291

Yin, S., Radwan, A. E., Xiao, F., Xie, G. C., and Lai, P. F. (2024). Developmental characteristics of vertical natural fracture in low-permeability oil sandstones and its influence on hydraulic fracture propagation. *Geomech. Geophys. Geo-Energy Geo-Res.* 10 (1), 165. doi:10.1007/s40948-024-00889-0

Zhai, G. Y., Li, J., Jiao, Y., Wang, Y., Liu, G., Xu, Q., et al. (2019). Applications of chemostratigraphy in a characterization of shale gas sedimentary microfacies and predictions of sweet spots -taking the Cambrian black shales in Western Hubei as an example. *Mar. Petrol. Geol.* 109, 547–560. doi:10.1016/j.marpetgeo.2019.06.045

frontiers | Frontiers in Earth Science

TYPE Original Research
PUBLISHED 13 August 2024
DOI 10.3389/feart.2024.1448238

OPEN ACCESS

EDITED BY
Hu Li,
Sichuan University of Science & Engineering, China

REVIEWED BY
Guoping Liu,
Peking University, China
Hongsheng Wang,
The University of Texas at Austin, United States

*CORRESPONDENCE
Lei Gong,
kcgonglei@foxmail.com
Shuai Gao,
349684871@qq.com

RECEIVED 13 June 2024
ACCEPTED 29 July 2024
PUBLISHED 13 August 2024

CITATION
Wang J, Wang J, Zhang Y, Zhang D, Sun L, Luo J, Wang W, Gong L, Liu Z and Gao S (2024) Multi-scale fracture patterns and their effects on gas enrichment in tight sandstones: a case study of the Upper Paleozoic in the Qingshimao gas field, Ordos Basin, China. *Front. Earth Sci.* 12:1448238. doi: 10.3389/feart.2024.1448238

Multi-scale fracture patterns and their effects on gas enrichment in tight sandstones: a case study of the Upper Paleozoic in the Qingshimao gas field, Ordos Basin, China

Jie Wang[1], Jiping Wang[2,3], Yuanyuan Zhang[2,3], Daofeng Zhang[2,3], Lei Sun[2,3], Jianning Luo[2,3], Wei Wang[2,3], Lei Gong[1,4]*, Zongbao Liu[1] and Shuai Gao[1,4]*

[1]College of Geosciences, Northeast Petroleum University, Daqing, China, [2]Exploration and Development Research Institute of China Petroleum Changqing Oilfield Company, Xi'an, China, [3]National Engineering Laboratory for Exploration and Development of Low Permeability Oil and Gas Fields, Xi'an, China, [4]Bohai-Rim Energy Research Institute, Northeast Petroleum University, Qinhuangdao, China

A well-connected network formed by multi-scale fractures is a key factor in the formation of high-quality reservoirs and the achievement of high and stable oil and gas production in tight sandstones. Taking the Upper Paleozoic of the Qingshimao gas field in the Ordos Basin, China, as an example, based on data from image logs, cores, and thin sections, fine quantitative characterization of multi-scale natural fractures in tight sandstone reservoirs was carried out. We also established a method for dividing network patterns of multi-scale fractures and discussed the effect of each fracture network pattern on the gas enrichment and production capacity. Results indicate regular changes in the length, density, aperture, porosity, permeability, and connectivity of natural fractures at different scales. Based on the spatial combination patterns and connectivity of fractures of different scales, four types of fracture network patterns were established: multi-scale fracture network with high density and multi-orientations, multi-scale fracture network with moderate-high density and dual orientations, small-scale fracture network with moderate density and dual orientations, small-scale fracture network with low density and single orientation. The first fracture network pattern can destroy the integrity of the cap layer, causing natural gas leakage. The second fracture network pattern is a favorable area for natural gas enrichment. The third fracture network pattern requires the use of hydraulic fracturing to obtain commercial airflow. The fourth fracture network pattern has little effect on reservoir control and storage. The study of natural fractures in tight sandstone reservoirs is usually based on a single-scale perspective. Understanding the development characteristics of multi-scale fractures and their controlling effects on the reservoir helps to

comprehensively understand the spatial configuration relationship of multi-scale fracture network structure patterns and promotes the development of multi-scale fractures in tight reservoir research.

KEYWORDS

Qingshimao gas field, tight sandstone, multi-scale fractures, fracture network pattern, gas enrichment

1 Introduction

Tight sandstone gas has become one of the essential fields for global unconventional natural gas exploration and development (Farouk et al., 2024). According to statistics from the Federal Geological Survey of the United States, approximately 70 tight gas basins have been discovered or speculated to develop globally, with tight gas resources of approximately 310 × 10^{12}m^3-510 × 10^{12}m^3 (German et al., 2023; Jia et al., 2012). As of the end of 2023, the cumulative proven reserves of the Upper Paleozoic in the Qingshimao area were 1,459 × 10^8 m^3, demonstrating good exploration prospects (He et al., 2021). The preliminary exploration results have confirmed that natural fractures are the key factor for obtaining high gas flow in the tight sandstone reservoir (Balsamo et al., 2023; Vásquez Serrano et al., 2024).

Natural fractures are not only effective storage spaces for tight sandstone reservoirs, but also essential seepage channels (Ortega et al., 2006; Gale et al., 2007; Gale et al., 2014; Gong et al., 2021b; Gong et al., 2023a; Zeng et al., 2024). Numerous studies by scholars have shown that the development of natural fractures exhibits multi-scale distribution characteristics (Guerriero et al., 2011; Micheal et al., 2021; Sweeney M R, 2023). They can quantitatively characterize fracture parameters at different scales based on observation methods or data such as nano CT, scanning electron microscopy, microscopic thin sections, core observation, logging interpretation, field outcrops, and drone photography (Loza Espejel et al., 2020; Birkholzer et al., 2021). The parameter characterization of fractures of different scales can span multiple orders of magnitude, and scholars have also studied different scales of fractures based on their own research purposes (Ortega et al., 2006; Strijker et al., 2012). The multi-scale natural fracture system not only communicates various pores and enhances the reservoir's permeability, but also is a key factor affecting the high production of tight sandstone reservoirs (Gong L. et al., 2019; Birkholzer et al., 2021; Nwabia and Leung, 2021; Sweeney et al., 2023). Fractures of different scales have different lengths and openings, resulting in varying degrees of connectivity and significant differences in their contributions to tight sandstone reservoirs (Bertrand et al., 2015; Laubach et al., 2018; Prabhakaran et al., 2021). The configuration combination and spatial distribution pattern of fractures of different scales are the key to determining whether an effective continuous reservoir can be formed (Fu J. H. et al., 2022; Fu X. F. et al., 2022; Sweeney M R, 2023). The degree of development, porosity, and permeability of fractures at different scales vary to some extent, but they have a positive effect on productivity (Watkins et al., 2018; Aubert et al., 2021; Cao et al., 2024). In other words, there is a positive correlation between the development degree of the multi-scale natural fractures and production capacity. The higher the development degree of the multi-scale natural fractures, the higher the production capacity of the oil and gas wells (Bagni et al., 2020; Fu et al., 2023; Zeng et al., 2023).

However, with the deepening of exploration and development of tight sandstone gas reservoirs, the contradiction between the fracture development degree and natural gas production capacity has become increasingly prominent, that is, there may not necessarily be a positive correlation between the fracture intensity and production capacity (Gong Lei. et al., 2019). Part of the reason for this contradiction is that there are scale differences in the sources of obtaining fracture strength data, resulting in poor comparability of fracture strength across different wells. At the same time, the differences in connectivity and contribution to reservoir properties of fractures of different scales were also ignored, exposing the problem of unclear understanding of the development characteristics and spatial configuration patterns of multi-scale fractures in tight sandstone reservoirs (Zeng et al., 2022). The fracture development degree is not the only factor determining the high and stable production of a single well. Previous studies on multi-scale fractures have been limited, and currently only targeted research has been conducted on fractures of a certain scale, lacking evaluation of the development characteristics of fractures at multiple scales. (Watkins et al., 2015; Casini et al., 2016; Fernández-Ibáñez et al., 2018; Prabhakaran et al., 2021). Meanwhile, the role of multi-scale fracture development characteristics in reservoir control and storage also needs to be studied. As a typical tight sandstone gas development area in China, the Qingshi Mao gas field also faces such problems.

Therefore, taking the Upper Paleozoic tight sandstone reservoir of the Qingshimao gas field in Ordos Basin as an example, we quantitatively characterized the genesis types and distribution characteristics of multi-scale fractures, clarified the distribution mode of multi-scale fractures and their contributions to the reservoir, established the fracture network pattern of the Qingshimao gas field, and discussed the fracture development characteristics of each fracture network pattern and their controlling effect on gas accumulation.

2 Geological setting

The Qingshimao gas field is located in the western part of the Ordos Basin in China (Figure 1A). Structurally, it is situated on the southern wing of the central uplift of the Tianhuan Depression in the Ordos Basin and is in contact with the Majiatan Fault on the west side (Figure 1B). The Majiatan Fault is mainly characterized by a Y-shaped reverse thrust and detachment, exhibiting an overall SN-oriented asymmetric syncline shape with obvious north-south segmentation and east-west zoning (Guo et al., 2020). The

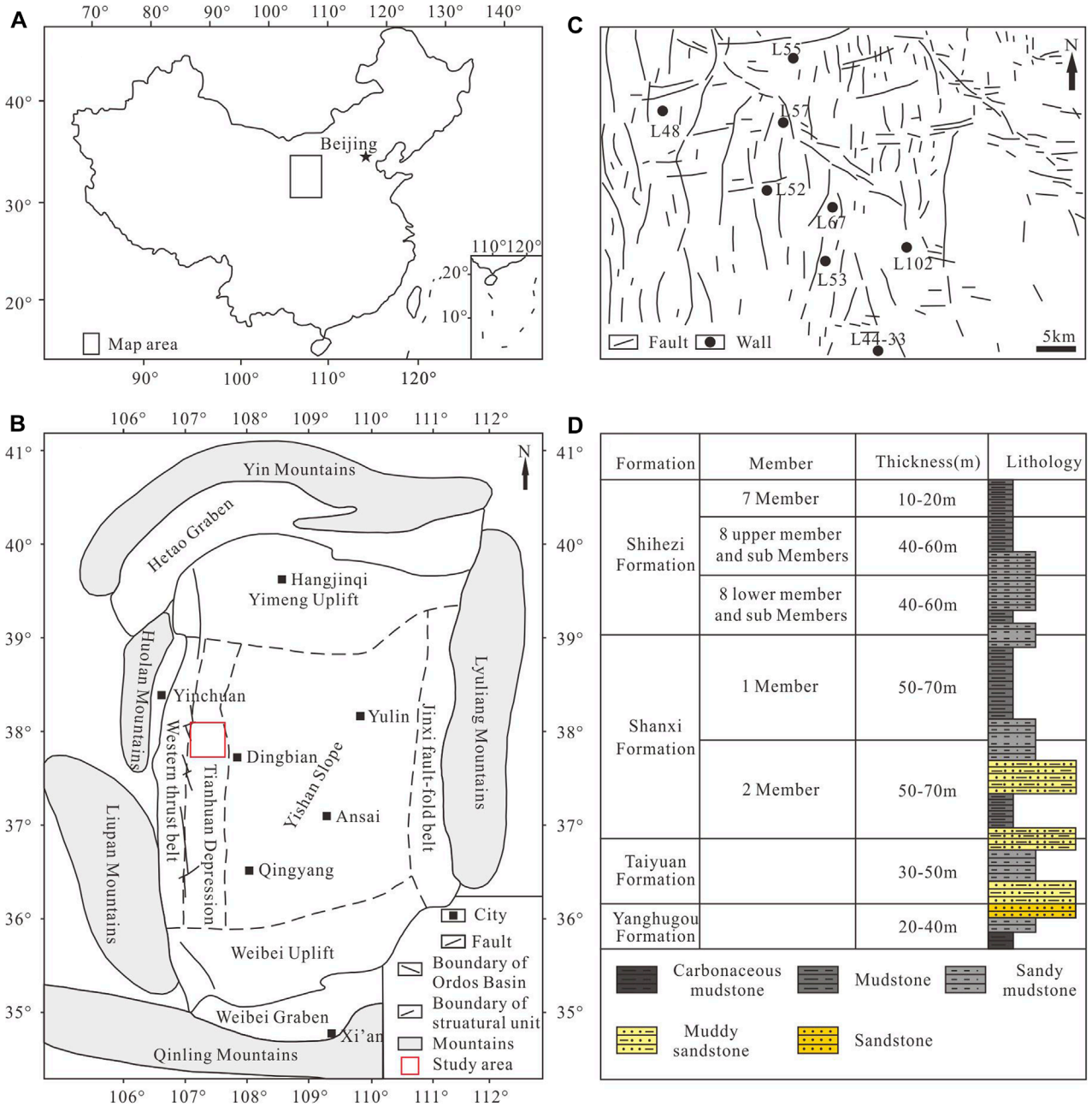

FIGURE 1
Location, structural outline, and stratigraphic overview of the Qingshimao gas field. **(A)** The location of the Ordos Basin. **(B)** The location of the Qingshimao gas field. **(C)** Overview of the Structure of Qingshimao Gas Field **(D)** Overview of the Strata of Qingshimao Gas Field.

overall structural morphology of the research area is high in the north and low in the south, with a northwest-southeast trending nose-shaped uplift. Three northwest southeast trending faults are developed on the nose uplift belt, and nearly north-south trending secondary faults are developed in the south and east (Yin et al., 2022) (Figure 1C).

The strata in the Qingshimao area are tight sandstone reservoirs, with the Carboniferous Benxi Formation, Permian Taiyuan Formation, Shanxi Formation, Lower Shihezi Formation, Upper Shihezi Formation, and Shiqianfeng Formation developed from bottom to top (Figure 1D). The internal sedimentation is continuous, all of which are integrated contacts, mainly composed of transitional facies between sea and land and inland lake basin sedimentation. The main gas-bearing intervals are the He 8 section of the Permian Shihezi Formation, the Shan 1 and Shan 2 sections of the Shanxi Formation, and the Taiyuan Formation. The thickness of the Upper Paleozoic strata is relatively stable in this area, with a total sedimentary rock thickness of about 700 m and minimal planar variation (Jiang et al., 2023). Its lithology is mainly composed of tight sandstone, with the main rock types being siltstone, fine sandstone,

quartz sandstone, and interbedded mud and sand. The Taiyuan and Shanxi formations of the Permian are mainly sedimentary coal-bearing strata, the main source rocks of the Upper Paleozoic. The physical properties of the reservoir in the typical well of tight sandstone in the Qingshimao gas field are different, with porosity distribution ranging from 5% to 11%, with an average of 7.9%. The permeability distribution is between 0.1 and 4.2mD, with an average of 0.36mD. The differences in the physical properties of sandstone reservoirs may be related to the quartz content and cement types in different regions, with higher quartz content areas having better reservoir properties (Wang et al., 2022; Su et al., 2023).

3 Method

3.1 Materials and samples

We use image logs data from 36 wells to identify natural fractures and quantitatively characterize parameters such as fracture occurrence (strikes and dip angles), density, and aperture. We observed and described 210 m core samples from 5 wells in the Qingshimao gas field (Figure 1C). We measured parameters such as the type, mechanical properties, dip angle, height, aperture, and filling degree of 1,320 fractures. At the same time, we selected characteristic wells from the distance of the fault and integrated their gas and water production data to analyze the reservoir control effect in the study area. The Zeiss Axio Image Z1 polarizing microscope was used to statistically analyze the fracture parameters (fracture type, filling degree, aperture, length) of 40 cast thin sections. According to the method proposed by Zeng et al. (2010), the aperture of fractures under formation-confining pressure conditions was corrected, and the porosity and permeability of fractures of different scales were calculated using the Monte Carlo method.

3.2 Characterization of fracture connectivity

Sanderson et al. (2018) proposed a topological representation method for fracture network patterns, which provides convenience for characterizing fracture connectivity. They divided the types of fracture nodes into isolated nodes (Type I), adjacent nodes (Type Y), and intersecting nodes (Type X), indicating that the degree of fracture connectivity has gradually improved. At the same time, they used the ratio of the number of branches to the number of fractures (NB/NL) and the number of nodes occupied by each fracture (CL) to characterize the connectivity of fractures (Balberg and Binenbaum, 1983; Berkowitz, 1995; Manzocchi, 2002; Sanderson and Nixon, 2015). A large number of real fracture network pattern statistics and numerical simulations confirm that the NB/NL values are distributed between 2–10, and the larger the NB/NL value, the better the connectivity. When CL < 2, it indicates that the fracture network is not connected. When CL > 3.57, the fracture network reaches a percolation state (Balberg et al., 1984; Nixon et al., 2012). Attila Petrik et al. (2023) improved and optimized the characterization of fracture connectivity based on the Sanderson topology using high-resolution image logs technology (Petrik et al., 2023). However, this method must be based on a definite fracture network graph. Since our study area can directly observe very few intersecting fractures on core and image logs, it is difficult to observe adjacent nodes (Y-shaped nodes) and intersecting nodes (X-shaped nodes). It is difficult for us to directly use Sanderson and Attila Petrik's methods to quantitatively characterize the connectivity of fractures in the study area. Ghosh and Mitra. (2009) and Gong et al., 2023a studied the factors affecting fracture connectivity and pointed out that fracture density, fracture orientation and sets, and fracture length are the main factors affecting fracture connectivity (Ghosh and Mitra, 2009; Gong et al., 2023a). We are inspired by this and propose a fracture connectivity prediction method based on considering these influencing factors. Firstly, the Monte Carlo random simulation method is used to create a fracture pattern with the actual fracture density, sets and orientation, fracture length, and other parameters in the study area as constraints. Then, Sanderson's method is used for connectivity characterization. The connectivity of the fractures in the study area can be equivalently calculated through dozens of simulations and characterisations.

4 Results

Based on the identification methods and scale of natural fractures, as well as the arrangement relationship between fractures and mechanical layers, natural fractures in tight sandstone in the study area can be divided into three types: large-scale fractures, small-scale fractures and micro-scale fractures. Large-scale fractures are manifested as throughgoing fractures and small faults, which generally cut through multiple rock mechanical units. Some small faults can cut through mudstone interbeds or throughgoings. Small-scale fractures are mainly manifested as bed-confined fractures (including intraformational fractures), which develop within a single rock mechanical layer and are mainly controlled by beddings and lithological interfaces. Micro-scale fractures are smaller in scale, generally less than 50 μm in aperture, and can only be identified under microscope.

4.1 Large-scale fractures

Three types of fractures, conductive, resistive and induced, were identified on image logs. Conductive fractures are characterized by dark sinusoidal curves, generally open fractures that are not filled with minerals. Resistive fractures are characterized by bright sinusoidal curves, typically natural fractures filled with calcite or quartz (Figures 2A,B). Induced fractures are usually caused by drilling tool disturbance or stress release, indicating the direction of the current maximum principal stress at present and thus indirectly used to evaluate the effectiveness of the fracture. Large-scale fractures exhibit dark (or bright) sinusoidal curves at medium to high dip-angles in image logs and have continuous and good penetrability (Figures 3A,B), with some showing apparent bedding plane displacement or small displacement on both sides of the fracture surface. On the core, it exhibits high dip-angle throughgoing fractures that cut through multiple rock mechanical layers (interfaces) (Figures 3C,D).

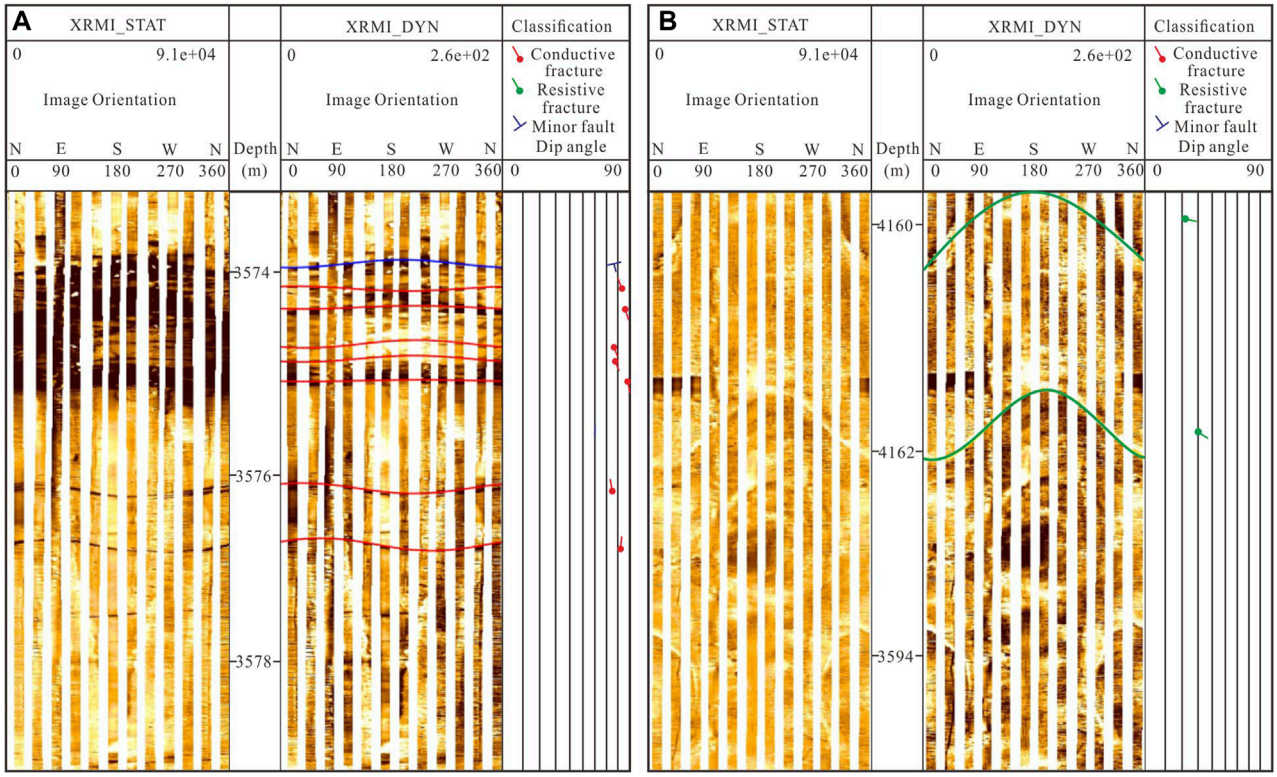

FIGURE 2
Types of image logs fractures in the study area. **(A)** The characteristics of high conductivity fractures and small faults were identified by image logs. **(B)** High resistance fracture characteristics identified by image logs.

The tight sandstone reservoir in the Qingshimao gas field mainly develops four sets of fractures: northeast-southwest, northwest-southeast, nearly north-south, and nearly east-west. Most of the wells mainly comprise two sets of fractures: northeast-southwest and nearly north-south. Some wells exhibit a single orientation, but the wells near the fault are greatly affected by the structure. The fracture orientation is relatively complex, with three to four sets of fractures developed. The inclination angle of large-scale fractures is mainly medium to high dip-angle, mainly distributed at 60°–90°, accounting for more than 85%, while a small number of low dip-angle fractures are developed (Figure 4). High conductivity fractures account for about 92% of the image logs fractures in large-scale fractures, and their effectiveness is good. Consistent with the observation results of the core. The density of fracture lines is distributed between 0.3–0.6 lines/m, with an average of 0.47 lines/m, and there are differences in fracture density among different wells. The aperture of large-scale fractures is mainly distributed between 55–180° μm. The average is 108 μm. According to the Monte Carlo method, the porosity and permeability of fractures were calculated, and it was found that the porosity of large-scale fractures is relatively low, mainly distributed in the range of 0.07%–0.15%, with an average of 0.10%. Its permeability is relatively high, with a main distribution range of 8-10mD and an average of 9.2mD.

A planar fracture connectivity network model was established based on the constraints of the fracture group and orientation, fracture scale, and fracture density mentioned above. Sanderson's fracture connectivity characterization method is used to characterize natural fractures in the tight sandstone reservoir of the Qingshimao gas field under this mode. Twenty simulations were conducted on large-scale fractures, and the simulation results showed that the proportion of isolated type nodes (Type I nodes) in the study area ranged from 34.6% to 47.2%, with an average of 40.9%; The proportion of adjacent nodes (Y-shaped nodes) is distributed between 3.5% and 18.4%, with an average of 10.3%; The proportion of intersecting nodes (X-shaped nodes) is distributed between 45.6% and 54.4%, with an average of 48.6%. The number of nodes (CL) for each fracture is mainly distributed between 3.35–5.84, with an average of 5.18, and the majority of them are greater than 3.27. In the IYX triangle diagram, the simulation results are generally located in the fracture seepage zone, with a small portion located in the critical seepage zone.

4.2 Small-scale fractures

Small-scale fractures in tight sandstone reservoirs in the Qingshimao area are manifested on the core as intraformational fractures developed within the rock mechanics layer and bed-confined fractures terminated at the rock mechanics interface at the end. The intraformational fractures within the layer are characterized by no contact between the two ends and the interface of the rock mechanics layer. The fracture size is small, the height is smaller than the thickness of the developed rock mechanics

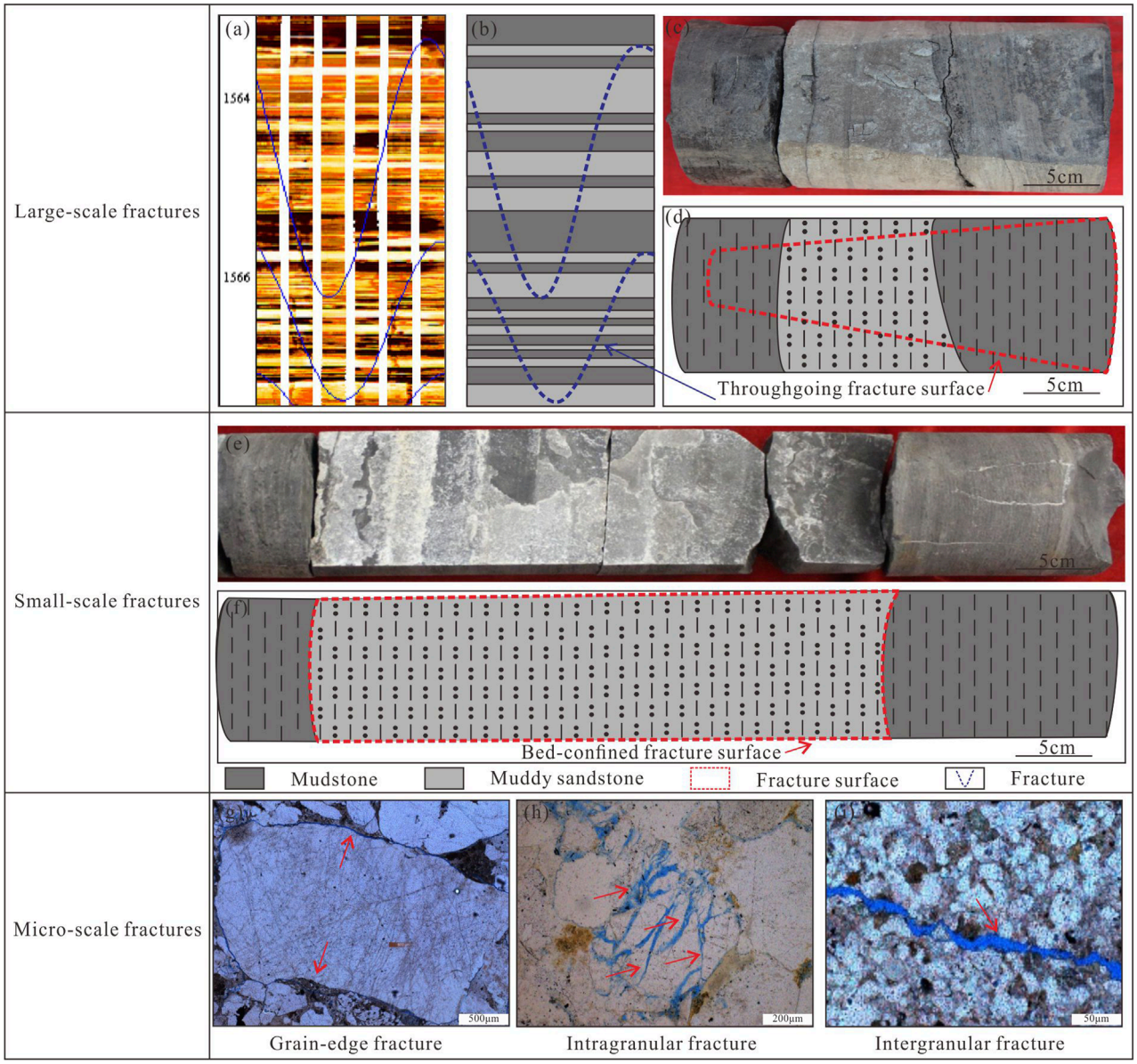

FIGURE 3
Characteristics of multi-scale fractures. **(A)** and **(B)** Throughgoing fractures in image logs; **(C)** and **(D)** Throughgoing fractures in cores; **(E)** and **(F)** Bed-confined fractures in cores; **(G)** Grain-edge fractures in thin section; **(H)** Intragranular fractures in thin section; **(I)** Intergranular fractures in thin section.

layer, and the fracture aperture is smaller. Bed-confined fractures are limited by the interface between the rock mechanics layers on both sides, with one or both ends terminating at the rock mechanics layer interface. The fracture height is less than or equal to the thickness of the developed rock mechanics layer, the fracture surface is rough, the aperture is greater than the aperture of the intraformational fracture, the fracture inclination is large, and it is distributed nearly perpendicular to the rock mechanics interface. The fracture distribution is regular, and the spacing is good (Figures 2E,F).

The inclination angle of small-scale fractures in the tight sandstone reservoir of the Qingshimao gas field is mainly high dip-angle, mainly distributed at 80°–90°. The height of fractures is mainly distributed between 5 and 25cm, with an average of 19.2 cm. The filling degree of small-scale fractures is very low, with 10.47% fully filled, 1.16% partially filled, 88.37% unfilled, and 89.53% effective fractures. The effectiveness of fractures is good, and the filling minerals are mainly calcite, quartz, and mud (Figure 5). The linear density of small-scale fractures is mainly distributed between 0.52–2.07/m, with an average of 1.04/m. The degree of fracture development varies among different wells and regions. The aperture of small-scale fractures is mainly distributed between 80–100° μm. The average is 85 μm. The porosity of fractures is mainly distributed between 0.17% and 0.23%, with an average of 0.20%. The permeability of fractures is mainly distributed between 2-8mD, with an average of 3.6mD.

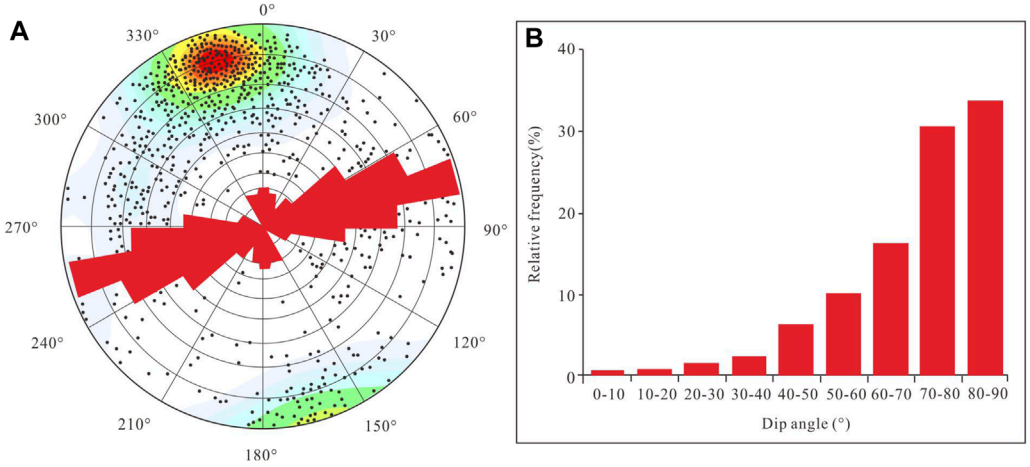

FIGURE 4
Rose plot and dip distribution of natural fractures in the study area. **(A)** Rose diagram of natural fracture direction. **(B)** Distribution map of natural fracture inclination angle.

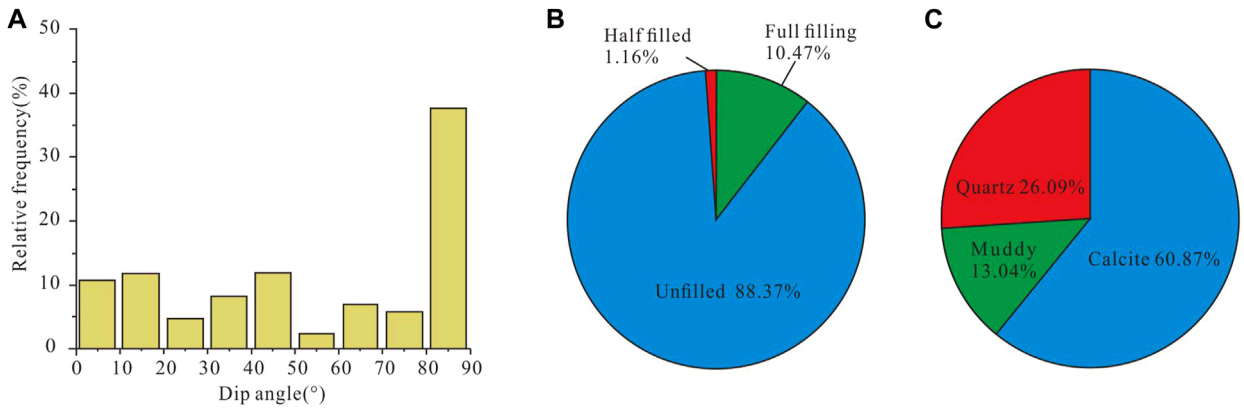

FIGURE 5
Various parameters of small-scale fractures. **(A)** Distribution map of dip angle of bed-confined fractures. **(B)** Distribution map of fracture filling degree. **(C)** Fill with minerals.

Due to the core's unoriented nature, we cannot obtain the orientation information of small-scale fractures. Since the study area is mainly composed of structural fractures, small-scale and large-scale fractures have the same composition and orientation. Therefore, we used the composition and orientation of large-scale fractures determined by image logs and the density, scale, and composition of small-scale fractures on the core to constrain their connectivity and conducted 20 simulations of their fracture connectivity. The simulation results show that the proportion of isolated small-scale fracture nodes (Type I nodes) in the study area is distributed between 47.5%–60.1%, with an average of 53.6%; The proportion of adjacent nodes (Y-shaped nodes) is distributed between 4.2% and 19.3%, with an average of 12.5%; The proportion of intersecting nodes (X-shaped nodes) is distributed between 31.8% and 45.6%, with an average of 33.9%. The number of nodes (Cl) for each fracture ranges from 2.85 to 3.74, with an average of 3.22. In the IYX triangle diagram, the simulation results are generally located in the critical seepage area of the fracture, with a small portion located in the seepage area of the fracture (Figure 6).

4.3 Micro-scale fractures

According to the particle relationship between micro-fractures and minerals, they can be divided into intragranular fractures, grain edge fractures, and intergranular fractures (Figures 2G–I). According to the observation and statistics of micro-fractures in 40 casting thin sections, the micro-fractures in the Qingshimao gas field are mainly manifested as intergranular fractures on the thin sections and its content accounts for about 90%, with a relatively small proportion of intragranular fractures and grain-edge fractures and the content of both accounts for about 10%. The intergranular fracture usually cuts through multiple mineral particles, with a large aperture and long extension, partially penetrating the entire

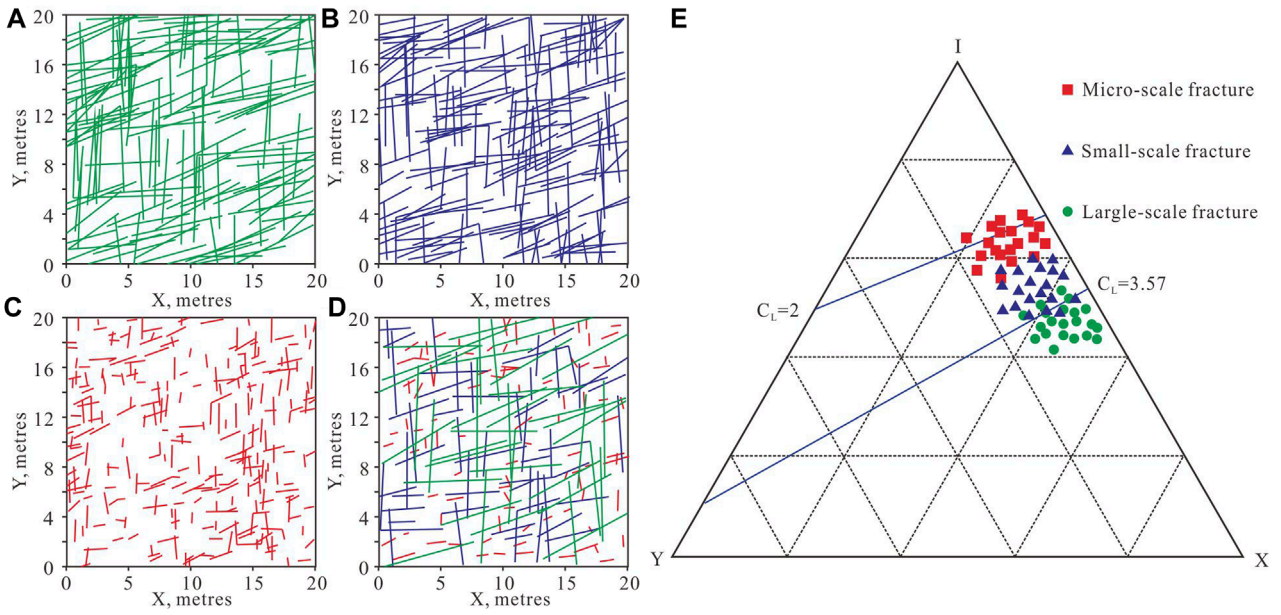

FIGURE 6
Characterization of fracture connectivity at different scales. **(A)** Simulation of multi-scale fracture connectivity. **(B)** Large-scale fracture connectivity simulation **(C)** Small-scale fracture connectivity simulation **(D)** Micro-scale fracture connectivity simulation **(E)** Multi-scale fracture connectivity triangle diagram.

thin film development, mainly playing a role in communicating the pores between particles and within particles. Intragranular fractures are manifested as quartz fractures or feldspar cleavage fractures, usually distributed inside mineral particles without cutting through the edges of the particles, and their aperture is relatively small; The grain-edge fractures are distributed along the edges of mineral particles, with a smaller aperture.

The filling degree of micro-scale fractures in the tight sandstone reservoir of the Qingshimao gas field is relatively low, with full filling accounting for 16%, semi-filling accounting for 32%, unfilled accounting for 52%, and effective fractures accounting for 84%. The effectiveness of fractures is good, and the minerals used for fracture filling are calcite, quartz, and mud. The development degree of micro-scale fractures is high, and the density of fracture surfaces is mainly distributed between 1 and 6.8 m/m^2, with an average of 4.2 m/m^2. The aperture of micro-fractures is mainly distributed between 10 and 75 μm. Its peak value is 128 μm. The average is 48.6 μm. The aperture of unfilled fractures is mainly distributed between 8–145° μm. Its peak value is 143 μm. The average is 42.2 μm. The porosity of micro-fractures is mainly distributed between 0.1% –0.6%, with an average of 0.48%. The permeability of micro-fractures is mainly distributed between 0.01 and 0.1mD, with an average of 0.08mD (Figure 7).

Due to the core's unoriented nature, we cannot obtain information on the orientation of micro-scale fractures. Since that the study area is mainly composed of structural fractures, micro-scale and large-scale fractures have the same composition and orientation. Therefore, we used the composition and orientation of small-scale and large-scale fractures determined by image logs and the length, density, and composition of micro-scale fractures on thin sections, to constrain their connectivity, and conducted 20 simulations. The simulation results show that the proportion of isolated micro-scale fracture nodes (Type I nodes) in the study area is distributed between 55.6%–68.2%, with an average of 62.8%; The proportion of adjacent nodes (Y-shaped nodes) is distributed between 3.2% and 19.6%, with an average of 12.8%; The proportion of intersecting nodes (X-shaped nodes) is distributed between 19.2% and 35.6%, with an average of 24.4%. The number of nodes (CL) for each fracture ranges from 1.82 to 3.06, with an average of 2.52. In the IYX triangle diagram, the simulation results are generally located in the critical seepage area of the fracture, with a small portion located in the area of poor fracture connection and poor fracture connectivity (Figure 6).

5 Discussion

5.1 The control effect of multi-scale fractures on reservoirs

Scholars have found through reports on the characterization of fractures at different scales that there are regular variations in fracture parameters, such as fracture size, fracture effectiveness, fracture density, fracture aperture, porosity, permeability, and connectivity (Ortega et al., 2006; Guerriero et al., 2010; Guerriero et al., 2011; Strijker et al., 2012; Ghanizadeh et al., 2015). From micro-scale to small-scale to large-scale fractures, their fracture apertures are significantly different, showing an overall upward trend, distributed between 10–180° μm. However, the density and size of fractures at different scales exhibit opposite patterns. There are certain differences in the effectiveness of fractures of different scales, but this difference seems to have a

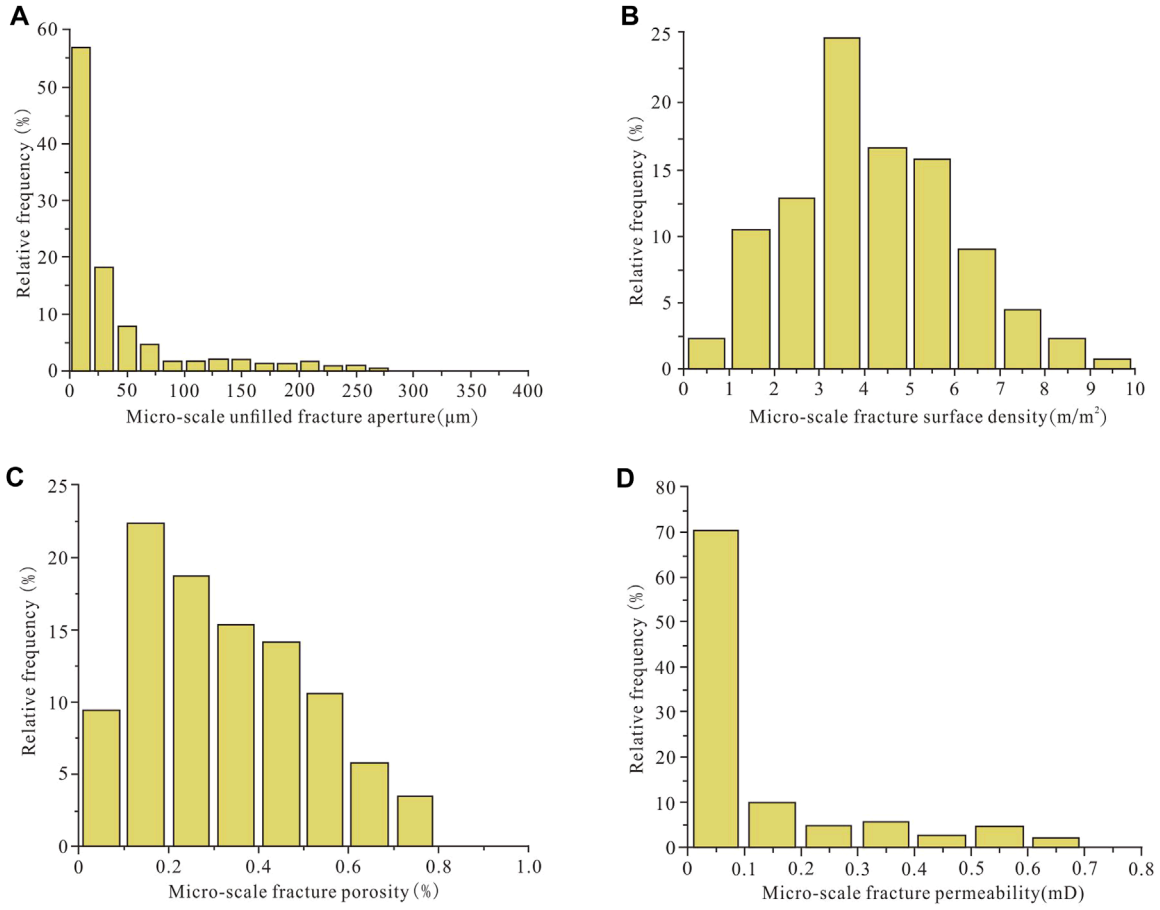

FIGURE 7
Distribution of various parameters of micro-scale fractures. **(A)** Distribution of micro-scale unfilled fracture aperture. **(B)** Distribution of micro-scale surface fracture density. **(C)** Distribution of micro-scale fracture porosity. **(D)** Permeability distribution of micro-scale fractures.

certain pattern: Micro-scale fractures have the worst effectiveness, while large-scale fractures have the best effectiveness. The reason for this difference may be that, from a microscopic perspective, the aperture of micro-scale fractures is smaller and more easily filled by minerals. On the other hand, from a macro perspective, some large-scale filled fractures may not be easily identified and may also create an illusion of good effectiveness. The Monte Carlo method is used to calculate the porosity and permeability of multi-scale fractures, and there is a negative correlation between porosity and scale size. The order from large to small is micro-scale, small-scale, and large-scale. The magnitude of permeability at different scales shows an opposite pattern to porosity; that is, the larger the scale of the fracture, the greater the permeability. From the perspective of fracture connectivity, there is a positive correlation between fracture connectivity and fracture scale, with large-scale fractures having the best connectivity and micro-scale fractures having the worst connectivity. This difference is because the fracture scale, density, and orientation of different scale fractures are different, which affects the degree of fracture connectivity (Figure 8). This is consistent with Ortega et al. (2006) recognition that the impact of fracture scale effects on fracture parameters (fracture density, aperture) needs to be considered when calculating fracture parameters (Ortega et al., 2006).

Multiscale fractures are important storage spaces, and production practice has shown that natural fractures of different scales have significantly different effects on tight and low-permeability reservoirs and on oil and gas. Large scale fractures usually affect the preservation of oil and gas, while small and medium-sized fractures control the permeability system of tight reservoirs. Microscale fractures mainly play a storage role (Strijker et al., 2012; Lyu et al., 2019). Therefore, we compared the contribution rates of porosity and permeability in the multi-scale fracture system of the Qingshimao gas field, as well as the porosity and permeability in the matrix. Here, we established the relationship between multi-scale fracture porosity and permeability by analyzing the relevant parameters of matrix porosity and permeability, as well as the density distribution of multi-scale fractures (Figure 9). It can be seen that the contribution of matrix and fractures of different scales to the porosity and permeability of the reservoir is different. The contribution to porosity in descending order is matrix, micro-scale fractures, small-scale fractures, and large-scale fractures. The contribution rate of matrix porosity is 85%–95%, with an average of 88.6%; The contribution rate of micro-scale fracture

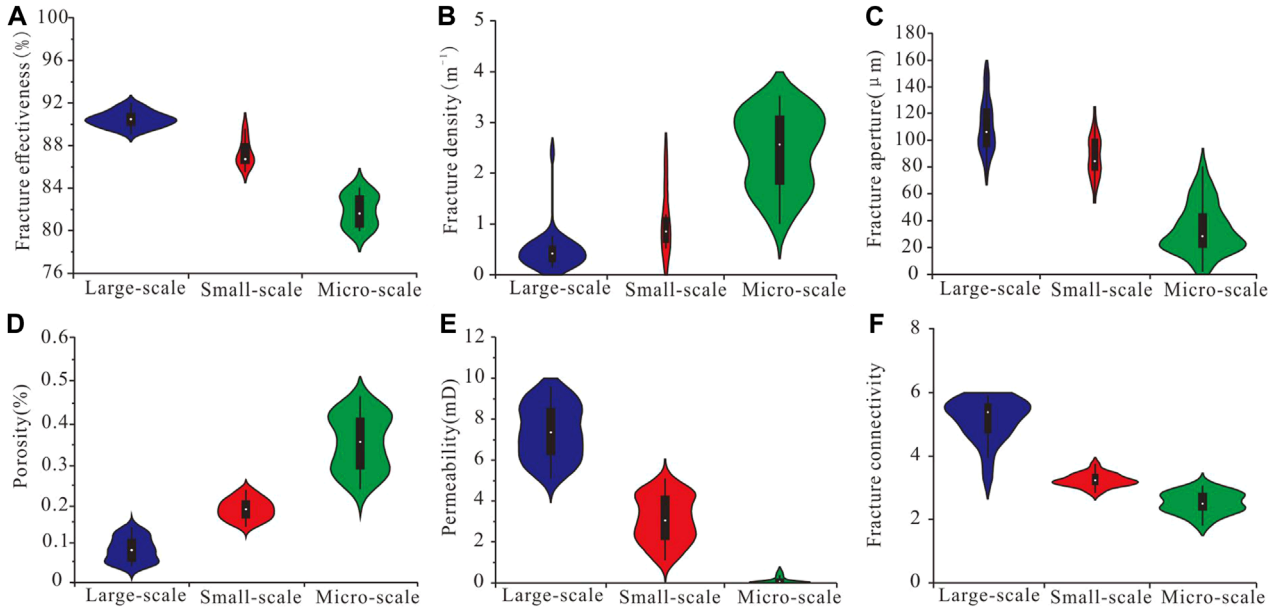

FIGURE 8
Distribution of fracture parameters at different scales. **(A)**Distribution of fracture effectiveness at different scales **(B)**Distribution of fracture density at different scales **(C)**Distribution of fracture aperture at different scales **(D)**Distribution of fracture porosity at different scales **(E)**Distribution of fracture permeability at different scales **(F)**Distribution of fracture connectivity at different scales.

porosity is 5%–11%, with an average of 7.4%; The contribution rate of small-scale fracture porosity is 0%–4%, with an average of 2.8%; The contribution rate of large-scale fracture porosity is 0%–2%, with an average of 1.2%. From the perspective of the contribution of permeability, its contribution in descending order is large-scale fractures, small-scale fractures, matrix, and micro-scale fractures. The contribution of permeability provided by the matrix is 5%–17%, with an average of 10%; Micro-scale fractures do not contribute significantly to reservoir permeability, averaging 3.2%, but they provide good porosity and can effectively communicate between intergranular and intragranular pores; The contribution of permeability of small-scale and large-scale fractures is 5–100 times that of matrix permeability. Small-scale fractures contribute 16%–43% to reservoir permeability, with an average of 24.4%. Due to the influence of layer control, they can provide important seepage channels and storage space for the tight sandstone reservoir in the Qingshimao gas field. Large-scale fractures have a significant contribution to reservoir permeability, mainly distributed in the range of 56%–70%, with an average of 62.4%. Due to the influence of throughgoing penetration, they have good connectivity and damage the reservoir, which can greatly improve the permeability and permeability of the reservoir (Figure 10).

Debenham et al. (2019) described and discussed the spatial distribution of porosity and permeability of microscale fractures in tight sandstone reservoirs and determined that micro-scale fracture changes can effectively improve reservoir permeability (Debenham et al., 2019). Hennings et al. (2012) determined through the analysis of the contribution of large-scale fractures to reservoirs and their control over reservoir performance that large-scale fractures can significantly improve reservoir properties and enhance reservoir performance (Hennings et al., 2012). Although

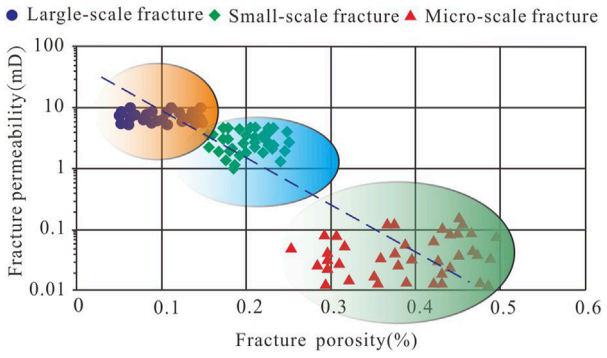

FIGURE 9
Relationship between fracture porosity and permeability.

they have made significant contributions to the study of the effect of fractures on reservoirs, there needs to be more research on the effect of multi-scale fractures on reservoirs. Therefore, we systematically evaluated and discussed the contribution and control of multi-scale fractures on reservoirs in the study area by considering the changes in the distribution patterns of different parameters of multi-scale fractures. We determined that different scale fractures have different control effects on the reservoir. Namely, micro-scale fractures can effectively communicate intergranular and intragranular pores, small-scale fractures can provide important seepage channels and reservoir space, and large-scale fractures can damage the reservoir. However, they can greatly improve the permeability and seepage capacity of the reservoir.

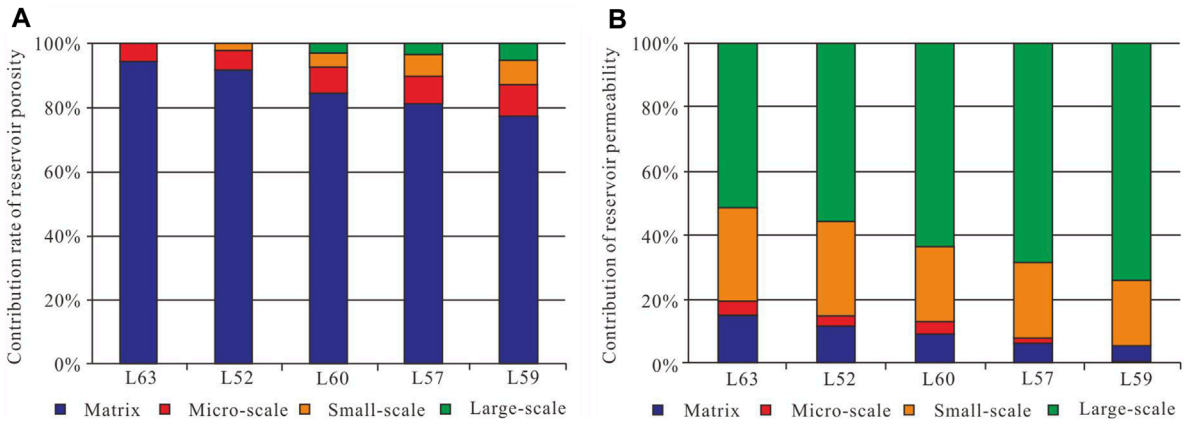

FIGURE 10
Shows the contribution rate of multi-scale fractures to the reservoir. **(A)** Multi-scale fracture porosity contribution rate. **(B)** Contribution of multi-scale fracture permeability.

5.2 The impact of multi-scale fracture development on the productivity of oil and gas wells

The porosity and permeability of tight sandstone reservoirs are relatively low, and fractures of different scales form a well-connected continuous network in space, which can serve as effective seepage channels and provide certain storage space for tight sandstone reservoirs. A well-connected network is a key factor for the formation of high-quality contiguous reservoirs and the achievement of high and stable production in tight sandstone reservoirs (Sanderson et al., 2018; Braathen et al., 2020; Lucca et al., 2020; Mercuri et al., 2020; Rabbel et al., 2021). Due to the different fracture sizes and connectivity of different scale configurations in different blocks of the Qingshimao area, the effectiveness and connectivity of fractures, as well as the contribution of fractures to reservoirs under different network structure modes are affected. Therefore, based on the quantitative characterization of multi-scale fractures in the tight sandstone reservoir in the Qingshimao area, we considered factors such as the fracture group and orientation, the size of the fracture scale, and the density of fractures. Based on the spatial combination patterns of fractures of different scales, we divided the study area into network structure patterns. Four types of seam network structures have been established: multi-scale fracture network with high density and multi multi-orientations, multi-scale fracture network with moderate-high density and dual orientations, small-scale fracture network with moderate density and dual orientations, small-scale fracture network with low density and single orientation (Figure 11).

The structural pattern of the first type of fracture network is located at the end and overlapping area of the fault. It has a multi-scale fracture network system with high fracture density, multiple orientations (mainly developing three to four fracture orientations), strong connectivity, and greatly improves the physical properties of the tight reservoir. It can form a large area of continuous, high-quality reservoirs. According to the distance relationship diagram between water and gas production and the fault (Figure 12), in this mode, the water production of a single well is high, and the gas production is low. This situation may be due to the large-scale fractures (throughgoing fractures and small faults) developed in this type of fracture network, which are prone to vertical connectivity, thereby damaging the integrity of the cap rock and causing natural gas leakage or upward layers-system adjustment. The fractures formed by it have played a destructive role in controlling storage and reservoirs.

The second type of fracture network structure pattern is located 0.5km–1.3 km near the fault, mainly developing two sets of fractures, with multi-scale throughgoing fractures as the main type. The degree of fracture development is high, and the connectivity is good, effectively improving the tight reservoir's physical properties and horizontal continuity. It can form a high-quality reservoir with regional continuity. The gas and water production relationship diagram shows that this mode has high gas and water production, making it the mode with the highest single well production and a favorable area for natural gas enrichment. This phenomenon may be because the fracture density is relatively high and the connectivity is relatively good in this mode, which can effectively improve the reservoir. However, it does not cause damage to the reservoir and is conducive to the enrichment of natural gas. The fractures formed in this mode are key in controlling reservoir and reservoir.

The third type of fracture network structure pattern is located within the range of 1.3–2.3 km from the fault. It mainly develops two sets of fractures, mainly small and medium-sized bed-confined fractures and partially throughgoing fractures. The fracture density and connectivity are moderate, which can obtain a certain production capacity. Fracturing is needed to improve the reservoir effectively. Its gas and water production are relatively low and cannot form a continuous high-quality reservoir. The fractures formed in this pattern play an adjusting role in controlling the reservoir.

The fourth type of fracture network structure mode is located in the parent rock area with high mud content > 2.3 km away from the fault. The orientation of the fractures is single, mainly consisting of small-scale bed-confined and micro-scale fractures. The fracture density is low, the connectivity is poor, and it cannot form a

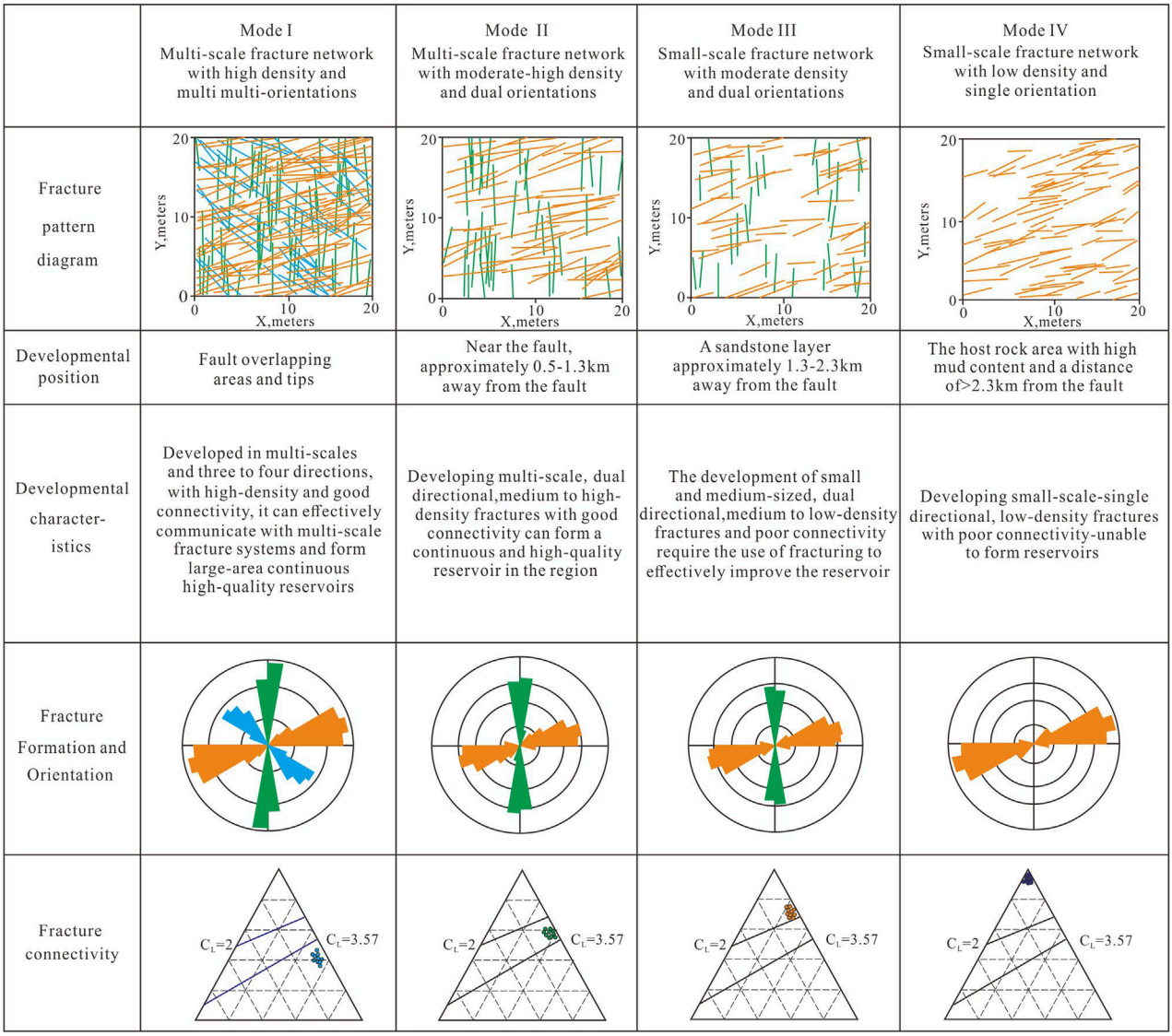

FIGURE 11
Structural pattern division of multi-scale fracture network.

reservoir. Its role in controlling the tight sandstone reservoir in the Qingshimao area is insignificant. Therefore, the Qingshimao area is greatly influenced by different fracture network structural patterns, and the differences between these patterns play an important role in the distribution of gas and water, which is one of the important reasons for the complexity of gas and water in the Qingshimao area.

Prabhakaran et al. (2021) studied the network structure pattern of reservoirs using large-scale fractures, emphasizing the inherent changes in the natural fracture network structure pattern. The results showed that the changes in the fracture network structure pattern cannot only consider the influence of a single factor (Prabhakaran et al., 2021). Ghosh and Mitra. (2009) considered the influence of fracture set and orientation, fracture density in their study of fracture connectivity and spatial configuration relationships. They concluded that multiple fracture systems and high density have a significant impact on connectivity (Ghosh and Mitra, 2009). Although scholars' research results have played an important role in fracture connectivity and network spatial structure patterns, there is still a lack of research on multi-scale and multi-factor aspects. Therefore, we propose a multi-scale fracture network structure pattern prediction method that considers multiple factors. By comprehensively discussing the spatial configuration relationship of multi-scale fractures in tight sandstone reservoirs, taking into account multiple factors such as fracture set and orientation, fracture scale, fracture density, fracture length, etc. and the control effect of fractures on the reservoir, we have determined the development patterns of fractures under different network structure patterns.

Understanding the spatial configuration relationship of fractures and their control over reservoirs can help determine the impact of fractures on reservoirs and the development of fractures under this network pattern. If one wants to understand the spatial configuration relationship of fractures and their control over

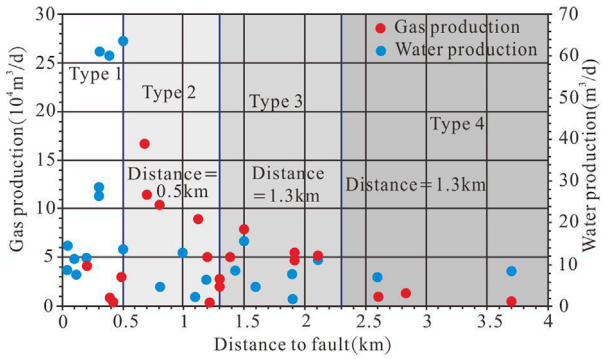

FIGURE 12
The relationship between gas production, water production, and distance from faults under four types of fracture network structure modes.

reservoirs, it is necessary to classify the scale of fractures and clarify the development characteristics of fractures at different scales rather than analyzing and discussing fractures at a single scale. When studying the spatial configuration relationship of fractures, it is necessary to consider multiple factors, including the fracture set and orientation of fractures, fracture scale, fracture density, fracture length, etc., rather than just considering the influence of one factor. This multi-scale and multi-factor consideration method helps to infer how fracture density, fracture connectivity, and fracture scale control reservoirs and helps to understand better and promote the development of multi-scale fracture network structure patterns in spatial configuration relationships.

6 Conclusion

1. A multi-scale fracture system is developed in the tight sandstone reservoir of the Qingshimao gas field in the Ordos Basin. The related parameters of micro, small, and large-scale fractures differ, but there are regular changes. Micro-scale fractures have high density, high porosity (0.1%–0.6%), and low permeability (0.01–0.1mD), it has the function of communicating matrix pores and reservoir space. Small-scale fractures are moderate compared to micro and large-scale fractures and are important flow channels for tight sandstone reservoirs in the study area. Large-scale fractures have a large length and aperture, good connectivity, and can provide important permeability (8-10mD) for tight reservoirs. However, the fracture density is relatively low, and the porosity provided for the reservoir is limited (0.07%–0.15%).
2. Based on the development characteristics of different types of fractures in the Qingshimao area, four types of fracture network structural models have been established. Different fracture network structures have different impacts on the production capacity of the Qingshimao gas field. Multi-scale fracture network with high density and multi-orientations can damage the integrity of the cover layer, causing natural gas leakage or adjustment to the upper layer system. Multi-scale fracture network with moderate-high density and dual orientations can effectively improve the physical properties and lateral continuity of tight reservoirs, making it a favorable area for natural gas enrichment. Small-scale fracture network with moderate density and dual orientations can achieve certain production capacity, but it requires the use of hydraulic fracturing to obtain commercial airflow. Small-scale fracture network with low density and single orientation cannot form a reservoir, and it has little effect on the control of tight sandstone reservoirs in the Qingshimao area.
3. The research results of this work are of great significance for future studies on the development characteristics and quantitative evaluation of multi-scale fractures. At the same time, they provide insights into the control and storage effects of multi-scale fractures and the development of multi-scale fracture network structural patterns in spatial configuration relationships. Increasing oil and gas development capacity has become crucial in the current context of energy transition. It is necessary to focus on this aspect of development not only in conventional oil and gas extraction, but also in the exploration and development of unconventional oil and gas and hydrocarbons.

Data availability statement

The raw data supporting the conclusions of this article will be made available by the authors, without undue reservation.

Author contributions

JeW: Conceptualization, Writing–original draft, Writing–review and editing. JpW: Conceptualization, Writing–original draft, Writing–review and editing. YZ: Data curation, Writing–review and editing. DZ: Formal Analysis, Writing–review and editing. LS: Data curation, Writing–review and editing. JL: Formal Analysis, Writing–review and editing. WW: Investigation, Writing–review and editing. LG: Methodology, Writing–review and editing. ZL: Writing–review and editing. SG: Writing–review and editing.

Funding

The author(s) declare that financial support was received for the research, authorship, and/or publication of this article. This research was funded by Research on Key Technologies for Improving Oil Recovery of Tight Sandstone Gas Reservoirs in China National Petroleum Corporation's Major Science and Technology Project (2023ZZ25); "Research on Reservoir Formation Characteristics, Main Control Factors, and Development Technology Countermeasures of Qingshimao Gas Field" Technology Project of Changqing Oilfield Company of China National Petroleum Corporation (2022D-JB04); National Natural Science Foundation of China (Grant No. 42172161), Natural Science Foundation of Heilongjiang Province (Grant No. YQ2021D006).

Conflict of interest

Authors JpW, YZ, DZ, LS, JL, and WW were employed by Exploration and Development Research Institute of China Petroleum Changqing Oilfield Company.

The remaining authors declare that the research was conducted in the absence of any commercial or financial relationships that could be construed as a potential conflict of interest.

The authors declare that this study received funding from China National Petroleum Corporation and Changqing Oilfield Company of China National Petroleum Corporation. The funder had the following involvement in the study: data collection and analysis.

Publisher's note

All claims expressed in this article are solely those of the authors and do not necessarily represent those of their affiliated organizations, or those of the publisher, the editors and the reviewers. Any product that may be evaluated in this article, or claim that may be made by its manufacturer, is not guaranteed or endorsed by the publisher.

References

Aubert, I., Lamarche, J., and Léonide, P. (2021). Ternary fault permeability diagram: An innovative way to estimate fault zones hydraulics. *J. Struct. Geol.* 147, 104349. doi:10.1016/j.jsg.2021.104349

Bagni, F. L., Bezerra, F. H., Balsamo, F., Maia, R. P., and Dall'Aglio, M. (2020). Karst dissolution along fracture corridors in an anticline hinge, Jandaíra Formation, Brazil: implications for reservoir quality. *Mar. Petroleum Geol.* 115, 104249. doi:10.1016/j.marpetgeo.2020.104249

Balberg, I., Anderson, C. H., Alexander, S., and Wagner, N. (1984). Excluded volume and its relation to the onset of percolation. *Phys. Rev. B, Condens. matter* 30 (7), 3933–3943. doi:10.1103/PhysRevB.30.3933

Balberg, I., and Binenbaum, N. (1983). Computer study of the percolation threshold in a two-dimensional anisotropic system of conducting sticks. *Phys. Rev. B, Condens. matter* 28 (7), 3799–3812. doi:10.1103/PhysRevB.28.3799

Balsamo, F., La Bruna, V., Bezerra, F. H., Dall Aglio, M., Bagni, F. L., Silveira, L. G., et al. (2023). Mechanical stratigraphy controls fracture pattern and karst epigenic dissolution in folded Cretaceous carbonates in semiarid Brazil. *Mar. Petroleum Geol.* 155, 106409. doi:10.1016/j.marpetgeo.2023.106409

Berkowitz, B. (1995). Analysis of fracture network connectivity using percolation theory. *Math. Geol.* 27 (4), 467–483. doi:10.1007/BF02084422

Bertrand, L., Geraud, Y., Garzic, E. L., Place, J., Diraison, M., Walter, B., et al. (2015). A multiscale analysis of a fracture pattern in granite; a case study of the Tamariu Granite, Catalunya, Spain. *J. Struct. Geol.* 78, 52–66. doi:10.1016/j.jsg.2015.05.013

Birkholzer, J. T., Morris, J., Bargar, J. R., Brondolo, F., Cihan, A., Crandall, D., et al. (2021). A new modeling framework for multi-scale simulation of hydraulic fracturing and production from unconventional reservoirs. *Energies (Basel)* 14 (3), 641. doi:10.3390/en14030641

Braathen, A., Petrie, E., Nystuen, T., Sundal, A., Skurtveit, E., Zuchuat, V., et al. (2020). Interaction of deformation bands and fractures during progressive strain in monocline - san Rafael Swell, Central Utah, USA. *J. Struct. Geol.* 141 (104219), 104219. doi:10.1016/j.jsg.2020.104219

Cao, D. S., Zeng, L. B., Gomez-Rivas, E., Gong, L., Liu, G. P., Lu, G. Q., et al. (2024). Correction of linear fracture density and error analysis using underground borehole data. *J. Struct. Geol.* 105152, 105152. doi:10.1016/j.jsg.2024.105152

Casini, G., Hunt, D. W., Monsen, E., and Bounaim, A. (2016). Fracture characterization and modeling from virtual outcrops. *AAPG Bull.* 100 (01), 41–61. doi:10.1306/09141514228

Debenham, N., Farrell, N. J. C., Holford, S. P., King, R. C., and Healy, D. (2019). Spatial distribution of micrometre-scale porosity and permeability across the damage zone of a reverse-reactivated normal fault in a tight sandstone: insights from the Otway Basin, SE Australia. *Basin Res.* 31, 640–658. doi:10.1111/bre.12345

Farouk, S., Qteishat, A., Sen, S., Ahmad, F., El-Kahtany, K., Collier, R., et al. (2023). Characterization of the gas-bearing tight paleozoic sandstone reservoirs of the risha field, Jordan: inferences on reservoir quality and productivity. *Arabian J. Sci. Eng.* doi:10.1007/s13369-024-09000-x

Fernández-Ibáñez, F., DeGraff, J. M., and Ibrayev, F. (2018). Integrating borehole image logs with core: a method to enhance subsurface fracture characterization. *AAPG Bull.* 102 (06), 1067–1090. doi:10.1306/0726171609317002

Fu, J. H., Li, S. X., Guo, Q. H., Guo, W., Zhou, X. P., and Liu, J. Y. (2022a). Enrichment conditions and favorable area optimization of continental shale oil in Ordos Basin. *Acta Pet. Sin.* 43 (12), 1702–1716. doi:10.7623/syxb202212003

Fu, X. F., Gong, L., Su, X. C., Liu, B., Gao, S., Yang, J. G., et al. (2022b). Characteristics and controlling factors of natural fractures in continental tight-oil shale reservoir. *Miner. (Basel).* 12 (12), 1616. doi:10.3390/min12121616

Fu, X. F., Su, X. C., Gong, L., Wang, Q. Q., Gao, S., and Xie, Z. H. (2023). Control of faults and fractures on shale oil enrichment. *Geoenergy Sci. Eng.* 228, 212080. doi:10.1016/j.geoen.2023.212080

Gale, J. F. W., Laubach, S. E., Olson, J. E., Eichhubl, P., and Fall, A. (2014). Natural fractures in shale: a review and new observations. *AAPG Bull.* 98 (11), 2165–2216. doi:10.1306/08121413151

Gale, J. F. W., Reed, R. M., and Holder, J. (2007). Natural fractures in the Barnett Shale and their importance for hydraulic fracture treatments. *AAPG Bull.* 91 (4), 603–622. doi:10.1306/11010606061

German, M., Salim, A. H., Michael, R., Russell, F., Mohamed, B., and Carlos, T. V. (2023). Assessment of true formation resistivity and water saturation in deeply invaded tight-gas sandstones based on the combined numerical simulation of mud-filtrate invasion and resistivity logs. *Petrophysics.* 64 (4), 502–517. doi:10.30632/PJV64N4-2023a2

Ghanizadeh, A., Clarkson, C. R., Aquino, S., Ardakani, O. H., and Sanei, H. (2015). Petrophysical and geomechanical characteristics of Canadian tight oil and liquid-rich gas reservoirs: I. Pore network and permeability characterization. *Fuel Guildf.* 153 (2015), 664–681. doi:10.1016/j.fuel.2015.03.020

Ghosh, K., and Mitra, S. (2009). Two-dimensional simulation of controls of fracture parameters on fracture connectivity. *AAPG Bull.* 93 (11), 1517–1533. doi:10.1306/07270909041

Gong, L., Cheng, Y. Q., Gao, S., Gao, Z. Y., Feng, J. R., and Wang, H. T. (2023a). Fracture connectivity characterization and its controlling factors in the Lower Jurassic tight sandstone reservoirs of eastern Kuqa. *Earth Sci.* 48 (07), 2475–2488. doi:10.3799/dqkx.2022.066

Gong, L., Fu, X. F., Wang, Z. S., Gao, S., Jabbari, H., Yue, W. T., et al. (2019a). A new approach for characterization and prediction of natural fracture occurrence in tight oil sandstones with intense anisotropy. *AAPG Bull.* 103 (6), 1383–1400. doi:10.1306/12131818054

Gong, L., Liu, K., and Ju, W. (2023b). Editorial: advances in the study of natural fractures in deep and unconventional reservoirs. *Front. earth Sci. (Lausanne)* 2023, 10. doi:10.3389/feart.2022.1096643

Gong, L., Su, X. C., Gao, S., Fu, X. F., Jabbari, H., Wang, X. X., et al. (2019c). Characteristics and formation mechanism of natural fractures in the tight gas sandstones of Jiulongshan gas field, China. *J. Petroleum Sci. Eng.* 175, 1112–1121. doi:10.1016/j.petrol.2019.01.021

Gong, L., Wang, J., Gao, S., Fu, X. F., Liu, B., Miao, F. B., et al. (2021b). Characterization, controlling factors and evolution of fracture effectiveness in shale oil reservoirs. *J. Petroleum Sci. Eng.* 203, 108655. doi:10.1016/j.petrol.2021.108655

Guerriero, V., Iannace, A., Mazzoli, S., Parente, M., Vitale, S., and Giorgioni, M. (2010). Quantifying uncertainties in multi-scale studies of fractured reservoir analogues; implemented statistical analysis of scan line data from carbonate rocks. *J. Struct. Geol.* 32 (9), 1271–1278. doi:10.1016/j.jsg.2009.04.016

Guerriero, V., Vitale, S., Ciarcia, S., and Mazzoli, S. (2011). Improved statistical multi-scale analysis of fractured reservoir analogues. *TECTONOPHYSICS* 504 (1-4), 14–24. doi:10.1016/j.tecto.2011.01.003

Guo, Y. Q., Wang, M. X., Guo, B. C., Cai, Z. C., and Hui, L.(2020). Sedimentary system characteristics and paleographic evolution of upper paleozoic of northern west margin, Ordos Basin. *J. North. University (Nat. Sci. Edi.)* 50(01), 93–104. doi:10.16152/j.cnki.xdxbzr.2020-01-013

He, J. C., Yu, H. J., He, G. H., Zhang, J., and Li, Y. (2021). Natural gas development prospect in Changqing gas province of the Ordos Basin. *Nat. Gas. Ind.* 41 (08), 23–33. doi:10.3787/j.issn.1000-0976.2021.08.003

Hennings, P., Allwardt, P., Paul, P., Zahm, C., Reid, R., Jr., Alley, H., et al. (2012). Relationship between fractures, fault zones, stress, and reservoir productivity in the Suban gas field, Sumatra, Indonesia. *AAPG Bull.* 96 (4), 753–772. doi:10.1306/08161109084

Jia, C. Z., Zheng, M., and Zhang, Y. F. (2012). Unconventional hydrocarbon resources in China and the prospect of exploration and development. *Petroleum Explor. Dev.* 39 (02), 139–146. doi:10.1016/S1876-3804(12)60026-3

Jiang, F. J., Jia, C. Z., Pang, X. Q., Jiang, L., and Zhang, C. L. (2023). Upper paleozoic total petroleum system and geological model of natural gas enrichment in Ordos Basin, NW China. *Petroleum exploration and development* 50 (02), 250–261. doi:10.11698/PED.20220602

Laubach, S. E., Lamarche, J., Gauthier, B. D. M., Dunne, W. M., and Sanderson, D. J. (2018). Spatial arrangement of faults and opening -mode fractures. *J. Struct. Geol.* 108, 2–15. doi:10.1016/j.jsg.2017.08.008

Loza Espejel, R., Alves, T. M., and Blenkinsop, T. G. (2020). Multi-scale fracture network characterisation on carbonate platforms. *J. Struct. Geol.* 140 (104160), 104160. doi:10.1016/j.jsg.2020.104160

Lucca, A., Storti, F., and Molli, G. (2020). Extensional fracture network attribute distribution in faulted thick sandstone strata: compione Fault, Northern Apennines, Italy. *J. Struct. Geol.* 131 (103954), 103954. doi:10.1016/j.jsg.2019.103954

Lyu, W., Zeng, L., Zhou, S., Du, X., Xia, D., Liu, G., et al. (2019). Natural fractures in tight-oil sandstones: a case study of the upper triassic Yanchang formation in the southwestern Ordos Basin, China. *AAPG Bull.* 103 (10), 2343–2367. doi:10.1306/0130191608617115

Manzocchi, T. (2002). The connectivity of two-dimensional networks of spatially correlated fractures. *Water Resour. Res.* 38 (9), 1162. doi:10.1029/2000WR000180

Mercuri, M., Carminati, E., Tartarello, M. C., Brandano, M., Mazzanti, P., Brunetti, A., et al. (2020). Lithological and structural control on fracture frequency distribution within a carbonate-hosted relay ramp. *J. Struct. Geol.* 137, 104085. doi:10.1016/j.jsg.2020.104085

Micheal, M., Xu, W., Xu, H., Zhang, J., Jin, H., Yu, H., et al. (2021). Multi-scale modelling of gas transport and production evaluation in shale reservoir considering crisscrossing fractures. *J. Nat. gas Sci. Eng.* 95 (104156), 104156. doi:10.1016/j.jngse.2021.104156

Nixon, C. W., Sanderson, D. J., and Bull, J. M. (2012). Analysis of a strike-slip fault network using high resolution multibeam bathymetry, offshore NW Devon U.K. *Tectonophysics* 541-543, 69–80. doi:10.1016/j.tecto.2012.03.021

Nwabia, F. N., and Leung, J. Y. (2021). Probabilistic history matching of multi-scale fractured reservoirs: Integration of a novel localization scheme based on rate transient analysis. *J. Nat. Gas Sci. Eng.* 94, 104067. doi:10.1016/j.jngse.2021.104067

Ortega, O. J., Marrett, R. A., and Laubach, S. E. (2006). A scale-independent approach to fracture intensity and average spacing measurement. *AAPG Bull.* 90 (2), 193–208. doi:10.1306/08250505059

Petrik, A., Vahle, C., Gianotten, I. P., Trøan, L. L., Rojo, L., and Galbraith, K. (2023). Quantitative characterisation of fracture connectivity from high-resolution borehole image logs. *Mar. petroleum Geol.* 155, 106405. doi:10.1016/j.marpetgeo.2023.106405

Prabhakaran, R., Urai, J. L., Bertotti, G., Weismuller, C., and Smeulders, D. M. J. (2021). Large-scale natural fracture network patterns: insights from automated mapping in the Lilstock (Bristol Channel) limestone outcrops. *J. Struct. Geol.* 150 (104405), 104405. doi:10.1016/j.jsg.2021.104405

Rabbel, O., Palma, O., Mair, K., Galland, O., Spacapan, J. B., and Senger, K. (2021). Fracture networks in shale-hosted igneous intrusions: processes, distribution and implications for igneous petroleum systems. *J. Struct. Geol.* 150 (104403), 104403. doi:10.1016/j.jsg.2021.104403

Sanderson, D. J., and Nixon, C. W. (2015). The use of topology in fracture network characterization. *J. Struct. Geol.* 72, 55–66. doi:10.1016/j.jsg.2015.01.005

Sanderson, D. J., Peacock, D. C. P., Nixon, C. W., and Rotevatn, A. (2018). Graph theory and the analysis of fracture networks. *J. Struct. Geol.* 125, 155–165. doi:10.1016/j.jsg.2018.04.011

Strijker, G., Bertotti, G., and Luthi, S. M. (2012). Multi-scale fracture network analysis from an outcrop analogue: a case study from the Cambro-Ordovician clastic succession in Petra, Jordan. *Mar. Petroleum Geol.* 38 (1), 104–116. doi:10.1016/j.marpetgeo.2012.07.003

Su, X. C., Gong, L., Fu, X. F., Gao, S., Zhou, X. P., and Lu, Q. (2023). Fracture distribution characteristics and effectiveness evaluation of tight sandstone reservoir of chang 7 member in Sanbian area, Ordos Basin. *Earth Sci.* 48 (07), 2601–2613. doi:10.3799/dqkx.2022.116

Sweeney, M. R., Hyman, J. D., Malley, D. O. ', Santos, J. E., Carey, J. W., and Stauffer, P. H. (2023). Characterizing the impacts of multi-scale heterogeneity on solute transport in fracture networks. *Geophys. Res. Lett.* 21 (50), 1–26. doi:10.1029/2023GL104958

Vasquez Serrano, A., Sampayo Rodriguez, M. F., Fitz Diaz, E., and Tolson, G. (2024). Kinematics, intensity, and spatial arrangement of extensional fractures in the Tuxtla-Malpaso fault system: Chiapas strike-slip fault province, southern Mexico. *J. Struct. Geol.* 180, 105062. doi:10.1016/j.jsg.2024.105062

Wang, J., Hu, C. G., Pan, Y. L., Huang, Q. J., Yuan, H. Q., and Gong, L. (2022). Fracture development characteristics and comprehensive evaluation of buried hill metamorphic reservoir in Jihua 1 area. *Chin. J. Geol.* 57 (02), 463–477. doi:10.12017/dzkx.2022.027

Watkins, H., Bond, C. E., Healy, D., and Butler, R. W. H. (2015). Appraisal of fracture sampling methods and a new workflow to characterise heterogeneous fracture networks at outcrop. *J. Struct. Geol.* 72, 67–82. doi:10.1016/j.jsg.2015.02.001

Watkins, H., Healy, D., Bond, C. E., and Butler, R. W. H. (2018). Implications of heterogeneous fracture distribution on reservoir quality; an analogue from the Torridon Group sandstone, Moine Thrust Belt, NW Scotland. *J. Struct. Geol.* 108, 180–197. doi:10.1016/j.jsg.2017.06.002

Yin, S., Sun, X. G., Wu, Z. H., Wang, Y. B., Zhao, J. Z., and Sun, W. H. (2022). Coupling control of tectonic evolution and fractures on the Upper Paleozoic gas reservoirs in the northeastern margin of the Ordos Basin. *J. Central South Univ. Sci. Technol.* 53 (09), 3724–3737. doi:10.11817/j.issn.1672-7207.2022.09.033

Zeng, L.B.(2010). Microfracturing in the upper triassic sichuan basin tight gas sandstones: tectonic, overpressure, and diagenetic origins. *AAPG Bull.* 94(12), 1811–1825. doi:10.1306/06301009191

Zeng, L. B., Gong, L., Guan, C., Zhang, B. J., Wang, Q. Q., Zeng, Q., et al. (2022). Natural fractures and their contribution to tight gas conglomerate reservoirs: a case study in the northwestern Sichuan Basin, China. *J. petroleum Sci. Eng.* 210, 110028. doi:10.1016/j.petrol.2021.110028

Zeng, L. B., Gong, L., Su, X. C., and Mao, Z. (2024). Natural fractures in deep to ultra-deep tight reservoirs:Distribution and development. *Oil Gas Geol.* 45 (01), 1–14. doi:10.11743/ogg20240101

Zeng, L. B., Gong, L., Zhang, Y. Z., Dong, S. Q., and Lyu, W. Y. (2023). A review of the genesis, evolution, and prediction of natural fractures in deep tight sandstones of China. *AAPG Bull.* 107 (10), 1687–1721. doi:10.1306/07052322120

frontiers | Frontiers in Earth Science

TYPE Original Research
PUBLISHED 13 September 2024
DOI 10.3389/feart.2024.1453098

OPEN ACCESS

EDITED BY
Gang Rao,
Southwest Petroleum University, China

REVIEWED BY
Jingshou Liu,
China University of Geosciences
Wuhan, China
Wei Yang,
China University of Petroleum, Beijing, China

*CORRESPONDENCE
Dongxi Liu,
ldxi@petrochina.com.cn
Hu Li,
lihu860628@126.com,
lihu@suse.edu.cn

RECEIVED 22 June 2024
ACCEPTED 16 August 2024
PUBLISHED 13 September 2024

CITATION
Tang W, Tuo C, Ma S, Yao Y, Liu D, Yang X, Yang L and Li H (2024) Shale reservoir characterization and implications for the exploration and development of the upper Permian Wujiaping Formation, Longmen–Wushankan area, eastern Sichuan Basin.
Front. Earth Sci. 12:1453098.
doi: 10.3389/feart.2024.1453098

Shale reservoir characterization and implications for the exploration and development of the upper Permian Wujiaping Formation, Longmen–Wushankan area, eastern Sichuan Basin

Wen Tang[1], Cong Tuo[1], Shaoguang Ma[2], Yongjun Yao[1], Dongxi Liu[1]*, Xinrui Yang[1], Licheng Yang[2] and Hu Li[3]*

[1]Chongqing Gas Field, PetroChina Southwest Oil and Gasfield Company, Chongqing, China, [2]Southwest Oil and Gas Field Company Development Department, Chengdu, China, [3]School of Economics, Sichuan University of Science and Engineering, Yibin, China

Recent exploration efforts have revealed significant industrial gas flow from the Wujiaping Formation marine shale in the Longmen–Wushankan area of the eastern Sichuan Basin, underscoring its considerable exploration potential. In this study, the reservoir characteristics and exploration potential of the Wujiaping Formation shale gas in this area are further evaluated. On the basis of well rock electrical properties, experimental analyses, and depositional and structural patterns in the eastern region, we characterize the reservoir properties and identify the primary factors controlling shale gas accumulation. The results indicate that the Wujiaping shale is characterized by a high organic matter content, favorable pore types, high porosity, and a high content of brittle minerals, which are conducive to subsequent development and fracturing. A positive correlation is observed between the total organic carbon (TOC) content, porosity, brittle mineral content, and shale gas content. The TOC content is strongly correlated with the gas content (the correlation coefficient is 0.75). The high shale gas yield of the Wujiaping Formation is attributed to a combination of favorable sedimentary environments, pore conditions, roof and floor conditions, and fracturing capabilities. However, compared with the Longmaxi Formation in the Sichuan Basin, the Wujiaping Formation shale is characterized by a lower porosity, thinner shale, and deeper burial, posing challenges for exploration and development. In this study, criteria for evaluating Wujiaping Formation shale gas are established, and four favorable exploration areas are identified. Overall, the Permian Wujiaping Formation marine shale in the Longmen–Wushankan area holds promising exploration and development

potential. Further exploration and an enhanced understanding of this formation will provide valuable guidance for future marine shale gas exploration and development in this area.

KEYWORDS

shale gas, reservoir characteristics, geological conditions, Nanya Syncline, Wujiaping Formation, Longmen-Wushankan area

1 Introduction

The southern Sichuan Basin has emerged as a focal point for shale gas exploration and production in China, highlighted by the recent establishment of a supergiant shale gas field with an annual production capacity exceeding 200×10^8 m^3 (Nie et al., 2018; Tang et al., 2019; Li, 2022). This remarkable development stems from successful exploration and production efforts targeting the Silurian Longmaxi Formation, which is widely recognized as a prolific shale gas reservoir. Success in the southern Sichuan Basin has prompted broader exploration activities, which have delineated shallow shale gas production zones (at depths less than 3,500 m) in key areas, such as Fuling, Weiyuan, Changning, and Zhaotong (Zhang et al., 2015; Chen et al., 2024). These shallower zones typically target organic-rich shales within the Longmaxi Formation and are characterized by favorable combinations of the total organic carbon (TOC) content, thermal maturity, thickness, and gas content. Building on these successes, exploration efforts have expanded into deeper portions of the Sichuan Basin (at depths of 3,500–4,500 m), with areas such as Luzhou showing significant promise for deep shale gas discoveries. These deeper plays often target the Longmaxi Formation and the underlying Permian Wujiaping Formation. The exceptional exploration and production potential of the marine shales in the Sichuan Basin and its adjacent areas can be attributed to a combination of favorable geological factors: depositional environments conducive to the accumulation of organic-rich sediments, suitable burial histories leading to optimal thermal maturation of organic matter, the presence of extensive overpressure, and the development of natural fractures enhancing permeability (Li et al., 2021; Yang et al., 2021; Yang et al., 2023). These factors, along with ongoing technological advancements in drilling and completion techniques, have positioned these marine shales as the primary target for shale gas exploration and production in China (Zou et al., 2022; Wang et al., 2022a).

Recent exploration has revealed that the HY1H and DY1H wells deployed and implemented by Sinopec and the CNPC in the Wujiaping Formation, respectively, yielded gas at rates of 8.9 $\times$ 10^4 m^3/d and 32.06 $\times$ 10^4 m^3/d, respectively (Feng et al., 2016; Zhu et al., 2019; Li, 2023; Smedley et al., 2024). This finding reveals new blocks and stratigraphic layers for marine shale gas exploration in the Sichuan Basin beyond the Ordovician Longmaxi Formation, Cambrian Danshancheng Formation, Cambrian Qiongzhusi Formation, Permian Dalong Formation, and Triassic Xujiahe Formation (Chen et al., 2019; Chen et al., 2021; Li et al., 2019; Dang et al., 2022; He et al., 2022a; He et al., 2022b; Jiang et al., 2023). Previous studies have investigated the distribution, sedimentary environment, and main factors controlling shale gas enrichment in the Wujiaping Formation in the western Hubei Province in depth (Zhai et al., 2019; Zeng et al., 2020; Wang et al., 2022b; Wang et al., 2024; Li et al., 2022a; Chen et al., 2022). Liang and Li (2021) clarified the geological conditions and exploration potential of shale gas in the Wujiaping Formation in eastern Chongqing–West Hubei, whereas Bao et al. identified the main factors controlling the high productivity of shale gas in the Hongxing area of western Hubei (Bao et al., 2023; Cao et al., 2021) defined the characteristics of organic-rich siliceous shale reservoirs in the Wujiaping Formation in the Lichuan area of western Hubei. However, the Wujiaping Formation in the Kaijiang-Liangping trough in the eastern Sichuan Basin has not received much attention. Existing studies have focused mostly on areas of non-deep-water carbonate facies along the Kaijiang-Liangping trough in northern and northwestern Sichuan (Liu and Xie, 2017; Zhang et al., 2022; Du et al., 2023) or have focused on the extension and expansion of the DY1H well. Limited detailed research has focused on the deep-water shale adjacent to the area of the DY1H well (He et al., 2021c). In this study, the characteristics of shale reservoirs in the Wujiaping Formation of the Nanya Syncline, eastern Sichuan Basin, are examined, drawing upon the electrical properties of well rocks and the sedimentary background of the eastern Sichuan Basin. In this research, the relationship between shale reservoir characteristics and the gas content is investigated, key factors controlling these reservoirs are identified, and they are compared to those of the Longmaxi Formation in the Sichuan Basin. By providing a clearer understanding of the Wujiaping Formation shale, in this study, insight into the exploration and exploitation of new shale gas resources in the Sichuan Basin is provided.

2 Geological setting

2.1 Structural setting

The eastern Sichuan Basin is part of the high and steep fold zone of eastern Sichuan, a relatively active tectonic area within the stable block. NE–SW-trending barrier-type folds have developed across the area from west to east. The Longtan and Wujiaping Formations are extensively developed in the eastern Sichuan Basin (Chen et al., 2020; Luo et al., 2024). These two formations represent isochronous heterotopic deposits. The Wujiaping Formation is exposed in northeastern Sichuan and adjacent areas and is characterized by marine carbonate rock deposits. In some parts of the eastern Sichuan Basin, thin to thick layers of shale and Emeishan basalts are interbedded and exposed (Wang et al., 2021). From the Guang'an–Chongqing area southeastward, the Wujiaping Formation gradually transitions into the Longtan Formation.

The study area is located mainly in the Nanya Syncline, which is a secondary structural unit of the high and steep fold zone in

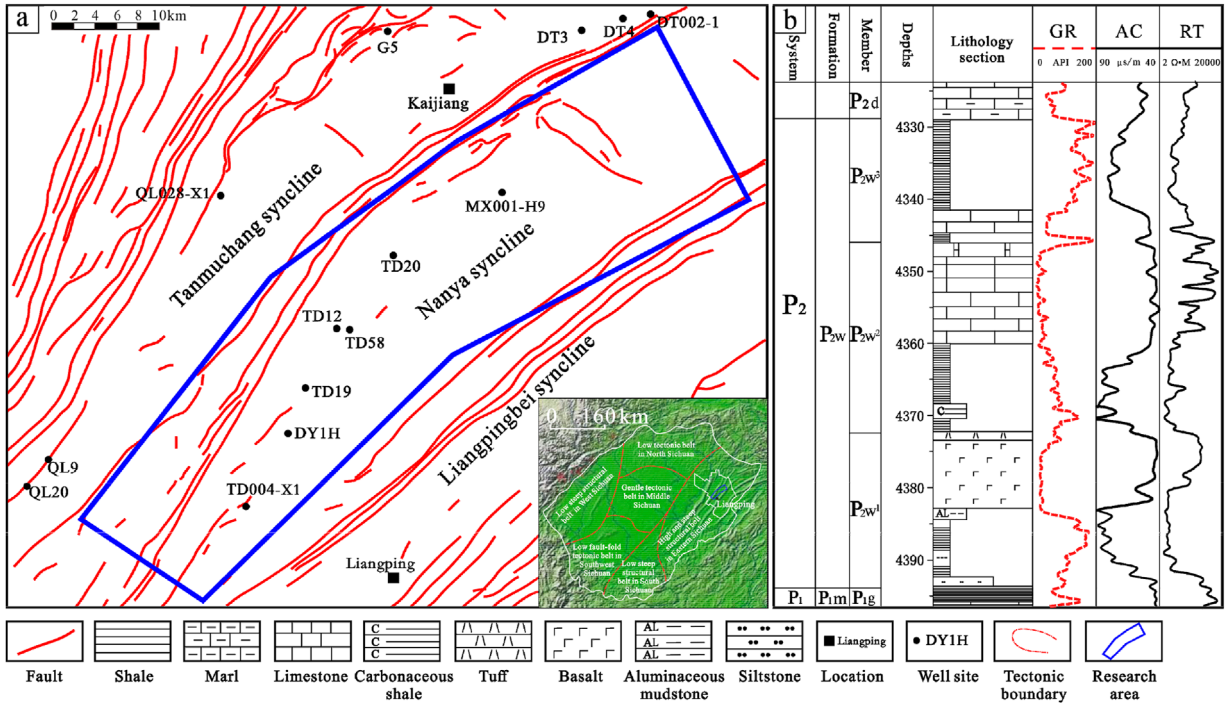

FIGURE 1
Structural location of the study area **(A)** and lithological profile of the Wujiaping Formation **(B)**.

the eastern Sichuan Basin. The structural position is stable. Within the syncline, burial depths range from 4,000 m to 5,500 m, with predominant NE–SW-trending structures. The structural width gradually decreases from north to south, forming an overall elongated shape with significant folding intensity. The Datianchi structural belt and the eastern boundary of the Nanmenchang structural belt mark the western boundary. The southern part features a concealed Longmen structure, whereas the northern part features a concealed Wushankan structure (Figure 1A). Owing to the impact of the Dongwu Movement, the top of the Maokou Formation in the study area has been completely eroded, with only remnants of the Gufeng Member remaining (Wang et al., 2021). With fluctuating sea levels, coastal swamp deposits with interbedded thin coal seams and volcanic rocks subsequently developed in the lower part of the Wujiaping Formation in the early late Permian. This unit is in disconformable contact with the underlying Gufeng Member of the Maokou Formation. The upper part of the Wujiaping Formation is characterized by interbedded shale and limestone, which developed predominantly in a shelf facies environment (Yang et al., 2021; Yang et al., 2023).

2.2 Stratigraphy

On the basis of the electrical, geochemical, and paleontological characteristics observed in well logs from wells in the study area, the Wujiaping Formation can be divided into three members. The shale and argillaceous mudstone at the base of the first member of the Wujiaping Formation unconformably overlie the carbonaceous and siliceous mudstone of the Gufeng Member (uppermost Maokou Formation) (Tang et al., 2020; Fan et al., 2024a; Li et al., 2024a). The shale and argillaceous mudstone (or thin coal seams) at the base of the second member of the Wujiaping Formation conformably overlie the volcanic rocks of the first member. The shale and marl at the base of the third member of the Wujiaping Formation conformably overlie the limestone with siliceous chert nodules of the second member. Finally, the marl and siliceous rocks at the base of the Changxing/Dalong Formation conformably overlie the shale and carbonaceous–calcareous–siliceous shale of the uppermost third member of the Wujiaping Formation (Figure 1B). The boundaries between these three members are distinct and easily recognizable, supporting the validity of this subdivision.

3 Samples and methods

3.1 Samples

In this study, we conducted core observations of well DY1H and collected more than 80 core samples. These core samples were subjected to thin section and scanning electron microscopy (SEM) observations, total organic carbon (TOC) analysis, porosity measurements, X-ray diffraction (XRD) analysis, and gas content determination (Table 1). All the experiments were conducted at the Analytical Laboratory of the Exploration and Development Research Institute of PetroChina Southwest Oil & Gasfield Company.

TABLE 1 Test items and samples.

Test item	Test instrument	Sample number
Shale slice identification	PH100-PG-B	10
TOC	LECO CS230	14
Porosity	HEP-P	18
SEM	TESCAN CLARA	9
XRD	TTR-08070518	13
Shale isothermal adsorption experiment	H-Sorb X600	12

3.2 Methods

3.2.1 TOC analysis

TOC analysis was conducted via the acid dissolution method. The samples were ground to particle sizes smaller than 0.2 mm and then heated to 60°C–80°C after 3 mL of dilute hydrochloric acid was added (Zhang et al., 2023a; Tan et al., 2020). After a thorough reaction, the samples were washed with water and dried. The TOC content was subsequently measured via a LECO CS230 carbon-sulfur analyzer. The measurement method followed the Chinese National Standard GB/T19145-2003 "Determination of TOC in Sedimentary Rocks."

3.2.2 SEM observations

SEM was used to characterize the pore structures and types in the shale samples (Li et al., 2024b). The procedure involved the following steps: shale samples were cut into 10 mm × 5 mm × 5 mm cubes along the axial line via a water-free cutting technique and then embedded in cubic epoxy resin molds. Next, the samples were polished under vacuum conditions using a high-energy argon ion beam (Leica EM RES 102). Finally, the polished samples were imaged and analyzed via SEM (Zhao et al., 2022; Zhang et al., 2023b).

3.2.3 Characterization of the whole-rock mineral composition

A Rigaku X-ray diffractometer (Model TTR, 08070158) was used for mineral composition analysis (Shan et al., 2022; Xia et al., 2023). The steps involved the following: 50 g of the prepared sample was crushed to a size of 1 mm via an iron mortar. The crushed sample (50 g) was then placed in a porcelain mortar and mixed with a small amount of distilled water, followed by repeated grinding. The mixture was transferred to a beaker and mixed with 500 mL of distilled water. After stirring for approximately 10 min, the mixture was allowed to settle for at least 8 h. The clay fraction of the suspension (<2 μm) was extracted via a centrifuge. Approximately 40 mg of the clay fraction was mixed with 7 mL of distilled water and stirred thoroughly. The mixture was then spread evenly on a frosted glass slide and allowed to air dry. Finally, the sample was scanned via XRD to determine the mineral composition. The analysis followed the standard procedure outlined in the "Method for X-ray Diffraction Analysis of Clay Minerals in Sedimentary Rocks" (SY/T5163-2018), published by the China National Petroleum Corporation.

3.2.4 Isothermal adsorption

An isothermal adsorption experiment was conducted in which the collected shale samples were crushed and heated to remove adsorbed shale gas (Shan et al., 2018; Qi et al., 2022). The shale samples were subsequently placed in a sealed container. The temperature was kept constant, and the pressure inside the container was gradually increased. The amount of natural gas adsorbed by the experimental samples was observed and measured. Finally, the experimental data were fitted via the Langmuir equation to obtain the isothermal adsorption curve. In this study, nitrogen isothermal adsorption was employed to analyze the pore size distribution. This method effectively characterizes mesoporous structures with a measurement range of 1.5–100 nm and a sensitivity range of 2–50 nm.

4 Results

4.1 Organic matter abundance

Organic matter abundance is a crucial indicator for evaluating the hydrocarbon generation potential of shale (Dessouky, 2024; Xu et al., 2024). The TOC content was used to evaluate the abundance of organic matter in the shale. According to the experimental results, 64% of the samples presented TOC values exceeding 5%, whereas 28.5% had TOC values less than 2%. Notably, wells TD19 and TD58 had the highest TOC values, reaching 7.4%. The Wujiaping Formation exhibited high TOC contents, indicating significant hydrocarbon generation potential. Additionally, the TOC values in the deep-water shelf facies samples were significantly higher than those in the shallow-water shelf facies samples. The TOC value in well TD19 (7.4%), located in the deep-water shelf facies, was 5.2% higher than the TOC value in well TD4 (2.2%), located in the shallow-water shelf facies. The average TOC content in the deep-water shelf facies was 6.2%, whereas the average TOC content in the shallow-water shelf facies was 1.8%, indicating a significant difference (Figure 2A). From a vertical perspective, the TOC enrichment and high values in the third member of the Wujiaping Formation were significantly greater than those in the other members. From a planar distribution perspective, the TOC contents ranged from 3.0% to 7.0%, and the high-TOC zones were consistent with the morphology of trough development, with the average TOC

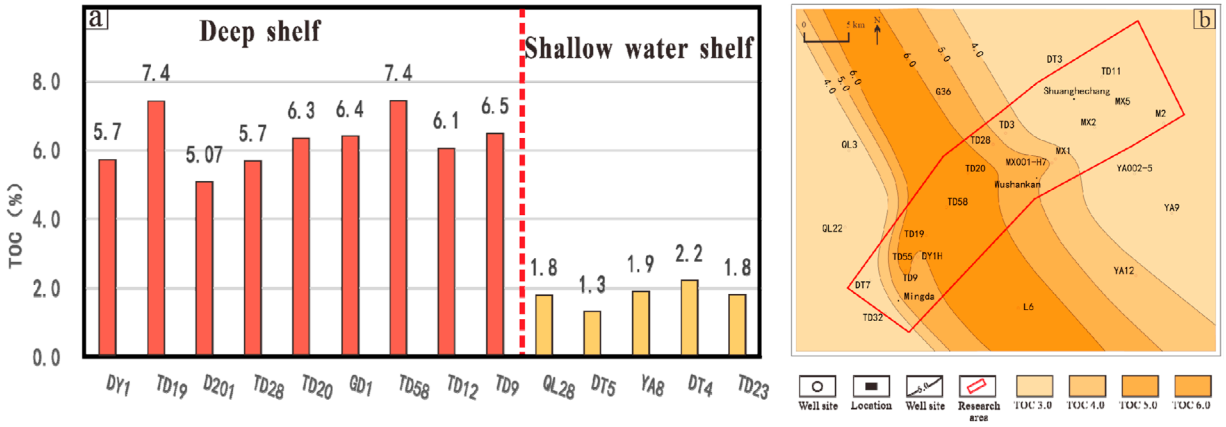

FIGURE 2
TOC contents shown in column format and plan view of the study area. **(A)** TOC contents of the main wells in the study area; **(B)** TOC contents of the third member of the Wujiaping Formation in the study area.

generally exceeding 4.0% within the trough (Figure 2B). Overall, the TOC content in the study area rapidly changed, with high values occurring along the trough, indicating a significant patchy trend of enrichment.

4.2 Spatial and physical characteristics of the reservoir

Three types of nanoscale pores were observed in the third member of the Wujiaping Formation: inorganic pores, organic pores, and microfractures (Figure 3). In accordance with the International Union of Pure and Applied Chemistry (IUPAC) pore diameter classification standard, these pores are classified into micropores (diameters < 2 nm), mesopores (diameters 2–50 nm), and macropores (diameters > 50 nm) (Guo et al., 2019; Li, 2022). The pores exhibited irregular shapes, with elliptical and circular shapes being the most common (Figure 3).

The third member of the Wujiaping Formation in the study area was dominated by meso- and macropores, with a pore size distribution ranging from 20 to 200 nm (Figure 4B). The average porosity values were between 4.0% and 5.0%. Significant high-value zones, similar in morphology to the trough, were observed in the central and southern areas (Figure 4C). Additionally, the correlation between porosity and permeability was weak when the porosity was less than 6%. However, the correlation became more prominent when the porosity exceeded 6%, and the permeability was greater than 520 nD, reaching a correlation coefficient of 0.98 (Figure 4A). This suggests that the shale in the study area has a strong gas storage capacity with good pore connectivity.

4.3 Brittle mineral content

The variation in the brittle mineral content directly affects the mechanical properties of shale. A higher brittle mineral content indicates that shale is more prone to fracturing under the same stress conditions, leading to the formation of fractures, which are beneficial for hydraulic fracturing and gas desorption (Yin et al., 2018a; Yin et al., 2018b; Li, 2022). The brittle mineral content in the study area was calculated via the following equation.

$$V_{BM} = \left(V_{quarz} + V_{calcite} + V_{pyrite}\right) / \left(V_{quarz} + V_{calcite} + V_{pyrite} + V_{clay}\right)$$

where V_{BM} is the brittle mineral content (%), V_{quartz} is the silicate content (%), $V_{calcite}$ is the carbonate content (%), V_{pyrite} is the pyrite content (%), and V_{clay} is the clay content (%).

The shale in the third member of the Wujiaping Formation in well DY1H was primarily composed of quartz, carbonate, and clay minerals, with minor amounts of feldspar and pyrite (Figure 5A). Planarly, a high-value zone formed around well DY1H, with values exceeding 80%. Vertically, the shale in the Wujiaping Formation exhibited some heterogeneity, with silicate minerals consistently exceeding 40%. Statistical analysis revealed that the brittle mineral contents ranged from 60.1% to 87.2%, with an average value of 77.54% (Figure 5B).

4.4 Gas content

The gas content is the most direct parameter for evaluating the commercial viability of shale gas reservoirs. The total gas content in the main wells of the study area was generally high, averaging approximately 3.5 m^3/t. The gas contents in wells DY1H and G18 reached 6.3 m^3/t and 4.9 m^3/t, respectively (Figure 6A). The third member of the Wujiaping Formation had the highest total gas content, with that in DY1H reaching 9.3 m^3/t (Figure 7). Planarly, the total gas content reached high values along the trough zone, exhibiting a banded distribution (Figure 6B).

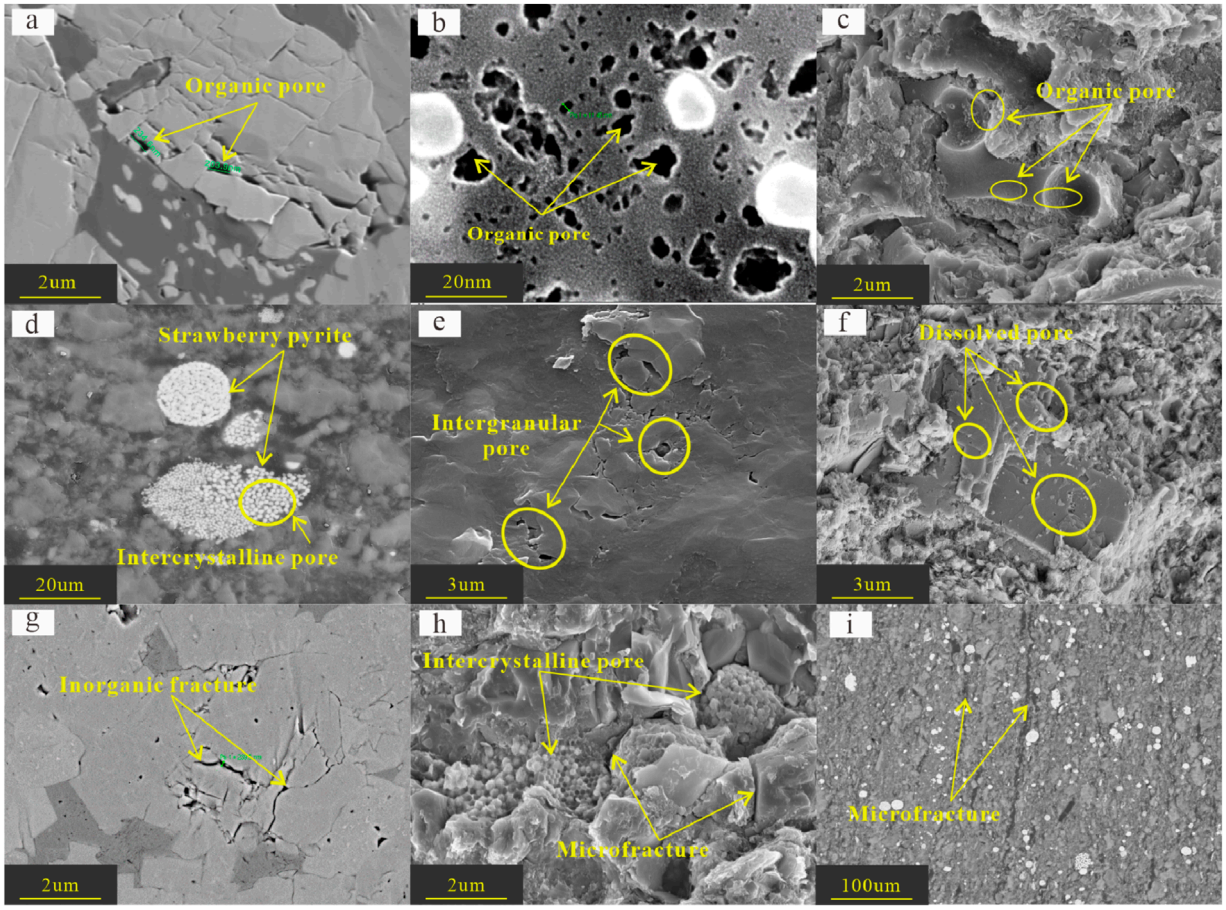

FIGURE 3
Micropore types in shale reservoirs of the Wujiaping Formation. **(A)** DY1H, 4,335.76 m, organic pores; **(B)** DY1H, 4,338.21 m, abundant interconnected organic pores developed from organic matter; **(C)** D201, 4,567.71 m, rounded organic pores; **(D)** DY1H, 4,337.20 m, intercrystalline pores developed in strawberry-shaped pyrite; **(E)** DY1H, 4,337.20 m, intergranular micropores, and microfractures; **(F)** D201, 4,568.53 m, a few dissolution pores developed in microcrystalline dolomite; **(G)** FT1, 4,578 m, microfractures; **(H)** D201, 4,564.12 m, concentrated distribution of strawberry-shaped pyrite, with microfractures developed at the edges; **(I)** DY1H, 4,334.15 m, bedding microfractures filled with organic matter.

5 Discussion

5.1 Main factors controlling shale gas reservoirs

Shale gas, a hydrocarbon resource found in organic-rich shale layers or interlayers, exists in free, adsorbed, or dissolved states, respectively, and migrates *in situ* or over short distances to form reservoirs (Tian et al., 2024; Fan et al., 2024; Lascelles, 2024). In the Longmen–Wushankan area of the eastern Sichuan Basin, deepwater shelf shale gas within the Wujiaping Formation is significantly influenced by the TOC content, porosity, and brittle mineral content. The presence of clay minerals in the lower Wujiaping Formation results in high experimental porosity but low effective porosity in the clay-rich shale. Consequently, the correlation between the porosity and gas content in the Wujiaping Formation is only 0.04 (Figure 8A). However, within the third member of the Wujiaping Formation, a positive correlation of 0.55 is observed between the porosity and shale gas content (Figure 8B).

Similarly, the high clay mineral content and low brittle mineral content in the lower Wujiaping Formation lead to a weak correlation of 0.22 between the brittle mineral and gas contents for the entire formation (Figure 8C). In contrast, the third member has a stronger positive correlation of 0.60 between the brittle mineral content and gas content (Figure 8D), suggesting that the high brittle mineral content in this member facilitates fracture development, thereby increasing shale gas accumulation. A strong positive correlation exists between the TOC content and gas content in the shale gas, with correlations of 0.75 and 0.73 for the entire Wujiaping Formation and its third member, respectively (Figures 8E, F).

Considering the three influential factors, the presence of clay minerals in the lower Wujiaping Formation means that a positive correlation with the gas content is observed only for the porosity and brittle mineral content of the third member. However, the TOC content positively correlates with the gas content throughout the Wujiaping Formation. Therefore, while the porosity, brittle mineral content, and TOC content are positively correlated with the shale gas content in the Wujiaping Formation, the TOC content is the

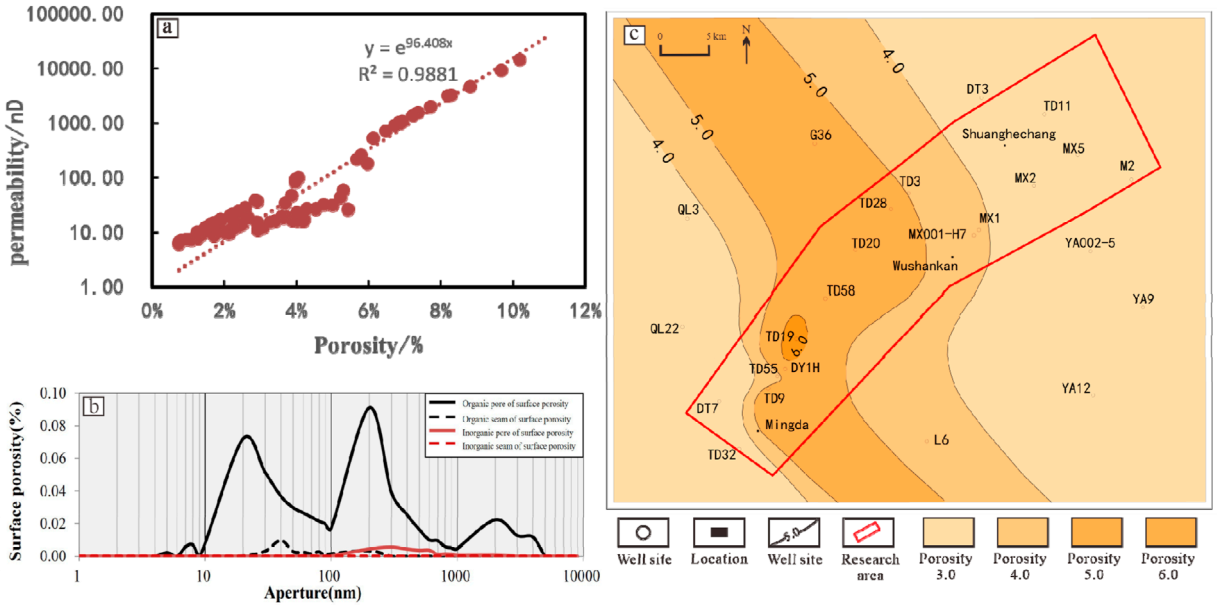

FIGURE 4
Shale porosity and distribution of the Wujiaping Formation. **(A)** Correlation between shale porosity and permeability in well DY1H; **(B)** Pore size characteristics of the shale samples; **(C)** Planar distribution of porosity.

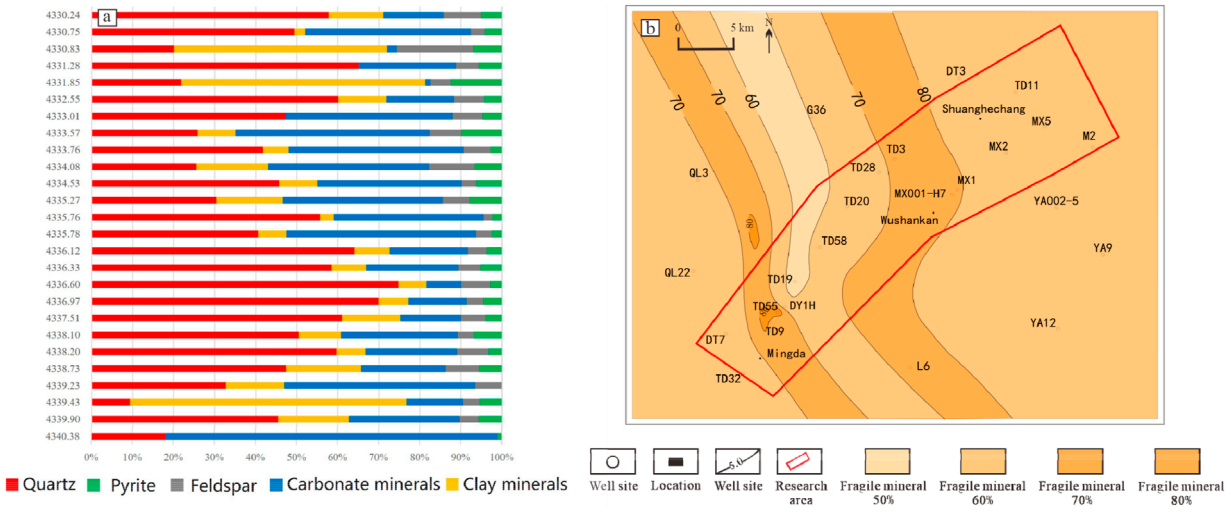

FIGURE 5
Characteristics and planar distribution of brittle minerals in the third member of the Wujiaping Formation. **(A)** Mineral composition in well DY1H; **(B)** Contour map showing the brittle mineral distribution.

most influential factor. This suggests that the TOC content is a key factor driving the high shale gas content observed in the Wujiaping Formation.

5.2 Main factors controlling shale gas enrichment and high yield

Multiple factors influence the enrichment and preservation of shale gas (Li et al., 2022b). The study area is located in the depositional center of the Kaijiang-Liangping Trough in the eastern Sichuan Province and is characterized by deepwater shelf facies. This deepwater environment, which was typically anoxic and reducing, positively impacted the enrichment and preservation of shale gas. Within the study area, the TOC content exhibits noticeable heterogeneity and longitudinal differentiation. Shales deposited in the trough's deepwater shelf facies display relatively high TOC contents, particularly those formed in the deepwater reducing environment of the third member of the Wujiaping Formation. These findings suggest that the deepwater shelf sedimentary

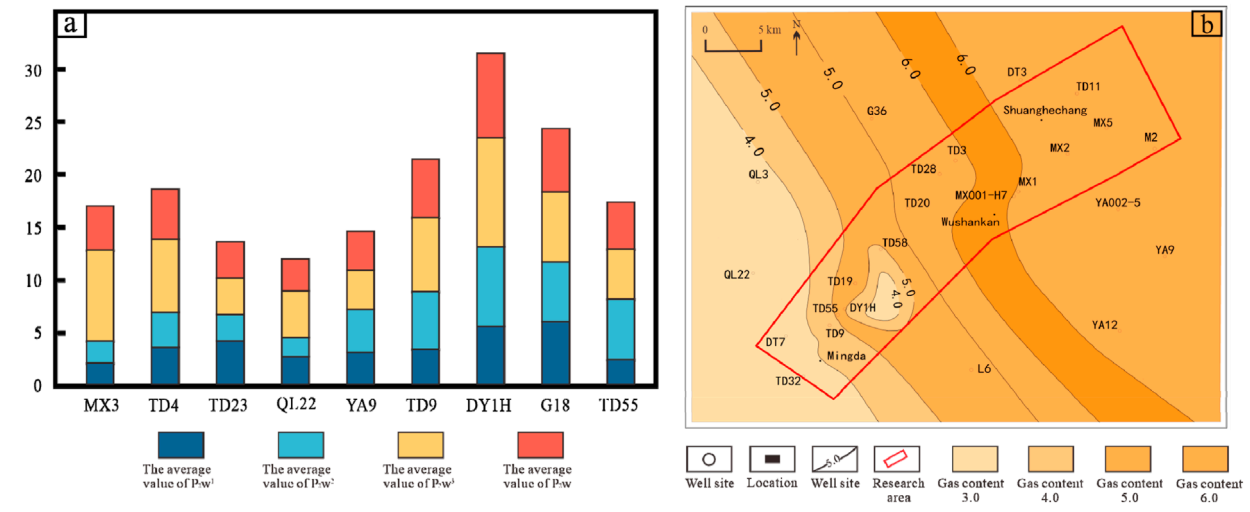

FIGURE 6
Column diagram of the gas contents in the study area and isogram of the gas contents of the third member of the Wujiaping Formation. **(A)** Column of the gas contents of some wells in the study area; **(B)** Isocontour plot of the gas contents in the study area.

environment provided the conditions for the development of organic-rich shales.

The Wujiaping Formation in the study area has average porosities ranging from 4% to 5%. These porosities, characterized by diverse pore types, contribute to shale gas preservation. Furthermore, the Wujiaping Formation's roof and floor lithologies are crucial for gas preservation. The roof comprises dense limestone or marl belonging to the Dalong or Changxing Formations, whereas the floor consists of thickly layered limestone of the Maokou Formation in the eastern area. These bounding layers provide effective sealing capacity, sandwiching the Wujiaping Formation shale and further facilitating shale gas preservation.

Finally, the fracturing capacity is crucial for achieving high shale gas yields. The Wujiaping Formation shale contains abundant brittle minerals, as exemplified in well DY1H, and it has an average brittle mineral content of 77.54%. This high brittle mineral content enhances the effectiveness of later-stage fracturing operations, ultimately increasing shale gas production.

In summary, the high yield of shale gas in the Wujiaping Formation is controlled by a combination of factors: the sedimentary environment, pore conditions, roof and floor conditions, and fracturing ability. The sedimentary environment provides the material basis, pore conditions provide reservoir space, favorable preservation conditions govern shale gas enrichment, and the fracturing ability enables high production rates.

5.3 Comparison with shale gas in other areas of the Sichuan Basin

The brittle mineral content affects the effectiveness of hydraulic fracturing. The Wujiaping Formation shale has a high overall brittle mineral content, reaching a maximum of 94%, which is significantly higher than those in other areas, such as western Chongqing (maximum of 68%), Luzhou (maximum of 72%), and Weiyuan (maximum of 71%) (Figure 9A). The range of TOC contents of the Wujiaping Formation is broad, with contents varying from 2.8% to 6.7%, with an average exceeding 4.0% within the trough. These values are also significantly higher than those in other areas in the Sichuan Basin, indicating that the Wujiaping Formation has a high TOC content, which is conducive to hydrocarbon generation and results in high-quality shale gas (Figure 9B). The organic matter maturity (Ro) of the Wujiaping Formation is comparable to that in other areas (Figure 9D). However, in terms of the porosity, shale thickness, and burial depth, the Wujiaping Formation shale is slightly inferior to the Longmaxi Formation shale. The porosity values of the Wujiaping Formation shale range from 5.6% to 6.8%, which are slightly lower than those in areas such as Changning and Weiyuan (Figure 9C). The shale thickness is generally less than that of the Longmaxi Formation. Although the Wujiaping Formation shale is widely distributed, it interlayers with limestone vertically, resulting in significant variations in shale thickness. The single-layer shale thicknesses range from 1 to 45 m (generally less than 20 m), which are less than the 20–66 m thickness of the Longmaxi Formation (Figure 9E). With respect to the burial depth, the area of the Longmaxi Formation with mature rocks is buried between 2,000 and 4,500 m, with a relatively small thickness. However, the Wujiaping Formation in the eastern Sichuan Basin is generally buried between 3,000 and 6,000 m. The study area predominantly comprises deep shale formations buried at depths exceeding 4,500 m, posing significant challenges for exploration and development (Figure 9F).

The gas content is a direct indicator of shale gas production. The adsorbed gas content in the third member of the Wujiaping Formation in well DY1H is 4.2 m^3/t, which is higher than that in the Longmaxi Formation in areas such as Changning (1.7 m^3/t

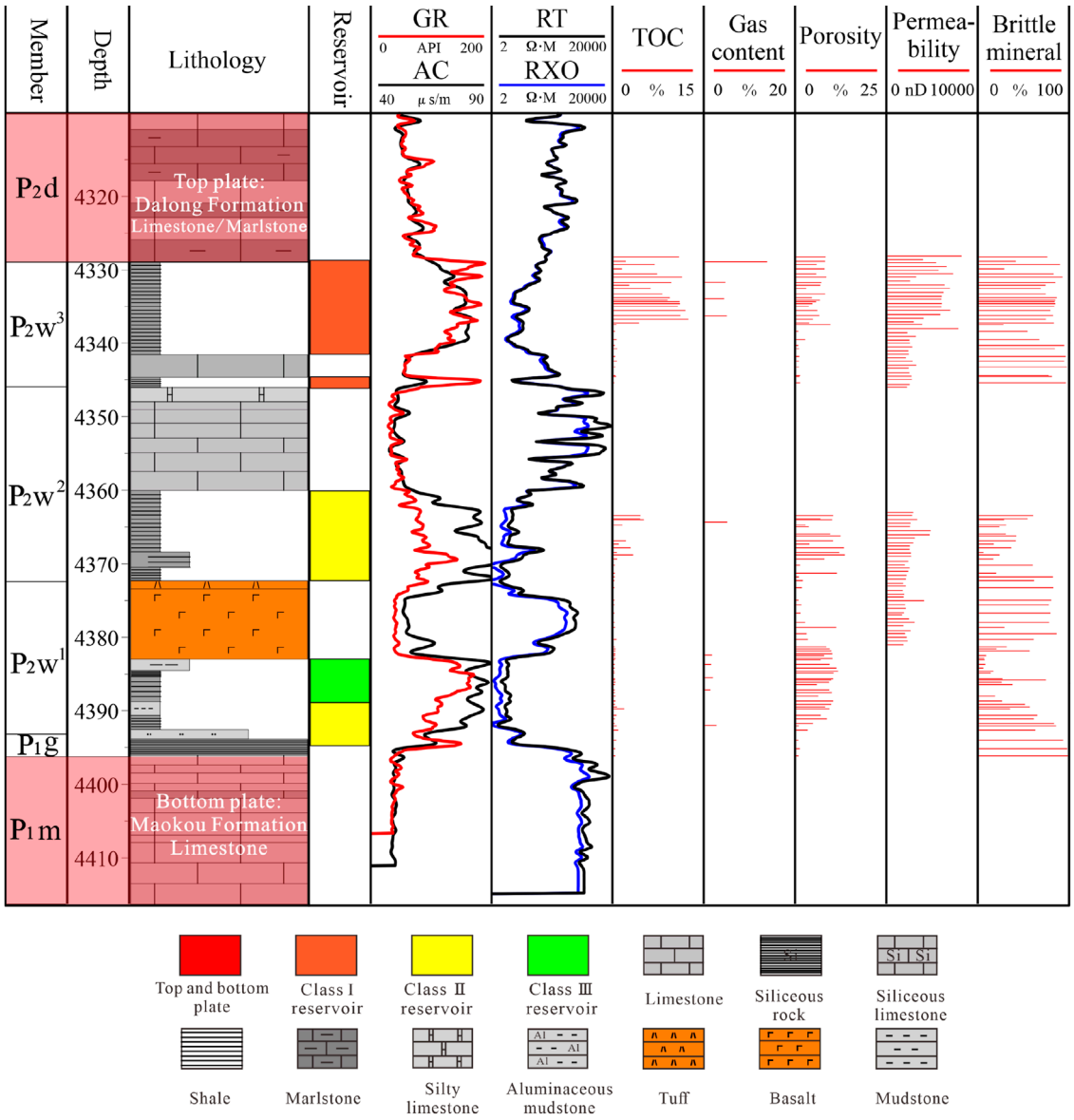

FIGURE 7
Comprehensive gas column of reservoir parameters in well DY1H.

to 3.4 m^3/t), Luzhou (1.5 m^3/t to 2.0 m^3/t), and Weiyuan (2.2 m^3/t to 2.5 m^3/t), indicating that the shale reservoir in the third member of the Wujiaping Formation has a strong adsorption capacity. The free gas content is 6.2 m^3/t, which is slightly higher than those in Changning (2.5 m^3/t to 4.4 m^3/t), Luzhou (2.4 m^3/t to 4.7 m^3/t), and Weiyuan (4.3 m^3/t to 6.1 m^3/t). The total gas contents range from 7.2 m^3/t to 10.67 m^3/t, which are significantly greater than that of the Longmaxi Formation. Overall, the gas content in the third member of the Wujiaping Formation in the study area is relatively high, with significant exploration potential (Figure 10).

In general, the shale of the Permian Wujiaping Formation in the eastern Sichuan Basin has brittle mineral contents as high as 94% and a high organic matter content, which is conducive to shale gas formation. However, compared with the Longmaxi Formation, the Wujiaping Formation has no obvious advantage in terms of organic matter maturity, and it has a slightly poorer porosity, smaller shale thickness, and deeper burial depth, so exploration and development are more difficult (Yang et al., 2022; Du et al., 2022). However, the shale reservoir in the third member of the Wujiaping Formation has a strong adsorption capacity, and the total gas content is higher than that in the Longmaxi Formation, so the study interval has great development potential.

5.4 Classification criteria for favorable zones

Currently, the Longmaxi Formation shale in areas such as Weiyuan, Changning, Luzhou, and western Chongqing in the

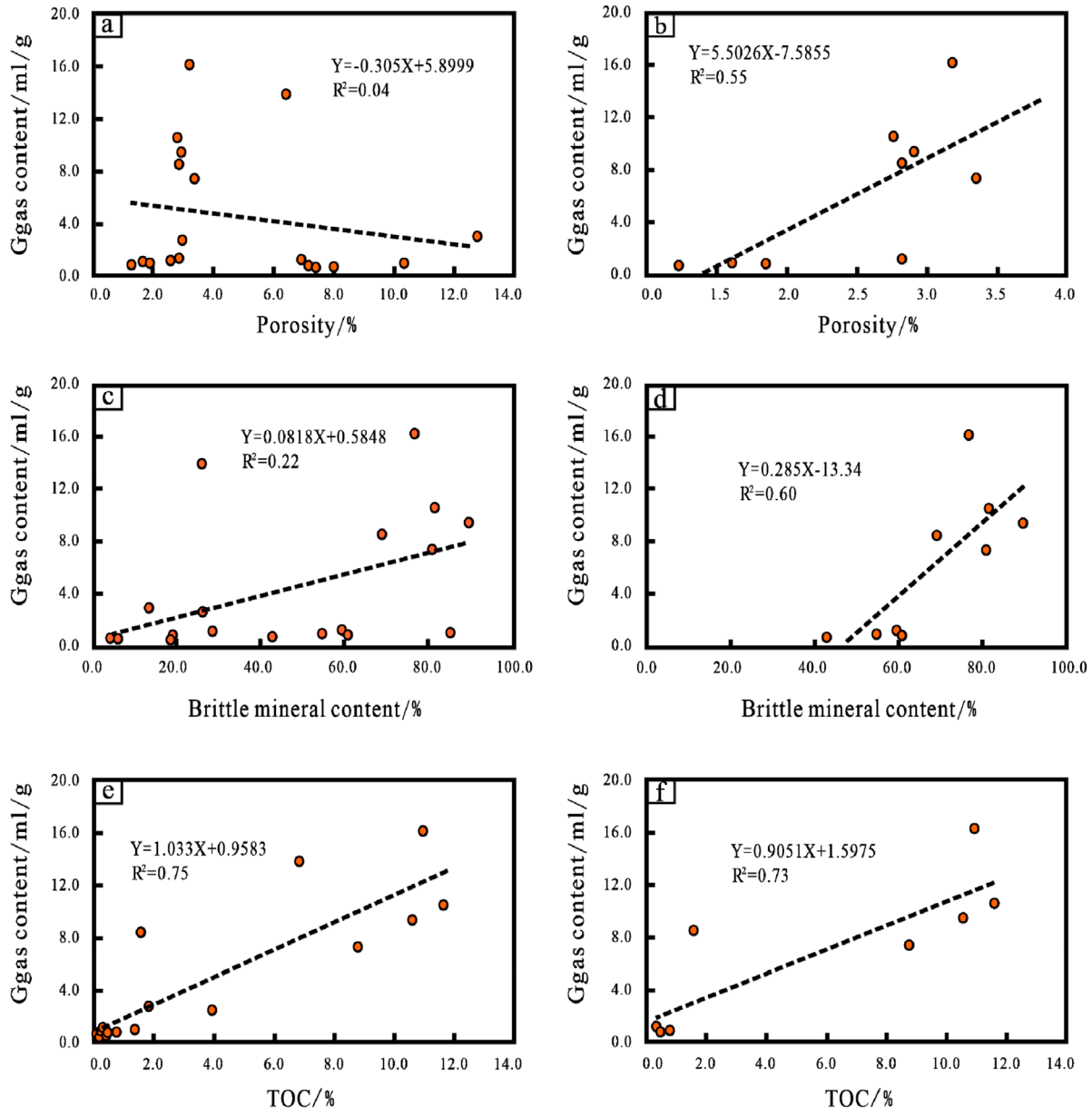

FIGURE 8
Relationship between reservoir parameters and the gas content. **(A)** Porosity and gas content of the Wujiaping Formation. **(B)** Porosity and gas content of the third member of the Wujiaping Formation. **(C)** Brittle mineral content and gas content of the Wujiaping Formation. **(D)** Brittle mineral content and gas content of the third member of the Wujiaping Formation. **(E)** TOC content and gas content of the Wujiaping Formation. **(F)** TOC content and gas content of the third member of the Wujiaping Formation.

Sichuan Basin exhibits promising exploration results, with some areas demonstrating good value for commercial exploration and development (Fan et al., 2020). The Wujiaping Formation has certain similarities with the Longmaxi Formation shale. Therefore, we can utilize the evaluation criteria for the Longmaxi Formation shale to conduct a comprehensive assessment of shale gas.

The CNPC Southwest Oil & Gasfield Company has classified the Longmaxi Formation shale on the basis of well logging evaluation via four categories: source rocks, physical properties, gas contents, and rock mechanics. The classification used four indicators: total organic carbon (TOC), porosity, free and adsorbed gas contents, and brittle mineral content. Three reservoir types were defined: Type I reservoirs (TOC contents >2%, porosity values >5%, gas contents >2 m^3/t, and brittle mineral contents >55%); Type II reservoirs (TOC contents between 1% and 2%, porosity values between 3% and 5%, gas contents between 1 m^3/t and 2 m^3/t, and brittle mineral contents between 35% and 55%); and Type III reservoirs (TOC contents <1%, porosity values <3%, gas contents <1 m^3/t, and brittle mineral contents <35%).

Bai et al. (2023) evaluated the shale gas in the Wujiaping Formation of the northeastern Sichuan Basin. They established favorable zones of Type I and Type II reservoirs based on the

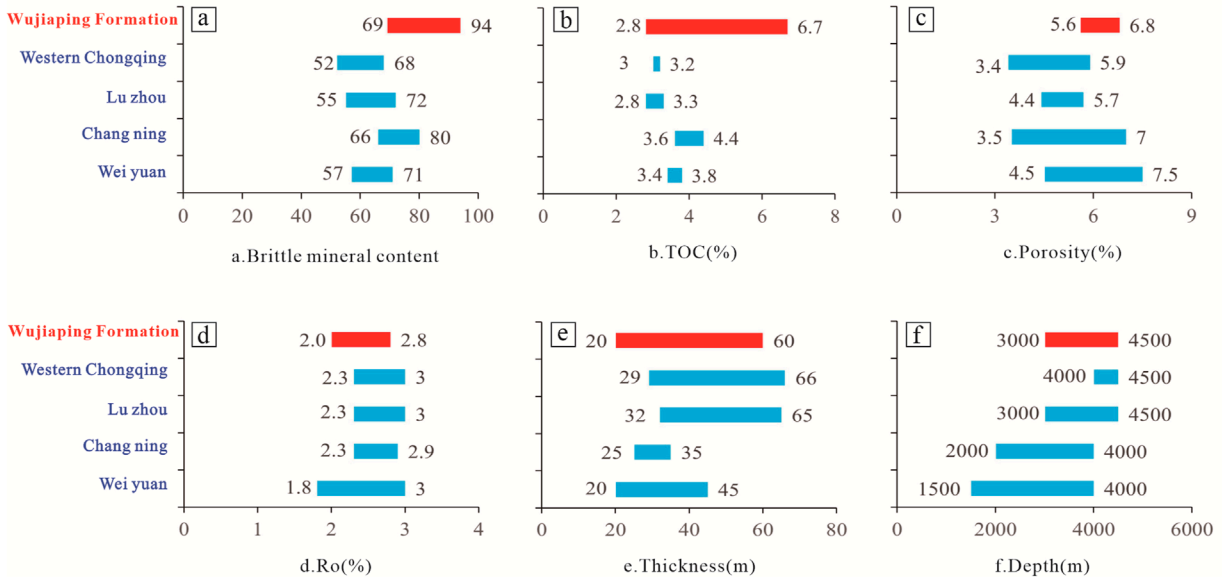

FIGURE 9
The characteristics of the Wujiaping Formation in the eastern Sichuan Basin are compared with those of the Longmaxi Formation shale in other major areas of the Sichuan Basin. **(A)** Brittle mineral content; **(B)** TOC; **(C)** Porosity; **(D)** Ro; **(E)** Thickness; **(F)** Burial depth.

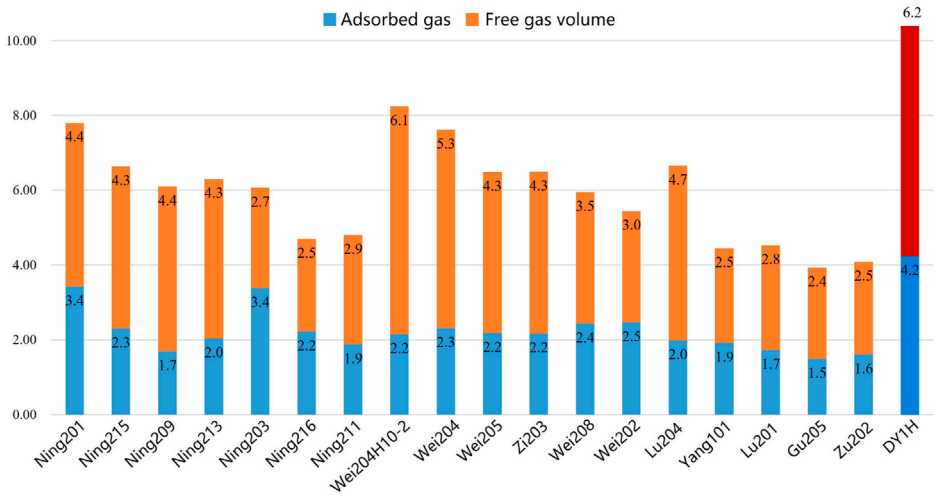

FIGURE 10
Gas content of the Wu3 Member in the study area compared with that of the Longmaxi Formation shale in other areas of the Sichuan Basin.

shale effective thickness, TOC, Ro, gas content, distance to the erosion line, and burial depth (Table 2). The Type I favorable zone characteristics are as follows: effective thickness >20 m, TOC >2%, Ro >1.1%, gas content >1 m^3/t, distance to the erosion line >5 km, burial depths between 1,000 and 4,000 m; the Type II favorable zone characteristics are as follows: effective thickness >10 m, TOC >1%, Ro >1.1%, gas content >0.7 m^3/t, distance to the erosion line >5 km, burial depths between 4,000 and 4,500 m.

Organic-rich shale, deposited in favorable sedimentary environments, is widely distributed in the Longmen–Wushankan area. The overall depositional setting was a shelf environment, with the deep-water shelf facies of the third member of the Wujiaping Formation being the most favorable for shale gas. Multiple factors influence the enrichment and preservation of shale. In this study, evaluation criteria for high-quality shale in the study area are established on the basis of multiple indicators, including source rocks, physical properties, rock mechanics, and gas contents. The criteria are based on the evaluation standards for shale gas in the Longmaxi Formation in the Sichuan Basin and Bai et al.'s evaluation standards for shale gas in the Wujiaping Formation in the northeastern Sichuan Basin, while also incorporating industry standards NB/T 10398-2020 (Table 3).

TABLE 2 Optimization criteria for the favorable area of shale gas in the Wujiaping Formation.

Major parameter	Class I favorable area	Class II favorable area
Effective shale thickness (m)	>20	>10
TOC (%)	>2	>1
Ro (%)	>1.1	
Gas content (m^3/t)	>1	>0.7
Distance denudation line (km)	>5	
Depth (m)	1,000–4,000	4,000–4,500

TABLE 3 Classification and evaluation criteria for high-quality shale from the Wujiaping Formation.

Major parameter	Class I favorable area	Class II favorable area
TOC (%)	≥3	≥2
Brittle mineral content (%)	≥60	≥40
Thickness (m)	≥20	≥10
Gas content (m^3/t)	≥3	≥2
Porosity (%)	≥5	≥4
Ro	≤3.5	≤3.7
Configuration	The fold strength is low	Moderate fold strength

5.5 Prospects of shale gas exploration and development

Within the "Kaijiang–Liangping Trough," the favorable zone of the Wujiaping Formation (buried between 4,500 and 5,000 m) can be divided into four synclinal belts from west to east: the Tanmuchang Syncline, the Nanya Syncline, the Liangping North Syncline, and the Yunyang–Wanxian Syncline (Yang et al., 2023). The shale reservoir in the deep-water shelf facies in the Wujiaping Formation in the Nanya Syncline, which is the southeastern end of the "Kaijiang–Liangping Trough," exhibits stable lateral continuity. The third member of the Wujiaping Formation shale has good gas contents, high TOC contents, good compressibility, and high porosity. Organic-rich shale, with a generally low drilling density, is widely distributed in this area. The marine shale gas in the Wujiaping Formation in the Nanya Syncline has good exploration and development prospects. The area shallower than 5,000 m in the Wujiaping Formation covers more than 450 km^2, with estimated geological resources of approximately $1{,}650 \times 10^{12}$ m^3.

Considering factors such as reservoirs, engineering, preservation, and surface conditions, the favorable zone in the Longmen–Wushankan area can be divided into four (1~4) units of development (Figure 11).

1) Located on a structural slope in the southwestern portion of the Nanya Syncline, this unit contains well DY1H at its center. It is characterized by a single secondary fault, indicating low fracture risk. The reservoir has consistent thicknesses of 15–20 m, a stable distribution, and burial depths ranging from 4,000 to 4,500 m. 2) Located on a structural slope in the northwestern portion of the Nanya Syncline, this unit is bound to the west by the Datianchi #1 fault. Two secondary faults are present in the northeast. The reservoir is characterized by a consistent thickness greater than 20 m, a stable distribution, and burial depths ranging from 4,000 to 5,000 m. 3) Located within the main stable area of the Nanya Syncline, this unit is characterized by a relatively gentle structural setting. With the Nanmenchang #1 fault as its eastern boundary, this unit is not internally faulted. The reservoir has consistent thicknesses of 15–20 m and is buried at depths ranging from 4,300 to 5,000 m. 4) Located in the northeastern portion of the Nanya Syncline, this unit is characterized by a relatively gentle structural setting within the stable synclinal area. Two secondary faults are present at the northeastern margin. Burial depths predominantly range from 4,300 to 5,000 m, locally exceeding 5,000 m.

6 Conclusion

(1) The Wujiaping Formation shale in the Longmen–Wushankan area exhibits favorable characteristics for shale gas accumulation, including high TOC contents, abundant pore

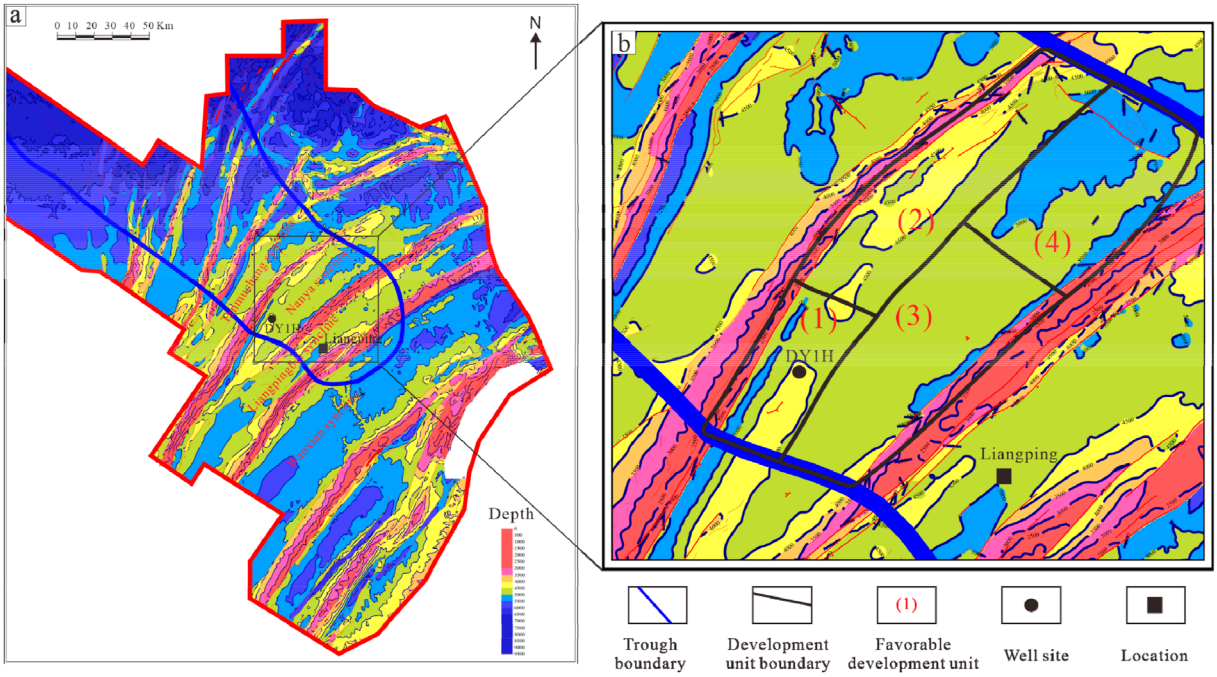

FIGURE 11
Location of the surface structure **(A)** and division of favorable areas for shale gas exploration **(B)** in the Nanya Syncline.

types (organic pores, inorganic pores, and microfractures), high porosities, and significant brittle mineral contents. These properties are particularly pronounced within the third member of the Wujiaping Formation, highlighting its potential for shale gas exploration and development. While positive correlations exist between the TOC content, porosity, brittle mineral content, and shale gas content, the TOC content emerges as the dominant controlling factor.

(2) The high shale gas yield observed in the Wujiaping Formation is attributed to a combination of factors: a favorable sedimentary environment (providing source material), suitable pore characteristics (governing storage capacity), effective roof and floor conditions (enhancing gas preservation), and good fracability (enabling high production rates). However, compared with the well-established Longmaxi Formation in the Sichuan Basin, the Wujiaping Formation presents challenges because of its lower porosity, reduced thickness, and deeper burial depths.

(3) In this study, a framework for evaluating the Wujiaping Formation shale gas potential is established, drawing upon existing evaluation standards for both the Longmaxi and Wujiaping Formations and incorporating the unique characteristics of the study area. In this evaluation, four favorable exploration areas within the Nanya Synclinorium are identified, highlighting its potential for future exploration. Development strategies should leverage the high-yield model of well DY1H, focusing on replicating its design within a pilot test platform for a well group and gradually expanding development within a small, representative test area.

Data availability statement

The original contributions presented in the study are included in the article/supplementary material, further inquiries can be directed to the corresponding authors.

Author contributions

WT: Conceptualization, Data curation, Formal Analysis, Methodology, Resources, Writing–original draft. CT: Conceptualization, Data curation, Formal Analysis, Methodology, Resources, Writing–original draft. SM: Conceptualization, Data curation, Methodology, Resources, Writing–review and editing. YY: Data curation, Formal Analysis, Investigation, Methodology, Resources, Writing–review and editing. DL: Conceptualization, Formal Analysis, Methodology, Resources, Writing–original draft, Writing–review and editing. XY: Conceptualization, Formal Analysis, Resources, Writing–review and editing. LY: Conceptualization, Data curation, Resources, Writing–review and editing. HL: Conceptualization, Methodology, Investigation, Project administration, Writing–original draft, Writing–review and editing.

Funding

The authors declare that financial support was received for the research, authorship, and/or publication of this article. This study was financially supported by the scientific research project of Southwest Oil and Gas Field Company (20230304-10).

Conflict of interest

Authors WT, CT, YY, DL, and XY were employed by PetroChina Southwest Oil and Gasfield Company. Authors SM and LY were employed by Southwest Oil and Gas Field Company Development Department.

The remaining author declares that the research was conducted in the absence of any commercial or financial relationships that could be construed as a potential conflict of interest.

Publisher's note

References

Bai, W., Sun, X., and Han, H. (2023). Hydrocarbon generation potential and favorable area selection of shale in Wujiaping Formation of Permian in north Eastern Sichuan. *IFEDC*, 255–241. doi:10.26914/c.cnkihy.2023.059446

Bao, H. Y., Zhao, S., Liang, B., Zhou, L., and Liu, H. T. (2023). Enrichment and high yield of shale gas in the Permian Wujiaping Formation in Hongxing area of Eastern Sichuan and its exploration implications. *China Petrol. expl.* 28 (1), 71–82. doi:10.3969/j.issn.1672-7703.2023.01.007

Cao, T. T., Deng, M., Liu, H., Cao, Q. G., and Liu, G. X. (2021). Reservoir characteristics and methane adsorption capacity of the Wujiaping formation shale: a case study in Lichuan area, western Hubei. *J. China Univ. Min. Tech.* 50 (1), 138–153. doi:10.13247/j.cnki.jcumt.001245

Chen, F. R., Wei, X. F., Liu, Z. J., Ao, M. C., and Yan, J. H. (2020). Pore development characteristics and main controlling factors of the Permian marine-continent transitional shale in the Sichuan Basin. *Nat. Gas. Geosci.* 31 (11), 1593–1602. doi:10.11764/j.issn.1672-1926.2020.04.028

Chen, Y., Tang, S. H., Tang, H. M., Xi, Z., Zhao, N., Sun, S., et al. (2024). Pore structure heterogeneity of deep marine shale in complex tectonic zones and its implications for shale gas exploration. *Energy Fuel* 38 (3), 1891–1905. doi:10.1021/acs.energyfuels.3c03882

Chen, Y. H., Liu, S. H., Zhu, Z. W., Wang, Z., Sun, X., and Xu, T. (2021). Geochemical characteristics and sedimentary setting of chang 9 shale in the upper triassic yanchang Formation of southEastern ordos basin (NW China). *J. Petrol. Sci. Eng.* 196, 108081. doi:10.1016/j.petrol.2020.108081

Chen, Y. H., Zhu, Z. W., and Zhang, L. (2019). Control actions of sedimentary environments and sedimentation rates on lacustrine oil shale distribution, an example of the oil shale in the Upper Triassic Yanchang Formation, south Eastern Ordos Basin (NW China). *Mar. Petrol. Geol.* 102, 508–520. doi:10.1016/j.marpetgeo.2019.01.006

Chen, Z. P., Liao, Y., Li, L., Chen, L., Wang, P., Zuo, Y., et al. (2022). Implication of alkane carbon and hydrogen isotopes for genesis and accumulation of over-mature shale gas: a case study of Longmaxi Formation shale gas in Upper Yangtze area. *Front. Earth Sci.* 10, 901989. doi:10.3389/feart.2022.901989901989

Dang, W., Nie, H. K., Zhang, J. C., Tang, X., Jiang, S., Wei, X., et al. (2022). Pore-scale mechanisms and characterization of light oil storage in shale nanopores: new method and insights. *Geosci. Front.* 13 (5), 101424. doi:10.1016/j.gsf.2022.101424

Dessouky, O. K. (2024). Geochemical characteristics and genesis of niobium–yttrium–fluorine granite pegmatite from Hmrat El Sorwhyia area, North Eastern Desert, Egypt. *Appl. Earth Sci. Online First*. doi:10.1177/25726838241262934

Du, W., Yang, W., Li, X. Y., Shi, F., Lin, R., Wang, Y., et al. (2022). Differential reservoir-forming mechanisms of the lower paleozoic wufeng-longmaxi and niutitang marine gas shales in northern Guizhou Province, SW China: theories and models. *Energies* 15 (4), 5137. doi:10.3390/en15145137

Du, Y., Wang, X. Z., Tang, R. F., Zhu, Y., Yang, C., Zhou, H., et al. (2023). Extraordinarily high organic matter enrichment in upper permian Wujiaping Formation in the Kaijiang-Liangping trough, Sichuan Basin. *Energies* 16 (1), 349. doi:10.3390/en16010349

Fan, C. H., Li, H., Qin, Q. R., He, S., and Zhong, C. (2020). Geological conditions and exploration potential of shale gas reservoir in Wufeng and Longmaxi Formation of southeastern Sichuan Basin, China. *J. Petrol. Sci. Eng.* 191, 107138. doi:10.1016/j.petrol.2020.107138

Fan, C. H., Nie, S., Li, H., Pan, Q. C., Shi, X. C., Qin, S. M., et al. (2024a). Geological characteristics and major factors controlling the high yield of tight oil in the Da'anzhai member of the western Gongshanmiao in the central Sichuan basin, China. *Geomech. Geophys. Geol.* 10 (1), 67. doi:10.1007/s40948-024-00783-9

Fan, C. H., Nie, S., Li, H., Radwan, A. E., Pan, Q. C., Shi, X. C., et al. (2024). Quantitative prediction and spatial analysis of structural fractures in deep shale gas reservoirs within complex structural zones: a case study of the Longmaxi Formation in the Luzhou area, southern Sichuan Basin, China. *J. Asian Earth Sci.* 263, 106025. doi:10.1016/j.jseaes.2024.106025

Feng, J. H., Cai, X. Y., Mou, Z. H., and Gao, S. L. (2016). Oil and gas exploration of China petroleum and chemical corporation during the 12th Five-Year Plan and the prospect for the 13th Five-Year Plan. *China Petrol. expl.* 21 (3), 1–13. doi:10.3969/j.issn.1672-7703.2016.03.001

Guo, X. B., Huang, Z. L., Zhao, L. B., Han, W., Ding, C., Sun, X., et al. (2019). Pore structure and multi-fractal analysis of tight sandstone using MIP, NMR and NMRC methods: a case study from the Kuqa depression, China. *J. Petrol. Sci. Eng.* 178, 544–558. doi:10.1016/j.petrol.2019.03.069

He, S., Li, H., Qin, Q. R., and Long, S. X. (2021c). Influence of mineral compositions on shale pore development of Longmaxi Formation in the Dingshan area, southEastern Sichuan Basin, China. *Energy Fuel* 35 (13), 10551–10561. doi:10.1021/acs.energyfuels.1c01026

He, S., Qin, Q. R., Li, H., and Wang, S. L. (2022b). Deformation differences in complex structural areas in the southern Sichuan Basin and its influence on shale gas preservation: a case study of Changning and Luzhou area. *Front. Earth Sci.* 9, 818155. doi:10.3389/feart.2021.818155

He, S., Qin, Q. R., Li, H., and Zhao, S. X. (2022a). Deformation differences in complex structural areas in the southern Sichuan Basin and its influence on shale gas preservation: a case study of changning and Luzhou areas. *Front. Earth Sci.* 9, 818543. doi:10.3389/feart.2021.818534

Jiang, S. L., Zhou, Q. H., Li, Y. J., and Yang, R. L. (2023). Fracability evaluation of the middle–upper Permian marine shale reservoir in well HD1, western Hubei area. *Sci. Rep.* 13, 14319. doi:10.1038/s41598-023-40735-z

Lascelles, D. F. (2024). Plate tectonics caused the demise of banded iron formations. *Appl. Earth Sci.* 122 (4), 230–241. doi:10.1179/1743275814Y.0000000043

Li, H. (2022). Research progress on evaluation methods and factors influencing shale brittleness: a review. *Energy Rep.* 8, 4344–4358. doi:10.1016/j.egyr.2022.03.120

Li, H. (2023). Coordinated development of shale gas benefit exploitation and ecological environmental conservation in China: a mini review. *Front. Ecol. Evol.* 11, 1232395. doi:10.3389/fevo.2023.1232395

Li, H., Tang, H. M., Qin, Q. R., Wang, Q., and Zhong, C. (2019). Effectiveness evaluation of natural fractures in Xujiahe Formation of Yuanba area, Sichuan basin, China. *Arab. J. Geosci.* 12 (6), 194. doi:10.1007/s12517-019-4292-5

Li, H., Wang, Q., Qin, Q. R., and Ge, X. Y. (2021). Characteristics of natural fractures in an ultradeep marine carbonate gas reservoir and their impact on the reservoir: a case study of the Maokou Formation of the JLS Structure in the Sichuan Basin, China. *Energy Fuel* 35 (16), 13098–13108. doi:10.1021/acs.energyfuels.1c01581

Li, H., Zhou, J. L., Mou, X. Y., Guo, H., Wang, X., et al. (2022a). Pore structure and fractal characteristics of the marine shale of the Longmaxi Formation in the changning area, southern Sichuan Basin, China. *Front. Earth Sci.* 10, 1018274. doi:10.3389/feart.2022.1018274

Li, J., Li, H., Jiang, W., Cai, M., He, J., Wang, Q., et al. (2024a). Shale pore characteristics and their impact on the gas-bearing properties of the Longmaxi Formation in the Luzhou area. *Sci. Rep.* 14, 16896. doi:10.1038/s41598-024-66759-7

Li, H., He, S., Radwand, A. E., Xie, J. T., and Qin, Q. R. (2024b). Quantitative analysis of pore complexity in lacustrine organic-rich shale and comparison to marine shale: Insights from experimental tests and fractal theory. *Energy Fuel.* 38 (17), 16171–16188. doi:10.1021/acs.energyfuels.4c03095

Li, J. J., Qin, Q. R., Li, H., and Wan, Y. F. (2022b). Numerical simulation of the stress field and fault sealing of complex fault combinations in Changning area, Southern Sichuan Basin, China. *Energy Sci. Eng.* 10 (2), 278–291. doi:10.1002/ese3.1044

Liang, X., and Li, L. (2021). Geological conditions and exploration potential for shale gas in upper permian Wujiaping Formation in the eastern of western Hubei-Eastern Chongqing. *Petrol. Geol. Exp.* 43 (3), 386–394. doi:10.11781/sysydz202103386

Liu, C., and Xie, Q. B. (2017). Depositional, sedimentary, and diagenetic controls on reservoir quality in carbonate successions: a case study from the carbonate gas reservoirs of the Lower Triassic Feixianguan Formation, Eastern Sichuan Basin, China. *J. Petrol. Sci. Eng.* 163, 484–500. doi:10.1016/j.petrol.2017.12.063

Luo, T., Guo, X. W., He, Z. L., Dong, T., Tao, Z., Yang, R., et al. (2024). Fluid evolution and gas enrichment in the Wufeng-Longmaxi shale reservoirs of the Eastern Sichuan Basin, SW China. *J. Asian Earth Scie.* 259, 105905. doi:10.1016/j.jseaes.2023.105905

Nie, H. K., Jin, Z. J., and Zhang, J. C. (2018). Characteristics of three organic matter pore types in the Wufeng-Longmaxi shale of the Sichuan Basin, southwest China. *Sci. Rep.* 8, 7014. doi:10.1038/s41598-018-25104-5

Qi, R., Qin, X., Lu, C., Ma, C., Mao, W., and Zhang, W. (2022). Experimental study on the isothermal adsorption of methane gas in natural gas hydrate argillaceous silt reservoir. *Adv. Geo-Energy Res.* 6 (2), 143–156. doi:10.46690/ager.2022.02.06

Shan, C., Ye, C., Zhang, Z., Zou, C., He, F., Zhang, H., et al. (2022). Reservoir characteristics and resource potential analysis of transitional shale gas in Southern Sichuan Basin. *Front. Earth Sci.* 10, 909469. doi:10.3389/feart.2022.909469

Shan, C., Zhang, T., Liang, X., Zhang, Z., Zhu, H., Yang, W., et al. (2018). Influence of chemical properties on CH 4 adsorption capacity of anthracite derived from southern Sichuan Basin, China. *China. Mar. Petrol. Geol.* 89, 387–401. doi:10.1016/j.marpetgeo.2017.10.008

Smedley, P. L., Allen, G., Baptie, B. J., Fraser-Harris, A., Ward, R., Chambers, R., et al. (2024). Equipping for risk: lessons learnt from the UK shale-gas experience on assessing environmental risks for the future geoenergy use of the deep subsurface. *Sci. Total Environ.* 921, 171036. doi:10.1016/j.scitotenv.2024.171036

Tan, B., Cheng, G., Zhu, X. M., and Yang, X. B. (2020). Experimental study on the physisorption characteristics of O_2 in coal powder are effected by coal nanopore structure. *Sci. Rep.* 10, 6946. doi:10.1038/s41598-020-63988-4

Tang, L., Song, Y., Jiang, S., Li, L. X., Li, Z., Li, Q. W., et al. (2020). Sealing mechanism of the roof and floor for the Wufeng-Longmaxi shale gas in the southern Sichuan Basin. *Energy Fuel* 34 (6), 6999–7018. doi:10.1021/acs.energyfuels.0c00983

Tang, X. L., Jiang, Z. X., Jiang, S., Cheng, L. J., Zhong, N. N., Tang, L., et al. (2019). Characteristics, capability, and origin of shale gas desorption of the Longmaxi Formation in the southeastern Sichuan Basin, China. *Sci. Rep.* 9, 1035. doi:10.1038/s41598-018-37782-2

Tian, H. N., Tang, J. P., Zhang, S. P., and Zhang, X. (2024). Adsorption-desorption characteristics of coal-bearing shale gas under three-dimensional stress state studied by low field nuclear magnetic resonance spectrum experiments. *Sci. Rep.* 14, 5566. doi:10.1038/s41598-024-54532-9

Wang, E. Z., Guo, T. L., L, B., et al. (2022a). Lithofacies and pore features of marine-continental transitional shale and gas enrichment conditions of favorable lithofacies: a case study of Permian Longtan Formation in the Lintanchang area, southeast of Sichuan Basin, SW China. *Petrol. explor. Dev.* 49 (6), 1310–1322. doi:10.11698/PED.20220273

Wang, J., Zhu, C. G., Li, X., Wang, B., and Zhang, Y. T. (2024). Experimental study on triaxial disturbance and failure characteristics of rock-like specimens. *J. Min. Strata Control Eng.* 6 (2), 023034. doi:10.13532/j.jmsce.cn10-1638/td.20240015.004

Wang, P., Liu, Z., Li, X., et al. (2022b). Development of the upper permian wujiaping shale in hongxing area, eastern Sichuan Basin, and its significance to shale gas enrichment. *Oil Gas. Geol.* 43 (5), 1102–1114. doi:10.11743/ogg20220508

Wang, X. Z., Li, B., Yang, X. Y., et al. (2021). Characteristics of "Guangyuan-Wangcang" trough during late Middle Permian and its petroleum geological significance in northern Sichuan Basin, SW China. *Petrol. Expl. Dev.* 48 (3), 562–574. doi:10.11698/PED.2021.03.11

Xia, Y., Xu, S., Lu, C., Andersen, P. Ø., and Cai, J. (2023). Characterization and capillary pressure curve estimation of clayey-silt sediment in gas hydrate reservoirs of the South China Sea. *Adv. Geo-Energy Res.* 10 (3), 200–207. doi:10.46690/ager.2023.12.06

Xu, S., Wen, J., Liu, K., Shi, X., and Dong, T. (2024). Brittle minerals, mechanical properties and fracability evaluation of shales. *Adv. Geo-Energy Res.* 214 (1), 8–11. doi:10.46690/ager.2024.10.03

Yang, W., Wang, Y. H., Du, W., Song, Y., Jiang, Z., Wang, Q., et al. (2022). Behavior of organic matter-hosted pores within shale gas reservoirs in response to differential tectonic deformation: potential mechanisms and innovative conceptual models. *Gas. Sci. Eng.* 102, 104571. doi:10.1016/j.jngse.2022.104571

Yang, Y., Chen, Y., Liu, S., et al. (2021). Status, potential and prospect of shale gas exploration and development in the Sichuan Basin and its periphery. *Nat. Gas. Ind.* 41 (1), 42–58. doi:10.3787/j.issn.1000-0976.2021.01.004

Yang, Y., Wang, H., Xie, J., et al. (2023). Exploration breakthrough and prospect of permian marine shale gas in the kaijiang-liangping trough, Sichuan Basin. *Nat. Gas. Ind.* 43 (11), 19–27. doi:10.3787/j.issn.1000-0976.2023.11.003

Yin, S., Jia, Q., and Ding, W. L. (2018b). 3D paleotectonic stress field simulations and fracture prediction for marine-continental transitional facies forming a tight-sandstone reservoir in a highly deformed area. *J. Geophys. Eng.* 15 (4), 1214–1230. doi:10.1088/1742-2140/aaad97

Yin, S., Lv, D. W., Jin, L., and Ding, W. L. (2018a). Experimental analysis and application of the effect of stress on continental shale reservoir brittleness. *J. Geophys. Eng.* 15 (2), 478–494. doi:10.1088/1742-2140/aaa5d2

Zeng, Q., Hu, X., Qu, H., et al. (2020). Division of strata and distribution of favorable reservoir rocks of the Upper Permian Wujiaping formation in the northwestern Sichuan Basin. *Nat. Gas. Expl. Dev.* 43 (4), 33–47. doi:10.12055/gaskk.issn.1673-3177.2020.04.004

Zhai, G. Y., Li, J., Jiao, Y., Wang, Y., Liu, G., Xu, Q., et al. (2019). Applications of chemostratigraphy in a characterization of shale gas sedimentary microfacies and predictions of sweet spots -taking the Cambrian black shales in Western Hubei as an example. *Mar. Petrol. Geol.* 109, 547–560. doi:10.1016/j.marpetgeo.2019.06.045

Zhang, H., Wu, Y. P., and Xie, P. S. (2023a). Experimental study on evolution law of compressive mechanical properties of interbedded roofrock. *J. Min. Strata Control Eng.* 5 (1), 013011. doi:10.13532/j.jmsce.cn10-1638/td.20220923.001

Zhang, P. W., Hu, L. M., Meegoda, J., and Gao, S. Y. (2015). Micro/nano-pore network analysis of gas flow in shale matrix. *Sci. Rep.* 5, 13501. doi:10.1038/srep13501

Zhang, Y., Huang, H. S., Zeng, Q., et al. (2022). Microfacies of limestones from upper permian Wujiaping Formation at gediba section in the northwestern Sichuan, southwest China. *J. Earth Sci. Env.* 44 (2), 287–297. doi:10.19814/j.jese.2021.08007

Zhang, Y. X., Pan, H. F., Bai, Y. B., Chen, G., and Luo, J. (2023b). Pore characteristics, oil contents and factors influencing laminated shale in the first member of the Qingshankou Formation in the Gulong sag, northern Songliao basin. *Minerals* 13 (9), 1220. doi:10.3390/min13091220

Zhao, J. P., Chen, H., Zhang, J. Y., Zhang, W. J., and Chen, G. (2022). Quantitative characterization of organic and inorganic pores in shale based on FIB-SEM. *Front. Earth Sci.* 10, 994312. doi:10.3389/feart.2022.994312

Zhu, W. C., Niu, L. L., Li, S. H., and Li, S. (2019). Creep-impact test of rock: status-of-the-art and prospect. *J. Min. Strata Control Eng.* 1 (1), 013003. doi:10.13532/j.jmsce.cn10-1638/td.2019.02.007

Zou, C., Yang, Z., Dong, D. Z., Zhao, Q., Chen, Z., Feng, Y., et al. (2022). Distribution and prospect of unconventional hydrocarbons in source rock strata in China. *Earth Sci.* 47 (5), 1517–1533. doi:10.3799/dqkx.2022.160

frontiers | Frontiers in Earth Science

TYPE Original Research
PUBLISHED 07 November 2024
DOI 10.3389/feart.2024.1436573

OPEN ACCESS

EDITED BY
Hu Li,
Sichuan University of Science and Engineering, China

REVIEWED BY
Wendong Wang,
China University of Petroleum, China
Quanyou Liu,
SINOPEC Petroleum Exploration and Production Research Institute, China
Qianyou Wang,
University of Liverpool, United Kingdom

*CORRESPONDENCE
Maoyun Wang,
wmy950904@163.com
Jianhui Zeng,
zengjh@cup.edu.cn

RECEIVED 22 May 2024
ACCEPTED 28 October 2024
PUBLISHED 07 November 2024

CITATION
Wang M, Zeng J, Li C, Qiao J, Wei W, Zhang H and Cui H (2024) The impacts of CO_2 on sandstone reservoirs in different fluid environments: insights from mantle-derived CO_2 gas reservoirs in Dongying Sag, Bohai Bay Basin, China.
Front. Earth Sci. 12:1436573.
doi: 10.3389/feart.2024.1436573

The impacts of CO_2 on sandstone reservoirs in different fluid environments: insights from mantle-derived CO_2 gas reservoirs in Dongying Sag, Bohai Bay Basin, China

Maoyun Wang[1,2]*, Jianhui Zeng[1,2]*, Chuanming Li[1,2], Juncheng Qiao[1,2], Wenfei Wei[1,2], Huanle Zhang[1,2] and Huwang Cui[1,2]

[1]National Key Laboratory of Petroleum Resources and Engineering, China University of Petroleum, Beijing, China, [2]College of Geosciences, China University of Petroleum, Beijing, China

Introduction: Mantle-derived CO_2, as an important component of hydrothermal fluids, is widely distributed in petroliferous basins. While previous experimental studies have suggested that CO_2 can improve sandstone reservoir quality through mineral dissolution in open fluid setting, they have overlooked its nagetive effects to sandstone reservoir quality by carbonate cementation. Additionally, the roles of various fluid environments in CO_2-reservoir interactions have not been studied in detail.

Methods: To systematically investigate the influences of CO_2 on sandstone reservoirs, we examine a typical mantle-derived CO_2 gas reservoir, Bohai Bay Basin, China. This study employs integrated methods, including electron microscopy, scanning electron microscopy, X-ray diffraction, stable C- and O-isotope analysis, and physical property data. The aim is to investigate the evidence and mechanisms by which mantle-derived CO_2 impacts sandstone reservoirs, particularly focusing on its effects in open and closed fluid environments.

Results and Discussion: Our findings reveal that dawsonite and ankerite are prevalent within the mantle-derived CO_2 gas reservoir, while isotopic analysis of carbonate cements indicates values ($\delta^{13}C$: −9.0‰ to −1.6‰; $\delta^{18}O$: −21.7‰ to −12.7‰) consistent with mantle-derived CO_2 and hydrothermal fluids. These pieces of evidence indicate that CO_2-rich hydrothermal fluids participate in water-rock interactions, thereby significantly influencing the diagenesis of reservoirs. Further, we notice that CO_2 reservoirs adjacent to faults exhibit an open fluid environment, characterized by superior porosity and permeability, more quartz, but fewer feldspar, carbonate, and clay minerals compared to those in closed fluid environments. Notably, kaolinite predominates in open fluid environments, while illite/smectite (I/S) is more common in closed settings. The dual roles of mantle-derived CO_2 are highlighted in our analysis: while it enhances reservoir storage and permeability through mineral dissolution, the carbonate cement generated by CO_2-water-rock interaction can also adversely affect reservoir quality. In open fluid environments, CO_2 facilitates

the dissolution of feldspar and carbonate minerals, promoting the timely removal of dissolution by-products (clay mineral) and inhibiting carbonate cementation, thereby improving reservoir properties. Conversely, in closed fluid environments, decreasing CO_2 concentrations with depth leads to diminishing dissolution effects and increased carbonate cementation, resulting in reduced reservoir porosity and permeability. Overall, the significance of this study is to correct the deviation in the impacts of CO_2 on sandstone reservoirs at laboratory setting through case study of typical mantle-source CO_2 gas reservoir.

This work can be applied to the studies of reservoir homogeneity and sweet spots in regions with hydrothermal and mantle-derived CO_2 activities. However, due to the limitation of CO_2 content range (about 15%–70%) in the study case, we are unable to investigate the effects of low-concentration CO_2 on sandstone reservoirs, which may affect the generalizability of this work. Besides, the formation temperature and pressure, and salinity of formation water, should be considered when dealing with other cases.

KEYWORDS

CO_2-water-rock interaction, fluid environment, mantle-derived CO_2, diagenesis, Dongying Sag

1 Introduction

Hydrothermal activities have occurred in petroliferous basins during their formation and evolution (Zhang et al., 2023; Zhu et al., 2017). Mantle-derived CO_2, as a primary component of hydrothermal fluids (Diker et al., 2024; Liu et al., 2024; Ranta et al., 2023; Sun and Dasgupta, 2023), significantly influences reservoir quality, and hydrocarbon expulsion and migration (Dmitriyevskiy et al., 2010; Guo et al., 2011; Zhu, et al., 2017; Liu et al., 2017; Lu et al., 2022; Huang et al., 2021). Furthermore, basins with rift tectonic background frequently experience hydrothermal activities, leading to the development of CO_2-rich oil and gas fields, such as The South Atlantic Ocean margin (Anderson et al., 2023; Liu et al., 2022; Wright, 2020), Hailar (Yang et al., 2021; Liu et al., 2009), Songliao (Liu N. et al., 2019; Yang et al., 2009), Bohai Bay (Miao et al., 2020), Subei (Liu J. et al., 2023; Zhou et al., 2020; Liu et al., 2017), Sanshui (Zhu et al., 2017), Yinggehai (Liu Q. et al., 2019; Yang et al., 2023), and other rift basins in eastern China (Zhao et al., 2017). This mantle-derived CO_2 migrates into the reservoirs and dissolves in formation water, generating H^+ and CO_3^{2-} (Li et al., 2015), where H^+ leads to the dissolution of aluminosilicate and carbonate minerals (Portier and Rochelle, 2005), while CO_3^{2-} combines with ions like Ca^{2+}, Mg^{2+}, and Fe^{2+} (Li et al., 2015), forming carbonate minerals that occupy pore space within the reservoirs. Therefore, in regions with hydrothermal activity, as well as high CO_2 concentrations, CO_2 is one of the critical factors that cannot be overlooked in contributing to reservoir heterogeneity. However, previous studies on mantle-derived CO_2 have mostly emphasized its positive effects on reservoirs (Liu Q. et al., 2023; Yuan et al., 2023; Liu et al., 2016; Zhou et al., 2020; Zhang et al., 2018), with little evidence showing its participation in carbonate cementation that could reduce reservoir quality (Hu, 2016). As a result, the overall impacts of mantle-derived CO_2 on reservoirs has not been comprehensively understood.

Most studies of CO_2-water-rock reaction experiments suggest that the dissolution of minerals by CO_2 does not always enhance reservoir porosity and permeability. In these experiments, the dissolution of feldspar and carbonate minerals by CO_2 increases the porosity of the core plugs (Wu et al., 2019; Fu et al., 2016; Yu et al., 2016; Fischer et al., 2010), while the permeability typically decreases as the pore throats are blocked by dissolution by-products, such as clay minerals (Pearce et al., 2019; Wu et al., 2019; Aminu et al., 2018). In the geological conditions, due to frequent fault activities in rift basins, reservoirs near faults often have relatively open fluid environments during geological history (Gudmundsson, 2022; Ward et al., 2016; Zhou et al., 2020; Wei et al., 2017; Li et al., 2016). The open fluid environments are conducive to the timely discharge of dissolution by-products, leading to significant improvements in reservoir porosity and permeability (Hu, 2016; Wei et al., 2017; Yuan et al., 2013a). However, most oil and gas reservoirs actually have a stable pressure system, and the fluid environment is relatively closed, making fluid migration and discharge of dissolution by-products relatively difficult (Yuan et al., 2013a; Zhao et al., 2016). Currently, there is a lack of systematic study on the impacts of mantle-derived CO_2 on reservoirs in different fluid environments, which, to some extent, limits the research on the reservoir homogeneity and the prediction of sweet spots in regions with hydrothermal activity, as well as high CO_2 concentrations.

Dongying Sag, located in Bohai Bay Basin, is characterized by numerous anticline oil and gas traps that have been modified by normal faults and are rich in mantle-derived CO_2 (Miao et al., 2020; Li et al., 2016). The mantle-derived CO_2 has unique stable carbon isotope compositions (Dai et al., 2001), which can contribute to confirming if the mantle-derived CO_2 participates in water-rock interactions and affects reservoirs (Liu R. et al., 2019; Hu, 2016; Liu et al., 2016). Therefore, Dongying Sag is an ideal place to research the synergistic impacts of fluid environments and CO_2 on reservoirs.

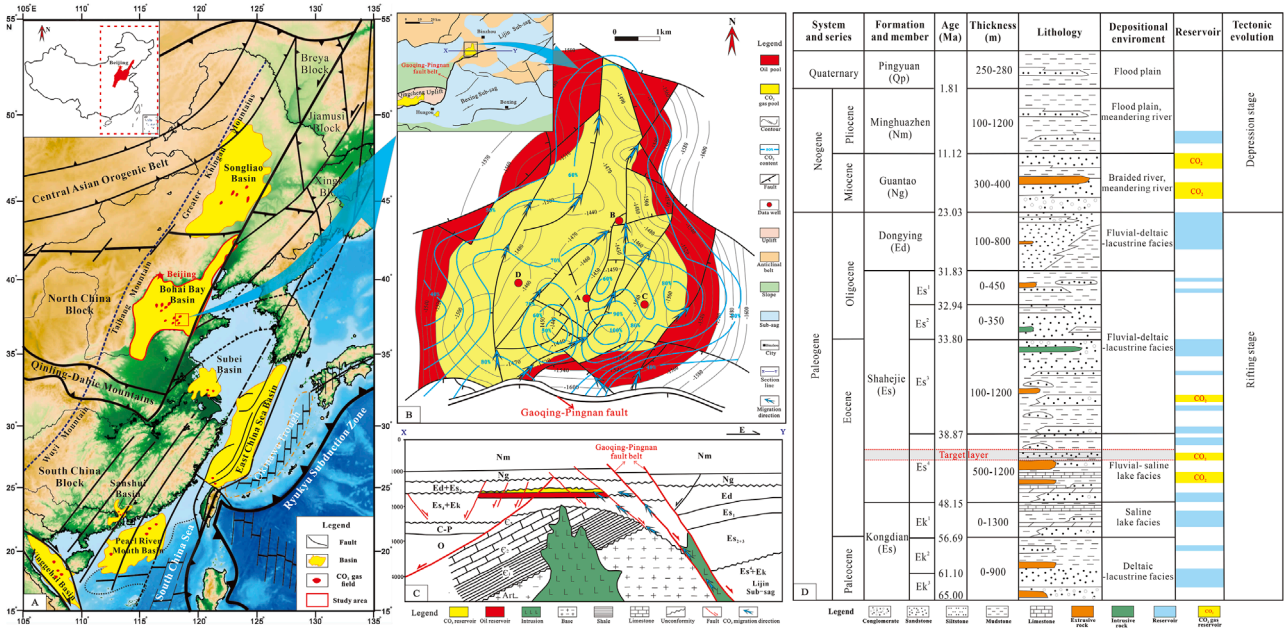

FIGURE 1
(A) Distribution of rift basins and CO_2 gas fields in eastern China [modified from Zhao et al. (2017)]. **(B)** Distribution of CO_2 gas fields in Dongying Sag, the top structure, CO_2 content distribution, and migration map of Pingfangwang CO_2 gas reservoir (modified from the Shengli Oilfield). **(C)** Profile map (see Figure 1B for location) and CO_2 source of study area (modified from Zeng, 2000). **(D)** Stratigraphy, lithology, tectonic movements, and reservoir distribution in the Dongying Sag [modified from Wei et al. (2017)].

This study examines typical mantle-derived CO_2 gas reservoirs in Dongying Sag as a case study, aiming to better understand the impacts of mantle-derived CO_2 on sandstone reservoirs in open and closed fluid environments using a multi-technique approach of combined mineralogy (Thin section, Scanning electron microscopy, and X-ray diffraction) and geochemistry (stable C- and O-isotopes). The main objectives of the current study are:

(1) To identify the mineralogical and geochemical evidence for the impacts of CO_2 on reservoirs.
(2) To investigate the characteristics of diagenetic minerals in mantle-derived CO_2 reservoirs and their impact on the sandstone reservoirs.
(3) To elucidate the impact mechanisms of CO_2 on sandstone reservoirs, with a focus on the impact laws of CO_2 on reservoirs in different fluid environments.

2 Geological setting

Due to the influence of the Pacific Plate's subduction, oil and gas fields rich in mantle-derived CO_2 are widely distributed in the rift basins of eastern China (Zhao et al., 2017) (Figure 1A). The Dongying Sag, located in the southeastern of the Bohai Bay Basin, is a graben of Mesozoic and Cenozoic (Niu et al., 2022). Along the Gaoqing-Pingnan deep fault in the Dongying Sag, there are several CO_2 gas fields (Han et al., 2010) (Figure 1B). These CO_2 mainly migrate from the mantle to sedimentary basins through magmatic activity and deep faults (Figure 1C) (Zhang et al., 2023; Guo et al., 2006), have special stable carbon isotope compositions (with $\delta^{13}C$ mostly around −6‰ ± 2‰) (Dai et al., 2001).

Since the Cenozoic, the Gaoqing-Pingnan deep fault has been active, accompanied by multiple magmatic and mantle-derived CO_2 activity events, forming multiple sets of CO_2-rich reservoirs (Figure 1D) (Kang et al., 2014; Cheng et al., 2020). According to drilling data, the Cenozoic stratigraphic unit includes the Kongdian Formation (Ek), Shahejie Formation (Es), Dongying Formation (Ed), Guantao Formation (Ng), Minghuazhen Formation (Nm), and Pingyuan Formation (Qp) (Figure 1D). Sediments of the Cenozoic strata in the Dongying Sag include the saline lake-delta-fluvial (the rifting stage) and fluvial (the depression stage) (Niu et al., 2022).

Pingfangwang CO_2 gas field, the typical mantle-derived CO_2 gas reservoir selected in this study, is an anticlinal trap that has been reformed by normal faults (Figure 1B). The target layer is a set of beach-bar sand in the 4th member of Shahejie Formation (Es^4) (Figure 1D). Its natural gas is mainly composed of CO_2, with a content of 61.2%–98.6%, CO_2 content decreases from south to north (Figure 1B). The $\delta^{13}C_{CO2}$ ranges from −5.08‰–−4.32‰. CO_2 from the mantle first migrates vertically to the target layer through the Gaoqing-Pingnan deep fault and then migrates northward through some nearly south-north trend normal faults (Figures 1B, C) (Wang et al., 2004; Zeng, 2000).

3 Data and methods

To investigate the characteristics of mantle-derived CO_2 reservoirs in the study area, 1,343 sets of porosity and permeability data and 46 sandstone samples of target layers from 4 wells

(represented as red circles in Figure 1B) were collected from the PEDRI, Shengli Oilfield. Four types of experiments were performed on these sandstone samples. 21 casting thin sections were observed using an optical microscope. Selected typical samples underwent scanning electron microscopy. X-ray diffraction analysis was conducted on 15 groups for whole rock and clay minerals. Additionally, C and O isotope analysis was carried out on a total of 10 sandstone samples and carbonate veins.

3.1 Analysis of thin sections

Thin sections were impregnated with blue epoxy resin to highlight the pore space and were dyed with Alizarin Red-S and K-ferricyanide for carbonate mineral identification. Calcite was dyed red, ferrocalcite was dyed purplish red, and ankerite was dyed blue-purple. Thin sections were observed using the Leica 4500P polarizing microscope. ImageJ software was used for quantitative analysis of surface porosity.

3.2 Scanning electron microscopy (SEM)

The Quanta-200F SEM was used to observe the fresh surface of gold-plated rock samples, facilitating the identification of diagenetic phenomena and minerals. The SEM was operated at an acceleration voltage of 20 kV and an emission current of 3 nA.

3.3 Whole rock and clay X-ray diffraction analysis (XRD)

Each group of samples was crushed and mixed evenly. A portion of the powder was used for whole rock XRD analysis, while the remainder was analyzed for clay XRD. This approach was adopted to minimize the effect of lithologic heterogeneity. The D8 Advance X-ray diffractometer was used for whole rock and clay X-ray diffraction analysis. This allowed for quantitative analysis of the types and contents of the whole rock and clay minerals in CO_2 reservoirs.

3.4 Stable C- and O-isotope analysis

Eight whole rocks and two calcite vein samples were selected for C- and O-isotope analysis. A ThermoFisher MAT-253 stable isotope mass spectrometer was used to determine the $\delta^{13}C$ and $\delta^{18}O$ of carbonate cement.

3.5 Calculation of carbonate cement formation temperature

To confirm the correlation between carbonate minerals in CO_2 reservoirs and mantle-derived CO_2 with high crystallization temperature properties, we calculated the precipitation temperatures of carbonate minerals in mantle-derived CO_2 gas reservoirs using the Formula 1 established by Friedman and O'Neil (1977).

$$1000 * \ln \alpha_{carbonate-water} \approx \delta^{18}O_{carbonate} - \delta^{18}O_{water} = 2.78 * 10^6/T^2 - 2.89 \quad (1)$$

Where $\alpha_{carbonate\text{-}water}$ is the fractionation coefficient, $\delta^{18}O_{carbonate}$ is the $\delta^{18}O_{PDB}$ value of carbonate, The $\delta^{18}O_{V\text{-}SMOW}$ value of pore water in the study area is −2.55‰ (Han et al., 2012), T is the temperature of carbonate precipitation.

4 Results

4.1 Petrology characteristics and mineral compositions of CO_2 gas reservoirs

The identification results from the thin sections (Table 1) show that the terrigenous detrital components of CO_2 reservoirs consist of quartz (average: 73.0%, range: 58.8%–86.8%), feldspars (average: 13.4%, range: 3.8%–23.7%), and rock fragments (average: 13.7%, range: 4.6%–24.3%). There is a significant difference between the reservoirs near the faults (wells A and B) and the reservoirs far away from the faults (wells C and D). The former has a higher quartz content and a lower feldspar content, with the lithology consisting of feldspathic litharenite and sublitharenite (Li et al., 2024), while the latter mainly consists of lithic arkose (Figure 2).

The XRD results for whole rock and clay minerals (Table 2) show that the mineral composition of the CO_2 sandstone reservoir in the study area is predominantly quartz, with an average of 58.2%, with a relatively low content of feldspar (K-feldspar and plagioclase). Moreover, carbonate minerals are widely developed, comprising an average content of 12.6% calcite, 6.0% ankerite, 3.1% dawsonite, and small amounts of siderite. Among them, Wells A, B, C, and D have average quartz contents of 69.8%, 67.1%, 47.3%, and 45.5%, respectively. The average contents of total carbonate minerals (calcite, ankerite, siderite, and dawsonite) are 10.2%, 11.6%, 36.6%, and 40.3%, respectively. The average contents of clay minerals are 7.1%, 6.9%, 9.0%, and 12.4%, respectively. As for clay minerals, kaolinite dominates with an average of 40.9%, followed by the illite/smectite (I/S) mixed layer, with an average of 35.3%. Among them, the average relative content of kaolinite in Wells A, B, C and D are 52%, 58%, 23%, and 27%, respectively, and the average relative content of I/S is 28%, 21%, 52%, and 42%, respectively.

The mineral composition exhibits a noticeable contrast between reservoirs near and far from faults (Figure 3). The former displays higher quartz content and lower content of calcite, ankerite, and clay minerals compared to the latter. Furthermore, the clay minerals in the reservoirs near faults are predominantly kaolinite, whereas these in the reservoirs far from the faults primarily consist of I/S.

4.2 Porosity and permeability of CO_2 gas reservoirs

According to the statistical results of porosity and permeability data (Figure 4), The porosity of CO_2 reservoirs is concentrated

10.3389/feart.2024.1436573

TABLE 1 Thin section identification results of CO_2 gas reservoirs in the study area.

Location	Well	Depth(m)	The detrital grain volume fraction			Surface porosity			Ratio of DSP (%)
			Quartz (%)	Feldspar (%)	Rock fragment (%)	PSP (%)	DSP (%)	TSP (%)	
Near faults	A	1,464.80	86.4	8.6	4.9	6.8	20.5	27.3	75.1
	A	1,496.90	76.9	3.8	19.3	9.2	26.0	35.2	73.9
	A	1,531.49	85.2	9.3	5.6	6.5	25.0	31.5	79.4
	A	1,557.11	86.8	6.6	6.6	7.4	22.0	29.4	74.8
	A	1,582.64	71.4	11.9	16.7	6.1	20.0	26.1	76.6
	Means of Well A		81.4	8.0	10.6	7.2	22.7	29.9	76.0
	B	1,442.00	76.4	9.9	13.7	4.4	18.0	22.4	80.4
	B	1,457.00	86.5	5.6	7.8	5.6	20.0	25.6	78.0
	B	1,472.26	73.3	10.0	16.7	6.0	16.0	22.0	72.7
	B	1,496.90	70.6	9.6	19.8	8.5	18.4	26.9	68.5
	B	1,518.70	69.8	12.9	17.3	5.9	16.3	22.2	73.4
	B	1,537.62	66.3	14.1	19.6	7.8	13.8	21.6	63.9
	Means of Well B		73.8	10.4	15.8	6.4	17.1	23.5	72.8
Far from faults	C	1,503.00	75.4	20.0	4.6	6.0	16.4	22.4	73.2
	C	1,527.90	72.2	13.9	13.9	4.9	11.5	16.4	70.1
	C	1,543.40	65.7	10.0	24.3	6.6	6.0	12.6	47.6
	C	1,569.96	63.2	23.7	13.2	1.3	7.0	8.3	84.3
	C	1,626.80	58.8	23.5	17.6	0.0	4.2	4.2	100.0
	Means of Well C		67.1	18.2	14.7	3.8	9.0	12.8	75.1
	D	1,460.23	75.0	18.8	6.3	7.7	19.1	26.8	71.3
	D	1,495.30	75.0	12.5	12.5	6.0	12.5	18.5	67.6
	D	1,512.80	67.9	16.7	15.4	6.6	8.0	14.6	54.8
	D	1,530.45	64.9	15.6	19.5	5.9	5.0	10.9	45.9
	D	1,556.30	64.7	23.5	11.8	4.5	4.0	8.5	47.1
	Means of Well D		69.5	17.4	13.1	6.1	9.7	15.9	57.3
Means			73.0	13.4	13.7	5.9	14.7	20.6	70.4

Abbreviation: Q–quartz; F–feldspar; RF–rock fragment; PSP–primary surface porosity; DSP–dissolution surface porosity; TSP–total surface porosity.

between 20% and 30% (Figure 4A), with an average of 23.6%. The permeability of CO_2 reservoirs near faults is mainly distributed in the range of 10 ~ 1,000 mD, with an average of 131.7 mD, while CO_2 reservoirs far from faults have permeability mainly distributed in the range of 1 ~ 100 mD, with an average of 24.3 mD (Figure 4B). As a whole, the physical properties of reservoirs near faults is better than that far from faults (Figure 4). The linear correlations between the porosity and permeability of CO_2 reservoirs are fair (Figure 4C),

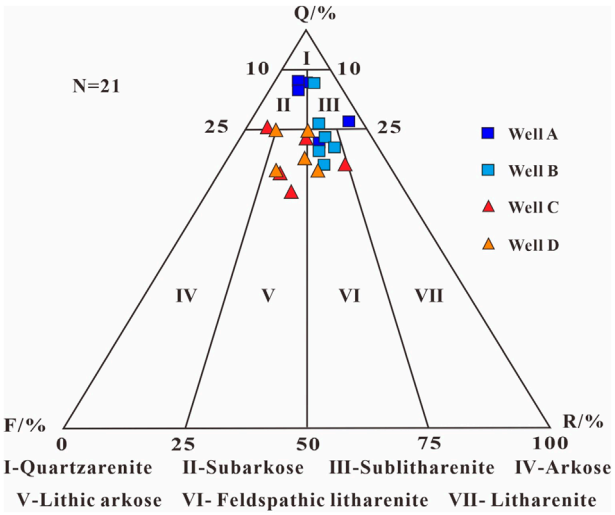

FIGURE 2
Detrital grain composition triangle diagram in the CO_2 gas reservoirs [revised from Folk (1968)]. Well A and B are near the faults, while well C and D are far from the faults. Q, Quartz; F, Feldspar; R, Rock fragment.

suggesting that the pores are the main seepage channels in CO_2 reservoirs.

4.3 Typical diagenesis in CO_2 gas reservoirs

4.3.1 Carbonate mineral cementation

Carbonate cementation is the predominant cementation process of CO_2 reservoirs in the study area, mainly developing dawsonite (Figures 5A–C), calcite (Figures 5C–F), ankerite (Figures 5C, F, G), and a small amount of siderite (Figures 5D, H) and dolomite (Figure 5I).

4.3.1.1 Dawsonite

Dawsonite, a special carbonate mineral, can stably exist in high-concentration CO_2 environments. It is generated by the continuous reaction of K-feldspar, plagioclase, or kaolinite with CO_2 and the formation water (Ryzhenko, 2006; Johnson et al., 2011). Observation of thin sections and SEM confirms that all CO_2 gas reservoirs have dawsonite, with extremely high recognition. It is filled in the pores of sandstone, forming a hairlike or radial aggregate with a size of approximately 100–200 μm (Figures 5A–C).

4.3.1.2 Calcite

Calcite is the most carbonate mineral in CO_2 reservoirs (Table 1), with pack-pore cementation (Figure 5C) or filling dissolution pores (Figure 5D). It frequently coexists with kaolinite (Figure 5E), indicating that these calcites formed after CO_2 injection into the reservoir. The coexistence of kaolinite and calcite is due to the acidic environment generated by CO_2, which causes feldspar to dissolve and form kaolinite. Later, the geological environment changes to alkaline, allowing calcite to precipitate within the pre-existing dissolution pores. Notably, some dissolution pores have not yet been incompletely filled (Figure 5D).

4.3.1.3 Ankerite

Ankerite is commonly developed in CO_2 reservoirs, filling dissolution pores and intergranular pores (Figures 5C, F, G). Some ankerites replaced calcite (Figure 5F), indicating that the formation time of ankerite was later than that of calcite.

4.3.1.4 Siderite and dolomite

Additionally, the CO_2 reservoir contains minor amounts of authigenic siderite (Figures 5D, H) and dolomite (Figure 5I). The dolomite was only observed under the microscope but not detected in the whole rock XRD analysis (Table 2).

4.3.2 Dissolution

The CO_2 reservoir in the study area exhibits intensive dissolution of feldspars, rock fragments, and calcites, forming numerous dissolution pores (Figure 5J–L). Remarkably, certain feldspar particles and calcite have undergone near-complete dissolution, forming mold pores (Figures 5J, K). Although some of the dissolution products, such as kaolinite and authigenic quartz, are filled in the dissolution pores (Figure 5L), and the carbonate minerals in the later stage are partially or completely filled in the dissolution pores (Figures 5C–E), the identification results of CO_2 reservoir thin sections show that the dissolution pores in the CO_2 reservoir still occupy an absolutely dominant position, with an average dissolution surface porosity of 14.7% and an average proportion of 70.4% (Table 1). In addition, the average dissolution porosity in the reservoirs near the faults is 19.4%, while the average dissolution porosity of reservoirs far from the faults is 9.4%. Obviously, the former is much greater than the latter.

4.4 The characteristics of carbon and oxygen isotopes in CO_2 gas reservoirs

Analysis results from carbonate veins and whole rock carbon and oxygen isotopes (Table 3) show that the $\delta^{13}C$ of carbonate minerals in mantle-derived CO_2 gas reservoirs are −9.0‰–−1.6‰, with an average of −5.2‰, and the $\delta^{18}O$ are −21.7‰–−12.7‰, with an average of −17.0‰. The average precipitation temperature of carbonate minerals in the study area was 121.9°C, which is much higher than the formation temperature.

5 Discussions

5.1 Evidence of the impact of mantle-derived CO_2 on reservoirs

CO_2 from the mantle has a unique range of C- and O-isotopes and high-temperature properties of mantle-derived fluids (e.g., Morishita, 2023; Ewa et al., 2012; Jin et al., 2013; Hou et al., 2019), and following prolonged interactions with the formation water and rocks, it ultimately generates carbonate minerals (e.g., Johnson et al., 2011; Harrison et al., 2019; Wei, et al., 2023). Thus, the impact of CO_2 on reservoirs can be confirmed based on the carbonate minerals generated during the mantle-derived CO_2-water-rock interactions and their isotopic characteristics.

TABLE 2 Whole rock and clay X-ray diffraction analysis results of CO_2 gas reservoirs in the study area.

Well		Depth (m)	Content of whole-rock minerals (%)								Relative content of clay minerals (%)				
			Quartz	K-feldspar	Plagioclas	Calcite	Ankerite	Siderite	Dawsonite	TCCM	I/S	I	K	C	Ratio of I/S
Near faults	A	1,464.80	81.5	8.7	0.0	0.0	1.0	0.0	0.2	7.1	26	11	59	4	45
	A	1,496.90	70.6	10.2	0.0	5.6	1.6	1.3	4.7	6.0	24	16	48	12	50
	A	1,531.49	64.4	7.2	5.7	3.3	1.7	1.1	8.5	8.1	30	11	52	7	40
	A	1,557.11	62.6	9.8	8.8	8.0	2.9	0.7	0.0	7.2	32	15	49	4	35
	Means of Well A		69.8	9.0	3.6	4.2	1.8	0.8	3.4	7.1	28	13	52	7	43
	B	1,442.00	62.3	9.4	7.4	6.8	1.0	0.9	4.1	8.1	32	15	46	7	50
	B	1,457.00	75.0	8.2	8.0	3.8	0.8	0.0	0.0	4.2	8	6	82	4	55
	B	1,496.90	71.1	5.1	9.5	5.9	1.8	0.0	0.0	6.6	19	14	57	10	35
	B	1,537.62	60.1	6.4	3.6	10.4	7.7	0.4	2.9	8.5	24	19	48	9	50
	Means of Well B		67.1	7.3	7.1	6.7	2.8	0.3	1.8	6.9	21	14	58	8	48
Far from faults	C	1,503.00	67.1	8.7	0.9	6.3	4.3	0.9	3.4	8.4	63	10	15	12	50
	C	1,527.90	56.3	8.4	1.2	15.8	4.6	0.3	3.5	9.9	43	14	38	5	45
	C	1,569.96	21.8	2.5	0.0	9.8	50.8	1.3	6.6	7.2	52	22	23	3	55
	C	1,626.80	43.8	6.7	0.0	35.1	3.8	0.0	0.0	10.6	50	20	14	16	55
	Means of Well C		47.3	6.6	0.5	16.8	15.9	0.6	3.4	9.0	52	17	23	9	51
	D	1,512.80	57.8	7.6	1.3	11.6	5.4	0.6	3.2	12.5	43	25	19	13	45
	D	1,530.45	34.7	7.4	1.1	26.8	3.2	2.3	10.0	14.5	39	23	30	8	45
	D	1,556.30	44.1	5.4	0.0	40.3	0.0	0.0	0.0	10.2	44	17	33	6	55
	Means of Well D		45.5	6.8	0.8	26.2	2.9	1.0	4.4	12.4	42	22	27	9	48
Means			58.2	7.4	3.2	12.6	6.0	0.7	3.1	8.6	35.3	15.9	40.9	8.0	47.3

Abbreviation: TCCM–total content of clay minerals, I/S–illite and smectite mixed layer, I–illite, K–kaolinite, C–chlorite.

10.3389/feart.2024.1436573

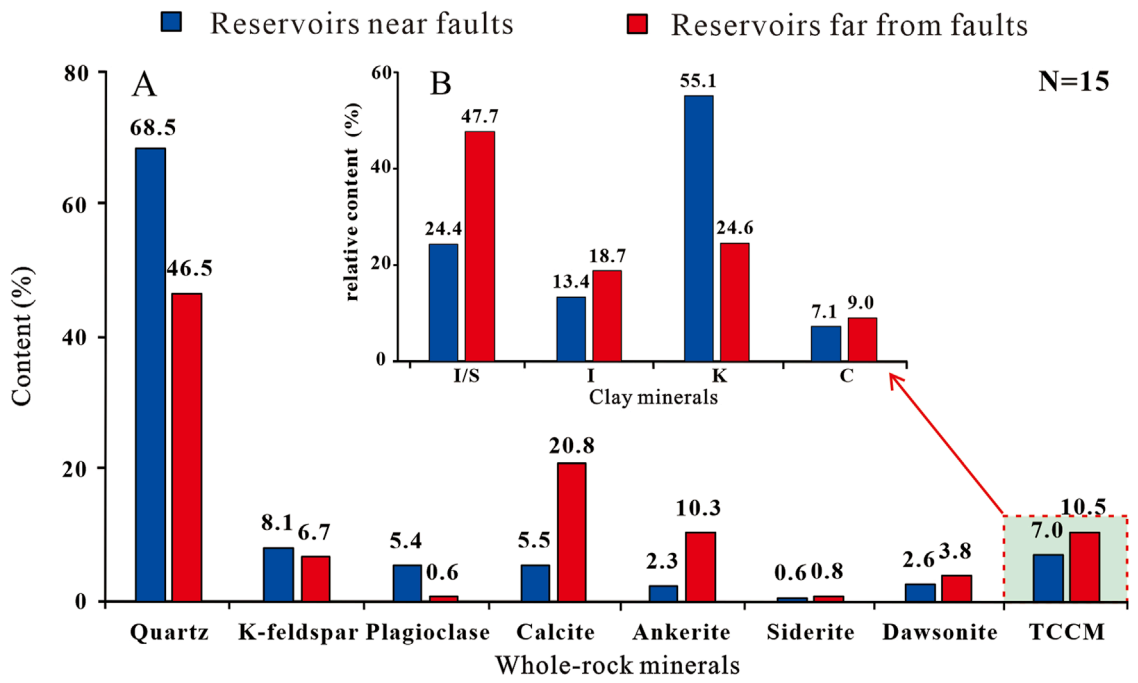

FIGURE 3
Mineral compositions of CO_2 gas reservoirs near and far from faults in the study area. **(A)** Histogram of mineral whole-rock content. **(B)** Histogram of relative content of clay minerals. TCCM–total contents of clay minerals.

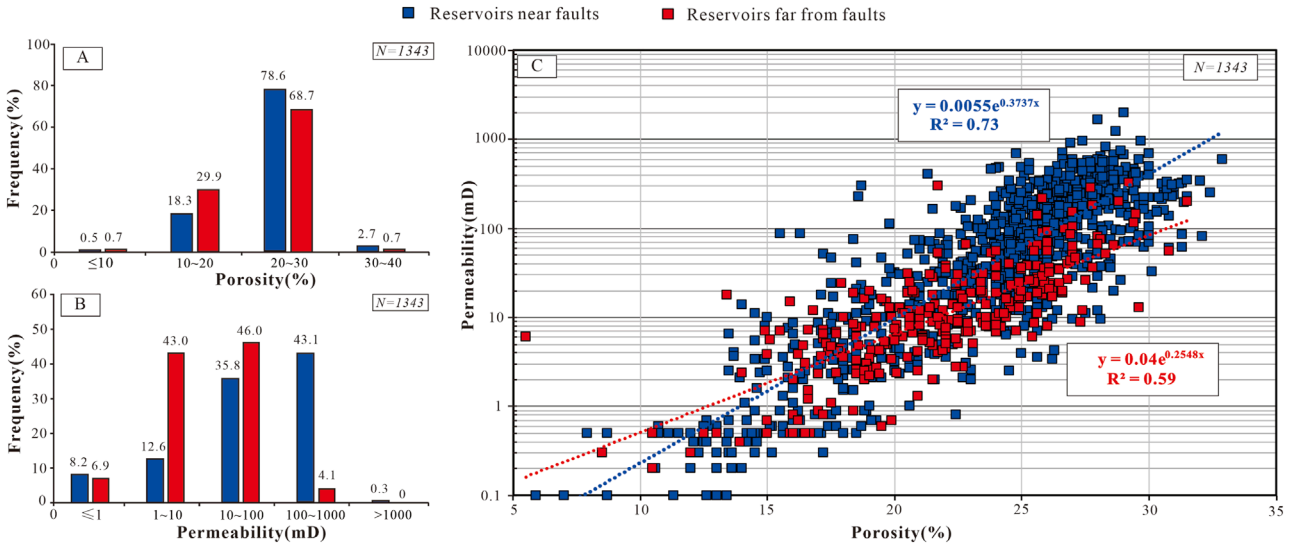

FIGURE 4
Characteristics of porosity and permeability of reservoirs near and far from faults. **(A)** Histogram of porosity frequency distribution. **(B)** Histogram of permeability frequency distribution. **(C)** The relationship of porosity and permeability in the CO_2 gas reservoirs.

5.1.1 Evidence from carbonate minerals

Dawsonite is the product of the long-term reaction between high-concentration mantle-derived CO_2 and formation water, as well as various feldspar (Equations 2–4), and is considered a "tracer mineral" for mantle-derived CO_2 fluid migration and accumulation (Ryzhenko, 2006; Liu et al., 2009; Johnson et al.,

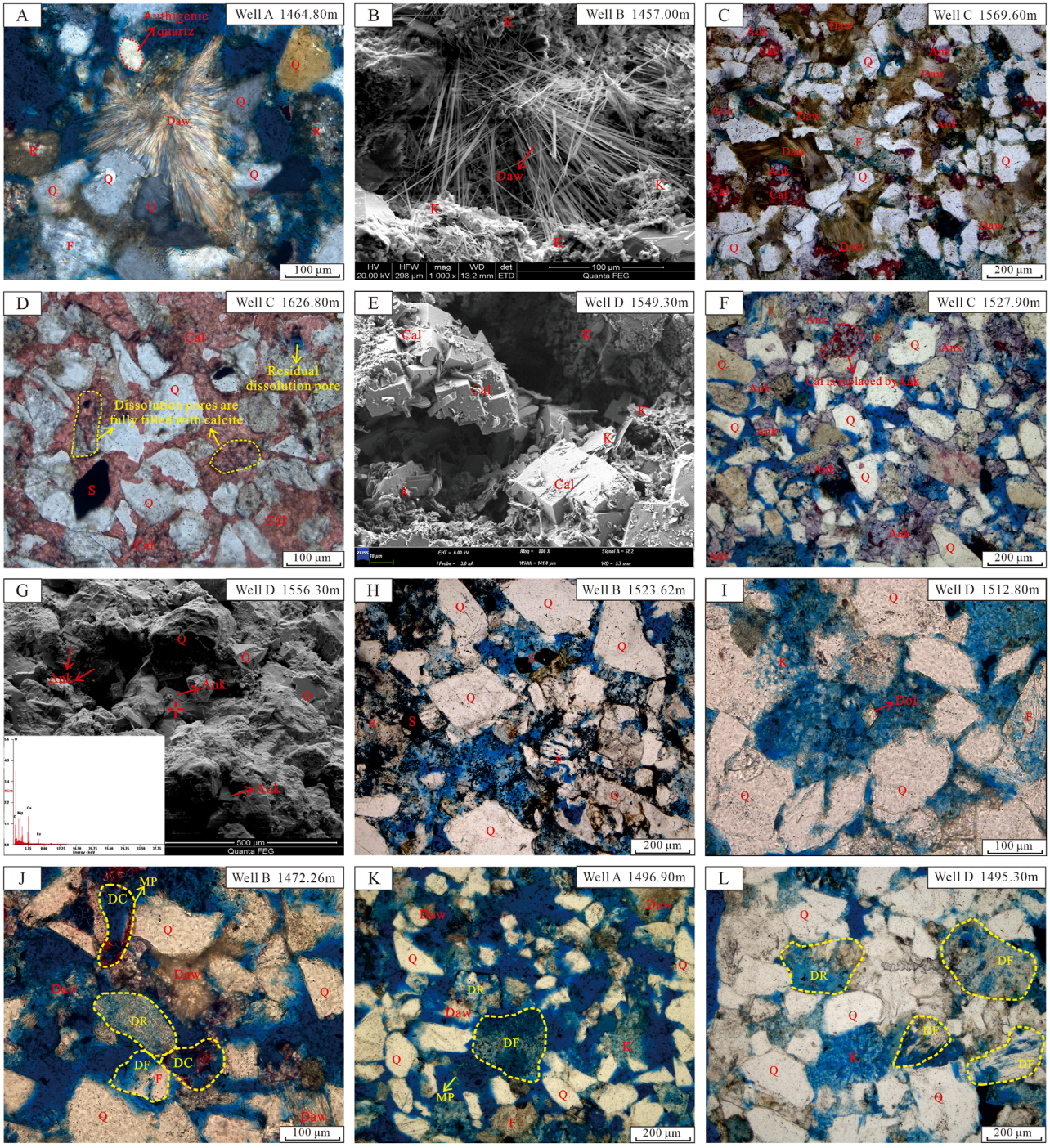

FIGURE 5
Pictures of carbonate cements and dissolution in CO_2 reservoirs. Picture **(A)** is derived from observations under cross-polarized light. Pictures **(B, E, G)** are derived from observations under SEM. Pictures **(C, D, F)**, and H-L are derived from observations under single polarized light. **(A)** Dawsonite accompanied with authigenic quartz **(B)** Dawsonite; **(C)** Dawsonite, calcite (dyed red) and ankerite (dyed blue-purple) cement; **(D)** calcite cement (dyed red), dissolution pores filled with calcites and unfilled residual dissolution pore; **(E)** Paragenesis of calcite and kaolinite; **(F)** Ankerite and calcite replaced by ankerite; **(G)** Ankerite and its energy dispersive spectrum analysis results **(H)** Rhombic authigenic siderite; **(I)** Authigenic dolomite; **(J)** Coexistence of dawsonite cement and intensive dissolution (feldspar, rock fragment, and calcite); **(K)** Coexistence of dawsonite, kaolinite and intensive dissolution (feldspar and rock fragment), some particles are completely dissolved and formed mold holes; **(L)** Coexistence of kaolinite and obvious dissolution (feldspar and rock fragment). Q, quartz; F, feldspar; R, rock fragment; Daw, dawsonite; Cal, calcite; Ank, ankerite; S, siderite; K, kaolinite; DR, dissolution of rock fragment; DF, dissolution of feldspar; DC, dissolution of calcite; MP, mold pore.

TABLE 3 The carbon and oxygen isotope data of whole rock and veins and the precipitation temperature of carbonate minerals of CO_2 gas reservoirs.

Well	Depth (m)	Sample types	$\delta^{13}C_{PDB}$(‰)	$\delta^{18}O_{PDB}$(‰)	FT (°C)	CPT (°C)
A	1,496.90	Whole rock	−6.4	−17.6	76.9	124.5
A	1,557.11	Vein	−8.0	−19.3	79.2	145.3
B	1,442.00	Vein	−4.8	−12.7	74.8	78.5
B	1,457.00	Whole rock	−1.7	−16.2	75.4	109.6
B	1,537.62	Whole rock	−4.2	−19.3	78.4	145.3
C	1,527.90	Whole rock	−5.0	−13.7	78.1	86.6
C	1,569.96	Whole rock	−1.6	−16.3	79.7	110.6
C	1,626.80	Whole rock	−6.6	−19.4	81.8	146.6
D	1,530.45	Whole rock	−5.0	−14.2	78.2	90.9
D	1,556.30	Whole rock	−9.0	−21.7	79.1	181.0
Mean			−5.2	−17.0	78.1	121.9

Abbreviation: GT, formation temperature; CPT, carbonate precipitation temperature.

2011). In the study area, dawsonite cement is generally developed (Figures 5A–C, J, K), while only a small amount of plagioclase and K-feldspar are present (Table 2), suggesting that the reaction between feldspar and mantle-derived CO_2 has generated dawsonite.

$$KAlSi_3O_{8(K-feldspar)} + Na^+ + CO_2 + H_2O \rightarrow NaAlCO_3(OH)_{2(Dawsonite)} + 3SiO_{2(Quartz)} + K^+ \quad (2)$$

$$NaAlSi_3O_{8(Albite)} + CO_2 + H_2O \rightarrow NaAlCO_3(OH)_{2(Dawsonite)} + 3SiO_{2(Quartz)} \quad (3)$$

$$CaAl_2Si_2O_{8(Anorthite)} + 2Na^+ + 3CO_2 + 3H_2O \rightarrow 2NaAlCO_3(OH)_{2(Dawsonite)} + CaCO_{3(Calcite)} + SiO_{2(Quartz)} + 2H^+ \quad (4)$$

Moreover, ankerite is generally considered a kind of cement in the middle to late diagenetic stage (e.g., Oluwadebi et al., 2018; Ma et al., 2018; Han et al., 2012), with a high precipitation temperature, and the precipitation temperatures of ankerite in Dongying Sag are about 110°C–135°C (Han et al., 2012). The ratio of I/S in mantle source CO_2 reservoirs is mainly between 40% and 55% (Table 2), indicating that the current diagenetic evolution is still in the early to middle diagenetic stage. However, the theoretical burial temperature of CO_2 reservoirs is 74.8°C–81.8°C in the study area (Table 3) (Gong et al., 2013), which is much lower than the precipitation temperature of ankerite. That is to say, the formation of ankerite (Figures 5C, F, G) occurs in a high-temperature environment formed by hydrothermal fluids rich in CO_2. And there is a close genetic relationship between ankerite and mantle-derived CO_2 in the study area.

5.1.2 Evidence from carbon and oxygen isotopes

According to the results of C- and O-isotopes analysis (Table 3), the $\delta^{13}C$ values of carbonate minerals in the mantle-derived CO_2 reservoir range from −9.0‰–−1.6‰, with an average of −5.2‰. Which basically fall within the range suggested for mantle-derived CO_2 (−8‰–4‰VPDB; Morishita, 2023; Dai et al., 2001). Moreover, the precipitation temperature of carbonate minerals is generally much higher than the maximum theoretical formation temperature (Table 3). Furthermore, the carbon and oxygen isotope data were submitted to the genetic chart of carbonate cement in the Bohai Bay Basin established by (Wang and Zhang, 2001), which showed that carbonate cement in mantle-derived CO_2 reservoirs was mainly formed in a transitional environment of low-temperature hydrothermal and high-temperature magmatic-hydrothermal fluids (Figure 6; e.g., Hou et al., 2019).

In summary, evidence from minerals and carbon and oxygen isotopes suggests that mantle-derived CO_2 indeed interacts with formation water and rocks, ultimately generating diverse carbonate cements precipitated in fractures and pores.

5.2 The dual effects of mantle-derived CO_2 on sandstone reservoirs

The mechanism of the impact of CO_2 on reservoirs by previous studys mainly comes from CO_2-water-rock reaction experiments. In these experiments, CO_2 fluids were injected into core plugs to make CO_2, water, and rock to fully react. And the porosity, permeability, and mineral changes of core plugs were measured pre- and post-experiment (e.g., Fischer et al., 2010; Aminu et al., 2018; Pearce et al., 2019; Wu et al., 2019; Fu et al., 2016). These studies generally indicate that dissolution is the main reaction between CO_2 and rocks, resulting in an increase in porosity (Wu et al.,

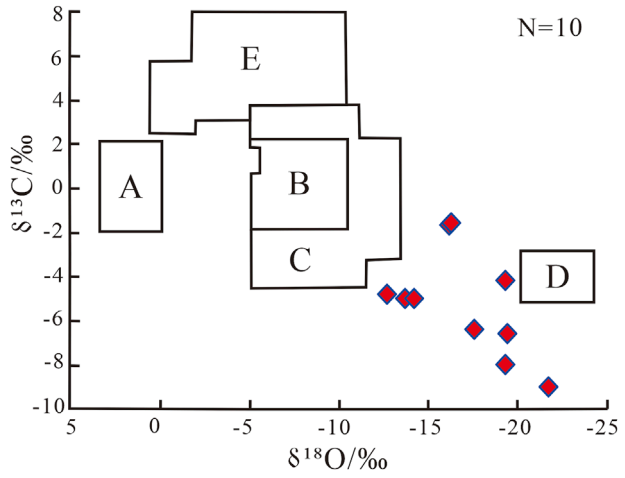

FIGURE 6
Origin of carbonate minerals (veins and cement) of mantle-derived CO_2 reservoirs in the study area [modified from Wang and Zhang (2001)]. A–carbonates sediment in low salinity solution. B–carbonate sediment in seawater salinity solution. C–carbonate sediment of cryogenic hydrothermal origin. D–carbonate sediment of magmatic-hydrothermal origin. E–carbonate sediment of lacustrine.

2019; Fu et al., 2016; Yu et al., 2016; Fischer et al., 2010) and a decrease in permeability due to blockage of throats by by-products of dissolution (Pearce et al., 2019; Wu et al., 2019; Aminu et al., 2018). However, the open fluid environment in the formation is relatively limited and generally found near faults (Zhou et al., 2020; Wei et al., 2017). On the contrary, most oil and gas reservoirs feature relatively closed fluid environments, making fluid migration relatively difficult (Yuan et al., 2013a; Zhao et al., 2016). Additionally, various ions can also participate in the water-rock reactions (Ahmat et al., 2022; Portier and Rochelle, 2005; Li et al., 2015). Therefore, the previous works cannot fully elucidate the impact of CO_2 on reservoirs.

In the high-temperature and high-pressure environment of the formation, the CO_2-water-rock reaction theoretically has dual effects on the sandstone reservoirs (Portier and Rochelle, 2005; Li et al., 2015). On the one hand, A large amount of CO_2 dissolves in the formation water and forms weak acids (H^+) (Equation 5), which then dissolve the carbonate minerals and aluminosilicate minerals, such as K-feldspar, plagioclase, and so on (Portier and Rochelle, 2005). On the other hand, the CO_3^{2-} formed in (Equation 5) combines with Ca^{2+}, Mg^{2+}, and Fe^{2+} in the formation water to generate stable carbonate minerals (Equation 6; Li et al., 2015).

$$CO_2 + H_2O \rightarrow CO_3^{2-} + 2H^+ \quad (5)$$

$$(Ca, Mg, Fe)^{2+} + CO_3^{2-} \rightarrow (Ca, Mg, Fe)\,CO_{3\,(Carbonates\,minerals)} \quad (6)$$

5.2.1 The impacts of dissolution by mantle-derived CO_2 on reservoirs

During the diagenetic evolution of reservoirs, dissolution is the key factor for good physical properties of oil and gas reservoirs (Ehrenberg and Baek, 2019). The dissolution in the mantle-derived CO_2 reservoirs is extremely strong (e.g., Liu N. et al., 2023; Liu et al., 2016; Zhou et al., 2020). The intensive dissolution of feldspars, rock fragments, and calcites forms a large number of dissolution pores (Figure 5J–L), and even some feldspar and calcite almost completely dissolved to form mold pores (Figures 5J, K). As a result, the dissolution pores occupy the absolute dominant position in the pore system of the study area (Table 1). Therefore, the dissolution of feldspar and early calcite by CO_2 in the study area greatly increases the storage space for oil and gas, and simultaneously, the seepage channels are also improved (Figure 4). Mantle-derived CO_2 plays a crucial role in improving the physical properties of reservoirs in the study area.

5.2.2 The impacts of cementation by mantle-derived CO_2 on reservoirs

Cementation is the most destructive diagenesis in oil and gas reservoirs, and carbonate minerals are the most common types of cement and can negatively impact reservoir properties (Ketzer et al., 2003; Ehrenberg and Baek, 2019). In mantle-derived CO_2 gas reservoirs, after a prolonged CO_2-water-rock interaction, CO_2 gas reservoirs will also precipitate carbonate cement such as dawsonite, calcite, siderite, ankerite, and dolomite (Figures 5A–I, e.g., Ahmat et al., 2022; Worden, 2006; Liu et al., 2009). These minerals will occupy the pore spaces (Figures 5A–I), leading to the deterioration of reservoir quality. There are fair negative correlations between the content of carbonate minerals, porosity, and permeability of mantle-derived CO_2 reservoirs (Figures 7A, B), indicating that the cementation of carbonate minerals affected by CO_2 is the primary factor leading to the deterioration of CO_2 reservoir quality (e.g., Ahmat et al., 2022).

In addition, dawsonite cements are commonly accompanied by authigenic quartz (Figure 5A) (Equations 2–4), and feldspar dissolution can generate authigenic quartz and diverse clay minerals, like kaolinite, I/S (Li et al., 2021). These authigenic quartz fill the pores and reduce the porosity of the reservoirs, while the clay minerals may block the pores and throats and decrease the permeability (Pearce et al., 2019; Wu et al., 2019; Aminu et al., 2018), which can to some extent decrease the quality of the reservoirs.

5.3 The impacts of mantle-derived CO_2 on reservoirs in different fluid environments

5.3.1 The impacts of mantle-derived CO_2 on sandstone reservoirs in open fluid environments

In oil and gas fields with faults, reservoirs near faults typically exhibit relatively good reservoir properties and relatively open fluid environments compared to reservoirs far from faults (Gudmundsson, 2022; Wei et al., 2017; Ward et al., 2016). The good reservoir properties are largely attributed to the dissolution effects of organic acids and the timely migration of dissolution by-products facilitated by formation fluids (Wuelstefeld et al., 2017; Zhou et al., 2020; Li et al., 2016). Similarly, the reservoirs near the faults in the study area all have good porosity and permeability (Figure 4; e.g., Hu, 2016; Wei et al., 2017). For example, the well A, located

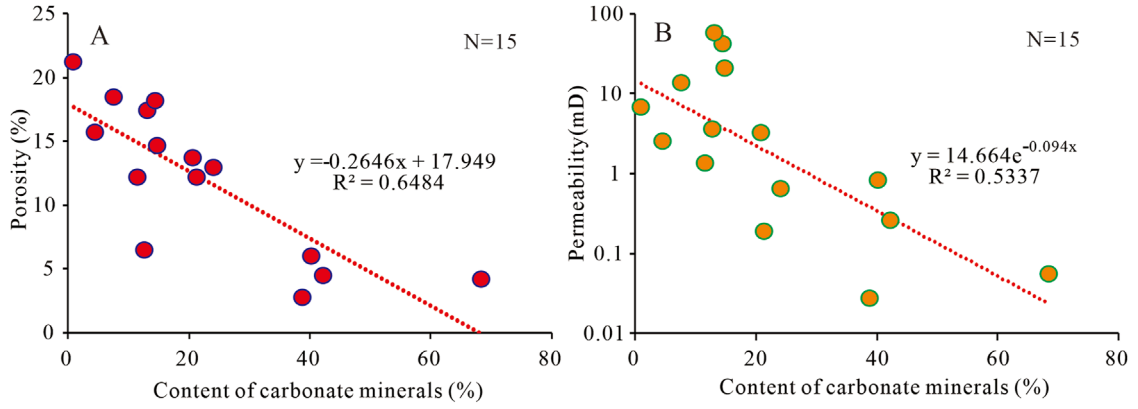

FIGURE 7
The relationship between contents of carbonate minerals and porosity **(A)** and permeability **(B)** in the mantle-derived CO_2 reservoirs.

near the fault, has an average porosity of 23.6% and an average permeability of 84.0 mD. According to the curves of average porosity and permeability, the vertical variation between porosity and permeability is relatively small (Figure 8). The dissolution of feldspar and early calcite in the reservoir is extremely intensive (Figure 8). The by-products of dissolution, clay minerals, are few and mainly composed of kaolinite (Figure 3). The carbonate cementation in Well A is weak, with only a small amount of other carbonate cement, except dawsonite that can stably exist in high CO_2 concentrations environment (Table 2).

Accordingly, In the open fluid environment near the fault in the study area, the by-products of feldspar dissolution (clay minerals and siliceous cement) are carried out from the reservoir by the flow of formation fluid (e.g., Wuelstefeld et al., 2017; Hu, 2016; Wei et al., 2017). In addition, the high-temperature environment provided by the influx of deep fluids also effectively intensifies the dissolution of feldspars and carbonate minerals (e.g., Wuelstefeld et al., 2017). All of these will lead to a significant improvement in reservoir quality. The abundant presence of kaolinite (Table 2) indicates that the fluid environment is acidic, which can inhibit the carbonate cementation (Boyer, 1983). Therefore, there is only a small amount of carbonate cement in the CO_2 reservoirs with open fluid environments (Table 2). Although there may be some dawsonite in high-concentration CO_2 environments, it cannot prevent the overall trend of improving reservoir quality (Figure 8).

In summary, an open fluid environment facilitates the dissolution of reservoirs by CO_2, facilitating the removal of dissolution products from the reservoirs, and high CO_2 concentration inhibits carbonate mineral cementation, greatly increasing reservoir porosity and permeability.

5.3.2 The impacts of mantle-derived CO_2 on sandstone reservoirs in closed fluid environments

In reservoirs located far from faults, the fluid environment is generally more closed, leading to limited fluid flow and complex diagenesis (Macaulay et al., 2001; Wang et al., 2017; Ahmat, et al., 2022; Yuan et al., 2013b). Clay minerals assemblages were used to identify closed fluid environments (Azzam et al., 2023; Lv et al., 2022). In the study area, the mantle-derived CO_2 reservoirs far away from faults have rare plagioclase, massive carbonate minerals, and I/S (Table 2; e.g., Azzam et al., 2023; Lv et al., 2022), which may imply the relatively closed fluid environment and mineral formation process. Initially, CO_2 entered the reservoirs to form an acidic environment, causing significant dissolution of plagioclase, generating dissolution pores and massive I/S. However, due to the difficulty of fluid flow in reservoirs far from faults, the dissolution by-products, such as Na^+, Ca^{2+}, and Al^{3+}, were not discharged timely, forming a local alkaline environment. Because I/S cannot be converted into kaolinite in alkaline environments (Yuan et al., 2013b), a large amount of I/S remains in the reservoirs. Meanwhile, the alkaline environments also lead to the precipitation of carbonate minerals in pre-existing dissolution pores (Figures 5C–E; e.g., Macaulay et al., 2001). In addition, reservoirs far from faults generally keep lower CO_2 content. For example, the well C is in a low CO_2 content area (Figure 1B), which also proves that the fluid environment of CO_2 reservoirs in well C is relatively closed.

After mantle-derived CO_2 enters the trap, CO_2 gradually migrates towards the top of the reservoir by the action of buoyancy (Wei et al., 2023; Gudmundsson, 2022), eventually leading to a decrease in CO_2 concentration with increasing depth (Figure 9). The higher the concentration of CO_2, the stronger the acidity of the fluid and the more intense the dissolution of reservoirs. Therefore, as the depth increases, the dissolution of the reservoir gradually weakens (Figure 9). The acidity of the fluid can also inhibit the cementation of carbonate minerals (Sun et al., 2020), so the carbonate cementation at the top of the reservoir is relatively weak (Figure 9). The prolonged contact between high concentrations of mantle-derived CO_2, formation water, and debris particles leads to strong dissolution of feldspar and early carbonate minerals (Figure 5J–L, e.g., Azzam et al., 2023; Lv et al., 2022), resulting in increased salinity of formation water (Giles and Boer, 1990; Yuan et al., 2013b). Due to the vertical difference of CO_2 concentration in the reservoir, the salinity of the formation water

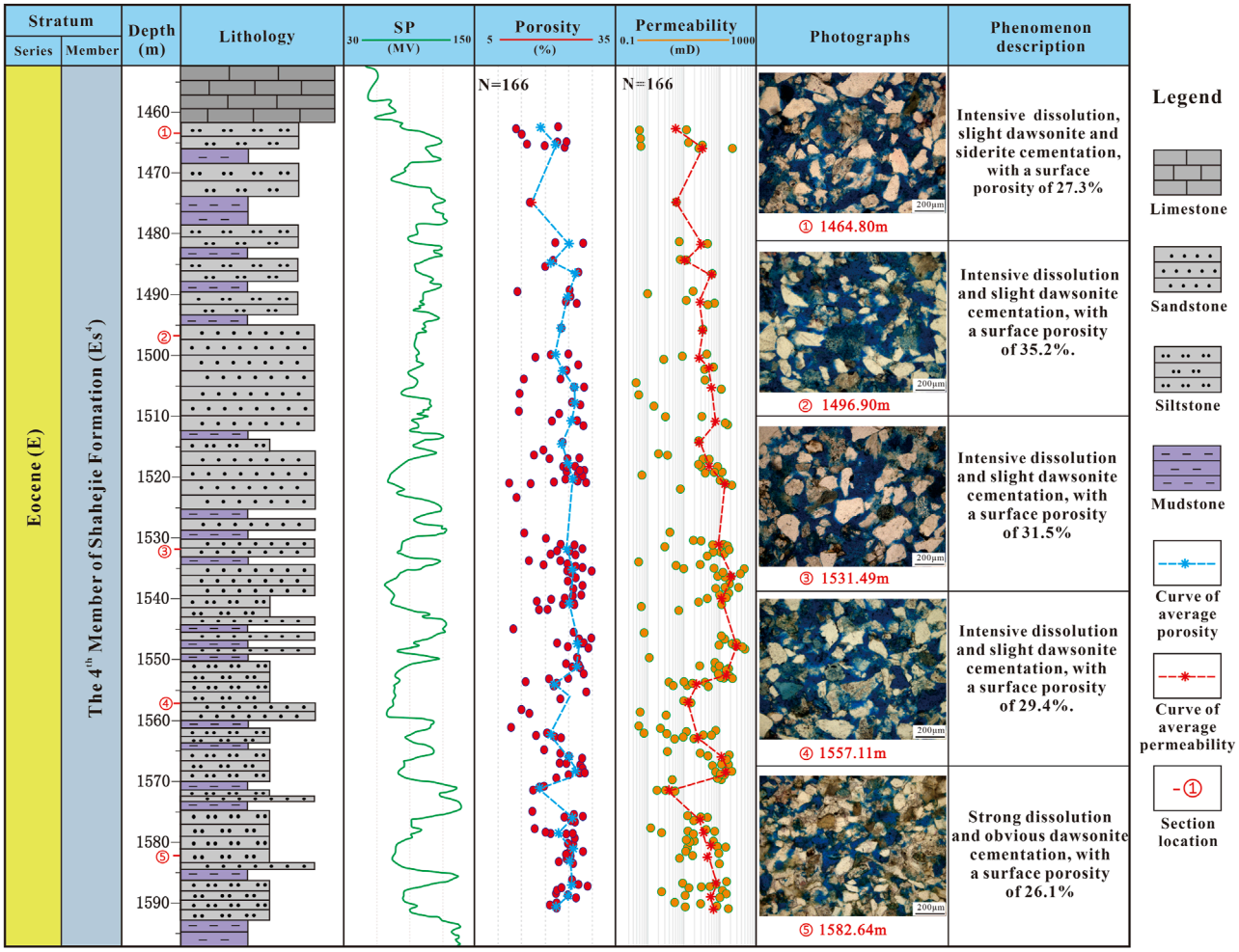

FIGURE 8
Composite columnar section of lithology, porosity, permeability, and diagenesis characteristics of Well A in an open fluid environment.

at the top of the reservoir would be higher than that at the bottom after a long-term CO_2-water-rock interaction. Naturally, high salinity formation water and dissolution by-products migrate and diffuse downwards under the influence of the difference in salinity. Therefore, the dissolution products at the top of the reservoir will also migrate downwards and recrystallize. In addition, as the depth increases, the CO_2 concentration decreases, the fluid alkalinity increases, and CO_2 gradually participates in carbonate minerals cementation (Figure 9).

In summary, within closed fluid environment reservoirs, as depth increases, dissolution gradually weakens while carbonate cementation strengthens (Figure 9). The constructive effects of dissolution and the destructive effects of carbonate cementation work synergistically, resulting in a gradual decrease in porosity and permeability (Figure 7). This trend is observed across each sand layer (Figure 9).

5.3.3 Impact pattern of mantle-derived CO_2 on reservoirs in open and closed fluid environments

Based on the argument above, a comprehensive pattern of the impact of CO_2 on reservoirs within open and closed fluid environments in the study area has been established (Figure 10). The reservoirs near the faults keep an open fluid environment, while the further away from the faults, the more closed the fluid environment is (e.g., Gudmundsson, 2022; Ward et al., 2016; Macaulay et al., 2001; Wang et al., 2017; Ahmat, et al., 2022). As the distance from the fault increases, the dissolution weakens, carbonate cementation strengthens, contents of clay minerals and the relative content of I/S increase, while the relative content of kaolinite decreases (e.g., Azzam et al., 2023; Lv et al., 2022). In an open fluid environment, feldspar strongly dissolves and generates a large number of dissolution pores (e.g., Hu, 2016; Wei and Sun, 2017), and the dissolution by-products (clay minerals) are timely removed from the reservoirs and migrate northward along the faults with the fluids. Moreover, the acidic environment formed by CO_2 inhibits the precipitation of carbonate minerals (Boyer, 1983), so there are only a few carbonate cements. All of these effectively improve the physical properties of reservoirs. In a relatively closed fluid environment, as the depth increases, the CO_2 concentration decreases, the acidity of the formation water weakens, and the dissolution weakens, but the cementation of carbonate minerals strengthens. Due to the higher CO_2 content at the top of the reservoir

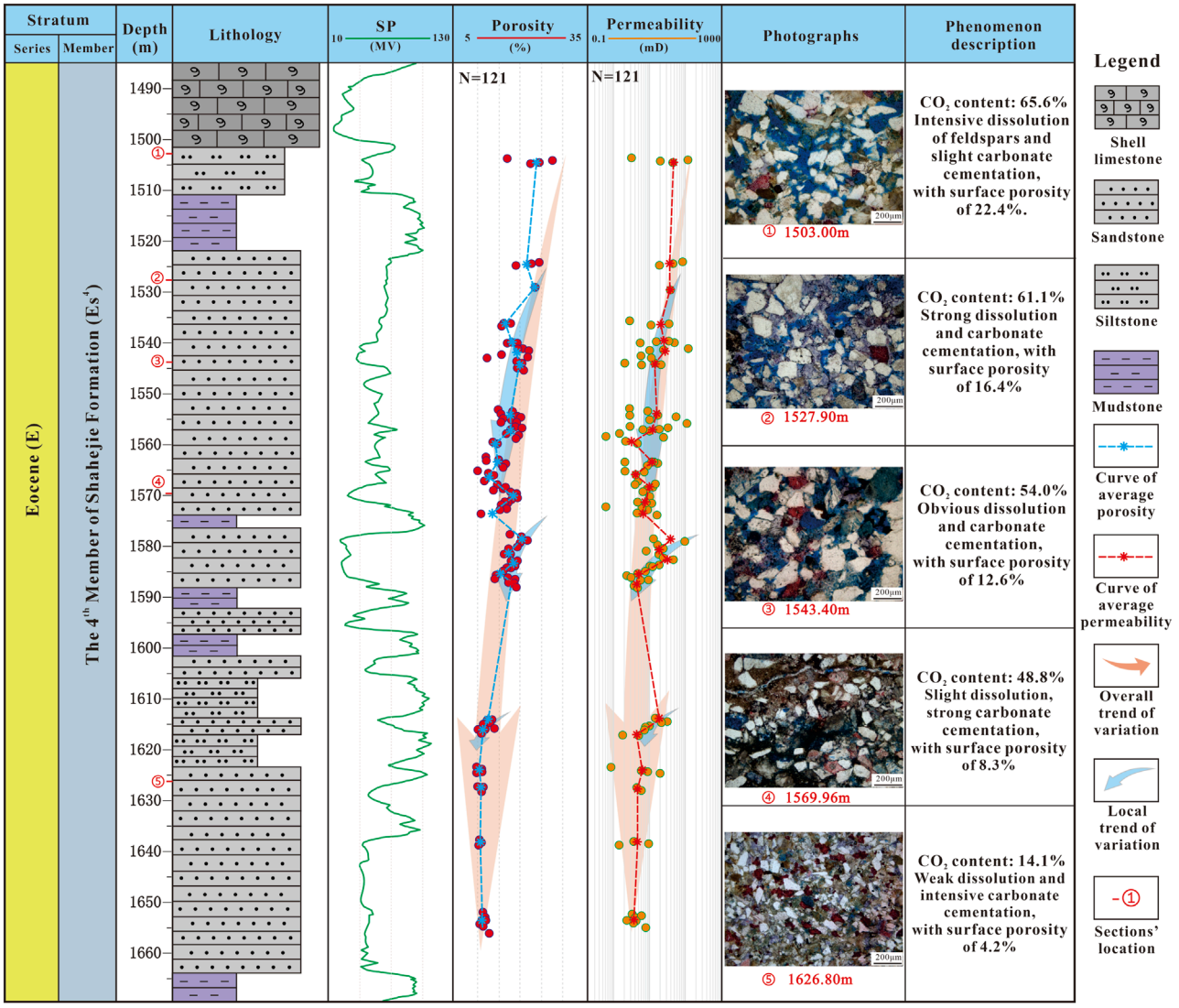

FIGURE 9
Composite columnar section of lithology, porosity, permeability, and diagenesis characteristics of Well C in a relatively closed fluid environment.

compared to the bottom, the CO_2-water-rock interactions are more intense, leading to differences in the concentration of dissolution by-products between the upper and lower parts of the reservoirs. Although dissolution products cannot be effectively discharged from the reservoir or transported over long distances (Yuan et al., 2013b), they would migrate downwards and recrystallize due to the concentration gradient of the by-products. Ultimately, the porosity and permeability of reservoirs gradually decrease with depth.

Previous experiments have demonstrated that CO_2 primarily participates in mineral dissolution, often overlooking the dual effects of CO_2 on reservoirs and the roles of fluid environments in this context under geological conditions. This is why it's important to select geological cases to illustrate the impact of CO_2 on reservoirs. This work confirms the influence of mantle-derived CO_2 on reservoirs through mineralogy (dawsonite and ankerite) and geochemistry (stable C- and O-isotopes), and further demonstrates the dual effects (dissolution and cementation) of mantle-derived CO_2 on reservoirs integrated with reservoir physical properties, with a particular focus on how CO_2 influences reservoirs in different fluid environments. However, due to the limitation of CO_2 content range (about 15%–70%) in the study area, we are unable to investigate the effects of low-concentration CO_2 on sandstone reservoirs, which may affect the generalizability of this study. Besides, the formation temperature and pressure, and salinity of formation water should be considered when dealing with other cases. Overall, this work can be applied to the studies of reservoir homogeneity and sweet spots in regions with hydrothermal and mantle-derived CO_2 activities.

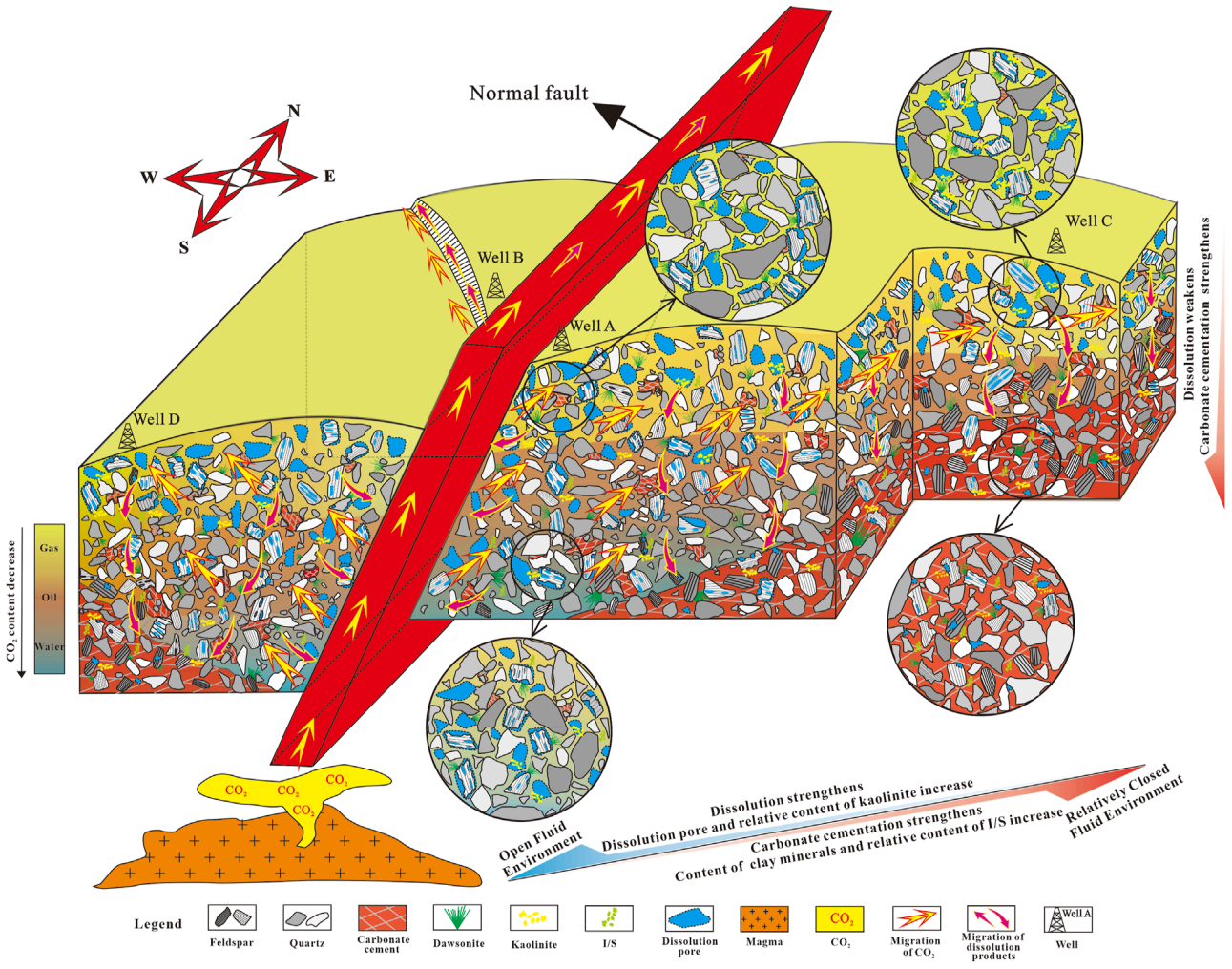

FIGURE 10
The pattern diagram of the impacts of CO_2 on reservoirs in open and relatively closed fluid environments.

6 Conclusion

In this paper, we take a CO_2 gas reservoir in the Dongying Sag, Bohai Bay Basin, China, as an example, using a multi-technique approach in mineralogy and geochemistry to investigate evidence of the impact of mantle-derived CO_2 on the reservoir. Combining with the charateristics of the reservoir's physical properties, we elucidate the mechanisms through which mantle-derived CO_2 influences the sandstone reservoirs and discuss the patterns of its impact on reservoir properties in open and closed fluid environments. The conclusions can be drawn as follows:

(1) Dawsonite (a special tracer mineral of mantle-derived CO_2) and ankerite (its crystallization temperature is much higher than the normal geothermal gradient of the study area) are widely distributed in the CO_2 reservoir of the Dongying Sag. Moreover, the $\delta^{13}C$ (−9.0‰–−1.6‰) and $\delta^{18}O$ (−21.7–−12.7‰) of carbonate cements in the mantle-derived CO_2 gas reservoir basically fall within the range suggested for mantle-derived CO_2 and hydrothermal fluids. These mineralogical and geochemical evidence indicate that CO_2-rich hydrothermal fluids have actively participated in water-rock reactions within the reservoir, thereby impacting its diagenesis.

(2) The CO_2 reservoirs near faults in the study area are an open fluid environment, while the CO_2 reservoirs far from faults keep a relatively closed fluid environment. There are significant differences in the debris particles, mineral composition, and physical properties between reservoirs in open fluid environments and closed fluid environments. The former has better porosity and permeability, more quartz, as well as fewer feldspar, carbonate, and clay mineral cement. Furthermore, the clay minerals in open fluid environments are predominantly kaolinite, whereas these in closed fluid environments primarily consist of I/S.

(3) The mantle-derived CO_2 has dual effects on sandstone reservoirs. On the one hand, the dissolution by CO_2 greatly increases the reservoir's storage and seepage capacity. On the other hand, the carbonate cement formed by the CO_2-water-rock reaction can also lead to serious deterioration of

reservoir quality. In open fluid environments, CO_2 strongly dissolves feldspar and carbonate minerals in reservoirs, and the dissolution by-products (clay minerals) are carried out from the reservoirs timely, and the acidic environment formed by CO_2 inhibits carbonate cementation, which synergistically improves the physical properties of reservoirs. In closed fluid environments, decreasing CO_2 concentrations with depth leads to diminishing dissolution effects and increased carbonate cementation, resulting in reduced reservoir porosity and permeability.

However, the CO_2 content, the formation temperature and pressure, and salinity of formation water should be considered when dealing with other cases. Overall, this study provides a good understanding for the impacts of mantle-derived CO_2 on sandstone diagenesis and reservoir properties in open and closed fluid environments, which may contribute to the studies of reservoir homogeneity and sweet spots in regions with hydrothermal and mantle-derived CO_2 activities.

Data availability statement

The original contributions presented in the study are included in the article/supplementary material, further inquiries can be directed to the corresponding authors.

Author contributions

MW: Conceptualization, Investigation, Methodology, Writing–original draft, Writing–review and editing. JZ: Project administration, Resources, Supervision, Writing–review and editing. CL: Writing–review and editing, Investigation. JQ: Supervision, Validation, Writing–review and editing. WW: Investigation, Writing–original draft. HZ: Investigation, Writing–review and editing. HC: Investigation, Writing–review and editing.

Funding

The author(s) declare that financial support was received for the research, authorship, and/or publication of this article. This work is supported by the National Natural Science Foundation of China, Grant number 42302144.

Acknowledgments

We would like to express our sincere gratitude to the Petroleum Exploration and Development Research Institute of Shengli Oilfield, China Petroleum and Chemical Corporation, for providing us with the core samples and data used in this study. Additionally, we would like to extend our special thanks to the reviewers and editors for their insightful comments and suggestions, which have greatly helped to improve the quality of this article.

Conflict of interest

The authors declare that the research was conducted in the absence of any commercial or financial relationships that could be construed as a potential conflict of interest.

Publisher's note

References

Ahmat, K., Cheng, J., Yu, Y., Zhao, R., and Li, R. (2022). CO_2-water-rock interactions in carbonate formations at the tazhong uplift, Tarim basin, China. *Minerals* 12, 635. doi:10.3390/min12050635

Aminu, D. M., Nabavi, A. S., and Manovic, V. (2018). CO_2-brine-rock interactions: the effect of impurities on grain size distribution and reservoir permeability. *Int. J. Greenh. Gas Control* 78, 168–176. doi:10.1016/j.ijggc.2018.08.008

Anderson, C. D. S., Gabriella, D. O. Q., Julio, C. M., João, M., Mauro, C. G., Fred, J., et al. (2023). Petrogenetic insights on tephritic magmatism from davis bank South Atlantic ocecan-vitória-trindade ridge VTR, Brazil: the role of a CO_2-enriched mantle source. *J. S. Am. Earth Sci.* 122, 104170. doi:10.1016/j.jsames.2022.104170

Azzam, F., Blaise, T., Dewla, M., Patrier, P., Beaufort, D., Abd Elmola, A., et al. (2023). Role of depositional environment on clay coat distribution in deeply buried turbidite sandstones: insights from the agat field, Norwegian North Sea. *Mar. Petroleum Geol.* 155, 106379. doi:10.1016/j.marpetgeo.2023.106379

Boyer, F. (1983). *Depositional environments and diagenetic history of the springer formation: ardmore basin, Oklahoma*. Dallas: The University of Texas at.

Cheng, X., Cao, Y., Yuan, G., Wang, Y., and Zan, N. (2020). Origin and distribution model of the lower Paleozoic carbonate reservoirs in pingfangwang pingnan buried hills, Dongying Sag. *J. China Univ. Petroleum Ed. Nat. Sci.* 44, 1–14. doi:10.13969/j.issn.1673-5005.2020.03.001

Dai, J., Shi, X., and Wei, Y. (2001). Summary of the abiogenic origin theory and the abiogenic gas pools (fields). *Acta Pet. Si-Nica* 22, 5–10.

Diker, C., Ulusoy, İ., Akkaş, E., Aydın, E., Gümüş, E., Gümüş, E., et al. (2024). Hydrothermal fluid circulation within the restless structural frame of Hasandağ volcanic system (Central Anatolia, Türkiye) inferred from self-potential, CO_2, and temperature measurements. *J. Volcanol. Geotherm. Res.* 446, 107994. doi:10.1016/J.JVOLGEORES.2023.107994

Dmitriyevskiy, N. A., Kireyev, A. F., Bochko, A. R., and Fedorova, T. A. (2010). Hydrothermal origin of oil and gas reservoirs in basement rock of the southern vietnam continental shelf. *Int. Geol. Rev.* 35 (7), 621–630. doi:10.1080/00206819309465547

Ehrenberg, S. N., and Baek, H. (2019). Deposition, diagenesis and reservoir quality of an oligocene reefal-margin limestone succession: asmari formation, United Arab Emirates. *Sediment. Geol.* 393, 105535. doi:10.1016/j.sedgeo.2019.105535

Ewa, S., Hervé, M., Morihisa, H., Michał, Ś., Andrzej, D., Jens, G., et al. (2012). Evidence in archaean alkali feldspar megacrysts for high-temperature interaction with mantle fluids. *J. Petrology* 53, 67–98. doi:10.1093/petrology/egr056

Fischer, S., Axel, L., and Maren, W. (2010). CO_2-brine-rock interaction - first results of long-term exposure experiments at *in situ* P-T conditions of the ketzin CO_2 reservoir. *Chem. Erde* 70, 155–164. doi:10.1016/j.chemer.2010.06.001

Folk, R. L. (1968). *The petrology of sedimentary rocks*. Austin, Texas: Hemphill Publishing Company, 127.

Friedman, N., and O'Neil, J. R. (1977). *Data of geochemistry: compilation of stable isotope fractionation factors of geochemical interest*. Washington: D.C: US Government Printing Office.

Fu, M., Song, R., Xie, Y., Zhang, S. n., Gluyas, J. G., Zhang, Y. z., et al. (2016). Diagenesis and reservoir quality of overpressured deep-water sandstone following inorganic carbon dioxide accumulation: upper miocene huangliu formation, Yinggehai Basin, South China Sea. *Mar. Petroleum Geol.* 77, 954–972. doi:10.1016/j.marpetgeo.2016.08.005

Giles, M. R., and de Boer, R. B. (1990). Origin and significance of redistributional secondary porosity. *Mar. Petroleum Geol.* 7, 378–397. doi:10.1016/0264-8172(90)90016-a

Gong, J., Zhang, J., Zhang, S., and Zhang, L. (2013). The effect of the Paleogene-Neogene magmation on hydrocarbon-generating region of the upper Es_{3-4}-middle Es_3 dark argillaceous rocks in Dongying Depression. *J. Northwest Univ. Nat. Sci. Ed.* 43, 101–108. doi:10.16152/j.cnki.xdxbzr.2013.01.016

Gudmundsson, S. (2022). Transport of geothermal fluids along dikes and fault zones. *Energies* 15, 7106. doi:10.3390/en15197106

Guo, D., Xia, B., Wang, X., and Zhang, S. (2006). Relationship between faulting and reservoiring of CO_2 in jiyang depression. *Nat. Gas. Ind.* 26, 40–42.

Guo, X., He, S., Liu, K., Cao, F., Shi, H., and Zhu, J. (2011). Condensates in the PY30-I structure, Panyu uplift, Pearl River Mouth basin, South China Sea: evidence for hydrothermal activity associated with petroleum migration and accumulation. *J. Petroleum Geol.* 34 (2), 217–232. doi:10.1111/j.1747-5457.2011.00502.x

Han, H., Zhang, J., Zhang, J., Wu, H., Xiang, X., and Lei, Y. (2010). A study on the phase of CO_2 pools underground, Jiyang depression. *J. Northwest Univ. Nat. Sci. Ed.* 40, 493–496. doi:10.16152/j.cnki.xdxbzr.2010.03.020

Han, Y., He, S., Song, G., Wang, Y., Hao, X., Wang, B., et al. (2012). Origin of carbonate cement in the overpressured top seal and adjacent sandstones in Dongying Depression. *Acta Pet. Sin.* 33, 385–393.

Harrison, A. L., Tutolo, B. M., and DePaolo, D. J. (2019). The role of reactive transport modeling in geologic carbon storage. *Int. Mag. Mineralogy, Geochem. Petrology* 15, 93–98. doi:10.2138/gselements.15.2.93

Hou, Z., Chen, S., Liu, H., Yang, H., and Wang, Y. (2019). Hydrothermal fluid activity and its hydrocarbon geological significance in Dongying Depression. *J. China Univ. Min. and Technol.* 48, 1090–1101. doi:10.13247/j.cnki.jcumt.000999

Hu, W. (2016). Origin and Indicators of deep-seated fluids in sedimentary basins. *Bull. Mineralogy, Petrology Geochem.* 35, 817–826. doi:10.3969/j.issn.1007-2802.2016.05.002

Huang, X., Jin, Z., Liu, Q., Meng, Q., Zhu, D., Liu, J., et al. (2021). Catalytic hydrogenation of post-Mature hydrocarbon source rocks under deep-derived fluids: an example of early Cambrian Yurtus formation, Tarim basin, NW China. *Front. Earth Sci.* 9. doi:10.3389/FEART.2021.626111

Jin, Z., Zhu, D., Meng, Q., and Hu, W. (2013). Hydrothermal activities and influences on migration of oil and gas in Tarim Basin. *Acta Petrol. Sin.* 29, 1048–1058.

Johnson, G., Nightingale, B. M., Shevalier, M., and Hutcheon, I. (2011). Using oxygen isotope ratios to quantitatively assess trapping mechanisms during CO_2 injection into geological reservoirs: the pembina case study. *Chem. Geol.* 283, 185–193. doi:10.1016/j.chemgeo.2011.01.016

Kang, Y., Zou, L., Liu, Z., Han, M., Lu, H., and Yao, S. (2014). Faulted structure and its effect on oil–gas reservoir forming in Qingcheng arch. *Petroleum Geol. Recovery Effic.* 21, 45–48. doi:10.13673/j.cnki.cn37-1359/te.2014.06.011

Ketzer, J. M., Holz, M., Morad, S., and Al-Aasm, J. S. (2003). Sequence stratigraphic distribution of diagenetic alterations in coal-bearing, paralic sandstones: evidence from the rio bonito formation (early permian), southern Brazil. *Sedimentology* 50 (5), 855–877. doi:10.1046/j.1365-3091.2003.00586.x

Li, J., Li, H., Jiang, W., Cai, M. L., He, J., Wang, Q., et al. (2024). Shale pore characteristics and their impact on the gas-bearing properties of the Longmaxi Formation in the Luzhou area. *Sci. Rep.* 14, 16896. doi:10.1038/s41598-024-66759-7

Li, L., Zhong, D., Yang, C., and Zhao, L. (2016). Faults role in formation and distribution of the mantle derived carbon dioxide gas pools: case study of the Jiyang depression in Bohai Bay Basin, China. *Acta Petrol. Sin.* 32, 2209–2216.

Li, M., Song, L., Yu, H., Cao, Y., and Yuan, G. (2021). Influence of pH value on feldspar dissolution and pore-increasing effect. *J. China Univ. Petroleum Ed. Nat. Sci.* 45, 33–41. doi:10.3969/j.issn.1673-5005.2021.05.004

Li, Z., Guo, J., Zhang, Y., and Chen, J. (2015). High–temperature supercritical CO_2 water-rock simulation experiment of sandstone and its geological significance. *Nat. Gas. Ind.* 35, 31–38. doi:10.3787/j.issn.1000-0976.2015.05.0075

Liu, H., Liu, C., Zhang, H., Zhou, Z., and Han, F. (2024). The precipitation mechanisms of scheelite from CO_2-rich hydrothermal fluids: Insight from thermodynamic modeling. *Appl. Geochem.* 175, 106187. doi:10.1016/J.APGEOCHEM.2024.106187

Liu, J., Ge, Z., and Li, X. (2023). The accumulation law and helium-rich genesis of CO_2 gas reservoir in Subei Basin. *Nat. Gas. Geosci.* 34, 477–485. doi:10.11764/j.issn.1672-1926.2022.11.005

Liu, J., Pujol, M., Zhou, H., Selby, D., Li, J., and Cheng, B. (2022). Origin and evolution of a CO_2-Rich gas reservoir offshore Angola: insights from the gas composition and isotope analysis. *Appl. Geochem.* 148, 105552. doi:10.1016/j.apgeochem.2022.105552

Liu, L., Ming, X., Liu, N., Yang, H., Yu, L., Bai, H., et al. (2016). Characteristics and formation mechanism of Muti-layer distribution of dawsonite in the Honggang oil field, southern Songliao Basin. *Bull. Mineralogy, Petrology Geochem.* 35, 817–826. doi:10.3969/j.issn.1007-2802.2016.05.007

Liu, L., Zhu, D., Qu, Z., Jin, Z., Wang, X., and Dong, L. (2009). Impacts of mantle–genetic CO_2 influx on the reservoir quality of lower cretaceous sandstone from wuerxun depression, Hailaer Basin. *Acta Petrol. Sin.* 25, 2311–2319.

Liu, N., Wu, K., Liu, L., Yu, L., and Sun, Y. (2019). Dawsonite characteristics and its implications on the CO_2 in Yinggehai-Huangliu formation of Ledong area, Yinggehai Basin. *Earth Sci.* 44, 2695–2703. doi:10.3799/dqkx.2019.106

Liu, Q., Wu, X., Wang, X., Jin, Z., Zhu, D., Meng, Q., et al. (2019). Carbon and hydrogen isotopes of methane, ethane, and propane: a review of genetic identification of natural gas. *Earth-Science Rev.* 190, 247–272. doi:10.1016/j.earscirev.2018.11.017

Liu, Q., Zhu, D., Jin, Z., Meng, Q., and Yu, H. (2017). Effects of deep CO_2 on petroleum and thermal alteration: the case of the Huangqiao oil and gas field. *Chem. Geol.* 469, 214–229. doi:10.1016/j.chemgeo.2017.06.031

Liu, Q., Zhu, D., Jin, Z., Tian, H., Zhou, B., Jiang, P., et al. (2023). Carbon capture and storage for long-term and safe sealing with constrained natural CO_2 analogs. *Renew. Sustain. Energy Rev.* 17, 113000. doi:10.1016/J.RSER.2022.113000

Liu, R., Heinemann, N., Liu, J., Zhu, W., Wilkinson, M., Xie, Y., et al. (2019). CO_2 sequestration by mineral trapping in natural analogues in the Yinggehai Basin, South China Sea. *Mar. Petroleum Geol.* 104, 190–199. doi:10.1016/j.marpetgeo.2019.03.018

Lu, J., Li, C., Wang, M., and Zhang, C. (2022). Review of deep fluids in sedimentary basins and their influence on resources, with a focus on oil and geothermal exploitation. *Front. Earth Sci.* 10. doi:10.3389/feart.2022.896629

Lv, X., Fu, M., Zhang, S., Meng, X., Liu, Y., Ding, X., et al. (2022). Effect of diagenesis on the quality of sandstone reservoirs Exposed to high-temperature, overpressure, and CO_2-Charging conditions: a case study of upper Miocene Huangliu sandstones of Dongfang District, Yinggehai Basin, South China Sea. *Front. Earth Sci.* 10. doi:10.3389/feart.2022.885602

Ma, P., Lin, C., Zhang, S., Dong, C., Zhao, Y., Dong, D., et al. (2018). Diagenetic history and reservoir quality of tight sandstones: a case study from Shiqianfeng sandstones in upper Permian of Dongpu Depression, Bohai Bay Basin, eastern China. *Mar. Petroleum Geol.* 89, 280–299. doi:10.1016/j.marpetgeo.2017.09.029

Macaulay, C. I., Beckett, D., Beckett, D., Braithwaite, K., Bliefnick, D., and Philps, B. (2001). Constraints on diagenesis and reservoir quality in the fractured hasdrubal field, offshore Tunisia. *J. Petroleum Geol.* 24 (1), 55–78. doi:10.1111/j.1747-5457.2001.tb00661.x

Miao, Q., Xu, C., Hao, F., Yin, J., Wang, Q., Xie, M., et al. (2020). Roles of fault structures on the distribution of mantle-derived CO_2 in the Bohai Bay Basin, NE China. *J. Asian Earth Sci.* 197, 104398. doi:10.1016/j.jseaes.2020.104398

Morishita, Y. (2023). Hydrothermal calcite precipitation in veins: Inspired by experiments for oxygen isotope fractionation between CO_2 and calcite from 1°C to 150°C. *Appl. Sci.* 13 (9), 5610. doi:10.3390/app13095610

Niu, Z., Wang, Y., Wang, X., Meng, W., Liu, X., Wang, R., et al. (2022). Characteristics of crude oil with different sulfur content and genesis analysis of high-sulfur crude oil in the eastern section of the southern slope of Dongying Sag. *Petroleum Geol. Recovery Effic.* 19, 15–27. doi:10.13673/j.cnki.cn37-1359/te.202108024

Oluwadebi, A. g., Taylor, K. G., and Dowwey, P. J. (2018). Diagenetic controls on the reservoir quality of the tight gas Collyhurst sandstone formation, lower Permian, East Irish sea basin, United Kingdom. *Sidementary Geol.* 371, 55–74. doi:10.1016/j.sedgeo.2018.04.006

Pearce, J. K., Dawson, G. K. W., Sommacal, S., and Golding, S. D. (2019). Experimental and modelled reactions of CO_2 and SO_2 with core from a low salinity aquifer overlying a target CO_2 storage complex. *Geosciences* 9, 513. doi:10.3390/geosciences9120513

Portier, S., and Rochelle, C. (2005). Modeling CO_2 solubility in pure water and NaCl-type waters from 0 to 300°C and from 1 to 300 bar application to the utsira formation at sleipner. *Chem. Geol.* 217, 187–199. doi:10.1016/j.chemgeo.2004.12.007

Ranta, E., Halldórsson, S. A., Barry, P. H., Ono, S., Robin, J. G., Kleine, B. I., et al. (2023). Deep magma degassing and volatile fluxes through volcanic hydrothermal systems: insights from the askja and kverkfjöll volcanoes, Iceland. *J. Volcanol. Geotherm. Res.* 436, 107776. doi:10.1016/j.jvolgeores.2023.107776

Ryzhenko, B. N. (2006). Genesis of dawsonite mineralization: thermodynamic analysis and alternatives. *Geochem. Int.* 44, 835–840. doi:10.1134/S0016702906080088

Sun, C., and Dasgupta, R. (2023). Carbon budget of earth's deep mantle constrained by petrogenesis of silica-poor ocean island basalt. *Earth Planet. Sci. Lett.* 611, 1–12. doi:10.1016/j.epsl.2023.118135

Sun, D., Li, W., Lu, S., Liu, X., He, T., Zhu, P., et al. (2020). Reservoir characteristics and controlling factors of shushanhe formation in yingmaili area of tabei uplift. *J. Northeast Petroleum Univ.* 44, 82–93. doi:10.3969/j.issn.2095-4107.2020.06.009

Wang, D., and Zhang, Y. (2001). A study on the origin of the carbonate cement within the reservoir in the external metamorphic belt of the Bohai Bay oil–gas bearing region. *Petroleum Explor. Dev.* 28, 40–42.

Wang, J., Cao, Y., Song, G., and Liu, H. (2017). Diagenetic evolution and formation mechanisms of high-quality reservoirs under multiple diagenetic environmental constraints: an example from the paleogene beach-bar sandstone reservoirs in the dongying depression, Bohai Bay Basin. *Acta Geol. Sin.* 91, 232–248. doi:10.1111/1755-6724.13074

Wang, X., Qiu, L., and Jiang, Z. (2004). The relativity of igneous activity and CO_2 gas reservoir in jiyang depression. *Nat. Gas. Geosci.* 15, 422–427.

Ward, N. I. P., Alves, T. M., and Blenkisop, T. G. (2016). Reservoir leakage along concentric faults in the southern north Sea: implications for the deployment of CCS and EOR techniques. *Toctonophysics* 690, 97–116. doi:10.1016/j.tecto.2016.07.027

Wei, W., Zhu, X., Lu, P., and Tan, M. (2023). Effects of inorganic CO_2 intrusion on diagenesis and reservoir quality of lacustrine conglomerate sandstones: implications for geological carbon sequestration. *Geoenergy Sci. Eng.* 229, 212111–212280. doi:10.1016/j.geoen.2023.212111

Wei, W., Zhu, X., Tan, M., Wu, C., Xue, M., Guo, D., et al. (2017). The early cretaceous thermal fluid activities and their impacts on clastic reservoir rocks in the bayingebei formation of chagan sag. *Oil and Gas Geol.* 38, 270–280. doi:10.11743/ogg20170207

Wei, X., and Sun, Y. (2017). Fault characteristics and controlling factors of hydrocarbon accumulation in qingxi area of dongying depression. *Fault-Block Oil and Gas Field* 4, 154–158. doi:10.6056/dkyqt201702004

Worden, R. H. (2006). Dawsonite cement in the triassic lam formation, shabwa basin, yemen: a natural analog for a potential mineral product of subsurface CO_2 storage for greenhouse gas reduction. *Mar. Petroleum Geol.* 23, 61–77. doi:10.1016/j.marpetgeo.2005.07.001

Wright, V. P. (2020). The mantle, CO_2, and the giant aptian chemogenic lacustrine carbonate factory of the South Atlantic: some carbonates are made, not born. *Sedimentology* 69, 47–73. doi:10.1111/sed.12835

Wu, S., Zou, C., Ma, D., Zhai, X., Yu, H., and Yu, Z. (2019). Reservoir property changes during CO_2 –brine flow through experiments in tight sandstone: implications for CO_2 enhanced oil recovery in the triassic chang 7 member tight sandstone, Ordos Basin, China. *J. Asian Earth Sci.* 179, 200–210. doi:10.1016/j.jseaes.2019.05.002

Wuelstefeld, P., Hilse, U., Koehrer, B., Adelmann, D., and Hilgers, C. (2017). Critical evaluation of an upper carboniferous tight gas sandstone reservoir analog: diagenesis and petrophysical aspects. *Mar. Petroleum Geol.* 86, 689–710. doi:10.1016/j.marpetgeo.2017.05.034

Yang, C., Liu, Q., Zhou, Q., et al. (2009). Genetic identification of natural gases in qingshen gas field, Songliao Basin. *Earth Science-Journal China Univ. Geosciences* 34, 792–798.

Yang, J., Qi, N., Ireland, M., Lu, S., Wang, M., Lu, M., et al. (2021). Geological controls on the natural CO_2 accumulation in the surennuoer oilfield of the hailar basin, China. *Mar. Petroleum Geol.* 133, 105319. doi:10.1016/j.marpetgeo.2021.105319

Yang, K., He, S., Yang, C., Wang, M., Zhang, R., Ren, S., et al. (2023). Diagenesis characteristics of tight sandstone reservoirs with high temperature, overpressure, and high CO_2 content: a case study of neogene meishan-huangliu formation in LD10 area, Yinggehai Basin. *Lithol. Reserv.* 35, 83–95. doi:10.12108/yxyqc.20230108

Yu, M., Liu, L., Yang, S., Yu, Z., Li, S., Yang, Y., et al. (2016). Experimental identification of CO_2-oil-brine-rock interactions: implications for CO_2 sequestration after termination of a CO_2-EOR project. *Appl. Geochem.* 75, 137–151. doi:10.1016/j.apgeochem.2016.10.018

Yuan, G., Cao, Y., Xi, K., Wang, Y., Li, X., and Yang, T. (2013b). Feldspar dissolution and its impact on physical properties of Paleogene clastic reservoirs in the northern slope zone of the Dongying Sag. *Acta Pet. Sin.* 34, 853–866. doi:10.7623/syxb201305006

Yuan, G., Cao, Y., Yang, T., Wang, Y., Li, X., Xi, K., et al. (2013a). Porosity enhancement potential through mineral dissolution by organic acids in the diagenetic process of the clastic reservoir. *Earth Sci. Front.* 20, 207–219.

Yuan, J., Zhou, T., and Zhao, G. (2023). Identification marks of deep thermal fluid activity and its effect on reservoir transformation. *Acta Geol. Sin.* 97, 2067–2083. doi:10.19762/j.cnki.dizhixuebao.2023235

Zeng, J. (2000). Thermal fluid activities and their effects on water-rock interaction in Dongying Sag. *Earth Science-Journal China Univ. Geoscience.* 25, 133–136.

Zhang, C., Liu, D., Liu, Q., Jiang, S., Wang, X., Wang, Y., et al. (2023). Magmatism and hydrocarbon accumulation in sedimentary basins: a review. *Earth-Science Rev.* 244, 104531. doi:10.1016/j.earscirev.2023.104531

Zhang, Y., Hu, W., Yao, S., Yu, H., Kang, X., Wu, H., et al. (2018). The interaction of CO_2-rich fluid with sandstone and its significance for sandstone reservoirs of Permian Longtan Formation in Huangqiao area, Subei Basin. *Geol. Bull. China* 37, 1944–1955.

Zhao, F., Jiang, S., Li, S., Cao, W., Wang, G., Zhang, H., et al. (2017). Correlation of inorganic CO_2 reservoirs in East China to subduction of paleo-pacific plate. *Earth Sci. Front.* 24, 370–384. doi:10.13745/j.esf.yx.2017-3-12

Zhao, J., Cao, Q., Bai, Y., Er, C., Li, J., Wu, W., et al. (2016). Petroleum accumulation from continuous to discontinuous: concept, classification, and distribution. *Acta Pet. Sin.* 37, 145–159. doi:10.7623/syxb201602001

Zhou, B., Jin, Z., Liu, V., Lun, Z., Meng, Q., and Zhu, D. (2020). Alteration of reservoir-caprock systems by using CO_2-rich fluid in the huangqiao area, North Jiangsu Basin. *Oil and Gas Geol.* 41, 1151–1161. doi:10.11743/ogg20200604

Zhu, D., Liu, Q., Jin, Z., Meng, Q., and Hu, W. (2017). Effects of deep fluids on hydrocarbon generation and accumulation in Chinese petroliferous basins. *Acta Geol. Sin. Engl. Ed.* 91, 301–319. doi:10.1111/1755-6724.13079

frontiers | Frontiers in Earth Science

TYPE Original Research
PUBLISHED 20 December 2024
DOI 10.3389/feart.2024.1520502

OPEN ACCESS

EDITED BY
Hu Li,
Sichuan University of Science and Engineering, China

REVIEWED BY
Caifang Wu,
China University of Mining and Technology, China
Yumeng Wang,
Helmholtz Association of German Research Centres (HZ), Germany

*CORRESPONDENCE
Baoqing Li,
19951233305@163.com

RECEIVED 31 October 2024
ACCEPTED 03 December 2024
PUBLISHED 20 December 2024

CITATION
Ye Z, Li B and Cao J (2024) Enrichment characteristics and genesis mechanism of critical elements (Nb-Ta-Zr-Hf-REE-Y) in coals: a case study of Late Permian coalfield in Northeastern Guizhou, China.
Front. Earth Sci. 12:1520502.
doi: 10.3389/feart.2024.1520502

Enrichment characteristics and genesis mechanism of critical elements (Nb-Ta-Zr-Hf-REE-Y) in coals: a case study of Late Permian coalfield in Northeastern Guizhou, China

Ziyi Ye, Baoqing Li* and Jialiang Cao

Key Laboratory of Tectonics and Petroleum Resources, China University of Geosciences, Ministry of Education, Wuhan, China

The discovery of coal-type beneficial metal deposits and corresponding genesis mechanisms are cutting-edge issues in current sedimentary environment research. Based on industrial analysis, mineralogy, and geochemical measurement of seven typical mines in the Late Permian coalfield of northeastern Guizhou, the enrichment characteristics and mineralization mechanisms of critical metal elements in coal rocks have been revealed in this study. The chemical composition of coal from the Late Permian Wujiaping Formation in northeastern Guizhou is mainly characterized by ultra-low moisture content, medium ash and medium volatile matter yield, and medium high sulfur content. The content of coal-hosted critical metal elements is very high. There are significant differences in elemental composition of coalbeds from different mines, and they are mostly enriched vertically in the coal between and near tonsteins. For example, the K1 coalbed of XX Mine is characterized by Se-Nb-Ta-Zr-Hf enrichment, while the K3 coalbed only has Se enrichment characteristics. TDY Mine has the characteristics of Zr-Nb-Be-Se-Hf-Ta and rare earth element (REE) -Y enrichment. The differences in assemblage type and abundance of critical metal elements in coal rock are mainly controlled by the input of terrestrial detrital materials, environmental conditions, seawater, and hydrothermal fluids. The weathering products of acidic volcanic ash, basalt, and intermediate acidic rocks in the Kangdian Upland provide material sources for the enrichment of critical metal elements. Specifically, the input of intermediate acidic volcanic ash is the main factor for the enrichment of Nb-Ta-Zr-Hf-REY (REE plus Y) in most coal mines. The coastal swamp environment in marine-continental transitional zone, periodic seawater transgression, and hydrothermal fluids control the alteration, transformation, and formation of detrital minerals, affecting the activation and migration of some critical metal elements.

KEYWORDS

late permian, critical elements, coal, terrigenous materials, volcanic ash, genesis mechanism

1 Introduction

Critical metal elements (including REY, Nb, Ta, Zr, Hf, Ga, Li, etc.) are valuable strategic resources that play important roles in industries such as new materials, energy, information technology, aerospace, and military industry (Zhai et al., 2019; Dai et al., 2022). Due to the growing demand and rising economic significance of these critical elements (Martin et al., 2017; Per and Erika, 2018), the demand for critical metals is increasing in recent years. In above context, the study of sedimentary deposits abundant with critical elements has received great attention from academic community of environmental science. As a sedimentary organic-rich rock with reduction and adsorption barrier properties, coal can serve as a carrier for the enrichment of various metal elements under special geological and geochemical conditions (Dai et al., 2012; Zhang et al., 2023). In terms of abundance, critical metal enrichment using coal as a carrier can even exceed that of traditional metal deposits (Zhao et al., 2019; Yang et al., 2017; Hower et al., 2019; Dai et al., 2020). Previous studies suggest that coalbeds, tonstein, roof, as well as other types of sedimentary rocks, volcanic ash altered clay rocks, and tuffs, can all enrich various strategic metals, forming a scale for industrial exploitation (Zhou et al., 2023; Dai et al., 2022; Dai et al., 2024; Jin et al., 2024).

The enrichment of trace elements in coal can be summarized into following models: terrestrial detrital enrichment model, tuff enrichment model, infiltration or atmospheric groundwater driven model, and exudation enrichment model related to fluid rise of various origins (Seredin and Finkelman, 2008). The genesis types of strategic metallic minerals in coalfields are complex. As of now, various genesis types including volcanic ash type, volcanic ash-hydrothermal alteration composite type, syngenetic or epigenetic hydrothermal leaching type, submarine exhalation type, hydrothermal-sedimentary environment composite type, etc., Have been reported successively (Crowley et al., 1993; Dai et al., 2005; Dai et al., 2012; Dai et al., 2022; Liu et al., 2019). The total coal resources in the northeast Guizhou coalfield are not abundant compared with those in the northern, western and southwestern parts of Guizhou (Zhang et al., 2023), but several mining areas in coals are highly enriched in critical elements, with higher average than those of Chinese coal (Dai et al., 2012), such as REY (573 μg/g)-Nb (90 μg/g)-Ta (9 μg/g)-Zr (869 μg/g)-Hf (18 μg/g)-Ga (48 μg/g)-Li (110 μg/g). In addition, the abundance of critical metal elements in the coal of Northeast Guizhou has obvious spatiotemporal heterogeneity, which is manifested in the fact that the abundance of elements in different coal seams in the same coal seam and in different mining areas is very different, which has become a key factor restricting the research for rich ore horizons. As for the causes of the enrichment of critical elements in coals in the late Permian of Guizhou, many scholars have put forward their own opinions. Ren (2006) and Dai et al. (2012) suggested that terrestrial detrital materials are one of the main controlling factors for mineral and trace element anomalies in coal in southwestern China, and the terrestrial input of Emeishan basalt from the Kangdian Upland has a significant impact on the enrichment of critical elements in the late Permian coals from western Guizhou (Wang et al., 2012; Shen et al., 2023). The volcanic ash input, hydrothermal activity after deposition, and alteration of acidic fluids have been proposed to control the enrichment of critical metals in coal in north and northwest Guizhou (Li et al., 2020; 2022; Jin et al., 2024). Zhang et al. (2023) summarized the research results of coal geochemistry in Guizhou in the past 20 years and concluded that the enrichment of Nb, Ta, Zr, Hf and REY in Late Permian coal is mainly affected by the supply of weathering products from Emeishan basalt, the mixing of syn-diagenetic volcanic ash and low-temperature hydrothermal activity after coal deposition.

The coal-bearing strata of the Late Permian coalfield in northeastern Guizhou were not affected by volcanic activity during depositional process, and the coupling enrichment of REE-Nb-Ta-Zr-Hf-Ga cannot be attributed to conventional tuff type enrichment mechanism (Dai et al., 2024). The spatiotemporal heterogeneity of critical metal element abundance has not been thoroughly studied. Controlling factors for the spatiotemporal heterogeneity, and the coupling relationship between geological controlling factors and the critical metal element enrichment remain unknown. Based on mineralogy, and geochemical measurement of seven different mines in the Late Permian coalfield of northeastern Guizhou, the objectives of this study are to reveal the coupling relationship between geological factors and critical element enrichment and to determine mechanism of element enrichment and mineralization.

2 Geological setting

The Late Permian coalfield in northeastern Guizhou Province is located in the Central Yangzi Plate (Figure 1A). During the Middle Permian, under extensive transgression, thick shallow marine carbonate formations (Maokou Formation and Qixia Formation) were deposited in southwest China. To the beginning of Late Permian, influenced by the Dongwu Movement, seawater retreated to deep water basins in southern Guizhou, and most of the northeastern part of Guizhou rose to land and altered by weathering. Meanwhile, a large-scale basaltic magma eruption occurred in the northwest of Guizhou Province, and formed Emeishan Large Igneous Province (ELIP). The ELIP can be divided into three zones: inner zone, middle zone and outer zone. The inner zone is the central position of the mantle plume of Emeishan, and the huge thick Emei basalt is deposited in the inner zone, forming a topographic plateau, namely, the Kangdian Upland (Figure 1B). After the large-scale Emei basalt eruption, influenced by basement subsidence and hot and humid climate, large-scale coal accumulation began in the southwest China of the early Late Permian (Li et al., 2022).

The ELIP had a significant controlling effect on the Late Permian coal-hosted rare metal deposits in southwestern China (Figure 1B). These controlling effects are manifested in the following four aspects: 1) The topography formed by ELIP (high in the west and low in the east) provides favorable conditions for peat accumulation, leading to the distribution of most coal-bearing strata in the middle and outer zones of ELIP; 2) The Kangdian Upland is a positive tectonic unit located in the western part of Guizhou, extending in a north-south direction, and has become the main provenance area in Northeastern Guizhou. 3) The volcanic ash generated by the weakening of mantle plume activity can serve as a basis for peat accumulation (forming the bottom of coal seams) or terminate peat accumulation (forming the

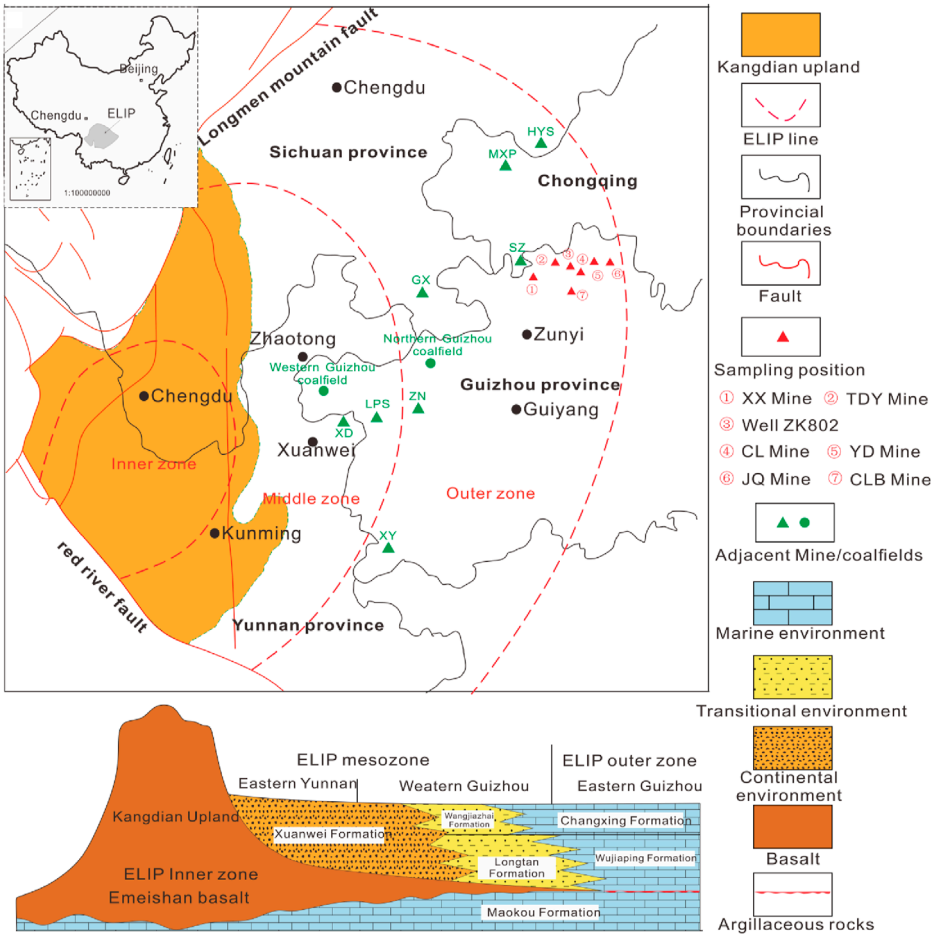

FIGURE 1
Distribution of inner, intermediate, and outer zones of the Emeishan Large Igneous Province (ELIP) and location of the study area [modified after He et al. (2003); Shen et al. (2021)].

roof of coal seams); 4) Frequent volcanic activity and related hydrothermal activity are conducive to the accumulation of organic matter in the Late Permian coal-bearing strata in South China (China Coal Geology Bureau, 1996; Li et al., 2020).

In the middle zone of ELIP, the Maokou Formation limestone, Emeishan basalt and coal bearing rock series (Xuanwei Formation or Longtan Formation) formed an accumulation sequence from bottom to up. In the outer zone, the Maokou Formation limestone, argillaceous rock and coal bearing rock series (Wujiaping Formation) constitute a stacking sequence (Figure 1B). The coal-bearing strata studied belong to the Upper Permian Wujiaping Formation, which is a set of shallow marine sediments. The lithology of Wujiaping Formation includes carbonate rocks interbedded with siliceous rocks and clastic rocks (Figure 2A). Two coalbeds are identified, one of which has commercial value for mining. In the early Late Permian, Wujiaping belonged to the transgression period, with the direction of transgression from southeast to northwest. The seawater moved back and forth frequently, forming a lithofacies paleogeographic feature consisting of continental facies-transitional facies-marine facies from northwest to southeast (China Coal Geology Bureau, 1996).

3 Methodology

3.1 Samples

The coal and non coal samples collected in this study were from K1 and K3 Coalbed of XX Mine in the Late Permian coalfield of northeastern Guizhou, as well as the 4th Coalbed of CL Mine, TDY Mine, JQ Mine, YD Mine, CLB Mine, and the drilling core of Well ZK802. The location of sampling points is shown in Figure 1A. A total of 77 samples were collected, including 62 coal samples, 6 tonstein samples, and 9 roof (or floor) samples (Figure 2B).

3.2 Analytical techniques

Firstly, the collected samples are crushed step by step. Then conduct industrial analysis, total sulfur analysis, mineralogical and geochemical analysis on the processed samples. According to ASTM Standard D3173/D3173M-17a (2017), ASTM Standard D3174-12 (2018), and ASTM Standard D3175-17

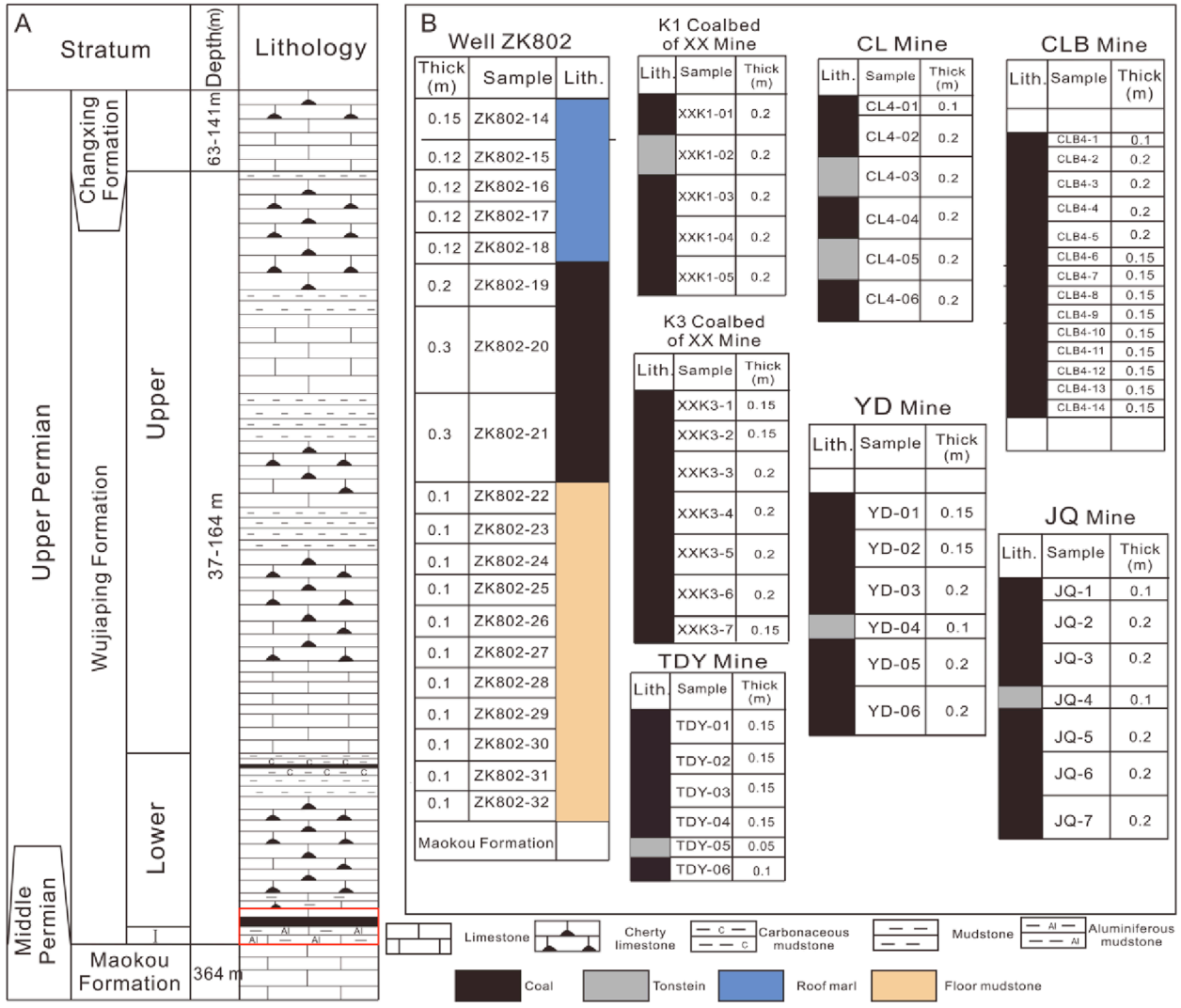

FIGURE 2
(A) Stratigraphic column of the Late Permian in northeast Guizhou, the red box indicates the layer of sampling location. **(B)** The quantity and distribution of collected samples in different mining areas of the Late Permian coalfield in northeast Guizhou.

(2011), the moisture content, ash yield, and volatile matter yield of coal and tonstein were measured. Use Bruker D8 A25 Advance powder diffractometer to scan the X-ray spectrum of samples. Qualitative identification of mineral phases was carried out using PDF-2 and EVA software (Bruker), and semi-quantitative analysis of mineral content was performed using normalized reference intensity ratio (Chung, 1974). Utilizing a field emission scanning electron microscope (FE-SEM, FEI Quanta) equipped with energy dispersive X-ray spectroscopy (EDS; Genesis Apex 4) ™ 450 FEG), to determine the morphological characteristics of minerals and the distribution of elements in minerals. Use Thermo's ARL ADVENT'XP+X-ray fluorescence spectroscopy (XRF) to determine the content of major elements. According to the two-step digestion method proposed by Querol et al. (1997), the sample was digested and the content of trace elements and rare earth elements was determined using inductively coupled plasma-mass spectrometry (ICP-MS, X-Series II Thermo). The experimental steps are as follows:

Step 1: Weigh 0.1 g of the sample and place it in a polytetrafluoroethylene (PFTE) tank. Add 2.5 mL of HNO_3 to the sample, cover it with a lid, and place it in a constant temperature incubator at 90°C for at least 4 h. Transfer the obtained solution to a 100 mL centrifuge tube and clean the dissolution tank with deionized water to recover the samples. Ensure that all samples enter the centrifuge tube and centrifuge at 3,000 rpm for 20–25 min;

Step 2: Remove the upper clear liquid and place it in a conical flask. The solid residue was recovered using 2.5 mL of HNO_3, poured into the previous PFTE tank, and 7.5 mL of HF (2.5 mL, 2.5 mL, 2.5 mL) was added again. All solid samples were recovered into the PFTE dissolution tank. Place the dissolution tank in a constant temperature chamber at 90°C and maintain it for 24 h. Place the dissolution tank on a heating plate (230°C) for acid quenching operation, and add 2.5 mL of $HClO_4$ during this process. After the liquid has

evaporated, add 1 mL of HNO_3 and evaporate again. After evaporation, 1 mL of HNO_3 was added for sample recovery, and the dissolution tank was cleaned with deionized water. All the liquid was poured into the previous conical flask, and then diluted to 100 mL with deionized water to obtain a 2.5% HNO_3 solution for ICP-MS analysis.

3.3 Principal component analysis (PCA) method

PCA is a multivariate data analysis technique that can be used to capture much of the information in a large multi-dimension data matrix in fewer dimensions (Meglen, 1992; Iwamori et al., 2017). One of its main applications is to reveal relationships among variables (Yamashita and Tanoue, 2003; Boehme et al., 2004), since it chooses the new axes to lie along directions of highest correlation (Gotelli and Ellison, 2004). The projection of each variable on the new axis is called its loading, which indicates the relative importance of each variable on that axis; the projection of each sample in the new axis is called its score (Meglen, 1992). PC is a linear combination of variables, with the first sample of all samples being scored on the first axis, the second sample being scored on the second axis, and so on. PCs are orthogonal to each other (right angles: "orthogonal" is a dimensional analogy of "vertical") and are therefore not correlated. In this article, we use an Origin 2022 program to build PCAs. The detailed introduction and use method can be referred to Xue et al. (2011).

4 Results

4.1 Coal quality characteristics

The measurement results of moisture content, ash content, volatile matter yield, and sulfur content of coal samples from different mines are shown in Table 1. The moisture content ranges from 0.7% to 4.1%, with most results distributed between 1.0% and 1.5% and an average of 1.5%, indicating that the coal sample belongs to ultra-low moisture coal (MT/T 850-2000, 2000). The ash content ranges from 7.4% to 69.9%, concentrated between 15% and 30%, with an average of 22.14%. According to GB/T 15224.1–2018, it belongs to low ash to medium ash yield coal. The yield of volatile matter is mostly distributed in a range of 15%–29%, with an average of 21.9%, belonging to low volatile to medium volatile bituminous coal (MT/T849-2000, 2000). The ash yield of coal samples shows a good positive correlation with the yield of volatile matter (R^2 = 0.65), indicating that the yield of volatile matter is influenced by inorganic components. The total sulfur content ranges from 1.1% to 24%, with an average of 4.4%. According to the classification criteria for sulfur content in coal by Chou. (2012), coal samples in this study are mainly composed of medium and high sulfur coal (>3%). There is a good positive correlation between sulfur content and ash yield (R^2 = 0.48–0.97), especially in high sulfur samples (R^2 of 0.85, 0.96, 0.96 for CLB, XX, and CL coal mines, respectively). It is suggested that sulfur in coal mainly exists in inorganic components, such as sulfide minerals (pyrite), sulfate minerals, etc. (Finkelman, et al., 2018; Finkelman, et al., 2019).

4.2 Mineral characteristics

4.2.1 Mineral compositions and contents

The coal samples in this study are composed of clay minerals (including kaolinite, illite, ammonium illite, and zeolite), oxide minerals (quartz and rutile), sulfide minerals (pyrite and sphalerite), carbonate minerals (calcite, dolomite, and siderite), and sulfate minerals (gypsum, pyrite) (Figure 3). Taking the coal sample from the CLB Mine as an example, pyrite (2.4%–38%) is the main mineral component, followed by ammonium illite (0%–5.8%) and a small amount of kaolinite (0%–4.4%) (Table 2).

The mineral content of the tonstein sample differs from that of the coal sample. In the TDY Mine, the main mineral type of tonstein is kaolinite (60%), followed by pyrite (1.2%). Kaolinite is the main mineral (51%) in the YD Mine, and contains trace amounts of pyrite (0.88%). In the CL mine, the main mineral of tonstein is kaolinite (with an average value of 51%), followed by pyrite (with an average value of 2.6%) and a small amount of calcite (with an average value of 1.2%). Tonstein in the JQ Mine is mainly composed of kaolinite (65%), followed by illite (4.4%). Only kaolinite (75%) and a small amount of rutile (4.8%) were detected in tonstein samples from the K1 coalbed of XX Mine.

4.2.2 Mineral distribution and occurrence characteristics

Kaolinite is the main clay mineral in coal samples, occurring in strip or lens-shaped (Figures 4A, B). Kaolinite can also serve as a matrix for pyrite, rutile, and quartz particles (Figures 4C, D). A small amount of kaolinite is a fracture-filling cement (Figure 4A), formed by precipitation of aluminum and silicon-containing solutions. A small amount of kaolinite appears in the organic matter cell lumens (Figure 4C), indicating syndiagenetic-early diagenetic origin. Worm-like kaolinite may be of volcanic ash origin (Figure 4E). Illite has a low content and is often present as a cell-filling cement for microscopic components (Figures 4F, I), or dispersed in granular form in organic matter (Figure 4G).

In some samples, quartz and illite are co-filled in the cell lumens and micro-fractures of organic matter (Figure 4F), indicating a authigenic origin. In other samples, quartz occurs in granular form in organic matter matrix or kaolinite matrix (Figure 4G). The long axis of this type of quartz is parallel to the bedding plane and has a certain degree of roundness, belonging to terrigenous detrital origin. Calcite occurs in fractures or vein forms in organic matter (Figure 4H). It is suggested that calcite precipitates directly from Ca-rich hydrothermal fluids. In floor samples, calcite occurs in granular form in the kaolinite matrix (Figure 4M). Siderite is only observed in coal samples from the YD Mine and JQ Mine, filling the organic pores in an irregular shape (Figure 4J), suggesting a hydrothermal precipitation origin.

The occurrence forms of pyrite include 1) subeuhedral to euhedral crystal aggregates (Figures 4D, E); 2) Cell lumen-filling cement (Figure 4K); 3) Spherical polycrystalline framboidal (Figure 4I); 4) Other granular forms in organic matter matrix or kaolinite matrix (Figure 4P); 5) The fracture-filling cement (Figure 4L) is of hydrothermal origin.

The forms of gypsum occurrence include euhedral crystals (Figure 4N) and fracture-filling cements (Figure 4K). Gypsum clusters are concentrated near pyrite or iron sulfate, indicating that they are

TABLE 1 Industrial analysis and total sulfur analysis results of coal samples from 7 mines of the Late Permian coalfield in northeast Guizhou. (Mad, moisture; Ad, ash yield; V_{daf}, volatile matter; S, total sulfur; ad, air-dried basis; d, dry basis; daf, dry and ash-free basis).

Mine/Well	Coalbed	Sampling quantity			Industrial analysis results			S (%)
		Coal	Tonstein	Roof (or floor)	M_{ad} (%)	A_d (%)	V_{daf} (%)	
CLB	4th	14			0.7–1.8 (1.33)	7.4–40.6 (15.7)	12.8–26.37 (15.35)	2.3–24.1 (7.0)
TDY	4th	5	1		1–1.7 (1.33)	11.5–62.1 (26.48)	17–35.4 (22.58)	1.3–2.7 (1.88)
YD	4th	5	1		0.9–4.1 (1.76)	16.7–27 (21.38)	19.3–26.9 (22.34)	1.1–7.5 (2.5)
CL	4th	4	2		1–1.9 (1.3)	17.5–30.4 (21.23)	18.9–20.2 (22.75)	1.8–5.2 (3.08)
JQ	4th	6	1		0.9–2.4 (1.67)	7.7–69.9 (30.96)	16.7–33.6 (24.57)	1.5–11 (3.33)
XX	K1	3	1		1.3–2.4 (1.65)	19.1–40.2 (30.35)	13.8–18.9 (16.6)	3.2–6.3 (5)
XX	K3	7			0.9–2.0 (1.74)	13.2–34.9 (18.13)	12.6–21.1 (15.21)	1–16 (5.07)
ZK802	4th	3	11	5	1.2–1.4 (1.33)	22.8–23.9 (23.33)	19.8–29 (23.57)	1.9–2.9 (2.33)

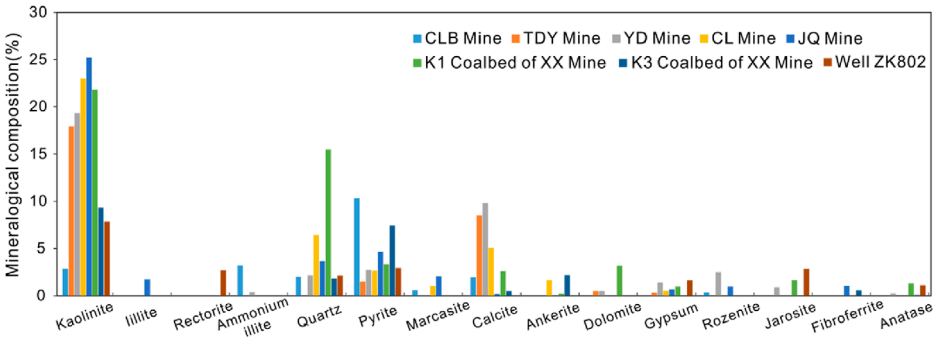

FIGURE 3
Mineral compositions of coal samples from the Late Permian coalfield in northeast Guizhou.

TABLE 2 Mineral compositions of coal samples from the Late Permian coalfield in northeast Guizhou. (Kln, Kaolinite; Qz, Quartz; Py, Pyrite; Cal, Calcite; Ank, Ankerite; Dol, Dolomite; Gyp, Gypsum; Roz, Rozenite; Jar, Jarosite; Fib, Fibroferrite; Mar, Marcasite; Ana, Anatase; Amm, Ammonium illite; Rec, Rectorite).

Mine/Well	Kln	Qz	Py	Cal	Ank	Dol	Gyp	Roz	Jar	Fib	Mar	Ana	Amm	Ilt	Rec
CLB	2.87	2.00	10.32	1.94				0.36			0.59		3.20		
TDY	17.93		1.49	8.48		0.50	0.31								
YD	19.35	2.15	2.74	9.80		0.51	1.39	2.47	0.88			0.25	0.38		
CL	23.00	6.42	2.65	5.06	1.64		0.52				1.00				
JQ	25.21	3.67	4.63	0.19			0.70	0.95		1.04	2.05			1.71	
XX (K1 Coalbed)	21.82	15.48	3.35	2.60	0.22	3.17	0.96		1.64			1.29			
XX (K3 Coalbed)	9.32	1.81	7.44	0.51	2.17					0.57		0.09			
ZK802	7.87	2.13	2.93				1.63		2.83			1.10			2.70

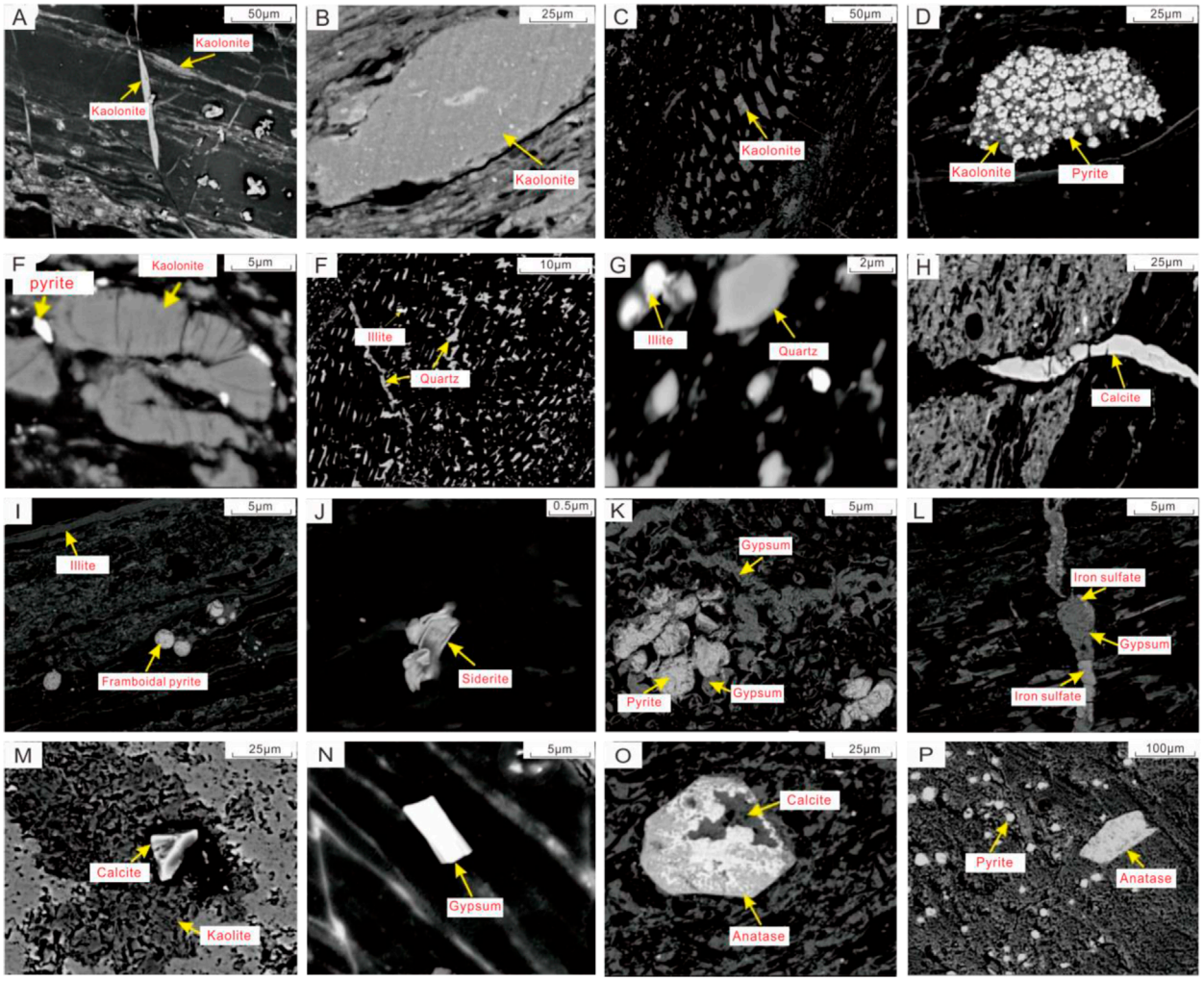

FIGURE 4
SEM back scattered images of different mineral phases from the Late Permian coalfield in northeast Guizhou. **(A)** Striped-shaped kaolinite filled fractures **(B)** Lens-shaped kaolinite; **(C)** Kaolinite cement in the cell lumen; **(D)** Pyrite in the kaolinite matrix; **(E)** Worm-like kaolinite and pyrite; **(F)** Illite and quartz filling the cell lumen, and quartz filling the organic fractures; **(G)** Granular illite and semi-rounded quartz; **(H)** Calcite filled in fractures; **(I)** Striped-shaped illite and strawberry-shaped pyrite; **(J)** Irregular-shaped siderite; **(K)** Pyrite filling the cell lumen and gypsum filling the fractures; **(L)** Gypsum and iron sulfate fill fractures; **(M)** Calcite in kaolinite matrix; **(N)** Euhedral gypsum crystals; **(O)** Euhedral rutile crystal; **(P)** Granular pyrite and rutile in organic matter.

likely formed by the interaction between sulfuric acid formed by the oxidation of pyrite and calcite (Figure 4L). A small amount of rutile is distributed in small dispersed particles in the organic matter matrix (Figure 4P), indicating that rutile originates from the reprecipitation of Ti-rich solution. Anatase occurs as cylindrical form in the kaolinite matrix. Low roundness of the anatase indicates its terrigenous detrital origin. There are dissolved spaces in the self-shaped crystal rutile, which are filled with kaolinite (Figure 4O), indicating the influence of hydrothermal solutions.

4.3 Geochemical characteristics

4.3.1 Major element oxides

The average content and proportion of major element oxides are shown in Table 3 and Figure 5A. The distribution of major elements in different coal mines exhibits strong heterogeneity. Taking CLB Mine as an example, its major elemental composition is Fe_2O_3 (7.05%), followed by SiO_2 (5.0%) and Al_2O_3 (2.96%). Compared with the average value of Chinese coal (Figure 5B), Si, Al, K, and Ti are more enriched in coal samples in this study, especially in the K1 Coalbed of XX Mine and the 4th Coalbed of Well ZK802. Fe, Na, and other minerals are relatively depleted, especially TY and YD Mines. Furthermore, Ca is depleted in the 4th coal seam of JQ Mine, K3 Coalbed of XX Mine, and the 4th Coalbed of ZK802 well, but is more enriched in TYD Mine and CL Mine. K is only depleted in the K3 Coalbed of XX Mine.

4.3.2 Trace elements enrichment

According to the enrichment coefficient proposed by Dai et al. (2012) (CC = element content/average trace element content in coal worldwide), the enrichment levels of critical metal elements are

TABLE 3 Average of major element oxides (%) from the Late Permian coalfield in northeast Guizhou (based on bulk samples). *, data of average values for Chinese coals (Dai et al., 2012).

Mine/Well	SiO_2	Al_2O_3	CaO	Fe_2O_3	K_2O	MgO	Na_2O	P_2O_5	TiO_2
CL	16.92	7.53	2.40	3.30	0.30	0.35	0.10	0.10	0.35
JQ	13.36	6.77	0.11	2.89	0.39	0.17	0.10	0.10	0.43
TYD	13.28	6.97	3.18	1.00	0.30	0.27	0.10		0.38
XXK1	22.54	7.68	0.90	5.36	0.35	0.42	0.28	0.10	1.16
YD	9.52	8.80	2.48	2.50	0.35	0.25	0.10		0.40
XX (K3 Coalbed)	7.94	3.61	0.39	5.83	0.10	0.10	0.10		0.31
ZK802	33.22	26.50	0.38	5.05	0.71	0.41	0.10	0.10	2.97
Chinese coals*	8.47	5.98	1.23	4.85	0.19	0.22	0.16	0.09	0.33

TABLE 4 Average of trace element (μg/g) in northeast Guizhou and adjacent coalfields/coal mines in the Late Permian (on whole coal or rock basis). 1, data of average values for Chinese coals (Dai et al., 2012); 2, data of average values for world hard coals (Ketris and Yudovich, 2009).

Mine/Well/coalfield	Se	Zr	Nb	Mo	Hf	Ta	Th	U	REY
XX (K1 Coalbed)	7.5	290	42	3.6	6.6	2.0	9.6	4.2	303
XX (K3 Coalbed)	11	104	17	2.1	2.8	1.3	6.5	1.9	96
CLB	9.9	67	10	16	1.6	0.06	2.5	4.5	105
TDY	7.4	468	49	6.9	9.7	1.8	9.1	6.0	347
CL	14	987	77	7.5	17	0.68	8.4	6.5	534
YD	14	820	81	4.5	18	5.7	19	6.5	621
JQ	16	886	62	23	16	2.7	12	15	660
ZK802	8.4	384	61	9.5	9.5	2.7	13	6.6	374
North Guizhou coalfield	1.0	162	26	2.0	2.4	0.90	6.0	2.5	111
ZN	3.2	173	22	7.2	2.6	3.2	5.4	9.3	136
LPS	3.6	141	15	4.8	2.2	2.3	4.6	5.2	89
XY	1.8	162	19	39	2.5	0.80	4.5	17	109
West Guizhou coalfield	2.8	157	19	12	2.4	2.3	4.9	7.5	98
MXP	66	411	43	6.5	11	2.9	12	376	423
GX	4.9	410	38	2.5	7.4	1.5	6.8	15	276
XD	6.6	112	11	1.8	3.0	0.92	7.1	2.1	465
SZ	13	444	24	3.7	9.9	1.8	9.4	18	460
HYS	7.0	695	76	4.1	10	0.68	8.5	4.1	1,423
Chinese coals[1]	2.47	89.5	9.44	3.08	3.71	0.62	5.84	2.43	117.69
World hard coals[2]	1.3	36.00	3.70	2.2	1.2	0.28	3.3	2.40	60.07

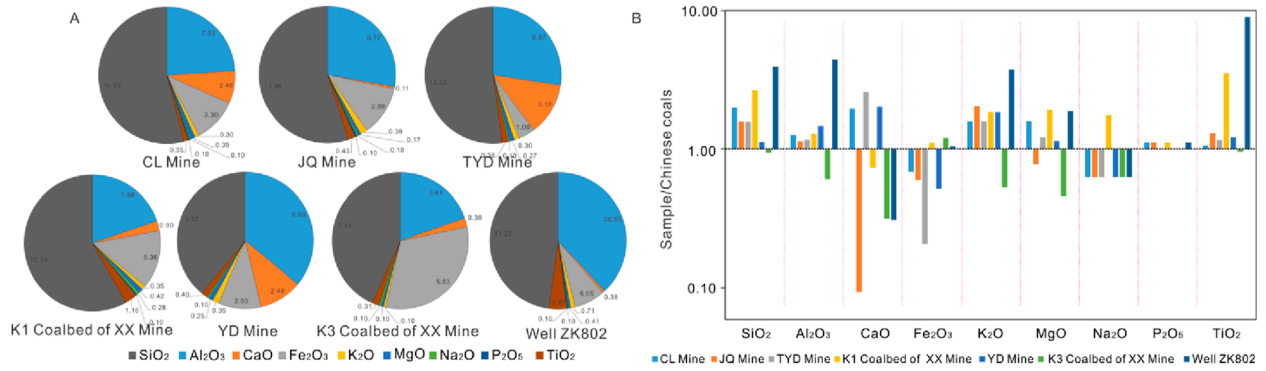

FIGURE 5
(A) Mineral compositions of the Late Permian coalfield in northeast Guizhou. **(B)** Concentration coefficient of major element oxides for coal samples from the Late Permian coalfield in northeast Guizhou.

divided into six categories: CC<0.5 (depleted), 0.5<CC<2 (normal), 2<CC<5 (slightly enriched), 5<CC<10 (enriched), and 10<CC<100 (highly enriched) (Figure 6). The K1 Coalbed of XX Mine is mainly enriched in Se-Nb-Ta-Zr-Hf, while the K3 Coalbed of XX Mine shows Se enrichment. TDY Mine is enriched in both Zr-Nb-Be-Se-Hf-Ta and REY. CL Mine exhibits enrichment characteristics of Zr-Nb-Be-Se-REY-Hf-Ta. The YD Mine is characterized by enrichment of Se-Zr-Hf-Nb-Ta-REY-Be-Th, while the JQ Mine is characterized by enrichment of Se-Zr-Hf-Nb-Ta-REY-Mo-U. CLB Mine is characterized by Se-Mo-U enrichment. The coal samples from Well ZK802 have Se-Nb-Ta-Zr-Hf-REY-Mo-U-V enrichment, with a higher degree of enrichment of critical elements compared to samples from coal mines.

The Late Permian coalfields in northeastern Guizhou have enriched elements such as Nb, Ta, Zr, Hf, REY, Se, Th, and U to varying degrees, these enrichment element combinations were also found in adjacent coalfields/coal mines, such as MXP Mine, HYS Mine, SZ Mine, XD Mine, Northern Guizhou and Western Guizhou coalfields, etc. In addition, there were certain differences in the combination and content of enrichment elements among different mines in northeastern Guizhou coalfields (Table 4).

For example, the Zr content ranges from 8.9 to 3,083 μg/g, with an average value of 393 μg/g, far higher than the world hard coal (average value of 36 μg/g). It is also higher than the average value of Zr in XD, LPS, ZN, XY Mine and Northern Guizhou, Western Guizhou coalfields (<200 μg/g), slightly lower than the content of Zr in MXP, GX and SZ Mine (>400 μg/g), and lower than that in HYS Mine (695 μg/g). In the three coal mines of CL, YD, and JQ, the average value of Zr is relatively high, at 987 μg/g, 820 μg/g, and 886 μg/g, respectively. In the coal samples collected from the CLB Mine, the degree of Zr enrichment is the lowest (average value of 67 μg/g), but still higher than the Zr content in the world hard coal.

Figure 7 shows that critical metal elements such as Li, Nb, Ga, and REY are most enriched in or near tonstein, while their enrichment in roof (or floor) samples is relatively weak. The variation trends of Al2O3, ash content, kaolinite, and critical metal elements are basically consistent (Figure 7), indicating that detrital input is the main factor controlling the enrichment of trace elements.

4.3.3 Rare earth element and yttrium (REY) enrichment

The average REY content of coal samples from JQ and YD coal mines was the highest, at 660 μg/g and 621 μg/g, respectively (Table 5), followed by CL Mine. Compared with the other coalfields in Guizhou, the coal in the northeastern Guizhou coalfield is more enriched in REY. Compared with the coal samples from adjacent Mines, the content of REY is significantly lower in HYS, lower than that of MXP, SZ and XD (423 μg/g, 460 μg/g and 465 μg/g), and higher than the average content of REY in GX (276 μg/g). From the continental environment in the western study area to the marine environment in the east, there is a trend of increasing REY content in coal, which is related to the influence of terrestrial input on peat deposition (Zhuang et al., 2000). The classification and enrichment types of REY were based on the classification scheme proposed by Seredin and Dai (2012). Taking the K1 Coalbed of XX Mine as an example, LREY ranges from 157 to 328 μg/g (average 263 μg/g), and MREY ranges from 34 to 68 μg/g (average 52.0 μg/g). HREY ranges from 12 to 6.3 μg/g (average 9.4 μg/g), and LREY content is significantly higher than MREY and HREY. The δEu value ranges from 0.42 to 0.37, indicating a significant negative Eu anomaly. δCe ranges from 0.77 to 1.01, showing a weak negative Ce anomaly. Except for one sample characterized by weak negative La anomaly (<1), all other samples exhibit positive La anomalies (1.08–1.15). All samples showed varying degrees of positive anomalies in Gd (1.11–2.83).

As shown in the REY curves of K1 Coalbed in XX Mine (Figure 8A), the REY content of tonstein (Sample No. XXK1-2) is significantly higher than that of other samples. XXK1-2, XXK1-4, and XXK1-5 exhibit LREY enrichment with $La_N/Yb_N>1$. XXK1-1 and XXK1-3 exhibit MERY enrichment, with $La_N/Sm_N<1$ and $Gd_N/Yb_N>1$. Tonstein (Sample No. XXK1-2) showed significant negative Ce anomalies, while the rest samples had normal or weak negative Ce anomalies. All samples exhibit Eu negative anomaly. The REY characteristics of coal samples from other coal mines/drilling wells are shown in Figure 8. The coals of Well ZK802 occur weakly negative Eu anomalies only (Figure 8H), this may be explained by the influence of high-temperature hydrothermal solutions (Hower et al., 2015; Zhou et al., 2023).

FIGURE 6
Concentration coefficients (CC) of trace elements from the Late Permian coalfield in northeast Guizhou.

5 Enrichment mechanism of critical elements

5.1 Control of terrestrial input

5.1.1 Using PCA to determine the impact of terrigenous detrital inputs

Terrigenous detrital input has a significant controlling effect on the abnormal enrichment of minerals and trace elements in coal in southwest China (Ren, 2006; Dai et al., 2012; Shen et al., 2023). In order to determine whether terrigenous detrital input has an effect on the enrichment of key elements in coal in this area, principal component analysis (PCA) was used to explore the relationship between sulfur content, ash content, mineral composition and geochemical elements in coal (Figure 9). Based on the ordination diagram Figure 9A, we noted that the loadings angle of the variables in red dotted box such as Zr, Al_2O_3, REY, Ga, Hf, Ta, etc., is very small, and the projection value on the *X*-axis (PC1) is significantly larger and closer, while Mo, U, Fe_2O_3, Se has a larger projection value on the *Y*-axis (PC2). This indicates that the sources and genesis of Zr, Al_2O_3, REY, Ga, Hf, Ta, etc., Are similar, and they are obviously affected by terrestrial sources, but the enrichment of U, Mo, Se and Fe elements was of non-terrigenous origin. Similarly, we find that the kaolinite and ash content in Figure 9B are projected on PC1 with high values, which also proves that the enrichment of these elements in the red dotted box is obviously influenced by terrigenous detritus. In addition, we find that the loadings of sulfur content and pyrite content in Figure 9B are very close, and the projection value on PC2 is higher, which indicates that most of the sulfur in coal originates from pyrite, and also proves that the enrichment of U, Mo, Se is related to pyrite and sulfur.

5.1.2 Basalt debris input from Kangdian Upland

The weathering products of ELIP in Kangdian Upland provide the main provenance of terrestrial input for the Late Permian coalfields in Yunnan and Guizhou provinces in SW China, and are an important basis for the enrichment of REY and trace elements in coals (Yang et al., 2011; Shen et al., 2021). In this study, Al_2O_3-TiO_2, Zr/TiO_2-Nb/Y, and Zr-Ti cross-plots were applied to discuss the influence of basaltic provenance in the Kangdian Upland on the Late Permian coalfields (Figure 10). The Al_2O_3/TiO_2 ratio can be used to determine the magma source of altered volcanic ash in coal-bearing strata. Hayashi et al. (1997) proposed that Al_2O_3/TiO_2 ratios ranging from 3–8, 8–21, and 21–70 respectively indicate the presence of ferromagnesian, neutral rock, and felsic provenance. Winchester and Floyd (1977) found the abundance and distribution of selected minor, trace elements (Ti, Zr, Y, Nb, Ce, Ga and Sc) and their cross-plot may be used to distinguish common volcanic rock types. Although elements including Al, Ti, Nb, and Y, can be relatively mobile in a few specific supergene environments (Ward, 2016; Dai et al., 2015). The Al_2O_3/TiO_2-Nb/Y, Zr-Ti and Zr/TiO_2-Nb/Y

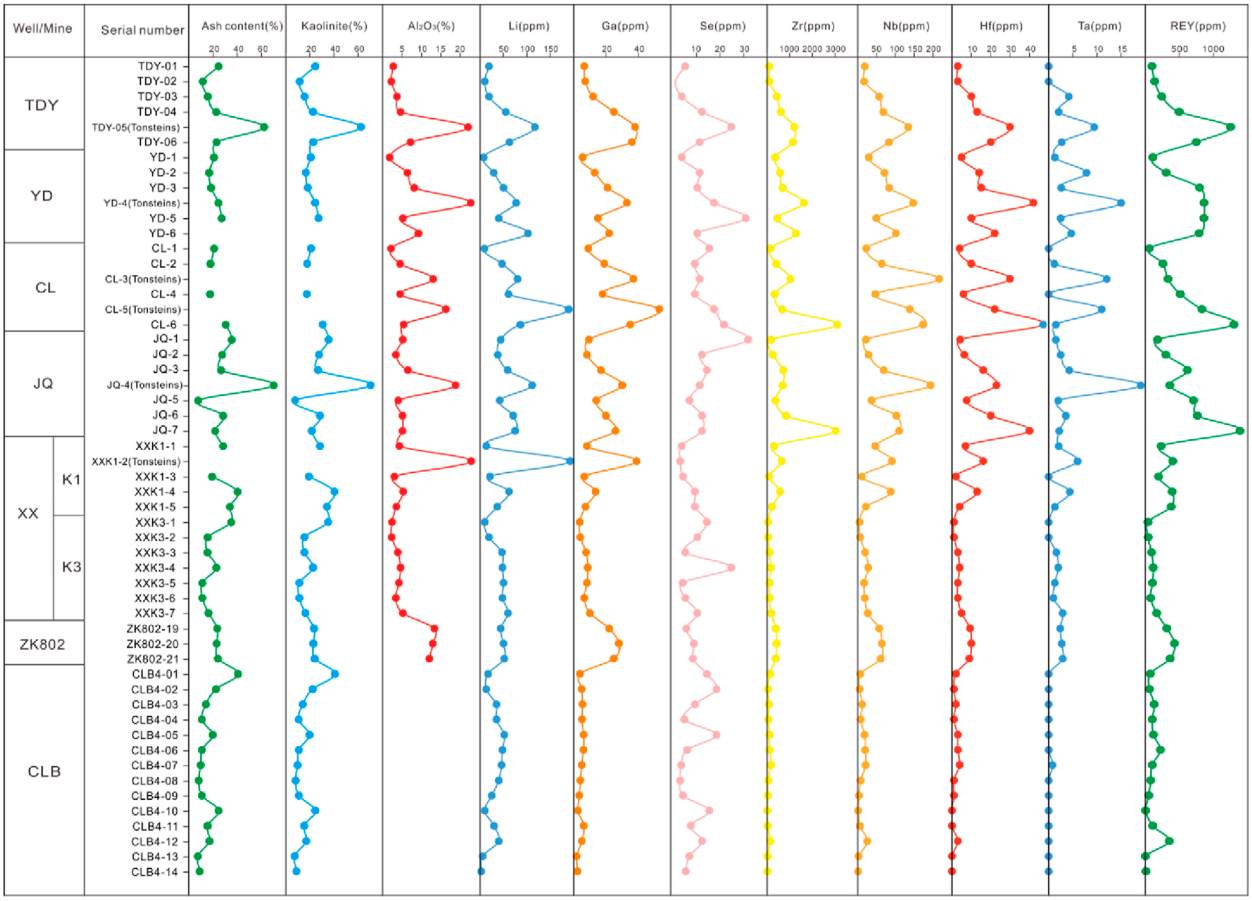

FIGURE 7
Variations of ash, kaolinite, Al_2O_3, REY, and critical trace element contents of the Late Permian coalfield in northeast Guizhou.

TABLE 5 REY geochemical parameters of coal and tonstein samples in the Late Permian coalfield in northeast Guizhou. L, M, and H are light, medium, and heavy REY; $(La/Yb)_N$, $(La/Sm)_N$, $(Gd/Yb)_N$ are the standardized ratios; N, Upper Continental Crust Normalized; $\delta Eu = Eu_N/(Sm_N + Gd_N)^{0.5}$; $\delta Ce = Ce_N/(La_N + 0.5Pr_N)^{0.5}$; $\delta La = La_N/(3Pr_N - 2Nd_N)^{0.5}$; $\delta Gd = Gd_N/(0.33Sm_N + 0.67Tb_N)^{0.5}$.

	REY (μg/g)	LREY (μg/g)	MREY (μg/g)	HREY (μg/g)	δCe	δEu	δLa	δGd	$(La/Yb)_N$	$(La/Sm)_N$	$(Gd/y)_N$
XX (K1 Coalned)	324.00	262.80	51.80	9.34	0.93	0.72	1.08	1.47	1.44	1.03	1.39
XX (K3 Coalbed)	95.57	75.43	17.71	2.34	0.96	0.75	1.17	3.12	1.10	0.96	1.15
CLB Mine	105.60	85.86	17.40	2.52	1.24	0.61	1.21	2.64	1.32	1.08	1.23
TDY Mine	497.17	378.00	99.17	20.18	1.10	0.38	1.05	1.82	0.86	0.75	1.21
CL Mine	550.17	423.33	104.83	22.10	1.05	0.31	1.04	1.46	0.95	0.84	1.08
YD Mine	621.00	469.67	125.67	25.98	1.04	0.38	1.13	1.10	0.84	0.86	1.02
JQ Mine	617.57	452.29	139.14	26.24	1.03	0.39	1.12	1.40	1.22	1.02	1.23
Well ZK802	373.33	308.33	54.00	11.33	0.90	0.89	1.10	0.98	1.30	0.98	1.13

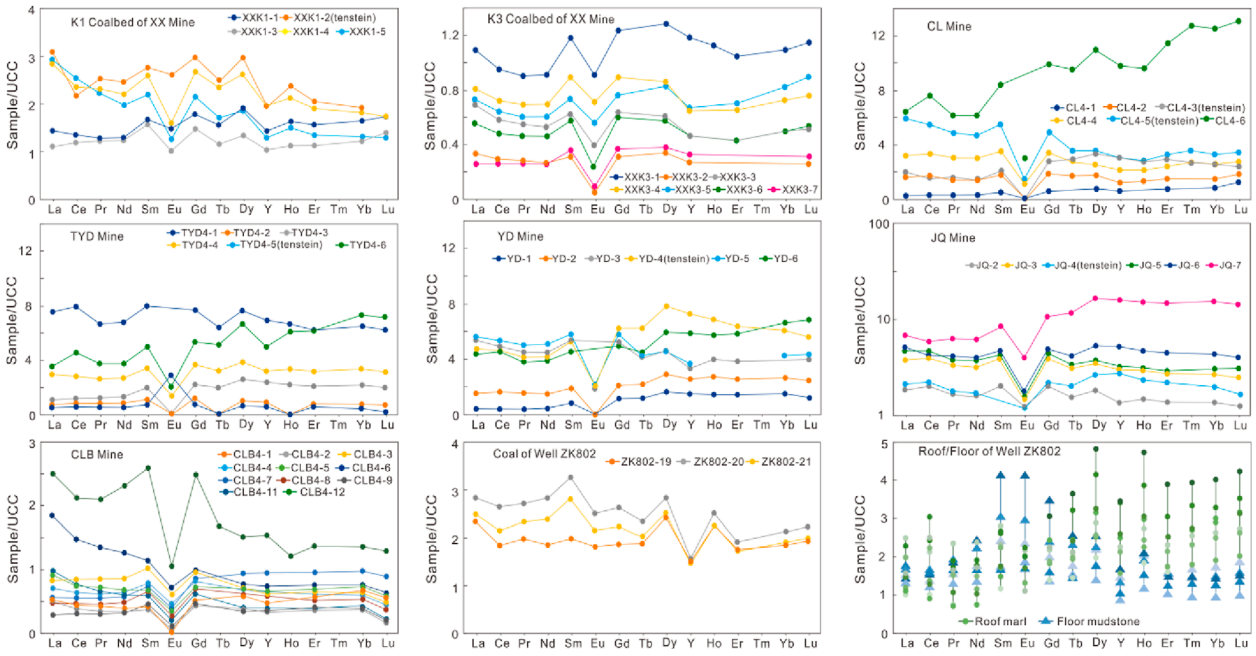

FIGURE 8
REY distribution patterns in the coal, roof, and floor samples from the Late Permian coalfield in northeast Guizhou. UCC are cited from Taylor and McLennan. (1985).

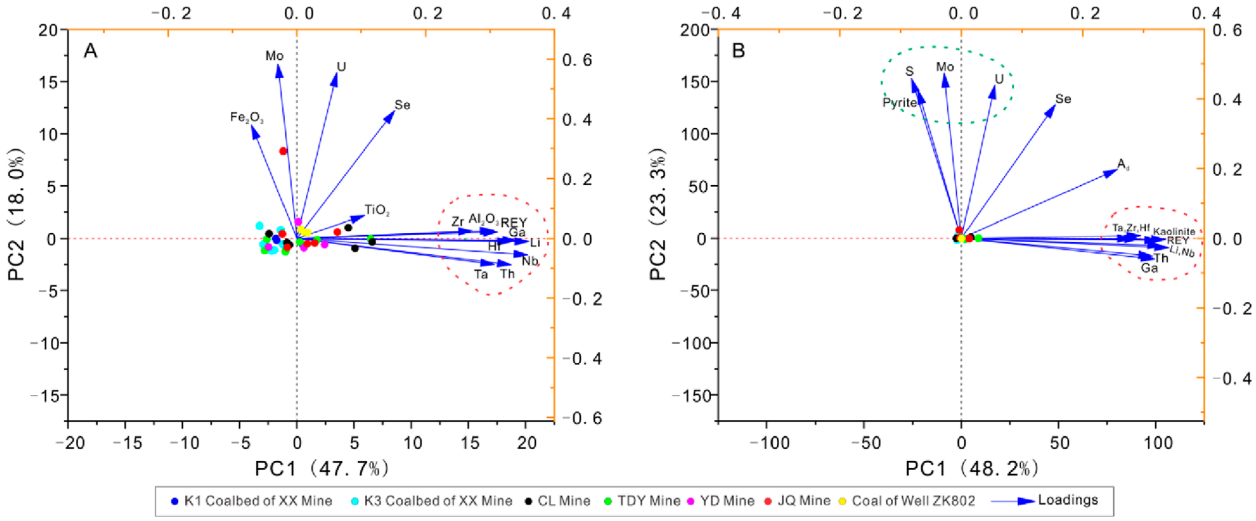

FIGURE 9
Principal component analysis (PCA) of all measured variables in the Late Permian coalfield in northeast Guizhou. Arrows represent variables. **(A)** Comprises major elements and critical elements; **(B)** comprises sulfur content, ash content, mineral composition, and critical elements. Principal component 1 in **(A)** and **(B)** explained 47.7% and 48.2% of the total variances, respectively.

discrimination diagrams are used in this study as these elements appear immobile in our study (Liu et al., 2020).

The coal samples and clay rocks from the Well ZK802, as well as tonstein samples from the K1 Coalbed of XX Mine, all exhibit low Al_2O_3/TiO_2 ratio (3–8) (Figure 10A). In Figure 10B, the data points corresponding to these samples fall within the range of alkaline basalt and are close to Emeishan basalt. In Figure 10C, data points fall within the range of intraplate volcanic rocks, while in Figure 10D, they are close to the low titanium basalt of the Kangdian Upland, suggesting that the inorganic components in this sample come from the low titanium basalt of the Kangdian Upland. These samples have the characteristics of low Ti/Y (427–452) and low Nb/La (0.75–0.82), similar to the low titanium basalt of the Kangdian Upland (Ti/Y<500, and Nb/La ranging between 0.6 and 1.4). It is suggested that the inorganic components in coal samples and overlying clay rocks come from low titanium basalts in the

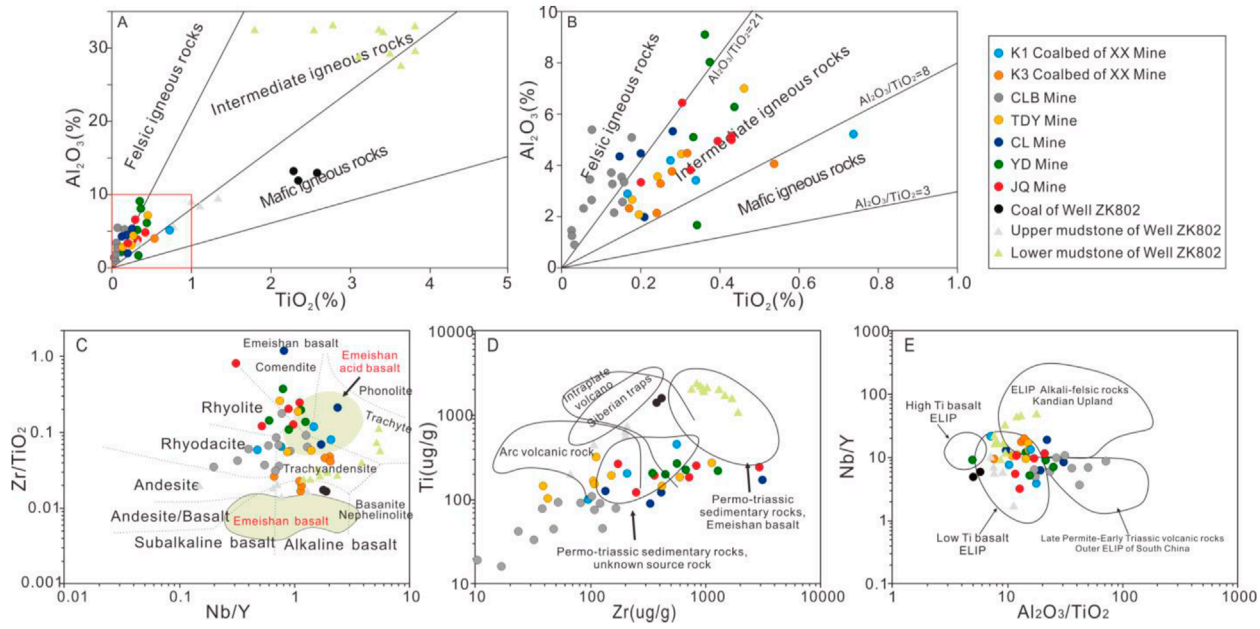

FIGURE 10
Relationship between Al_2O_3 versus TiO_2 **(A, B)**, Zr/TiO_2 versus Nb/Y **(C)**, Ti versus Zr **(D)**. And Nb/Y versus Al_2O_3/TiO_2 **(E)** in the Late Permian coalfield in northeast Guizhou.

Kangdian Upland. In study area, only coal samples from Well ZK802 showed varying degrees of enrichment in Sc, V, Cr, Co., Ni, Cu, Zn, and Se. This enrichment feature was discovered in coal samples from the Late Permian period, which were sourced from Kangdian Upland basalt (Xiao et al., 2004), indirectly confirming the view that the inorganic components in the Well ZK802 samples come from Kangdian Upland basalt.

5.1.3 The input of acidic volcanic ash during the late permian

Except for coal samples and clay rocks from CLB Mine and Well ZK802, almost all data points of other coal samples fall within the range of neutral rocks, indicating that the provenance belongs to neutral rocks (Figures 10A, B). Most studies propose that the characteristics of acidic rocks and intermediate acidic volcanic ash in the Upper Permian strata in Southwest China and the weathering debris input of acidic rocks at the top of the Emeishan basalt are related (Li et al., 2020; Zhao et al., 2019; Liu et al., 2020). Figure 9C shows that most of the coal samples and tonstein samples from TDY, CL, YD, and JQ Mines fell into the rough rock and alkali flow rock areas, and overlapped with the Emeishan acidic volcanic rock area, indicating that the main source of inorganic components in these coal mines is the input of intermediate acidic volcanic ash. In addition, the data points of these samples are concentrated within the range of Permian-Triassic sedimentary rocks with unknown volcanic rock provenance (Figure 10D). Moreover, in Figure 10E, these data points are concentrated in the alkaline rock range of Emeishan, which also implies the presence of volcanic rock provenance. Comparison of REY distribution patterns shows that these coal samples and tonstein samples differ significantly from ELIP felsic intrusive rocks (such as granite and diorite) (Figure 11), but are more similar to alkaline rhyolite, indicating the input of volcanic ash from eruptions rather than the weathering products of felsic intrusive rocks.

The mineral content and morphological characteristics in coal samples also indicate that the inorganic components come from the input of intermediate acidic volcanic ash. The quartz content is low (Table 2), and it has not even been detected in most samples. Under SEM, quartz occurs as extremely fine particles (Figures 4F, G), belonging to authigenic origin rather than terrestrial detrital origin. It has been reported that the intermediate acidic rocks at the top of the Emeishan basalt have a high quartz content (Shellnutt and Jahn, 2010). Quartz deposition in peat bogs can lead to an increase in quartz content in coal seams and surrounding rocks (Liu et al., 2019). In addition, worm-like kaolinite was observed in coal samples (Figure 4E), which also confirms that the provenance belongs to volcanic rocks (Dai et al., 2017). Vertically, the Al_2O_3/TiO_2 of tonstein is significantly higher than that in coal sample, belonging to the range of felsic provenance. This indicates that the increased input of intermediate acidic volcanic ash led to the termination of peat accumulation and the formation of interbedded tonstein (Figures 12D–G). The variation of Al_2O_3/TiO_2 in coal samples is small. However, Al_2O_3/TiO_2 showed high values (>21) in the samples near the tonstein and at the bottom of the coalbed (Figures 12D–G), reflecting input from intermediate acidic volcanic materials.

5.1.4 Input of weathered debris from acidic rocks at the top of ELIP

Most of the sample data points from XX Mine fall within the range of neutral provenance (Figures 10A, B), while a small number of coal samples and tonstein samples fall within the range

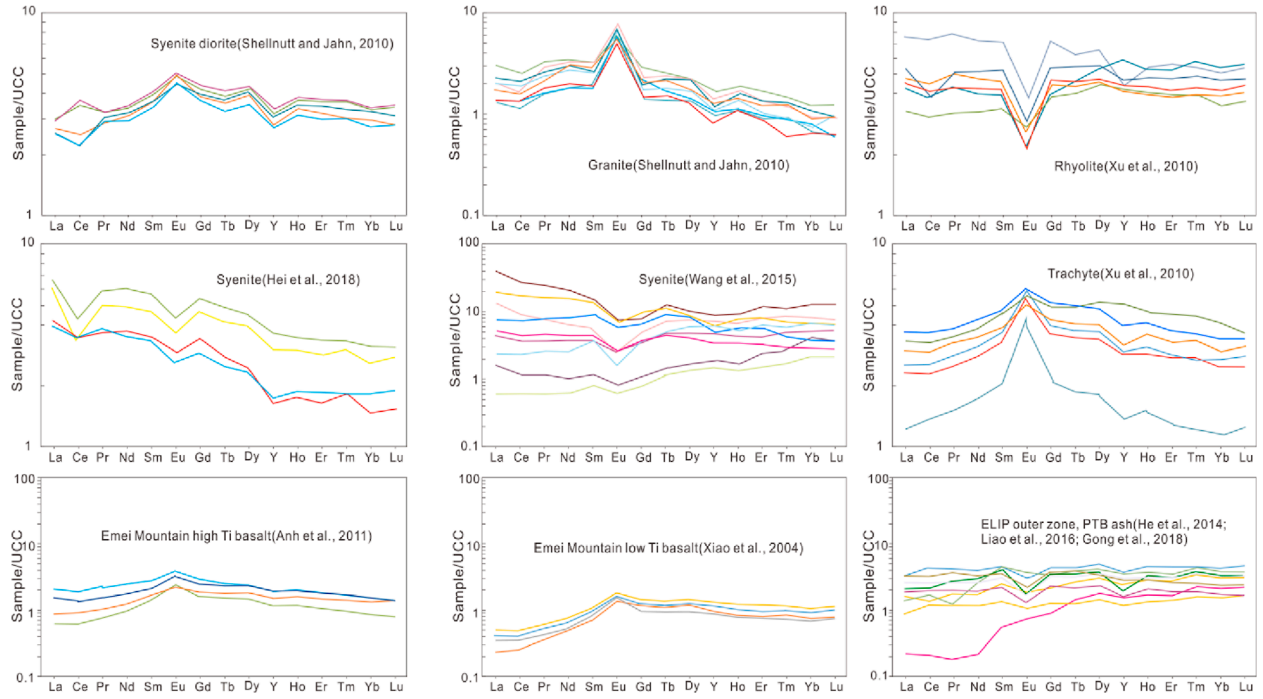

FIGURE 11
ELIP felsic intrusive rocks and volcanic rocks with rare earth element partition model [modified from Li et al. (2020); Shen et al. (2023)].

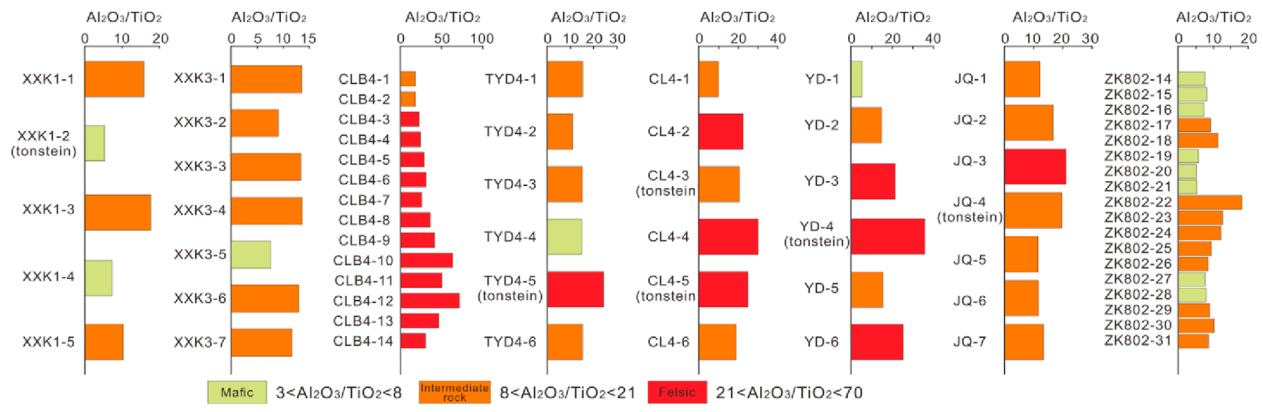

FIGURE 12
Vertical variations of Al_2O_3/TiO_2 of the Late Permian coalfield in northeast Guizhou.

of ferromagnesian provenance. The data points corresponding to the K1 Coalbed are distributed at the common boundary of coarse-grained rock and coarse-grained andesite, as well as at the common boundary of coarse-grained andesite and rhyolite (Figures 10C–E). The tonstein sample is close to the range of Emeishan basalt. The data points corresponding to the K3 Coalbed are distributed within the range of coarse andesite and alkaline basalt. Compared to samples influenced by intermediate acidic volcanic rocks, the samples from XX Mine are closer to the alkaline basalt range. Liu et al. (2019) proposed that the main factor contributing to the enrichment of REY and critical elements in coalfields of western Guizhou Province is the input of alkaline volcanic material from the top of ELIP. It can be inferred that the plagioclase neutral rocks at the top of ELIP are the main provenance of XX Mine (Dai et al., 2016; Xie et al., 2017). Similar to the coal samples from southern Sichuan Province, there is a negative Ce anomaly in the samples from XX Mine, indicating a provenance dominated by felsic or felsic neutral rocks (Dai et al., 2015).

The coal samples from XX Mine have a high quartz content. Quartz particles are large and have a certain degree of roundness, indicating terrestrial debris origin. Meanwhile, some small self-generated quartz particles have also been observed, which are the weathering products of basalt in the Kangdian Upland or siliceous hydrothermal precipitation products (Dai et al., 2012). Vertically,

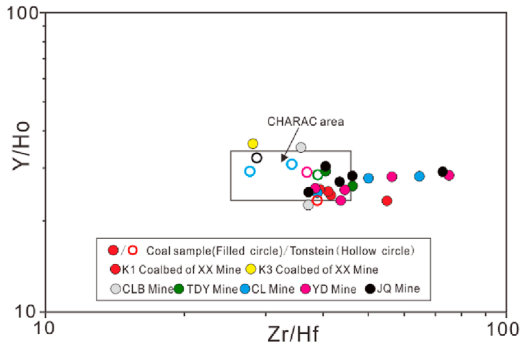

FIGURE 13
Plot of Y/Ho versus Zr/Hf from northeast Guizhou coal field, CHARAC area are modified from Bau M. (1996).

some samples have low Al_2O_3/TiO_2, corresponding data points falling within the range of mafic provenance (Figures 11A, 12B), suggesting terrigenous detrital input from Kangdian Upland basalt.

5.1.5 Volcanic arc or paleozoic orogenic belt

Most of the clay rocks and coal samples from Well ZK802 belong to alkaline basalt (Figure 12E). The low titanium Emeishan basalt exhibits sub-alkaline characteristics, indicating that these samples have other provenance regions. The deposition of alkaline volcanic ash in coal-accumulating environments is an important factor in the enrichment of critical metal elements in Late Permian coal in the study area (Dai et al., 2016; 2017). Some studies have suggested that the felsic inorganic components in coalfields in western Guizhou come from remote volcanic arcs or Paleozoic orogenic belts, rather than ELIP (Liu et al., 2020). The coal samples from CLB Mine have the highest Al_2O_3/TiO_2 content, indicating that the inorganic components come from the input of felsic substances. The Nb/Y-Zr/TiO2 cross-plot indicates the input of alkaline and sub-alkaline intermediate acidic volcanic ash (Figure 10C). The extrusive rocks induced by the Emeishan mantle plume belong to the alkaline - peralkaline category (Hei et al., 2018), providing an alkaline-peralkaline provenance for the study area. The acidic volcanic ash at the Permian-Triassic boundary in southern China provides sub-alkaline volcanic debris (Liao et al., 2016). In Figure 9D, the coal sample from CLB Mine is closer to the arc volcano range, while most of the data points fall within the Late Permian-Early Triassic volcanic rock range (Figure 10E), showing the contribution of more distant volcanic arcs to inorganic components. In the coal samples from CLB Mine, the element enrichment combination is Se-Mo-Ge-Nb-U, which differs significantly from the enrichment combinations of Kangdian Upland basalt, felsic volcanic rocks at the top of basalt, and intermediate acidic volcanic ash, but is similar to two reported coalbeds in western Guizhou Province (Liu et al., 2020). The inorganic components of these two coalbeds are considered to originate from unknown volcanic arcs and/or distal orogenic belts. Vertically, Al_2O_3/TiO_2 shows a decreasing trend, indicating a continuously decreasing input intensity of volcanic arcs and/or distal orogenic belt debris (Figure 12C).

5.2 The influence of hydrothermal fluids

In southwestern China, hydrothermal fluids are an important factor affecting the mineralogy and geochemical anomalies of coal (Dai et al., 2004; 2012). Widespread fluid activity plays an important role in the activation, migration, and enrichment of critical metal elements in coal (Cheng et al., 2015; Li et al., 2017; Yang et al., 2017).

5.2.1 Formation and transformation of minerals

The presence of ammonium illite is direct evidence of high-temperature fluid activity, and it is commonly observed in samples from CLB Mine. Ammonium illite occurs in two ways in coal: 1) illite is formed by alteration through the substitution of NH_4^+ and K^+ (Williams et al., 1992); 2) Kaolinite and nitrogen interact with coalification to form (Dai et al., 2012). Illite was not detected in the CLB Mine samples, therefore the formation of ammonium illite is related to the second way. The nitrogen involved in the formation of ammonium illite may come from bacterial decay and thermal decomposition of organic matter, reacting with H+ to form $NH4^+$. Under reducing and acidic conditions, $NH4^+$ easily enters the pore fluid. Ammonium illite occurs in pores or cell lumen, coexisting with kaolinite, indicating that ammonium illite may originate from the kaolinite precursor produced by the interaction between kaolinite and $NH4^+$ during coalification process (Williams et al., 1989; 1992).

Kaolinite was detected in coal and tonstein samples from TDY, YD, CL, and XX mines, while other types of clay minerals were not detected. However, various types of clay minerals were detected in the samples of CLB, JQ Mine, and Well ZK802. The clay minerals in the coal samples of study area are mainly kaolinite, which is induced by the decomposition of debris in the highly acidic solution of peat swamp, promoting the transformation of other aluminosilicates into kaolinite. In the coal sample from Well ZK802, zeolite is also evidence of low-temperature hydrothermal fluid activity. Letoshite is mainly formed in some low-temperature hydrothermal alteration zones and widely replaces potassium feldspar along this vein, or it may have been formed during low-grade metamorphism (Susilawati and Ward, 2006). Kaolinite, montmorillonite, zeolite, and plagioclase can all form zeolite through weathering. The process of kaolinite deformation into zeolite requires additional material supply, including SiO_2, Na^+, and K^+, and the most likely provider of these substances is hydrothermal fluid (Hower and Gayer, 2002). Due to the fact that the coal sample mainly contains kaolinite and quartz, this indicates that zeolite is mainly formed through low-temperature hydrothermal alteration.

Carbonate minerals and sulfate minerals can also confirm hydrothermal fluid activity. Calcite is widely distributed in various coalbeds in the study area. Except for CL Mine, no carbonate minerals were detected in the tonstein and floor samples of other mines. Calcite mainly appears in the form of fracture cement in coal (Figure 4H). The fractures formed after coalbed rupture provide permeable channels for Ca^{2+} rich hydrothermal fluids to pass through the coalbed (rather than the tonstein). The gypsum content that occurs as fracture cement is low and coexists with pyrite (Figures 4I–K). Iron sulfides near fractures are easily oxidized, and fluids rich in oxygen and calcium may be more likely to promote the production of iron containing sulfate minerals along fractures (Figure 4L) (Dai et al., 2013). In addition, the authigenic small quartz (Figure 4F), fracture-cemented pyrite

TABLE 6 The maximum and minimum values of Nb/Ta and Zr/Hf in coal samples from the Late Permian coalfield in northeast Guizhou.

Mine/Well	XX (K1 coalbed)	XX (K3 coalbed)	CLB	TDY	CL	YD	JQ	ZK802
Nb/Ta	17–22	9–18	27	14–33	12–119	9–33	10–50	18–29
Zr/Hf	39–56	35–46	35–69	35–56	29–66	38–77	29–75	35–47

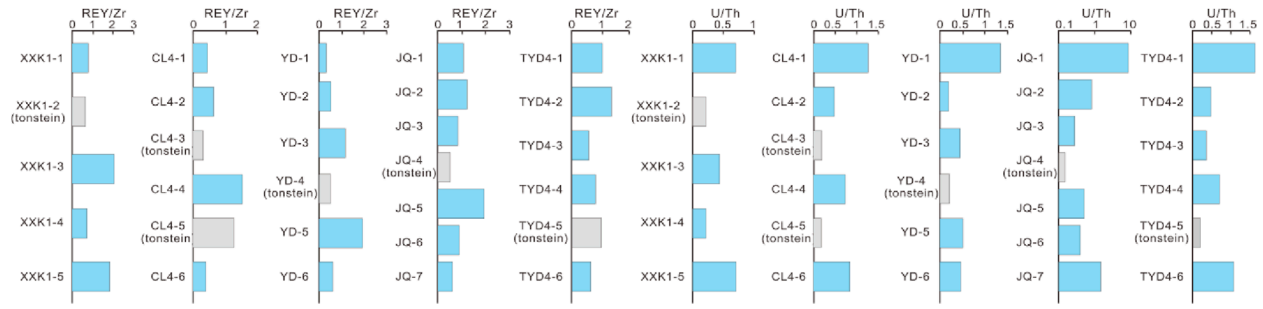

FIGURE 14
Vertical variation of REY/Zr and U/Th in coal samples from the Late Permian coalfield in northeast Guizhou.

(Figure 4L), and authigenic siderite (Figure 4J) all suggest the input of hydrothermal fluids.

5.2.2 Activation and migration of enriched elements

As a high field strength element, Nb-Ta-Zr-Hf-REY is believed to not migrate under low-temperature hydrothermal conditions (Arbuzov et al., 2019), migration occurs only under the action of strong acidic hydrothermal solution (Spears and Arbuzov, 2019). In Figure 13, all data points of the tonstein samples fall within the CHARAC range. Some data points of coal samples fall outside the CHARAC range, indicating that the fluid has fractionated Zr-Hf and Y-Ho (Bau M.,1996). For samples from different coal mines, Nb/Ta and Zr/Hf vary greatly, especially in CL, YD, and JQ coal mines (Table 6). Under the action of acidic fluid, the two elements with strong migration ability, Nb and Zr, undergo migration, resulting in fractionation of the combination of Nb-Ta and Zr-Hf elements. The Nb/Ta and Zr/Hf ratios in the coal samples are higher than those in the tonstein sample, indicating that Nb and Zr are relatively more actively leached from the tonstein and then deposited in the underlying organic matter. The re-deposition of elements is the reason for the enrichment of Nb and Zr in multiple coalfields in southwestern China (Dai et al., 2013). Meanwhile, few samples in the present study are characterized by Gd-maximum as well as MREY enrichment (Figures 8A, B), which is indicative of acid solutions (e.g., high P_{CO2}-waters) (Shand et al., 2005).

Compared to Nb, Ta, Zr, and Hf, REY has a higher mobility in aqueous solutions (Liu et al., 2019). Therefore, the vertical variation of REY content is inconsistent with Nb, Ta, Zr, and Hf. In XX, CL, YD, and JQ coal mines, the REY/Zr ratio of the interbedded tonstein is lower than that of the underlying coalbed (Figure 14), indicating that some REY leaches out of the interbedded tonstein and subsequently re-enriches in the underlying coalbed. Meanwhile, in the tonstein of TDY and CL coal mines, the REY/Zr ratio is higher than that of the underlying coalbed (Figures 14B, E), indicating that the overlying coalbed provides a source of REY. Under the action of gravity, fluids rich in REY enter the underlying tonstein. However, due to the barrier effect or changes in acidity or alkalinity, REY precipitates in the tonstein and no longer penetrates downwards. Acidic water can cause leaching and migration of REY, while alkaline water can cause re-precipitation of REY. The variation of U/Th can be used to reflect the migration and re deposition of acidic aqueous solutions between coalbeds and tonstein. In all coalbeds, the U/Th of the interbedded tonstein is lower than that of the underlying coal sample, indicating that U leaches out of the interbedded tonstein and then re precipitates in the underlying coalbed. It is worth noting that in the samples from the top of the coalbed, U/Th is higher than in other positions. This reflects the leaching of U elements from the overlying roof, which entered the top coalbed and led to an increase in U/Th. In addition, the roof composed of carbonate rock is easily influenced by seawater and may contain a high content of U, which may also lead to a high U content in the coalbed.

5.3 The influence of seawater

Wang et al. (2008) proposed that the variations in REY content in coal are due to the mixing of weathering products of Emeishan basalt under the influence of regression and transgression. Coalbeds formed in environments less affected by seawater have relatively high levels of REY. Previous studies have shown that coal affected by the ocean has a higher sulfur content than coal formed in freshwater environments (Chou, 2012). In this study, the total sulfur content of coal samples is between 1.1% and 24%, belonging to medium-high sulfur coal. Sulfur mainly occurs as pyrite (Figure 9B), with a small amount occurring as organic matter and sulfate. The occurrence form of pyrite implies the influence of seawater. The Sr/Ba value has been successfully used as a marine-influence indicator for

peat depositional environments, with Sr/Ba>1 indicating a marine influence for coal samples (Spiro et al., 2019). In this study, the Sr/Ba ratio of most coal samples was higher than 1, indicating that the coalbed was affected by seawater. The diffusion of varying degrees of seawater into peat bogs may lead to changes in the mineralogical and geochemical patterns of coal, as well as the enrichment of marine derived elements. In this study, the correlation between Se, U, and Mo with Nb, Ta, Zr, Hf, and REY was weak, but the correlation between Se and U, S was good (Figure 9B), indicating that Se may be related to sulfides represented by pyrite. The formation of pyrite is influenced by seawater, therefore the enrichment of Se and U in coal is also related to the influence of seawater.

6 Conclusion

(1) The chemical composition of coal from the Late Permian Wujiaping Formation in northeastern Guizhou is characterized by ultra-low moisture content, moderate ash content, moderate volatile matter yield, and medium high sulfur content. These coal samples are composed of clay minerals (including kaolinite, illite, ammonium illite, etc.), quartz, rutile, pyrite, calcite, gypsum and other minerals. There are certain differences in mineral composition among coal samples from different coal mines. The content of critical metal elements in coal is high, and the elemental composition of different minerals varies greatly. Vertically, critical metal elements are enriched in the tonstein and nearby coalbeds.

(2) The input of terrestrial debris is the main factor affecting the abundance of critical metal elements in coal, and the weathering products of acidic volcanic ash, basalt, and intermediate acidic rocks in the Kangdian Upland provide the material sources of critical metal elements. The input of intermediate acidic volcanic ash is the main factor for the enrichment of Nb-Ta-Zr-Hf-REY in most coal mines. The coastal swamp environment of the transitional facies, seawater infiltration, and hydrothermal fluids control the alteration and transformation of detrital minerals and the precipitation of authigenic minerals. The activation and migration of some critical metal elements are also controlled by these factors.

Data availability statement

The raw data supporting the conclusions of this article will be made available by the authors, without undue reservation.

Author contributions

ZY: Conceptualization, Investigation, Visualization, Writing–original draft. BL: Investigation, Methodology, Supervision, Writing–original draft. JC: Methodology, Resources, Supervision, Visualization, Writing–review and editing.

Funding

The author(s) declare that financial support was received for the research, authorship, and/or publication of this article. This study was funded by the National Natural Science Foundation of China (No. 41972182).

Conflict of interest

The authors declare that the research was conducted in the absence of any commercial or financial relationships that could be construed as a potential conflict of interest.

Generative AI statement

The author(s) declare that no Generative AI was used in the creation of this manuscript.

Publisher's note

References

Arbuzov, S. I., Spears, D. A., Vergunov, A. V., Ilenok, S. S., Mezhibor, A. M., Ivanov, V. P., et al. (2019). Geochemistry, mineralogy and genesis of rare metal (Nb-Ta-Zr-Hf-Y-REE-Ga) coals of the seam XI in the south of kuznetsk basin, Russia. *Ore Geol. Rev.* 113, 103073. doi:10.1016/j.oregeorev.2019.103073

ASTM Standard D3173/D3173M – 17a (2017). *Standard test method for moisture in the analysis sample of coal and coke*. West Conshohocken, PA: ASTM International.

ASTM Standard D3174-12 (Reapproved 2018) (2018). *Ash in the analysis sample of coal and coke from coal*. West Conshohocken, PA: ASTM International.

ASTM Standard D3175-17 (2011). *Standard test method for volatile matter in the analysis sample of coal and coke*. West Conshohocken, PA: ASTM International.

Bau, M. (1996). Controls on the fractionation of isovalent trace elements in magmatic and aqueous systems: evidence from Y/Ho, Zr/Hf, and lanthanide tetrad effect. *Contributions Mineralogy and Petrology* 123, 323–333. doi:10.1007/s004100050159

Boehme, J., Coble, P., Conmy, R., and Stovall-Leonard, A. (2004). Examining CDOM fluorescence variability using principal component analysis: seasonal and regional modeling of three-dimensional fluorescence in the Gulf of Mexico. *Mar. Chem.* 89, 3–14. doi:10.1016/j.marchem.2004.03.019

China Coal Geology Bureau (1996). "Sedimentary environments and coal accumulation of late permian coal Formation in western Guizhou," in *Southern sichuan and eastern yunnan*. China: Chongqing University Press. Ch.

Chou, C. L. (2012). Sulfur in coals: a review of geochemistry and origins. *Int. J. Coal Geol.* 100, 1–13. doi:10.1016/j.coal.2012.05.009

Chung, F. K. (1974). Quantitative interpretation of X-ray diffraction patterns of mixtures. II. Adiabatic principle of X-ray diffraction analysis of mixtures. *J. Appl. Crystallogr.* 7, 526–531. doi:10.1107/S0021889874010387

Crowley, S. S., Ruppert, L. F., Belkin, H. E., Stanton, R. W., and Moore, T. A. (1993). Factors affecting the geochemistry of a thick, subbituminous coal bed in the Powder

River Basin: volcanic, detrital, and peat-forming processes. *Org. Geochem.* 20 (6), 843–853. doi:10.1016/0146-6380(93)90067-L

Dai, S., Li, D., Ren, D., Tang, Y., Shao, L., and Song, H. (2004). Geochemistry of the late Permian No. 30 coal seam, Zhijin Coalfield of Southwest China: influence of a siliceous low-temperature hydrothermal fluid. *Appl. Geochem.* 19 (2004), 1315–1330. doi:10.1016/j.apgeochem.2003.12.008

Dai, S., Liu, C., Zhao, L., Liu, J., Wang, C., and Ren, D. (2022). Strategic metal mineral resources in coal measures: significance and challenges. *J. China Coal Sci.* 47 (5), 1743–1749. doi:10.13225/j.cnki.jccs.MJ22.0011

Dai, S., Liu, J., Ward, C. R., Hower, J. C., French, D., Jia, S., et al. (2015). Mineralogical and geochemical compositions of Late Permian coals and host rocks from the Guxu Coalfield, Sichuan Province, China, with emphasis on enrichment of rare metals. *Int. J. Coal Geol.* 166, 71–95. doi:10.1016/j.coal.2015.12.004

Dai, S., Ren, D., Chou, C., Finkelman, R., Seredin, V., and Zhou, Y. (2012). Geochemistry of trace elements in Chinese coals: a review of abundances, genetic types, impacts on human health, and industrial utilization. *Int. J. Coal Geol.* 94, 3–21. doi:10.1016/j.coal.2011.02.003

Dai, S., Ren, D., Tang, Y., Yue, M., and Hao, L. (2005). Concentration and distribution of elements in late permian coals from western Guizhou province, China. *Int. J. Coal Geol.* 61, 119–137. doi:10.1016/j.coal.2004.07.003

Dai, S., Shen, M., Liu, G., and Zhao, L. (2024). Enrichment mechanism of rare earth elements in Late Permian coal measure basement tuff in western Guizhou. *Acta Geol. Sin.* 98 (8), 2316–2335. doi:10.19762/j.cnki.dizhixuebao.2024188

Dai, S., Ward, C. R., Graham, I. T., French, D., Hower, J. C., Zhao, L., et al. (2017). Altered volcanic ashes in coal and coal-bearing sequences: a review of their nature and significance. *Earth-Science Rev.* 175, 44–74. doi:10.1016/j.earscirev.2017.10.005

Dai, S., Xie, P., Jia, S., Ward, C. R., Hower, J. C., Yan, X., et al. (2016). Enrichment of U-Re-V-Cr-Se and rare earth elements in the Late Permian coals of the Moxinpo Coalfield, Chongqing, China: genetic implications from geochemical and mineralogical data. *Ore Geol. Rev.* 80, 1–17. doi:10.1016/j.oregeorev.2016.06.015

Dai, S., Zhang, W., Ward, C. R., Seredin, V. V., Hower, J. C., Li, X., et al. (2013). Mineralogical and geochemical anomalies of late Permian coals from the Fusui Coalfield, Guangxi Province, southern China: influences of terrigenous materials and hydrothermal fluids. *Int. J. Coal Geol.* 105, 60–84. doi:10.1016/j.coal.2012.12.003

Dai, S., Zhao, L., Wei, Q., Song, X., Wang, W., Liu, J., et al. (2020). Resources of critical metals in coal-bearing sequences in China: enrichment types and distribution. *Sci. China Press* 65 (33), 3715–3729. doi:10.1360/TB-2020-0112

Finkelman, R. B., Dai, S., and French, D. (2019). The importance of minerals in coal as the hosts of chemical elements: a review. *Int. J. Coal Geol.* 212, 103251. doi:10.1016/j.coal.2019.103251

Finkelman, R. B., Palmer, C. A., and Wang, P. P. (2018). Quantification of the modes of occurrence of 42 elements in coal. *Int. J. Coal Geol.* 185, 138–160. doi:10.1016/j.coal.2017.09.005

GBT 15224.1-2018 (2018). "Classification for quality of coal in P.R. China," in *Part 1 ash*.

Gotelli, N. J., and Ellison, A. M. (2004). *A primer of ecological statistics*. Sunderland, MA: Sinauer Associates.

Hayashi, K., Fujisawa, H., Holland, H. D., and Ohmoto, H. (1997). Geochemistry of ~1.9 Ga sedimentary rocks from northeastern Labrador, Canada. *Geochimica Cosmochimica Acta* 61 (19), 4115–4137. doi:10.1016/S0016-7037(97)00214-7

He, B., Xu, Y. G., Chung, S. L., Xiao, L., and Wang, Y. M. (2003). Sedimentary evidence for a rapid, kilometer-scale crustal doming prior to the eruption of the Emeishan flood basalts. *Earth Planet. Sci. Lett.* 213, 391–405. doi:10.1016/S0012-821X(03)00323-6

Hei, H., Su, G., Wang, Y., Mo, X., Luo, Z., and Liu, W. (2018). Rhyolites in the emeishan large igneous province (SW China) with implications for plume-related felsic magmatism. *J. Asian Earth Sci.* 164, 344–365. doi:10.1016/j.jseaes.2018.05.032

Hower, J., Eble, C., O'Keefe, J., Dai, S., Wang, P., Xie, P., et al. (2015). Petrology, palynology, and geochemistry of gray hawk coal (early pennsylvanian, langsettian) in eastern Kentucky, USA. *Minerals* 5 (3), 592–622. doi:10.3390/min5030511

Hower, J. C., Cantando, E., Eble, C. F., and Copley, G. C. (2019). Characterization of stoker ash from the combustion of high-lanthanide coal at a Kentucky bourbon distillery. *Int. J. Coal Geol.* 213, 103260. doi:10.1016/j.coal.2019.103260

Hower, J. C., and Gayer, R. A. (2002). Mechanisms of coal metamorphism: case studies from Paleozoic coalfields. *Int. J. Coal Geol.* 50, 215–245. doi:10.1016/S0166-5162(02)00119-2

Iwamori, H., Yoshida, K., Nakamura, H., Kuwatani, T., Hamada, M., Haraguchi, S., et al. (2017). Classification of geochemical data based on multivariate statistical analyses: complementary roles of cluster, principal component, and independent component analyses. *Geochem. Geophys. Geosystems* 18 (3), 994–1012. doi:10.1002/2016GC006663

Jin, C., Liu, L., Zhang, X., Gao, S., Cheng, Z., Li, B., et al. (2024). Characteristics and genetic mechanism of Li- Nb- Ta enrichment in Late Permian coal in the coalfield of northwestern Guizhou, Southwest China. *Acta Geol. Sin.* 98 (8), 2316–2335. doi:10.19762/j.cnki.dizhixuebao.2024188

Ketris, M. P., and Yudovich, Y. (2009). Estimations of Clarkes for Carbonaceous biolithes: world averages for trace element contents in black shales and coals. *Int. J. Coal Geol.* 78, 135–148. doi:10.1016/j.coal.2009.01.002

Lattin, J. M., Carroll, J. D., Green, P. E., and Green, P. E. (2003). *Analyzing multivariate data*. Pacific Grove, CA: Thomson Brooks/Cole.

Li, B., Zhaung, X., Querol, X., Li, J., Moreno, N., Córdoba, P., et al. (2019). Geological controls on enrichment of Mn, Nb (Ta), Zr (Hf), and REY within the early permian coals of the jimunai depression, xinjiang province, NW China. *Int. J. Coal Geol.* 215, 103298. doi:10.1016/j.coal.2019.103298

Li, B., Zhuang, X., Li, J., Querol, X., Font, O., and Moreno, N. (2017). Enrichment and distribution of elements in the late permian coals from the zhina coalfield, Guizhou province, southwest China. *Int. J. Coal Geol.* 171, 111–129. doi:10.1016/j.coal.2017.01.003

Li, B., Zhuang, X., Ning, S., Li, J., Wang, X., Huang, S., et al. (2022). Mobilization, migration and enrichment mechanism of zr (Hf)-Nb(Ta)-Ga rare earth elements: a case study of the coal bearing strata of the Upper Permian Wujiaping Formation in Wuzhengdao Area. *J. China Coal Soc.* 47 (5), 1822–1839. doi:10.13225/j.cnki.jccs.MJ22.0136

Li, B., Zhuang, X., Querol, X., Moreno, N., Córdoba, P., Shangguan, Y., et al. (2020). Geological controls on the distribution of REY-Zr (Hf)-Nb (Ta) enrichment horizons in late Permian coals from the Qiandongbei Coalfield, Guizhou Province, SW China. *Int. J. Coal Geol.* 231, 103604. doi:10.1016/j.coal.2020.103604

Liu, J., Song, H., Dai, S., Nechaev, V. P., Graham, I. T., French, D., et al. (2019). Mineralization of REE-Y-Nb-Ta-Zr-Hf in wuchiapingian coals from the liupanshui coalfield, Guizhou, southwestern China: geochemical evidence for terrigenous input. *Ore Geol. Rev.* 115, 103190. doi:10.1016/j.oregeorev.2019.103190

Liu, J. J., Nechaev, V. P., Dai, S., Song, H., Nechaeva, E. V., Jiang, Y., et al. (2020). Evidence for multiple sources for inorganic components in the Tucheng coal deposit, western Guizhou, China and the lack of critical-elements. *Int. J. Coal Geol.* 223, 103468. doi:10.1016/j.coal.2020.103468

Martin, G., Rentsch, L., H¨ock, M., and Bertau, M. (2017). Lithium market research – global supply, future demand and price development. *Energy Storage Mater.* 6, 171–179. doi:10.1016/j.ensm.2016.11.004

Meglen, R. R. (1992). Examining large databases: a chemometric approach using principal component analysis. *Mar. Chem.* 39, 217–237. doi:10.1016/0304-4203(92)90103-H

MT/T 849–2000 (National Standard of P.R. China), 2000. Classification for volatile matter of coal.

MT/T 850–2000 (National Standard of P.R. China), 2000. Classification for moisture of coal.

Per, K., and Erika, M. (2018). Examining the rare-earth elements (REE) supply–demand balance for future global wind power scenarios. *Geol. Surv. Den. Greenl. Bull.* 41, 87–90. doi:10.34194/geusb.v41.4350

Querol, X., Whateley, M. K. G., Fernfindez-Turiel, J. L., and Tuncali, E. (1997). Geological controls on the mineralogy and geochemistry of the Beypazari lignite, central Anatolia, Turkey. *Int. J. Coal Geol.* 33, 255–271. doi:10.1016/S0166-5162(96)00044-4

Ren, D. Y. (2006). *Geochemistry of trace elements in coal*. Beijing, China: Science Press.

Seredin, V. V., and Dai, S. (2012). Coal deposits as potential alternative sources for lanthanides and yttrium. *Int. J. Coal Geol.* 94, 67–93. doi:10.1016/j.coal.2011.11.001

Seredin, V. V., and Finkelman, R. B. (2008). Metalliferous coals: a review of the main genetic and geochemical types. *Int. J. Coal Geol.* 76, 253–289. doi:10.1016/j.coal.2008.07.016

Shand, P., Johannesson, K. H., Chudaev, O., Chudaeva, V., and Edmunds, W. M. (2005). "Rare earth element contents of high pCO2 groundwaters of Primorye, Russia: mineral stability and complexation controls," in *Rare earth elements in groundwater flo* (Netherlands: Springer).

Shellnutt, J. G., and Jahn, B. M. (2010). Formation of the Late Permian Panzhihua plutonic-hypabyssal-volcanic igneous complex: implications for the genesis of Fe–Ti oxide deposits and A-type granites of SW China. *Earth Planet. Sci. Lett.* 289, 509–519. doi:10.1016/j.epsl.2009.11.044

Shen, M., Dai, S., Graham, I. T., Nechaev, V. P., French, D., Zhao, F., et al. (2021). Mineralogical and geochemical characteristics of altered volcanic ashes (tonsteins and K-bentonites) from the latest Permian coal-bearing strata of western Guizhou Province, southwestern China. *Int. J. Coal Geol.* 237, 103707. doi:10.1016/j.coal.2021.103707

Shen, M. L., Dai, S. F., Nechaev, V. P., French, D., Graham, I. T., Liu, S. D., et al. (2023). Provenance changes for mineral matter in the latest Permian coals from western Guizhou, southwestern China, relative to tectonic and volcanic activity in the Emeishan Large Igneous Province and Paleo-Tethys region. *Gondwana Res.* 113, 71–88. doi:10.1016/j.gr.2022.10.011

Spears, D. A., and Arbuzov, S. I. (2019). A geochemical and mineralogical update on two major tonsteins in the UK Carboniferous Coal Measures. *Int. J. Coal Geol.* 210, 103199. doi:10.1016/j.coal.2019.05.006

Spiro, B. F., Liu, J., Dai, S., Zeng, R., Large, D., and French, D. (2019). Marine derived $^{87}Sr/^{86}Sr$ in coal, a new key to geochronology and palaeoenvironment: elucidation of

the India-Eurasia and China-Indochina collisions in Yunnan, China. *Int. J. Coal Geol.* 215, 103304. doi:10.1016/j.coal.2019.103304

Susilawati, R., and Ward, C. R. (2006). Metamorphism of mineral matter in coal from the Bukit Asam deposit, south Sumatra, Indonesia. *Int. J. Coal Geol.* 68, 171–195. doi:10.1016/j.coal.2006.02.003

Taylor, S. R., and Mclennan, S. H. (1985). *The continental Crust: its composition and evolution*. Oxford: Blackwell.

Wang, Q., Yang, R., and Miao, B. (2008). Rare earth elements stratigraphic significance in late Permian coal measure from Bijie City, Guizhou Province, China. *J. rare earths* 26 (5), 760–764. doi:10.1016/S1002-0721(08)60178-7

Wang, X., Dai, S., Chou, C., Zhang, M., Wang, J., Song, X., et al. (2012). Mineralogy and geochemistry of late permian coals from the taoshuping mine, yunnan province, China: evidences for the sources of minerals. *Int. J. Coal Geol.* 96-97, 49–59. doi:10.1016/j.coal.2012.03.004

Ward, C. R. (2016). Analysis, origin and significance of mineral matter in coal: an updated review. *Int. J. Coal Geol.* 165, 1–27. doi:10.1016/j.coal.2016.07.014

Williams, L. B., Ferrell, R. E., Chinn, E. W., and Sassen, R. (1989). Fixed-ammonium in clays associated with crude oils. *Appl. Geochem.* 4 (6), 605–616. doi:10.1016/0883-2927(89)90070-X

Williams, L. B., Wilcoxon, B. R., Ferrell, R. E., and Sassen, R. (1992). Diagenesis of ammonium during hydrocarbon maturation and migration, Wilcox Group, Louisiana, U.S.A. *Appl. Geochem.* 7 (2), 123–134. doi:10.1016/0883-2927(92)90031-W

Winchester, J. A., and Floyd, P. A. (1977). Geochemical discrimination of different magma series and their differentiation products using immobile elements. *Chem. Geol.* 20, 325–343. doi:10.1016/0009-2541(77)90057-2

Xiao, L., Xu, Y., Mei, H., Zheng, Y., He, B., and Pirajno, F. (2004). Distinct mantle sources of low-Ti and high-Ti basalts from the western Emeishan large igneous province, SW China: implications for plume–lithosphere interaction. *Earth Planet. Sci. Lett.* 228, 525–546. doi:10.1016/j.epsl.2004.10.002

Xie, P., Zhang, S., Wang, Z., Wang, L., and Xu, Y. (2017). Geochemical characteristics of the Late Permian coals from the Yueliangtian Coalfield, western Guizhou, southwestern China. *Arabian J. Geosciences* 10 (5), 98. doi:10.1007/s12517-017-2916-1

Xue, J., Lee, C., Wakeham, S. G., and Armstrong, R. A. (2011). Using principal components analysis (PCA) with cluster analysis to study the organic geochemistry of sinking particles in the ocean. *Org. Geochem.* 42, 356–367. doi:10.1016/j.orggeochem.2011.01.012

Yamashita, Y., and Tanoue, E. (2003). Distribution and alteration of amino acids in bulk DOM along a transect from bay to oceanic waters. *Mar. Chem.* 82, 145–160. doi:10.1016/S0304-4203(03)00049-5

Yang, R., Cheng, W., Gao, J., Chen, J., Wei, H., Shen, M., et al. (2017). U, Li, Nb and V Element Enrichment of Coal Seams and Potential Resource Evaluation in Southwest Guizhou. *Guizhou Geol.* 34 (2), 77–81. doi:10.3969/j.issn.1000-5943.2017.02.003

Yang, R. D., Liu, L., Wei, H. R., Cui, Y. C., and Cheng, W. (2011). Geochemical characteristics of Guizhou Permian coal measure strata and analysis of the control factors. *J. Coal Sci. and Eng.* 17 (1), 55–68. doi:10.1007/s12404-011-0112-6

Zhai, M., Wu, F., Hu, R., Jiang, S., Li, W., Wang, R., et al. (2019). Critical metal mineral resources: current research status and scientific issue. *Sci. Found. China* 33 (2), 116–111. CNKI:SUN:ZKJJ.0.2019-02-002.

Zhang, Y., Cheng, W., Yang, R., Yang, B., Lv, F., Luo, C., et al. (2023). A review on the abnormal enrichment of some metals in coals from Guizhou. *Geol. Rev.* 69 (1), 247–265. doi:10.16509/j.georeview.2022.10.045

Zhao, L., Dai, S., Nechaev, V. P., Nechaeva, E. V., Graham, I. T., French, D., et al. (2019). Enrichment of critical elements (Nb-Ta-Zr-Hf-REE) within coal and host rocks from the Datanhao mine, Daqingshan Coalfield, northern China. *Ore Geol. Rev.* 111, 102951. doi:10.1016/j.oregeorev.2019.102951

Zhou, J. H., Chen, H. Y., Zhao, L., Wang, X. H., Li, H., Li, T., et al. (2023). Enrichment of critical elements (Li-Ga-Nb-Ta-REE-Y) in the coals and host rocks from the Daping Mine, Yudongnan Coalfield, SW China. *Ore Geol. Rev.* 152, 105245. doi:10.1016/j.oregeorev.2022.105245

Zhuang, X. G., Querol, X., Zeng, R. S., Xu, W. D., Alastuey, A., Lopez-Soler, A., et al. (2000). Mineralogy and geochemistry of coal from the Liupanshui mining district, Guizhou, south China. *Int. J. Coal Geol.* 45, 21–37. doi:10.1016/S0166-5162(00)00019-7

frontiers | Frontiers in Earth Science

TYPE Original Research
PUBLISHED 11 March 2025
DOI 10.3389/feart.2025.1491334

OPEN ACCESS

EDITED BY
Hu Li,
Sichuan University of Science and Engineering, China

REVIEWED BY
Jianguo Zhang,
China University of Geosciences, China
Zikun Zhou,
Panzhihua University, China

*CORRESPONDENCE
Yang Li,
7891235@qq.com

RECEIVED 04 September 2024
ACCEPTED 12 February 2025
PUBLISHED 11 March 2025

CITATION
Fan Z, Hu C, Jiang S, Li M, Cai Y, Jiang Y, Li Y and Tian M (2025) Logging-data-driven lithology identification in complex reservoirs: an example from the Niuxintuo block of the Liaohe oilfield.
Front. Earth Sci. 13:1491334.
doi: 10.3389/feart.2025.1491334

Logging-data-driven lithology identification in complex reservoirs: an example from the Niuxintuo block of the Liaohe oilfield

Zuochun Fan[1,2], Changhao Hu[2], Shu Jiang[3], Man Li[2], Ye Cai[2], Yue Jiang[2], Yang Li[2]* and Mei Tian[2]

[1]Institute of Advanced Studies, China University of Geosciences, Wuhan, China, [2]Petrochina Liaohe Oilfield Company, Panjin, China, [3]School of Sustainable Energy, China University of Geosciences, Wuhan, China

For lithologic oil reservoirs, lithology identification plays a significant guiding role in exploration targeting, reservoir evaluation, well network adjustment and optimization, and the establishment of reservoir models. Lithology is usually predicted from well log data based on limited core observations. In recent years, machine learning algorithms have been applied to lithology identification to enhance prediction accuracy. In this paper, five algorithms, including Bayes discriminant analysis, Random Forest (RF), Support Vector Machine (SVM), Back Propagation Neural Network (BPNN), and Convolutional Neural Network (CNN) are evaluated for lithology identification using data from the Niuxintuo reservoir. This reservoir is characterized by complex structural and sedimentary features, strong heterogeneity, and intricate lithological properties, all of which present considerable challenges for well logging identification. First, we conducted a detailed observation of the core lithology. Based on the requirements for reservoir evaluation and the principles of logging identification, we reclassify the lithology of the study area into two categories: clastic rocks and dolomite. The clastic rocks are further subdivided into five rock types: fine sandstone, medium-coarse sandstone, conglomerate, mudstone, and transitional rock. The well log series were selected through sensitivity analysis. Then, Bayes discriminant analysis and four machine learning methods were trained to identify the lithology of the study area. The results indicate that except for Bayes discriminant analysis, all the constructed machine learning classifiers demonstrate high prediction accuracy, with the accuracy rate exceeding 85%. Among them, SVM classifier shows the best performance achieving a prediction accuracy as high as 93%. Additionally, the well-trained SVM model was successfully used to predict the lithology profile of blind wells. Our findings provide valuable guidance for predicting the remaining oil distribution and further exploration potential in the Niuxintuo oilfield. Furthermore, this study gains insight into the process and methodology of rapidly predicting lithology of hydrocarbon reservoirs using easily accessible well logging data.

KEYWORDS

lithology classification, machine learning, support vector machine, random forest, convolutional neural networks, back propagation neural network, bayes distinguish analysis

1 Introduction

Lithology identification is a crucial issue in reservoir characterization, as it helps correlate critical reservoir properties such as porosity, permeability and oil saturation, and plays a vital role in constructing field-scale reservoir models. Well log data have advantages such as high vertical resolution, good continuity, and convenient data acquisition. Therefore, they are an important resource for obtaining underground lithological information. Lithology classification based on well log data forms the foundation for reservoir characterization and provides a basis for geological studies such as sedimentary facies and environmental analysis. In addition to its significance in formation evaluation and geological analysis, lithology interpretation plays an important role in predicting sweet spot reservoirs and forecasting remaining oil distribution. The traditional methods for interpreting lithology mainly include cross-plot technique (e.g., Sanyal et al., 1980), curve feature method (Anifowose et al., 2019), imaging logging chart method (Cohn et al., 1996), multiple linear regression method (Delfiner et al., 1987), and discriminant analysis method (Dong et al., 2016; Dong et al., 2022). However, each of the method have some limitations (Sun et al., 2019). For example, a lack of clarity in the relationships between the data points may result in the cross-plot technique failed. Moreover, and it cannot display higher dimensional spatial information, and usually only two parameters can be considered at the same time (McDowell et al., 1998). Multiple linear regression method is very sensitive to highly correlated independent variables, and the relationship between variables is often nonlinear, which may lead to a decrease in the explanatory power of the model (Delfiner et al., 1987). Discriminant analysis methods require a large number of high-quality datasets, and are limited by some assumed premises (Dong et al., 2016). Overall, these methods generally require a large number of samples, which are very time-consuming. Recognizing lithology boundaries from well log data is inherently a nonlinear problem, primarily because log curves are influenced by rock properties like pore fluids. Therefore, it is essential to develop a suitable nonlinear approach that can effectively address these challenges.

The rapid advancement of computer technology has enabled machine learning methods to offer more time and cost-effective solutions with higher lithology identification accuracy, compared to traditional lithology identification methods (e.g., Ashraf et al., 2021; Bressan et al., 2020). Nowadays, numerous machine learning methods have emerged and been successfully applied to lithology identification (e.g., Wang et al., 2014; Bhattacharya et al., 2016; Biau and Scornet, 2016; Saporetti et al., 2018; Wang et al., 2020; Zhang et al., 2023). Machine learning can be categorized into three types: unsupervised learning, semi-supervised learning, and supervised learning. Unsupervised learning techniques, such as expectation maximisation (Miyahara et al., 2020), K-mean clustering (Huang et al., 2016), hierarchical clustering (Vichi et al., 2022), and deep autocoders (Kampffmeyer et al., 2018), are used only by arranging the lithology according to its intrinsic characteristics to provide an overall perspective. They are helpful when the dataset is limited (there are no available labels). In contrast, semi-supervised learning techniques (SSL), such as forward and unlabeled machine learning (Helm et al., 2023), active semi-supervised algorithms (Xu et al., 2021a; Shan et al., 2021), and Laplace Support Vector Machines (Yang and Xu, 2018), are beneficial when there is a limited amount of labelled data accessible. On the contrary, supervised learning techniques, which are suitable for learning a pattern in a known labelled species and inferring new instances in accordance with this pattern, can provide precise training data and therefore give very accurate results (Jordan and Mitchell, 2015). Several well-known supervised shallow learning algorithms are used for petrographic classification of core-tagging-based logs. This category includes backpropagation neural networks (Amari, 1993; Dong et al., 2023), support vector machine (SVM) (Wang et al., 2014), K-nearest neighbours (Wang et al., 2023; Li et al., 2024), and decision trees (DT) (Zhou et al., 2020). In addition, uniform integration techniques such as Random Forest (RF) (Yan et al., 2024), Extreme Gradient Boosting (Chen and Guestrin, 2016; Zheng et al., 2022), and Logistic Boosting Regression (Huang et al., 2019) belong to the same category, and such supervised algorithms use geological rules to make petrographic estimation more credible. In addition, several popular deep learning (DL) algorithms (Goodfellow et al., 2016; Miclea et al., 2020), such as convolutional neural networks (Xu et al., 2021b), recurrent neural networks (Tian et al., 2021) and long- and short-term memory networks (Lin et al., 2020), and TabNet (Madani et al., 2018; Li et al., 2022), possess very excellent properties such as weight sharing, local connectivity, and translational isotropy to effectively handle high-dimensional data.

The Niuxintuo reservoir is a typical lithological reservoir. Previous studies have shown that sedimentary environments significantly influence the lithology distribution. Moreover, the lithology controls petrophysical properties, and petrophysical properties control oil saturation (Zhou, 2022; Li, 2022). In this article, we applied multiple methods for lithology identification in the study area and select the most appropriate method for lithology prediction. Firstly, based on the detailed observation and description of rock cores, the lithology of the Niuxintuo area in is divided into six categories: fine sandstone, medium coarse sandstone, conglomerate, mudstone, transitional rock, and dolomite. Subsequently, the logging sequence is standardized and normalized to eliminate systematic errors, thereby improving the accuracy in describing, interpreting, and predicting reservoirs. Building on this, extensive cross plots are employed to evaluate the sensitivity of logging sequences. By integrating lithology sensitivity, data reliability, and curve complementarity, six key parameters—acoustic transmit time (AC), compensated neutron (CNL), density (DEN), gamma ray (GR), resistivity (RT), and conductivity (CON_CAL)—are selected as predictive curves for lithology identification. The initial step in multi-method lithology identification involves classifying lithology using Bayes discriminant analysis. However, with a prediction accuracy of only 58.20%, this approach falls short of meeting the requirements for reliable lithology prediction. Then, the focus shifted to exploring lithology identification using advanced machine learning algorithms, including RF, SVM, BPNN, and CNN. The developed machine learning classifiers demonstrate high prediction accuracy, with SVM achieving the best performance, boasting a prediction accuracy of up to 93%. The findings offer crucial guidance for forecasting remaining oil distribution and evaluating further exploration potential in the Niuxintuo oilfield. Moreover, this study provides valuable insights into the methodology and process of

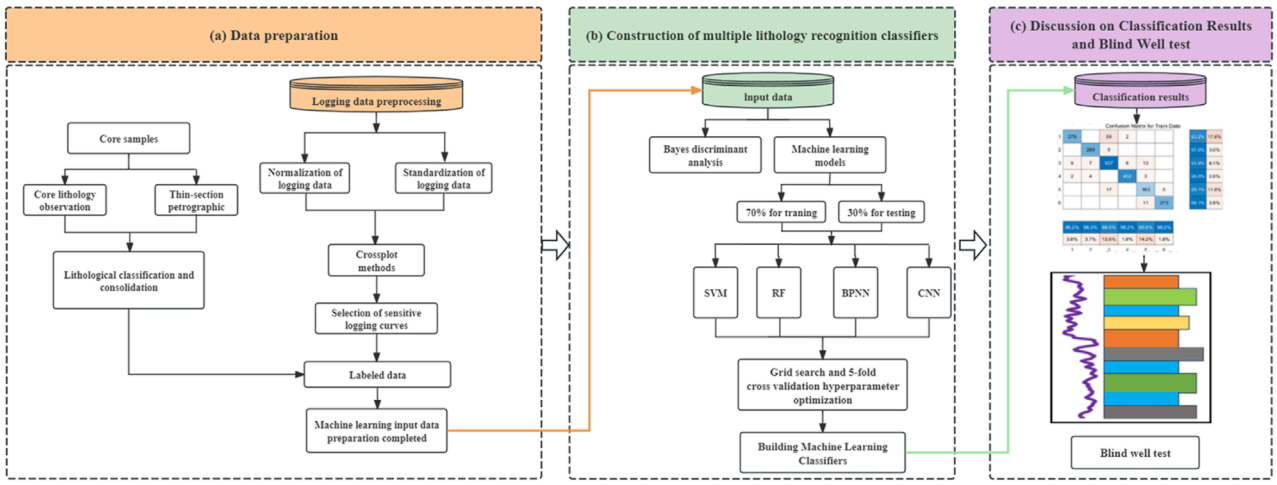

FIGURE 1
Lithology identification flowchart of this study. **(A)** Data preparation. **(B)** Construction of multiple lithology recognition classifiers. **(C)** Discussion on Classification Resultsand Blind Well test.

rapidly predicting hydrocarbon reservoir lithology using a large amount of logging data.

2 Methodology

This section provides a detailed overview of lithology identification methods, including core lithology observation and statistics, well logging data preprocessing, Bayes discriminant analysis, and four machine learning methods for lithology identification. The overall workflow is show in Figure 1.

2.1 Core lithology observation and statistics

The lithology types of Niuxintuo Oilfield are complex. Based on the detailed observation of core samples along with thin section data, the lithology types in the study area are summarized. Overall, the lithology of Niuxintuo reservoir can be divided into two categories: one is the alluvial fan type clastic rock composed of fine sandstone, siltstone, medium sandstone, coarse sandstone, and gravel rock; The other type is laminated dolomite and muddy dolomite with transitional fan edge lake facies (Figures 2, 3).

Furthermore, through the observation of cast thin sections and analysis of mineral composition, genetic processes, compositional content, and sedimentary structures, the lithology has been further subdivided into 19 fundamental rock types (Table 1).

Cross plot is the most commonly used method for displaying the relationships between variables and is widely used in reservoir research (Ehsan and Gu, 2020). It can display different logging data on the same plane and evaluate the relationships between these data through the position and shape of the intersection points. Accurate lithology identification and characterization require first understanding the physical property differences among various rock types, followed by selecting suitable logging parameters for quantitative differentiation.

Using the preprocessed logging sequences and core lithology labels, a cross-plot analysis was conducted to identify lithology-sensitive logging curves (Figure 4). Considering lithology sensitivity, data quality reliability, and curve complementarity, AC, CNL, DEN, GR, RT, and CON_CAL were selected as lithology-sensitive curves for subsequent research on logging-based lithology identification.

Figures 4A, B illustrates that the AC-CNL and AC-DEN cross-plots exhibit strong lithological differentiation, whereas the RT-GR and DEN-CON_CAL cross-plots yield moderate results (Figures 4C, D). In contrast, the CNL-DEN and GR-AC cross-plots demonstrate the least effectiveness (Figures 4E, F). Figure 5 indicates that dolomite has a higher GR value and slightly larger neutron response, making it easy to distinguish. The characteristics of mudstone are high GR value, low RT value, high AC value, and low density, with high discrimination. The GR value of fine siltstone shows a medium to low value, with a slightly higher neutron response. The GR value of sandy conglomerate shows a medium to low value, while the CNL value is small.

2.2 Standardization of logging data

Logging sequence data preprocessing provides near-wellbore stratigraphic information, which can be used to identify changes in stratigraphic interfaces, lithology, and sedimentary environments. However, in practical work, due to measurement errors, noise and outliers, depth migration or missing data, directly using raw logging data for lithology inversion may lead to data mismatch, lack of spatial constraints, low signal-to-noise ratio, and parameter mismatch, which will inevitably affect the accuracy of inversion results (Zheng et al., 2022). Therefore, preprocessing logging curves can improve data quality and availability, eliminate

FIGURE 2
Typical core photographs for different lithologies of Niuxintuo reservoir. **(A)** Tuo22,1693.72 m, fine sandstone; **(B)** Tuo 32–34, 1713.56 m, medium sandstone; **(C)** Tuoguan 2, 1790.08 m, coarse sandstone; **(D)** Tuo 22, 1707.66 m, gravel rock; **(E)** Tuo 31–39, 1860.71 m, argillaceous limestone; **(F)** Tuo 25–33, 2,328.86 m, silty mudstone; **(G)** Tuo 32–34, 1745.69 m, argillaceous dolomite; **(H)** Tuo 12, 2,103.66 dolomite; **(I)** Tuo 32–34, 1748.77 m, dolomitic mudstone.

the influence of non-geological factors, and truly reflect stratigraphic characteristics.

The Niuxintuo Oilfield in Liaohe has a long history of development. Over the course of extensive exploration and production activities, systematic errors have emerged in the logging data due to ongoing updates and changes in logging instruments. If the original logging sequence data is directly used for reservoir description, it will affect the accuracy and reliability of the results. Therefore, standardizing logging data can help eliminate systematic errors and enhance the ability to describe, interpret, and predict reservoirs (Zheng et al., 2022).

The key to standardizing logging data is the selection of standard layers, usually selecting mudstones or coal seams with a certain thickness that are stably developed throughout the area. There is a total of seven sets of oil bearing formations in the Niuxintuo oil reservoir. Using GES (Geological Evaluation System) software, the AC, CNL, DEN, GR, RT, and CON_CAL logging curves were standardized in batches.

2.3 Bayes discriminant analysis

Discriminant analysis is a statistical learning method used to establish one or more discriminant functions and assign sample points to different categories (Cui et al., 2023). The goal is to identify features or variables that can distinguish different categories to the greatest extent by analyzing training samples of known categories, and use these features or variables to construct discriminant functions to classify unknown samples.

2.4 Random forest

RF uses Bagging to construct multiple training datasets through self-sampling, and then constructs a base classifier for each sample set, which can improve the overall performance and robustness of the model (Breiman, 2001). Evaluate the contribution of each feature to the model's predictive performance during classification

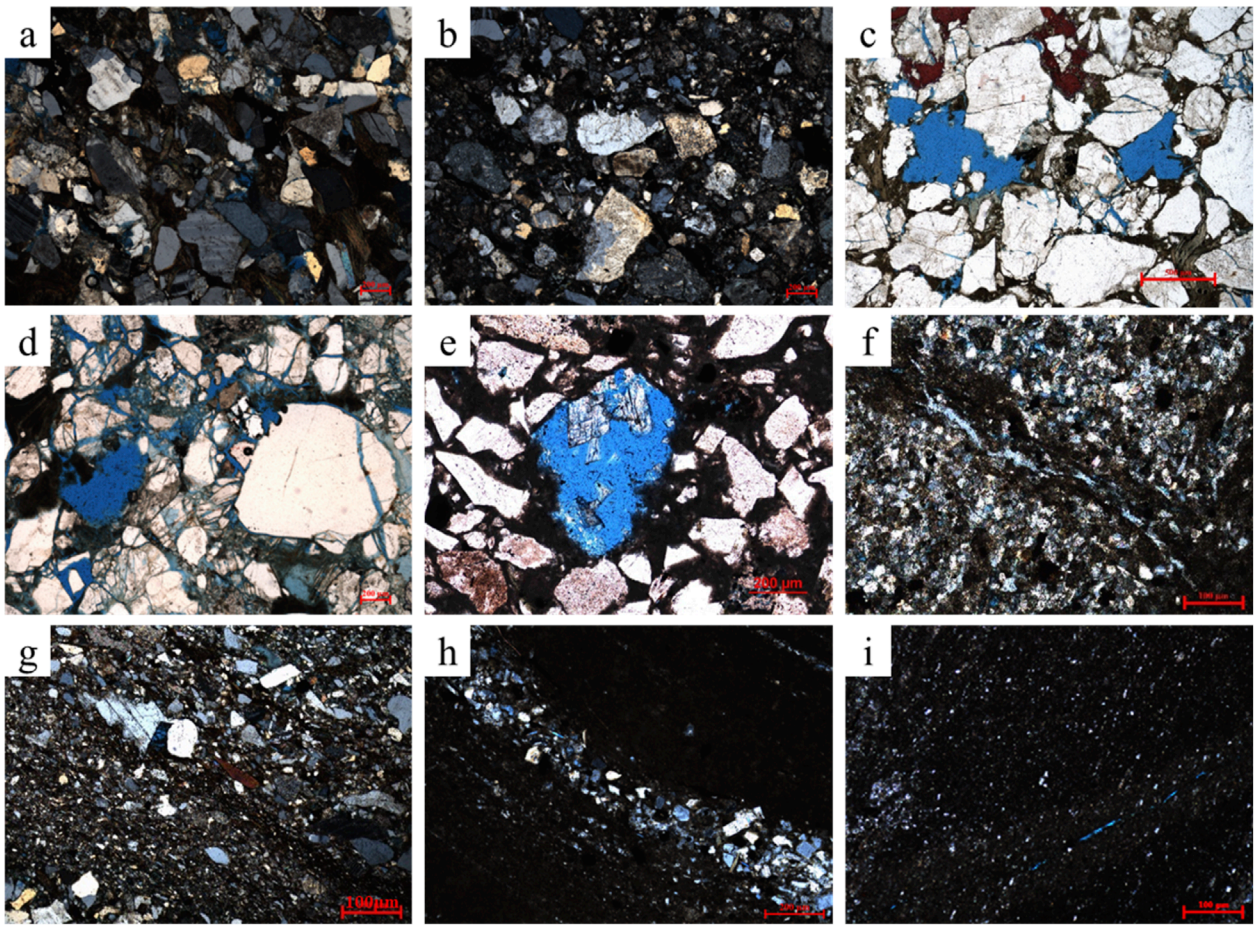

FIGURE 3
Casting thin section of different lithologies. **(A)** Tuo 31–39, 1,690.28 m, fine sandstone; **(B)** Tuo 25–33, 2,396.43 m, gravelly fine sandstone; **(C)** Tuo 31–39, 1785.74 m, medium sandstone; **(D)** Tuo 14, 1,557.87 m, coarse sandstone; **(E)** Tuo 25–33, 2,324.63 m, conglomerate; **(F)** Tuo 25–33, 2,321.46 m, silty mudstone; **(G)** Tuo 31–39, 1719.58 m, fine sand mixed with mudstone; **(H)** Tuo 12, 1,663.19 m, dolomite; **(I)** Tuo 32–34, 1745.6 m, muddy dolomite.

TABLE 1 Lithology types of the niuxintuo oil reservoir.

Basic rock types from cores		Classification of logging lithology
Clastic rock	Unequal-grained sandstone, conglomerate	Conglomerate
	Coarse sandstone, pebbly coarse sandstone	Medium-coarse sandstone
	Medium sandstone, pebbly medium sandstone	
	Fine sandstone, pebbly fine sandstone, and dolomitic fine sandstone	Fine sandstone
	Mudstone	Mudstone
Transitional rocks	Mudstone with gravel, silty mudstone, and dolomitic mudstone	Transitional rocks
	Siltstone, pebbly siltstone, argillaceous siltstone	
Carbonate	Dolomite	Dolomite
	Argillaceous dolomite	

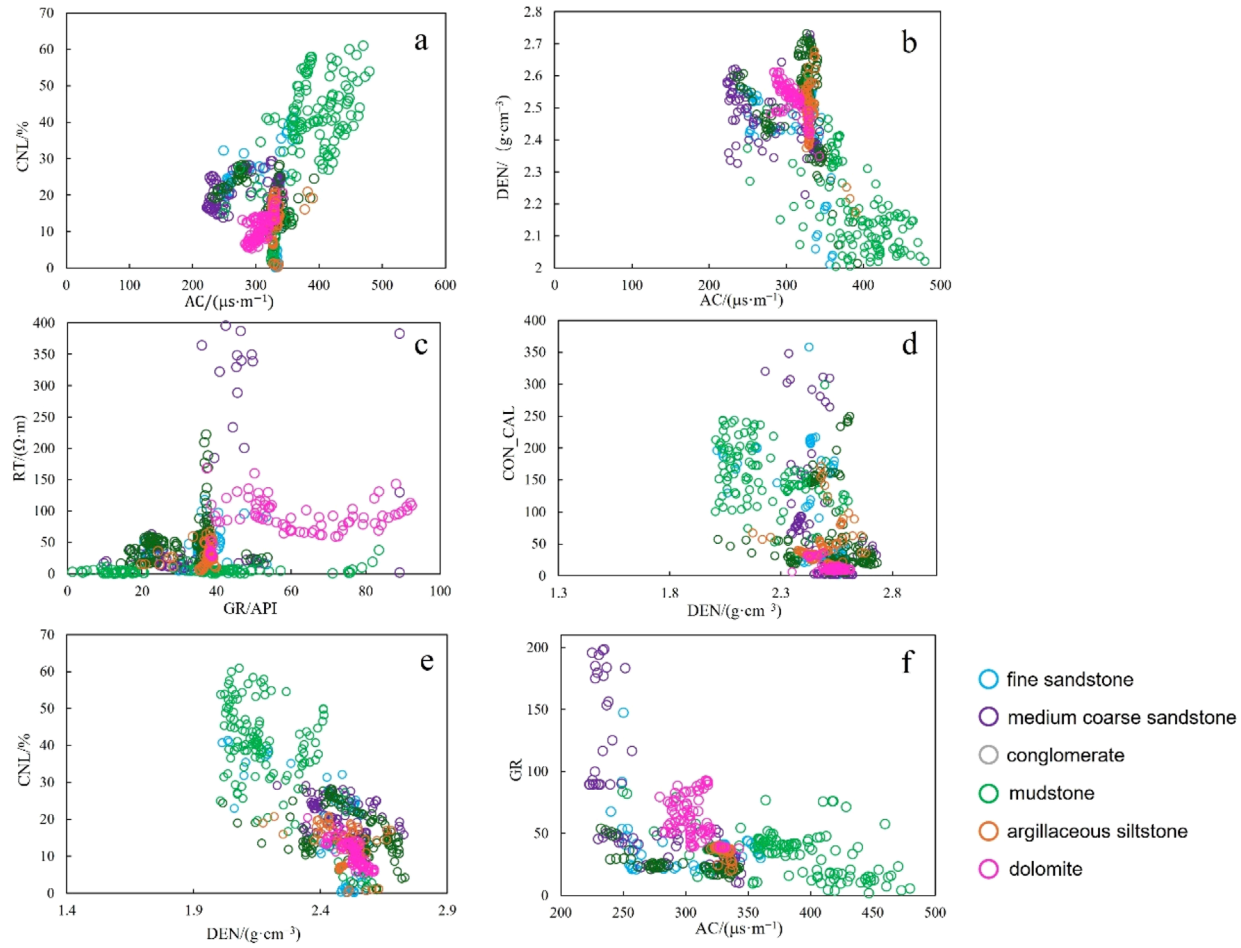

FIGURE 4
Well logging cross plots of different lithologies. **(A)** AC-CNL cross plot; **(B)** AC-DEN cross plot; **(C)** DEN-CON_CAL cross plot; **(D)** DEN-CNL cross plot; **(E)** GR-RT cross plot; **(F)** AC-GR cross plot.

by calculating the information gain rate of variables. This approach quantifies the importance of each feature parameter, allowing for the selection of variables with higher information gain rates. By focusing on these key variables, the modeling process becomes more streamlined, the influence of redundant features is minimized, and both the model's performance and its generalization capability are enhanced.

2.5 Support vector machine

SVM is a binary classification model. The basic principle is to construct a hyperplane with maximum spacing in a specific space to achieve correct partitioning of samples of different categories (Wang et al., 2014). For a given training dataset, multiple hyperplanes may satisfy the separation conditions. However, the objective of SVM is to identify the unique hyperplane that maximizes the margin, ensuring the greatest possible separation between classes. Lithology recognition belongs to multi classification problems. For multi classification problems, SVM can adopt one to many (One vs. Rest) or one to one (One vs. One) classification strategies (Wang et al., 2014). In the one-to-many method, each category is combined with other categories to construct multiple binary classification models for classification. In the one-on-one method, a binary classification model is constructed for each pair of categories, and the final result is determined as the category with the highest number of votes through voting or other strategies. Whether it is a binary classification problem or a multi classification problem, SVM can solve it and exhibits good performance in handling high-dimensional data and nonlinear problems.

2.6 Back propagation neural network

BPNN is a multi-layer feedforward neural network trained according to the error backpropagation algorithm (Rumelhart et al., 1986). The learning rule involves using the steepest descent method to iteratively adjust the network's weights and thresholds through backpropagation, aiming to minimize the network's total squared error (Dong et al., 2023; Wang and Wang, 2021). The neural network consists of three parts: input layer, hidden layer, and

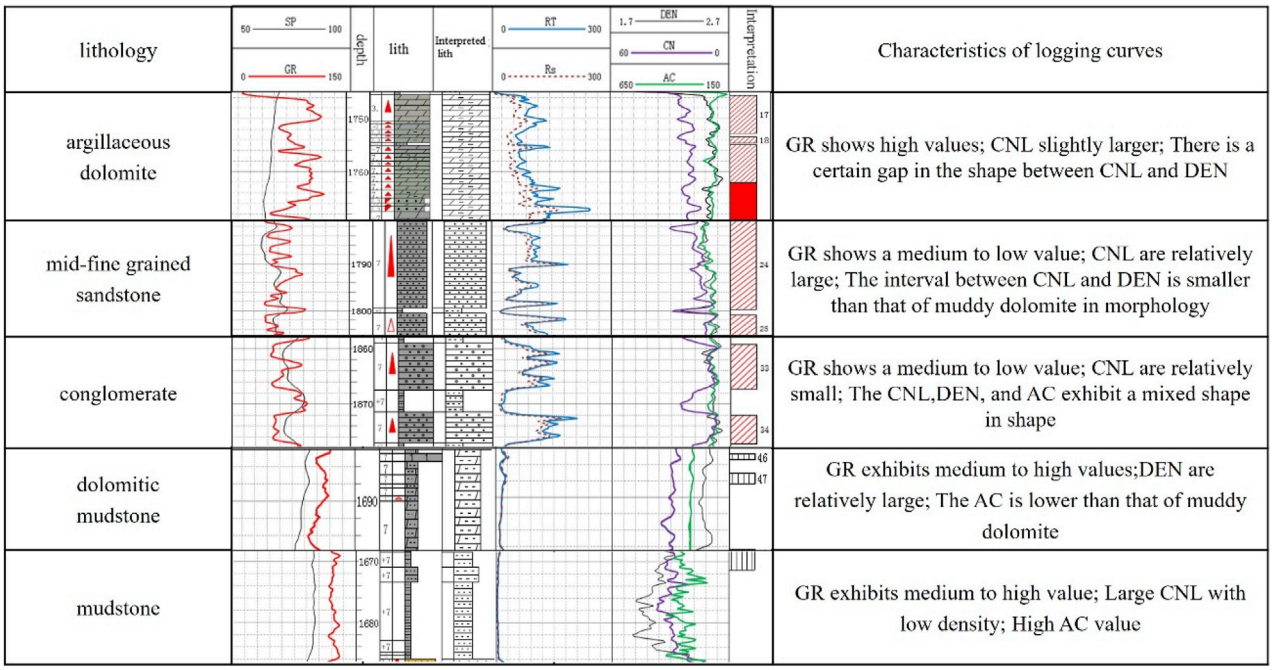

FIGURE 5
Logging response characteristics of different lithologies.

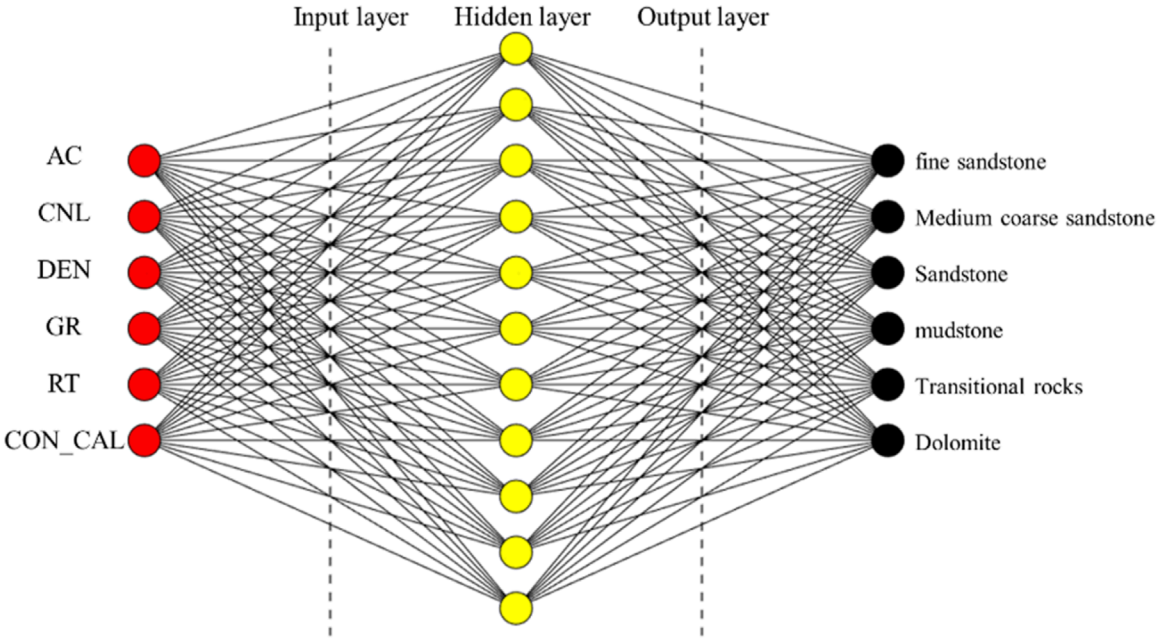

FIGURE 6
Basic architecture of a BP neural network.

output layer. The main process of BP neural networks is divided into two stages, namely, signal forward propagation and error back propagation. Signal forward propagation refers to the process of transmitting information from the input layer through the hidden layer to the output layer. In contrast, error backpropagation involves transmitting the error from the output layer to the input layer, sequentially adjusting the weights and biases of the hidden-to-output and input-to-hidden layers (Dong et al., 2023; Peng et al., 2024). The main factors affecting the performance of BP neural networks include the number of hidden layer nodes, the

TABLE 2 Bayesian discriminant analysis equation coefficients for different lithologies.

Logging curve	Fine sandstone	Medium coarse sandstone	Conglomerate	Mudstone	Transitional rocks	Dolomite
AC	1.048	1.050	1.065	1.126	1.078	1.065
CNL	2.038	2.129	2.055	2.224	2.051	2.027
DEN	304.246	308.284	311.549	304.854	310.230	307.489
GR	0.154	0.179	0.141	0.198	0.174	0.206
RT	0.126	0.138	0.127	0.128	0.121	0.123
CON_CAL	0.053	0.056	0.053	0.057	0.052	0.051
(constant)	−560.977	−576.291	−584.414	−596.900	−586.249	−576.476

TABLE 3 Lithology classification result matrix.

Lithology	1	2	3	4	5	6	Total
1	95.0	28.0	54.0	43.0	152.0	0.0	372.0
2	88	200	29	0	73	18	408
3	197	6	313	7	292	0	815
4	12	12	8	546	61	16	655
5	22	0	38	4	294	0	358
6	15	2	30	0	58	314	419

Note: 1-fine sandstone; 2-Medium coarse sandstone; 3-Sandstone; 4-mudstone; 5-Transitional rocks; 6-Dolomite.

TABLE 4 Lithology distribution of core samples in the study area.

Lithology	Number of samples
Fine sandstone	372
Medium coarse sandstone	408
Conglomerate	815
Mudstone	655
Transitional rocks	358
Dolomite	419
Total	3,027

selection of activation functions, and the parameter setting of learning rates.

Based on the preprocessing of logging data, we analyze the factors influencing lithology and select the preferred logging response parameters—AC, CNL, DEN, GR, RT, and CON_CAL—as input features for the model. This means the input layer consists of six neurons. The initial number of neurons in the hidden layer is set to 1–2 times the number of input neurons. The optimal number of hidden layer neurons is then determined automatically during the learning process through network structure optimization. The output layer consists of six types of lithology, that is, the number of output layer nodes is six. Basic architecture of a BPNN model is shown in Figure 6.

2.7 Convolutional neural networks

CNN are an important type of artificial neural network, but they are independent of traditional neural networks such as multi-layer perceptual neural networks, RBF neural networks, and fuzzy logic neural networks (Zhong et al., 2019). CNN consists of five layers: data input layer, convolutional computing layer, ReLU excitation layer, pooling layer, and fully connected layer. CNN combines three steps to achieve pattern recognition, including local acceptance domain, weight sharing, and under sampling. The local receptive field refers to the set of units within each layer of the neural network that are connected to the previous layer. Each neuron in this small neighborhood extracts fundamental visual features, such as line segments, endpoints, and angles, from the input data. Weight sharing refers to CNN sharing the weights of some neurons; Therefore, fewer parameters are optimized during the training process. Under sampling can reduce the feature resolution of displacement, amplification, and other forms of distortion invariance (Le and Borji, 2017; Zhong et al., 2019).

3 Results and discussion

3.1 Lithological classification based on bayes discriminant analysis

Binary classification problems are typically addressed using the Fisher criterion, while the Bayes criterion is commonly employed for multi-class classification problems. To tackle the lithology identification of clastic rocks using well logging data, this study

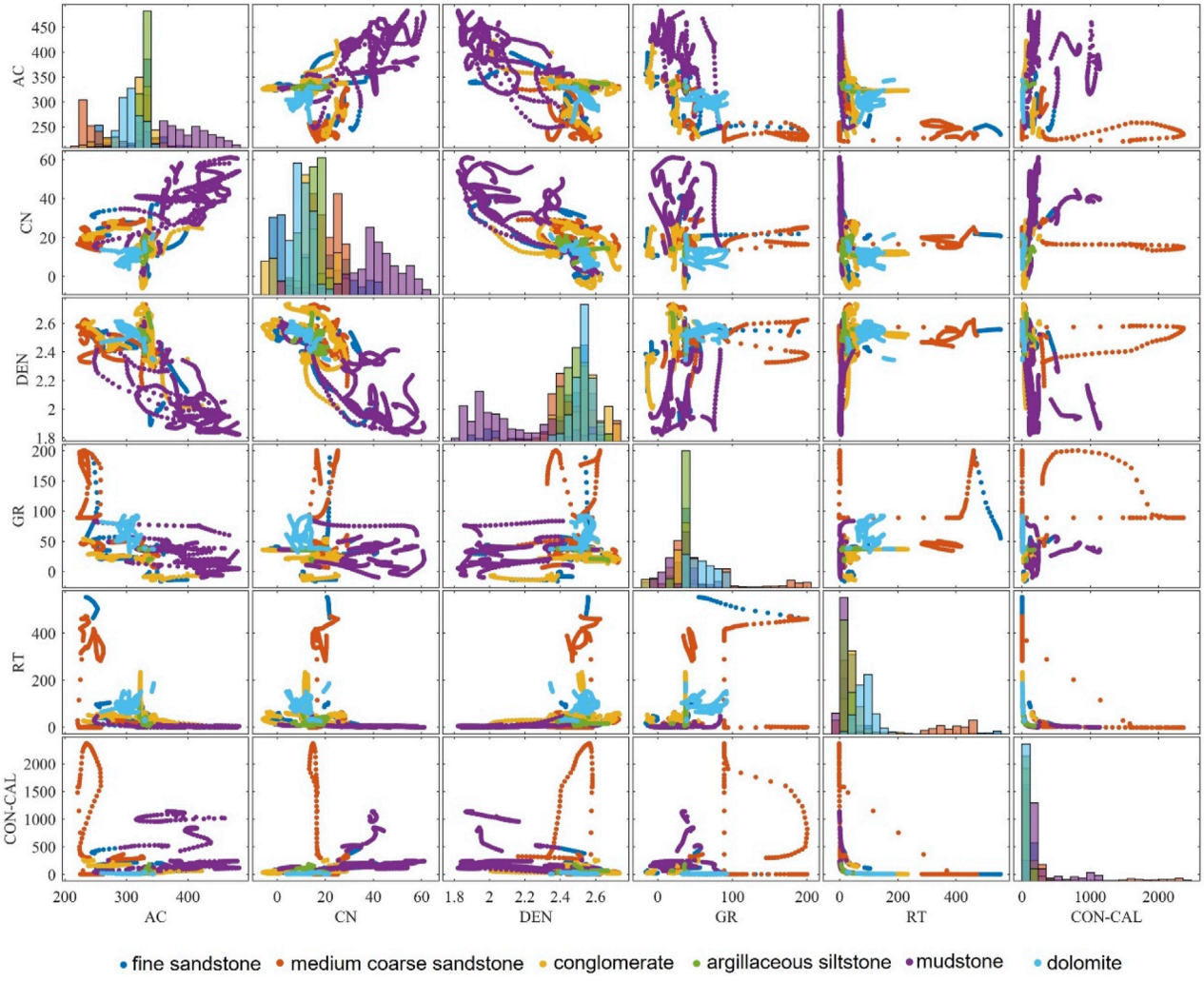

FIGURE 7
Correlation matrix of different lithology and logging parameters.

TABLE 5 Optimum parameter values for each model.

Classifier	Optimal hyperparameter
RF	cv folds = 5; criterion = "gini"; max depth = 29; min leaf size = 1; min parent = 13; num trees = 70
SVM	cv folds = 5; kernel = 'RBF'; C = 32; gamma = 32
BPNN	hidden layer size range = 16; epochs range = 1,000; goal range = 1e-2 learning rate range = 0.01
CNN	training options = "adam"'; max epochs = 200; initial learn rate = 1e-3 L2regularization = 1e-04; learn rate drop factor = 0.5; learn rate drop period = 150

develops a discriminant function based on the Bayes criterion. Substitute the logging curve data values for each lithology sample into the following six Bayes discriminant functions to calculate the corresponding function values. Comparing the values of these six functions, which function has the highest value can determine which category the sample is classified into. The coefficients of the Bayesian discriminant function are shown below (Table 2).

According to the Bayes discriminant coefficient table, the Bayes discriminant function can be listed as follows (Equations 1–6):

$$\begin{aligned}\text{Fine sandstone} = &-560.977 + 1.048 \times \text{AC} + 2.038 \times \text{CNL} + 304.246 \\ &\times \text{DEN} + 0.154 \times \text{GR} + 0.126 \times \text{RT} + 0.053 \\ &\times \text{CON\_CAL}\end{aligned} \tag{1}$$

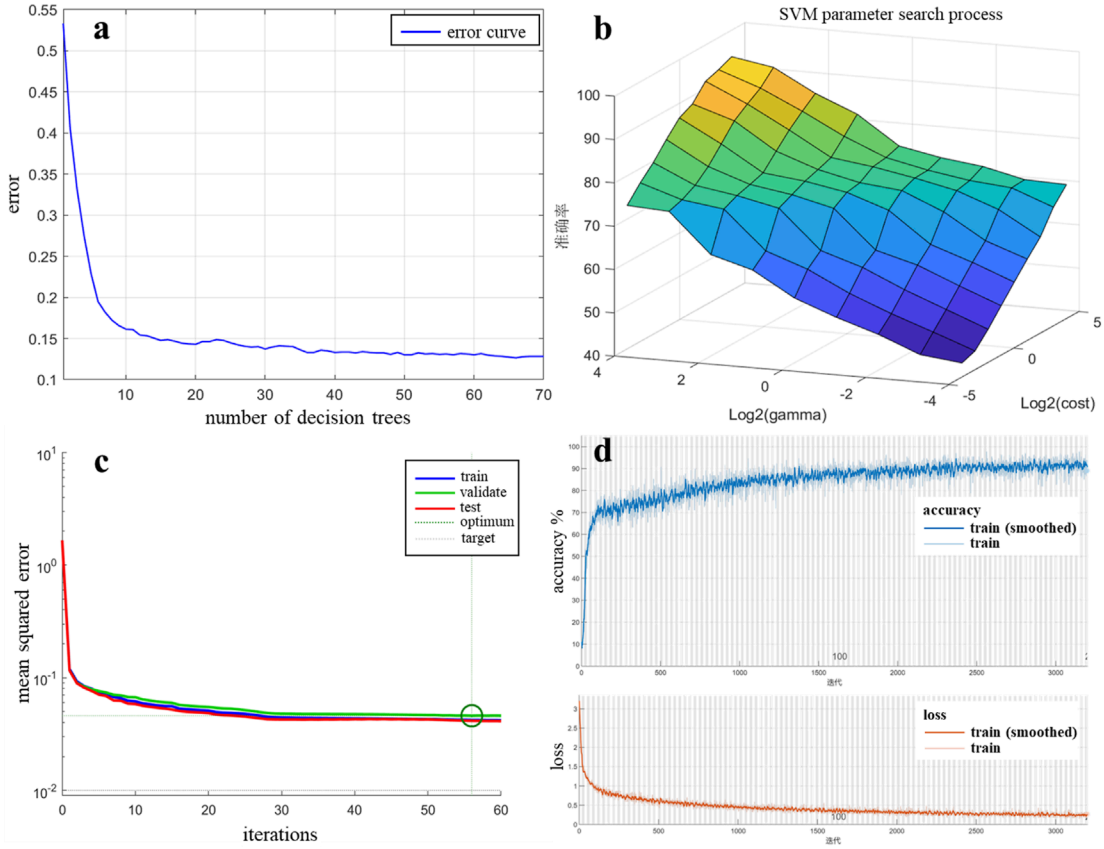

FIGURE 8
Machine learning algorithms partially hyperparameter optimization. **(A)** RF decision tree optimization; **(B)** SVM hyperparameter optimization; **(C)** BPNN mean square error; **(D)** CNN Training Progress.

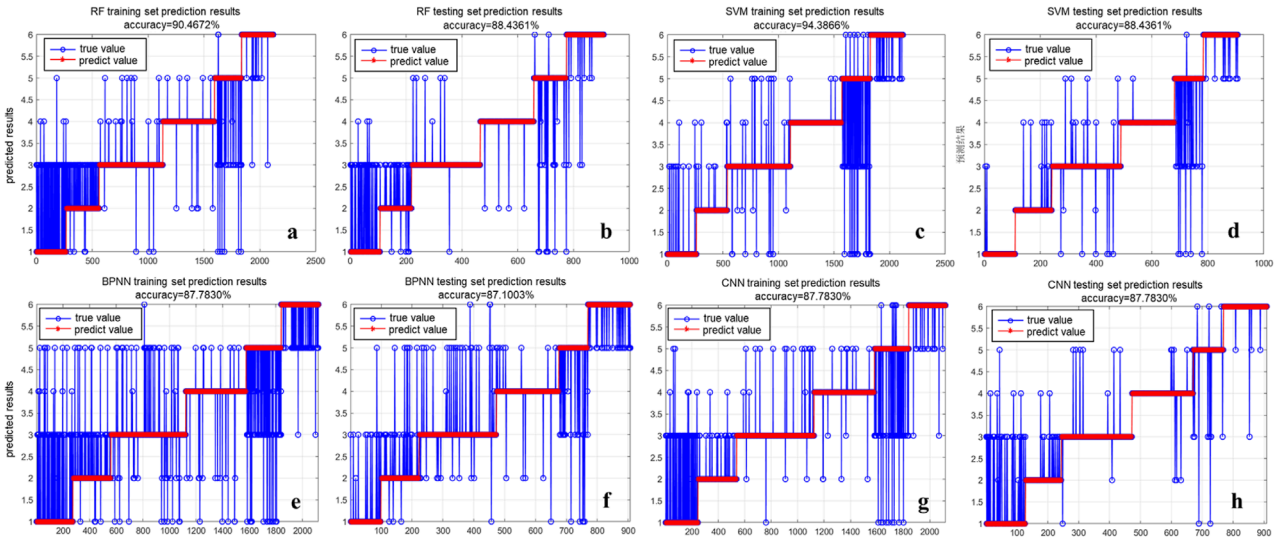

FIGURE 9
Prediction results of each machine learning classifier. **(A)** RF training set test results; **(B)** RF testing set test results; **(C)** SVM training set test results; **(D)** SVM testing set test results; **(E)** BPNN training set test results; **(F)** BPNN testing set test results; **(G)** CNN training set test results; **(H)** CNN testing set test results.

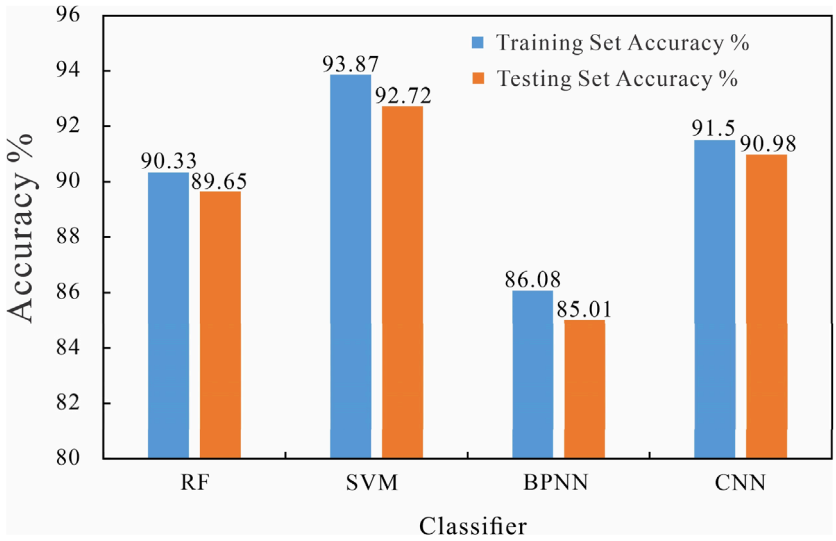

FIGURE 10
Comparison of prediction accuracy of four machine learning models.

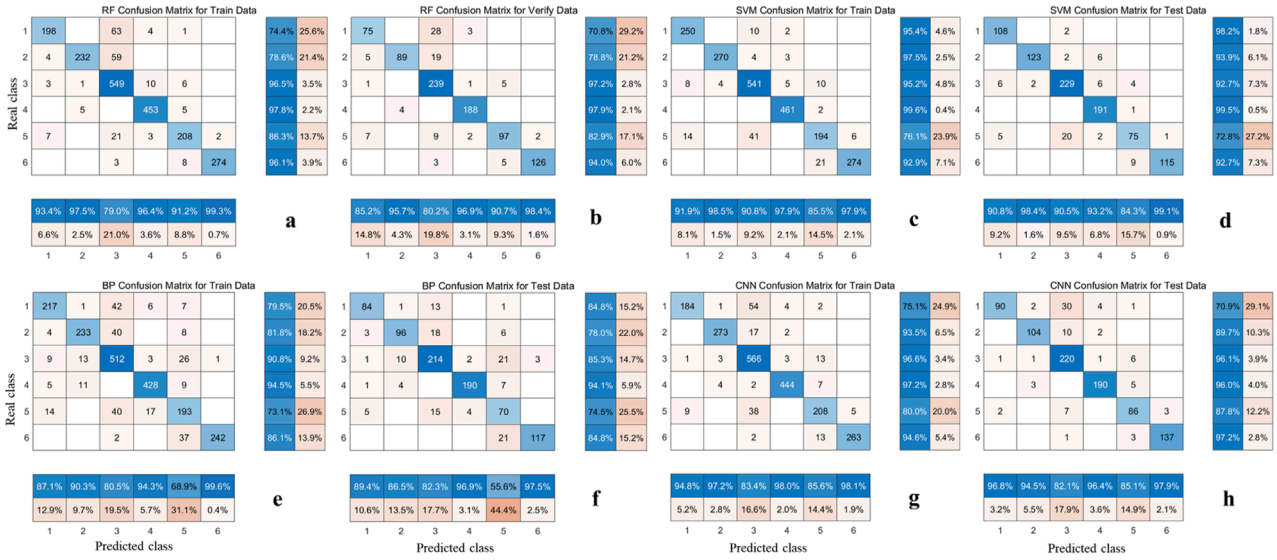

FIGURE 11
Confusion matrix of each machine learning classifier. **(A)** RF training set confusion matrix; **(B)** RF testing set confusion matrix; **(C)** SVM training set confusion matrix; **(D)** SVM testing set confusion matrix; **(E)** BPNN training set confusion matrix; **(F)** BPNN testing set confusion matrix; **(G)** CNN training set confusion matrix; **(H)** CNN testing set confusion matrix.

$$\text{Medium coarse sandstone} = -576.291 + 1.050 \times \text{AC} + 2.129 \times \text{CNL} + 308.284 \times \text{DEN} + 0.179 \times \text{GR} + 0.138 \times \text{RT} + 0.056 \times \text{CO}N\_CAL \quad (2)$$

$$\text{Conglomerate} = -584.414 + 1.065 \times \text{AC} + 2.055 \times \text{CNL} + 311.549 \times \text{DEN} + 0.141 \times \text{GR} + 0.127 \times \text{RT} + 0.053 \times \text{CO}N\_CAL \quad (3)$$

$$\text{Mudstone} = -596.900 + 1.126 \times \text{AC} + 2.224 \times \text{CNL} + 304.854 \times \text{DEN} + 0.198 \times \text{GR} + 0.128 \times \text{RT} + 0.057 \times \text{CON\_CAL} \quad (4)$$

$$\text{Transitional rocks} = -586.249 + 1.078 \times \text{AC} + 2.051 \times \text{CNL} + 310.230 \times \text{DEN} + 0.174 \times \text{GR} + 0.121 \times \text{RT} + 0.052 \times \text{CON\_CAL} \quad (5)$$

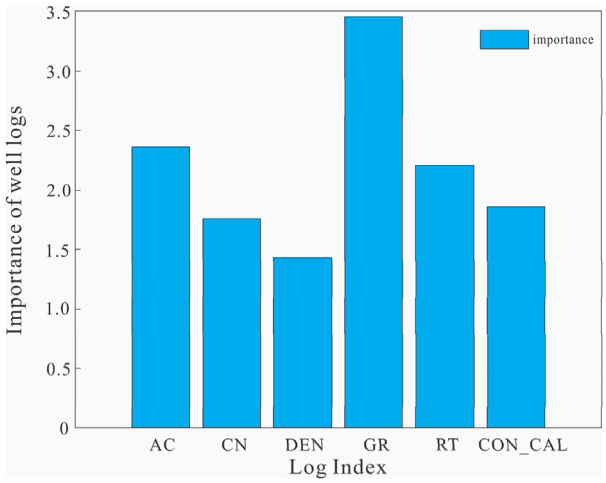

FIGURE 12
Analysis of the importance of logging parameters in RF classifier.

$$\begin{aligned}\text{Dolomite} = &-576.476 + 1.065 \times \text{AC} + 2.027 \times \text{CNL} + 307.489 \\ &\times \text{DEN} + 0.206 \times \text{GR} + 0.123 \times \text{RT} + 0.05 \\ &\times \text{CON\_CAL}\end{aligned} \tag{6}$$

As shown in Table 3, the discriminant coincidence rate was determined by comparing the classification results obtained by substituting the observed lithology values into the discriminant function with the original classifications. The lithology codes are indicated in Table 3 footnote. In this case, the accuracy is 58.2%, indicating that the discriminant analysis method demonstrates limited accuracy in identifying lithology within this study area. The limitations of Bayesian discriminant analysis in lithology identification primarily arise from the following factors. First, the algorithm's underlying assumptions pose significant challenges: it presumes that the data conforms to a specific probability distribution, typically a normal distribution for different categories. However, real-world lithological data often deviates from this assumption, leading to inaccurate classification outcomes. Additionally, the method assumes that all features are independent, a condition rarely met in practice. In lithological datasets, features frequently exhibit interdependencies, and ignoring these correlations can diminish the model's accuracy. Furthermore, Bayesian discriminant analysis struggles with handling the inherent complexity of lithological data, limiting its effectiveness in more intricate classification tasks. When addressing complex lithological types, Bayesian discriminant analysis often fails to capture underlying nonlinear relationships, resulting in suboptimal performance under intricate geological conditions.

3.2 Machine learning methods for lithology recognition

3.2.1 Data preparation

This study used 3,027 sets of logging and core data from 8 core wells in the study area, with 70% of the data for training and 30% for testing. These two datasets each have different functions. The training set is used to create machine learning models and model hyperparameter optimization, while the testing set is used to evaluate the performance of trained machine learning model. The lithological labels of 1–6 correspond to six main lithologies: fine sandstone, medium to coarse sandstone, conglomerate, mudstone, transitional rocks, and dolomite (Table 4).

The following six conventional logging parameters—AC, CNL, DEN, GR, RT, and CON_CAL—are selected as sample attribute values. These parameters form a 7-dimensional vector, comprising six dimensions of parameter values and one dimension for the corresponding lithology label. In machine learning, feature normalization is often essential to eliminate dimensional differences, minimize feature biases, and mitigate the impact of outliers. Normalizing data not only accelerates the training model's convergence but also facilitates reaching the optimal solution more efficiently. The normalization of logging curves maps the values of the curves to (0,1) through linear transformation. The definition is defined as Equation 7:

$$x^* = \frac{x - x_{min}}{x_{max} - x_{min}} \tag{7}$$

Among them, x_{max} and x_{min} represents the maximum and minimum values in the set of curve values, respectively. Through this processing method, the normalized logging data values will fall within the [0,1] interval, making it easier to compare and analyze.

Exploratory data analysis is performed by creating correlation matrix diagrams to visualize the relationships between different lithologies and logging parameters. Figure 7 presents the correlation matrix diagram illustrating the relationships between various lithologies and logging parameters. The horizontal and vertical axes correspond to six logging parameters, while the diagonal showcases the distribution histograms of different lithologies associated with the parameters on the horizontal axis. Different colors represent various lithologies, and the significant overlap among most logging parameters indicates a lack of clear boundaries, making model classification challenging.

3.2.2 Model parameter optimization

To obtain the optimal machine learning model, grid search and 5-fold cross validation methods were used to optimize the hyperparameters of RF, SVM, BPNN, and CNN models (Table 5). The optimization process for the key parameters is illustrated in Figure 8, while unmentioned parameters are set to default values to enhance the model's accuracy. 5-fold cross-validation provides a reliable estimate of model performance, helps identify optimal parameter settings, and mitigates the risks of overfitting or underfitting. It is widely used for evaluating models and selecting the best parameters, making it suitable for a variety of datasets. The main step of 5-fold cross-validation involves randomly splitting the dataset into five equal parts. Each time, one part is used as the test set, while the remaining four parts serve as the training set. This process is repeated for each part. The optimal parameter combination is then selected based on the highest cross-validation score from the candidate set. After parameter tuning, we optimized the classifier parameters to achieve the best combination (Table 5).

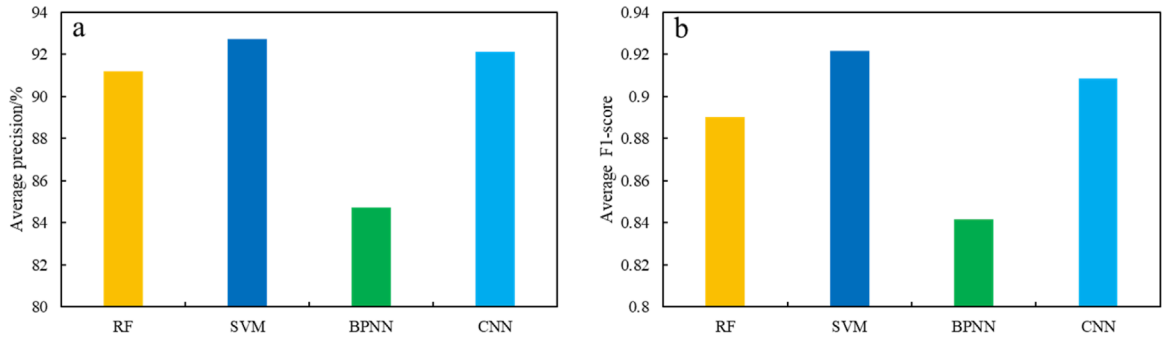

FIGURE 13
Comparison of lithology identification results of different models. **(A)** Average prediction accuracy of different models; **(B)** Average F1-score for different models.

TABLE 6 F1-Score for different lithologies using different models.

Lithology	RF	SVM	BPNN	CNN
Fine sandstone	0.77	0.94	0.87	0.82
Medium coarse sandstone	0.86	0.96	0.82	0.92
Conglomerate	0.88	0.92	0.84	0.89
Mudstone	0.97	0.96	0.95	0.96
Transitional rocks	0.87	0.78	0.64	0.86
Dolomite	0.96	0.96	0.91	0.98

3.3 Comparison of four machine learning lithology methods

3.3.1 Evaluation criterion

The performance of the classification models is evaluated using indicators such as accuracy, precision, recall, and F1-score (Zheng et al., 2022) (Equations 8–11). Accuracy represents the proportion of correct predictions (both positive and negative) out of all predictions. Precision measures the proportion of true positives among the samples predicted as positive. Recall refers to the proportion of correct positive samples among the total actual positives. F1 score is the harmonic average of recall rate and precision rate, which considers the accuracy of the model in predicting positive samples (recall rate) and its recognition ability for positive samples (recall rate). These standard calculation formulas are as follows:

$$\text{Accuracy} = \frac{TP + TN}{TP + \text{TN} + FP + FN} \tag{8}$$

$$\text{Precision} = \frac{TP}{TP + \text{FP}} \tag{9}$$

$$\text{Recall} = \frac{TP}{TP + \text{FN}} \tag{10}$$

$$F1 - score = 2 \cdot \frac{Precision \times Recall}{Precision + Recall} \tag{11}$$

TP refers to the cases where both the prediction and the actual value are positive. FP refers to the cases where the prediction is positive but the actual value is negative. FN refers to the cases where the prediction is negative but the actual value is positive. TN refers to the cases where both the prediction and the actual value are negative.

3.3.2 Analysis of single point prediction results

After building each machine learning model, the performance of the models is validated and tested. The results are then compared across the four classifiers to evaluate their relative effectiveness (Figure 9). Figure 10 shows the comparison of prediction accuracy results among different models. Among them, SVM has the best classification performance, with a prediction accuracy of 93.87% in the training set and 92.72% in the test set. CNN took second place, with a prediction accuracy of 91.50% for the training set and 90.98% for the test set. The prediction accuracy of the RF training set is 90.33%, and the prediction accuracy of the test set is 89.65%. BPNN has the lowest accuracy, with a prediction accuracy of 86.08% for the training set and 85.01% for the test set. From the above, each machine learning classifier constructed has a high prediction accuracy, with an accuracy rate above 85%. SVM has the best classification performance, with a prediction accuracy rate of up to 93%. The confusion matrices (Figure 11) reveal the misclassification patterns of lithology classes for each model, emphasizing which classes are mistakenly predicted as others. In addition, RF can be used to explain the importance of different parameters in various classification and regression models for model prediction results. The importance ranking of logging parameters for lithology identification based on RF is: GR, AC, RT, CON_ CAL, CNL, DEN (Figure 12).

The comparison of average precision (Figure 13A) and average F1-score results (Figure 13B) for different models. It can be observed that the BPNN model has the lowest average precision (84.7%) and F1-score (0.84). The RF model ranks second, with an average precision of 91.2% and an F1-score of 0.89. The CNN model achieves a relatively high average accuracy of 92.1%, with an F1-score of 0.91. The SVM model delivers the highest performance, with an average precision of 92.7% and an F1-score of 0.92. In summary, SVM has the best lithology recognition performance,

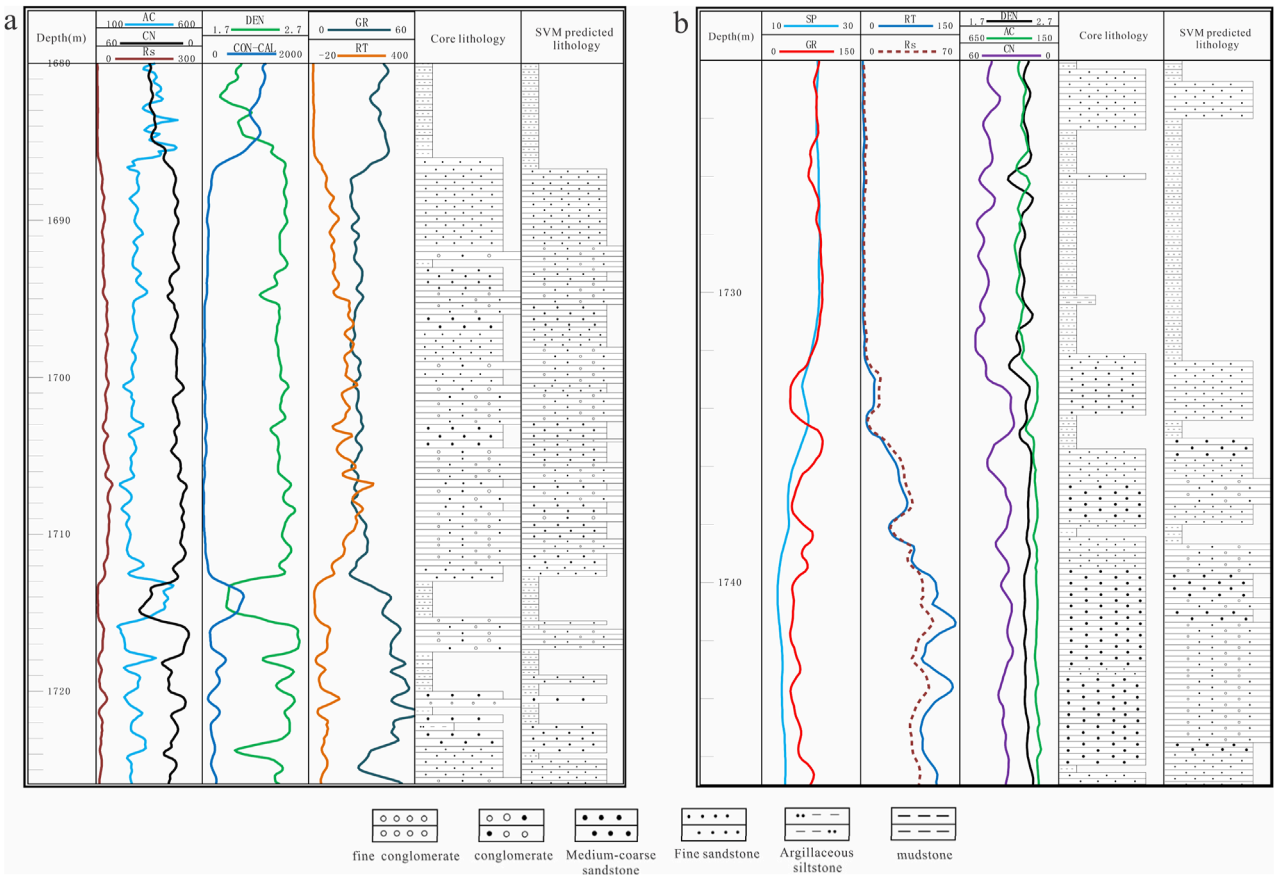

FIGURE 14
Comparison of core lithology and predicted lithology using well trained SVM classifier. **(A)** Tuo 31–39 well; **(B)** Tuo 35–33 well.

followed by CNN, with both F1-score higher than 0.9, superior to RF and BPNN.

As shown in Table 6, each model demonstrates varying recognition capabilities for different lithology types. SVM showed the highest average F1-score, reaching 0.92. Among them, except for transitional rocks, the F1-score of all other lithologies exceeds 0.92, and the transitional rocks are mainly divided into fine sandstone and medium to coarse sandstone. This could be attributed to the fact that the siltstone class is a non-reservoir in the study area, and the logging response characteristics of fine sandstone and siltstone are quite similar. When classifying lithology, they are classified as transitional rocks, resulting in the lowest prediction accuracy of other models in transitional rocks. The F1-score of CNN and RF is second to SVM, with a high F1-score of 0.96 for both mudstone and dolomite, and the classification of lithology types is relatively similar. The main classification is that fine sandstone and medium to coarse sandstone are divided into conglomerate and transitional rocks are divided into sandy conglomerate and fine sandstone. BPNN also has a high F1-score of 0.91 for both mudstone and dolomite, and the lowest F1-score of 0.64 for transitional rocks. In summary, the SVM classifier demonstrates the best overall performance in lithology identification and is therefore used for lithology prediction in the study area.

3.3.3 Lithology prediction in the uncored well

We further validated the effectiveness of the SVM classifier in lithology identification using two blind wells (Figure 14). The results show a high consistency between the lithology predicted by the well-trained SVM model and the lithology observed in the cores, indicating that the well-trained SVM model provides reliable lithology predictions for uncored wells.

4 Conclusion

The main conclusions drawn in this article are as follows:

1. The cross-plot method is not effective in distinguishing lithology, but can help identify sensitive logging curves. The selected sensitive logging curves are: gamma ray (GR), acoustic transmit time (AC), resistivity (RT), conductivity (CON_CAL), compensated neutron (CNL), and density (DEN).
2. Except for Bayes discriminant analysis, all the constructed machine learning classifiers [i.e., Random Forest (RF), Support vector machine (SVM), Back propagation neural network (BPNN), and Convolutional neural networks (CNN)] demonstrate high prediction accuracy, with the accuracy rate exceeding 85%. Among them, SVM classification shows the best performance achieving a prediction accuracy as high as

93%. Blind well tests have confirmed the reliability of the well trained SVM model.

3. RF can be used to explain the importance of different parameters in various classification and regression models for model prediction results. The importance ranking of logging parameters for lithology identification in this study is: GR, AC, RT, CON_ CAL, CNL, DEN.

Data availability statement

The original contributions presented in the study are included in the article/supplementary material, further inquiries can be directed to the corresponding author.

Author contributions

ZF: Conceptualization, Investigation, Methodology, Resources, Writing–original draft, Writing–review and editing. CH: Methodology, Supervision, Writing–original draft. SJ: Methodology, Supervision, and Writing–original draft. ML: Data curation, Formal Analysis, Writing–original draft. YC: Resources, Validation, Writing–original draft. YJ: Investigation, Software, Writing–original draft. YL Data curation, Formal Analysis, Investigation, Writing–review and editing. MT: Investigation, Resources, Writing–original draft.

Funding

The author(s) declare that financial support was received for the research, authorship, and/or publication of this article. The authors declare that this study received funding from CNPC Science and Technology special Project "Research on Greatly Improved Oil recovery Technology in Ultra-high water cut period of medium and high permeability Oilfield" (number: 2023ZZ22). The funder was not involved in the study design, collection, analysis, interpretation of data, the writing of this article, or the decision to submit it for publication.

Conflict of interest

Authors ZF, CH, ML, YC, YJ, YL, and MT were employed by Petrochina Liaohe Oilfield Company.

The remaining author declares that the research was conducted in the absence of any commercial or financial relationships that could be construed as a potential conflict of interest.

Publisher's note

References

Amari, S. I. (1993). Backpropagation and stochastic gradient descent method. *Neurocomputing* 5 (4-5), 185–196. doi:10.1016/0925-2312(93)90006-O

Anifowose, F., Abdulraheem, A., and Al-Shuhail, A. (2019). A parametric study of machine learning techniques in petroleum reservoir permeability prediction by integrating seismic attributes and wireline data. *J. Petroleum Sci. Eng.* 176, 762–774. doi:10.1016/j.petrol.2019.01.110

Ashraf, U., Zhang, H., Anees, A., Mangi, H. N., Ali, M., Zhang, X., et al. (2021). A core logging, machine learning and geostatistical modeling interactive approach for subsurface imaging of lenticular geobodies in a clastic depositional system, SE Pakistan. *Nat. Resour. Res.* 30, 2807–2830. doi:10.1007/s11053-021-09849-x

Bhattacharya, S., Carr, T. R., and Pal, M. (2016). Comparison of supervised and unsupervised approaches for mudstone lithofacies classification: case studies from the Bakken and Mahantango-Marcellus Shale, USA. *J. Nat. Gas Sci. Eng.* 33, 1119–1133. doi:10.1016/j.jngse.2016.04.055

Biau, G., and Scornet, E. (2016). A random forest guided tour. *Test* 25, 197–227. doi:10.1007/s11749-016-0481-7

Breiman, L. (2001). Random forests. *Mach. Learn.* 45, 5–32. doi:10.1023/a:1010933404324

Bressan, T. S., de Souza, M. K., Girelli, T. J., and Junior, F. C. (2020). Evaluation of machine learning methods for lithology classification using geophysical data. *Comput. and Geosciences* 139, 104475. doi:10.1016/j.cageo.2020.104475

Chen, T., and Guestrin, C. (2016). "Xgboost: a scalable tree boosting system," in *Proceedings of the 22nd acm sigkdd international conference on knowledge discovery and data mining*.

Cohn, D. A., Ghahramani, Z., and Jordan, M. I. (1996). Active learning with statistical models. *J. Artif. Intell. Res.* 4, 129–145. doi:10.1613/jair.295

Cui, H., Deng, Y., Zhong, R., Li, W., Yu, C., Danyushevsky, L. V., et al. (2023). Determining the ore-forming processes of Dongshengmiao Zn-Pb-Cu deposit: evidence from the linear discriminant analysis of pyrite geochemistry. *Ore Geol. Rev.* 163, 105782. doi:10.1016/j.oregeorev.2023.105782

Delfiner, P., Peyret, O., and Serra, O. (1987). Automatic determination of lithology from well logs. *SPE Form. Eval.* 2 (03), 303–310. doi:10.2118/13290-PA

Dong, S., Wang, Z., and Zeng, L. (2016). Lithology identification using kernel Fisher discriminant analysis with well logs. *J. Petroleum Sci. Eng.* 143, 95–102. doi:10.1016/j.petrol.2016.02.017

Dong, S., Zeng, L., Du, X., He, J., and Sun, F. (2022). Lithofacies identification in carbonate reservoirs by multiple kernel Fisher discriminant analysis using conventional well logs: a case study in A oilfield, Zagros Basin, Iraq. *J. Petroleum Sci. Eng.* 210, 110081. doi:10.1016/j.petrol.2021.110081

Dong, Y., Ma, Z., Xu, F., Su, X., and Chen, F. (2023). Combining the back propagation neural network and particle swarm optimization algorithm for lithological mapping in North China. *Remote Sens.* 15 (17), 4134. doi:10.3390/rs15174134

Ehsan, M., and Gu, H. (2020). An integrated approach for the identification of lithofacies and clay mineralogy through Neuro-Fuzzy, cross plot, and statistical analyses, from well log data. *J. Earth Syst. Sci.* 129, 101–113. doi:10.1007/s12040-020-1365-5

Goodfellow, I., Bengio, Y., and Courville, A. (2016). *Deep learning*. The MIT Press.

Helm, H. S., Basu, A., Athreya, A., Park, Y., Vogelstein, J. T., Priebe, C. E., et al. (2023). Distance-based positive and unlabeled learning for ranking. *Pattern Recognit.* 134, 109085. doi:10.1016/j.patcog.2022.109085

Huang, X., Ye, Y., Xiong, L., Lau, R. Y., Jiang, N., and Wang, S. (2016). Time series k-means: a new k-means type smooth subspace clustering for time series data. *Inf. Sci.* 367, 1–13. doi:10.1016/j.ins.2016.05.040

Huang, Y., Liu, Y., Li, C., and Wang, C. (2019). GBRTVis: online analysis of gradient boosting regression tree. *J. Vis.* 22, 125–140. doi:10.1007/s12650-018-0514-2

Jordan, M. I., and Mitchell, T. M. (2015). Machine learning: trends, perspectives, and prospects. *Science* 349 (6245), 255–260. doi:10.1126/science.aaa8415

Kampffmeyer, M., Løkse, S., Bianchi, F. M., Jenssen, R., and Livi, L. (2018). The deep kernelized autoencoder. *Appl. Soft Comput.* 71, 816–825. doi:10.1016/j.asoc.2018.07.029

Le, H., and Borji, A. (2017). What are the receptive, effective receptive, and projective fields of neurons in convolutional neural networks? *arXiv Prepr. arXiv 1705.07049*. doi:10.48550/arXiv.1705.07049

Li, H. (2022). Research progress on evaluation methods and factors influencing shale brittleness: a review. *Energy Rep.* 8, 4344–4358. doi:10.1016/j.egyr.2022.03.120

Li, H., He, S., Radwand, A. E., Xie, J. T., and Qin, Q. R. (2024). Quantitative analysis of pore complexity in lacustrine organic-rich shale and comparison to marine shale: insights from experimental tests and fractal theory. *Energy Fuel* 38 (17), 16171–16188. doi:10.1021/acs.energyfuels.4c03095

Li, H., Zhou, J. L., Mou, X. Y., Guo, H. X., Wang, X. X., An, H. Y., et al. (2022). Pore structure and fractal characteristics of the marine shale of the Longmaxi Formation in the Changning area, southern Sichuan basin, China. *Front. Earth Sci.* 10, 1018274. doi:10.3389/feart.2022.1018274

Lin, J., Li, H., Liu, N., Gao, J., and Li, Z. (2020). Automatic lithology identification by applying LSTM to logging data: a case study in X tight rock reservoirs. *IEEE Geoscience Remote Sens. Lett.* 18 (8), 1361–1365. doi:10.1109/LGRS.2020.3001282

Madani, A., Arnaout, R., Mofrad, M., and Arnaout, R. (2018). Fast and accurate view classification of echocardiograms using deep learning. *NPJ Digit. Med.* 1 (1), 6. doi:10.1038/s41746-017-0013-1

McDowell, G. M., King, A., Lewis, R. E., Clayton, E. A., and Grau, J. A. (1998). "In-site nickel assay by prompt gamma neutron activation wireline logging," in *SEG Annual Meeting* (New Orleans, Louisiana: Society of Exploration Geophysicists), 772–775. doi:10.1190/1.1820589

Miclea, A. V., Terebes, R., and Meza, S. (2020). "One dimensional convolutional neural networks and local binary patterns for hyperspectral image classification," in 2020 IEEE International Conference on Automation, Quality and Testing, Robotics (AQTR), Cluj-Napoca, Romania, 21-23 May 2020, 1–6. doi:10.1109/AQTR49680.2020.9129920

Miyahara, H., Aihara, K., and Lechner, W. (2020). Quantum expectation-maximization algorithm. *Phys. Rev. A* 101 (1), 012326. doi:10.1103/PhysRevA.101.012326

Peng, Y. Y., Li, Y. F., Yu, H., Han, P. R., Zhu, C., and He, M. C. (2024). Mechanical properties of coal and rock with different dip angles based on true triaxial unloading test. *J. Min. Strata Control Eng.* 6 (2), 023037. doi:10.13532/j.jmsce.cn10-1638/td.20231222.001

Rumelhart, D. E., Hinton, G. E., and Williams, R. J. (1986). Learning representations by back-propagating errors. *Nature* 323 (6088), 533–536. doi:10.1038/323533a0

Sanyal, S. K., Juprasert, S., and Jubasche, J. (1980). An evaluation of a rhyolite-basalt-volcanic ash sequence from well logs. *Log. Anal.* 21 (1), 3–9.

Saporetti, C. M., da Fonseca, L. G., Pereira, E., and de Oliveira, L. C. (2018). Machine learning approaches for petrographic classification of carbonate-siliciclastic rocks using well logs and textural information. *J. Appl. Geophys.* 155, 217–225. doi:10.1016/j.jappgeo.2018.06.012

Shan, S. C., Wu, Y. Z., Fu, Y. K., and Zhou, P. H. (2021). Shear mechanical properties of anchored rock mass under impact load. *J. Min. Strata Control Eng.* 3 (4), 043034. doi:10.13532/j.jmsce.cn10-1638/td.20211014.001

Sun, J., Li, Q., Chen, M., Ren, L., Huang, G., Li, C., et al. (2019). Optimization of models for a rapid identification of lithology while drilling-A win-win strategy based on machine learning. *J. Petroleum Sci. Eng.* 176, 321–341. doi:10.1016/j.petrol.2019.01.006

Tian, M., Omre, H., and Xu, H. (2021). Inversion of well logs into lithology classes accounting for spatial dependencies by using hidden markov models and recurrent neural networks. *J. Petroleum Sci. Eng.* 196, 107598. doi:10.1016/j.petrol.2020.107598

Vichi, M., Cavicchia, C., and Groenen, P. J. (2022). Hierarchical means clustering. *J. Classif.* 39 (3), 553–577. doi:10.1007/s00357-022-09419-7

Wang, A. X., Chukova, S. S., and Nguyen, B. P. (2023). Ensemble k-nearest neighbors based on centroid displacement. *Inf. Sci.* 629, 313–323. doi:10.1016/j.ins.2023.02.004

Wang, G., Carr, T. R., Ju, Y., and Li, C. (2014). Identifying organic-rich Marcellus Shale lithofacies by support vector machine classifier in the Appalachian basin. *Comput. and Geosciences* 64, 52–60. doi:10.1016/j.cageo.2013.12.002

Wang, J., and Wang, X. L. (2021). Seepage characteristic and fracture development of protected seam caused by mining protecting strata. *J. Min. Strata Control Eng.* 3 (3), 033511. doi:10.13532/j.jmsce.cn10-1638/td.20201215.001

Wang, P., Chen, X., Wang, B., Li, J., and Dai, H. (2020). An improved method for lithology identification based on a hidden Markov model and random forests. *Geophysics* 85 (6), IM27–IM36. doi:10.1190/geo2020-0108.1

Xu, H., Li, L., and Guo, P. (2021a). Semi-supervised active learning algorithm for SVMs based on QBC and tri-training. *J. Ambient Intell. Humaniz. Comput.* 12, 8809–8822. doi:10.1007/s12652-020-02665-w

Xu, Z., Ma, W., Lin, P., Shi, H., Pan, D., and Liu, T. (2021b). Deep learning of rock images for intelligent lithology identification. *Comput. and Geosciences* 154, 104799. doi:10.1016/j.cageo.2021.104799

Yan, T., Xu, R., Sun, S. H., Hou, Z. K., and Feng, J. Y. (2024). A real-time intelligent lithology identification method based on a dynamic felling strategy weighted random forest algorithm. *Petroleum Sci.* 21 (2), 1135–1148. doi:10.1016/j.petsci.2023.09.011

Yang, Z., and Xu, Y. (2018). A safe screening rule for Laplacian support vector machine. *Eng. Appl. Artif. Intell.* 67, 309–316. doi:10.1016/j.engappai.2017.10.011

Zhang, X., Wen, J., Sun, Q., Wang, Z., Zhang, L., and Liang, P. (2023). Lithology identification technology of logging data based on deep learning model. *Earth Sci. Inf.* 16 (3), 2545–2557. doi:10.1007/s12145-023-01051-2

Zheng, D., Hou, M., Chen, A., Zhong, H., Qi, Z., Ren, Q., et al. (2022). Application of machine learning in the identification of fluvial-lacustrine lithofacies from well logs: a case study from Sichuan Basin, China. *J. Petroleum Sci. Eng.* 215, 110610. doi:10.1016/j.petrol.2022.110610

Zhong, Z., Carr, T. R., Wu, X., and Wang, G. (2019). Application of a convolutional neural network in permeability prediction: a case study in the Jacksonburg-Stringtown oil field, West Virginia, USA. *Geophysics* 84 (6), B363–B373. doi:10.1190/geo2018-0588.1

Zhou, K., Zhang, J., Ren, Y., Huang, Z., and Zhao, L. (2020). A gradient boosting decision tree algorithm combining synthetic minority oversampling technique for lithology identification. *Geophysics* 85 (4), WA147–WA158. doi:10.1190/geo2019-0429.1

Zhou, X. (2022). Reservoir characteristics and main controlling factors of the fourth member of shahejie formation in Niuxintuo area of western Liaohe sag. *Special Oil and Gas Reservoirs* 29 (5), 49. (in Chinese with an English abstract). doi:10.3969/j.issn.1006-6535.2022.05.007

frontiers | Frontiers in Earth Science

TYPE Original Research
PUBLISHED 07 April 2025
DOI 10.3389/feart.2025.1494518

OPEN ACCESS

EDITED BY
Peng Tan,
CNPC Engineering Technology R&D Company Limited, China

REVIEWED BY
Aleksandar Valjarević,
University of Belgrade, Serbia
Andres Felipe Alonso Rodriguez,
Great Colombia University, Colombia
Qilu Xu,
China University of Petroleum, China
Jintong Liang,
Chengdu University of Technology, China
Sherif Farouk,
Egyptian Petroleum Research Institute, Egypt

*CORRESPONDENCE
Xiyan Yang,
✉ 15181427705@163.com

RECEIVED 11 September 2024
ACCEPTED 17 March 2025
PUBLISHED 07 April 2025

CITATION
Yang R, Yang X, Zhang Y, Du Y, Qiao L, Lei Y and Fan X (2025) Reservoir characteristics and main controlling factors of argillaceous limestone in the Mao-1 Member, middle permian Maokou formation, southeastern Sichuan basin, southwest China.
Front. Earth Sci. 13:1494518.
doi: 10.3389/feart.2025.1494518

Reservoir characteristics and main controlling factors of argillaceous limestone in the Mao-1 Member, middle permian Maokou formation, southeastern Sichuan basin, southwest China

Rong Yang[1,2], Xiyan Yang[1,2]*, Yu Zhang[3], Yao Du[3], Lin Qiao[3], Yunjing Lei[1,2] and Xiangyu Fan[1,2]

[1]State Key Laboratory of Shale Oil and Gas Enrichment Mechanisms and Effective Development, Beijing, China, [2]School of Geoscience and Technology, Southwest Petroleum University, Chengdu, China, [3]Exploration Business Department, PetroChina Southwest Oil and Gasfield Company, Chengdu, China

In recent years, various acidizing tests have been conducted to obtain information about the industrial gas flows from acidizing tests in vertical wells JS1 and YH1 in eastern Sichuan Province, China. The results indicated that the Mao-1 Member of the Maokou Formation in southeastern Sichuan consists of good source rocks and a reservoir with high gas content. In this study, through investigations of outcrop sections, core drilling observations, thin-section identification, SEM, XRD, and TOC measurements, combined with nitrogen adsorption and logging analysis, we systematically studied the characteristics of tight argillaceous limestone reservoirs in the Mao-1 Member of southeastern Sichuan and summarized the main controlling factors for their formation. In the study area, the reservoir lithologies of the Mao-1 Member were composed of micrite limestone, bioclastic micrite limestone, and argillaceous limestone. Argillaceous limestone exhibited the highest content of clay minerals and TOC, while bioclastic micrite limestone showed relatively lower values. Six types of reservoir spaces were identified: intergranular pores, solution pores, organic pores, bioclastic-related fractures, clay mineral interlayer fractures, and macroscopic fractures. Argillaceous limestone also exhibited relatively high porosity in the Mao-1a subsegment. The reservoir pores are mainly divided into micro-pores and medium-pores, with diameters of less than 4 nm. The reservoir is primarily distributed vertically in the Mao-1a sub-member and the upper part of the Mao-1c sub-member. The formation of the tight carbonate reservoir is primarily influenced by diagenetic processes, including rock type, mineral composition, pore type, organic matter content, clay mineral transformation, dissolution, and cementation. Our analysis demonstrated that argillaceous limestone with high TOC content and good porosity is the best reservoir rock type in the study area.

KEYWORDS

reservoir space types, pore characteristics, unconventional reservoirs, south region of eastern Sichuan, Mao-1 member of Maokou formation

1 Introduction

Nodular limestone is also known as limestone-marl alternation (Miiller and Fabrieius, 1977; Moller and Vingan, 1988). Nodular limestones have been widely recorded in shallow marine basin sediments of the Phanerozoic era (e.g., Davaud and Lombard, 1975; Courtinat, 1993; Holmden et al., 1998; Samtleben et al., 2000; Westphal and Munnecke, 2003; Chacrone et al., 2004; Rey et al., 2004). Previous studies have primarily focused on investigating their origin (Wendler et al., 2016; Westphal and Munnecke, 1997; Reinhardt et al., 2000; Westphal et al., 2000; Westphal et al., 2008). In recent years, with the further exploration of unconventional reservoirs (Fan et al., 2020a; Li et al., 2024), it has been proposed that the argillaceous limestone in nodular limestone can serve not only as a source rock for hydrocarbons but also has storage capacity. Considering the numerous fractures discovered in the argillaceous limestone, these fractures can serve both as channels for hydrocarbon migration and as storage spaces for oil and natural gas (Li et al., 2025a).

Natural gas exploration of the Permian Maokou Formation in the Sichuan Basin, China, using conventional methods began in the 1950s and continues to this day. The beach facies and weathered crust paleo-karst reservoirs in members 2–3 of the Maokou Formation form a target stratum containing a group of medium-sized gas fields (Chen, 2007; Jiang et al., 2012; Cao et al., 2022; Hao et al., 2020). Among these, the "eyeball-eyelid" structure ("nodular limestone") in the Mao-1 Member is composed of marine carbonate source rocks that have been systematically studied (Huang et al., 2016; Liang et al., 2008; Hu et al., 2021; Huang and Lü, 2011). Recent studies have confirmed that the natural gas in the Mao-1 Member is primarily sourced from its own source rock (Li et al., 2021; Bao et al., 2024; Zhai et al., 2024). These findings suggest the existence of a new type of unconventional exploration field. The carbonate source rock gas reservoir (source-reservoir integration) in the Mao-1 Member holds great potential for natural gas exploration (Hu et al., 2018; Ma et al., 2010). In the past 2 years, significant gas volumes have been detected during tests in wells JS1, YH1, TT1, JH1, and DS1HF in the Mao-1 Member in Eastern and Southern Sichuan. Specifically, industrial gas flows of 20×10^4 m^3, 12.5×10^4 m^3, and 22.6×10^4 m^3 have been obtained from wells TT1, JH1, and DS1HF, respectively (Li et al., 2021; Lei et al., 2020; Li et al., 2012). This outcome proves that the Mao-1 Member of the Maokou Formation in eastern Sichuan contains a substantial amount of high-quality source rock and is also a productive gas-bearing reservoir. According to the literature, the Mao-1 Member is composed of nodular limestone strata with an "eyeball-eyelid" structure and is associated with a gentle slope sedimentary environment (Hao et al., 2020; Liu et al., 2019). Its primary reservoir spaces consist of shrinkage pores and talc fractures formed by the transformation of sepiolite into talc (Li et al., 2021). Some studies suggest that the formation of nodular limestone results from the sequential enhancement of sedimentation and diagenesis (Yuan et al., 2020). It has also been reported that the Milankovitch cycle caused the original sedimentary variations in the eyeball-eyelid limestone layers. In contrast, variations in terrigenous input, organic matter content, and paleoproductivity are considered crucial to its formation (Lei, 2021). It has also been confirmed that the Mao-1 Member exhibits self-generation and self-storage characteristics. Moreover, a unique carbonate reservoir exists between a shale reservoir and a fractured reservoir (Hao et al., 2020). Although considered a carbonate source rock, its pore characteristics differ from those of a shale reservoir (Hu et al., 2019). Previous studies have focused on the origin of talc in reservoir spaces (Li et al., 2021). However, the reservoir characteristics and principal controlling factors have been inadequately studied, limiting the exploration and development of the Mao-1 Member. To address this issue, this study focuses on the marly limestone of the Mao-1 Member in the Maokou Formation of the eastern Sichuan Basin. This study combines outcrop investigation, core drilling, thin-section identification, SEM, XRD, TOC analysis, liquid nitrogen adsorption, and logging analysis to thoroughly investigate and characterize the features of tight carbonate reservoirs. Additionally, the key controlling factors of reservoir development are analyzed in detail.

2 Geological background

The Yunnan movement at the end of the Carboniferous period caused the uplift of the Sichuan Basin's basement as a whole, which was subjected to levelling and filling (Taylor and Hayes, 2013). During the deposition of the Liangshan Formation, a large-scale transgression occurred, and the sedimentary environment was changed from terrestrial to marine. As a result, a set of clastic coastal deposits was formed in the Liangshan Formation (Yang et al., 2021; Su et al., 2020; Yang et al., 2023). During the deposition of the Qixia Formation, the sedimentary environment was transformed into a carbonate platform (Xie et al., 2022). During the sedimentary period of the Maokou Formation, based on the platform facies of the Qixia Formation sedimentary environment, a sedimentary process of rapid transgression and slow regression took place. The overall sedimentary environment exhibits a gentle carbonate slope, carbonate slope, and carbonate basin (Hao et al., 2020; Zeng et al., 2023). From southwest to northeast, the sedimentary environment of the Sichuan Basin possesses shallow, gentle slope facies, medium gentle slope facies, deep gentle slope facies, and shallow shelf facies (Figure 1a), which are characterised as being high in the southwest and low in the northeast.

The study area of this work is located in the southeastern part of Sichuan Province. The whole Mao-1 member has a deep, gentle slope sedimentary environment. The lithology is mainly composed of dark-grey, a grey-black, thin-thick layer of organic-containing argillaceous limestone (due to obvious external structural characteristics, referred to as an "eyelid") and a grey-to-dark-grey medium-thick–thick layer of bioclastic micrite limestone ("eyeball"). The existence of this type of limestone constitutes a typical eyeball-like structure in the vertical direction (Figure 2a; Fan et al., 2023). According to the rock structure and the logging curve characteristics, the Mao-1 member can be divided into three sub-members, namely, a, b and c from the top to the bottom, as shown in Figure 1b. The rock type of the Mao-1a member is mainly composed of dark-grey micrite limestone, whereas grey

Abbreviations: Mao-1 member, The Mao-1 member of the Maokou Formation; TOC, Total organic carbon content; SEM, Scanning electron microscopy; XRD, X-ray diffraction of total rock.

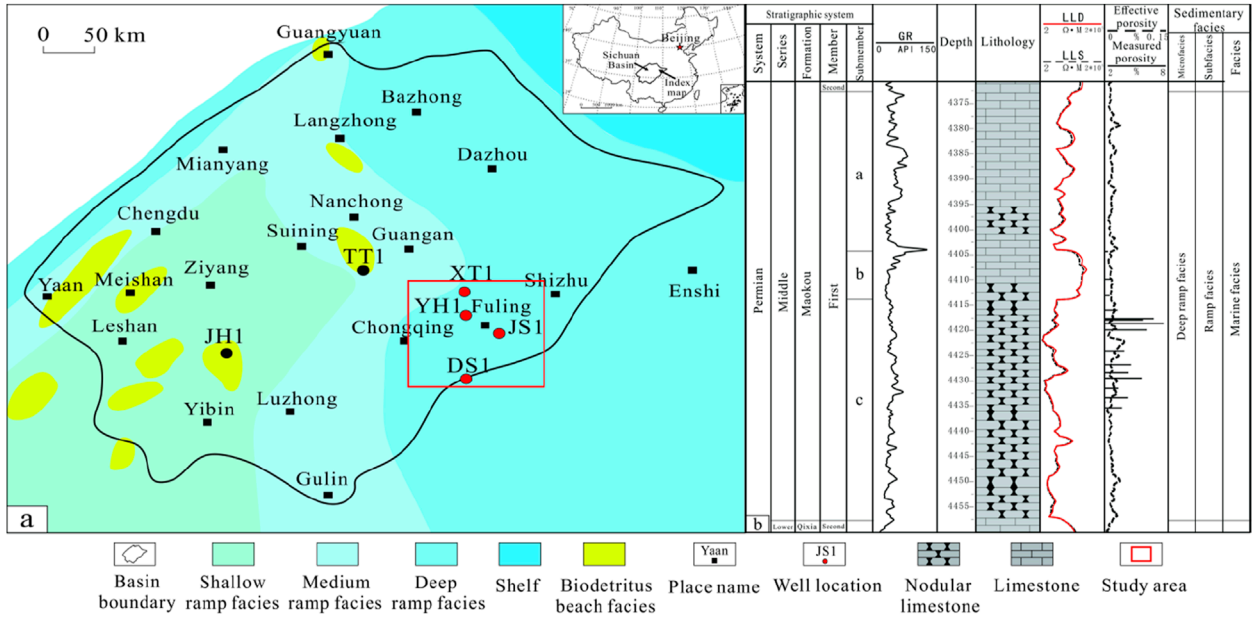

FIGURE 1
(a) Plane graph of the Mao-1 member, Maokou Formation, Sichuan Basin (Zhao, 2021). **(b)** Comprehensive well log of Well XT1.

nodular limestone can be detected at the bottom. The characteristics of the interface curve of Mao-1a and Mao-1b are obvious, while the gamma and resistivity curves exhibit significant increasing trends. The lithology type of Mao-1b sub-member is mainly composed of dark-grey micrite limestone. Mao-1b, Mao-1a, and Mao-1c exhibit obvious differences in their electrical measurement curves, with the resistivity of Mao-1b being significantly higher than those of Mao-1a and Mao-1c. The rock type of Mao-1c is mainly composed of dark-grey nodular limestone. When the Mao-1c sub-member transits to the Qixia Formation, the logging curve is characterised by a decrease in the gamma value and an increase in the resistivity.

The Mao-2 and Mao-3 members of the Maokou Formation can be described as regressive system tracts. The lithology of the Mao-2 member is mainly composed of interbedded, bright, crystal bioclastic limestone, micritic bioclastic limestone, and bioclastic micritic limestone with a low shale content. The whole of the Mao-3 member is grey, thick massive limestone. A thick granular limestone is interbedded in the middle and upper parts with thin micrite limestone. In the lower part, grey bioclastic micrite limestone, and argillaceous limestone have been developed (Hu et al., 2019; Su et al., 2020; Tian et al., 2021).

3 Samples and experimental methods

The samples for this work were primarily collected from Well XT1 in the eastern Sichuan Basin. Samples of different rock types were obtained and sequentially subjected to observations with thin sections. Various measurements were conducted including SEM imaging, whole-rock XRD and TOC analyses, as well as nitrogen adsorption tests.

A total of 82 samples were prepared into thin sections for a detailed observation of their lithological characteristics. SEM observations were conducted using a FEI Quanta 250 FEG field emission scanning electron microscope. Twenty-five regular samples of 2 cm × 2 cm were prepared, and their surfaces were initially polished with sandpaper. Subsequently, some samples were further polished using an argon ion polishing machine and coated with a gold layer. After the treatment, SEM observations were carried out under a scanning voltage of 10 kV and a working distance of approximately 9 mm.

A total of 82 samples were analysed carrying out whole-rock XRD and TOC content experiments. The XRD whole-rock analysis can semi-quantitatively analyse the mineral composition of rocks. In this work, the X'pert PRO X-ray diffractometer produced by the Dutch PANalytical company was used to test the sample powder that was ground to 200 mesh. The sample powder was initially dried to a constant weight at 110°C. Then, it was evenly spread on a microscope slide after cooling, and subsequently subjected to XRD analysis. The determination of THE TOC content was performed using a Leco CS-400 carbon and sulfur analyser. The test samples were first treated with acid (a concentration of 50% hydrochloric acid) to remove inorganic carbon contaminants from the samples; then, the measurement was carried out at temperatures exceeding 800°C. During this process, the organic carbon in the samples was oxidized under high-temperature and oxygen-rich conditions, and the generated carbon dioxide was quantitatively detected by the analyser. Finally, the total organic carbon content in the samples was calculated using the external standard method (He et al., 2025; Li et al., 2025b).

Four samples were subjected to liquid nitrogen adsorption experiments to study the pore structure. A Micromeritics ASAP2460 surface area analyser was used to conduct the liquid nitrogen adsorption experiments. Oil-containing samples were required prior to the de-oiling treatment; the representative samples were ground and

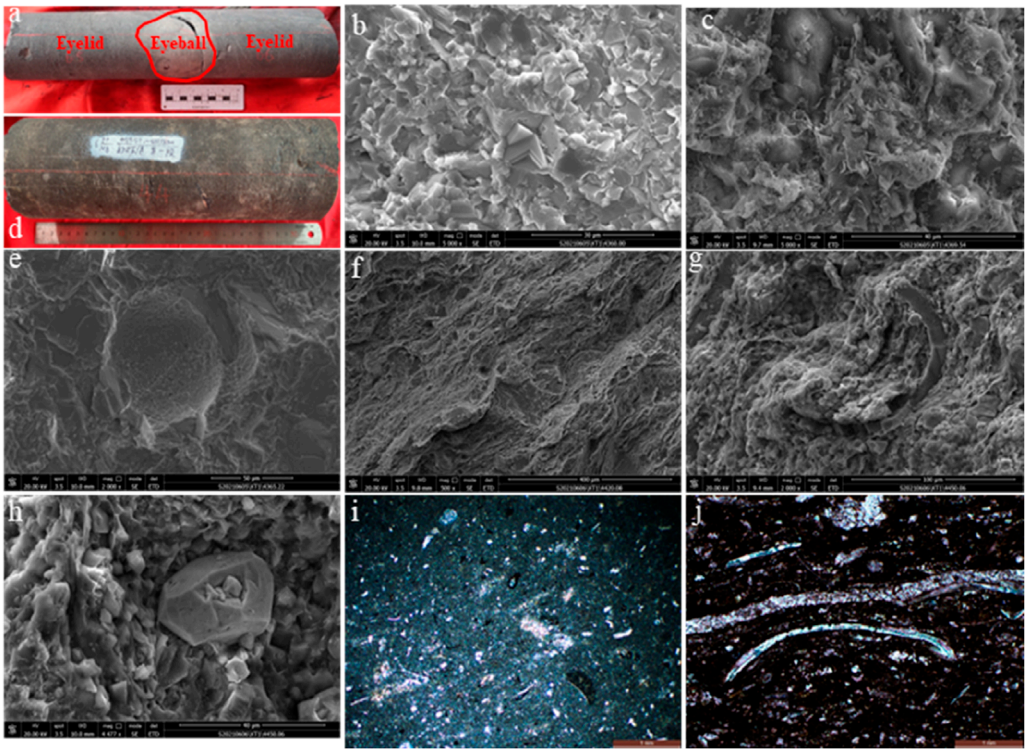

FIGURE 2
Rock images of the first member of the Maokou Formation in southeastern Sichuan. **(a)** Well XT1, 4373.57m, micritic limestone. **(b)** Well XT1, 4360 m, micrite limestone, calcite grain near embedded contact, see the self-shaped crystal calcite grain. **(c)** Well XT1, 469.54m, micritic limestone, flaky magnesium silicate mineral distribution. **(d)** Well XT1, 4449–4450m, nodular limestone, dark gray part is eyelid, light colour part is eyeball. **(e)** Well XT1, 4365.22m, micritic limestone, bioclastic. **(f)** Well XT1, 4420.08 m, bioclastic argillaceous limestone, argillaceous mineral lamellar distribution, directionality, in which calcareous and siliceous particles are dispersed. **(g)** Well XT1, 4450.06m, siliceous thin shell-like bioclasts. **(h)** Well XT1, 4450.06 m. Pyrite grains. **(i)** Well XT1, 4435.75 m, micrite limestone, see biological debris. **(j)** Well XT1, 4431.55 m, eyelid limestone, bioclastic development, mostly filled with calcite.

sieved, and 2 g of particles with sizes ranging from 20 to 40 mesh were selected and degassed under vacuum at 100°C for 10 h. Oil-containing samples were automatically de-oiled for an extended period using a Soxhlet extractor with dichloromethane until the extractant was clear. The samples were crushed using a jaw crusher and ball mill, and a vibrating sieve machine was used to select particles with sizes between 20 and 40 mesh, taking more than 10 g. The sieved particle samples were then loaded into sample tubes, placed in the degassing position of the analyser, and degassed at 105°C for 10 h. After degassing, the mass of the samples was measured using a balance with a precision of one ten-thousandth. The thermostat bath was filled with a cooling medium (liquid nitrogen for N_2) to the required level; the test control software was activated to perform the test and analyse the results (using multi-point BET, BJH, and DFT methods to calculate the specific surface area and pore size distribution).

4 Results

4.1 Petrological characteristics of reservoir

The existence of micrite limestone is not common in the Mao-1 member and is mainly distributed in the middle and upper sections of the Mao-1b member. Its colour is grey and dark-grey on the whole, with calcite contents of 80%–90% (Figure 2a) and very low dolomite contents. In addition, a small amount of authigenic pyrite can be detected on the surface of these rocks. Under SEM imaging, near-embedded contacts of calcite grains, self-shaped calcite grains, and a distribution of flaky magnesium silicate minerals can be seen (Figures 2b, c).

The presence of bioclastic micrite limestone (Figure 2d) is common in the Mao-1 member of the Maokou Formation. It is mainly distributed at the bottom of Mao-1a and in Mao-1c, and is often interbedded with bioclastic argillaceous limestone. The rock colour is grey and brown-grey. The content of bioclasts is 20%–30%, the biological particles are poorly sorted and rounded, gastropods are well preserved, while ostracods and bivalves are half-shaped to broken (Figures 2e, i).

The existence of argillaceous limestone (Figure 2d) is common and is mainly developed in Mao-1a. Most of it is interbedded with dark-grey bioclastic micritic limestone. Biological debris is also common. In addition to bivalves, there are often small amounts of gastropods and ostracods mixed with deep and shallow-water organisms. The bivalves are filled with argillaceous and micritic calcite (Figures 2g, j). The SEM analysis showed that the argillaceous minerals are layered and directional, whereas calcareous and

siliceous particles are dispersed and distributed. The presence of bioclasts can be also seen. The outer layer of bioclasts is a siliceous shell and pyrite grains (Figures 2f–h).

4.2 Types of reservoir spaces

According to the observations of thin sections and SEM images of different rock types in the Mao-1 member combined with existing data, it can be inferred that the reservoir spaces of the Mao-1 member are mainly formed by intergranular pores, dissolution pores, organic matter pores, fractures associated with bioclasts, and clay mineral interlayer fractures. Among them, clay mineral interlayer fractures and organic matter pores play a leading role (Liu et al., 2024).

The intergranular pores are mostly developed between the mineral grains and are primary pores. In the study area, the intercrystalline pores of Mao-1 members are mainly distributed between the calcite grains (Figures 3a–d). The intercrystalline pores between the clay minerals are mostly flaky, their pore widths range from tens to hundreds of nanometres, and the extension lengths are 1–15 μm. However, the connectivity of both is poor. This kind of pore is considered an important type of reservoir space in the carbonate reservoir of the Maokou Formation in southeastern Sichuan.

The dissolution pores in the study area are mostly developed in calcite crystals due to calcite dissolution in the deposit. Calcite is strongly corroded, often residual and harbour-like, forming irregular dissolution pores. The dissolution pores are developed in groups. The pore size distribution of the dissolution pores is wide, ranging from tens of nanometres to tens of microns (Figures 3e–h).

After the pyrolysis of organic matter, the residual organic matter is mostly filled and broken in the intergranular pores of minerals, inducing the formation of organic hydrocarbon generation pores. Organic matter pores are mostly developed in bioclastic micrite and bioclastic argillaceous limestones with high organic matter content. Organic matter pores are relatively isolated and honeycomb-like with pore sizes ranging generally from tens to hundreds of nanometres and the connectivity is poor (Figures 3i, j).

Bioclasts are well developed in the Mao-1 member. The existence of Intercrustal and pericrustal fractures at the edges of bioclast fossil shells are considered common types of pores and fractures in carbonate rocks. The original fabric of individual large shells is mostly preserved, and the fractures are caused by an extrusion process when the shell is closely arranged with the shell or shell edge. In these regions, fractures are formed between the shell and the clay minerals (Figure 3k). It is interesting to notice that a number of the unstable shells retain some of the original fabric, while the remaining shells develop calcite grains, showing fractures in the shell. This shell part has a certain stress inheritance (Figure 3l).

When the buried depth of the formation is increasing, the ground temperature and the gradual alkalinisation of formation water are also increased. As a result, the clay minerals become dehydrated and a precipitation of a large amount of interlayer water is induced. Then, micro-fractures are formed between the layers. Considering the SEM observations of the samples from the southeastern Sichuan area, the existence of many interlayer pores and fractures developed between the layered and flaky talc aggregates in the samples can be seen, which are linear or triangular. The widths of the fractures are generally 0.5–8 μm, and the connectivity is good (Figures 3m, n).

Fractures are also developed in the core samples from the Mao-1 member. Nonetheless, most of them are half-filled with calcite (Figures 3o, p).

4.3 Reservoir distribution characteristics

The Mao-1 members in southeastern Sichuan exhibit stable and continuous formation characteristics. The reservoir is characterized by high Gamma Ray (GR) values and low resistivity values. Vertically, the Mao-1 member reservoir is mainly developed at the bottom of the Mao-1a sub-member and the top of the Mao-1c sub-member, the Mao-1b sub-member reservoir is hardly developed at all (Figure 4). The reservoir lithology is mostly argillaceous limestone, followed by bioclastic micrite limestone. Horizontally, the reservoir is mainly produced in the deep, gentle slope, argillaceous limestone microfacies and the deep, gentle slope, bioclastic micrite microfacies.

4.4 Mineral composition characteristics of reservoir

The XRD results (Table 1) show that the mineral composition of the Mao-1 member of Maokou Formation in the study area is mainly calcite. In contrast, dolomite, quartz, clay minerals, siderite, pyrite, orthoclase, and plagioclase can be also seen. The clay minerals mainly include talc and a talc-mixed layer. The calcite mineral content is 12%–100%, with a mean of 82.69%. The dolomite content, the content of quartz, the content of talc, and the content of clay minerals lie between 0% and 79.5%, 0% and 86.5%, 0% and 22.4%, and 0%–19%, an average content of 6.81%,6.76%, 1.55%, and 1.34%, respectively. The clay minerals are mainly composed of a mixed layer and talc. The content of plagioclase can be found between 0% and 4.1%, with an average content of 0.12%. The content of orthoclase, siderite, and pyrite minerals is 0%–8.2%, 0%–6.5%, and 0%–4.6% with an average content of 0.2%, 0.26%, and 0.28%, respectively. In general, calcite and dolomite are the main minerals in the rock of the Mao-1 member, whereas the content of brittle minerals is high. The content of calcite in the micritic limestone is 60%–99%, the content of quartz is 0%–20%, and the content of clay minerals is very small at <3%. The calcite content in bioclastic micrite limestone is 60%–95%, the content of quartz is 1%–23%, and clay minerals is 1%–10%. The calcite content in argillaceous limestone is 55%–85%, the content of quartz is 0%–11%, and clay minerals is 10%–27% (Figure 5). Vertically, the content of calcite of Mao-1a is 60%–90%, the content of quartz is 0%–30%, and the content of clay minerals is 0%–20%. Additionally, the content of calcite of Mao-1b is 60%–90%, the content of quartz is 0%–10%, and the content of clay minerals is 3%–20%. The calcite content of Mao-1c is 60%–99%, quartz is 0%–30%, and clay minerals is 0%–20% (Figure 6).

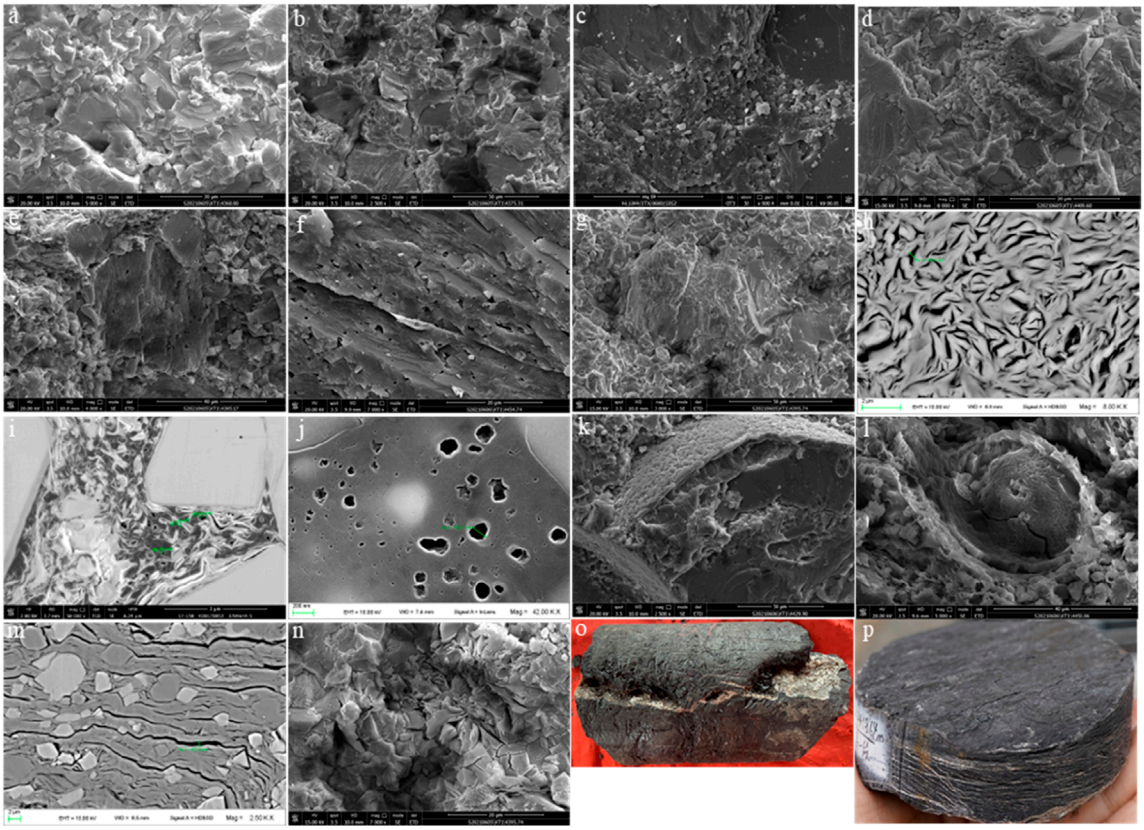

FIGURE 3
Rock images of the first member of the Maokou Formation in southeastern Sichuan **(a)** XT1 well, 4360 m, calcite intercrystalline pore. **(b)** XT1 well, 4375.31 m, calcite intercrystalline pore. **(c)** XT1 well, 4461.64m, calcite intercrystalline pore. **(d)** XT1 well, 4409.6 m. Intergranular pores and grain edge fractures. **(e)** XT1 well, 4385.17 m, calcite intragranular dissolved pore. **(f)** XT1 well, 4454.74 m, calcite intracrystalline dissolution pores. **(g)** XT1 well, 4395.74 m, calcite intragranular dissolved pore. **(h)** XT1 well, 4431.5m, flaky talc aggregates developed interlayer fractures. **(i)** YH1 well, a small amount of pores are developed in organic matter. **(j)** TY1 well, 2834.06m, organic pore. **(k)** XT1 well, 4429.90 m, bioclastic grain edge fracture, intragranular fracture. **(l)** XT1 well, 4450.06m, intragranular fractures. **(m)** XT1 well, 4420 m, lamellar talc aggregate development interlayer fracture. **(n)** XT1 well, 4395.74m, clay interlamellar fracture. **(o)** XT1 well, 4410.34–4410.50 m, eyeball limestone (calcite half filling seam). **(p)** XT1 well, 4420.85m, eyelid limestone, well-developed foliation.

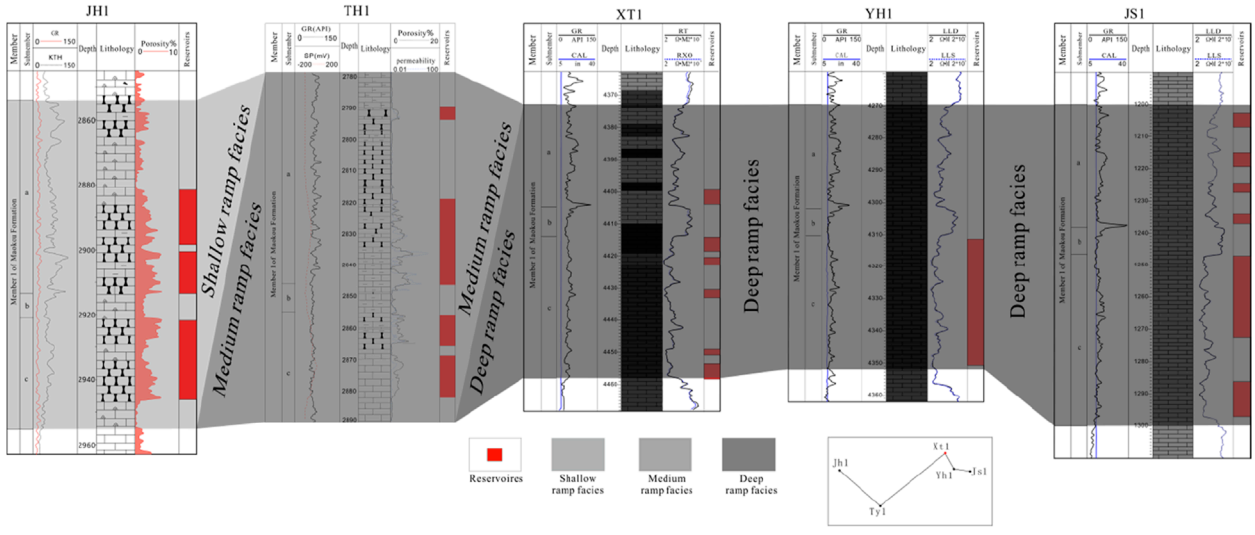

FIGURE 4
Sedimentary reservoir correlation diagram of the JH1 well, TY1 well, XT1 well, YH1 well, JS1 well, 1-YH1 well, and JS1 well.

TABLE 1 TOC, porosity, and XRD mineral composition table of the samples.

Depth (m)	Lithology	TOC (%)	Porosity (%)	Calcite (%)	Dolomite (%)	Siderite (%)	Pyrite (%)	Quartz (%)	Orthoclase (%)	Plagioclase (%)	Clay mineral (%)
4373.88	Micrite limestone	0.83	1.98	64.9	30.6	0	0.7	3.7	0	0	0
4375.31	Bioclastic micrite limestone	0.52	1.39	95.2	0.4	0	0	2.2	0	0	2.3
4376.13	Micrite limestone	0.4	1.39	95.6	1.2	0	0	3.2	0	0	0
4376.95	Micrite limestone	0.57	0.74	63.3	27.9	0	0.6	8.3	0	0	0
4379.13	Micrite limestone	1.66	1.77	77.2	4.9	0	0.5	17.4	0	0	0
4380.38	Micrite limestone	0.26	0.4	92.3	5.6	0	0	2.1	0	0	0
4381.29	Micrite limestone	0.16	0.67	98.6	0.6	0	0	0.8	0	0	0
4382.02	Micrite limestone	1.63	1.51	89.8	3	0	0	7.1	0	0	0
4382.93	Micrite limestone	1.31	2.37	89.3	3.4	0	0	7.3	0	0	0
4383.99	Micrite limestone	1.44	1.19	89.6	3.2	0	0	7.2	0	0	0
4385.17	Micrite limestone	0.35	0.46	99.5	0	0	0	0.5	0	0	0
4386.4	Micrite limestone	0.46	0.19	12.2	1.3	0	0	86.5	0	0	0
4387.89	Micrite limestone	0.41	0.58	96.3	0.7	0	0	2.9	0	0	0
4388.69	Micrite limestone	1.15	1.47	88.4	3.9	0	0	7.6	0	0	0
4389.81	Micrite limestone	0.38	1.44	93.1	4	0	0	2.9	0	0	0
4391.05	Bioclastic micrite limestone	0.96	1.46	88.9	1.3	0	0	6	0	0	3.7
4391.91	Bioclastic micrite limestone	0.47	1.08	85.1	7.6	0	0	4.2	0	0	3.1
4392.92	Bioclastic micrite limestone	1.31	1.94	78.1	3.4	0	0	14.8	0	0	3.6
4394.02	Bioclastic micrite limestone	0.17	1.72	90.8	5.2	0	0	1.2	0	0	2.8
4395.74	Bioclastic micrite limestone	0.37	0.31	91.3	2.1	0	0	3.8	0	0	2.8

(Continued on the following page)

10.3389/feart.2025.1494518

TABLE 1 (*Continued*) TOC, porosity, and XRD mineral composition table of the samples.

Depth (m)	Lithology	TOC (%)	Porosity (%)	Calcite (%)	Dolomite (%)	Siderite (%)	Pyrite (%)	Quartz (%)	Orthoclase (%)	Plagioclase (%)	Clay mineral (%)
4396.71	Bioclastic micrite limestone	0.32		58.4	33.5	0	0.4	5.9	0	0	1.9
4397.99	Micrite limestone	0.57		68.5	18.3	1.7	0	9.6	1.9	0	0
4399.12	Argillaceous limestone	0.26	0.35	81.4	2.9	0	0	3.3	0	0	12.4
4400.38	Bioclastic micrite limestone	0.11	0.61	91.9	0	0	2.8	1.5	2.2	0	1.7
4400.9	Micrite limestone	0.8	2.7	61.7	17.2	6.5	0	14.5	0	0	0
4401.52	Argillaceous limestone	1.36	3.78	70.6	1.2	0	3.2	10.6	0	0	14.4
4402.12	Argillaceous limestone	0.77	1.71	84.1	0.8	0.9	2.1	0.7	0	0	11.4
4402.93	Micrite limestone	0.46	1.16	92	0	3.2	4.6	0.2	0	0	0
4403.99	Micrite limestone	0.09	0.54	87.1	1.8	2.9	4.5	0	0.8	2.8	0
4404.88	Argillaceous limestone	0.24	0.86	84.6	1.1	0	0	0.3	2.9	0	11.1
4405.39	Bioclastic micrite limestone	0.54	0.8	93	2.2	0	0	0.8	0	2.7	1.4
4406.48	Bioclastic micrite limestone	0.14	0.61	80.6	2.7	2.4	0	2.4	8.2	0	3.6
4407.57	Argillaceous limestone	0.67	0.88	59.2	13.5	3.5	0	1.8	0.4	4.1	17.5
4408.51	Bioclastic micrite limestone	0.12	0.69	88.1	3	0	0	0.3	0	0	8.6
4409.6	Bioclastic micrite limestone	0.13	0.38	74.5	3.7	0.3	0	3.1	0	12.9	5.5
4410.34	Argillaceous limestone	0.8	1.45	71	3.3	1.5	0	0	0	8.5	15.7
4411.41	Argillaceous limestone	0.42	0.56	78.3	0.4	0.5	0	2.7	0	0	18.2

(Continued on the following page)

10.3389/feart.2025.1494518

TABLE 1 (*Continued*) TOC, porosity, and XRD mineral composition table of the samples.

Depth (m)	Lithology	TOC (%)	Porosity (%)	Calcite (%)	Dolomite (%)	Siderite (%)	Pyrite (%)	Quartz (%)	Orthoclase (%)	Plagioclase (%)	Clay mineral (%)
4412.61	Argillaceous limestone	0.84		72.4	5.8	0	0	9.2	0	0	12.6
4413.64	Argillaceous limestone	0.8		67.2	1.1	0	0	9.4	0	0	22.4
4414.85	Micrite limestone	0.19		95.4	1.3	0	0	3.2	0	0	0
4416.12	Bioclastic micrite limestone	0.46	1.67	89.8	0.4	0	0	3.4	0	0	6.4
4418.1	Micrite limestone	0.62		84.4	2.4	0	0	13.2	0	0	0
4419.1	Argillaceous limestone	0.55		74.4	3	0	0	10.3	0	0	12.3
4420.08	Argillaceous limestone	0.78		58.5	5.2	0	0	9.8	0	0	26.6
4420.76	Bioclastic micrite limestone	0.25	0.87	95.1	0	0	0	1.4	0	0	3.6
4421.9	Micrite limestone	0.24	0.7	98.7	0.3	0	0	1	0	0	0
4423.05	Micrite limestone	0.2	0.46	100	0	0	0	0	0	0	0
4424.3	Bioclastic micrite limestone	0.32	0.61	93.7	0	0	0	3	0	0	3.3
4425.21	Micrite limestone	0.38	0.84	94	0	0	0.6	5.5	0	0	0
4426.09	Micrite limestone	0.39	0.8	96.9	0	0	0	3.1	0	0	0
4427.04	Micrite limestone	1.07		72.8	5.4	0	0.6	21.3	0	0	0
4428.2	Bioclastic micrite limestone	0.42	1.73	89.5	1.1	0	0	7.1	0	0	2.4
4428.99	Bioclastic micrite limestone	0.73		73.3	3.5	0	0.9	15.8	0	0	6.5
4429.9	Micrite limestone	0.17	0.5	98.8	0	0	0	1.2	0	0	0
4431.06	Micrite limestone	0.11	0.37	99.7	0	0	0	0.3	0	0	0
4432	Micrite limestone	0.24	0.3	96.8	0.7	0	0	2.5	0	0	0

(Continued on the following page)

10.3389/feart.2025.1494518

TABLE 1 (*Continued*) TOC, porosity, and XRD mineral composition table of the samples.

Depth (m)	Lithology	TOC (%)	Porosity (%)	Calcite (%)	Dolomite (%)	Siderite (%)	Pyrite (%)	Quartz (%)	Orthoclase (%)	Plagioclase (%)	Clay mineral (%)
4433.09	Bioclastic micrite limestone	0.77	3.01	83.1	1.7	0	0	9.9	0	0	5.3
4434.2	Micrite limestone	0.31	1.18	98.9	0	0	0	1.1	0	0	0
4435.06	Micrite limestone	0.59	2.07	95.2	0.5	0	0	4.3	0	0	0
4436.01	Micrite limestone	0.49	1.88	97.6	1.2	0	0	1.2	0	0	0
4437.01	Micrite limestone	0.46		86.1	13.9	0	0	0	0	0	0
4438.11	Micrite limestone	0.15	0.57	99.5	0	0	0	0.5	0	0	0
4439.2	Micrite limestone	1.12	1.4	79.6	2	0	0	18.4	0	0	0
4440.28	Micrite limestone	0.92	3.62	89	1.2	0	0	9.8	0	0	0
4441.3	Argillaceous limestone	0.61	1.7	75.9	0.8	0	0	11	0	0	12.2
4442.37	Micrite limestone	0.54	0.2	86.2	1.6	0	0	12.2	0	0	0
4443.59	Micrite limestone	0.22	0.99	99.2	0	0	0	0.8	0	0	0
4444.23	Micrite limestone	0.39	1.23	97.3	0	0	0	2.7	0	0	0
4445.03	Micrite limestone	0.14	0.71	99.1	0	0	0	0.9	0	0	0
4446.2	Micrite limestone	0.32	2.04	96.4	0.9	0	0	2.7	0	0	0
4447.43	Micrite limestone	0.63		72.2	1.5	0	0	26.3	0	0	0
4448.39	Bioclastic micrite limestone	0.56		56.6	13.8	0	0.5	22.7	0	0	6.4
4450.06	Micrite limestone	0.81		76.8	1.4	0	0	21.8	0	0	0
4451.17	Micrite limestone	0.47	0.99	84.4	10.2	0	0	4.4	0	0	1
4451.82	Micrite limestone	0.38	0.54	92.8	2.1	0	0	5.2	0	0	0
4452.63	Micrite limestone	0.18	0.82	94.9	1	0	0	4.1	0	0	0
4453.55	Argillaceous limestone	0.26		84.5	4.8	0	0	1.4	0	0	9.3

(Continued on the following page)

10.3389/feart.2025.1494518

10.3389/feart.2025.1494518

TABLE 1 (*Continued*) TOC, porosity, and XRD mineral composition table of the samples.

Depth (m)	Lithology	TOC (%)	Porosity (%)	Calcite (%)	Dolomite (%)	Siderite (%)	Pyrite (%)	Quartz (%)	Orthoclase (%)	Plagioclase (%)	Clay mineral (%)
4454.74	Micrite limestone	0.07	0.17	99.3	0	0	0	0.7	0	0	0
4455.14	Micrite limestone	0.04	0.32	95.9	0.5	0	0	3.6	0	0	0
4455.56	Micrite limestone	0.6	0.49	97.6	0	0	1.7	0.7	0	0	0
4456.32	Micrite limestone	0.04	0.57	98.5	1	0	0	0.5	0	0	0
4457.25	Micrite limestone	0.36	0.42	89.3	0	0	0.7	0.5	0	9.4	0

4.5 Organic matter abundance and evolutionary stages

The range of vitrinite reflectance (Ro) values for the organic matter in the Mao-1 member, is between 1.57% and 1.60% (Table 2), indicating that the organic matter is primarily in the high maturity stage of thermal evolution. There is little difference in the degree of thermal evolution among different rock types.

According to the TOC test results of 82 samples from the Maokou Formation (Table 1), the extracted TOC values ranged from 0.11% to 1.63%, with an average of 0.51% (Figure 7a). The TOC content of argillaceous limestone was the highest, ranging from 0.26% to 1.36%, with an average value of 0.64% (Figure 7b). The samples from the Mao-1a section were the most enriched in TOC, ranging from 0.09% to 1.66%, with an average value of 0.61% (Figure 7c).

4.6 Reservoir physical property characteristics

The porosity distribution ranges for Micrite limestone, Bioclastic micrite limestone, and Argillaceous limestone are from 0.17% to 3.62%, 0.31%–3.01%, and 0.35%–3.78%, respectively (Figure 8a). The primary physical properties of argillaceous limestone are significantly better than those of micrite and bioclastic micrite limestones. Vertically, the porosity ranges for Mao-1a, Mao-1b, and Mao-1c sub-member are from 0.19% to 3.78%, 0.38%–1.45%, and 0.17%–3.62%, respectively, with the Mao-1a sub-member reservoir having the best physical properties (Figure 8b).

4.7 Pore structure of reservoir

The pore types and characteristics can be directly observed with SEM imaging. However, local and individual carbonate rock samples can be only observed, while the overall pore characteristics of a sample cannot be quantitatively assessed (Loucks et al., 2009). Therefore, in this work, four argillaceous limestone samples were selected in the reservoir section for nitrogen adsorption experiments to quantitatively observe the overall pore characteristics of the samples (Table 3). The results showed that the N_2 adsorption-desorption curve of the sample is similar to the type-IV isothermal curve proposed by IUPAC (International Union of Applied Chemistry), and the whole system is transformed into a capillary condensation system of porous adsorbent (Figure 9). The adsorption capacity rapidly increased under lower relative pressure, and the curve became convex, indicating a strong interaction between the adsorbate and the surface, with the overall deviation occurring on the y-axis. No evident plateau was observed at the highest point of relative pressure, and the adsorption curve's upward trend was obvious (Figures 9a–d). These results indicate that either there are still larger macropores in the sample, which are not filled with nitrogen, or the interaction between the adsorbate molecules is strong. The adsorption process may be continued to form a multi-molecular layer, with a continuous rise in the adsorption isotherm. In the middle section of relative pressure (P/P0), hysteresis occurs between the adsorption-desorption curves, leading to the

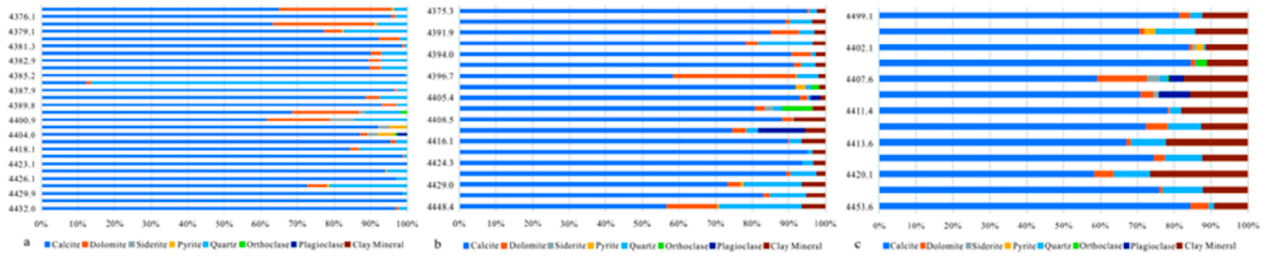

FIGURE 5
XRD mineral percentage bar chart of different lithofacies. **(a)** Micrite limestone; **(b)** Bioclastic micrite limestone; **(c)** Argillaceous limestone.

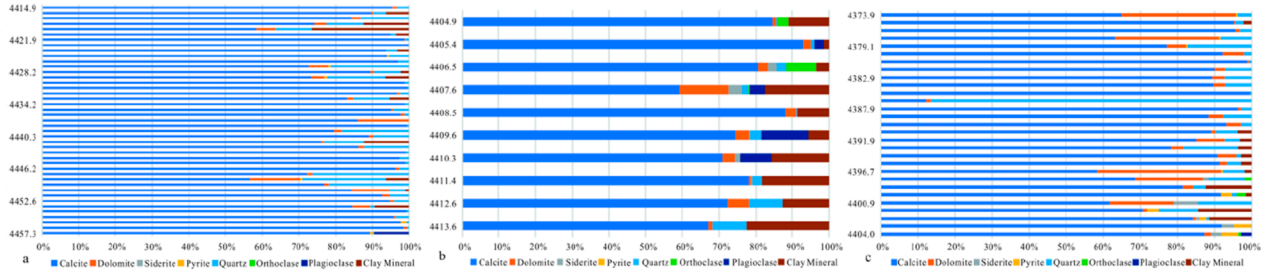

FIGURE 6
X-ray diffraction mineral percentage bar chart of different sub-members. **(a)** Mao-1a member; **(b)** Mao-1b member; **(c)** Mao-1c member.

TABLE 2 Vitrinite reflectance statistics table for Mao-1 member.

Depth (m)	Lithology	Ro (%)	Number of measurement points	Standard deviation
4369.54	Bioclastic micrite limestone	1.60	7	0.0140
4380.38	Bioclastic micrite limestone	1.57	5	0.0120
4409.60	Argillaceous limestone	1.58	6	0.0160

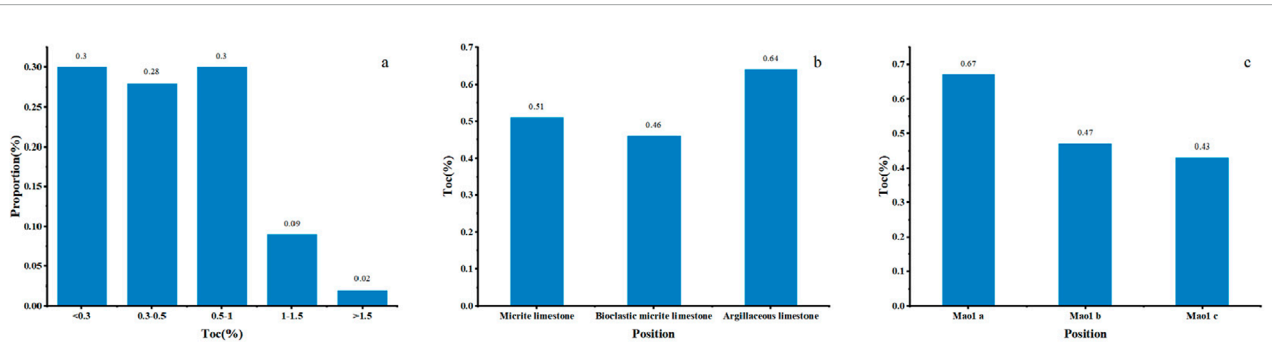

FIGURE 7
(a) Histogram of organic carbon distribution frequency. **(b)** Histogram of organic carbon content in different reservoir lithologies. **(c)** Histogram of organic carbon content in each sub-member of the Mao-1 member.

manifestation of a hysteresis loop. According to the industry standard GBT21650.2-2008, the hysteresis loop is between H3 and H4. This result indicates that the pores in the sample have mainly a slit-like morphology, with the pores composed of flaky clay and rigid particles. An obvious inflexion point can be also seen on the desorption curve, which is caused by the difference between the

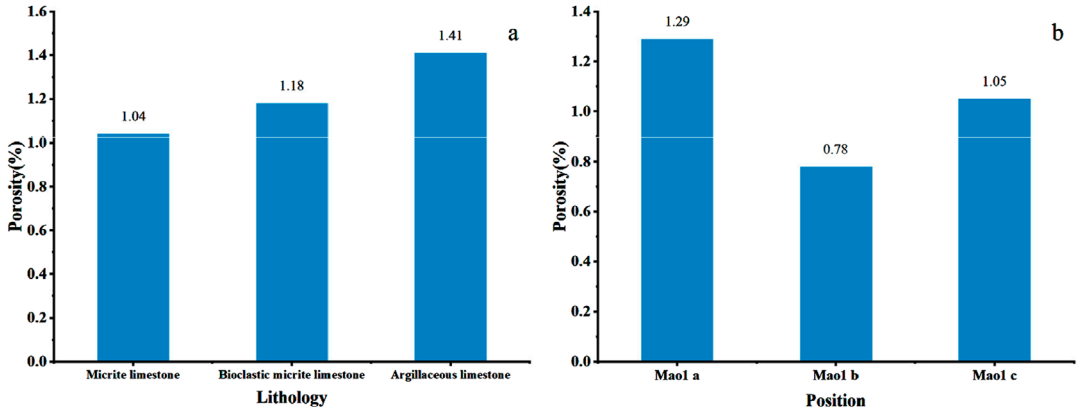

FIGURE 8
Physical property analysis histogram. **(a)** Histogram of porosity distribution in different reservoir lithologies. **(b)** Histogram of porosity distribution at different layers.

capillary condensation and the evaporation of thin-necked bottle-like pores (Wei et al., 2013). According to IUPAC (1994), the shale pores can be divided into three categories: micropores (<2 nm), mesopores (2–50 nm), and macropores (>50 nm). Considering the peaks in the pore size distribution maps (Figures 9a1–d1, a2–d2) induced by adsorption and desorption branches, it can be seen that the pores in the sample are mainly micropores and mesopores <4 nm. In summary, the pore morphology of carbonate reservoirs in the Mao-1 member is mainly lamellar clay (mainly talc) interlayer fractures, slit-like pores composed of rigid particles, and fine-necked bottle-like pores. The pores are primarily micropores and mesopores <4 nm.

5 Discussion

The development of carbonate reservoirs in the Mao-1 member is affected by many factors, with lithofacies, TOC, and diagenesis playing major roles.

5.1 Effect of rock type on reservoir development

From the above-mentioned analysis, it can be inferred that the Mao-1 member reservoir is mainly developed in the deep, gentle slope, bioclastic micritic limestone, and argillaceous limestone at the bottom of the Mao-1a sub-member and top of the Mao-1c sub-member. This effect can be explained by considering that the bioclastic and argillaceous contents in the micritic limestone are low, resulting in the development of fewer inter-layer pores and organic pores in clay minerals. Meanwhile, the bioclastic contents in the bioclastic micritic limestone and argillaceous limestone and the content of clay minerals are relatively high, which facilitates the development of pores.

5.2 Organic matter content has a positive effect on reservoir performance

Organic matter pores are formed by the existence of residual organic matter in the intergranular pores of minerals, which take the form of fillings and fragments after the pyrolysis of organic matter. As can be seen from Figure 7, the TOC content has a good positive correlation with porosity (Figure 10a), specific surface area (Figure 10c) and total pore volume (Figure 10b). This outcome shows that the organic matter content has a good effect on the pore structure of the reservoir. However, the organic matter content is regarded as one of the key factors determining the reservoir performance of shale gas reservoirs. High-quality reservoirs are often found in shale development sections with high organic matter contents (Chen, 2007). For the tight marl reservoir in the Mao-1 member, due to its low overall organic matter content (average TOC = 0.51%), the impact of organic matter pores on pore characteristics is positive but weak. This result reflects the fact that TOC content is one of the main factors affecting the reservoir in the Mao-1 member.

5.3 Diagenesis

The constructive diagenesis process that took place during the sedimentary period of the Mao-1 member mainly comprised the transformation of clay minerals and dolomitization. The cementation of calcite primarily caused destructive diagenesis.

As can be seen from the SEM results, a large number of talc shrinkage pores (fractures) are developed in Mao-1 (Figures 6h, m). It can be also observed that clay minerals are positively correlated with porosity (Figure 11b). According to the literature, sepiolite [$Mg_8Si_{12}O_{30}(OH)_4{\cdot}4H_2O$] will be transformed into talc [$Mg_3Si_4O_{10}(OH)_2$] under the combined influence of temperature and maturity Ro (Chen et al., 1985; Cai et al., 2019). In the laboratory, the structural transformation temperature of sepiolite is 310°C–330 °C (Yang and Xu, 1986). When the maturity

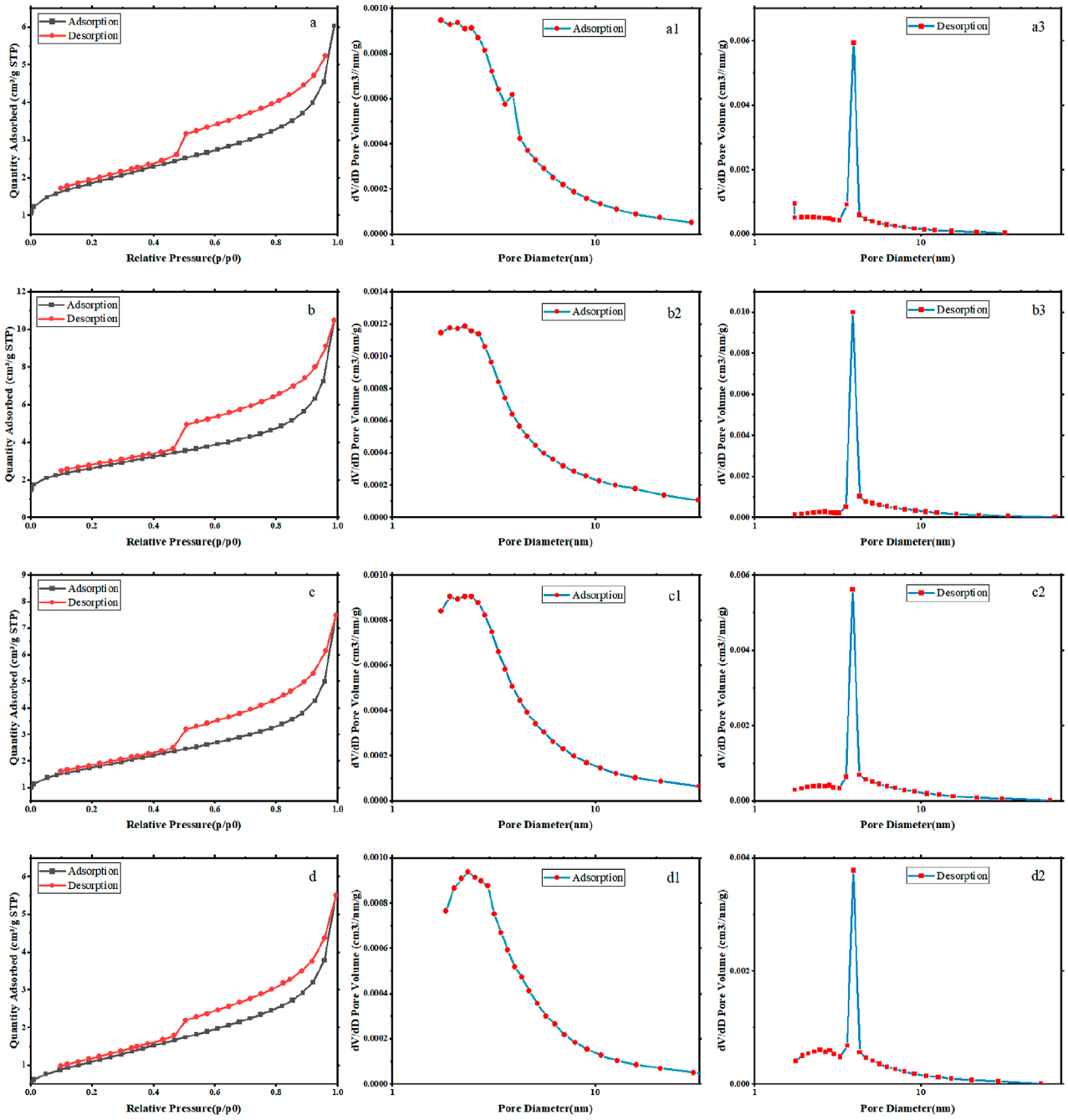

FIGURE 9
(a–d) Nitrogen adsorption-desorption isotherms of four argillaceous limestone samples; **(a1-d1)** Pore size distribution diagrams obtained from nitrogen adsorption of the samples; **(a2-d2)** Pore size distribution diagrams obtained from nitrogen desorption of the samples.

Ro value reaches 1.2% (Yang and Xu, 1986), sepiolite will be almost completely converted into talc. Nonetheless, this procedure may not necessarily occur in nature. Yang and Xu, (1986) argued that sepiolite can be converted to talc when the burial temperature reaches 120 °C. The measurement of three samples (Table 2) showed that the Ro value of rock maturity in the study area was 1.57%–1.6%, and the geothermal temperature at the end of the early Cretaceous was up to 140°C (Li et al., 2021), which offer suitable conditions for the conversion of sepiolite to talc. With the progress of talcisation, mineral crystals will be transformed from the trioctahedral chain of sepiolite to the fibrous flakes of talc. Thus, a large number of diagenetic shrinkage fractures will be formed. At the same time, the size of the talc crystals will become smaller than that of sepiolite. Several primary pores, such as intergranular pores, will be also formed during the transformation process. These diagenetic shrinkage pores and fractures are considered important reservoir spaces for the tight reservoirs in the Mao-1 member of the Maokou Formation.

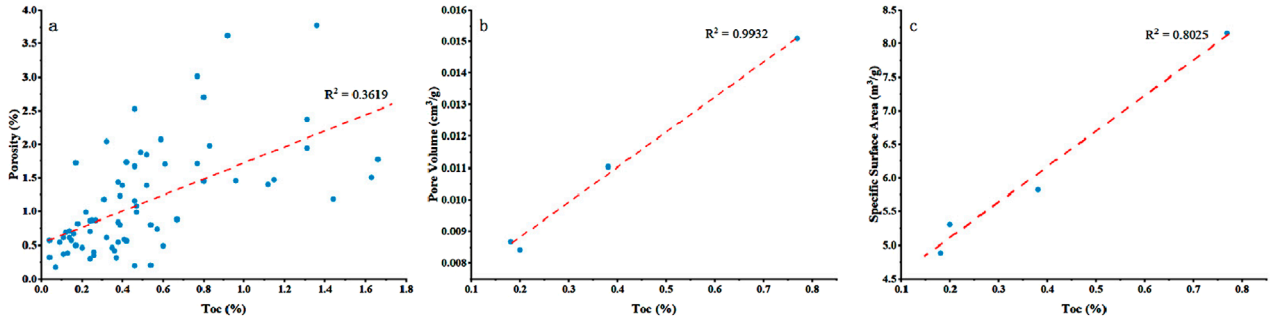

FIGURE 10
(a) Scatter plot of TOC *versus* Porosity. **(b)** Scatter plot of TOC *versus* Surface Area. **(c)** Scatter plot of TOC *versus* Pore Volume.

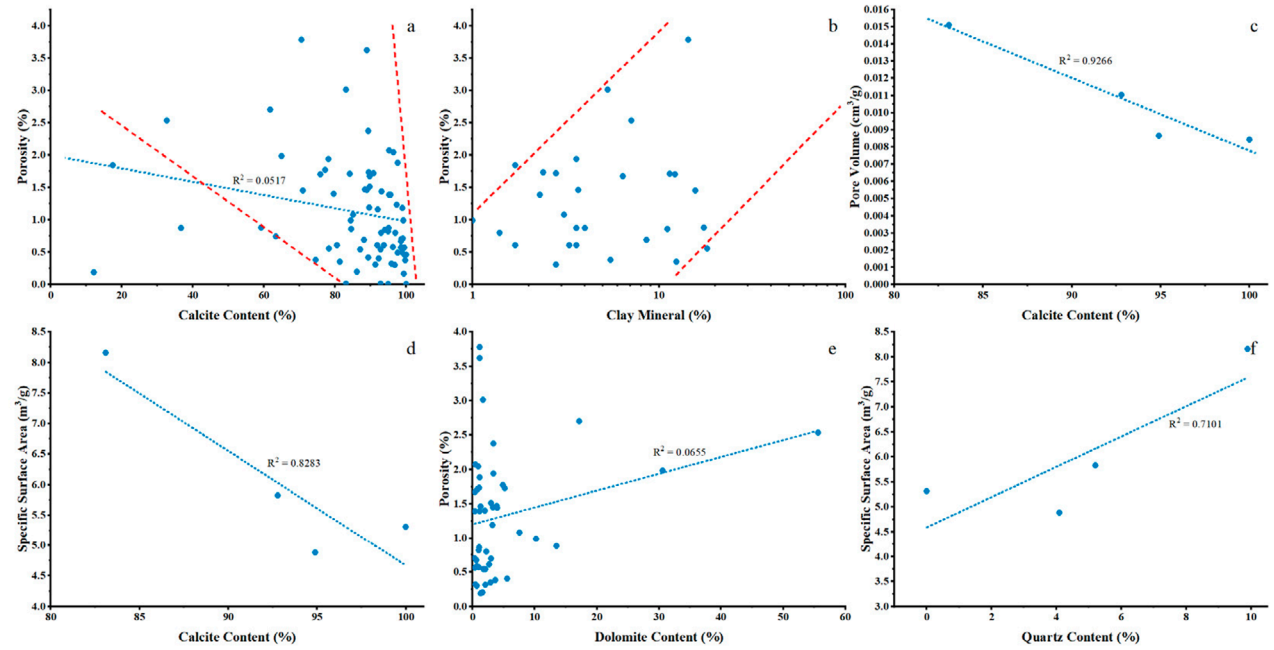

FIGURE 11
(a) Scatter plot of calcite versus porosity. **(b)** Scatter plot of clay minerals versus porosity. **(c)** Scatter plot of calcite versus pore volume. **(d)** Scatter plot of calcite versus surface area. **(e)** Scatter plot of dolomite versus porosity. **(f)** Scatter plot of quartz versus surface area.

Dolomitization is commonly developed along with the transformation of clay minerals. It is currently believed that the genetic mechanism of dolomite in the Permian strata of the Maokou Formation is associated with a thermal convection process driven by abnormal ground temperatures related to Emei ground fissure movement in a buried environment (Dong et al., 2020). Dolomite has a higher density than calcite. During the process of dolomitization, the precipitation volume of dolomite is less than the dissolution volume of calcite (Liu et al., 2021), and the porosity of the rock increases. The diagram in Figure 11e shows that there is a positive correlation between the dolomite content and porosity, indicating that dolomitization improves the Mao-1 reservoir in the study area. Another mineral, calcite, has a high content and is negatively correlated with porosity, specific surface area, and pore volume. This result also demonstrates that limestone dolomitization has a positive impact on reservoir improvement.

Dissolution is also prevalent in the Mao section of carbonate rocks in the study area, and is mainly evident as intracrystalline dissolution pores of brittle minerals such as calcite (Figures 6c, g). These dissolution pores can be used as reservoir spaces but also as fluid channels, which are conducive to the transformation of reservoirs.

In addition to clay mineral transformation, dolomitization, and dissolution, which play a constructive role in the reservoir, on the contrary, cementation (especially calcite mud crystal cementation) plays a destructive role in the reservoir. The microscopic photographs and SEM observations of the reservoir section of the Maokou Formation in the study area demonstrate that the cementation type of the reservoir section of the Maokou

10.3389/feart.2025.1494518

TABLE 3 TOC, porosity, XRD, and whole rock mineral composition analyses of the samples.

Number	Depth (m)	Lithology	TOC (%)	Porosity (%)	Calcite (%)	Dolomite (%)	Quartz (%)	Clay mineral (%)	Specific surface area (m^2/g)	Pore volume (cm^3/g)
a	4423.05	Argillaceous limestone	0.2	0.46	100	0	0	0	5.3090	0.008422
b	4433.09	Argillaceous limestone	0.77	3.01	83.1	1.7	9.9	5.3	8.1594	0.015098
c	4451.82	Argillaceous limestone	0.38	0.54	92.8	2.1	5.2	0	5.8230	0.011037
d	4452.63	Argillaceous limestone	0.18	0.82	94.9	1	4.1	0	4.8842	0.008655

Formation in the study area primarily consists of calcite mud crystal and mud cementations in the eyelid tuff section with high mud content. The impact of different mineral components on the reservoir in Figure 11 reveals a negative correlation among pore volume, specific surface area, pore structure parameters, and calcite content and a positive correlation with clay mineral content (Figures 11a–d). This finding indicates that the mud crystal cementation of calcite exerts a destructive effect on the reservoir.

5.4 Petroleum geology significance

Overall, the analysis of thin sections, physical properties, XRD, nitrogen adsorption, SEM, TOC, and logging indicates that the reservoirs are mostly developed in the lower part of Mao-1a and the upper part of Mao-1c. In contrast, the reservoirs in Mao-1b are largely undeveloped. The reservoir lithofacies are mostly composed of argillaceous limestone and bioclastic micritic limestone microfacies with a high shale content. The reservoir pores mainly possess micropores and mesopores, such as organic matter pores and clay mineral shrinkage pores. The nitrogen adsorption experiments showed that the pore sizes are mostly <4 nm, mainly being micropores. Hu et al. (2007) argued that as the pore size increases, the gas stored in the pore changes from an adsorbed state to a free state. The existence of a larger pore volume leads to a higher free gas content. In addition, a larger total volume of micropores induces a bigger specific surface area (Zhong et al., 2002; Xu et al., 2009). Taking into account that the spacing between the pore walls and adsorbate is very small, the ability to adsorb gas is stronger than that of wider pores. Therefore, the force between the pore surfaces and the adsorbate is stronger than that of larger pores (Lozano Castello et al., 2002). Hence, in this kind of ultra-low-porosity and low-permeability reservoir, the presence of nano-scale pores significantly improves natural gas enrichment; however, at the same time, it complicates the overall model.

In recent years, the exploration of dense carbonate reservoirs is constantly increasing (Farouk et al., 2024a; Farouk et al., 2024b; Farouk et al., 2024c; Farouk et al., 2024d). For example, the Dalan Formation in the Permian System of the Persian Gulf, the Apollonia Formation in the western desert of Egypt, and the S1 formation in the Indus Basin on the Pakistani landmass have all achieved gas discoveries in dense limestone reservoirs (Kidambi and Kumar, 2016; Gomaa et al., 2019; Durrani et al., 2020). Afşar et al. (2014) studied the dense carbonate reservoirs in the Bristol Channel and found that argillaceous limestone exhibits a higher non-interlayer fracture percentage than micrite limestone. This result suggests that argillaceous limestone reservoirs have better reservoir properties compared to micrite limestone. These cases prove that argillaceous limestone reservoirs have good exploration prospects in the field of unconventional reservoirs. This work provides a detailed analysis of the characteristics of argillaceous limestone reservoirs and proposes the main controlling factors affecting their development, which can be compared with similar dense carbonate reservoirs globally.

6 Conclusion

In this work, a systematic analysis was performed using SEM imaging, XRD and TOC analysis, as well as studying nitrogen adsorption and other experimental data to comprehensively analyse the reservoir characteristics of Mao-1 members in southeastern Sichuan, elucidating the primary controlling factors and filling in the gaps in this area. From our analysis, the following can be drawn.

1. The reservoir rock types of Mao-1 members in southeastern Sichuan are mainly composed of micritic limestone, bioclastic micritic limestone, and argillaceous limestone. The mineral composition is primarily calcite. Clay minerals are primarily talc.
2. The TOC content in argillaceous limestone is relatively high, and it is relatively enriched in the Mao-1a sub-member. The range of vitrinite reflectance (Ro) values for the organic matter in the Mao-1 member, is between 1.57% and 1.60%, indicating that the organic matter is primarily in the high maturity stage of thermal evolution.
3. There are six main types of reservoir spaces in the Mao-1 member: intergranular pores, dissolution pores, organic matter pores, fractures related to bioclastic, interlayer fractures of clay minerals, and macroscopic fractures. The porosity of argillaceous limestone is relatively high. The overall characteristics are of a low-porosity and low-permeability tight limestone reservoir.
4. The pores of the carbonate reservoir of the Mao-1 member are mainly composed of micropores and mesopores with a diameter of about 4 nm. Their morphology is mainly slit-like pores comprising flaky clay and rigid particles.
5. The reservoir formation in the Mao-1 member is mainly affected by the lithofacies, organic matter content, clay mineral transformation, dolomitization, dissolution, and other diagenesis. The transformation of clay minerals can create a large number of shrinkage pores, which is key to the quality of the reservoir; clay minerals also adsorb a significant amount of organic matter, promoting the formation of organic matter pores and enhancing the storage performance. Dissolution processes provide additional storage space, further modifying the reservoir, while micritic cementation of calcite has a destructive effect on the reservoir. Clay minerals and argillaceous limestone with higher TOC content are the main high-quality reservoirs.

Data availability statement

The original contributions presented in the study are included in the article/supplementary material, further inquiries can be directed to the corresponding author.

Author contributions

RY: Conceptualization, Investigation, Writing - review and editing, Validation, Writing - original draft. XY: Conceptualization, Investigation, Writing - original draft, Data curation, Validation, Writing - review and editing. YZ: Conceptualization, Writing - original draft, Data curation, Investigation. YD: Investigation, Validation, Writing - original draft. LQ: Investigation, Writing - original draft. YL: Data curation, Investigation, Writing - original draft. XF: Conceptualization, Investigation, Writing - original draft.

Funding

The author(s) declare that financial support was received for the research and/or publication of this article. Open funding of State Key Laboratory of Shale Oil and Gas Enrichment Mechanisms and Effective Development (G5800-20-ZS-KFGY010).

Conflict of interest

Authors YZ, YD, and LQ were employed by PetroChina Southwest Oil and Gasfield Company.

The remaining authors declare that the research was conducted in the absence of any commercial or financial relationships that could be construed as a potential conflict of interest.

Publisher's note

All claims expressed in this article are solely those of the authors and do not necessarily represent those of their affiliated organizations, or those of the publisher, the editors and the reviewers. Any product that may be evaluated in this article, or claim that may be made by its manufacturer, is not guaranteed or endorsed by the publisher.

References

Afşar, F., Westphal, H., and Philipp, S. L. (2014). How facies and diagenesis affect fracturing of limestone beds and reservoir permeability in limestone–marl alternations. *Mar. Pet. Geol.* 57, 418–432. doi:10.1016/j.marpetgeo.2014.05.024

Bao, H. Y., Zhao, S., Wang, B. J., Guo, Z. F., Liu, H. T., Zhang, L., et al. (2024). Exploration breakthrough and main controlling factors for shale gas enrichment in the Permian Maokou Formation in Hongxing area in eastern Sichuan Basin. *China Pet. Explor.* 29 (1), 65–75. doi:10.3969/j.issn.1672-7703.2024.01.005

Cai, Z. X., Li, J., Chen, H. R., Cong, F. Y., Wu, N., Wang, L. J., et al. (2019). Genesis of Mg-phyllosilicate occurrences in the middle permian marine successions of south China. *Appl. Clay Sci.* 181, 105242. doi:10.1016/j.clay.2019.105242

Cao, H., Chen, Y. G., Chen, C., Gao, Z. L., Shan, S. J., Li, T. J., et al. (2022). Controlling factors of karst reservoir in Maokou Formation, northeastern Sichuan Basin. *Nat. Gas Explor. Dev.* 45 (3), 1–10. doi:10.12055/gaskk.issn.1673-3177.2022.03.001

Chacrone, C., Hamoumi, N., and Attou, A. (2004). Climatic and tectonic control of Ordovician sedimentation in the western and central High Atlas (Morocco). *J. Afr. Earth Sci.* 39 (3), 329–336. doi:10.1016/j.jafrearsci.2004.07.035

Chen, Y. J., Wang, P. Y., and Ren, L. F. (1985). Transformation of sepiolite into talc during diagenesis. *Chin. Sci. Bull.* 36 (4), 284–287.

Chen, Z. Q. (2007). Exploration for natural gas in middle permian Maokou Formation of Sichuan Basin. *China Pet. Explor.* 05, 1–11. doi:10.3969/j.issn.1672-7703.2007.05.001

Courtinat, B. (1993). The significance of palynofacies fluctuations in the greenhorn formation (Cenomanian-Turonian) of the western interior basin, USA. *U. S. A Mar. Micropaleontolgy* 21 (1), 249–257. doi:10.1016/0377-8398(93)90017-R

Davaud, E., and Lombard, A. (1975). Statistical approach to the problem of alternating beds of limestone and marl (Upper Oxfordian of the French Jura). *Eclogae Geol. Helv.* 68 (3), 491–509.

Dong, Y. X., Chen, H. D., Wang, J. Y., Hou, M. C., Xu, S. L., Zhu, P., et al. (2020). Thermal convection dolomitization induced by the emeishan large igneous Province. *Mar. Pet. Geol.* 116, 104308. doi:10.1016/j.marpetgeo.2020.104308

Durrani, M. Z. A., Talib, M., Ali, A., Sarosh, B., and Naseem, N. (2020). Characterization and probabilistic estimation of tight carbonate reservoir properties using quantitative geophysical approach:a case study from a mature gas field in the Middle Indus Basin of Pakistan. *J. Pet. Explor. Prod. Technol.* 10 (7), 2785–2804. doi:10.1007/s13202-020-00942-0

Fan, C. H., Li, H., Qin, Q. R., He, S., and Zhong, C. (2020a). Geological conditions and exploration potential of shale gas reservoir in Wufeng and Longmaxi Formation of southeastern Sichuan Basin, China. *J. Petrol. Sci. Eng.* 191, 107138. doi:10.1016/j.petrol.2020.107138

Fan, J. P., Song, J. M., Liu, S. G., Jiang, Q. C., Li, Z. W., Yang, Di, et al. (2023). Paleotemperature evolution and its driving mechanism during the formation of limestone-marl alternations in first member of Middle Permian Maokou Formation in Sichuan Basin. *Shiyou shiyan dizhi* 45 (4), 726–738. doi:10.11781/sysydz202304726

Farouk, S., Fagelnour, M., Zaky, A. S., Arafat, M., Salama, A., Al-Kahtany, K., et al. (2024b). Petroleum system evaluation: hydrocarbon potential and basin dynamics in abu darag sub-basin, northern Gulf of suez (Egypt). *Minerals* 14 (11), 1154. doi:10.3390/min14111154

Farouk, S., Saada, S. A., Fagelnour, M., Tawfik, A. Y., Arafat, M., and El-Kahtany, K. (2024d). Geochemical evaluation and basin modelling of the cretaceous succession in the azhar oil field, west beni suef basin, Egypt. *Geol. J.* 59 (7), 1949–1967. doi:10.1002/gj.4979

Farouk, S., Saada, S. A., Fagelnour, M. S., and Arafat, M. (2024a). Petrophysical and gas chromatographic analysis integration for hydrocarbon identifications in cretaceous reservoirs, azhar field, beni suef basin, Egypt. *Egypt. J. Petroleum* 33 (1), 7. doi:10.62593/2090-2468.1018

Farouk, S., Sen, S., Ahmed, F., Qteishat, A., Al-Kahtany, K., Moreno, H. M., et al. (2024c). Assessment of the upper cretaceous abu roash carbonate source rocks from the beni suef field, western desert, Egypt. *J. Afr. Earth Sci.* 215, 105272. doi:10.1016/j.jafrearsci.2024.105272

Gomaa, S., Attia, A., and Abdelhady, A. (2019). Well testing analysis of unconventional gas reservoirs: real case study of tight gas carbonate reservoir, Apollonia Formation, Western Desert, Egypt. *Int. J. Petroleum Petrochem. Eng.* 5 (1), 1–5. doi:10.20431/2454-7980.0501002

Hao, Y., Yao, Q. Y., Tian, H., Gu, M. F., She, M., and Wang, Y. (2020). Sedimentary characteristics and reservoir-controlling factors of the permian Maokou Formation in Sichuan Basin. *Mar. Orig. Pet. Geol.* 25 (3), 202–209. doi:10.3969/j.issn.1672-9854.2020.03.002

He, S., Tan, W. C., Li, H., Wang, Y., Niu, P. F., and Qin, Q. R. (2025). Mineralogical and lithofacies controls on gas storage mechanisms in organic-rich marine shales. *Energy Fuel.* 39 (8), 3846–3858. doi:10.1021/acs.energyfuels.4c05685

Holmden, C., Creaser, R. A., Muehlenbachs, K., Leslie, S. A., and Bergström, S. M. (1998). Isotopic evidence for geochemical decoupling between ancient epeiric seas and bordering oceans: implications for secular curves. *Geology.* 26 (6), 567–570. doi:10.1130/0091-7613(1998)026<0567:iefgdb>2.3.co;2

Hu, A., Pan, Y. S., Tang, J. P., Li, C. Q., and Dong, Z. X. (2007). Experiment research of adsorption and NMR on the noulding coal. *Clean. Coal Technol.* 13 (3), 37–40. doi:10.13226/j.issn.1006-6772.2007.03.003

Hu, A. P., Pan, L. Y., Hao, Y., Shen, A. J., and Gu, M. F. (2018). Origin, characteristics and distribution of dolostone reservoir in Qixia Formation and Maokou Formation, Sichuan Basin, China. *Mar. Orig. Pet. Geol.* 23 (2), 39–52. doi:10.3969/j.issn.1672-9854.2018.02.006

Hu, D. F., Wang, L. J., Huang, R. C., Duan, J. B., Xu, Z. X., and Pan, L. (2019). Characteristics and main controlling factors of the Middle Permian Maokou dolomite reservoirs in the eastern Sichuan Basin. *Nat. Gas. Ind.* 39 (6), 13–21. doi:10.3787/j.issn.1000-0976.2019.06.002

Hu, D. F., Wang, L. J., Zhang, H. R., Duan, J. B., Xia, W. Q., Liu, Z. J., et al. (2021). Discovery of carbonate source rock gas reservoir and its petroleum geological implications: a case study of the gas reservoir in the first Member of Middle Permian Maokou Formation in the Fuling area, Sichuan Basin. *Nat. Gas. Ind. B* 8 (1), 13–23. doi:10.1016/j.ngib.2020.07.001

Huang, J. Z., and Lü, Z. G. (2011). How to judge carbonate rock as source rock: a case of Sichuan Basin. *Mar. Orig. Pet. Geol.* 16 (3), 8–14. doi:10.3787/j.issn.1000-0976.2020.07.003

Huang, S. P., Jiang, Q. C., Wang, Z. C., Su, W., Feng, Q. F., and Feng, Z. (2016). Differences between the middle permian Qixia and Maokou source rocks in the Sichuan Basin. *Nat. Gas. Ind.* 36 (12), 26–34. doi:10.3787/j.issn.1000-0976.2016.12.004

Jiang, Q. C., Hu, S. Y., Wang, Z. C., Chi, Y. L., Yang, Y., Lu, W. H., et al. (2012). Paleokarst landform of the weathering crust of middle permian Maokou Formation in Sichuan Basin and selection of exploration regions. *Acta Pet. Sin.* 33 (6), 949–960. doi:10.7623/syxb201206005

Kidambi, T., and Kumar, G. S. (2016). Mechanical earth modeling for a vertical well drilled in a naturally fractured tight carbonate gas reservoir in the Persian Gulf. *J. Pet. Sci. Eng.* 141, 38–51. doi:10.1016/j.petrol.2016.01.003

Lei, H. (2021). Enesis and reservoir microscopic characteristics of eyelid-eyeball-shaped limestone in the 1st member of Maokou Formation, Sichuan Basin. *China Univ. Geosci. (Beijing)*.

Lei, L., Zhang, L. S., and Xiong, W. (2020). Acid fracturing technology of Maokou Formation in well- dashi- 1HF, southeastern chongqing. *Reserv. Eval. Dev.* 10 (5), 84–90. doi:10.13809/j.cnki.cn32-1825/te.2020.05.012

Li, H., Duan, H. T., Qin, Q. R., Zhao, T. B., Fan, C. H., Luo, J., et al. (2025a). Characteristics and distribution of tectonic fracture networks in low permeability conglomerate reservoirs. *Sci. Rep.* 15, 5914. doi:10.1038/s41598-025-90458-6

Li, H., He, S., Radwand, A. E., Xie, J. T., and Qin, Q. R. (2024). Quantitative analysis of pore complexity in lacustrine organic-rich shale and comparison to marine shale: insights from experimental tests and fractal theory. *Energy Fuel.* 38 (17), 16171–16188. doi:10.1021/acs.energyfuels.4c03095

Li, H. J., Xie, X. N., Huang, J. H., Chen, H., and Lin, Z. L. (2012). Main factors controlling the formation of excellent marine source rocks in Permian Maokou formation of northwest Sichuan, China. *Earth Science-Journal China Univ. Geosciences* 37 (1), 171–180. doi:10.3799/dqkx.2012.017

Li, R., Su, C. P., Shi, G. S., Jia, H. F., Li, S. H., and Yu, Y. (2021). The genesis of nodular limestone reservoirs of the first period of Maokou Formation of Permian in southern Sichuan Basin. *Nat. Gas. Geosci.* 32 (6), 806–815. doi:10.11764/j.issn.1672-1926.2021.02.005

Li, J., Zhang, Q., Jiang, W., Li, H., Li, L., Xue, T. F., et al. (2025b). Lithological controls on pore structure and their ımplications for deep shale gas reservoir quality in the Longmaxi Formation, Luzhou area, Southern Sichuan Basin, China. *Energy Fuel.* 39 (3), 1541–1558. doi:10.1021/acs.energyfuels.4c05247

Liang, D. G., Guo, T. L., Chen, J. P., Bian, L., and Zhao, Z. (2008). Some progresses on studies of hydrocarbon generation and accumulation in marine sedimentary regions, southern China (Part 1): distribution of four suits of regional marine source rocks. *Mar. Qrigin Pet. Geol.* 13 (2), 1–16. doi:10.3969/j.issn.1672-9854.2011.03.002

Liu, J., He, X., and Xue, F. (2024). The influence of natural fractures of multi-feature combination on seepage behavior in shale reservoirs. *J. Min. Strata Control Eng.* 6 (1), 013437. doi:10.13532/j.jmsce.cn10-1638/td.20240018.001

Liu, J., Xia, W., Li, J. J., Zhang, X., Li, R., and Wang, L. (2019). Analysis of reservoir characteristics of the first member of Maokou Formation in southeastern Sichuan Basin. *Bull. Sci. Technol.* 35 (7), 26–32. doi:10.13774/j.cnki.kjtb.2019.07.006

Liu, W. D., Zhong, D. K., Yin, H., Sun, H., Liang, X., Li, R., et al. (2021). Development characteristics and main controlling factors of ultra-deep dolomite reservoirs of the Qixia Formation in the northwestern Sichuan Basin. *J. China Univ. Min. and Technol.* 50 (2), 342–362. doi:10.13247/j.cnki.jcumt.001203

Loucks, R. G., Reed, R. M., Ruppel, S. C., and Jarvie, D. M. (2009). Morphology, genesis, and distribution of nanometer-scale pores in siliceous mudstones of the mississippian barnett shale. *J. Sediment. Res.* 79 (12), 848–861. doi:10.2110/jsr.2009.092

Lozano Castello, D., Alcaniz Monge, J., Lillo, C., Cazorla Amoros, D., and Linares Solano, A. (2002). Advances in the study of methane storage in porous carbonaceous materials. *Fuel* 81 (14), 1777–1803. doi:10.1016/S0016-2361(02)00124-2

Ma, Y. S., Cai, X. Y., Zhao, P. R., Luo, Y., and Zhang, X. F. (2010). Distribution and further exploration of the large-medium sized gas fields in Sichuan Basin. *Acta Pet. Sin.* 31 (03), 347–354. doi:10.7623/syxb201003001

Miiller, J., and Fabrieius, F. (1977). Magnesian-Calcite nodules in the Ionian deep sea, an actualistic model for the formation of some nodular limestones Spec. *Publs Int. Ass.Sediment.* 1, 235–247. doi:10.1002/9781444304855.ch10

Moller, N. K., and Vingan, K. (1988). The genesis of nodular limestones in the Ordovician and Silurian of the Oslo Region (Norway). *Sedimentology.* 35 (3), 405–420. doi:10.1111/j.1365-3091.1988.tb00994.x

Reinhardt, E. G., Cavazza, W., Patterson, R. T., and Blenkinsop, J. (2000). Differential diagenesis of sedimentary components and the implication for strontium isotope analysis of carbonate rocks. *Chem. Geol.* 164 (3-4), 331–343. doi:10.1016/S0009-2541(99)00147-3

Rey, O., Simo, J. A., and Lorente, M. A. (2004). A record of long- and short-term environmental and climatic change during OAE3: La Luna Formation, Late Cretaceous (Santonian-early Campanian), Venezuela. *Sediment. Geol.* 170 (1-2), 85–105. doi:10.1016/j.sedgeo.2004.06.006

Samtleben, C., Munnecke, A., and Bickert, T. (2000). Development of facies and C/O-isotopes in transects through the Ludlow of Gotland: evidence for global and local influences on a shallow-marine environment. *Facies.* 43 (1), 1–38. doi:10.1007/BF02536983

Su, C. P., Tan, X. C., Wang, X. F., Li, F., Lu, F. F., Li, M. L., et al. (2020). Characteristics of eyeball-shaped limestone reservoir and its genesis of the middle

permian Maokou Formation in east Sichuan Basin. *Mar. Orig. Pet. Geol.* 25 (1), 55–62. doi:10.3969/j.issn.1672-9854.2020.01.006

Taylor, B., and Hayes, D. E. (2013). Origin and History of the South China Sea Basin. *The Tectonic and Geologic Evolution of Southeast Asian Seas and Islands: Part 2* 98, 23–56. doi:10.1029/GM027p0023

Tian, X., Shi, J., Dong, J., Tan, W. C., Yin, C. H., Li, Q., et al. (2021). New understanding of sedimentary facies of the first Member of Maokou Formation based on the latest drilling in central Sichuan Basin. Nat. *Gas. Geosci.* 32 (11), 1646–1655. doi:10.11764/j.issn.1672-1926.2021.05.001

Wei, X. F., Liu, R. B., Zhang, T. S., and Liang, X. (2013). Micro-pores structure characteristics and development control factors of shale gas resetvoir: a caxe of longmaxi Formation in xx area of southern sichuan and northern guizhou. *Nat. Gas. Geosci.* 24 (05), 1048–1059. doi:10.11764/j.issn.1672-1926.2013.05.1048

Wendler, I., Wendler, J. E., and Clarke, L. J. (2016). Sea-level reconstruction for Turonian sediments from Tanzania based on integration of sedimentology, microfacies, geochemistry and micropaleontology. *Palacogeogr. Palaeoclimatol. Palaeoecol.* 441 (3), 528–564. doi:10.1016/j.palaeo.2015.08.013

Westphal, H., Head, M. J., and Munnecke, A. (2000). Differential diagenesis of rhythmic limestone alternations supported by palynological evidence. *J. Sediment. Res.* 70 (3), 715–725. doi:10.1306/2DC40932-0E47-11D7-8643000102C1865D

Westphal, H., and Munnecke, A. (1997). Mechanical compaction versus early cementation in fine-grained limestones: differentiation by the preservation of organic microfossils. *Sediment. Geol.* 112 (1-2), 33–42. doi:10.1016/S0037-0738(97)00033-X

Westphal, H., and Munnecke, A. (2003). Limestone-marl alternations: a warm-water phenomenon? *Geology.* 31 (3), 263–266. doi:10.1130/0091-7613(2003)031<0263:lmaaww>2.0.co;2

Westphal, H., Munnecke, A., and Brandano, M. (2008). Effects of diagenesis on the astrochronological approach of defining stratigraphic boundaries in calcareous rhythmites: the Tortonian GSSP. *Lethaia.* 41 (4), 461–476. doi:10.1111/j.1502-3931.2008.00101.x

Xie, S. Y., Wang, X. Z., Li, B., Jiang, H., Du, Y., Zhang, R., et al. (2022). Analysis of the diagenetic fluid of deep dolomitic "Leopard-Spot" limestones in the middle permian Qixia Formation in shuangyushi region in northwest Sichuan Basin, China. *Front. Earth Sci.* 10, 931834. doi:10.3389/feart.2022.931834

Xu, M. G., Ma, Z. H., Chen, J., and Xu, S. Q. (2009). Experimental study on influencing factors of adsorption properties of methane on coal. *Mineral Eng. Res.* 24 (2), 51–54.

Yang, S., Chen, A. Q., Zhang, X. H., Li, Q., Xu, S. L., Chen, C., et al. (2021). Paleogeographic transition of the permian chihsia-maokou period in the Sichuan Basin and indications for oil-gas exploration. *Acta Sedimentol. Sin.* 39 (6), 1466–1477. doi:10.14027/j.issn.1000-0550.2021.072

Yang, W. J., Tan, X. C., Tang, D. H., Zhang, Z. K., Hu, X., Li, M. L., et al. (2023). Sequence lithofacies paleogeography evolution of the middle permian Maokou Formation in the northwest margin of the Sichuan Basin. *Front. Earth Sci.* 11, 1301302. doi:10.3389/feart.2023.1301302

Yang, Z. Q., and Xu, J. W. (1986). The formation and post-sedimentary alternation of sepiolite in Pingle Depression. *Bulletin* 12, 31–51.

Yuan, Z., Chen, L., Mu, Z. C., Liao, L., Lai, Y. G., Li, K. L., et al. (2020). Genesis of nodular limestones from the lower triassic yinkeng Formation in chaohu region. *J. Xi'an Univ. Sci. Technol.* 40 (4), 672–681. doi:10.13800/j.cnki.xakjdxxb.2020.0415

Zeng, D. M., Xie, X. B., Huang, D., Yu, L. Z., and Zhang, Y. (2023). Sedimentary characteristics of the Maokou Formation of the permian in northern Sichuan Basin and its petroleum significance. *J. Southwest Petroleum Univ.* 45 (1), 1–12. doi:10.11885/j.issn.1674-5086.2020.12.24.04

Zhai, C. B., Lin, L. B., You, D. H., Liu, F. B., and Liu, S. Y. (2024). Sedimentary microfacies characteristics and organic matter enrichment pattern of the 1st member of the Middle Permian Maokou Formation, southwestern Sichuan Basin. *Oil Gas Geol.* 45 (2), 440–456. doi:10.11743/ogg20240210

Zhao, P. R. (2021). Reservoir characteristics and gas exploration potential of permian Mao- 1 member of Maokou Formation in jiaoshiba area. *Reserv. Eval. Dev.* 11 (5), 772–781. doi:10.13809/j.cnki.cn32-1825/te.2021.05.016

Zhong, L. W., Zhang, H., Yun, Z. R., and Lei, C. L. (2002). Influence of specific pore area and pore volume of coal on adsorption capacity. *Coal Geol. and Explor.* 3, 26–29. doi:10.3969/j.issn.1001-1986.2002.03.008

frontiers | Frontiers in Earth Science

TYPE Original Research
PUBLISHED 11 April 2025
DOI 10.3389/feart.2025.1552826

OPEN ACCESS

EDITED BY
Hu Li,
Sichuan University of Science and Engineering, China

REVIEWED BY
Binfeng Cao,
Institute of Geology and Geophysics (CAS), China
Yuqiang Jiang,
Southwest Petroleum University, China

*CORRESPONDENCE
Fanghao Xu,
xufanghao17@cdut.edu.cn

RECEIVED 29 December 2024
ACCEPTED 21 March 2025
PUBLISHED 11 April 2025

CITATION
Li A, Xu F, Fan C, Li M, Jiang F, Xu G, Xiong X, Zhang X and Xie B (2025) Formation process and controlling factors of tight buried-basement hill reservoirs:a case study of Weixinan Depression, Northern Beibu Gulf Basin, South China.
Front. Earth Sci. 13:1552826.
doi: 10.3389/feart.2025.1552826

Formation process and controlling factors of tight buried-basement hill reservoirs:a case study of Weixinan Depression, Northern Beibu Gulf Basin, South China

Anran Li[1,2], Fanghao Xu[1]*, Caiwei Fan[3], Ming Li[3], Fan Jiang[3], Guosheng Xu[1], Xiaojun Xiong[1], Xichun Zhang[1] and Bing Xie[1]

[1]State Key Laboratory of Oil and Gas Reservoir Geology and Exploitation, Chengdu University of Technology, Chengdu, China, [2]Southwest Petroleum University, Chengdu, China, [3]China National Offshore Oil Corporation, Zhanjiang Branch, Zhanjiang, China

In relatively stable sedimentary basins, the formation of buried-basement hill reservoirs mainly occurs after the basin basement forms and before the overlying sedimentary cover layer is filled. Represented by the Beibu Gulf Basin in the South China Sea, buried-basement hill reservoirs are key targets for hydrocarbon exploration in deep sedimentary basins. Limited exploration and research in buried-basement hills hinder the understanding of hydrocarbon accumulation conditions, thereby restricting large-scale hydrocarbon exploration. Geophysical methods, including the balanced section method and stress field analysis, were used to restore the formation and burial processes of buried-hills in the Weixinan Depression of Beibu Gulf Basin. The formation process of these buried-basement hills consists of five stages including diapiric uplift (Caledonian period), thrust (Indosinian-Yanshanian period), multiple exposure (Late Caledonian, and Indosinian-Yanshanian period), multiple burials (Hercynian period and Early Himalayan Period), and finalization (Late Himalayan Period). Three controlling factors of these buried-basement hills are determined: ①differences in the degree of granite intrusion lead to differences in karst paleogeomorphology; ②thrust movement of NE-SW direction during the Hercynian period; ③ thrust movement of NW-SE direction during the Indosinian-Yanshanian. The main controlling factors for the development of buried-carbonate basement hill reservoirs are multi-stage tectonic stress, karstification, and lithology. The tight buried-carbonate hill reservoir mainly composed of dissolved pore and fracture is concentrated in horizontal underflow zone. The main controlling factors for the development of buried-granite (or metamorphic rock) hill reservoirs are tectonic stress, and karstification. The reservoir mainly composed of dissolved pore and fracture is concentrated in leaching zone located at the top of each buried-granite and metamorphic rocks hill.

KEYWORDS

paleozoic, buried-basement hill, tectonic evolution, controlling factor, Beibu Gulf Basin, Weixinan depression

1 Introduction

Basement oil and gas reservoirs refer to oil and gas accumulation in the crystalline basement of a basin, with reservoir rock types consisting of metamorphic or igneous rocks (Walters, 1953; P'an, 1982). As exploration deepens, the academic community has proposed that the formation of basement hydrocarbon reservoirs is linked to basin evolution (Kosachev et al., 2019). In recent years, basement reservoirs have been defined as hydrocarbon or fluid reservoirs formed in crystalline basement or sedimentary rocks prior to basin formation (Kutcherov and Krayushkin, 2010; Carvalho et al., 2013). The reservoir lithology can be metamorphic or igneous rocks, or sedimentary rocks (Ye et al., 2022; Parnell et al., 2017; Wang et al., 2023). The statistical results of hydrocarbon exploration cases worldwide indicate that hydrocarbon resources carried by basement are widely distributed worldwide (Gao et al., 2008; Azaiez et al., 2018; Rodríguez-Cuevas et al., 2024). The global number of basement oil and gas fields and the proportion of recoverable hydrocarbon reserves are 9.3%, 10.2%, and 2.7%, respectively (Wang et al., 2024). Buried-basement hill reservoirs are an major type of basement reservoirs (Salah and Alsharhan, 1998; Mazzullo et al., 2009). The formation of buried-basement hills often involves complex tectonic evolution, along with alterations in diagenetic fluids, which complicate the reservoir formation mechanism (Xing, 1993; Guo et al., 2017). Moreover, compared to carbonate and clastic reservoirs, the exploration risk of buried-basement hill reservoirs is high (Zhao et al., 2015; Zhao et al., 2018), the degree of exploration is low, and the understanding of reservoir formation conditions and distribution patterns is still unclear.

The tectonic zone between the Eurasian and Pacific Plates is a key area for basement oil and gas reservoir distribution (Liu et al., 2022). Due to the compression and subduction of the Indosinian Pacific Plate, numerous buried-basement hills formed in the South China Sea, including the Beibu Gulf Basin (Kerimov et al., 2019). In recent years, exploration has revealed the enormous potential of hydrocarbon resources in buried-basement hill reservoirs (Wang et al., 2024; Deng et al., 2024). The geological setting of Bohai Bay basin is similar to that of Beibu Gulf Basin, with complex stratigraphic structure and diverse types of buried-hills (Yi et al., 2022; Zhu et al., 2024). The tectonic dynamics, reservoir formation conditions and hydrocarbon accumulation model of buried-hill formation in Bohai Bay basin have been gradually revealed in recent years (Xu et al., 2024).

Compared with the Bohai Bay Basin, in the Beibu Gulf Basin, there are multiple lithologies present in the reservoir, and the differences in reservoir space types, porosity, and permeability among different lithologies are significant, which restricts the efficient exploration and development of this type of hydrocarbon resources. The complex structural history leads to complex diagenetic alteration in the later stage (Liu et al., 2017; Qin et al., 2020), with strong heterogeneity in the degree of alteration. There is a lack of research on the controlling factors of reservoir formation in different rock types of basement (Zhao et al., 2019). Extensive drilling, logging, and geophysical data from the Beibu Gulf Basin provide valuable insights into the genesis of buried-basement hill reservoirs. Using the latest 2D and 3D seismic and drilling data, the Weixinan Depression in the Beibu Gulf Basin was chosen as the research focus, revealing the formation mechanism of buried-hills under tectonic evolution conditions. By combining elements, isotopes, and microscopic temperature measurements, the controlling factors of buried-basement hill reservoirs are analyzed, providing a theoretical foundation for efficient exploration.

2 Geological setting

The Beibu Gulf Basin extends from the Guangdong-Guangxi Uplift in the north to the Hainan Uplift in the south and the Leizhou Peninsula in the east. It is a Cenozoic rift basin in the northern South China Sea. Based on the tectonic pattern formed during the Paleogene extensional stage, the basin is divided into three primary structural units from north to south: the northern depression zone, the Qixi Uplift, and the southern depression zone (Figure 1A). The Weixinan Depression is located in the northern depression of the Beibu Gulf Basin and is one of the two largest secondary structural units within the depression (Li et al., 2021). The stratigraphic column in the Weixinan Depression is composed of the Paleogene Changliu Formation, Liushagang Formation, Weizhou Formation, Neogene Xiayang Formation, Jiaowei Formation, Dengloujiao Formation, Wanglougang Formation, and Quaternary System from the bottom to the top (Figure 2). The basin has gone through two major stages of tectonic evolution: the rift stage in the Paleogene and the depression stage in the Neogene Quaternary. The rifting stage deposited continental clastic rocks including the Changliu Formation, Liushagang Formation, and Weizhou Formation, while the depression stage mainly consisted of marine clastic rock construction (Figure 1B).

3 Samples and methods

3.1 Petrographic and geochemical analysis

First, 25 samples from drilling cores of the buried-hill reservoir were polished twice, then impregnated with blue epoxy and stained with Alizarin red to identify different rock fabrics. Next, petrographic relationships of the different fabrics were delineated using a CL8200MK5 cathodoluminescence (CL) microscope. Fluid-inclusion microthermometry was performed on 25 samples using a calibrated Linkam THMS600 cooling-heating stage. The thermal cycling method was used to determine fluid inclusion homogenization temperature (Th) and melting ice temperature (Tm). The measurement precision for Th is ±1°C, and ±0.1°C for Tm. Forty-one samples were selected for Sr isotope measurement using a Finnigan Triton thermal ionization mass spectrometer (TIMS). Forty-one samples were selected for stable isotopic ($\delta^{18}O$, $\delta^{13}C$) measurement using MAT253 isotope mass spectrometer. The $\delta^{18}O$ and $\delta^{13}C$ data were normalized to Vienna Pee Dee Belemnite (V-PDB) standard and corrected by fractionation factors proposed by Fairchild and Spiro (1987). All the above tests were conducted at Chengdu University of Technology.

3.2 Seismic data analysis

The 3D seismic survey network mainly covers the No.2 and No.3 Main Faults in the study area. The post-stack 3D seismic channel

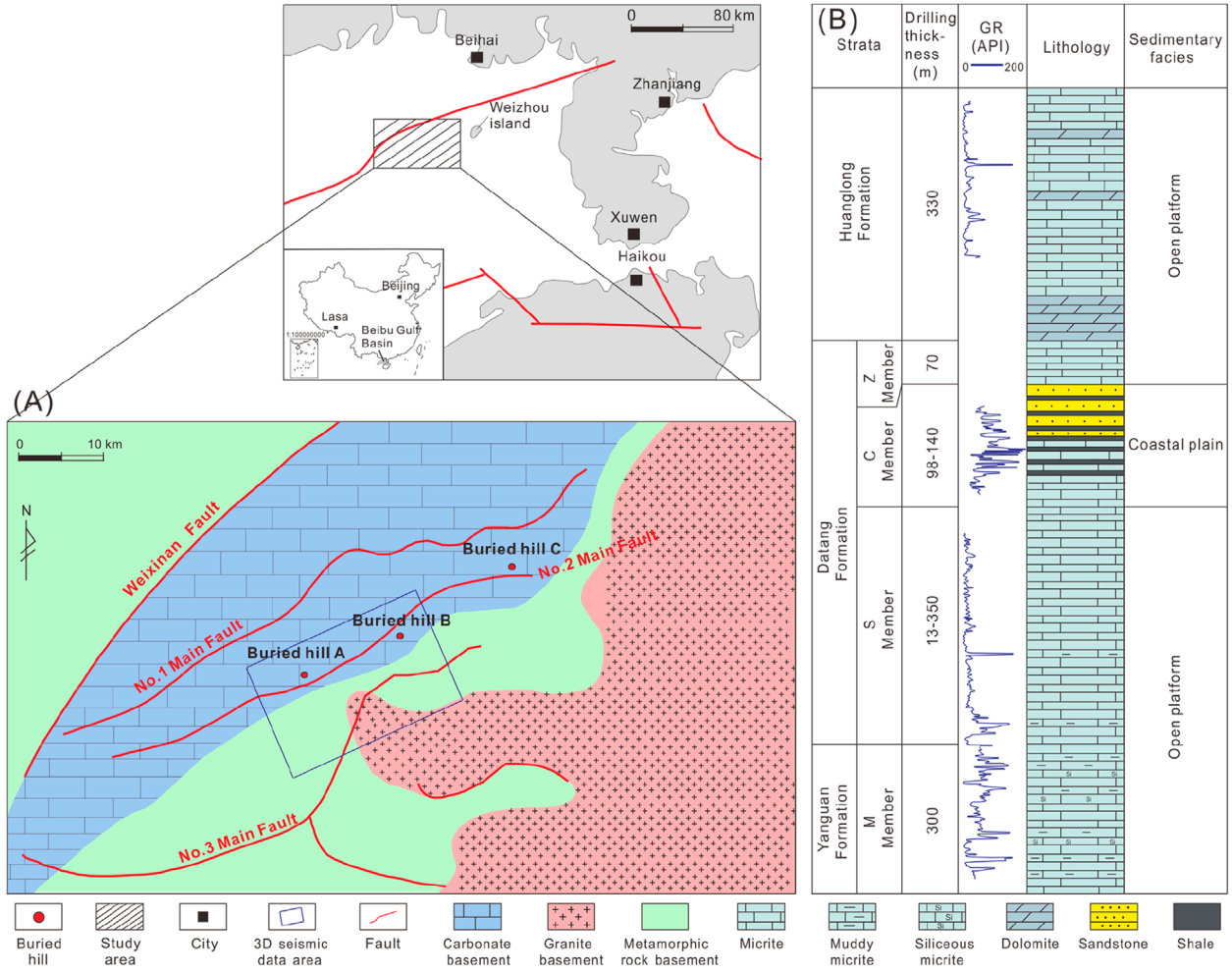

FIGURE 1
(A) Lithology of buried-basement hill and main fault distribution in Weixinan Depression of Northern Beibu Gulf Basin. **(B)** Stratigraphic column of buried-carbonate basement hill in Weixinan Depression of Northern Beibu Gulf Basin.

spacing is 12.5 m × 12.5 m, and the area is about 300 km^2. The logging stratification and lithologic data of all wells in 3D seismic area are complete. The borehole seismic calibration of 15 wells in the 3D seismic area has been completed. The synthetic records are basically consistent with the characteristics of the well side channel wave group, with high correlation coefficient, good well seismic matching relationship, accurate horizon calibration results, and the interface of the buried-hill is moderately strong wave crest reflection, laying the foundation for the subsequent detailed interpretation of seismic horizon and the analysis of interval velocity field. Due to the weak reflection energy within the buried-hill, directly interpreting the three-dimensional reflection of high, steep faults from the original data volume is challenging. Therefore, this study enhances the seismic data by amplifying steep dip angle reflections and applying low-pass filtering. The enhanced seismic data highlights the fault reflections (high, steep reflection signals) within the buried-hill, aiding in fault characterization. The interpretation of high, steep faults within the buried-hill was completed by combining the original data volume, enhanced data volume, and fully stacked data volume after optimizing the gathers.

3.3 Analytical techniques of stress field

Numerical simulation of structural deformation is an interdisciplinary research area that integrates methods from geology, geophysics, geochemistry, mathematics, computational mechanics, and computer science. The principle of numerical simulation experiments on geological structure deformation is to follow the basic laws of geological development, rely on advanced computer processing systems, and use geological models constructed from solid earth science data as the experimental research basis. Structural fractures are primarily controlled by changes in the tectonic stress field. In stress concentration zones, when stress exceeds the fracture threshold, rock deformation and fractures occur, forming structural fractures. The formation and development of structural fractures mainly focus on two types of structures: first, fractures, which can cause local stress concentration along the periphery of the fractures and the intersection of multiple fractures; The second is folding. When the strata undergo folding deformation, stress concentration areas will be formed at the turning points, and crack development areas will be formed in areas with significant changes

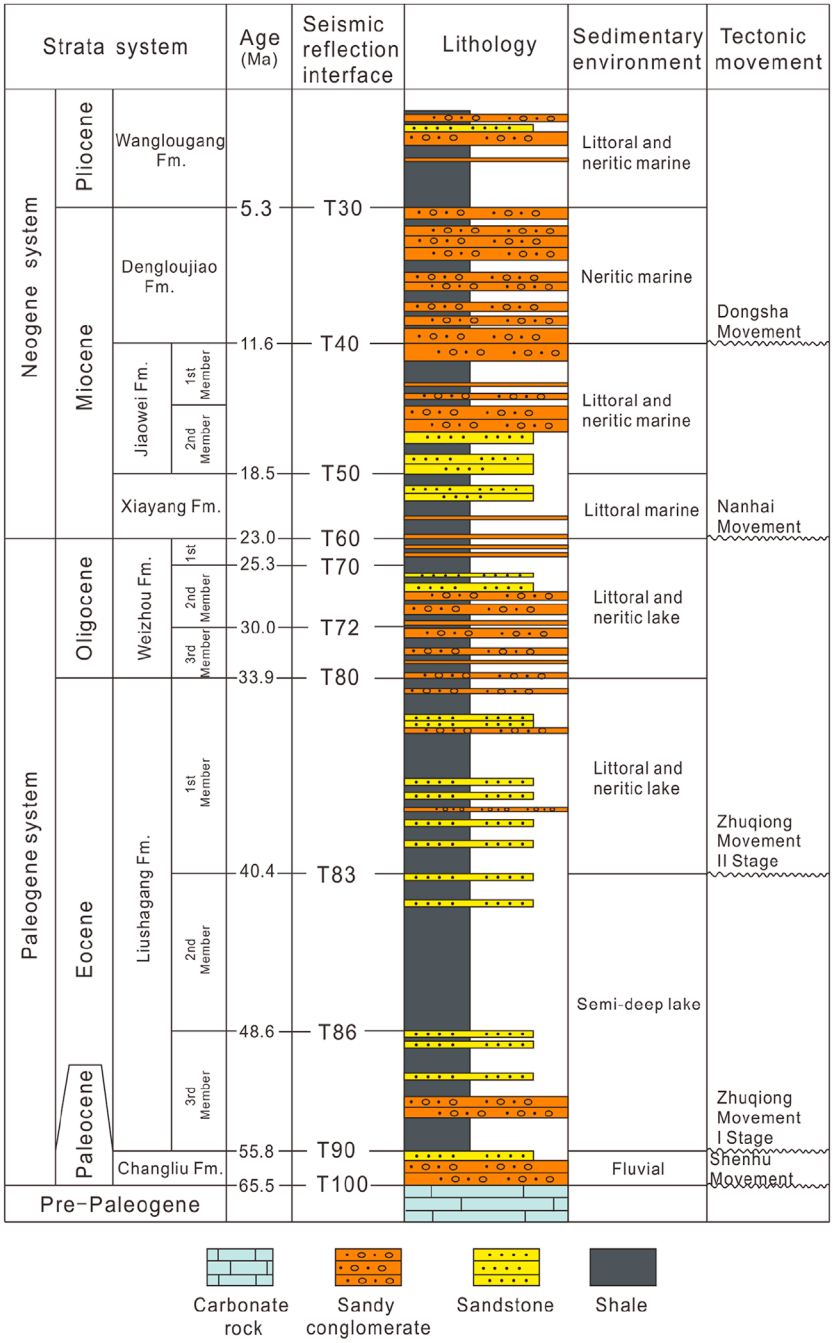

FIGURE 2
Stratigraphic column of overlying strata of buried-hill and tectonic evolution of Beibu Gulf Basin (modified from Li et al., 2018).

in folding curvature. In this study, to analyze the development of basement fractures in different structural units of the Beibu Gulf Basin, we selected drilling exploration wells for rock core observation and statistical fracture analysis. This was based on an analysis of the structural genesis system and the Cenozoic structural pattern. We constructed a geological model and applied numerical simulation methods for stress fields and fracture development across different periods of the basin. This allowed us to determine the extent and distribution of fractures in basement rocks across the main depressions of the basin. Based on the depth structure and elastic parameters of the top surface of the buried-hill (Figure 3A), the "thin-plate theory" is used for structural stress field analysis (Timoshenko and Woinowsky-Krieger, 1959; Zhou et al., 2011). Firstly, the elastic parameter data volume obtained from pre-stack seismic inversion is used to calculate the construction curvature and simulate stress distribution (Figure 3B).

Since Dahlstrom (1969) systematically proposed the balanced section method, this technique has gradually been widely adopted

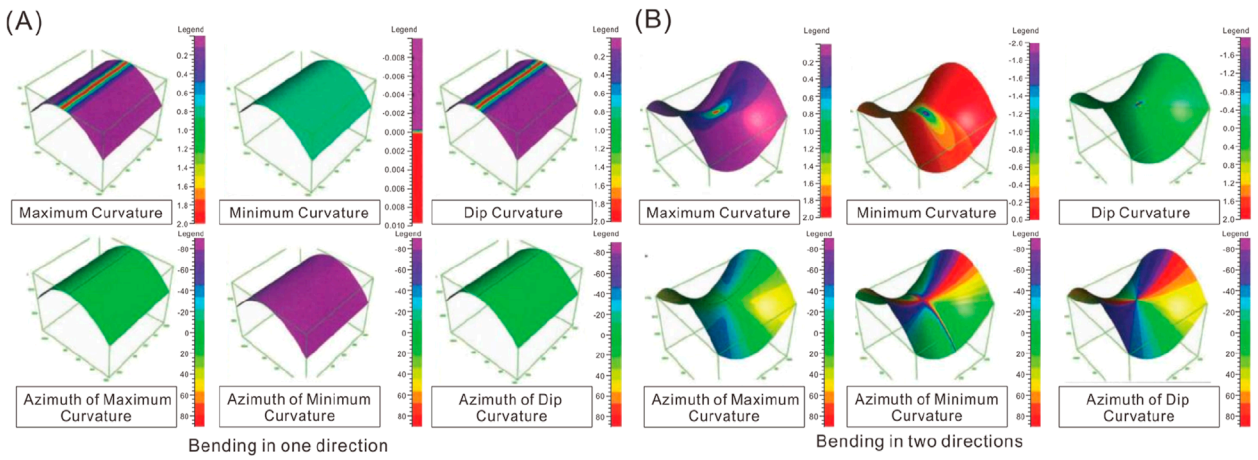

FIGURE 3
Schematic diagram of tectonic curvature and stress distribution applied in 3D seismic data. **(A)** Tectonic curvature and stress distribution in one direction. **(B)** Tectonic curvature and stress distribution in two direction.

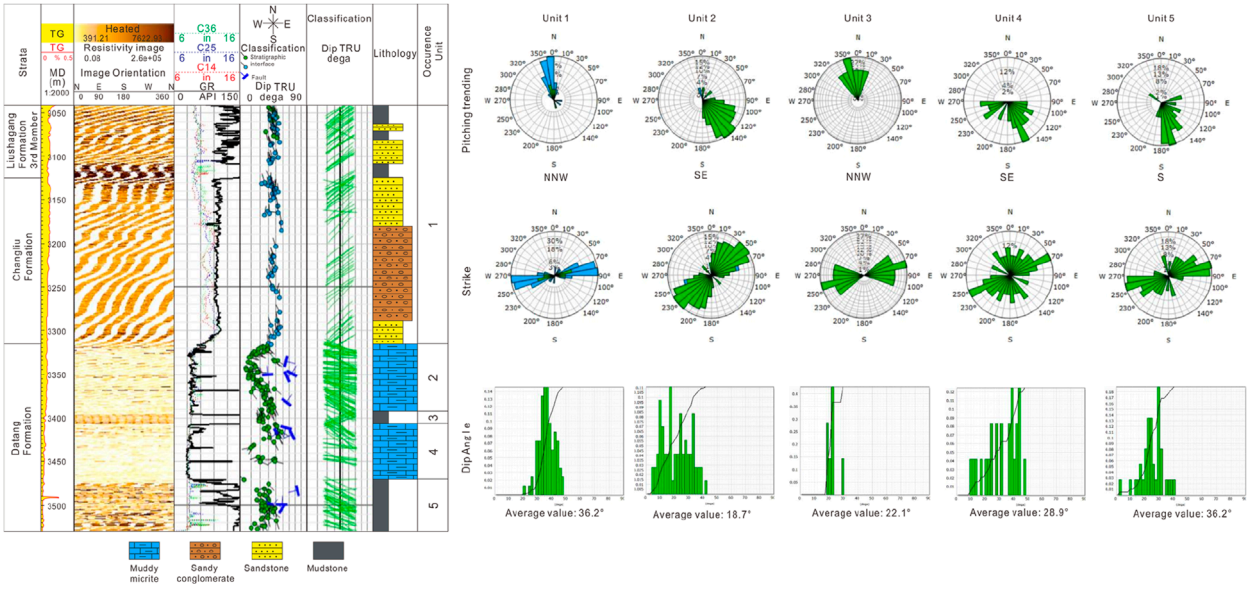

FIGURE 4
The occurrence of different stratigraphic units of buried-carbonate hill and overlying strata (Changliu Formation and Liu shagang Formation third Member) in Weixinan Depression (based on imaging logging data and drilling data).

by geologists and has played a key role in verifying seismic interpretation and restoring structural deformation. The balanced section method analyzes the regional tectonic background, selects appropriate deformation mechanisms for interpreting the section, and applies geometric and kinematic principles to restore the deformation structures to the initial sedimentary, undeformed state. This method allows the characteristics of structural deformation at each stage of structural evolution to be visually represented on the section. By measuring the length changes of the section, strain variables and strain rates can be calculated, providing a more accurate basis for quantitative analysis of structural evolution history. To constrain the arbitrariness of balanced sections, geologists have established a series of rules in years of practical work to ensure the accuracy of balanced sections (Butler, 1983; Castelluccio et al., 2015; Mazur et al., 2018). These rules mainly include: (1) The area of the conservation profile remains unchanged before and after deformation, that is, the shortened area should be the same as the overlapping area of the strata. (2) The layer length before and after deformation remains unchanged, provided that the thickness of the rock layer does not change during the deformation process, only fractures and folds occur. (3) The conservation of displacement should be maintained along the same fault, and the displacement of each equivalent layer should be consistent.

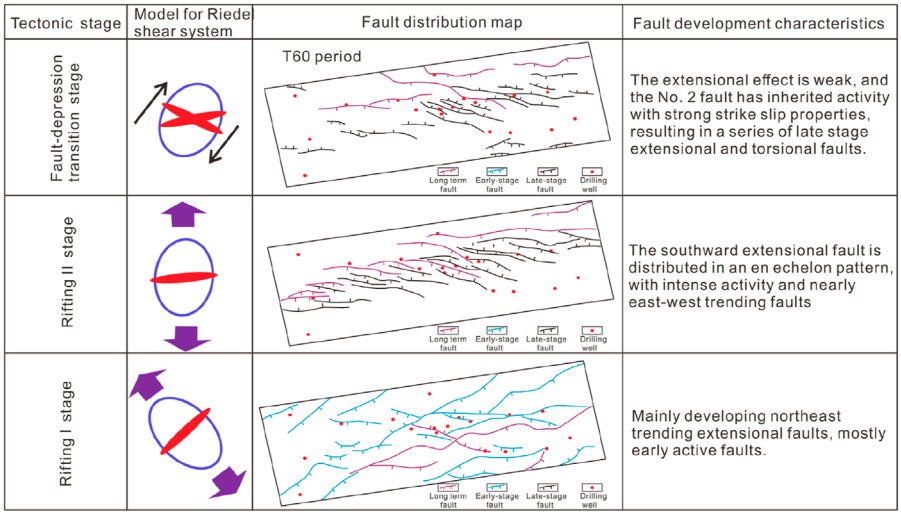

FIGURE 5
Structural stress field and faulting periods in Weixinan Depression.

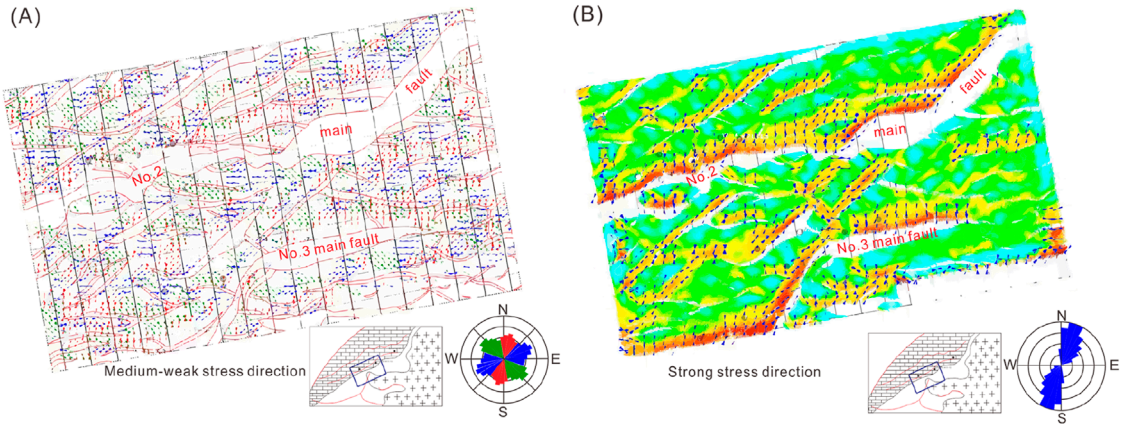

FIGURE 6
Characteristics of stress field at the top of buried-hills in Weixinan Depression. **(A)** Characteristics of medium and weak stress fields. **(B)** Characteristics of strong stress fields.

4 Stratigraphic framework of buried-carbonate hill

According to the imaging logging results, the inclination of the Carboniferous strata in Buried-carbonate Basement Hill is mainly southeast, with a low dip angle and an average of about 21.6° (Figure 4). Speculation on the distribution characteristics of the inner strata of the carbonate buried-hill: The strata of the Buried-carbonate Basement Hill A are divided into S Member and M Member from bottom to top, with missing Z Member and C Member overlying. In contrast, the strata of Buried-carbonate Basement Hill C are divided into S Member, M Member, Z Member and C Member from bottom to top, and the underlying strata are currently not involved in drilling (Figure 1B).

5 Tectonic evolution of buried-hill

5.1 Analysis of stress field at the top of buried-hill

The stress field simulation based on three-dimensional seismic data is mainly through the elastic thin plate theory, which establishes the relationship between curvature and strain, and then establishes the relationship between strain and stress, so as to realize the prediction of *in-situ* stress. The thin plate bending theory holds that the stratum studied is uniform, continuous, isotropic and completely elastic, and that the formation of the stratum is completely formed by tectonic stress. In the stress prediction method based on curvature stress analysis, the key parameters are curvature, Young's modulus, and Poisson's ratio. To improve the accuracy of simulation results,

10.3389/feart.2025.1552826

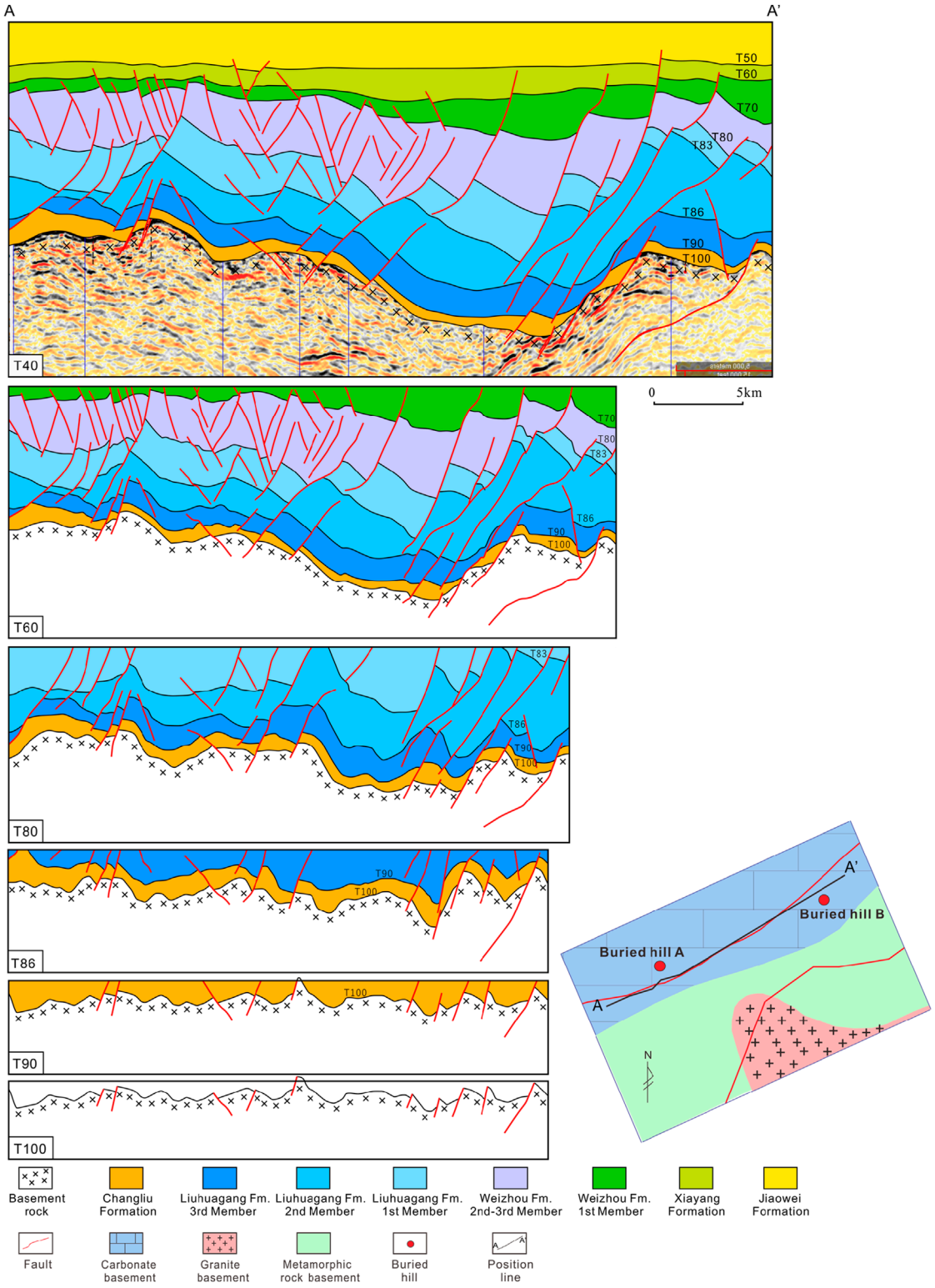

FIGURE 7
Cenozoic tectonic evolution process of Weixinan Depression.

a high-precision seismic layer velocity field is constructed based on multi-source information fusion. Time-depth conversion is performed on the interface of the submerged mountain top to obtain an accurate depth domain surface. The least squares method is then used to fit the trend surface and calculate its curvature. Young's modulus and Poisson's ratio data volumes are obtained

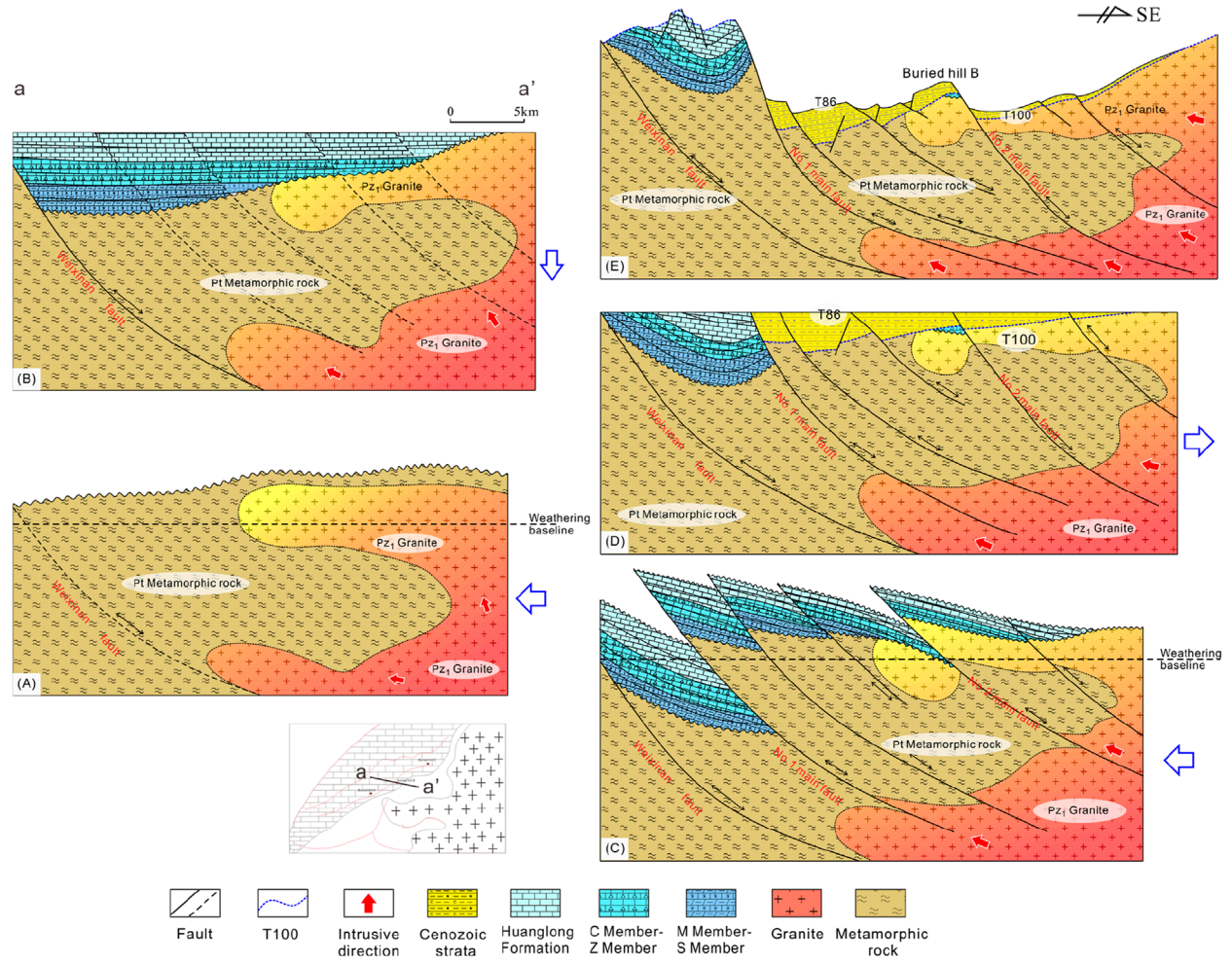

FIGURE 8
Tectonic evolution and formation process of buried-carbonate hill in Weixinan Depression. **(A)** The diapirism uplift of the basement leads to the exposure of granite and metamorphic rocks above the water surface. The first-stage buried-hills formed by weathering of granite and metamorphic rocks. **(B)** The sedimentary strata of the Carboniferous system led to the deep burial of the first-stage buried-hills (granite and metamorphic rocks). **(C)** The reverse thrust caused weathering of the Carboniferous carbonate rock, resulting in the formation of the second-stage of buried-hills (carbonate rock). **(D)** The Cenozoic sedimentary strata led to the deep burial of the second-stage of buried-hills. **(E)** The morphology of buried-hills was finally finalized in the Quaternary period.

through pre-stack inversion. The geostress is then calculated step by step, followed by outputting the structural stress field at the top of the buried-hill.

As mentioned earlier, the study area has developed both extensional controlled nearly EW oriented depression controlling faults that cut through the Paleogene (Wu et al., 2022), segmented NE oriented fault zones controlled by strike-slip, and a series of alternating NE oriented anticlines and synclines caused by compressive stress. Comprehensive analysis suggests that these structural phenomena are actually different manifestations of the same period of dextral shear deformation in different parts of the basin. Regional fault analysis shows that the inherited fault direction during the entire subsidence period in the study area is mainly NE-NNE, reflecting the overall NW in the study area (Figure 5). The simulation of tectonic stress field is based on the current deep tectonic surface, which is the comprehensive result of multiple tectonic processes. That is, the stress direction calculated by the strong stress plane diagram is the comprehensive result of multiple stress periods, approximately perpendicular to the direction of the current fault zone. The analysis of medium and weak stress fields can be used to analyze the stress characteristics of multiple tectonic periods, as shown in the three sets of stress directions in the figure (Figure 6A). Among them, the stress characteristics in the NW direction (green) are consistent with the stress direction of the first episode of the second belt rift. Characteristics of weak stress field at the top of buried-hill: In the area far away from the major fault, there are multiple sets of weak stress, whose direction is approximately consistent with the multi period stress direction in the study area. Characteristics of strong stress field at the top of buried-hill: Strong stress is concentrated near main faults (No. 2 and No. 3 main fault zones) (Figure 6), with a stress direction near the north-south direction (Figure 6B).

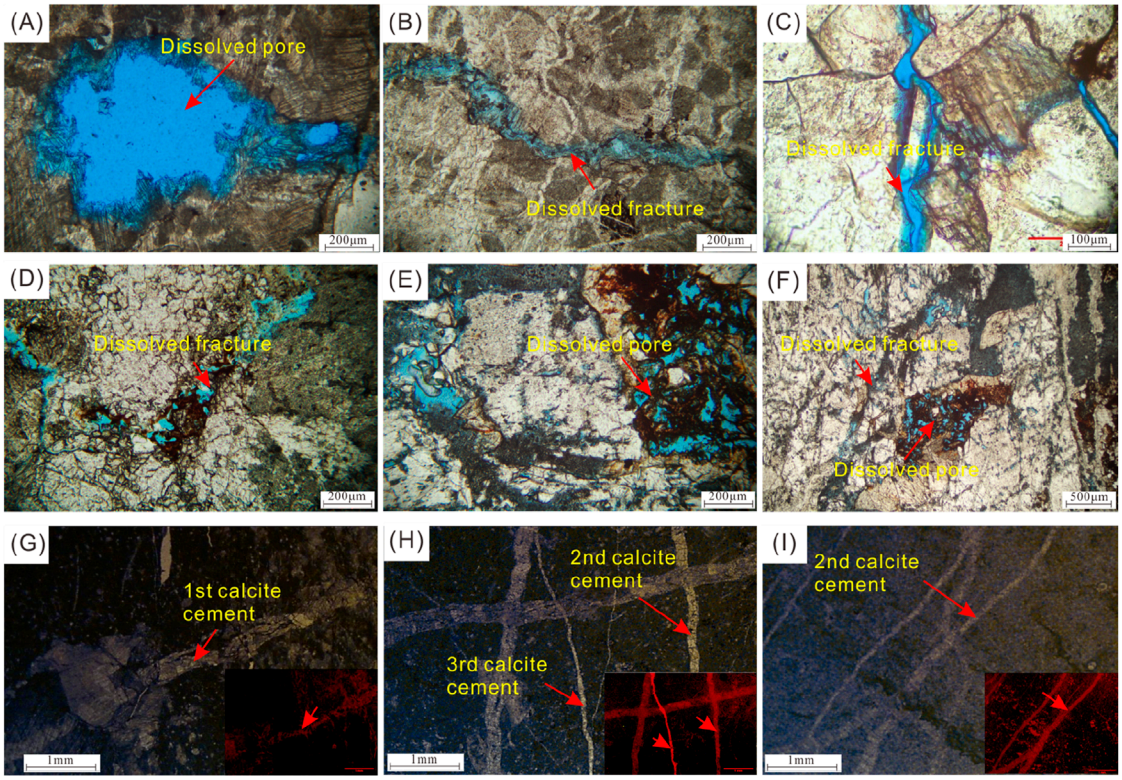

FIGURE 9
Petrological evidence of epidiagenetic-stage karstification in buried-basement hill in Weixinan Depression. **(A)** Intragranular dissolved pores in micrite. The pore size has exceeded 500 μm. **(B)** Dissolved fractures in micrite. The fracture width is 100 μm. **(C)** Dissolved fractures cutting through calcite crystals of the micrite matrix. The fracture width is 100 μm. **(D)** Dissolved fractures in granite cutting through feldspar grain. **(E)** Intragranular dissolved pores in feldspar grain of granite. **(F)** Intragranular dissolved pores and dissolved fractures in feldspar grains of granite. **(G)** The first-stage calcite cement of structural fracture in carbonate matrix. **(H)** The second-stage and third-stage calcite cement of structural fracture. **(I)** The second-stage calcite cement of structural fracture.

5.2 Seismic reflection characteristics of stratigraphic interfaces

Based on the seismic reflection characteristics of the main Paleogene interfaces in the Beibu Gulf Basin, and regional structural data, the geological structural attributes of each interface were analyzed, and the interfaces were classified. The first level unconformity is a tectonic cycle interface with tectonic transformation significance, corresponding to plate convergence events, with a large impact range. The secondary unconformity surface represents the interface for the transformation of the basin's internal structural system, corresponding to periodic structural events within the basin. Therefore, T100 and T60 belong to the first order sequence boundary, which is a regional structural boundary with significant structural unconformity characteristics. They can be identified, tracked, and compared in the Beibu Gulf Basin and even in the entire northern margin of the South China Sea. The T100 interface represents the interface at which the basin enters the initial stage of rifting, and belongs to the unconformity interface of faulting (Figure 7). In the Beibu Gulf Basin, the reflection characteristics of the T100 interface are relatively obvious, but in some areas, the reflection characteristics of the T100 interface are unclear and difficult to identify and track. The T60 interface is the interface where the basin transforms from a rift to a depression (Figure 7), belonging to a post rift unconformity interface. It is also the interface where structural inversion occurs in the basin area, and the interface reflection is relatively clear throughout the entire basin.

During the formation of the Beibu Gulf Basin, the regional stress field underwent a clockwise rotation due to the combined forces of the Indian-Australian Plate, Pacific Plate, and the subduction of the ancient South China Sea. Based on the period of significant changes in the regional stress field, a second-order sequence boundary can be identified: T83, which represents the interface where the regional stress field transitions from NW-NNW to near NS direction. Before the T83 interface, the Indian Plate moved northward and began to collide with the Eurasian Plate, forming a series of early NE-NEE trending faults, mainly developing fluvial lacustrine sediments; After the T80 interface, it was subjected to the southward extrusion of the Indosinian Plate and the subduction of the ancient South China Sea, forming a series of late stage near EW trending faults (Figure 7), mainly developing coastal shallow lake delta sediments. In the late stage of fracturing, the basin transformed into marine facies, mainly developing coastal shallow sea to shallow sea sedimentary facies. In addition, the T86, T80, T72, T70 and other interfaces in the basin represent local tectonic change events and are third-order sequence interfaces (Figure 7).

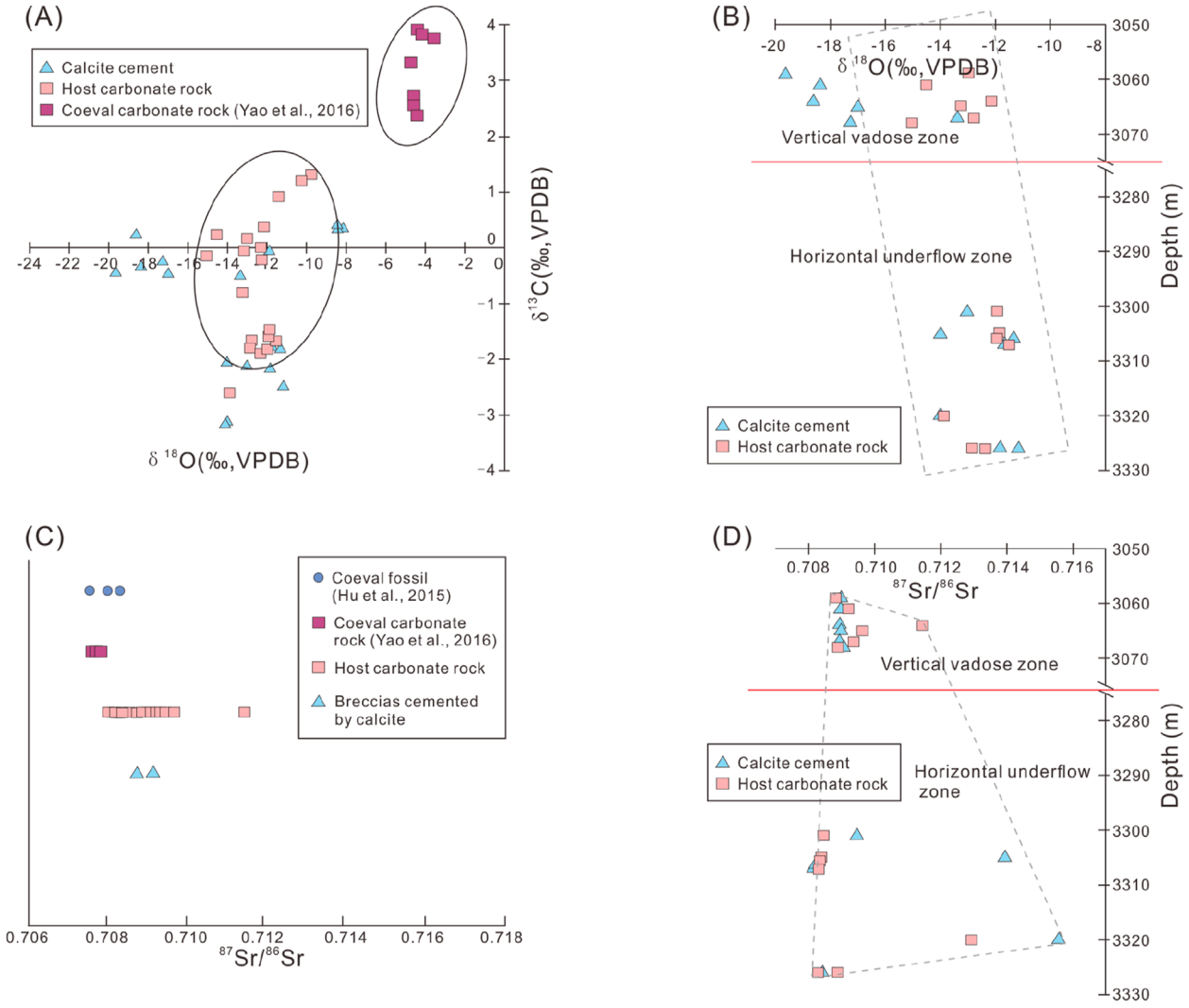

FIGURE 10
Inorganic geochemical characteristics of buried-hill reservoirs in Weixinan Depression. **(A)** Carbon and oxygen isotope crossplot. **(B)** Burial depth and oxygen isotope crossplot. **(C)** Strontium isotope distribution. **(D)** Burial depth and strontium isotope crossplot.(some data are from Hu et al., 2015; Yao et al., 2016).

5.3 Tectonic evolution and formation process of buried-carbonate hill

During the Jinning Movement, Precambrian metamorphic rocks formed the basin's basement. During the Silurian period, influenced by the Caledonian Orogeny, northwest-southeast compression caused crustal uplift and thickening, leading to the reactivation of the geosyncline fold. The Weixinan Fault formed during this period and began to experience reverse movement. The magma in the southeastern study area transformed the metamorphic basement through diapiric intrusion/fault intrusion, resulting in the formation of paleogeomorphology with significant height variations following the uplift of the study area (Figure 8A). The southeastern part of the study is characterized by intense magma intrusion and thin overlying metamorphic rocks, which have started to undergo differential weathering and erosion. During the Hercynian period, uplift caused by early magma intrusion and a relative sea-level decline prevented deposition of the Devonian system in the study area, leading to continued weathering and erosion. Entering the Carboniferous period, influenced by the Hercynian Movement, the Weixinan Fault slid back, causing overall subsidence in the study area (Figure 8B). Coastal clastic rocks and marine carbonate rocks were continuously deposited on a large scale, including the Lower Carboniferous M Member, S Member, C Member, Z Member, and Upper Carboniferous Huanglong Formation. During this period, the paleogeomorphology caused by the Caledonian thrust were still maintained to a certain extent. The overlying metamorphic rocks in the area where Buried-hill A is located were completely eroded, exposing granite and undergoing atmospheric freshwater leaching and alteration. The undulating paleogeomorphology result in differences in the Carboniferous strata, with the depocenter located in the northwest of the study area and gradually tapering off towards the southeast. During the Late Permian Dongwu Movement, under the influence of NE-SW compressive stress, local

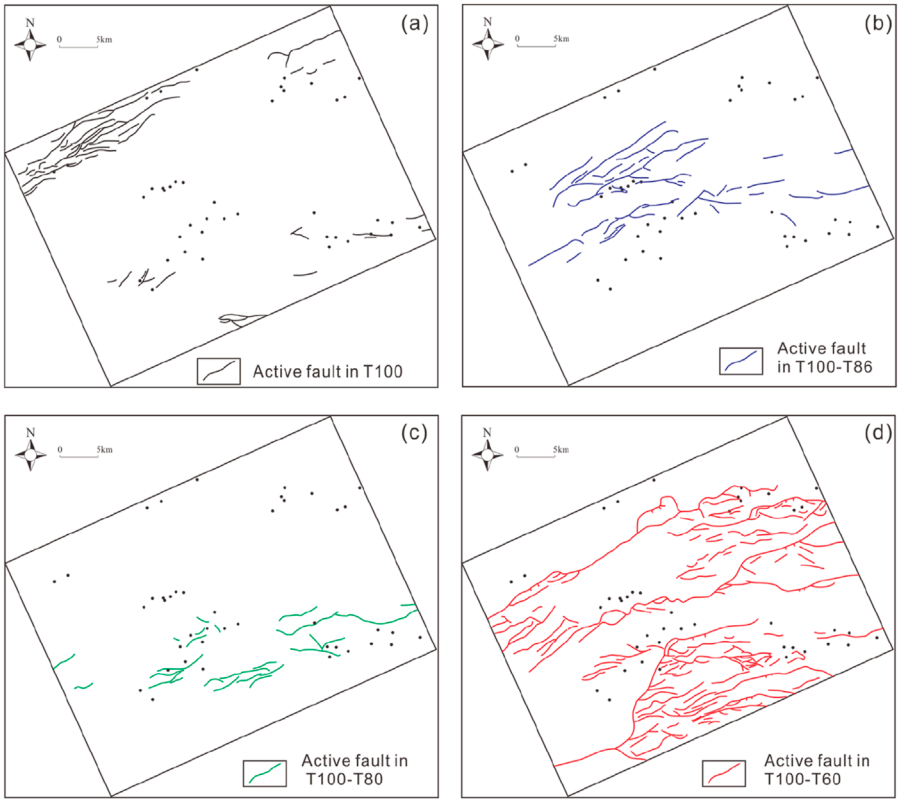

FIGURE 11
Distribution of active faults in different periods and drilling well locations in Weixinan Depression. **(A)** Active fault in T100. **(B)** Active fault in T100-T86. **(C)** Active fault in T100-T80. **(D)** Active fault in T100-T60.

thrust structures were formed due to active internal faults in the study area, and the overlying Carboniferous began to undergo differential erosion (Figure 8C).

During the Permian-Middle Triassic period, under the influence of the Indosinian Movement, strong compression occurred from the southeast to the northwest. The hidden faults formed during the Caledonian period were reactivated, and a series of strong northeast trending thrust structures were mainly formed by the Weixinan Fault, the No.1 main fault, the No.2 main fault, and the No.3 main fault. The Carboniferous system underwent stepped differential weathering and erosion. The stress primarily originates from the southeast direction, and the hanging plates of the No.1, No.2, and No.3 main faults being pushed to higher, more weathered positions, corresponding to stronger erosion. The lower plate of the No. 1 fault is positioned at a relatively lower elevation, corresponding to a lower degree of erosion. In the early stage of the Himalayan Movement from the Late Cretaceous to the Paleocene, there was regional northwest southeast tension, and the Weixinan Fault, the No.1 main fault, the No.2 main fault, and the No.3 main fault began to gradually reverse and slide back. The No.3 main fault experienced a late back slip, resulting in the interruption of Cenozoic sedimentation. The intensity of fault activity is strong in the southwest and gradually weakens towards the northeast, receiving alluvial fan sedimentation represented by the Changliu Formation (Figure 8D). In the late Himalayan period, the tensional-shear faulting ended, and the morphological characteristics of the Paleozoic buried-hills no longer changed (Figure 8E).

5.4 Tectonic evolution and formation process of buried-granite (and metamorphic rock) hill

During the Jinning Movement, the basement of the Weixinan Depression was composed of Proterozoic metamorphic rocks (Figure 8A). During the Silurian period, influenced by the Caledonian Orogeny, the crust was compressed in a northwest-southeast direction, resulting in uplift and thickening, with the geosyncline folds reactivating. The Weixinan Fault began to form and undergo reverse movement. The magma in the southeastern margin of the study area dissolved the metamorphic rock basement through basal intrusion/fault intrusion, while causing uplift. The uplifted granite and metamorphic rocks underwent differential weathering and erosion until the Devonian period (Figure 8A). Affected by the Carboniferous Hercynian Movement, the Weixinan Fault slid back, and the southwestern part of the study area sank and received Upper Carboniferous sediments (Figure 8B). During the Late Permian Dongwu Movement, NE-SW compressive stress induced internal fractures and formed local thrust structures, resulting in differential erosion of overlying Carboniferous

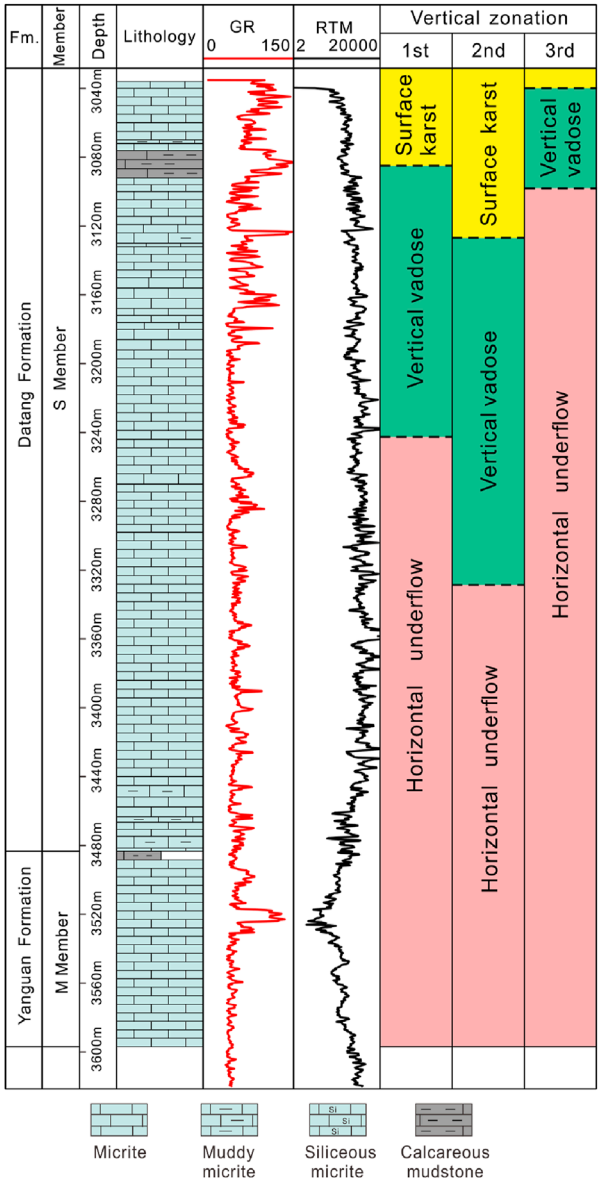

FIGURE 12
Vertical zonation of buried-carbonate basement hill in the Weixinan Depression.

carbonate rocks. During the Permian-Middle Triassic period, under the influence of the Indochina Movement, there was a strong compression from southeast to northwest, and the hidden faults formed during the Caledonian period were reactivated. A series of northeast trending thrust structures represented by the Weixinan Fault, the No.1 Main Fault, the No.2 Main Fault, and the No.3 Main Fault have caused the Carboniferous strata to be weathered again (Figure 8C).

During the Late Cretaceous Paleocene, there was regional NW-SE tension, and the Weixinan Fault, No.1 Main Fault, No.2 Main Fault, and No.3 Main Fault began to gradually reverse and slide back. The third main fault experienced a relatively late back slip, resulting in relatively thin Cenozoic sedimentary strata in the eastern study area (Figure 8D). Under the action of regional tension, many tensile fractures were formed inside the buried-hill (Figure 8D). In the late Himalayan period, the tensional-shear faulting ended, and the morphological characteristics of the Paleozoic buried-hills no longer changed (Figure 8E). In summary, there are two stages in the formation process of metamorphic rock buried-hills. The formation process of carbonate rocks buried-hills is limited to only one stage.

6 Controlling factors for gas reservoir

6.1 Epidiagenetic-stage karstification

6.1.1 Petrological evidence

Microscopic petrological characteristics suggest that both buried-carbonate and granite (metamorphic) hills have been altered by prolonged atmospheric freshwater exposure after being uplifted above sea level. The lithology of buried-carbonate hills is composed of micrite, and numerous of intraparticle dissolution pores and fractures have been observed inside the host rock (micrite) (Figure 9A). The dissolved rock fabric has no selective characteristics and aligns with the characteristics of epidiagenetic karstification. The reservoir spaces in the granite (metamorphic rock) buried-hill reservoir are also composed of dissolution pores and fractures resulting from weathering leaching (Figures 9B, C). In thin-section, intense leaching causes unstable mineral particles such as feldspar to transform into clay mineral (Figure 9D), and fracture leads to mylonization of feldspar (Figure 9E), mica, and other minerals (Figure 9F). Rock core observations show that the development of karst pores and fractures increases from bottom to top, while cementation strengthens in the same direction. Under cathodoluminescence (CL) microscopy, multi-stage calcite vein exhibit bright red, distinct from the host rock (micrite) (Figures 9G, H).

6.1.2 Carbon-oxygen stable isotope evidence

The abundance of $\delta^{13}C$ and $\delta^{18}O$ in marine carbonates is mainly influenced by factors such as sea level rise and fall, organic carbon sources and burial rates, and redox conditions in sedimentary diagenetic environments (Veizer et al., 1999; Berner, 2006). Thus, the carbon and oxygen isotope compositions of carbonate rocks vary depending on the sedimentary diagenetic environment and diagenetic fluid properties. In this study, according to the calculation formula proposed by Keith and Weber (1964), $\delta^{13}C$ and $\delta^{18}O$ were used to calculate the Z value and determine the diagenetic environment of calcite veins. The calculation formula is: paleo-salinity $Z = 2.048 \times (\delta^{13}C + 50) + 0.498 \times (\delta^{18}O + 50)$. When Z>120%, it is a marine diagenetic environment, and when Z<120%, it is a terrestrial diagenetic environment (Keith and Weber, 1964). The measured C-O isotopes of calcite vein and host rock are negatively biased compared to the original coeval seawater (Figure 10A), mainly due to the influence of atmospheric freshwater leaching. The calculated salinity Z value is mostly less than 120, suggesting marine limestone affected by fresh water. Moreover, the dilution effect of atmospheric fresh water on carbon and oxygen isotopes leads to negative measurement results (Figure 10A). The negative offset phenomenon in Vertical seepage zone is more significant than in horizontal runoff zone (Figure 10B).

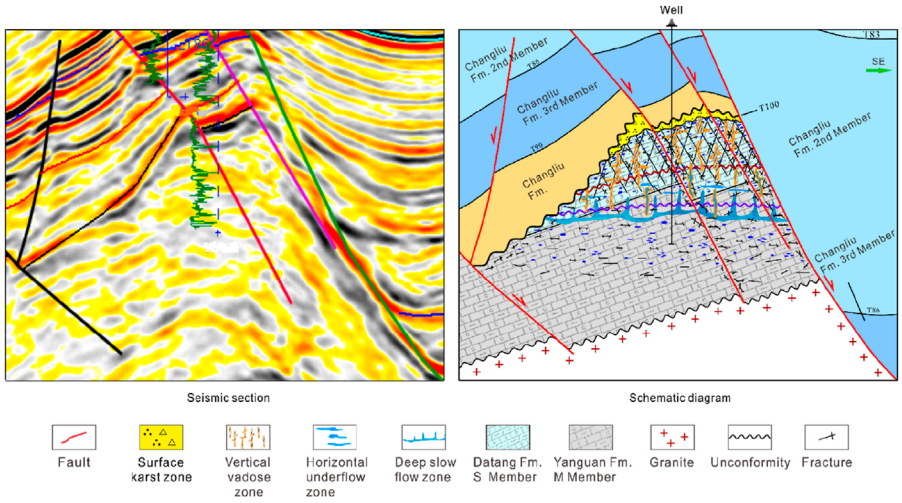

FIGURE 13
Formation model of buried-carbonate basement hill reservoir in Weixinan Depression (modified from Xie et al., 2024).

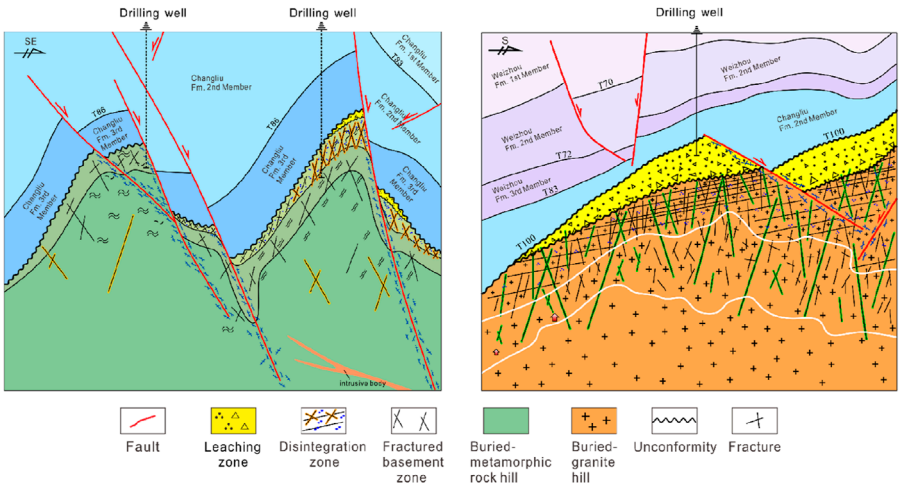

FIGURE 14
Formation model of buried-granite (or metamorphic rock) basement hill reservoir in the Weixinan Depression.

6.1.3 Strontium isotope evidence

The host rock composed of micrite belongs to the Carboniferous Visean stage, and the coeval conodont and carbonate $^{87}Sr/^{86}Sr$ is between 0.7076 and 0.7080 (Chen et al., 2018). In contrast, the strontium isotope values of host rock and calcite cement are higher (Figure 10C). Previous studies indicate that mantle-derived fluids and connate seawaters have considerably low Sr isotopic compositions (Gu et al., 2023). The elevated $^{87}Sr/^{86}Sr$ ratios should be ascribed to the diagenetic fluids of more radiogenic Sr It is suggested that freshwater constitutes the main body of diagenetic fluids. The $^{87}Sr/^{86}Sr$ ratios in horizontal underflow zone is higher than that of vertical vadose zone (Figure 10D).

6.2 Faulting activity

The South China Sea, which contains the Beibu Gulf Basin, has experienced multiple tectonic movements since the Mesozoic. These tectonic movements have resulted in the multi-stage development of faults (Figure 11), influencing the formation and evolution of buried-hills in the Beibu Gulf Basin. They are the dominant factor in the evolution of buried-hill structures, affecting both the internal structural styles and external morphology of the buried-hills.

Tectonic processes such as uplift, compression, and extension form large-scale faults, providing pathways for fluid transport in water-rock interactions. Fault activity produces numerous cracks and fractured zones in rocks. These cracks create channels for fluid

migration, allowing hydrothermal fluids, groundwater, and other fluids to move through rock layers. Hydrothermal fluids, carrying abundant minerals, rise or diffuse along fault zones. They undergo chemical reactions with surrounding rocks, dissolving mineral components and transforming pore structures, thus increasing porosity and permeability.

The rate of fault activity significantly affects reservoir properties and is a primary factor in fracture development. A higher rate of fault activity generates numerous fractures, increases pore space, promotes dissolution to form secondary pores, and thus enhances porosity. Simultaneously, more and wider fractures interconnect to become efficient flow channels, increasing reservoir permeability but also enhancing permeability heterogeneity. The impact of lower fault activity rates on these aspects is relatively weak.

7 Reservoir formation mechanism of buried-basement hill

The vertical zonation of buried-basement hill reservoir has been proposed by several literature (Salah and Alsharhan, 1998; Luo et al., 2005; Plotnikova, 2006), but the specific zonation scheme has not been unified (Zhang et al., 2024). Salah and Alsharhan (1998) divided the buried-basement hill into four zones based on the degree of alteration. On the basis of well logging interpretation, another more specific scheme was proposed (Luo et al., 2005), which is to divide the buried-hill reservoir into three zones: Top weathered zone, Middle fracture zone, and Lower tight zone. However, Xu et al. (2024) proposed that fractures only develop in the bottom and top zones, with the middle zone having low permeability. The vertical zonation of the buried-hill reservoir should be a joint result of basement lithology, faulting events, and diagenetic events (Wang et al., 2023; Zhang et al., 2024). By observing the core and logging curve shapes of different types of basement rock, the vertical zonation scheme of buried-hills that conforms to different types of basement was summarized in this study. For buried-carbonate basement hill reservoirs, the lithology is easily dissolved carbonate rocks with obvious vertical zonation characteristics (Figure 12). Based on previous studies and logging responses in this study (He et al., 2013), the vertical zonation of buried-carbonate hill are divided into four zones (Figure 13): surface karst zone, vertical vadose zone, horizontal underflow zone and deep slow flow zone (Xie et al., 2024). In surface karst zone, the filling of breccias and calcite cement leads to the underdevelopment of pores. The cementation effect of vertical vadose zone is strong, and the dissolved pores are almost completely cemented. The reservoir mainly composed of dissolved pore and fracture is concentrated in horizontal underflow zone. In addition to epidiagenetic karst, other diagenesis, including dolomitization, recrystallization and so on, can almost be ignored in the lithological transformation of buried-carbonate hills. Because the induction of these diagenesis requires harsh conditions, the range and intensity of action are extremely limited. The lithologic logging results of drilling also confirmed this view (Figure 12).

For aluminosilicate-rich rocks represented by granite and metamorphic rocks, Zhang et al. (2024) proposed a unified classification scheme for weathering crust structure. This classification scheme is composed of fractured basement zone, disintegration zone, and leaching zone from bottom to the top (Figure 14). Due to the minerals that form granite and metamorphic rocks is aluminosilicate minerals, their chemical properties are much more stable than those of carbonate rocks. Structural fractures play a decisive role in chemical alteration and dissolution of aluminosilicate minerals. From the bottom of the leaching zone to the surface of the buried-granite and metamorphic rocks basement hill, the chemical alteration of aluminosilicate minerals along various fractures is enhanced continuously, forming clay minerals and dissolved pores, and the rock sbecome loose and sandy. The reservoir mainly composed of dissolved pore and fracture is concentrated in leaching zone located at the top of each buried-granite and metamorphic rocks hill (Figure 14).

8 Conclusion

The petrographic features, seismic section and isotope evidence of the Pre-Paleogene, Paleogene and Neogene strata were studied to determine the Formation process of buried-hill and formation mechanism of reservoir in the Weixinan Depression of Northern Beibu Gulf Basin.

(1) The stress field at the top of the buried-basement hills has been revealed. Multiple sets of medium-weak stresses are observed far from the main fault area, and their directions are approximately consistent with the multi-stage stress directions in the Weixinan Depression of the Beibu Gulf Basin. Strong stress is concentrated near the main faults (No.2 and No.3 Main Fault), with the stress direction being nearly north-south.

(2) The buried-basement hills have undergone multiple periods of uplift, exposure, and burial. The formation of buried-basement hills involves several stages: diapiric uplift, thrusting, exposure, multiple burials, and finalization. Three factors control the formation of buried-basement hills: ① differences in the degree of granite intrusion, which lead to variations in karst paleogeomorphology; ②NE-SW thrusting during the Hercynian period; ③NW-SE thrusting during the Indosinian-Yanshanian.

(3) The reservoir spaces of tight buried-basement hills are composed of dissolved pores, dissolved fractures and structural fractures. The main controlling factors for the development of buried-carbonate basement hill reservoirs are multi-stage tectonic stress, karstification, and lithology. Lithology of buried-carbonate hill determines the degree of dissolution, while tectonic movements cause the uplift and erosion of the Carboniferous carbonate strata. Early-stage fractures provide favorable seepage space for subsequent karst processes, while late-stage fractures increase reservoir permeability. The main factors controlling the development of buried-granite (or metamorphic rock) hill reservoirs are tectonic stress and karstification.

Data availability statement

The raw data supporting the conclusions of this article will be made available by the authors, without undue reservation.

Author contributions

AL: Conceptualization, Methodology, Writing–original draft. FX: Funding acquisition, Investigation, Software, Visualization, Writing–original draft. CF: Data curation, Formal Analysis, Project administration, Writing–review and editing. ML: Investigation, Methodology, Writing–original draft. FJ: Methodology, Project administration, Supervision, Writing–review and editing. GX: Project administration, Resources, Supervision, Validation, Writing–review and editing. XX: Resources, Validation, Visualization, Writing–review and editing. XZ: Conceptualization, Investigation, Methodology, Writing–review and editing. BX: Data curation, Formal Analysis, Investigation, Writing–review and editing.

Funding

The author(s) declare that financial support was received for the research and/or publication of this article. This study was funded by the National Natural Science Foundation Youth Foundation Project of China (No. 42302186).

Conflict of interest

Author CF, ML and FJ are employed by China National Offshore Oil Corporation.

The remaining authors declare that the research was conducted in the absence of any commercial or financial relationships that could be construed as a potential conflict of interest.

Generative AI statement

The author(s) declare that no Generative AI was used in the creation of this manuscript.

Publisher's note

References

Azaiez, H., Gabtni, H., Bédir, M., and Campbell, S. (2018). Aeromagnetic study of buried basement structures and lineaments of sahel region (eastern Tunisia, north africa). *Arabian J. Geosciences* 11 (7), 140. doi:10.1007/s12517-018-3476-8

Berner, R. A. (2006). Geocarbsulf: a combined model for phanerozoic atmospheric O_2 and CO_2. *Geochimica Cosmochimica Acta* 70 (23), 5653–5664. doi:10.1016/j.gca.2005.11.032

Butler, R. W. H. (1983). Balanced cross-sections and their implications for the deep structure of the northwest Alps. *J. Struct. Geol.* 5 (2), 125–137. doi:10.1016/0191-8141(83)90038-X

Carvalho, I. S., Mendes, J. C., and Costa, T. (2013). The role of fracturing and mineralogical alteration of basement gneiss in the oil exhsudation in the Sousa Basin (Lower Cretaceous), Northeastern Brazil. *J. S. Am. Earth Sci.* 47, 47–54. doi:10.1016/j.jsames.2013.06.001

Castelluccio, A., Andreucci, B., Zattin, M., Ketcham, R. A., Szaniawski, R., Mazzoli, S., et al. (2015). Coupling sequential restoration of balanced cross sections and low-temperature thermochronometry: the case study of the western carpathians. *Lithosphere* 7 (4), 367–378. doi:10.1130/L436.1

Chen, J., Montanez, I. P., Qi, Y., Shen, S., and Wang, X. (2018). Strontium and carbon isotopic evidence for decoupling of pco(2) from continental weathering at the apex of the late paleozoic glaciation. *Geology* 46 (5), 395–398. doi:10.1130/G40093.1

Dahlstrom, C. (1969). Balanced cross sections. *Can. J. Earth Sci.* 6 (4), 743–757. doi:10.1139/e69-069

Deng, Y., Hu, D., Zhu, J., Liu, G., Chen, K., and Tong, C. (2024). Hydrocarbon accumulation regularities, newfields and new types of exploration,and resource potentials in Beibuwan Basin. *Acta Pet. Sin.* 45 (1), 202–225. doi:10.7623/syxb202401012

Fairchild, J., and Spiro, B. (1987). Petrological and isotopic implications of some contrasting late Precambrian carbonate, NE Spitsbergen. *Sedimentology* 34 (6), 793–989. doi:10.1111/j.1365-3091.1987.tb00587.x

Gao, X., Pang, X., Li, X., Chen, Z., Shan, J., Liu, F., et al. (2008). Complex petroleum accumulating process and accumulation series in the buried-hill trend in the rift basin:an example of Xinglongtai structure trend, liaohe subbasin. *Sci. China Ser. D Earth Sci.* 51 (Suppl. II), 108–116. doi:10.1007/s11430-008-6022-9

Gu, Y., Wang, Z., Yang, C., Luo, M., Jiang, Y., Luo, X., et al. (2023). Effects of diagenesis on quality of dengying formation deep dolomite reservoir, Central Sichuan Basin, China: insights from petrology, geochemistry and *in situ* U-Pb dating. *Front. Earth Sci.* 10, 1041164. doi:10.3389/feart.2022.1041164

Guo, Z., Ma, Y., Liu, W., Wang, L., Tian, J., Zeng, X., et al. (2017). Main factors controlling the formation of basement hydrocarbon reservoirs in the Qaidam Basin, western China. *J. Petroleum Sci. Eng.* 149, 244–255. doi:10.1016/j.petrol.2016.10.029

He, J., Fang, S. X., Hou, F. H., Yan, R. H., Zhao, Z. J., Yao, J., et al. (2013). Vertical zonation of weathered crust ancient karst and the reservoir evaluation and prediction-A case study of M_5^5-M_5^1 sub-members of Majiagou Formation in gas fields, central Ordos Basin, NW China. *Petroleum Explor. Dev.* 40 (5), 534–542. doi:10.11698/PED.2013.05.04

Hu, Z., Li, Y., Li, B., Huang, S., and Han, X. (2015). An overview of the strontium isotopic composition of phanerozoic seawater. *Adv. Earth Sci.* 30 (1), 37–49. doi:10.11867/j.issn.1001-8166.2015.01.0037

Keith, M. L., and Weber, J. N. (1964). Carbon and oxygen isotopic composition of selected limestones and fossils. *Geochimica Cosmochimica Acta* 28 (10-11), 1787–1816. doi:10.1016/0016-7037(64)90022-5

Kerimov, V. Y., Leonov, M. G., Osipov, A. V., Mustaev, R. N., and Hai, V. N. (2019). Hydrocarbons in the basement of the South China Sea (Vietnam) Shelf and structural–tectonic model of their formation. *Geotectonics* 53 (1), 42–59. doi:10.1134/S0016852119010035

Kosachev, I., Kayukova, G., and Mikhailova, A. N. (2019). Features of composition of oil extracts from the rocks of basement and sedimentary stratums of the novo-elkhovskoye field of tatarstan. *Petroleum Sci. Technol.* 37, 1016–1024. doi:10.1080/10916466.2018.1564771

Kutcherov, V. G., and Krayushkin, V. A. (2010). Deep-seated abiogenic origin of petroleum: from geological assessment to physical theory. *Rev. Geophys.* 48 (1), RG1001. doi:10.1029/2008RG000270

Li, C., Fan, C., Hu, L., Hu, Q., and Chen, L. (2021). Tectonic evolution characteristics and genesis of Weixi'nan low uplift in Beibu Gulf Basin. *Mar. Orig. Pet. Geol.* 26 (4), 319–325. doi:10.3969/j.issn.1672-9854.2021.04.004

Li, C., Yang, X., Fan, C., Hu, L., Dai, L., and Zhao, S. (2018). On the evolution process of the Beibu Gulf Basin and forming mechanism of local structures. *Acta Geol. Sin.* 92 (10), 2028–2039. doi:10.3969/j.issn.0001-5717.2018.10.005

Liu, L., Sun, Y., Chen, C., Lou, R., and Wang, Q. (2022). Fault reactivation in No.4 structural zone and its control on oil and gas accumulation in Nanpu sag, Bohai Bay Basin, China. *Petroleum Explor. Dev.* 49 (4), 824–836. doi:10.1016/s1876-3804(22)60313-6

Liu, N., Qiu, N., Chang, J., Shen, F., Wu, H., Lu, X., et al. (2017). Hydrocarbon migration and accumulation of the Suqiao buried-hill zone in Wen'an slope, Jizhong subbasin, Bohai Bay basin, China. *Mar. Petroleum Geol.* 86, 512–525. doi:10.1016/j.marpetgeo.2017.05.040

Luo, J., Morad, S., Liang, Z., and Zhu, Y. (2005). Controls on the quality of Archean metamorphic and Jurassic volcanic reservoir rocks from the Xinglongtai buried hill, western depression of Liaohe basin, China. *AAPG Bull.* 89 (10), 1319–1346. doi:10.1306/05230503113

Mazur, S., Ggaa, U., Kufrasa, M., and Krzywiec, P. (2018). Application of two-dimensional gravity models as input parameters to balanced cross-sections across the margin of the East European Craton in SE Poland. *J. Struct. Geol.* 116, 223–233. doi:10.1016/j.jsg.2018.05.013

Mazzullo, S. J., Wilhite, B. W., and Woolsey, I. W. (2009). Petroleum reservoirs within a spiculite-dominated depositional sequence: cowley formation (mississippian: lower carboniferous), south-central Kansas. *AAPG Bull.* 93 (12), 1649–1689. doi:10.1306/06220909026

P'an, C. H. (1982). Petroleum in basement rocks. *AAPG Bull.* 66 (10), 1597–1643. doi:10.1306/03b5a994-16d1-11d7-8645000102c1865d

Parnell, J., Baba, M., Bowden, S., and Muirhead, D. (2017). Subsurface biodegradation of crude oil in a fractured basement reservoir, Shropshire, UK. *J. Geol. Soc.* 174, 655–666. doi:10.1144/jgs2016-129

Plotnikova, I. N. (2006). Nonconventional hydrocarbon targets in the crystalline basement, and the problem of the recent replenishment of hydrocarbon reserves. *J. Geochem. Explor.* 89 (1-3), 335–338. doi:10.1016/j.gexplo.2005.12.012

Qin, C., Wang, H., Jiang, P., Yang, X., and Zou, K. (2020). Spacial distribution and evolution of axial deltaic system in continental rift basin:A case study of Weixinan sag. *Beibuwan Basin* 49 (3), 542–551. doi:10.13247/j.cnki.jcumt.001094

Rodríguez-Cuevas, M., Cardona, A., Monsalve, G., Zapata, S., and Valencia-Gómez, J. C. (2024). Fracture evaluation of the plutonic basement in the upper magdalena basin: implications for the development of naturally fractured reservoirs in the Northern Andes. *Geol. J.* 59, 1968–1997. doi:10.1002/gj.4980

Salah, M. G., and Alsharhan, A. S. (1998). The Precambrian basement: a major reservoir in the rifted basin, Gulf of Suez. *J. Petroleum Sci. Eng.* 19 (1998), 201–222. doi:10.1016/S0920-4105(97)00024-7

Timoshenko, S. P., and Woinowsky-Krieger, S. P. (1959). *Theory of plates and shells*. New York: McGraw-Hill.

Veizer, J., Ala, D., Azmy, K., Bruckschen, P., Buhl, D., Bruhn, F., et al. (1999). $^{87}Sr/^{86}Sr$, $\delta^{13}C$ and $\delta^{18}O$ evolution of phanerozoic seawater. *Chem. Geol.* 161 (30), 59–88. doi:10.1016/S0009-2541(99)00081-9

Walters, R. F. (1953). Oil production from fractured pre-Cambrian basement rocks in central Kansas. *AAPG Bull.* 37 (2), 300–313. doi:10.1306/5ceadc59-16bb-11d7-8645000102c1865d

Wang, H., Jiang, Y., Yang, C., Zhang, B., Gu, Y., Luo, X., et al. (2023). Hydrothermal silicification in Ediacaran Dengying Formation fourth member deep dolomite reservoir, Central Sichuan Basin,China:Implications for reservoir quality. *Geol. J.* 2023, 4257–4270. doi:10.1002/gj.4757

Wang, Z., Jiang, Q., Wang, J., Long, G., Cheng, H., Shi, Y., et al. (2024). Hydrocarbon accumulation characteristics in basement reservoirsand exploration targets of deep basement reservoirs in onshore China. *Petroleum Explor. Dev.* 51 (1), 31–43. doi:10.1016/s1876-3804(24)60003-0

Wu, K., Li, Y., Fan, C., Dong, F., and Hong, M. (2022). Characteristics of unconformity structure and its implication for petroleum accumulation during fault-depression transition period in the wushi sag, beibuwan basin. *Geotect. Metallogenia* 46 (2), 272–281. doi:10.16539/j.ddgzyckx.2022.02.006

Xie, B., Xu, F. H., Fan, C. W., Man, Y., Jiang, F., Xu, G. S., et al. (2024). Karst identification and development model of buried hill limestone reservoir in Weixinan Depression, Beibuwan Basin. *J. Jilin Univ. Earth Sci. Ed.* 54 (6), 2029–2046. doi:10.13278/j.cnki.jjuese.20240223

Xing, Y. (1993). A study of carbonate paleo buried hill reservoir in Beibu Gulf W10-3N field. *Petroleum Explor. Dev.* 20 (6), 100–108. CNKI:SUN:SKYK.0.1993-06-014.

Xu, C., Yang, H., Wang, F., and Peng, J. (2024). Formation conditions of deep to ultra-deep composite buried-hill hydrocarbon reservoirs in Bohai Sea, China. *Petroleum Explor. Dev.* 51 (6), 1–13. doi:10.11698/PED.20230576

Yao, L., Wang, X. D., Lin, W., Li, Y., Kershaw, S., and Qie, W. K. (2016). Middle Viséan (Mississippian) coral biostrome in central Guizhou, southwestern China and its palaeoclimatological implications. *Palaeogeogr. Palaeoclimatol. Palaeoecol.* 448 (2016), 179–194. doi:10.1016/j.palaeo.2015.08.031

Ye, T., Chen, A., Niu, C., Wang, Q., and Hou, M. (2022). Characteristics, controlling factors and petroleum geologic significance of fractures in the archean crystalline basement rocks: a case study of the south jinzhou oilfield in liaodong bay depression, north China. *J. Petroleum Sci. Eng.* 208, 109504. doi:10.1016/j.petrol.2021.109504

Yi, J., Li, H., Shan, X., Hao, G., Yang, H., Wang, Q., et al. (2022). Division and identification of vertical reservoir units in archaeozoic metamorphic buried hill of bozhong sag, Bohai Bay Basin, east China. *Petroleum Explor. Dev.* 49 (6), 1282–1294. doi:10.1016/s1876-3804(23)60349-0

Zhang, Y. J., Wang, G. M., and Yin, Z. Y. (2024). Classification scheme of weathering crusts structures for aluminosilicate rich rocks. *Acta Pet. Sin.* 45 (9), 1372–1384. doi:10.7623/syxb202409005

Zhao, S., Yang, X., Chen, L., Zhou, G., Jiao, L., and Zhao, Y. (2019). Hydrocarbon accumulation conditions and exploration potential of carbonate buried hills in Weixinan sag in western South China Sea. *China Offshore Oil Gas* 31 (2), 51–61. doi:10.11935/j.issn.1673-1506.2019.02.006

Zhao, S., Zhao, Y., Yang, X., Jiao, L., and Chen, C. (2018). An analysis on the characteristics and main controlling factors of reservoir in carbonate buried hill in the Weixi'nan Sag, Beibuwan Basin. *Haiyang Xuehao* 40 (9), 43–53. doi:10.3969/j.issn.0253-4193.2018.09.004

Zhao, X., Jin, F., Wang, Q., and Bai, G. (2015). Buried-hill play, Jizhong subbasin, Bohai Bay basin: a review and future propespectivity. *AAPG Bull.* 99 (1), 1–26. doi:10.1306/07171413176

Zhou, Z. H., Wong, K. W., Xu, X. S., and Leung, A. Y. T. (2011). Natural vibration of circular and annular thin plates by Hamiltonian approach. *J. Sound Vib.* 330 (5), 1005–1017. doi:10.1016/j.jsv.2010.09.015

Zhu, Y., Yan, Z., Qin, K., Li, Z., Xiong, R., and Sun, K. (2024). Lithological and physical characteristics and their controlling factors of the Archaean metamorphic rocks: a case study of the Damintun Sag, in Liaohe depression of Bohai Bay Basin, China. *Geoenergy Sci. Eng.* 241 (2024), 213088. doi:10.1016/j.geoen.2024.213088

frontiers | Frontiers in Earth Science

TYPE Original Research
PUBLISHED 11 April 2025
DOI 10.3389/feart.2025.1534598

OPEN ACCESS

EDITED BY
Peng Tan,
CNPC Engineering Technology R & D Company Limited, China

REVIEWED BY
Sherif Farouk,
Egyptian Petroleum Research Institute, Egypt
Wang Song,
China University of Petroleum, China
Weibiao Xie,
China University of Petroleum Beijing, China

*CORRESPONDENCE
Wu Kui,
wukui@cnooc.com.cn

RECEIVED 26 November 2024
ACCEPTED 18 March 2025
PUBLISHED 11 April 2025

CITATION
Dan L, Kui W, Yu Q and Shanshan Y (2025) Fine interpretation method for tight reservoirs based on core experiments and imaging logging: a case study of tight carbonate rocks in L area.
Front. Earth Sci. 13:1534598.
doi: 10.3389/feart.2025.1534598

Fine interpretation method for tight reservoirs based on core experiments and imaging logging: a case study of tight carbonate rocks in L area

Li Dan, Wu Kui*, Qi Yu and Yu Shanshan

Cnooc Research Institute Ltd., Beijing, China

Introduction: With the gradual reduction in conventional exploration and the gradual improvement of hydraulic fracturing technology, the exploration of tight oil and gas has gradually become general. Marine carbonate rocks are developed in the lower Paleozoic Ordovician in the eastern margin of Ordos Basin. According to the drilling results, the minerals in this area are mainly calcite and dolomite, and the secondary minerals are halite, anhydrite, quartz, feldspar and clay minerals. Core experiment reveals that the reservoir is tight, with porosity between 2 and 6% and permeability less than 2mD. Relationship between lithology and porosity established by conventional logging interpretation is not consistent with the results of gas logging, so it is impossible to accurately determine the reservoir location.

Method: The research in this paper is to interpret lithologic profile based on mineral X-ray diffraction data, to accurately evaluate pore type and permeability based on borehole electrical imaging and multipole array acoustic logging, and to interpret gas saturation by using the Archie formula with variable cementation index.

Results and discussion: This method improves the interpretation accuracy of geophysical logging methods for tight reservoirs in this block, and plays a key role in favorable evaluation of reservoir sweet spots.

KEYWORDS

carbonate rock, logging evaluation, imaging logging, tight gas, unconventional exploration

1 Introduction

The block L is an unconventional hydrocarbon exploration block of CNOOC. The exploration and development of Carboniferous and Permian tight sandstone gas and deep coalbed methane in the upper Paleozoic are important (Zhu G. et al., 2022; Guo et al., 2024; Yu et al., 2024; Zhang et al., 2023; Kang et al., 2024). At present, the exploration in these two fields comes to an end (Xu et al., 2024; Zhu Y. et al., 2022; Qi et al., 2023). The marine carbonate rock is developed in the lower Paleozoic of this block. The carbonate rock of the Ordovician Majiagou Formation is in unconformable contact with the Benxi Formation of the upper Paleozoic. The weathered crust reservoirs are developed in the upper combination, and mound beach reservoirs are developed

in the middle and lower combination (Yang et al., 2011; Yao et al., 2015; He et al., 2022; Fu et al., 2021). The gas bearing indications have been seen in drilling and have certain exploration potential. The Cambrian and Ordovician Majiagou Formation middle and lower assemblages both developed laminated argillaceous dolomite, which is an effective high-quality source rock with good hydrocarbon supply conditions. The adjacent ShenMu gas field drilled the undersalt carbonate rock in 2022, of which the open flow test of single well MT1 reached 3.5×10^5 m^3/d (Zhou et al., 2023). Liu et al. (2024) introduced in detail the types and characteristics of favorable sub-salt dolomite reservoirs in Ordos Basin, and gave detailed classification schemes of different types of reservoirs. Fu et al. (2023) and Meng et al. (2023) introduced the reservoir forming mode of well MT1 in detail, introduced the geological background of the well from source reservoir cap, and described the progress of carbonate acid fracturing technology. Jiang et al. (2022) analyzed the reservoir lithology of this section through conventional logging curves, and introduced the rapid interpretation of lithology by using envelope and cluster analysis through density curves and neutron curves. Lai et al. (2020) and Wang et al. (2020),Wang et al. (2021),Wang et al. (2022) classified the lithofacies of the fifth member of Majiagou Formation in the basin in detail by using conventional curves and electrical imaging data (Farouk et al., 2024a; Farouk et al., 2025; Farouk et al., 2024b).

In this paper, through conducting experiment data on drilled cores and combining them with conventional logging data, a rapid lithology interpretation method based on artificial intelligence algorithms is established. By processing borehole resistivity imaging logging data, the porosity spectrum and porosity curve are obtained to evaluate the effectiveness and connectivity of reservoir pores. By processing array acoustic logging data, the Stoneley waveform is obtained to further evaluate reservoir permeability parameters. Through the core rock resistivity experiment, the Archie formula with a variable m parameter is established to optimize the interpretation of gas saturation. Through the above processing methods, the experimental results and imaging logging are applied to the LITCR (logging interpretation for tight carbonate reservoirs), which improves the logging interpretation accuracy of conventional logging curves and is more conducive to LITCR.

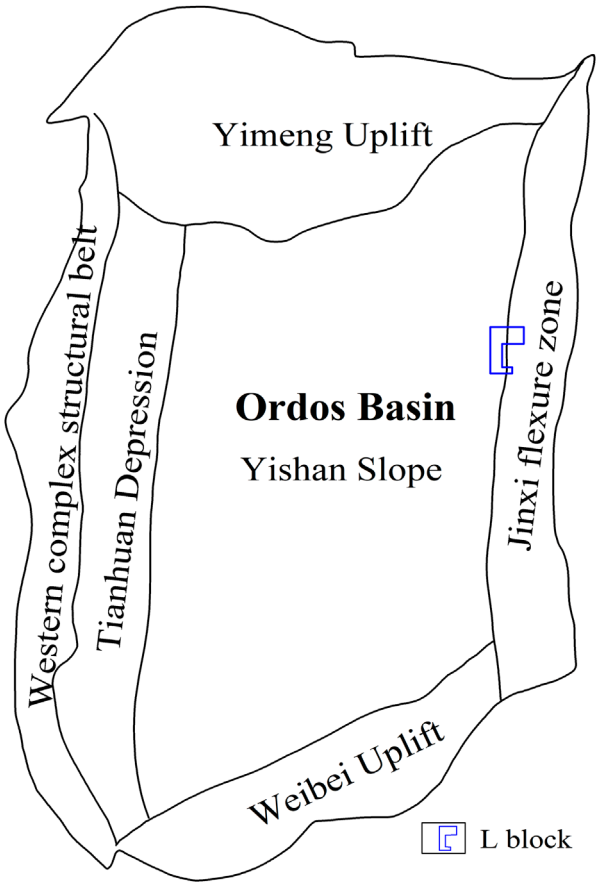

FIGURE 1
Overview map of Ordos basin and L work area location.

2 Regional overview

2.1 Geological overview

The Ordos Basin is a large multicycle craton basin featuring a relatively simple structure. The basin can be divided into six structural units, namely the Yimeng Uplift, Western complex structural belt, Tianhuan Depression, Yishan slope, Jinxi flexure zone, and Weibei uplift. Block L is structurally located in the Jinxi flexure zone on the eastern margin of the Ordos Basin,as shown in Figure 1 (Qi et al., 2024). The Middle Ordovician Majiagou Formation in this block experienced three major transgression-regression cycles and was divided into six members. Among them, the first, third, and fifth members of the Majiagou Formation are regressive sedimentary cycles, mainly developing gypsum salt rock and carbonate rock. The second, fourth, and sixth members are transgressive sedimentary cycles, mainly developing carbonate deposits. The sixth of Majiagou Formation at the top of the block is eroded. The fifth members of Majiagou Formation develop multi-frequency cycles, and thick gypsum salt rock is developed during the regression period. The strata of the Majiagou Formation in the upper part contact the overlying Carboniferous strata in an unconformable manner, and a set of karst weathering crust reservoir is developed. From the lower salt to the fourth member of the Majiagou Formation, a set of reef beach facies dolomite reservoir is developed. The main target reservoir is dolomite in limestone. The porosity of dolomite in this block is from 2% to 6%, the permeability is lower than 0.1 mD, and there is no natural productivity, so transformation is required (Tan et al., 2024a; Tan et al., 2024b).

2.2 Reservoir characteristics

The carbonate reservoir of the Majiagou Formation has complex mineral types. As shown in Table 1, X-ray diffraction analysis of core samples reveals that the main mineral components of carbonate rocks are calcite and dolomite, while the secondary minerals include halite, anhydrite, quartz, feldspar, and clay minerals. As depicted in the Figure 2, based on core observation

TABLE 1 Core X-ray diffraction mineral analysis.

Well name	Depth	Quartz/Shale	Calcite	Dolomite
Training well	1924.0	0	95	5
Training well	1925.2	0	15	85
Training well	1934.0	5	83	10
Training well	1935.0	0	15	85
Training well	1935.7	15	5	80
Training well	1937.0	5	15	80
Training well	1997.2	3	15	82
Training well	1941.3	5	93	2
Training well	1997.5	5	8	87
Training well	1997.6	5	10	85

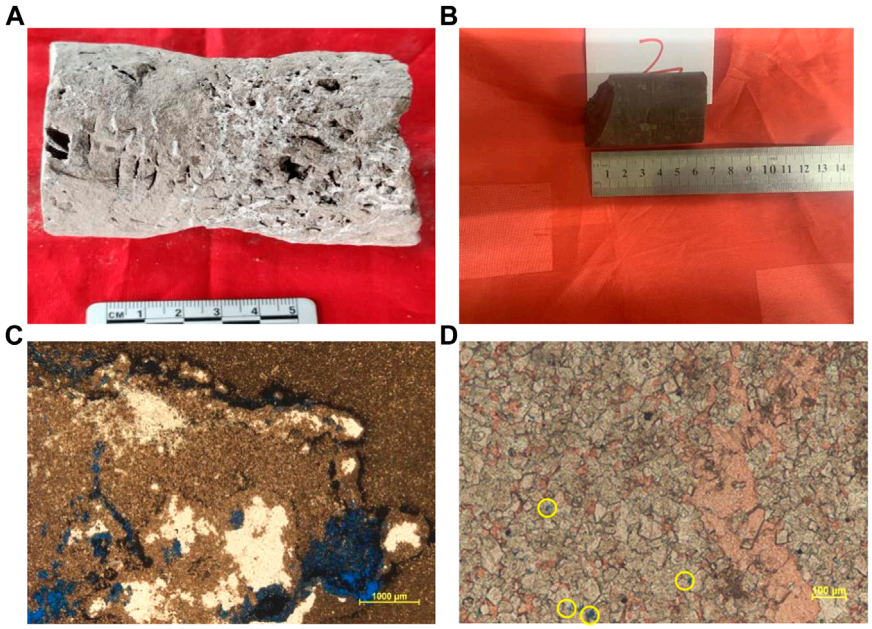

FIGURE 2
Core and microscopic photos of tight carbonate reservoirs in Zone L. **(a)** Dissolved cave,L-B, 2453.5-24534.3 m; **(b)** Anhydrite-moldic pore,L-A,1989-1995 m; **(c)** Fractures,L-B, 2410.2 m; **(d)** Crystal pores,L-B, 2420.3 m.

and scanning photos under the microscope, the pores can be classified as dissolved cave,anhydrite-moldic pore, fractures, crystal pores and so on. Some fractures can be observed to be filled with calcite in the reservoir. The reservoir has poor physical properties, with porosity ranging from 2% to 6% and permeability less than 1 millidarcy. The types of reservoir minerals are influenced by the sedimentary environment. Calcite and dolomite are the main minerals in the transgression stage, while gypsum rock, salt rock, and argillaceous dolomite are the main minerals in the regression stage.

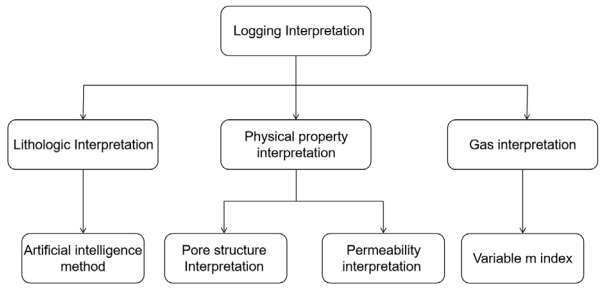

FIGURE 3
Flow chart of logging evaluation technology for tight carbonate reservoir.

3 Methodology

To enhance the accuracy of LITCR, researchers have conducted method research from three aspects: lithology, physical properties, and gas-bearing properties. 1. Employing artificial intelligence lithology interpretation based on core experimental data to replace the traditional mineral optimization method for rapid identification of rock properties. 2. Utilizing pore structure evaluation technology based on borehole resistivity imaging logging to replace conventional porosity interpretation and provide detailed explanations of pore types and structures (Khoshbakht et al., 2012; Brekke and Roenitz, 2021; Mazdarani et al., 2023). Applying permeability evaluation technology based on array acoustic logging to replace the traditional porosity-permeability model calculation and improve the accuracy of physical permeability evaluation (Winkler et al., 1989; Tang and Cheng, 1996). 3)Adopting variable parameter fluid evaluation technology based on core experiments to replace the traditional Archie formula interpretation model and enhance the accuracy of gas saturation evaluation parameters. The specific research idea flow is shown in Figure 3.

3.1 Artificial intelligence lithology interpretation based on core experiment

For the conventional logging lithology LITCR, researchers typically use the mineral optimization method for logging interpretation. This method relies on the logging response equation of rocks and minerals, as shown in Table 2. In the process of use, it only depends on the quality of the logging data, not refers to core experimental data. To a certain extent, it cannot obtain results of experimental correction. The fast lithology interpretation technology based on neural network algorithm, through the data analysis of the core experimental X-ray diffraction minerals and the measured well logging curve, establishes the correlation between the X-ray diffraction experimental mineral content and the logging curve, and extends the learning results to the logging interpretation application of the measured well for fast lithology identification and interpretation.

Multiple rock samples from the Majiagou Formation in well A of L area were subjected to X-ray diffraction experiments, and the experimental results are shown in Table 1. By using a small number of samples from this well as a learning well, the network relationship between lithologic content and logging curve is established. After training and learning, the application can finally obtain the rapid interpretation results of lithology, as shown in Figure 4. The first to ninth tracks are conventional logging curves and two-dimensional electrical imaging maps. The 10th track is the calculation result of the mineral optimization method. The 11th track is the calculation result of the neural network. The 12th track is the rapid lithologic interpretation result calculated by the neural network.

3.2 Physical property evaluation

The reservoir physical property evaluation established through conventional logging interpretation can characterize the ability of reservoir fluid. In tight carbonate rocks, favorable reservoirs are described by the effectiveness and connectivity of reservoir pores. The porosity spectrum and pore connectivity evaluation based on electrical imaging logging have higher accuracy in LITCR compared to the porosity evaluation based on conventional logging. The permeability evaluation based on acoustic imaging logging have more precision in LITCR compared to the Por-Perm relationship based on conventional logging. As a result, they are often more widely applied.

3.2.1 Porosity evaluation based on borehole electrical imaging

For tight carbonate reservoirs, borehole resistivity imaging logging is used to analyze porosity effectiveness by the porosity spectrum technology. Additionally, secondary porosity and face rate are further quantitatively characterized to form a fine interpretation of the reservoir and improve the vertical resolution and interpretation accuracy of porosity. The electrical imaging porosity spectrum technology is based on the Archie formula and dense sampling of electrical imaging logging, as shown in Equation 1. Through the circumferential change of resistivity, the circumferential change of porosity can be analyzed. Then, through analysis in the frequency domain, the primary and secondary pores of the formation can be distinguished and evaluated. In heterogeneous formations, considering the porosity changes in different directions around the well can help evaluate the effectiveness and connectivity of the pores and calculate the face rate. The technology of identifying different pore types based on electrical imaging logging images can quantify the contribution of connected pores, evaluate pore connectivity, and describe pore geometry.

$$S_w = n\sqrt{\frac{a \times b \times R_w}{R_t \times \emptyset^m}} \quad (1)$$

Fractured reservoirs are developed at 2,450–2,460 m in well L-B, as shown in Figure 5. The eighth channel is the electrical imaging full sidewall image, the ninth channel is

TABLE 2 Carbonate logging response in theory.

Lithology	Main minerals	Density g/cm3	Neutron porosity %	DTC us/ft	Pe B/e	Natural gamma API
Limestone	Calcite	2.71	0	47.5	5.084	0–5
Dolomite	Dolomite	2.87	1–3	43.5	3.142	5–20
Gypsum	Anhydrite	2.98	0	50.0	5.005	0–30
Salt	Salt	2.00	−2	67.0	4.169	0

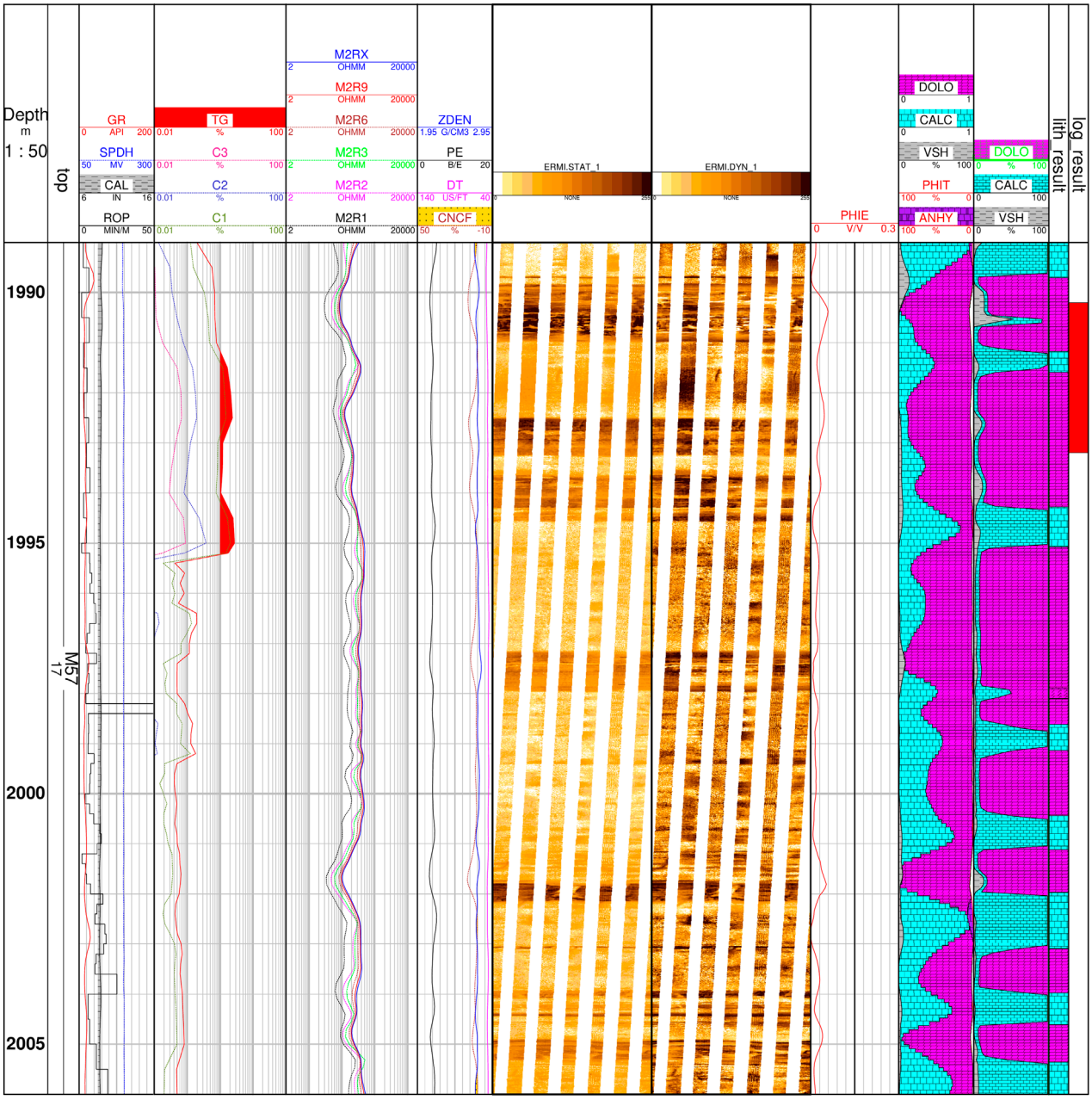

FIGURE 4
Fast interpretation chart of logging lithology based on Artificial Intelligence.

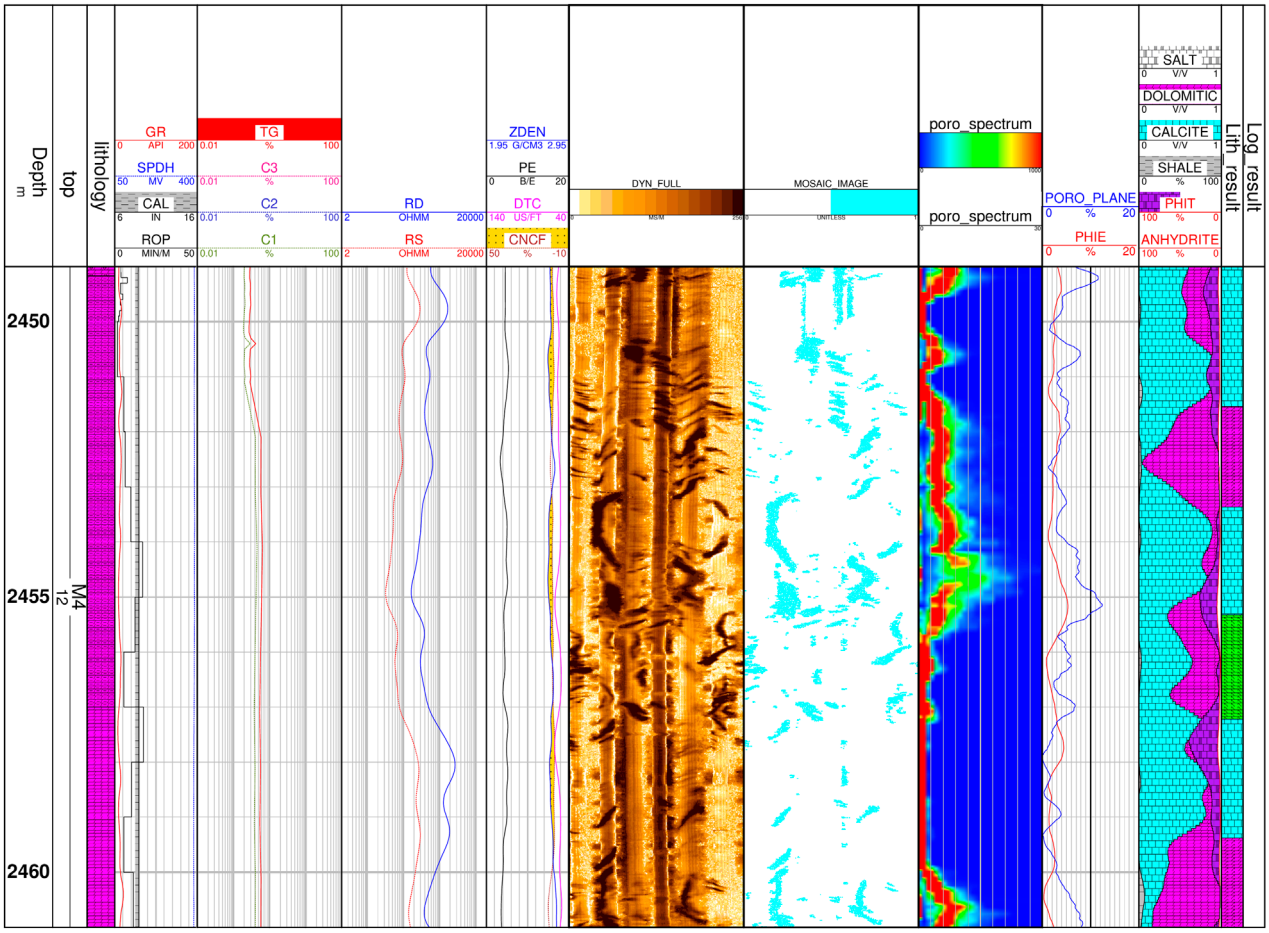

FIGURE 5
Fine evaluation results of porosity based on electrical imaging logging.

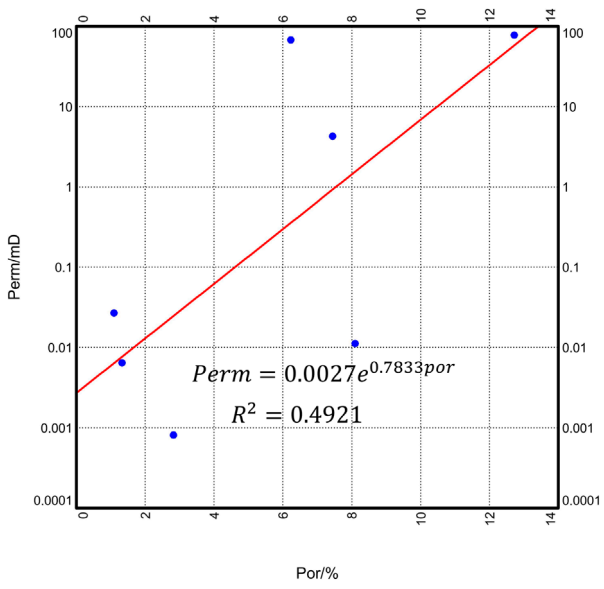

FIGURE 6
Permeability interpretation pore-perm fitting diagramfrom experiment.

the sidewall fracture image extracted by pore effectiveness analysis, the 10th channel is the porosity spectrum, and the 11th channel is the conventional porosity calculation and face rate calculation porosity respectively. The porosity related parameters calculated by electrical imaging have higher vertical and circumferential resolution and a better evaluation effect on connectivity.

3.2.2 Permeability evaluation based on array acoustic wave

For low porosity and low permeability reservoirs, the accuracy error of permeability interpretation by the conventional logging porosity-permeability relationship may be two orders of magnitude. The overburden pressure porosity and permeability experiment was carried out on the tight carbonate rocks in block L. The experimental results are shown in Figure 6. The relationship between porosity and permeability is shown in Equation 2.

$$Perm = 0.0027e^{0.7833por} \quad (2)$$

The correlation coefficient $R^2 = 0.4921$,verifies that the porosity and permeability relationship fluctuates greatly. Based on the

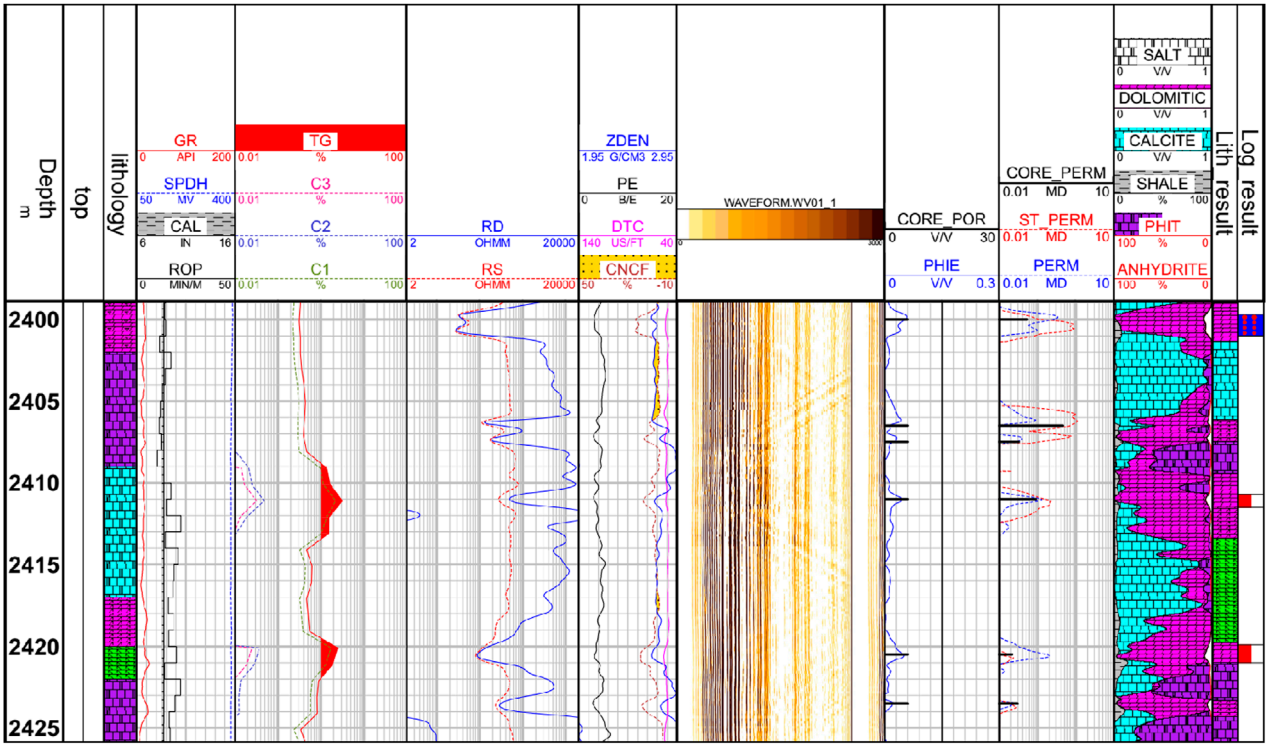

FIGURE 7
Fine evaluation results of permeability based on Stoneley wave inversion.

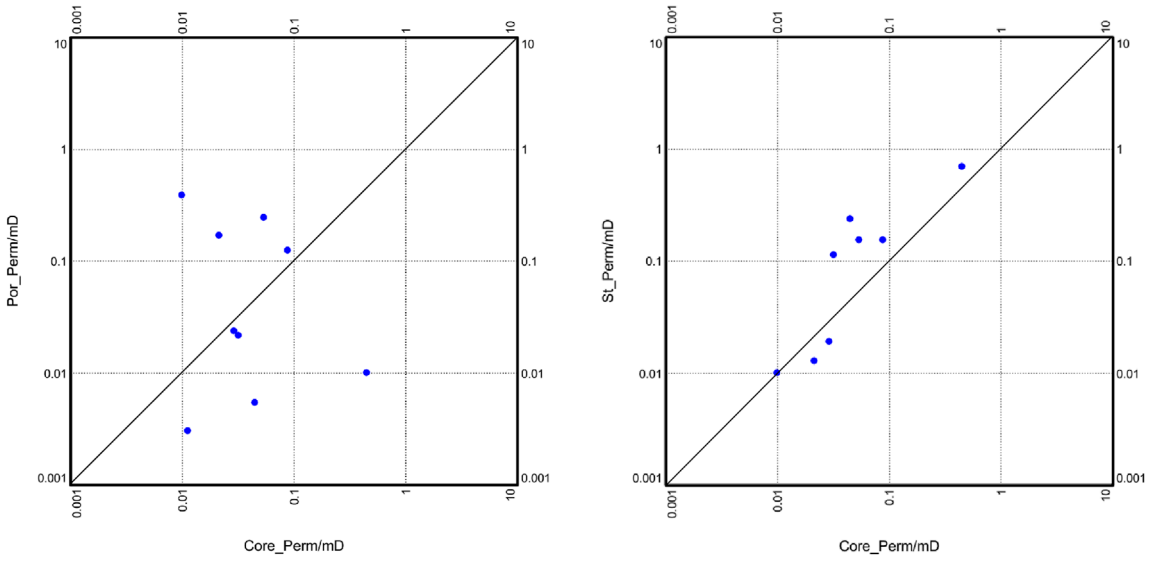

FIGURE 8
Comparison of interpretation accuracy between conventional permeability interpretation (left) and Stoneley wave inversion (right).

TABLE 3 Rock-electrical parameters experiment data.

Depth	a	m	b	n	Por
2,443.0	1	1.42	0.93	3.45	1.30%
2,444.9	1	1.32	0.97	2.26	1.50%
2,420.5	1	1.92	1.12	1.75	8.20%
2,440.8	1	1.39	1.13	2.17	1.10%

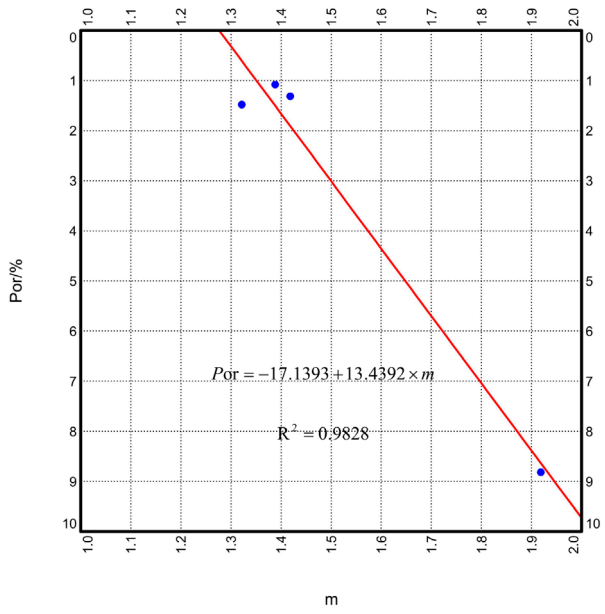

FIGURE 9
Relationship diagram between variable rock-electrical parameters m and porosity.

Stoneley wave method for evaluating reservoir permeability, the amplitude attenuation and time delay in the process of Stoneley wave passing through saturated fluid rock reflect the percolation of reservoir fluid, as shown in Equation 3.

$$E(K_0, Q^{-1}) = \left(\Delta f_c^{msd} - \Delta f_c^{theo}\right)^2 / \sigma_{syn}^2 + 2\pi\sigma_{syn}^2\left(\Delta T_c^{msd} - \Delta T_c^{theo}\right)^2 + \alpha\left(\sigma_{syn}^2 - \sigma_{theo}^2\right) \quad (3)$$

By controlling the minimum error between theoretical calculation and actual measurement, the permeability is inversed, and the permeability accuracy is improved by 1 - 2 orders of magnitude.

Stoneley wave permeability inversion is performed for well L-B, as shown in Figure 7. The eighth channel is acoustic two-dimensional imaging, the ninth channel is conventional interpretation porosity and experimental porosity, and the 10th channel is porosity and permeability model permeability, core permeability, and Stoneley wave inversion permeability. The porosity-permeability model permeability and core permeability, Stoneley wave permeability and core permeability are intersected at discrete points, as shown in Figure 8. The two standard errors are respectively 0.04424 and 0.01349, which verifies that Stoneley wave inversion has higher permeability accuracy.

3.3 Evaluation of variable index fluid based on core experiment

Due to the characteristics of low porosity and permeability, the traditional Archie formula is not very effective in evaluating the fluid properties of tight carbonate rocks. The L-A well in this area conducts a rock resistivity experiment on the core of the dolomite reservoir. The resistivity is measured by changing the rock water saturation, and then the rock-electrical parameters of each rock sample are calculated. The data are shown in Table 3. In this chapter, two methods of fluid quantitative evaluation are compared, and the accuracy of the two methods is compared through the qualitative identification technology of imaging logging and the total hydrocarbon curve of gas logging. The conventional Archie formula calculates the gas saturation through the rock-electrical parameters a, b, m, n obtained from the rock resistivity experiment, as shown in Formula 1. The variable index Archie method considers that the parameters a and b of rock electrical parameters have little change, and m is most susceptible to porosity. Therefore, m is fitted as the relevant formula of porosity to participate in the calculation of gas saturation. The fitting results of M and porosity in this area are shown in Figure 9. The relationship of parameter m and the porosity is shown in Equation 4, and the R^2 is 0.98.

$$Por = -17.1393 + 13.4392 \times m \quad (4)$$

Finally, combined with the total hydrocarbon curve of gas logging, the optimal fluid evaluation method of tight carbonate rock is given by comparing the two methods.

As shown in Figure 10, the eighth channel is the porosity and saturation channel. The blue curve is the water saturation calculated by the Archie formula, the red curve is the water saturation calculated by the variable index Archie formula, and the ninth channel is the apparent resistivity spectrum analysis of electrical imaging logging. The gas saturation interpreted at 2410 m and 2420 m is close to that interpreted by the gas bearing layer and gas water layer, respectively. The characteristics of the electrical imaging spectrum peak also have the corresponding characteristics of the gas layer and gas water layer. In the 2440 m section, the Archie formula is interpreted as the gas bearing layer and gas water layer, the variable index Archie formula is interpreted as the gas water layer, and the characteristics of the electrical imaging spectrum peak are interpreted as the gas water layer, which verifies the correctness of the variable index Archie formula.

4 Discussion

For the tight carbonate reservoir in Block L, we have studied and applied imaging logging series and core experimental data to finely calibrate the logging interpretation. Comparing the interpretation

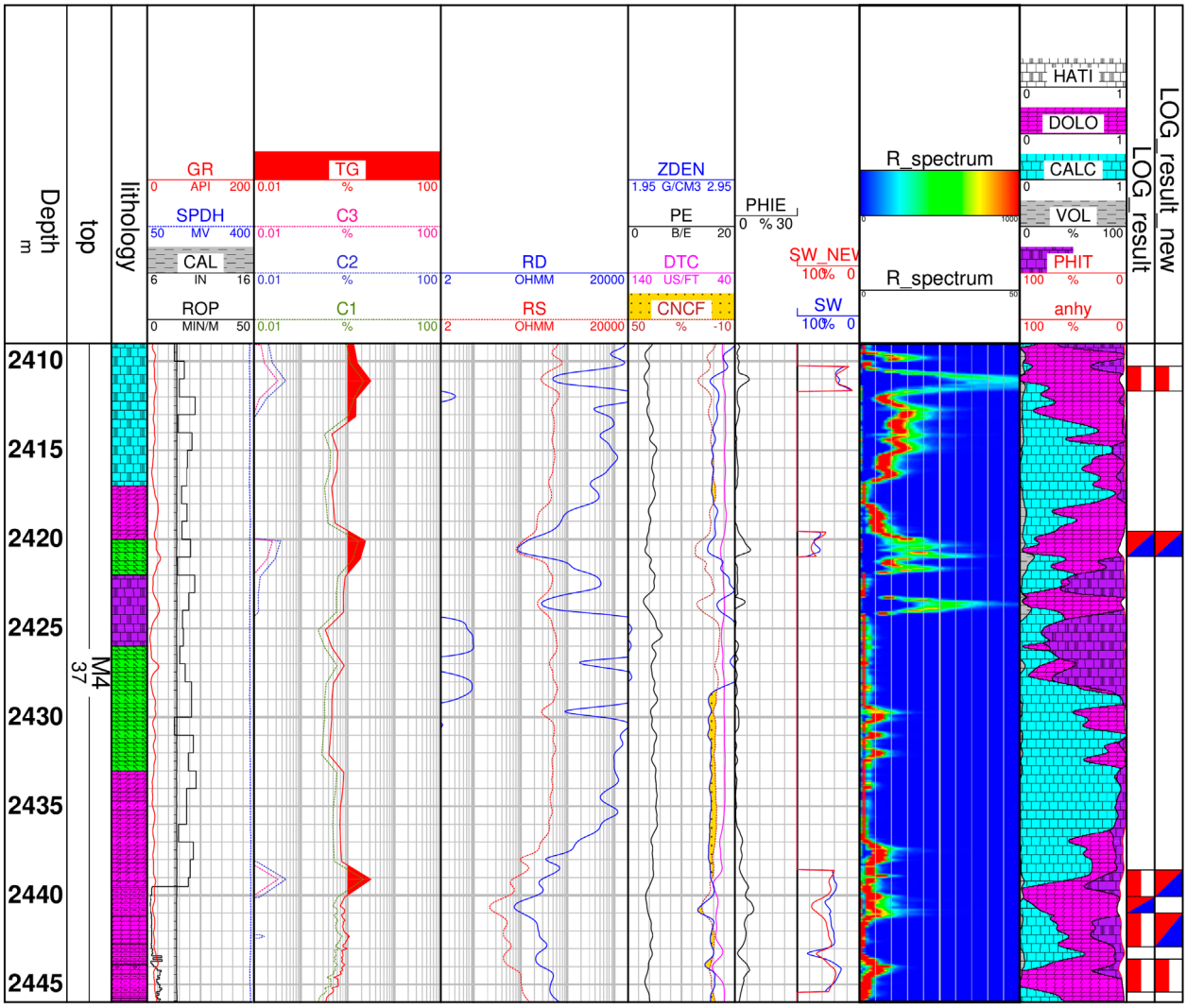

FIGURE 10
Fine interpretation and qualitative verification of gas saturation.

results of conventional logging methods with new results, we have found the following new advances: 1)Conduct rapid lithology interpretation based on artificial intelligence algorithms through core experiments. 2)Obtain porosity spectrum and porosity curve from borehole resistivity imaging logging data to evaluate the effectiveness and connectivity of reservoir pores. 3)Obtain Stoneley wave through array acoustic logging data and invert reservoir permeability parameters. 4)Establish the Archie formula with variable m parameter through core rock resistivity experiments to optimize the interpretation of gas saturation.

5 Conclusion

This study fine tuned the results of conventional logging interpretation through core experiments and imaging logging processing, improving the accuracy of logging interpretation. This method is mainly applied to unconventional reservoirs, including tight sandstones and tight carbonate rocks. For unconventional reservoirs, the application of more advanced instruments and methods can achieve precise interpretation.

Data availability statement

The original contributions presented in the study are included in the article/supplementary material, further inquiries can be directed to the corresponding authors.

Author contributions

LD: Conceptualization, Data curation, Formal Analysis, Funding acquisition, Investigation, Methodology, Project

administration, Resources, Software, Supervision, Validation, Visualization, Writing–original draft, Writing–review and editing. WK: Conceptualization, Data curation, Formal Analysis, Funding acquisition, Investigation, Methodology, Project administration, Resources, Software, Supervision, Validation, Visualization, Writing–review and editing. QY: Conceptualization, Data curation, Formal Analysis, Funding acquisition, Investigation, Methodology, Project administration, Resources, Software, Supervision, Validation, Visualization, Writing–review and editing. YS: Conceptualization, Data curation, Formal Analysis, Funding acquisition, Investigation, Methodology, Project administration, Resources, Software, Supervision, Validation, Visualization, Writing–review and editing.

Funding

The author(s) declare that financial support was received for the research and/or publication of this article. This work was financially supported by the technology project of China National Offshore Oil Corporation, titled "Reservoir Formation Conditions and Exploration Key Technologies for Bauxite and Ordovician in the Eastern Margin of the Ordos Basin" (KJZH-2023-2104). The funder was not involved in the study design, collection, analysis, interpretation of data, the writing of this article, or the decision to submit it for publication.

Conflict of interest

Authors LD, WK, QY, and YS were employed by Cnooc Research Institute Ltd.

Generative AI statement

The author(s) declare that no Generative AI was used in the creation of this manuscript.

Publisher's note

References

Brekke, H., and Roenitz, T. (2021). Using high-resolution microresistivity image logs to reconstruct paleoenvironments and stratal architectures: an example from the mcmurray formation, leismer area, northeastern alberta, Canada. *Aapg Bull.* 105, 1563–1593. doi:10.1306/01282118137

Farouk, S., Fagelnour, M., Zaky, A. S., Arafat, M., Salama, A., Al-Kahtany, K., et al. (2024a). Petroleum system evaluation: hydrocarbon potential and basin dynamics in abu darag sub-basin, northern gulf of suez (Egypt). *Minerals* 14 (11), 1154. doi:10.3390/min14111154

Farouk, S., Qteishat, A., Sen, S., Ahmad, F., El-Kahtany, K., Collier, R., et al. (2025). Characterization of the gas-bearing tight paleozoic sandstone reservoirs of the risha field, Jordan: inferences on reservoir quality and productivity. *Arabian J. Sci. Eng.* 50 (1), 215–235. doi:10.1007/s13369-024-09000-x

Farouk, S., Saada, S. A., Fagelnour, M. S., and Arafat, M. (2024b). Petrophysical and gas chromatographic analysis integration for hydrocarbon identifications in cretaceous reservoirs, azhar field, beni suef basin, Egypt. *Egypt. J. Petroleum* 33 (1), 7. doi:10.62593/2090-2468.1018

Fu, J., Zhao, H., Dong, G., Han, T., Ren, J., Huang, H., et al. (2023). Discovery and prospect of oil and gas exploration in new areas of Ordos Basin. *Nat. Gas. Geosci.* 34 (8), 1289–1304. doi:10.11764/j.issn.1672-1926.2023.06.004

Fu, J., Yu, Z., Li, C., Wang, W., Huang, Z., Wu, X., et al. (2021). New discovery and favorable areas of natural gas exploration in the 4th member of ordovician Majiagou Formation by well mitan 1 in the eastern Ordos Basin. *Nat. Gas. Ind.* 41 (12), 17–27. doi:10.3787/j.issn.1000-0976.2021.12.003

Guo, G., Xu, F. , Liu, L., Cai, Y., Qin, W., Chen, Z., et al. (2024). Enrichment and accumulation patterns and favorable area evaluation of deep coalbed methane in the Fugu area, Ordos Basin. *Coal Geol. Explor.* 52 (2), 81–91. doi:10.12363/issn.1001-1986.23.08.0521

He, H., Guo, X., Zhao, Z., Xi, S., Wang, J., Song, W., et al. (2022). New understandings on gas accumulation and major exploration breakthroughs in subsalt ma 4 member of ordovician Majiagou Formation, Ordos Basin, NW China. *Petroleum Explor. Dev.* 49 (3), 429–439. doi:10.11698/PED.20210659

Jiang, L., Yang, B., Wang, W., and Liu, L. (2022). Logging-based method to identify the lithology in carbonate rocks, Fuxian area. *Nat. Gas Technol. Econ.* 16 (2), 22–27. doi:10.3969/j.issn.2095-1132

Kang, S., Lv, Y., Wang, C., Wang, B., Li, Z., Zhang, Y., et al. (2024). Control of sedimentary environments on gas contents of coal seams: a case study of NO.15 coals bed of the Taiyuan Formation in Shouyang area, Qinshui Basin. *J. Palaeogeogr. Ed.* 26 (02), 416–430. doi:10.7605/gdlxb.2024.02.017

Khoshbakht, F., Azizzadeh, M., Memarian, H., Nourozi, G. H., and Moallemi, S. A. (2012). Comparison of electrical image log with core in a fractured carbonate reservoir. *J. Petrol. Sci. Eng.* 86-87, 289–296. doi:10.1016/j.petrol.2012.03.007

Lai, J., Liu, B., Feng, Q., Pang, X., Zhao, T., Wang, G., et al. (2020). Well logging identification and evaluation of depositional microfacies in dolostones from the 5th Member of the Ordovician Majiagou Formation in the Jingbian gas field, Ordos basin. *Acta Geol. Sin.* 94 (5), 1551–1567. doi:10.19762/j.cnki.dizhixuebao.2020201

Liu, X., He, J., Wei, L., Liu, B, Bao, H., Shi, K., et al. (2024). Sedimentary characteristics and evolution mechanism of Ordovician presalt dolomite reservoirs in the central and eastern Ordos Basin. *Chin. J. Geol.* 59 (3). doi:10.12017/dzkx.2024.045

Mazdarani, A., Kadkhodaie, A., Wood, D. A., and Soluki, Z. (2023). Natural fractures characterization by integration of fmi logs, well logs and core data: a case study from the sarvak formation (Iran). *J. Petroleum Explor. Prod. Technol.* 13, 1247–1263. doi:10.1007/s13202-023-01611-8

Meng, Q., Yu, X., Shi, J., Zhao, H., Liu, Y., Wang, Y., et al. (2023). Genesis and source of natural gas in well mitan-1 of ordovician Majiagou Formation, mid-eastern Ordos Basin, China. *Nat. Gas. Geosci.* doi:10.11764/j.issn.1672-1926.2023.05.011

Qi, Y., Li, D., Yu, S., and Li, Q. (2023). Geophysical exploration methods on bauxite reservoirs in L gasfield, Ordos Basin. *Front. Energy Res.* 11, 1328662. doi:10.3389/fenrg.2023.1328662

Qi, Y., Wu, K., Wang, B., Zheng, X., Li, W., and Li, D. (2024). Lithofacies identification of deep coalbed methane reservoir based on high-resolution seismic inversion. *Front. Earth Sci.* 12, 1440729. doi:10.3389/feart.2024.1440729

Tan, P., Chen, Z., Huang, L., Zhao, Q., and Shao, S. R. (2024b). Evaluation of the combined influence of geological layer property and *in-situ* stresses on fracture height growth for layered formations. *Petroleum Sci.* 21, 3222–3236. doi:10.1016/j.petsci.2024.07.014

Tan, P., Fu, S., Huang, L., Chen, Z., and Cao, J. (2024a). Effects of orthogonal cleat structures on hydraulic fracture evolution behavior. *Geoenergy Sci. Eng.* 241, 213119. doi:10.1016/j.geoen.2024.213119

Tang, X., and Cheng, C. H. (1996). Fast inversion of formation permeability from Stoneley wave logs using a simplified Biot-Rosenbaum model. *GEOPHYSICS* 61, 639–645. doi:10.1190/1.1443993

Wang, S., Wang, G., Huang, L., Song, L., Zhang, Y., Li, D., et al. (2021). Logging evaluation of lamina structure and reservoir quality in shale oil reservoir of Fengcheng Formation in Mahu Sag, China. *Mar. Petroleum Geol.* 133, 105299. doi:10.1016/j.marpetgeo.2021.105299

Wang, S., Wang, G., Lai, J., Li, D., Liu, S., Chen, X., et al. (2020). Logging identification and evaluation of vertical zonation of buried hill in Cambrian dolomite reservoir: a study of Yingmai-Yaha buried hill structural belt, northern Tarim basin. *J. Petroleum Sci. Eng.* 195, 107758. doi:10.1016/j.petrol.2020.107758

Wang, S., Wang, G., Li, D., Wu, X., Chen, X., Wang, Q., et al. (2022). Comparison between double caliper, imaging logs, and array sonic log for determining the *in-situ* stress direction: a case study from the ultra-deep fractured tight sandstone reservoirs, the Cretaceous Bashijiqike Formation in Keshen8 region of Kuqa depression, Tarim Basin, China. *Petroleum Sci.* 19 (6), 2601–2617. doi:10.1016/j.petsci.2022.08.035

Winkler, K. W., Liu, H.-L., and Linton Johnson, D. (1989). Permeability and borehole Stoneley waves: Comparison between experiment and theory. *GEOPHYSICS* 54, 66–75. doi:10.1190/1.1442578

Xu, C, Zhu, G., Ji, H., Zhu, Y., and Sun , Q. (2024). Exploration progress and reserve increase strategy of onshore natural gas of CNOOC. *China Pet. Explor.* 29 (1), 32–46. doi:10.3969/j.issn.1672-7703.2024.01.003

Yang, H., Fu, J., Wei, X., and Ren, J. (2011). Natural gas exploration domains in Ordovician marine carbonates, Ordos Basin. *Acta Pet. Sin.* 32 (5), 733–740.

Yao, J., Bao, H., Ren, J., Sun, L., and Ma, Z. (2015). Exploration of Ordovician subsalt reservoirs natural gas in Ordos Basin. *China Pet. Explor.* 20 (3), 1–12. doi:10.3969/j.issn.1672-7703.2015.03.001

Yu, S., Zhao, Z., Zhu, Y., Zhu, X., Lai, J., Li, D., et al. (2024). Reservoir characteristics and formation model of the bauxite gas reservoir: the Benxi Formation in the LX block, northeast of Ordos Basin, China. *ACS Omega* 9 (16), 18127–18136. doi:10.1021/acsomega.3c10097

Zhang, Y., Zhu, Y., Shao, L., Wang, C., Zhu, X., Liu, F., et al. (2023). Coal accumulation model of epicontinental sea in high-resolution sequence stratigraphic framework: a case study of Taiyuan Formation in Southern Qinshui Basin. *J. Northeast petroleum Univ.* 47 (04), 82–94+10. doi:10.3969/j.issn.2095-4107.2023.04.007

Zhou, J., Li, M., Wu, D., Yu, Z., Zhang, J., Zhang, T., et al. (2023). Characteristics and exploration potential of subsalt gas-bearing system in Majiagou Formation of middle ordovician in the eastern Ordos Basin. *Nat. Gas. Ind.* 43 (3), 34–45. doi:10.3787/j.issn.1000-0976.2023.03.004

Zhu, G., Li, B., Li, Z., Du, J., Liu, Y., and Wu, L. (2022a). Practices and development trend of unconvertional natural gas exploration in eastern margin of Ordos Basin: Taking Linxing-Shenfu gas field as an example. *China offshore Oil Gas* 34 (4), 16–29. doi:10.11935/j.issn.1673-1506.2022.04.002

Zhu, Y., Zhao, Z., Zhang, D., Chen, G., Liu, C., Zhang, L., et al. (2022b). Accumulation conditions and accumulation laws of tight gas in Shenfu area, northeast of Ordos Basin. *China Offshore Oil Gas* 34 (4), 55–64. doi:10.11935/j.issn.1673-1506.2022.04.005

frontiers | Frontiers in Earth Science

TYPE Original Research
PUBLISHED 19 May 2025
DOI 10.3389/feart.2025.1499533

OPEN ACCESS

EDITED BY
Ahmed E. Radwan,
Jagiellonian University, Poland

REVIEWED BY
Shuai Yin,
Xi'an Shiyou University, China
Xu Shenglin,
Chengdu University of Technology, China

*CORRESPONDENCE
Lixue Cheng,
415066437@qq.com

RECEIVED 21 September 2024
ACCEPTED 19 March 2025
PUBLISHED 19 May 2025

CITATION
Cheng L and Peng J (2025) Controls on lacustrine shale reservoir characteristics: insights from deposition, diagenesis, and geochemistry in the Jurassic Qianfoya Formation.
Front. Earth Sci. 13:1499533.
doi: 10.3389/feart.2025.1499533

Controls on lacustrine shale reservoir characteristics: insights from deposition, diagenesis, and geochemistry in the Jurassic Qianfoya Formation

Lixue Cheng[1,2]* and Jun Peng[1]

[1]School of Geoscience and Technology, Southwest Petroleum University, Chengdu, China, [2]College of Air Traffic Management, Civil Aviation Flight University of China, Guanghan, China

Continental lacustrine shales, which are distinct from marine shales in reservoir architecture, pose challenges for resource evaluation due to their complex multi-scale controls. The Middle Jurassic Qianfoya Formation in the Langzhong–Yuanba (LZ-YB) area of the northeastern Sichuan Basin represents a critical continental shale gas target, yet systematic studies of its reservoir quality drivers remain limited. Through integrated sedimentological, geochemical, and petrophysical analyses of core samples, three dominant sedimentary facies are identified: blocky, banded, and laminated, reflecting depositional energy variations. The formation shows favorable hydrocarbon potential with an average total organic carbon (TOC) content of 1.85% and is mineralogically dominated by clay minerals (illite and illite–smectite) and felsic components. Semi-deep lacustrine facies, especially clay-rich lithofacies, demonstrate superior reservoir quality due to higher total organic carbon content and pore networks dominated by silty intergranular pores, interlayer pores in clay minerals, and intragranular pores in pyrite and microfractures, contrasting with marine shales where organic matter-hosted pores prevail. Key controlling factors include organic matter-clay mineral synergy, depositional environment (anoxic conditions, freshwater influx, and terrigenous input), and diagenetic processes such as clay transformation and recompaction. Laminated facies exhibit optimal reservoir quality compared to blocky or banded types, with positive correlations between clay-organic content and storage capacity. These findings highlight the coupled depositional–diagenetic controls on continental shale reservoirs, providing critical insights for global exploration of analogous lacustrine shale systems.

KEYWORDS

lacustrine shale, reservoir characteristics, depositional–diagenetic controls, organic-clay synergy, Qianfoya formation, continental shale reservoirs

1 Introduction

Global advancements in unconventional resource exploration have revealed substantial potential in continental shale systems beyond traditional marine targets. Successful cases include the lacustrine Wolfcamp Formation in the Permian Basin (United States)

with estimated recoverable resources exceeding 20 billion barrels, the organic-rich Cretaceous La Luna Shale in South America, and the Permian Whitehill Formation in the Karoo Basin (South Africa), with total organic carbon (TOC) values as high as 14% (Iacoviello et al., 2019; Milkov et al., 2020; Sohail et al., 2022; Hakimi et al., 2023; Li et al., 2023). In China, recent discoveries highlight prolific continental shale plays, such as the Qingshankou Formation (Songliao Basin), the Chang 7 Member (Ordos Basin), and the Qianfoya (QFY) Formation (Sichuan Basin), which collectively hold over 10 billion tons of shale oil resources (Fan et al., 2020; Jin et al., 2022; Wang and Tang, 2023; Ma and Feng, 2023; Wang E. Z et al., 2023; Bian, 2024; Li H. et al., 2024; Li et al., 2024 J.; Li H et al., 2025). The marine shale of the Lower Silurian Longmaxi Formation in Southern Sichuan is the most typical shale gas reservoir in our country (Li, 2022; Li, 2023a; Radwan et al., 2023; He et al., 2025), while the continental shale strata of the Middle Jurassic QFY Formation is an important alternative area for exploration and development of shale oil and gas in the Sichuan Basin (Li et al., 2023c; Wu et al., 2024). In recent years, the Sinopec Group has successively deployed many exploration wells for the QFY Formation in the Langzhong-Yuanba (LZ-YB) area, northeastern Sichuan Basin, and better oil and gas shows have appeared. However, no commercial breakthrough has been achieved (Zhao et al., 2021; Zhang et al., 2021; Guo et al., 2022).

In the previous research on continental fine-grained sedimentary rocks, in the early stage, scholars around the world mostly studied the single and two controlling factors of reservoir quality (Jadoon et al., 2016; He et al., 2021; He et al., 2022; Liu J et al., 2024; Kasala et al., 2025; Ye et al., 2025; Hou et al., 2025). For example, Dai et al. believed that the total organic carbon (TOC) content and brittle mineral content in the continental shale reservoir of the Yanchang Formation in Ordos are the main factors controlling the development of nanoscale pores (Dai et al., 2016). According to the relationship between diagenetic sequence and pore evolution of the Paleogene lacustrine shale oil reservoir in the Dongying Depression, Zhang et al. suggested that the dissolution and hydrocarbon generation of organic matter can increase reservoir physical properties (Zhang et al., 2018). When Jadoon studied the lacustrine sedimentary environment of Roseneath and Murteree in Australia, it was found that organic-rich shale mainly developed in semi-deep and deep lake environments near the storm wave base (Jadoon et al., 2016). Natural fractures in shale oil formations play a significant role in fluid flow channels. Dong et al. proposed a fracture identification method (FRNN) based on deep learning, and the research results have been applied to the shale of the Yanchang Formation (Dong et al., 2024).

There is still no detailed study on the controlling factors of lacustrine fine-grained sedimentary reservoirs of the Middle Jurassic QFY Formation in the northeastern Sichuan Basin. Therefore, this paper systematically studies the main controlling factors affecting the reservoir quality of fine-grained sedimentary rocks in the QFY Formation from many aspects, which is significant for exploring the mechanism of petroleum enrichment in continental fine-grained sedimentary rocks and promoting the exploration of Jurassic continental shale gas in the northern Sichuan Basin.

2 Geological setting

The area under investigation is situated at the intersection of the depression in the northern Sichuan Basin and the low structural belt in the middle Sichuan Basin, crossing the Zitong–Cangxi nose structural belt, the NE structural belt, the depression in the northern Sichuan Basin, and the Yilong–Pyeongchang low structural belt, bordering the northern front of the Longmenshan in the west, the Micangshan uplift in the north, and the Dabashan arc structural belt in the east (Li et al., 2019; Sun, 2023; Qin and Lan, 2024; Hu et al., 2025) (Figure 1A). Since the Indo-China Movement, the orogenic belts in the margin of the basin (Longmenshan in the northwest and Micangshan in the north) began to uplift successively , providing many sedimentary materials for the study area. Because it is located inside the basin and far from the orogenic belt in the margin of the basin, the tectonic compression is not intensive in the study area, and the overall structure is simple, locally forming low-amplitude fold deformation and developing small-scale faults.

The Middle–Lower Jurassic strata in the LZ-YB area are developed and widely distributed. Controlled by tectonic subsidence of the basin with different orders and lake transgressions, organic-rich shales of semi-deep lacustrine subfacies are developed in the QFY Formation. As there are good terrestrial source rocks and shale reservoirs in the region, it has a huge oil and gas resource potential. According to the lithology, electrical properties, and oil and gas content, the QFY Formation can be divided vertically into 1st Member, 2nd Member, and 3rd Member from bottom to top, and it experiences an entire cycle of lake transgression-regression (Qiu et al., 2021) (Figure 1B). The lake transgressions continue from the 1st Member of the QFY Formation and reach the maximum flooding period in the 2nd Member. The black shale, dominated by semi-deep lacustrine subfacies, is developed, with a small amount of siltstone and fine sandstone. The shale is rich in organic matter and is of good quality (Chen, 2022). From then on, the lake regression gradually begins until the 3rd Member of the QFY Formation. The study area is a sedimentary system of shallow lake-semi-deep lake subfacies and develops sedimentary micro-facies, such as shallow lacustrine facies mudstone, semi-deep lacustrine facies mudstone, and various beach bars. The depth of the sedimentary water gradually increases from north to south.

3 Samples and methods

3.1 Samples

A multifaceted approach was adopted to investigate the reservoir characteristics and controlling factors influencing the quality of continental fine-grained sedimentary rocks within the Middle Jurassic QFY Formation in the LZ-YB area, northeastern Sichuan Basin. A total of 87 core samples were carefully collected from different lithofacies identified in several exploration wells, encompassing claystones, silty claystones, silt-bearing claystones, siltstones, muddy siltstones, and shell limestone. Before analysis, all core samples were cleaned, dried, and cut into smaller representative subsamples.

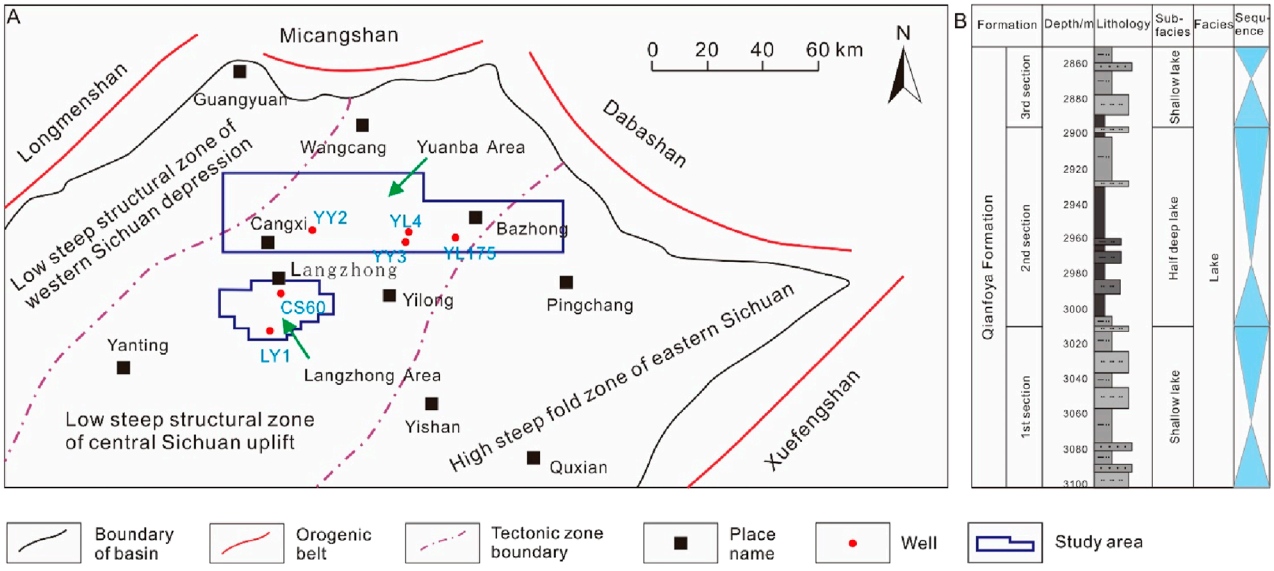

FIGURE 1
Geological setting of the LZ-YB area in the northeastern Sichuan Basin. **(A)** Structural location. **(B)** Stratigraphic column diagram.

3.2 Methods

Detailed macroscopic core observations were performed using a binocular microscope to document rock structures, including bedding characteristics (e.g., massive, banded, and laminated), bioturbation features, and any other visible rock structures indicative of the depositional environment. The lithological variations were documented by observing grain size variations, mineral composition based on visual inspection, and color changes. Additionally, any visible fractures were characterized based on their presence, orientation, and characteristics (e.g., open, filled, and mineralized), and evidence of hydrocarbons, such as oil staining, fluorescence, or gas shows, were recorded.

3.2.1 TOC analysis

The hydrocarbon generation potential of the QFY Formation was assessed by analyzing the TOC content of selected shale samples using a LECO CS-230 carbon-sulfur analyzer (He et al., 2022). Powdered samples were treated with hydrochloric acid (HCl) to remove carbonate minerals, and the TOC content was determined by combusting the treated samples at high temperatures in an oxygen-rich environment and measuring the evolved carbon dioxide (CO_2) using an infrared detector.

3.2.2 Whole-rock mineral composition analysis

The mineralogical composition of the core samples was determined through whole-rock X-ray diffraction (XRD) analysis. Representative rock samples were ground to a fine powder using a mortar and pestle and analyzed using a Bruker D8 Advance X-ray diffractometer. The resulting diffraction patterns were analyzed to identify and quantify the relative abundance of mineral phases, including quartz, clay minerals (e.g., illite, smectite, kaolinite, and chlorite), carbonate minerals (e.g., calcite and dolomite), and feldspar (Yang L. R et al., 2022; Nag et al., 2025; Peng et al., 2025). In whole-rock XRD analysis of fine-grained continental sedimentary rocks, acid combinations must be selected for sample digestion according to the mineral composition and target elements. HF + HNO_3 was used in this study, and the digestion process was as follows: (1) Sample preparation: ground to less than 200 mesh to ensure uniformity. (2) Acid mixing: 0.1–0.5 g of the sample was weighed into a polytetrafluoroethylene (PTFE) digestion tank, and 5–10 mL of HNO_3 and 3–5 mL of HF were added. (3) Closed digestion: using a microwave digester or high-pressure digester, the sample was heated to 180°C–200°C for 2–4 h (4) Acid treatment: After digestion, the solution was dried, and HNO_3 was added to redissolve and dry again (to remove residual HF and prevent damage to the ICP-MS atomizer). (5) Volume: Diluted HNO_3 (2%–5%) was added to bring the volume to 25–50 mL. The solution was filtered and tested on the machine.

3.2.3 Physical property analysis

Porosity and permeability, key parameters for reservoir quality assessment, were measured on cylindrical core plugs extracted from representative samples. Porosity was measured using a helium porosimeter (e.g., Quantachrome UltraPore) which measures the volume of helium gas permeating into the pore spaces of a core plug at a known pressure (Peng et al., 2018). Permeability, a measure of the ability of the rock to transmit fluids, was measured using a nitrogen gas permeameter (e.g., Vinci Technologies Permeameter) by flowing nitrogen gas through the core plug at a controlled pressure gradient and measuring the flow rate and pressure drop (Wen et al., 2024).

3.2.4 Reservoir pore characteristics

Scanning electron microscopy (SEM) was employed to visualize the pore structure and morphology of the QFY Formation. Small rock chips were mounted on SEM stubs, coated with gold to

prevent charging during imaging, and imaged using a high-resolution scanning electron microscope (e.g., FEI Quanta). Argon ion polishing was used to remove surface irregularities and expose the internal pore structure for better visualization. Large area backscattering scanning electron microscopy (MAPS) imaging technology, a technique that involves acquiring and stitching multiple high-resolution SEM images, was used to create a mosaic image of the sample surface (Jun and Liang, 2024). This approach allowed for the identification and quantification of different pore types (intergranular pores, interlayer pores in clay minerals, organic matter-hosted pores, and microfractures) based on their size, shape, and connectivity.

3.2.5 Geochemical analysis

Geochemical analyses were performed to determine the concentrations of specific elements and to understand the paleoenvironmental conditions during the deposition of the QFY Formation. Rock samples were digested using a combination of acids, and the concentrations of V, Cr, Ni, Sr, Ba, Al, Fe, Mn, and Mg were measured using inductively coupled plasma mass spectrometry (ICP-MS) or inductively coupled plasma atomic emission spectrometry (ICP-AES). The measured elemental concentrations were used to calculate various paleoenvironmental proxies, including V/Cr and V/(V + Ni) ratios for redox conditions, Sr/Ba ratios for paleosalinity, total rare earth elements (∑REE) and Fe/Mn and Mg/Ca ratios for paleoclimate, and Al content for paleoproductivity (Tang et al., 2023).

Diagenetic analysis was performed to evaluate the impact of post-depositional processes on the reservoir quality of the QFY Formation. Thin sections of selected core samples were prepared and examined under a polarized light microscope to identify diagenetic features, including compaction, cementation, dissolution, and clay mineral transformations. The compaction ratio was estimated based on the intensity of diagenetic alterations observed in the thin sections. The porosity loss due to cementation was evaluated using the Houseknecht method , which involves comparing the measured porosity with a theoretically calculated porosity based on the initial mineralogy of the rock.

4 Results

4.1 Reservoir petrological characteristics

Fine-grained sedimentary rocks have undergone multiple processes such as sedimentation, diagenesis, and tectonism, to form a complex rock fabric. Rock structure, organic matter abundance, and mineral composition are the main components of the petrological characteristics of the organic-rich, fine-grained sedimentary rocks (Gong et al., 2017; Wu and Kong, 2025).

4.1.1 Rock structure

The structural types of sedimentary rocks are determined by the arrangement of mineral components. Based on the observations of cores and thin sections, the rock structures of fine-grained sedimentary rocks of the QFY Formation in the study area can be divided into three types: blocky, banded, and lamellar.

The blocky structure is the most common structure in the fine-grained sedimentary rocks of the QFY Formation in the NE Sichuan Basin. It is characterized by no significant changes in mineral composition and particle size, and the rock is homogeneous with a thickness generally greater than 2.5 cm. Different rock structures and lithologic combinations indicate different forming environments. Blocky claystone and blocky silty claystone are fine-grained sedimentary rocks dominated by clay minerals that are transported to deepwater areas far from the provenance, reflecting the semi-deep lake environment with weak hydrodynamics (Figures 2A, B). In contrast, siltstone, muddy siltstone, and shell limestone, which are rapidly deposited under strong hydrodynamics in shallow lakes, are generally blocky in structure and well sorted (Figures 2C, D).

Banded structures are parallel overlaps of alternately dark and bright banded on the core. The majority are horizontal, a few are wavy, and the thickness is greater than 0.5 cm and less than 2.5 cm. The formation of this structure in the study area is mainly related to the sudden increase of hydrodynamics in shallow water areas, such as terrigenous events including storms and turbidity currents (Figure 2E).

The lamellar structure in the study area can be divided into straight laminae and wavy laminae. The horizontal lamellar structure in lamellar silt-bearing claystone, lamellar silty claystone, and laminated claystone is a typical microrock structure of terrigenous hydrostatic sedimentary fine-grained sedimentary rocks (Figures 2F–I). It is formed in a low-energy environment with a warm and humid climate and semi-enclosed or closed water, representing the shallow lake and semi-deep lake environment with weak hydrodynamics. The wavy laminar structure indicates that the sedimentary water is relatively volatile, and it is speculated that the wavy laminae are formed in the shallow lake environment with shallow water and strong hydrodynamics.

4.1.2 Organic matter abundance

Statistically, the TOC content of the QFY Formation in the study area ranges from 0.12% to 3.71%, with an average of 1.85%. In the middle 2nd Member of the QFY Formation, the TOC content is the highest and gradually decreases vertically upward and downward. Compared with marine fine-grained sedimentary rocks, continental fine-grained sedimentary rocks are characterized by rapid sedimentary changes and a complex sedimentary environment. The development of organic-rich fine-grained sedimentary rocks is mainly controlled by the sedimentary environment with deepwater reduction.

4.1.3 Mineral composition

Whole-rock XRD analysis shows that the fine-grained sedimentary rocks of the QFY Formation in the study area are mainly composed of quartz, clay minerals, and carbonate minerals, with a small amount of feldspar, pyrite, siderite, and anhydrite. Overall, the content of clay minerals and quartz is high, and the carbonate minerals show local enrichment. It is observed that the quartz content in the analyzed samples varies from 8.7% to 60.9%, with an average value of 38.5%. Similarly, the clay content ranges from 19.4% to 66.6%, with an average of 48.9%, while the carbonate content ranges from 0.2% to 17.8%, with an average value of 2.3%. The clay minerals identified in the QFY Formation of the study area

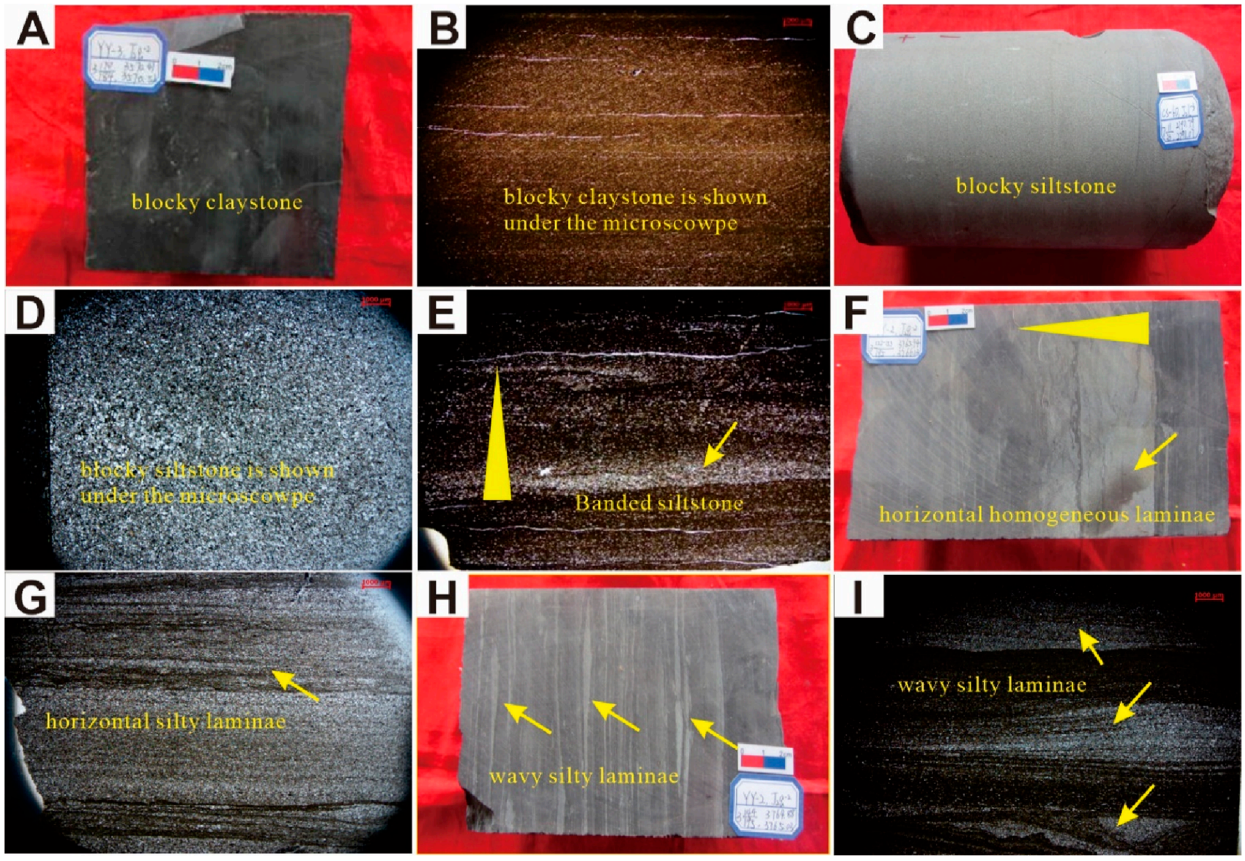

FIGURE 2
Different sedimentary structures of fine-grained sedimentary rocks in the QFY Formation. **(A)** Well YY3, 3570.52 m, 2nd Member, blocky claystone. **(B)** Well CS60, 2804.1 m, 2nd Member, blocky claystone. **(C)** Well CS60, 2792.79 m, 2nd Member, blocky siltstone. **(D)** Well YY3, 3556.16 m, 2nd Member, blocky siltstone. **(E)** Well LY1, 2779.7 m, 2nd Member, banding silty claystone. **(F)** Well YY2, 3725.94 m, 2nd Member, horizontal homogeneous laminae are developed. **(G)** Well YY3, 3603.06 m, 1st Member, horizontal silty laminae. **(H)** Well YY2, 3765.03 m, 2nd Member, wavy silty laminae. **(I)** Well YY3, 3523.98 m, 3rd Member, wavy silty laminae.

are illite, illite-smectite mixed layer, kaolinite, and chlorite. Notably, the highest content is observed for the illite-smectite mixed layer, which ranges from 28% to 55%, with an average of 42.48%, followed by illite, which ranges from 15% to 43%, with an average of 34%. The kaolinite content ranges from 2% to 35%, with an average of 6.39%, while the chlorite content ranges from 11% to 26%, with an average of 17% (Figure 3; Table 1).

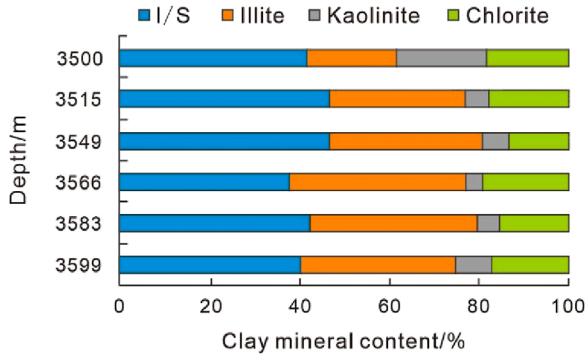

FIGURE 3
Percentage composition of clay minerals in the QFY Formation.

4.2 Reservoir physical properties

The shale gas exploration wells in the study area have a daily gas production of 0.71 × 10^4 m^3 and a daily oil production of 3 t in the fine-grained sedimentary rocks of the QFY Formation. To date, the cumulative gas production has reached 260.84 × 10^4 m^3 and the cumulative oil production has reached 2676.5 t. According to the test and analysis of the gas-bearing property for shale, the gas content of the fine-grained sedimentary rocks of the QFY Formation ranges from 0.25 m^3/t to 1.98 m^3/t, with an average of 1.03 m^3/t, and the gas-bearing property is quite good (the gas content is more than 1.00 m^3/t). The highest gas content is in organic-rich black blocky claystone (TOC is greater than 1.50%), grayish-black blocky silty claystone, and grayish-black laminated silty claystone, which range from 0.60 m^3/t to 1.98 m^3/t, with an average of 1.61 m^3/t (Figure 4).

The physical property tests of the core in the QFY Formation show that the porosity of black blocky claystones is between 0.4%

TABLE 1 XRD results of the clay minerals in the QFY Formation.

Sample number	Stratum	Depth/m	Relative content of clay minerals/%			
			Illite–smectite mixed layer	Illite	Kaolinite	Chlorite
1	QFY Formation	3505.16	55	25	6	14
2		3508.83	28	15	35	22
3		3510.17	46	30	4	20
4		3511.55	54	25	8	13
5		3514.78	53	29	2	16
6		3516.15	44	29	5	22
7		3518.26	37	32	5	26
8		3523.48	51	29	8	12
9		3526.59	48	31	6	15
10		3527.04	38	35	6	21
11		3529.2	49	33	4	14
12		3533.82	52	34	3	11
13		3539.02	46	30	13	11
14		3541.42	37	40	5	18
15		3545.43	43	35	5	17
16		3555.38	52	34	5	11
17		3558.66	34	43	4	19
18		3561.70	43	35	4	18
19		3562.51	34	40	3	23
20		3563.65	41	42	3	14
21		3565.10	37	36	6	21
22		3566.40	38	38	4	20
23		3569.51	32	41	5	22
24		3571.48	42	40	3	15
25		3574.66	52	32	5	11
26		3579.82	37	37	8	18
27		3583.15	41	39	4	16
28		3585.03	38	43	3	16
29		3602.55	42	32	6	16
30		3603.80	45	33	6	16
31		3605.33	28	39	14	19

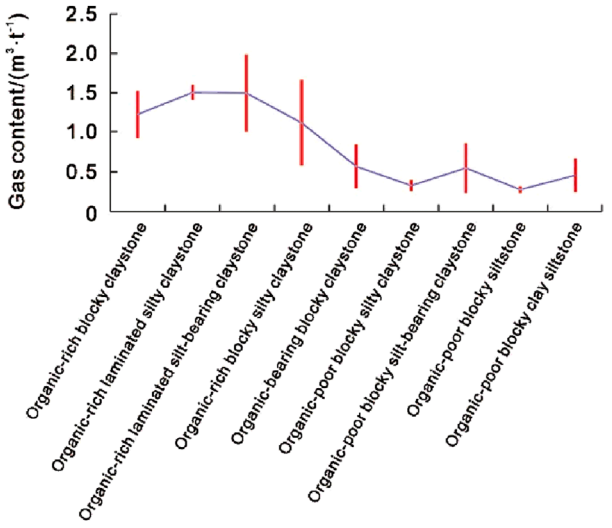

FIGURE 4
Gas-bearing test diagram of each lithofacies in the QFY Formation.

and 5.1%, with an average of 2.2%, and the permeability is between 0.004×10^{-3} μm^2 and 11.90×10^{-3} μm^2, with an average of 2.992×10^{-3} μm^2. The porosity of the grayish-black laminated silty claystone is between 0.6% and 3.3%, with an average of 1.9%, and the permeability is between 0.002×10^{-3} μm^2 and 0.689×10^{-3} μm^2, with an average of 0.289×10^{-3} μm^2. The porosity of the blocky silt-bearing claystone ranges from 1.0% to 4.8%, with an average of 3.2%, and the permeability is 0.144×10^{-3} μm^2 and 0.38×10^{-3} μm^2, with an average of 0.265×10^{-3} μm^2. According to the definition standard of the geological evaluation method for shale gas (GB/T 31,483–2015), the organic-rich continental shale in the semi-deep lake subfacies of the Middle Jurassic QFY Formation in the LZ-YB area, northeastern Sichuan Basin, satisfies the following conditions: the porosity, permeability, and TOC are greater than 2%, 0.1 × 10–^{3} μm^2, and 1%, respectively, and meet the standard of minimum industrial gas flow rate for continental shale gas (daily gas production is greater than 5,000 m^3), indicating that the fine-grained sedimentary reservoir in the QFY Formation can be used as a good reservoir.

4.3 Reservoir space types and characteristics

A total of 87 core samples of fine-grained sedimentary rocks in the QFY Formation from several coring wells in the study area were observed by argon ion polishing SEM. The examination of fine-grained sedimentary rocks under a microscope identified five distinct types of pores: silty intergranular pores, interlayer pores in clay minerals, intragranular pores in pyrite, organic matter-hosted pores, and microfractures.

4.3.1 Silty intergranular pores

Silty intergranular pores are one of the most common pores in the fine-grained sedimentary rocks of the QFY Formation in the study area. Because the LZ-YB area in the northeastern Sichuan Basin is close to the provenance of the Micangshan-Dabashan in the northern Sichuan Basin, the fine-grained sedimentary rocks are mixed with some silty sediments from the continental crust. These silty particles of terrigenous debris are dispersed in the shale. The intergranular pores are developed at the contact zones of mineral particles, but are affected by the shape of the detrital grains and the surrounding clay minerals. In particular, the silty intergranular pores formed by the dissolution of clay minerals and carbonate minerals are mostly irregular and pore-shaped. Some intergranular pores are distributed at the edges of brittle minerals such as quartz and feldspar grains, and the morphology of brittle minerals can also be seen through the distribution of intergranular pores (Figure 5A). In general, the porosity and permeability of brittle minerals are poor, and the pores are mostly filled with organic matter. Because of the influence of compaction and cementation in the diagenetic process, especially in the early diagenetic stage, a large number of intergranular pores are compressed and filled, resulting in relatively poor connectivity between pore throats.

4.3.2 Interlayer pores in clay minerals

According to the XRD analysis of clay minerals of rock samples in the QFY Formation, the content of illite–montmorillonite mixed layer is the highest in clay minerals of fine-grained sedimentary rocks of the QFY Formation in the study area, followed by illite, a small amount of kaolinite and chlorite, and montmorillonite is not developed. The illite–smectite mixed layer is the transitional mineral from montmorillonite to illite, which is honeycomb-shaped and flocculent. The illite is scaly and feathery, scattered on the surface of other mineral particles and filled between particles in the form of clay bridges. The morphology of these two clay minerals is mainly schistose. It gives the interlayer pores in the clay minerals in the study area a generally strong directionality and makes them show a parallel distribution and lamellar distribution with the cleavage plane of the clay minerals (Figure 5B). The interlayer pores can be filled by pyrite and organic matter (Chen et al., 2013). The grain boundary microfractures developed along the surface of clay minerals are mostly long banding. The long axis of the pores is generally between 10 nm and 50 nm, and the short axis is usually less than 1 μm. Due to the poor compressive resistance of clay minerals, the interlayer pores in clay minerals are sometimes curved under the influence of compaction in the early diagenetic stage. Because of the high content of clay minerals in fine-grained sedimentary rocks, the interlayer pore in clay minerals is the main pore type of the QFY Formation continental fine-grained sedimentary rocks in the study area, and its proportion is higher than that of other pores.

4.3.3 Intragranular pores in pyrite

Pyrite is formed in an anoxic reducing environment, and it is nodular-shaped and banded bedding or in a dispersed distribution in claystone and silty claystone. Pyrite is mainly developed in the form of framboidal aggregates in the fine-grained sedimentary rocks of the QFY Formation in the LZ-YB area (Figure 5C). Because the crystals are compacted, the spherical framboidal aggregates are formed. The aggregate diameters range from several microns to tens of microns. The pore size of the intragranular pores in the aggregates is large, approximately 10–80 nm. There are usually clay minerals or organic matter among framboidal pyrite, and the intragranular

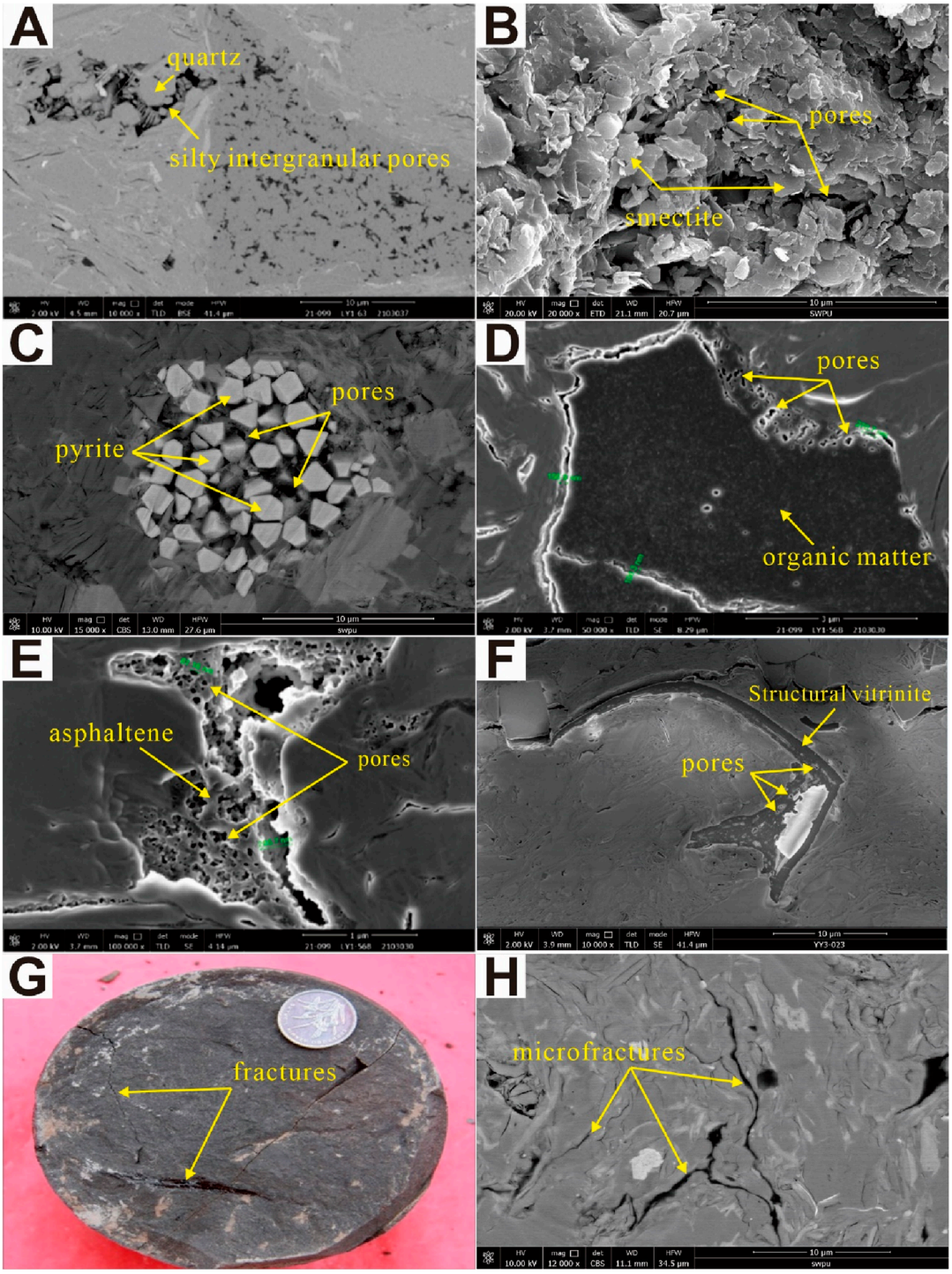

FIGURE 5
Pore characteristics of fine-grained continental sedimentary rocks in the QFY Formation. **(A)** Well LY1, 2746.36 m, 2nd Member, residual silty intergranular pores filled with quartz (SEM). **(B)** Well LY1, 2800.89 m, 2nd Member, smectite is distributed in sheets, and the pores between them have strong orientation (SEM). **(C)** Well YL4, 3647.14 m, 1st Member, intercrystalline pores in framboidal pyrite (SEM). **(D)** Well LY1, 2780.93 m, 2nd Member, scattered pores are developed around organic matter (SEM). **(E)** Well LY1, 2781.15 m, 2nd Member, pores are honeycomb-shaped (SEM). **(F)** Well YY3, 3518.26 m, 2nd Member, pores are developed in structural vitrinite (SEM). **(G)** Well LY1, 2785.46 m, 2nd Member, several fractures are developed with irregular surface and different widths, which are filled with asphaltene (photograph); **(H)** Well LY1, 2937.65 m, 1st Member, microfractures are developed (SEM).

pores in pyrite are easily blocked by surrounding organic matter or authigenic clay minerals.

4.3.4 Organic matter-hosted pores

Organic matter-hosted pores are usually formed in the process of hydrocarbon generation and exist within organic particles (Borjigin et al., 2021; Li H et al., 2022). The pore sizes of organic matter-hosted pores in the fine-grained sedimentary rocks of the QFY Formation in the study area are mainly nanoscale, with a diameter of approximately 30–50 nm, and the overall connectivity is poor. Two types of organic matter-hosted pores can be seen using SEM. One is in dispersed distribution with the organic matter filling in the silty intergranular pores as the main carrier (Figure 5D). Another is the honeycomb-shaped irregular oval or round hole (Figure 5E), with asphalt filled in microfractures as the main carrier, which is the main place for shale oil and gas preservation. The organic matter-hosted pores in fine-grained sedimentary rocks in the study area, observed by argon-ion-polishing SEM, are developed in the structural vitrinite (Figure 5F), and the pores are not developed in the vitrodetrinite and inertrodetrinite. With increasing burial depth and the influence of compaction, the scale of organic matter-hosted pores increases from microns to nanometers. In addition, organic matter-hosted pores are produced with the generation of organic hydrocarbons. Therefore, its pore characteristics are related to the type of organic matter, TOC, and maturity.

4.3.5 Microfractures

Macroscopically, shale bedding fractures and bedding slip scratches can be seen through the core (Li et al., 2021; Li H et al., 2025). Small-scale inclined joints and high-angle fractures are locally developed, with a length of 3–30 cm, and some fractures are filled with oil bloom and asphalt (Figure 5G). However, irregular inclined joints develop in the siltstone, while vertical fractures develop relatively, with a length of 3–24 cm and a width of 0.2–2 mm. Argon ion polishing SEM reveals that microfractures are mainly developed between clay mineral grains, the margins of organic matter, and the margins of the shell (Figure 5H).

According to the MAPS, the content of silty intergranular pores, interlayer pores in clay minerals, and intragranular pores in pyrite is the highest among all types of pores in continental fine-grained sedimentary rocks in the study area, followed by microfractures, and the content of organic matter-hosted pores is the lowest at less than 10%. (Figure 6).

5 Discussion

The QFY Formation in the study area is predominantly a shallow lacustrine to semi-deep lake sedimentary system. Within this system, semi-deep lacustrine subfacies claystones rich in organic matter and silty claystones are extensively developed, serving as the primary reservoir rock types for fine-grained sedimentary reservoirs. The influence of sedimentation on the fine-grained sedimentary rock reservoirs in the QFY Formation is mainly reflected in the following three aspects: (1) sedimentary facies control the enrichment of organic matter within fine-grained sedimentary rocks; (2) sedimentary facies dictate the types of rock structures that form fine-grained sedimentary rocks; and (3) sedimentary facies influence the mineral composition, thereby determining the distribution and development of different lithofacies within the fine-grained sedimentary rocks. Based on previous research methods, this paper comprehensively analyzed the effects of organic content, mineral composition, rock structure, sedimentary environment, and diagenesis on the reservoir quality of continental fine-grained sedimentary rocks in the study area.

5.1 Relationship between organic matter content and reservoir quality

According to previous studies, the organic matter content in fine-grained sedimentary rocks is closely related to the development of organic matter-hosted pores (Jiang et al., 2023; Zhou et al., 2025). The scatter plot conducted on the fine-grained sedimentary rocks in the studied region revealed a positive correlation between the TOC content and porosity (Figure 7). Furthermore, the results of the nano-CT experiment showed that the developing degree of organic matter-hosted pore development is positively associated with the content of organic matter and clay minerals (Aljamaan et al., 2017; Radwan et al., 2022; Wang B et al., 2023). With the increase of TOC and clay mineral content, the better the connectivity of shale pores and the higher the porosity.

5.2 Relationship between rock structure and reservoir quality

It is believed that natural microfractures are easily developed in lamellar and layered lithofacies (Gale et al., 2014; Wang and Wang, 2021; Li J et al., 2022; Liu G. Y et al., 2024). The porosity test results of more than 470 samples of the QFY Formation in the study area showed the following rules: the porosity of lamellar lithofacies was the highest, ranging from 1.3% to 5.9%, with an average of 4.0%. The porosity of banded lithofacies was the second, ranging from 1.0% to 4.8%, with an average of 2.7%, while the porosity of massive lithofacies was relatively low, ranging from 0.4% to 4.2%, with an average of 1.5% (Table 2).

According to the capillary pressure tested by the mercury intrusion method, the reservoir properties of lithofacies with different rock structures are different from each other (Luo et al., 2003; Yuan et al., 2016). The maximum connected pore throat radius of lamellar lithofacies was found to be between 0.011 μm and 0.148 μm with an average of 0.049 μm, and the median pore throat radius was found to be between 0.004 μm and 0.021 μm, with an average of 0.008 μm; the maximum connected pore throat radius of banded lithofacies ranged from 0.021 μm to 0.041 μm, with an average of 0.028 μm, and the median pore throat radius ranged from 0.004 μm to 0.006 μm, with an average of 0.005 μm; the maximum connected pore throat radius of massive lithofacies was found to be between 0.016 μm and 0.034 μm, with an average of 0.027 μm, and the median pore throat radius was found to be between 0.003 μm and 0.006 μm, with an average of 0.004 μm (Table 3). Comparing the three lithofacies, the lamellar lithofacies was found to have the largest maximum connected pore throat radius and the largest average pore throat radius, indicating that its lower limit of effective

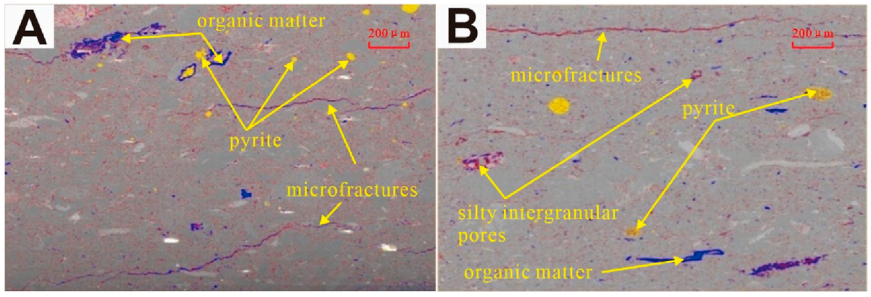

FIGURE 6
Void content analysis of fine-grained sedimentary rocks in the QFY Formation by macro-area backscatter imaging (MAPS). The pores are dominated by silty intergranular pores and microfractures between mineral particles (red is pores, blue is organic matter, and yellow is pyrite). **(A)** Well YY3, 3518.26 m, 2nd Member. **(B)** Well YY3, 3566.40 m, 2nd Member.

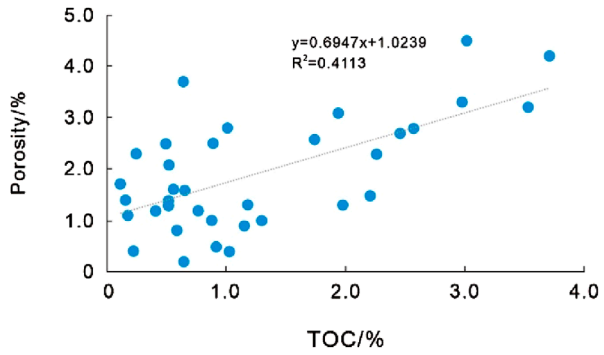

FIGURE 7
Relationship between TOC content and porosity.

TABLE 2 Porosity comparison of fine-grained sedimentary reservoirs with different rock structures.

Area	Well	Major lithofacies types	Porosity/%
LZ	LY1	Blocky claystone	0.40–2.50/1.35
		Banding silty claystone	1.00–3.10/1.80
		Blocky shell limestone	0.40–1.00/0.70
		Blocky siltstone	1.00–1.50/1.25
		Blocky clay siltstone	0.60–0.90/0.80
		Blocky silty claystone	0.60–1.40/1.00
		Laminated silt-bearing claystone	2.60–4.60/3.60
YB	YY3	Banding silty claystone	0.90–4.80/3.17
		Laminated claystone	4.10–5.10/4.60
		Blocky claystone	0.50–2.20/1.35
		Laminated silty claystone	3.20–5.90/4.83
		Blocky siltstone	0.90–1.50/1.20

pore throat radius was also the largest. From the perspective of mercury withdrawal efficiency, the numerical values of the lamellar facies and banded facies were significantly higher than those of the massive lithofacies, both of which were greater than 50%, indicating good reservoir connectivity. In general, the lamellar facies were found to have the best reservoir properties, followed by the banded lithofacies, while the massive lithofacies were found to have the worst reservoir properties.

5.3 Relationship between mineral composition and reservoir quality

The lithology of fine-grained sedimentary rocks of the QFY Formation in the study area can be classified into six types: claystone, silty claystone, silt-bearing claystone, siltstone, muddy siltstone, and shell limestone (Guo et al., 2014; Yang Y. M et al., 2022; Yang et al., 2023; He et al., 2023). The content of quartz in siltstones and muddy siltstones was found to be relatively high. Figures 8A–C show that the quartz content in fine-grained sedimentary rocks in the study area is negatively correlated with porosity, pore size, and pore volume. The higher the siliceous mineral content, the lower the reservoir space. Although quartz in fine-grained sedimentary rocks can increase the brittleness of fine-grained reservoirs, making them easier to fracture in the process of development, the main pores (intergranular pores) between the siliceous brittle particles are easily compressed and gradually decrease to non-existent during the burial process, indicating that the excessive siliceous minerals are not conducive to the development of pores (Zhang et al., 2020; Wan et al., 2025). According to the IUPAC classification standard, the curve of nitrogen adsorption has obvious hysteresis loops (Chen et al., 2023; Li J. J. et al., 2024). In the nitrogen adsorption experiment, the hysteresis loops of claystone, silt-bearing claystone, and silty claystone belong to H3 (Figure 9), reflecting the laminar pores. Because the clay minerals in the fine-grained sedimentary rocks of the QFY Formation in the study area were found to be dominated by the illite-smectite mixed layer and illite, the pores among the mineral compositions mainly composed of flaky particles mostly showed laminated features parallel to crystal structures under SEM. The pores with the laminated structure are beneficial in increasing

TABLE 3 Pore size comparison of fine-grained sedimentary reservoirs with different rock structures.

Well	Depth/m	Rock structure	Lithofacies types	Maximum connected pore throat radius/nm	Median pore throat radius/nm	Mercury removal efficiency/%
LY1	2810.81	Blocky	Blocky silty claystone	0.025	0.004	46.09
LY1	2790.66		Blocky claystone	0.034	0.005	30.17
LY1	2791.24		Blocky claystone	0.034	0.004	34.41
LY1	2793.78		Blocky claystone	0.031	0.005	33.17
YY3	3561.70		Blocky claystone	0.016	0.004	30.67
YY3	3566.40		Blocky silty claystone	0.024	0.004	34.53
YY3	3569.51		Blocky silty claystone	0.027	0.006	41.57
LY1	2807.40	Banding	Banding silty claystone	0.027	0.006	68.39
LY1	2794.68		Banding silty claystone	0.041	0.005	66.45
YY3	3585.74		Banding silty claystone	0.021	0.005	35.25
YY3	3606.43		Banding silty claystone	0.021	0.004	37.21
YY3	3562.51	Laminated	Laminated silt-bearing claystone	0.011	0.004	44.05
YY3	3563.65		Laminated silt-bearing claystone	0.013	0.004	71.57
YY3	3564.50		Laminated silty claystone	0.024	0.004	77.36
YY3	3538.24		Laminated silty claystone	0.148	0.021	76.95

the specific surface area of fine-grained sedimentary reservoirs and the adsorption of oil and gas.

It can be seen from Figures 8D–F that the clay mineral content in fine-grained sedimentary rocks in the study area is positively correlated with the volumes of micropores, mesoporous pores, and macropores, which indicates that with the increase of clay mineral content, the pores related to clay minerals are more developed in different pore sizes. Therefore, the clay minerals are the main controlling factor for the pore development of fine-grained sedimentary rocks in the QFY Formation in the LZ-YB area of the northeastern Sichuan Basin.

As can be seen from Figures 8G–I, there is no obvious correlation between carbonate mineral content and porosity, pore size, and pore volume.

5.4 Relationship between sedimentary environment and reservoir quality

5.4.1 Paleoredox environment

Jones and Manning (1994) drew the cross plot of the V/Cr and the degree of pyrite (DOP) in the Upper Jurassic mudstone in the Norwegian North Sea (Jones and Manning, 1994). Since then, other scholars have improved the accuracy of the V/Cr data points based on the analysis of the cross plot (Zhang et al., 2018). They believed that when V/Cr was less than 1.2, this was an indication of an oxidizing environment, while when V/Cr was more than 1.2, this indicated an anoxic–dysoxic environment. Combined with the theory by Hatch (Hatch and Leventhal, 1992), Zhang et al. (2018) studied the shale of the Wufeng–Longmaxi Formation in southeastern Chongqing, China, and found that when V/(V + Ni) was less than 0.46, this indicated an oxidizing environment; when the value ranged from 0.46 to 0.57, it indicated a weak oxidizing environment; if the value was observed to be between 0.57 and 0.83, it indicated an anoxic environment; and values between 0.83 and 1.00 indicated a euxinic environment. The value of V/Cr in the study area ranged from 1.22 to 1.54 with an average of 1.39, while the V/(V + Ni) ranged from 0.64 to 0.74 with an average of 0.71. These values reflect that in the sedimentary period, the QFY Formation in the study area was a sedimentary environment with an anoxic reducing condition. According to the scatter plot, V/Cr and V/(V + Ni) are positively correlated with specific surface area (S_{bet}) and total pore volume (V_{bjh}) (Figures 10A–D). The specific surface area of pores and pore volumes were observed to be larger in anoxic reducing conditions; in contrast, the two will shrink in oxygen-bearing oxidizing conditions. This shows that redox conditions can control the pore structures of the reservoir.

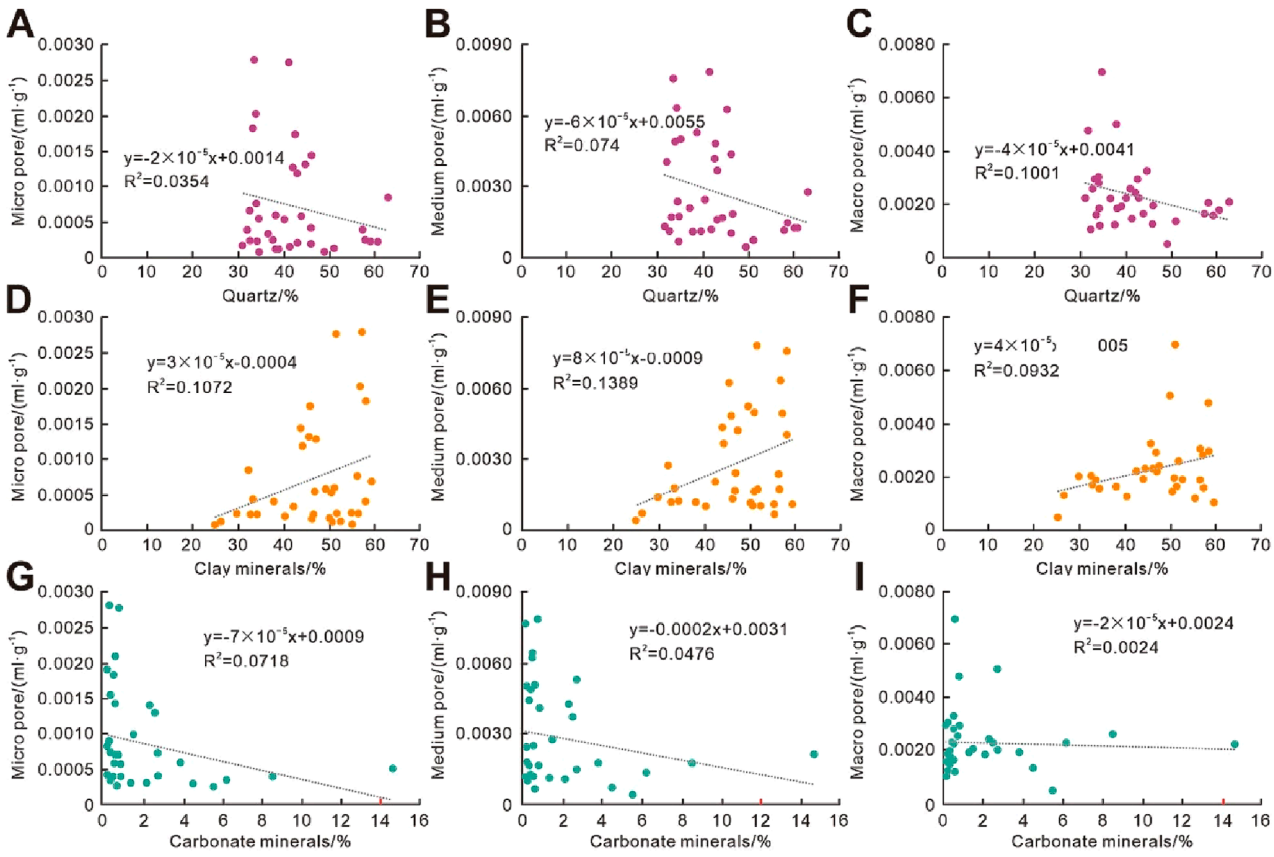

FIGURE 8
Correlation between pore volume and mineral content at different scales. **(A)** Relationship between quartz content and micropores. **(B)** Relationship between quartz content and middle pores. **(C)** Relationship between quartz content and macropores. **(D)** Relationship between clay mineral content and micropores. **(E)** Relationship between clay mineral content and middle pores. **(F)** Relationship between clay mineral content and macropores. **(G)** Relationship between carbonate mineral content and micropores. **(H)** Relationship between carbonate mineral content and medium pores. **(I)** Relationship between carbonate mineral content and macropores.

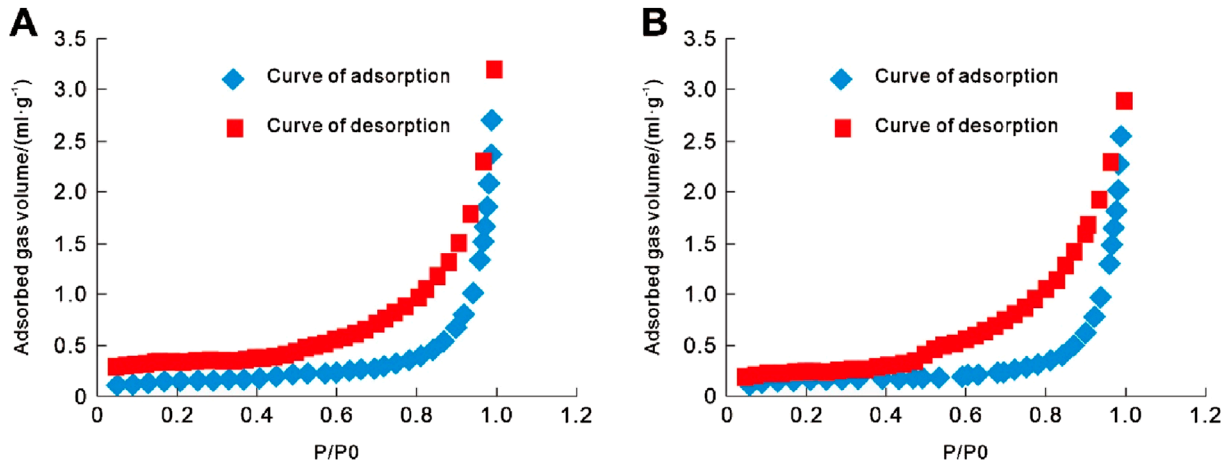

FIGURE 9
Nitrogen adsorption curve of claystone in the QFY Formation (P/P0: The ratio of gas pressure during adsorption to the vapor pressure at saturation, ranging from 0 to 1). **(A)** Well LY1, 2754.12 m, 2nd Member, claystone. **(B)** Well LY1, 2779.7 m, 2nd Member, silty claystone.

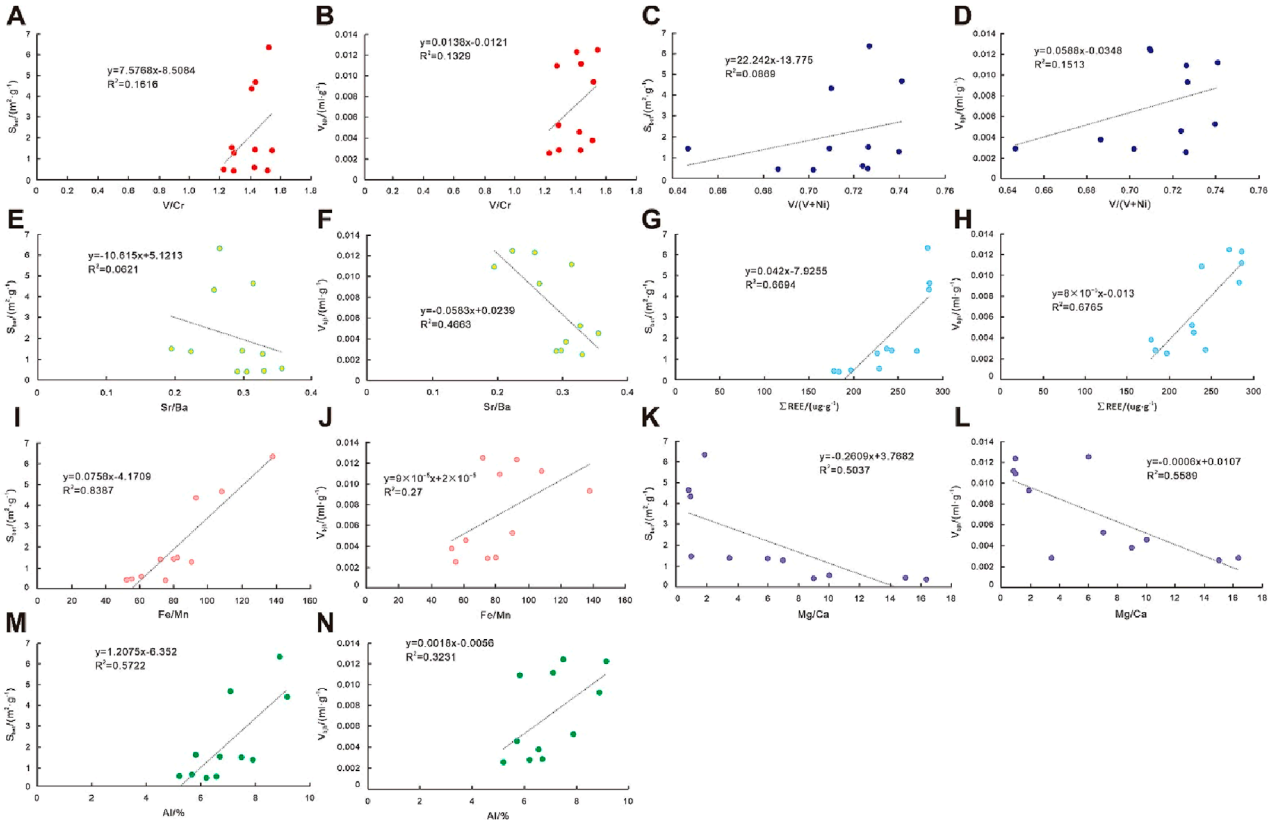

FIGURE 10
Relationships between geochemical indicators of different elements and specific surface area and total pore volume of the reservoir. **(A)** V/Cr vs. S_{bet}. **(B)** V/Cr vs. V_{bjh}. **(C)** V/(V + Ni) vs. S_{bet}. **(D)** V/(V + Ni) vs. V_{bjh}. **(E)** Sr/Ba vs. S_{bet}. **(F)** Sr/Ba vs. V_{bjh}. **(G)** ∑REE vs. S_{bet}. **(H)** ∑REE vs. V_{bjhs}. **(I)** Fe/Mn vs. S_{bet}. **(J)** Fe/Mn vs. V_{bjh}. **(K)** Mg/Ca vs. S_{bet}. **(L)** Mg/Ca vs. V_{bjh}. **(M)** Al vs. S_{bet}. **(N)** Al vs. V_{bjh}.

5.4.2 Paleosalinity

The value of Sr/Ba was used to determine the paleosalinity of sedimentary water in the QFY Formation, northeastern Sichuan Basin (Fu et al., 2023). The content of Sris relatively small in the freshwater zone, and the Sr/Ba is usually less than 1 in freshwater sediments, while the content of Sr increases correspondingly in saline-water sediments, and the Sr/Ba is greater than 1. The value of Sr/Ba in the study area ranged from 0.19 to 0.35, with an average of 0.28, indicating that in the sedimentary period, the QFY Formation in the LZ-YB area was a freshwater lake sedimentary environment. The value of Sr/Ba is negatively correlated with specific surface area (S_{bet}) and total pore volume (V_{bjh}) (Figures 10E, F). This indicates that the higher the salinity of the lake water, the smaller the reservoir space. Lake water with high salinity provides the material environment for the formation of shell limestone because the environment is suitable for the growth of lamellibranchiate organisms. With increasing carbonate content, it is easy for cementation to occur in the process of diagenesis blocking and filling pores and damaging the reservoir space.

5.4.3 Paleoclimate

According to the statistics, the total content of rare earth elements (∑REE) in the core samples of YL4 well in the study area was found to be approximately 237.68 μg/g, which is relatively high. This demonstrates the large terrestrial input and warm and humid climate in the sedimentary period. The ratios of two elements (Fe/Mn and Mg/Ca), which indicate paleoclimate, averaged 85.57 and 5.01, respectively, in the QFY Formation in the study area. Both high Fe/Mn and low Mg/Ca values reflect the warm and humid climate of the QFY Formation in the study area. The values of ∑REE and Fe/Mn are positively correlated with specific surface area (S_{bet}) and total pore volume (V_{bjh}), while the value of Mg/Ca is negatively correlated with them (Figures 10G–L). This means that the reservoir space in fine-grained sedimentary reservoirs develops more easily in warm and moist climates. A wetter climate will bring more precipitation, which will make the water level rise in the lake basin and the deepwater area enlarge (Falahatkhah et al., 2025). All these conditions facilitate the buildup of clay minerals and organic matter. The higher the content of clay minerals and organic matter in fine-grained sedimentary rocks, the more interlayer pores in clay minerals and organic matter-hosted pores, which makes it easier to form a better reservoir space.

5.4.4 Paleoproductivity

The content of the Al element in the study area was found to range from 5.82% to 9.15%, with an average of 7.05%, which indicates high paleoproductivity. By comparing the scatter plots,

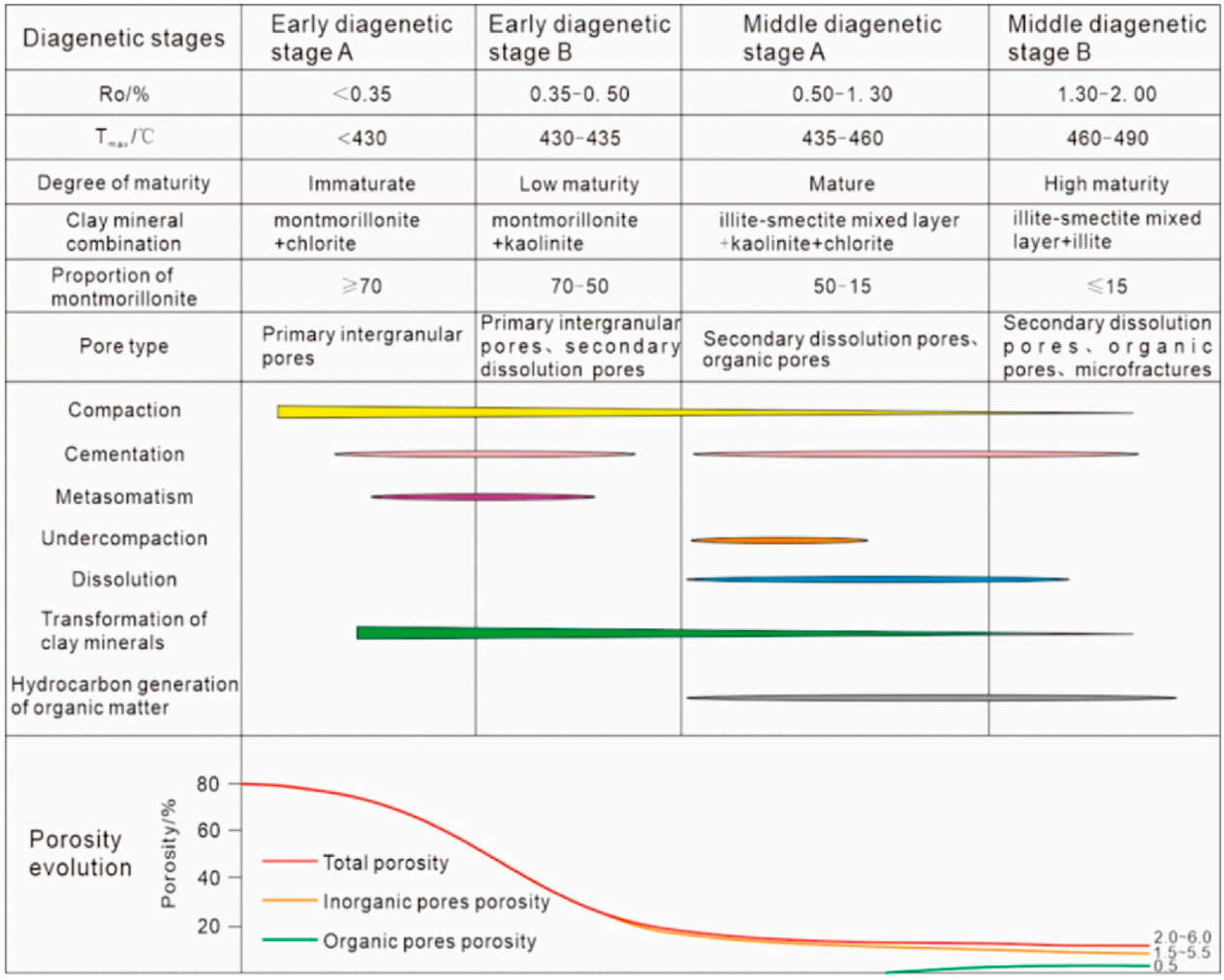

FIGURE 11
Diagenetic stage and diagenetic evolution of the reservoir.

it can be seen that the content of the Al element is positively correlated with the specific surface area (S_{bet}) and total pore volume (V_{bjh}) of the reservoir (Figures 10M, N). Because terrigenous debris can provide nutrients for organic matter production, the more terrigenous inputs into the lake basin, the more favorable it is for the formation of organic matter-hosted pores (Tan et al., 2024). The QFY Formation in the study area is in a warm climate during the sedimentary period, which is conducive to plant growth. The large runoff into the lake brought abundant terrestrial plants and nutrients to the lake basin; as a result, the aquatic plankton thrived, leading to an increase in the productivity of organic matter. With the rising organic matter content, organic matter-hosted pores also increased.

The reservoir space was found to be well developed in fine-grained sedimentary rocks formed in the sedimentary environment with anoxic reducing conditions, fresh water, wettability, and sufficient terrigenous debris. Therefore, the sedimentary environment of the QFY Formation in the study area was found to be one of the controlling factors of the reservoir space in continental fine-grained sedimentary rocks.

5.5 Relationship between diagenesis and reservoir quality

According to the oil and gas industry standard for the division of diagenetic stages in clastic rocks (SY/T 5477-2003), the continental fine-grained sedimentary rocks in the study area have entered the B phase of the middle diagenetic stage, which mainly experiences a series of diagenesis including compaction, cementation, dissolution, recompaction, clay mineral transformation, and the hydrocarbon generation from organic matter (Figure 11). Different diagenesis will constantly change the pore structure of fine-grained sedimentary reservoirs.

According to the intensity category of diagenesis, the compaction ratio in fine-grained sedimentary reservoirs in the study area mainly ranges from 21.3% to 83.6%, with an average of 60.5%, which is dominated by medium-strong compaction (Figure 12). This shows that fine-grained sedimentary rocks are greatly influenced by compaction, resulting in the shale bedding fractures dominated by lamellar fractures in the fine-grained sedimentary rocks that are strongly compressed and compacted. Under the function of stress,

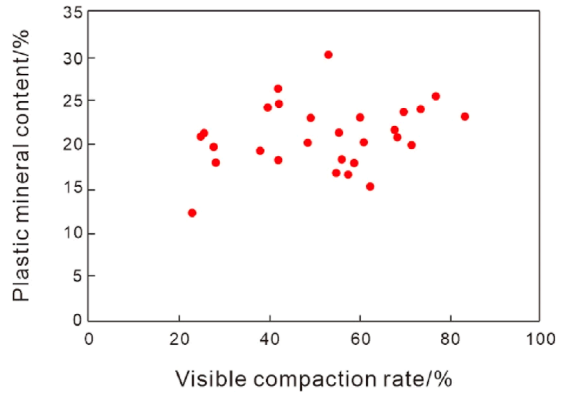

FIGURE 12
Relationship between plastic component content and compaction rate of fine-grained sedimentary reservoirs in the QFY Formation.

the particles in the sedimentary rocks show directional arrangement, and it can be seen that the lumachelles in shell limestone and shell mudstone are layered and overlapping. (Figure 13A).

The cast thin section, SEM, and X-ray diffraction studies of clay minerals show that there are mainly calcareous cementation and siliceous cementation, with a small amount of ferruginous cementation in fine-grained sedimentary reservoirs in the QFY Formation (Figures 13B, C). According to the Houseknecht evaluation method (Houseknecht, 1987), the porosity lost by cementation of fine-grained sedimentary reservoirs in the study area averages 16.55% (Figure 14). Overall, the influence of carbonate cement and siliceous cement on the pores of fine-grained sedimentary rocks is generally negative, and both dispersion and cementation will cause the reduction of the pores forming tight layers. Cementation is the main diagenesis resulting in poor reservoir properties in the study area.

In the study area, dissolution is developed in the carbonate minerals of the shell limestone and shell-bearing claystone, and the dissolution of calcite can be divided into early dissolution and late dissolution, with high intensity in the early stage. Carbonate minerals are easily dissolved by carbonate compounds, which are generated by the dissolution of carbon dioxide in water during the hydrocarbon generation process of organic matter, resulting in a certain number of secondary pores, such as intergranular dissolution pores (Figure 13D). XRD analysis of fine-grained sedimentary rocks in the QFY Formation shows that the content of calcite and dolomite is small, with an average of less than 3%. Therefore, carbonate minerals do not play an important role in the porosity evolution of fine-grained sedimentary reservoirs in the QFY Formation in the study area.

Although organic matter can provide material for organic matter-hosted pores, its content in continental shales cannot do much for organic matter-hosted pores. At the same time, the organic matter will occupy the development space of other pores. Therefore, the hydrocarbon generation of organic matter in continental fine-grained sedimentary rocks has little effect on improving reservoirs.

Zhao and Jin suggested that burial depth in the study area is generally greater than 2000 m (Zhao and Jin, 2021). When the formation temperature rises to 70°C–100°C, the rock has been completely consolidated under higher pressure, and the transformation among clay minerals is the main diagenesis in this period. Clay mineral X-ray diffraction results of core samples from several wells in the study area show that clay minerals basically do not contain montmorillonite but are dominated by illite and illite–smectite mixed layer (Figures 13E, F). This indicates that the montmorillonite or illite–smectite mixed layer in fine-grained sedimentary rocks will transfer into illite or illite–smectite mixed layer minerals with the increasing burial depth. The transformation of montmorillonite to illite is a spontaneous reaction with low energy consumption. The illite produced in this process is often in the form of irregular, tiny crystal plates and granular coatings, and the crystallinity improves with increasing burial depth. In the transformation process , montmorillonite precipitates interlayer water and structural water, causing the collapse of the crystal lattice and the shrinkage of the mineral particle volume, and forming a large number of interlayer pores in clay minerals. In addition, the pore volume also increases, which improves the adsorption capacity and reservoir space. With the increasing clay mineral transformation, many shale bedding fractures are formed, and clay laminae are developed. Compared with silt laminae, micro-nano pores and fractures are developed in the parts where clay laminae are developed, and the connectivity is relatively good, which effectively improves the reservoir capacity of fine-grained sedimentary rocks. In general, the clay minerals generated via transformation have the potential to augment the specific surface area of pores and enhance the oil and gas absorption capacity within fine-grained sedimentary reservoirs.

The recompaction merely develops in shale. The average of the acoustic time logging curve from the 2nd Member to the 1st Member in the QFY Formation (3500–3600 m) is close to the average of the curve near 2700–2800 m in the Lower Shaximiao Formation, which served as upper shallow strata. Both of them are greater than 80 μs/ft, which is obviously higher than the average of the acoustic time logging curve (less than 50 μs/ft) in the slow compaction area near 700 m from Lower Shaximiao Formation to the 3rd Member of the QFY Formation, which means that there is an overpressure area for the rocks in the shale section of the QFY Formation (Figure 15).

With the increasing burial depth and formation temperature, fine-grained sedimentary rocks are affected by mechanical and chemical compaction, and their internal sealing is enhanced, which makes solid organic matter mature into hydrocarbons. The fluid in the pores, with volume expansion and increased pressure, cannot be discharged in time and cannot bear the pressure from the overlying rock skeleton. The recompaction supports the internal pore structure of the fine-grained sedimentary rocks and preserves some pore structure in the rock.

Research shows that the fine-grained sedimentary reservoirs of the QFY Formation are dominated by unfilled to half-filled structural microfractures with good effectiveness (Figure 16). These microfractures can provide channels for the initial migration of oil and gas and storage space for organic matter-hosted pores. At the same time, the unstable components on both sides of the microfractures are broken under the action of pore water. Corrosion occurs along the edges of the broken particles, which results in secondary pores, increases rock porosity, and improves the physical properties of the reservoir. Microscopic observation of thin sections shows that a few of the microfractures in the reservoir are bifurcated.

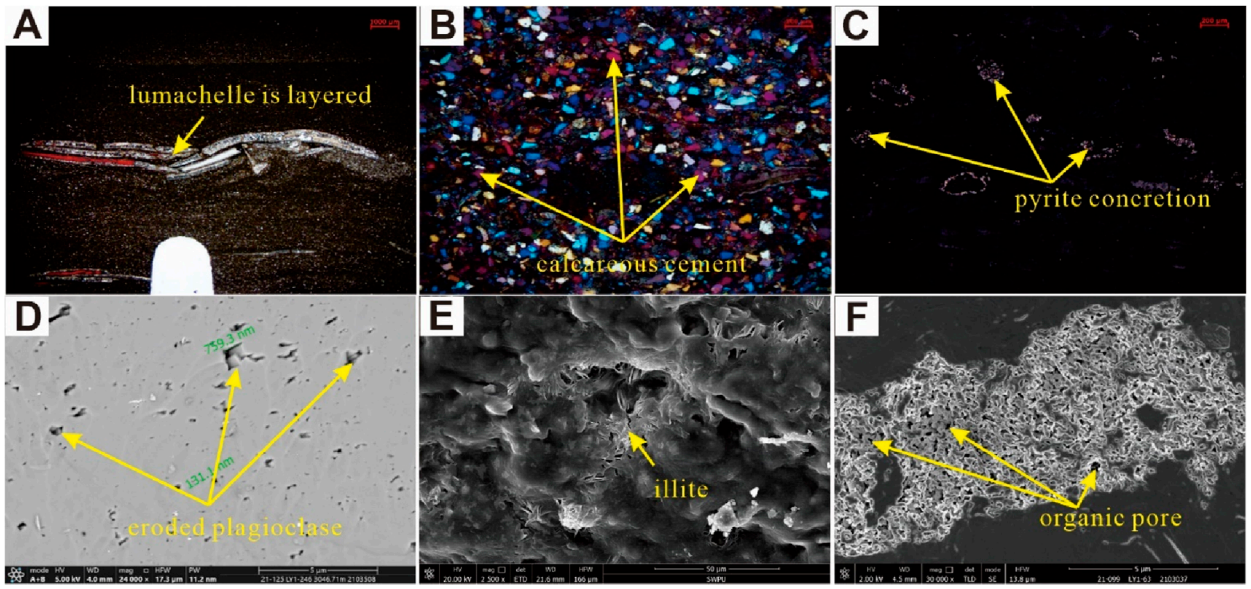

FIGURE 13
Characteristics of diagenesis in continental fine-grained sedimentary rocks in the QFY Formation. **(A)** Well YY3, 3609.28 m, 1st Member, the lumachelle is layered overlapping under compaction, 1X (–). **(B)** Well YY2, 3769.02 m, 2nd Member, the calcareous cement in siltstone, 5X (+). **(C)** Well YY2, 3777.56 m, 1st Member, the pyrite is an aggregated distribution, 10× (reflected light). **(D)** Well LY1, 2880.96 m, 1st Member, eroded plagioclase (SEM). **(E)** Well LY1, 2760.30 m, 2nd Member, clay minerals are transferred into illite (SEM). **(F)** Well LY1, 2784.67 m, 2nd Member, organic matter-hosted pores are developed in a complex of solid asphalt and the clay mineral kaolinite (SEM).

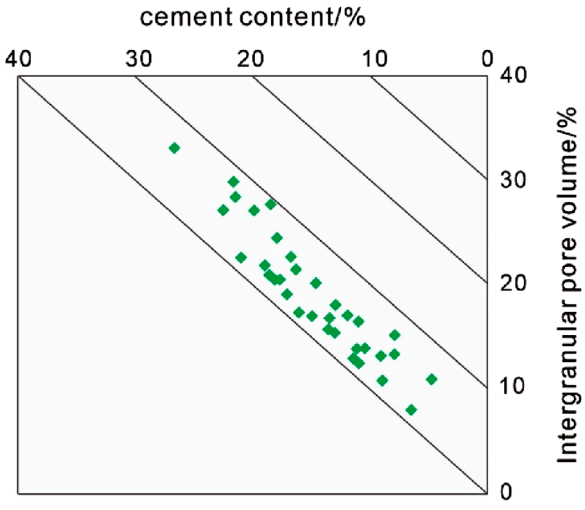

FIGURE 14
Relationship between cement and intergranular pore volume in fine-grained sedimentary reservoirs in the QFY Formation.

The bifurcated microfractures can connect other microfractures to form a complex network fracture system, which improves the seepage capacity of the reservoir to a certain extent and connects different reservoir spaces in the reservoir to form an aggregate of reservoir space. Thus, these microfractures formed by tectonism are the main filtrating channels for fluids in the reservoir and important storage space for oil and gas. During the later stages, when carrying out the fracture test production of oil and gas in fine-grained sedimentary reservoirs, the microfractures forming the fracture network also play an important and constructive role in the fracturing transformation of the reservoirs.

5.6 Implications for petroleum exploration and development

The abundance of organic matter is an important material basis for the formation of oil and gas in continental fine-grained sedimentary rocks, and the sedimentary environment can affect the burial and preservation of organic matter. In the semi-deep lake subfacies area, the water depth is deeper, the water is more reductive, the organic matter preservation conditions are better, and a set of fine sedimentary rocks with relatively large thickness and rich in organic matter and horizontal stratification can be deposited, such as claystones and silty claystones with good organic matter types, which provide the necessary material basis for oil and gas enrichment. The rock structure also has an important influence on oil and gas enrichment. The lamellar structure can not only affect the type of reservoir space, the distribution of pore size, and the development of pores and fractures but also control the porosity and permeability of the reservoir and greatly improve the horizontal seepage capacity of the reservoir. In this study, organic-rich laminar silty claystones develop a large number of laminar structures. Due to the different mineral properties in different laminates, many bedding fractures and mineral shrinkage fractures develop in the laminar segments, which are favorable spaces for oil and gas accumulation. Among them, bedding fractures are effective reservoir spaces and seepage

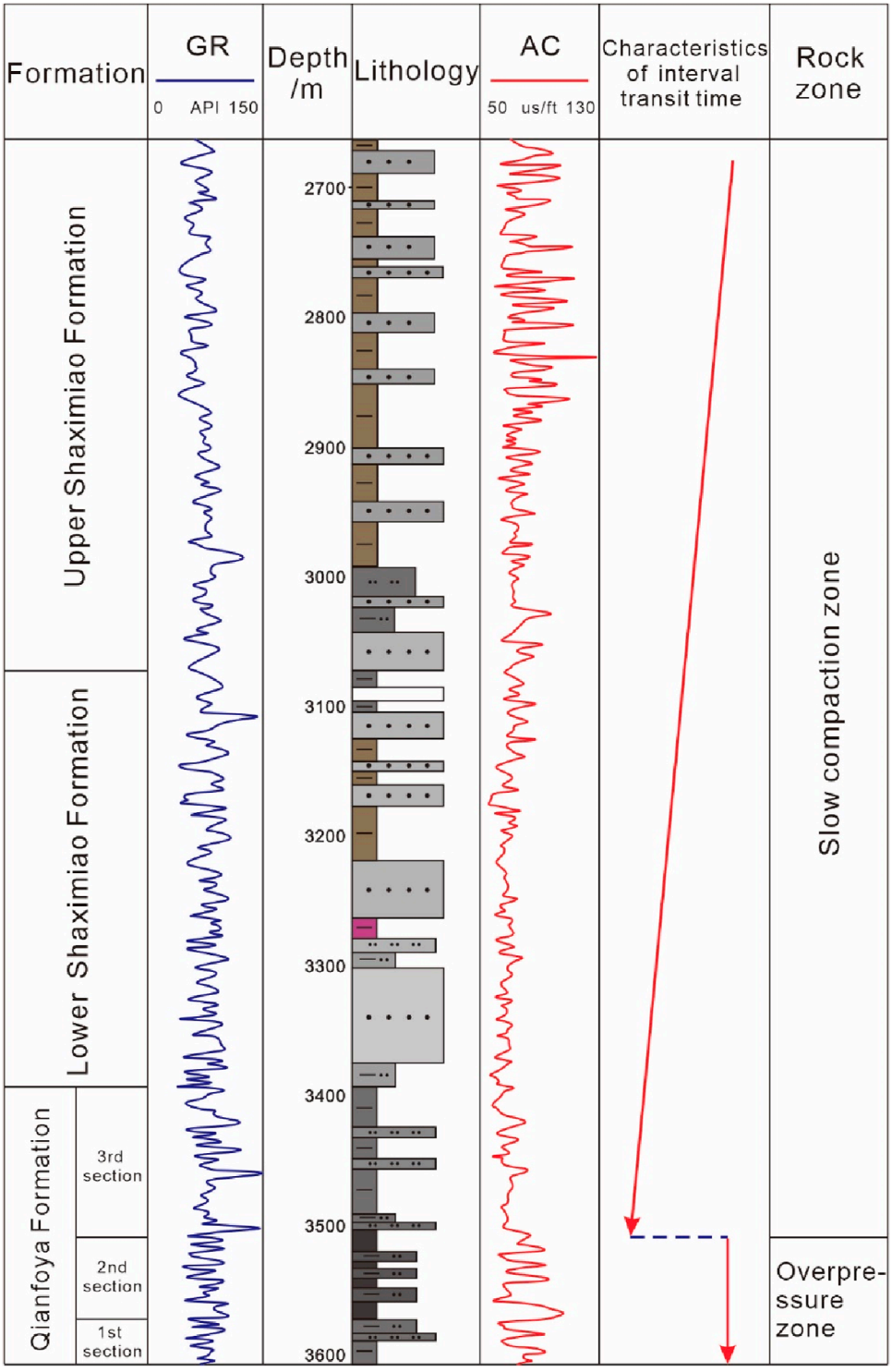

FIGURE 15
Characteristics of the undercompaction section in well YY3 (from 3500 m to 3600 m, the fine-grained sedimentary rocks from the 2nd to the 1st Member of the QFY Formation are an overpressure zone).

channels that affect the accumulation of oil and gas and the productivity of individual wells. Different mineral compositions also have an impact on oil and gas enrichment. Because the clay minerals in the fine-grained sedimentary rocks of the QFY Formation in the study area are mostly illite–smectite mixed layer and illite, the pores between the mineral compositions dominated by flake particles are mostly layered parallel to the crystal structure under scanning electron microscopy. The pore of this layered structure is

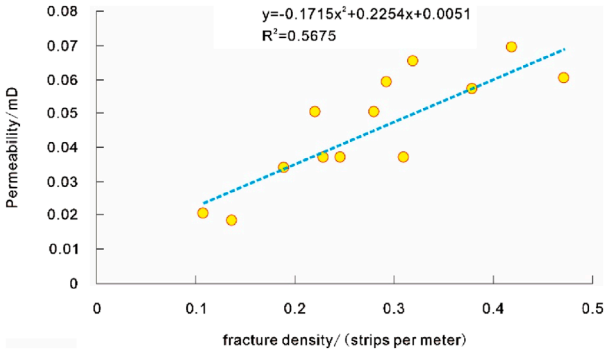

FIGURE 16
Relationship between tectonic fracture density and reservoir permeability.

conducive to increasing the specific surface area of the fine-grained sedimentary rock reservoir and is also conducive to the adsorption of oil and gas.

Overall, the continental fine-grained sedimentary rocks of the QFY Formation in the LZ-YB area have considerable oil and gas resource potential. By discussing the main controlling factors of oil and gas enrichment, the efficiency of oil and gas exploration and development of continental fine-grained sedimentary rocks in northeast Sichuan will be greatly improved.

6 Conclusion

(1) The fine-grained sedimentary rocks in the QFY Formation in the LZ-YB area, northeastern Sichuan Basin, mainly develop three rock structures. They are blocky, banded, and lamellar structures. The middle part of the 1st Member of the QFY Formation is a better source rock among the continental fine-grained sedimentary rocks whose TOC content is high, with an average of 1.85%. It also has a high potential for hydrocarbon generation. The mineral composition is dominated by clay minerals and felsic minerals, while the content of carbonate minerals is low. The clay minerals are mainly composed of illite and illite-smectite mixed layers.

(2) The porosity, permeability, TOC, and daily gas production of the organic-rich continental fine-grained sedimentary rocks of the semi-deep lacustrine subfacies of the QFY Formation in the LZ-YB area, northeastern Sichuan Basin, are greater than 2%, 0.1×10^{-3} μm^2, 1%, and 5 million cubic meters, respectively. All of them meet the standard of the minimum industrial gas flow rate for the continental shale gas; thus, it can be regarded as a good reservoir.

(3) According to the genesis of the reservoir space in continental fine-grained sedimentary rocks, the reservoir space identified from the fine-grained sedimentary rocks in the QFY Formation can be divided into silty intergranular pores, interlayer pores in clay minerals, intragranular pores in pyrite, organic matter-hosted pores, and microfractures. In the reservoir space, the proportion of silty intergranular pores is the highest, followed by interlayer pores in clay minerals and microfractures, a small number of intragranular pores exist in the strawberry-shaped pyrite, while the proportion of organic matter-hosted pores is less than 10%.

(4) The reservoir quality of continental fine-grained sedimentary rocks is controlled by multiple factors such as organic content, mineral composition, rock structure, sedimentary environment, and diagenesis. The claystone, which is rich with organic matter, horizontal laminae, and silt-bearing claystone, provides the material foundation for reservoirs with good reservoir properties and connectivity. The sedimentary environment with anoxic reducing conditions, fresh water, wettability, and sufficient terrigenous debris is conducive to the development of pore space in fine-grained sedimentary rocks. During the diagenetic process, the improvement of reservoir quality is mainly influenced by clay mineral transformation and recompaction, and the pores formed by clay mineral transformation are well preserved under recompaction. Microfractures formed by tectonism are the main filtration channels of fluids in the reservoir and an important reservoir space of oil and gas. They play an important role in the fracturing transformation of the reservoir.

Data availability statement

The original contributions presented in the study are included in the article/supplementary material; further inquiries can be directed to the corresponding author.

Author contributions

LC: conceptualization, data curation, formal analysis, investigation, methodology, software, writing – original draft, and writing – review and editing. JP: conceptualization, funding acquisition, project administration, resources, supervision, validation, and writing – review and editing.

Funding

The author(s) declare that financial support was received for the research and/or publication of this article. The 2025 Central University Basic Scientific Research Business Expense Support Project - Doctoral Innovation Capacity Enhancement Project, Project Number: 25CAFUC04059.

Conflict of interest

The authors declare that the research was conducted in the absence of any commercial or financial relationships that could be construed as a potential conflict of interest.

Generative AI statement

The author(s) declare that no Generative AI was used in the creation of this manuscript.

Publisher's note

References

Aljamaan, H., Ross, C. M., and Kovscek, A. R. (2017). Multiscale imaging of gas storage in shales. *SPE J.* 22 (6), 1760–1777. doi:10.2118/185054-PA

Bian, R. K. (2024). The formation and evolutionary characteristics of organic matter and pyrites in the continental shales of the 3rd submember of Chang 7 Member, Yanchang formation, Ordos Basin, China. *Energy Geosci.* 5 (2), 100250. doi:10.1016/j.engeos.2023.100250

Borjigin, T., Lu, L. F., Yu, L. J., Zhang, W. T., Pan, A. Y., Shen, B. J., et al. (2021). Formation, preservation and connectivity control of organic pores in shale. *Petrol. explor. Dev.* 48 (4), 798–812. doi:10.1016/S1876-3804(21)60067-8

Chen, L. X. (2022). A study on the inhomogeneous sedimentation-diagenesis-reservoir formation mode of deep tight marine clastic rock reservoirs in the Silurian Xiaoheba Formation, southeast Sichuan. *Front. Earth Sci.* 10, 900188. doi:10.3389/feart.2022.900188

Chen, W. L., Zhou, W., Luo, P., Deng, H. C., Li, Q., Shan, R., et al. (2013). Analysis of the shale gas reservoir in the lower silurian Longmaxi Formation, changxin 1 well, southeast Sichuan Basin, China. Acta petrol. *Sin.* 29 (3), 1073–1086.

Chen, Y. N., Yang, K., Wu, W., Yang, Y. R., Yang, X., and Ma, K. (2023). Favorable lithofacies and pore characteristics of the permian longtan formation shale in the southern Sichuan Basin. *Energy Geosci.* 4 (3), 100193. doi:10.1016/j.engeos.2023.100193

Dai, Q. Q., Luo, Q., Zhang, C., Lu, Z. J., Zhang, Y. Z., Lu, S. J., et al. (2016). Pore structure characteristics of tight-oil sandstone reservoir based on a new parameter measured by NMR experiment: a case study of seventh Member in Yanchang Formation, Ordos Basin. *Acta Petrol. Sin.* 37 (7), 887–897. doi:10.7623/syxb201607007

Dong, S. Q., Zeng, L. B., Wang, L. T., Lyu, W. Y., Xu, H., Ji, C. Q., et al. (2024). Fracture identification in shale reservoir using a deep learning method: Chang 7 reservoirs, Triassic Yanchang formation. *Geoenergy Sci. Eng.* 238, 212853. doi:10.1016/j.geoen.2024.212853

Falahatkhah, O., Ghaderi, A., Kadkhodaie, A., and Rezaee, R. (2025). Milankovitch-driven terrigenous deposit influx in Middle Ordovician marine successions of Western Australia: insights for paleoclimate and geochronology. *Mar. Petrol. Geol.* 173, 107282. doi:10.1016/j.marpetgeo.2024.107282

Fan, C. H., Li, H., Qin, Q. R., He, S., and Zhong, C. (2020). Geological conditions and exploration potential of shale gas reservoir in Wufeng and Longmaxi Formation of southeastern Sichuan Basin, China. *J. Petrol. Sci. Eng.* 191, 107138. doi:10.1016/j.petrol.2020.107138

Fu, Q., Hu, Z. Q., Feng, D. J., Huang, J. L., Xing, L. L., Zhu, Z. W., et al. (2023). Restoration and evolution of the Paleogene (E1f2) shale sedimentary environment in the Subei Basin, China. *ACS Omega* 8 (49), 46892–46903. doi:10.1021/acsomega.3c06603

Gale, J. F. W., Laubach, S. E., Olson, J. E., Eichhubl, P., and Fall, A. (2014). Natural fractures in shale: a review and new observations. *AAPG Bull.* 98 (11), 2165–2216. doi:10.1306/08121413151

Gong, X. X., Shi, Z. J., Wang, Y., Tian, Y. M., Li, W. J., and Liu, L. (2017). Characteristics and origin of the relatively high-quality tight reservoir in the Silurian Xiaoheba Formation in the southeastern Sichuan Basin. *PLOS One* 12 (7), e0180980. doi:10.1371/journal.pone.0180980

Guo, T. L., Xiong, L., Lei, W., Zhao, Y., and Pang, H. Q. (2022). Deep shale gas exploration and development in the Weirong and Yongchuan areas, South Sichuan Basin: progress, challenges and prospect. *Nat. Gas. Ind.* 42 (8), 45–59. doi:10.3787/j.issn.1000-0976.2022.08.005

Guo, X. S., Li, Y. P., Liu, R. B., and Wang, Q. B. (2014). Characteristics and controlling factors of micro-pore structures of Longmaxi shale play in the jiaoshiba area, Sichuan Basin. *Nat. Gas. Ind.* 34 (6), 9–16. doi:10.3787/j.issn.1000-0976.2014.06.002

Hakimi, M. H., Hamed, T. E., Lotfy, N. M., Radwan, A. E., Lashin, A., and Rahim, A. (2023). Hydraulic fracturing as unconventional production potential for the organic-rich carbonate reservoir rocks in the Abu El Gharadig Field, north western Desert (Egypt): evidence from combined organic geochemical, petrophysical and bulk kinetics modeling results. *Fuel* 334 (1), 126606. doi:10.1016/j.fuel.2022.126606

Hatch, J. R., and Leventhal, J. S. (1992). Relationship between inferred redox potential of the depositional environment and geochemistry of the upper pennsylvanian (missourian) Stark shale member of the dennis limestone, wabaunsee county, Kansas, USA. *Chem. Geol.* 99, 65–82. doi:10.1016/0009-2541(92)90031-Y

He, S., Li, H., Qin, Q. R., and Long, S. X. (2021). Influence of mineral compositions on shale pore development of Longmaxi Formation in the Dingshan area, southeastern Sichuan Basin, China. *Energy Fuel* 35 (13), 10551–10561. doi:10.1021/acs.energyfuels.1c01026

He, S., Qin, Q. R., Li, H., and Zhao, S. X. (2022). Deformation differences in complex structural areas in the southern sichuan Basin and its influence on shale gas preservation: a case study of changning and luzhou areas. *Front. Earth Sci.* 9, 818543. doi:10.3389/feart.2021.818534

He, S., Tan, W. C., Li, H., Wang, Y., Niu, P. F., and Qin, Q. R. (2025). Mineralogical and lithofacies controls on gas storage mechanisms in organic-rich marine shales. *Energy Fuel* 39 (7), 3846–3858. doi:10.1021/acs.energyfuels.4c05685

He, W., Li, T., Mou, B. X., Lei, Y. X., Song, J. H., and Liu, Z. C. (2023). Lithofacies types and physical characteristics of organic-rich shale in the Wufeng-Longmaxi Formation, Xichang Basin, China. *ACS Omega* 8 (20), 18165–18179. doi:10.1021/acsomega.3c01307

Hou, H. D., Yang, W., Yang, R., Jiang, Z. X., Miao, K., Sun, W. H., et al. (2025). Formation and evolution of complex pore-fracture systems in shale gas reservoirs: insights into controlling mechanisms. *Energy Fuel* 39 (6), 3008–3038. doi:10.1021/acs.energyfuels.4c05306

Houseknecht, D. W. (1987). Assessing the relative importance of compaction processes and cementation reduction of porosity in sandstone. *AAPG Bull.* 71 (5), 485–491. doi:10.1306/9488787F-1704-11D7-8645000102C1865D

Hu, H. Y., Wang, D. X., Li, W. P., Zhu, G. E., and Chen, X. Y. (2025). The heterogeneity characterization of lacustrine shale pores in the daanzhai member of the ziliujing Formation in the yuanba area, Sichuan Basin. *Minerals* 15 (1), 11. doi:10.3390/min15010011

Iacoviello, F., Lu, X. K., Mitchell, T. M., Brett, D. J. L., and Shearing, P. R. (2019). The imaging resolution and knudsen effect on the Mass transport of shale gas assisted by multi-length scale X-ray computed tomography. *Sci. Rep.* 9, 19465. doi:10.1038/s41598-019-55999-7

Jadoon, Q. K., Roberts, E., Blenkinsop, T., Wust, R. A. J., and Shah, S. A. (2016). Mineralogical modelling and petrophysical parameters in Permian gas shales from the Roseneath and Murteree formations, Cooper Basin, Australia. *Petrol. explor. Dev.* 43 (2), 277–284. doi:10.1016/S1876-3804(16)30031-3

Jiang, S. L., Tang, T., Zhong, S. C., Li, H., Gao, Z., Yang, C., et al. (2023). Intensive geological alteration and gas accumulation in Longmaxi Formation shales at moderate and great depths: a case study of the Luzhou area in the southern Sichuan fold zone, China. *Geol. J.* 8 (48), 4215–4228. doi:10.1002/gj.4788

Jin, Z. J., Liang, X. P., and Bai, Z. R. (2022). Exploration breakthrough and its significance of Gulong lacustrine shale oil in the Songliao Basin, Northeastern China. *Energy Geosci.* 3 (2), 120–125. doi:10.1016/j.engeos.2022.01.005

Jones, B. J., and Manning, A. C. (1994). Comparison of geochemical indices used for the interpretation of palaeoredox conditions in ancient mudstones. *Chem. Geol.* 111 (1-4), 111–129. doi:10.1016/0009-2541(94)90085-X

Jun, J., and Liang, W. (2024). Investigation of the pore structure characteristics and fluid components of Quaternary mudstone biogas reservoirs: a case study of the Qaidam Basin in China. *Sci. Rep.* 14 (1), 26512. doi:10.1038/s41598-024-78010-4

Kasala, E. E., Wang, J. J., Majid, A., and Nadege, M. N. (2025). Enhancing CO2 storage capacity and methane (CH4) production in the Yanchang shale gas reservoir: a simulation study on influencing factors and optimization strategies. *Fuel* 388, 134535. doi:10.1016/j.fuel.2025.134535

Li, H. (2022). Research progress on evaluation methods and factors influencing shale brittleness: a review. *Energy Rep.* 8, 4344–4358. doi:10.1016/j.egyr.2022.03.120

Li, H. (2023a). Advancing "carbon peak" and "carbon neutrality" in China: a comprehensive review of current global research on carbon capture, utilization, and storage technology and its implications. *ACS Omega* 8 (45), 42086–42101. doi:10.1021/acsomega.3c06422

Li H, H., Duan, H. T., Qin, Q. R., Zhao, T. B., Fan, C. H., and Luo, J. (2025). Characteristics and distribution of tectonic fracture networks in low permeability conglomerate reservoirs. *Sci. Rep.* 15 (1), 5914. doi:10.1038/s41598-025-90458-6

Li, H., He, S., Radwan, A. E., Xie, J. T., and Qin, Q. R. (2024a). Quantitative analysis of pore complexity in lacustrine organic-rich shale and comparison to marine shale: insights from experimental tests and fractal theory. *Energy Fuel* 38 (17), 16171–16188. doi:10.1021/acs.energyfuels.4c03095

Li, H., Tang, H. M., Qin, Q. R., Zhou, J. L., Qin, Z. J., Fan, C. H., et al. (2019). Characteristics, formation periods and genetic mechanisms of tectonic fractures in the

tight gas sandstones reservoir: a case study of Xujiahe Formation in YB area, Sichuan Basin, China. *J. Petrol. Sci. Eng.* 178, 723–735. doi:10.1016/j.petrol.2019.04.007

Li, H., Wang, Q., Qin, Q. R., and Ge, X. Y. (2021). Characteristics of natural fractures in an ultradeep marine Carbonate gas reservoir and their impact on the reservoir: a case study of the Maokou Formation of the JLS Structure in the Sichuan Basin, China. *Energy Fuel* 35 (16), 13098–13108. doi:10.1021/acs.energyfuels.1c01581

Li H, H., Zhou, J. L., Mou, X. Y., Guo, H. X., Wang, X. X., An, H. Y., et al. (2022). Pore structure and fractal characteristics of the marine shale of the Longmaxi Formation in the changning area, southern Sichuan Basin, China. *Front. Earth Sci.* 10, 1018274. doi:10.3389/feart.2022.1018274

Li, J., Li, H., Jiang, W., Cai, M. L., He, J., Wang, Q., et al. (2024b). Shale pore characteristics and their impact on the gas-bearing properties of the Longmaxi Formation in the Luzhou area. *Sci. Rep.* 14, 16896. doi:10.1038/s41598-024-66759-7

Li J, J., Li, H., Xu, J. L., Wu, Y. J., and Gao, Z. (2022). Effects of fracture formation stage on shale gas preservation conditions and enrichment in complex structural areas in the southern Sichuan Basin, China. *Front. Earth Sci.* 10, 921988. doi:10.3389/feart.2022.921988

Li, J. J., You, H., Zhang, X. W., Zhao, S. P., Jiang, F. J., Feng, G. Q., et al. (2024c). Influence of shale reservoir properties on shale oil mobility and its mechanism. *Energy Geosci.* 5 (4), 100329. doi:10.1016/j.engeos.2024.100329

Li, Q. W., Liu, Z. B., Chen, F. R., Zhang, K., and Tang, L. (2023). Behavior and controlling factors of methane adsorption in Jurassic continental shale, northeastern Sichuan Basin. *Energy Geosci.* 4 (1), 83–92. doi:10.1016/j.engeos.2022.08.007

Liu G. Y, G. Y., Tang, Y., Liu, K. Q., Liu, Z. Q., Zhu, T., Zou, Y., et al. (2024). Comparison of pore structure characteristics of shale-oil and tight-oil reservoirs in the Fengcheng Formation in Mahu Sag. *Energies* 17 (16), 4027. doi:10.3390/en17164027

Liu J, J., He, X., and Xue, F. (2024). The influence of natural fractures of multi-feature combination on seepage behavior in shale reservoirs. *J. Min. Strata Control Eng.* 6 (1), 013437. doi:10.13532/j.jmsce.cn10-1638/td.20240018.001

Luo, J. L., Guo, D. Y., Yi, P., Wang, Z. Z., and Yang, J. L. (2003). Major factors controlling reservoir-quality of the Upper Triassic Chang 2 sandstones in the Panlong oil area. *J. Northwest Univ.* 33 (6), 105–110. doi:10.16152/j.cnki.xdxbzr.2003.06.035

Ma, Y., and Feng, J. L. (2023). Depositional environment variations and organic matter accumulation of the first member of the Qingshankou Formation in the southern Songliao Basin, China. *Front. Earth Sci.* 11, 1249787. doi:10.3389/feart.2023.1249787

Milkov, A. V., Schwietzke, S., Allen, G., Sherwood, O. A., and Etiope, G. (2020). Using global isotopic data to constrain the role of shale gas production in recent increases in atmospheric methane. *Sci. Rep.* 10, 4199. doi:10.1038/s41598-020-61035-w

Nag, R., Cogne, N., Hrushikesh, H., Prabhakar, N., and Mishra, D. (2025). Petrochronology and geochemistry of migmatites from the Assam-Meghalaya gneissic complex (NE India): implications for the crustal anatexis and reworking during Gondwana assembly. *Precambrian Res.* 418, 107670. doi:10.1016/j.precamres.2024.107670

Peng, J., Zhang, H. B., and Lin, X. X. (2018). Study on characteristics and genesis of botryoidal dolostone of the Upper Sinian Dengying Formation: a case study from Hanyuan region, Sichuan, China. *Evaporite* 33 (2), 285–299. doi:10.1007/s13146-017-0343-8

Peng, M. H., Li, J., Tian, J. C., Zhang, X., Luo, J., Li, P. J., et al. (2025). Neoproterozoic rifting along the margin of the rodinia supercontinent: sedimentary evidence from the northwestern tarim block, northwest China. *Palaeogeogr. Palaeocl.* 660, 112662. doi:10.1016/j.palaeo.2024.112662

Qin, L. M., and Lan, X. D. (2024). Genesis of the wuchiapingian formation tuffs and their relationship with the tectonic background of the kaijiang-liangping trough in the northern Sichuan Basin. *Minerals* 14 (10), 1034. doi:10.3390/min14101034

Qiu, H. Y., Jiang, Z. X., Liu, Z. J., Chang, J. Q., Su, Z. F., Yang, Z. W., et al. (2021). Difference in pore structure characteristics between condensate and dry shale gas reservoirs: insights from the pore contribution of different matrix components. *J. Nat. Gas. Sci. Eng.* 96, 104283. doi:10.1016/j.jngse.2021.104283

Radwan, A. E., Wood, D. A., and Radwan, A. A. (2022). Machine learning and data-driven prediction of pore pressure from geophysical logs: a case study for the Mangahewa gas field, New Zealand. *J. Rock Mech. Geotech.* 14 (6), 1799–1809. doi:10.1016/j.jrmge.2022.01.012

Radwan, A. E., Yin, S., Hakimi, M. H., and Li, H. (2023). Petroleum geology of conventional and unconventional resources: introduction. *Geol. J. (Chichester).* 58 (11), 3965–3969. doi:10.1002/gj.4898

Sohail, G. M., Radwan, A. E., and Mahmoud, M. (2022). A review of Pakistani shales for shale gas exploration and comparison to North American shale plays. *Energy Rep.* 8, 6423–6442. doi:10.1016/j.egyr.2022.04.074

Sun, Z. M. (2023). Superimposed hydrocarbon accumulation through multi-source and multi-stage evolution in the Cambrian Xixiangchi Group of eastern Sichuan Basin: a case study of the Pingqiao gas-bearing anticline. *Energy Geosci.* 4 (1), 131–142. doi:10.1016/j.engeos.2022.09.001

Tan, J., Jiang, Y. Q., Li, X. T., Ji, C. H., Gu, Y. F., and Wang, Z. L. (2024). Paleoenvironment of marine-continental transitional shales in the lower Permian Shanxi formation, southeastern Ordos Basin, China. *Energy Geosci.* 5 (3), 100261. doi:10.1016/j.engeos.2023.100261

Tang, S. Q., Dong, S. F., Yang, X. Y., Fan, C. H., Li, H., Zhong, Z. Y., et al. (2023). Geochemical analysis of dolomite in the fourth member of the upper sinian dengying formation, northern Sichuan Basin, China. *ACS Omega* 8 (48), 45878–45895. doi:10.1021/acsomega.3c06638

Wan, J. L., Yu, Z. C., Yuan, Y. J., Huang, W. H., Dong, Z. T., and Rezaee, R. (2025). Lithofacies classification and reservoir property of lacustrine shale, the Cretaceous Qingshankou formation, Songliao basin, northeast China. *Mar. Petrol. Geol.* 173, 107262. doi:10.1016/j.marpetgeo.2024.107262

Wang B, B., Lu, C. L., Cui, F., and Zhang, Z. (2023). Uniaxial compression test research on rock creep disturbance characteristics based on CT scanning. *J. Min. Strata Control Eng.* 5 (3), 43–53. doi:10.13532/j.jmsce.cn10-1638/td.2023.03.002

Wang E. Z, E. Z., Guo, T. L., Li, M. W., Xiong, L., Dong, X. X., Wang, T., et al. (2023). Favorable exploration lithofacies and their formation mechanisms in lacustrine shales deposited under different salinity conditions: insights into organic matter accumulation and pore systems. *Energy Fuel* 37 (16), 11838–11852. doi:10.1021/acs.energyfuels.3c02038

Wang, J., and Wang, X. L. (2021). Seepage characteristic and fracture development of protected seam caused by mining protecting strata. *J. Min. Strata Control Eng.* 3 (3), 58–66. doi:10.13532/j.jmsce.cn10-1638/td.20201215.001

Wang, R. F., and Tang, Y. (2023). Study on the rock physical mechanical properties evaluation of tight oil reservoir in Chang 7 member, Longdong area, Ordos Basin, China. *Front. Earth Sci.* 11, 1249787. doi:10.3389/feart.2024.1342561

Wen, Z., Yao, Y. B., Sun, X. X., Lei, X., and Cui, C. (2024). The impact of gas flow on hydrate reformation and reservoir seepage characteristics in clayey silt sediments. *Energy Fuel* 38 (6), 5149–5158. doi:10.1021/acs.energyfuels.3c05096

Wu, H. J., and Kong, X. W. (2025). Analysis of geological characteristics and potential factors of formation damage in coalbed methane reservoir in Northern Qinshui basin. *Sci. Rep.* 15 (1), 3025. doi:10.1038/s41598-025-87026-3

Wu, X. Q., Yang, J., Wang, P., Li, H. J., Chen, Y. B., Ni, C. H., et al. (2024). Gas source of the middle jurassic Shaximiao Formation in the zhongjiang large gas field of western sichuan depression: constraints from geochemical characteristics of light hydrocarbons. *Energy Geosci.* 5 (2), 100263. doi:10.1016/j.engeos.2023.100263

Yang L. R, L. R., Li, J. J., and Jiang, C. (2022). Analysis of acoustic emission parameters and time-frequency characteristics in the process of rock sample fracture. *J. Min. Strata Control Eng.* 5 (1), 013015. doi:10.13532/j.jmsce.cn10-1638/td.20220923.003

Yang, S. P., Liu, P. Z., and Lu, W. Y. (2023). Study on triaxial compression tests on briquette coal specimens with different binder contents. *J. Min. Strata Control Eng.* 5 (2), 023027. doi:10.13532/j.jmsce.cn10-1638/td.2023.02.001

Yang Y. M, Y. M., Peng, J., Xu, T. Y., Wang, Y. B., and Zeng, Y. (2022). Characterization, classification, and evaluation of the reservoir pore structure features of lacustrine fine-grained sedimentary rocks. A case study of the fourth member of the shahejie Formation in the chenguanzhuang area of the southern gently sloping zone of the dongying depression, bohai bay basin. *Front. Earth Sci.* 10, 878089. doi:10.3389/feart.2022.878089

Ye, T. R., Meng, J., Xiao, Y. T., Liu, y.q., Zheng, A. W., and Liang, B. (2025). Integrated AutoML-based framework for optimizing shale gas production: a case study of the Fuling shale gas field. *Energy Geosci.* 6 (1), 100365. doi:10.1016/j.engeos.2024.100365

Yuan, D. D., Lu, S. F., Chen, F. W., Xiao, H., and Wu, Y. H. (2016). Shale microscopic pore structure characterization in well Pengye 1 of southeast Chongqing. *Spec. Oil Gas. Res.* 23 (1), 49–53. doi:10.3969/j.issn.1006-6535.2016.01.011

Zhang, B. L., Shen, B. T., Zhang, J. H., and Zhang, X. G. (2020). Experimental study of edge-opened cracks propagation in rock-like materials. *J. Min. Strata Control Eng.* 2 (3), 033035. doi:10.13532/j.jmsce.cn10-1638/td.20200313.001

Zhang, J. G., Jiang, Z. X., Liu, L., Yuan, F., Feng, L. Y., and Li, C. S. (2021). Lithofacies and depositional evolution of fine-grained sedimentary rocks in the lower submember of the Member 3 of Shahejie Formation in Zhanhua sag, Bohai Bay Basin. *Acta petro. Sin.* 42 (3), 293–306. doi:10.7623/syxb202103003

Zhang, S., Liu, H. M., Wang, M., Fu, A. B., Bao, S. Y., Wang, W. Q., et al. (2018). Pore evolution of shale oil reservoirs in Dongying sag. *Acta Petrol. Sin.* 39 (7), 754–766. doi:10.7623/syxb201807003

Zhao, D. F., Jiao, W. W., and Wei, Y. (2021). Diagenesis of a shale reservoir and its influence on reservoir brittleness: taking the deep shale of the Wufeng-Longmaxi Formation in western chongqing as an example. Acta sediment. *Sin.* 39 (4), 811–825. doi:10.14027/j.issn.1000-0550.2021.034

Zhao, J. H., and Jin, Z. J. (2021). Mudstone diagenesis: research advances and prospects. *Acta Sediment. Sin.* 39 (1), 58–72. doi:10.14027/j.issn.1000-0550.2020.133

Zhou, Q. M., Xu, H., Zhou, W., Zhao, X., Liu, R. Y., and Jiang, K. (2025). Sealing effects on organic pore development in marine shale gas: new insights from macro-to micro-scale analyses. *Energies* 18 (1), 193. doi:10.3390/en18010193

Frontiers in Earth Science

Investigates the processes operating within the major spheres of our planet

Advances our understanding across the earth sciences, providing a theoretical background for better use of our planet's resources and equipping us to face major environmental challenges.

Discover the latest Research Topics

See more →

Frontiers

Avenue du Tribunal-Fédéral 34
1005 Lausanne, Switzerland
frontiersin.org

Contact us

+41 (0)21 510 17 00
frontiersin.org/about/contact